Spectroscopic studies of defects in diamond including their formation and dissociation

De Weerdt, Filip

Spectroscopic studies of defects in diamond, including their formation and dissociation.

A thesis submitted for the degree of Doctor of Philosophy
in the University of London

Filip De Weerdt

Department of Physics
King's College London
University of London

Abstract

This thesis is about optical characterisation by photoluminescence, cathodoluminescence, Raman scattering, UV-VIS-NIR and FTIR absorption of defects in type Ia diamond and the change thereof after High Pressure High Temperature (HPHT) annealing.

Defects give colour to a diamond and colour is one of the price-determining factors of a cut and polished gem diamond. In some cases it is possible to enhance the colour of diamond with a low initial colour grade, potentially increasing its selling price by a factor of 10 or more. It is therefore extremely important for a gem-testing laboratory to have an understanding of defects in diamond, in general, and of the time-evolution of defects generated by HPHT treatment. The studies in this thesis, summarised below, will contribute to this understanding.

Chapter one is an introduction summarising the relevant defects in the natural diamonds under study, the theory of electron-phonon coupling and its consequences.

Chapter two illustrates the application of linear electron-phonon coupling on two defects, frequently encountered in brown diamond.

Chapter three illustrates a more fundamental consequence of linear electron-phonon coupling: sub-threshold excitation of the luminescence originating from defects in diamond.

Chapter four is concerned with vibrations of nitrogen aggregates in diamond as these should determine the attempt-to-escape frequency: the exponential pre-factor in the rate-constant for aggregation.

Chapter five characterises the annealing of irradiation defects produced in diamond. This is important because the migration of vacancies is one of the basic processes when brown type Ia diamond is annealed at HPHT.

Chapter six deals with the various nitrogen-vacancy defects which are created when brown type Ia diamond is annealed under HPHT conditions. A model is proposed which simulates the time evolution of defects in diamond.

Chapter seven draws the conclusions and points to further work.

Acknowledgements

It is a pleasure to thank the people and organisations who made this thesis possible. The HRD for supporting this study and making resources available. My supervisor Alan Collins for great support, critical review of the work and guidance. Also professors Alison Mainwood and Gordon Davies for support, aid and sharing their view on some of the results and analysis. Dr. I. Kiflawi for the interest in the work and sharing ideas, samples and reviewing some of the work.

The colleagues of HRD Research are acknowledged for their effort proof reading, and constructive remarks.

A number of collaborations have made other things possible and I'll try to thank everyone.

Professor Yuri Pal'yanov's group at Novosibirsk who grew the isotopically mixed diamonds and gave some thoughts on High Pressure High Temperature (HPHT) annealing. Igor Kupriyanov for excellent translation of Russian, discussions and sharing of articles.

The Exeter and Newcastle theoretical physics group: professor Bob Jones, dr. John Goss, dr. Steve Sque and dr. Luke Hounsome are thanked for their thoughts, reprints and preprints on vacancy clusters, radiation damage and dislocations.

Special thanks to David Fisher and the whole DTC Research group in Maidenhead for high temperature annealing of some of the samples under vacuum. The rest of the research group is thanked for their warm welcome at various conferences and meetings.

Special acknowledgements to dr. Konstantin (Kostya) Iakoubovskii, now at the AIST nanoscience group in Japan, for the data on irradiated and annealed type I diamonds. The analysis of this data gave substantial support to analysis of other data extracted from publications.

Sonny Pope, Russ Myers, Rob Galloway and Ken Jensen of Sundance company in Utah (USA) are acknowledged for the excellent HPHT annealings. Professors Minouri Akaishi and Hisao Kanda of NIMS are gratefully acknowledged for their help with CL measurements and some of the HPHT annealed diamonds.

The EPR group of the University of Ghent, Belgium – professor Freddy Callens, dr. Henk Frielinck and dr. Frank Loncke - for carrying out and giving advise on EPR measurements.

Professor dr. Jan D'Haen of the Physical analysis and Characterisation group of IMO for CL images and EBSD measurements.

Some researchers for giving their valuable view on the feasibility of experiments and for exchanging ideas, in particular dr. Mark Newton of the University of Warwick (UK) and dr. Dan Twitchen of e6 (UK).

Thanks also to dr. David Richards and dr. Minjas Zugnik of the King's College Solid State Physics group for the measurements on the Dilor XY spectrometer. They made some vital measurements on sub-threshold excitation possible.

Ludo Rossou and dr. Bert Willems of the EMAT group of the University of Antwerp are thanked for the annealing of some of the irradiated samples. These experiments were carried out with the kind permission of prof. G. Van Tendeloo.

Tom Anthony, GE researcher, now retired, gave some of the comments from the point of view of his work on HPHT annealing. Unfortunately, details could not be given as the work was and in some cases still is propriety. Nevertheless, on occasion I had the feeling "Tom has been there, done it already", and in most cases "was not allowed to publish". Despite the fact details on his experiments are missing, it confirmed some of the work which was carried out in this thesis.

I also would like to thank King's College PhD students Abdullah Shareef, Alex Conner, Zoya Shah and post-doc students dr. Lorenzo Milazzo, dr. Claire Glover, dr.

Hannah Smith, dr. Karl Johnston for enjoyable moments in the basement at King's and at the various conferences.

Finally thanks to my whole family and especially to my wife Sandra Van Osta for constant support and encouragement. During some periods of my research and study she has been more nervous then I was and I'm grateful for her patience.

Publications

Papers

"Absorption spectra of hydrogen in ^{13}C diamond, produced by high-pressure, high-temperature synthesis"
F. De Weerdt, Y.N. Pal'yanov, A.T. Collins, J. Phys.: Cond. Matter, vol. 15, (2003), p. 3163.

"Defect Aggregation and dissociation in type Ia diamonds by annealing at high pressure and temperature (HPHT)"
F. De Weerdt, R. Galloway, A. Anthonis , Defect and Diffusion Forum (Annual Retrospective - Ceramics VI), vol. 226-228, (2004), p. 49-60.

"Sub-threshold excitation luminescence of defects in diamond"
F. De Weerdt, A.T. Collins, M. Zugik, A. Conner, J. Phys. Cond. Matter, vol. 17, (2005), p. 8005.

"Broad band luminescence in brown type Ia diamonds"
F. De Weerdt, A.T. Collins, Diamond and Related Materials, accepted for publication

UK Conferences

A number of results have been presented at the annual UK Diamond conference, organised by DTC.

"Spectroscopic properties of type Ia diamonds with high concentrations of IR active hydrogen"
F. De Weerdt, A.T. Collins, 53rd Diamond conference, Oxford 2002

"Hydrogen related lines in the FTIR spectrum of isotopically mixed single crystal diamond"
F. De Weerdt, A.T. Collins, 54th Diamond conference, Cambridge 2003

"Sub-threshold excitation of optically active defects in diamond"
F. De Weerdt, A.T. Collins, 54th Diamond conference, Cambridge 2003

"Broad band luminescence in brown type Ia diamond"
F. De Weerdt, A.T. Collins, 55th Diamond conference, Warwick 2004

International conferences

Other results have been presented at international conferences as poster and oral presentation.

"The influence of pressure on high-pressure, high-temperature annealing of type Ia diamond"
F. De Weerdt, A.T. Collins, Diamond and Related Materials, vol. 12, (2003), p. 507
13th European Conference on Diamond, Diamond-like materials, Nitrides and Silicon-Carbide, Granada, Spain.

"Optical study of the annealing behaviour of the 3107 cm^{-1} defect"
F. De Weerdt, A.T. Collins, Diamond and Related Materials, vol. 15, (2006), p. 593
16th European Conference on Diamond, Diamond-like materials, Nitrides and Silicon-Carbide, Toulouse, France.

Index

Abstract 1

Acknowledgements 3

Publications 6

Index.....8

Table of figures.....14

Table of tables 34

Chapter One
Introduction.....39
1.1. Introduction.....39
1.2. Linear electron-phonon coupling theory and Jahn-Teller distortion 45
1.2.1. Linear electron-phonon coupling.....45
1.2.2. Jahn-Teller effects.....54
1.2.3. Vibronic coupling at nearly degenerate states 55
1.3. Diffusion in diamond 58
1.3.1. Introduction.....58
1.3.2. Thermodynamics of diffusion.....61
1.3.2.1. Equilibrium concentration of defects 61
1.3.2.2. The relation between equilibrium concentrations and the Gibbs free energy.....63
1.3.2.3. Influence of pressure 67
1.3.3. Other factors influencing the diffusion.....69
1.3.4. Dislocation diffusion.....70
1.4. Synthetic diamond growth 75
1.4.1. Growth of synthetic diamond by HPHT 75
1.4.2. Synthesis of diamond with iron nitride under HPHT conditions.....76
1.4.3. HPHT press used for HPHT treatment 76
1.4.4. Pressure and temperature measurements in HPHT presses 77
1.4.4.1. Temperature measurements.....77
1.4.4.2. Pressure measurements.....78
1.5. Spectroscopic techniques 78
1.5.1. UV-VIS spectroscopy 78
1.5.1.1. Light source.....61
1.5.1.1.1. Gas discharge 79
1.5.1.1.2. Filament lamps 80
1.5.1.2. Dispersive element 81
1.5.1.3. Slit width and focal length 82
1.5.1.4. Detectors: multi-channel systems and photomultipliers 83
1.5.1.5. Single beam systems 84
1.5.1.6. Double beam systems.....84
1.5.1.7. Double and triple monochromator systems.....84
1.5.1.8. Systems used 86

1.5.2. FTIR spectroscopy 87
1.5.2.1. Light source 87
1.5.2.2. Interferometer 88
1.5.2.3. Basic principles in FTIR spectroscopy 88
1.5.2.4. Systems used 91
1.5.3. EPR measurements 91
1.5.3.1. Basic principles and setup 91
1.5.3.2. Experimental procedure to determine the concentration of P1 defects 93
1.5.4. Cathodoluminescence spectroscopy 96
1.5.4.1. Basic principles and setup 96
1.5.4.2. Systems used 97
1.5.5. Energy Dispersive X-ray Fluorescence (EDXRF) 97
1.5.5.1. Basic principles and setup 97
1.5.6. Irradiation by with a linear electron accelerator (LINAC) 99
1.5.6.1. Basic principles and setup 99
1.5.6.2. System used 100
1.5.7. The DiamondView™ Instrument 101
1.5.6.1. Basic principles and setup 99
1.5.6.2. Device used 100
1.6. Sample cleaning 102
1.7. The concentration of infrared-active nitrogen-related defects in diamond 102
1.7.1. Defect induced infrared absorption 102
1.7.2. Concentration determination procedure 105
1.8. The concentrations of defects determined by UV-VIS absorption spectroscopy 107
1.9. Defect properties 108
1.9.1. Table of electronic transitions 108
1.9.2. Table of vibrational transitions 111
1.9.3. Defect production 112
1.9.3.1 General aspects of defects production by irradiation 112
1.9.3.2. Defect production by HPHT annealing of type Ia diamond 118
1.9.3.3. Defects in type Ia brown diamonds 119
1.9.4. Correlations between different absorption lines due to one defect 120
1.9.4.1. The A defect 120
1.9.4.2. The C defect 121

Chapter Two
Luminescence spectra of defects specific to brown type Ia diamonds. 123
2.1. Introduction 123
2.1.1. Chapter outline 123
2.1.2. Broad band luminescence 123
2.1.3. The 490.7 nm defect 125
2.2. Experimental 126
2.3. Results and discussion 127
2.3.1. Broad band luminescence 127
2.3.1.1. Photoluminescence data 127
2.3.1.2. X-Ray fluorescence data 134
2.3.2. The 490.7 nm defect 135
2.3.2.1. Photoluminescence data 135

2.3.2.2. Temperature behaviour of the ZPL 137
2.4. Conclusion 138
2.4.1. Broad band luminescence 138
2.4.2. The 490.7 nm defect 139

Chapter three
Sub-threshold excitation of luminescence of defects in diamond 140
3.1. Introduction.....140
3.2. Experimental.....142
3.2.1. Specimen details 142
3.2.2. Photoluminescence as a function of temperature 144
3.2.3. Photoluminescence as a function of exciting energy.....144
3.3. Results and discussion 145
3.3.1. Measurement of the transition probability.....145
3.3.2. Sub-threshold excitation as a function of temperature 146
3.3.2.1. Diamonds containing one type of defect excited by sub-threshold excitation.....146
3.3.2.2. Diamonds containing more then one type of defect 148
3.3.3. Sub-threshold excitation as a function of energy.....152
3.3.4. Higher excited states of the H3 defect.....154
3.4. Conclusions.....156

Chapter four
IR properties of impurities in diamond 158
4.1. Introduction.....158
4.1.1. Hydrogen in diamond. 158
4.1.2. Vibrational properties of the A defect in diamond. 162
4.2. Experimental.....163
4.3. Results and discussion 165
4.3.1. Correlation of the 3107 cm^{-1} with nitrogen and nitrogen aggregates 165
4.3.2. Results of 3107 cm^{-1} line in isotopically $^{12}C/^{13}C$ mixed HPHT synthetic diamonds. 168
4.3.2.1. Absorption near 3100 cm^{-1} 168
4.3.2.2. Intrinsic two-phonon absorption 169
4.3.2.3. Raman measurements.....170
4.3.2.4. Absorption near 1400 cm^{-1} 170
4.3.2.5. One-phonon absorption 171
4.3.2.6. Combination bands.....172
4.3.3. The shift of the A defect absorption peaks in isotopically $^{12}C/^{13}C$ mixed HPHT synthetic diamonds.....172
4.3.2.1. Sample details.....172
4.3.2.2. Raman measurements.....173
4.3.2.3. Infrared measurements 173
4.3.2.4 The peak position shift of the A defect in ^{13}C enriched diamond when assuming harmonic coupling to nearest neighbours only.176
4.3.4. Correlation between spectral features in the IR spectra of nitrogen aggregates.....177
4.4. Conclusion 180
4.4.1. Correlation of the 3107 cm^{-1} line with nitrogen and nitrogen aggregates. ....
.....180

4.4.2. Results of 3107 cm^{-1} line in isotopically $^{12}C/^{13}C$ mixed HPHT synthetic diamonds. 181
4.4.3. Results of the A defect in isotopically $^{12}C/^{13}C$ mixed HPHT synthetic diamonds. 181
4.4.4. Correlation between spectral features in the IR spectra of nitrogen aggregates. 182

Chapter Five
Vacancy capture by nitrogen aggregates and photo-induced changes of the H1b and H1c defect 183
5.1. Introduction 183
5.1.1. Chapter outline and motivation 183
5.1.2. Radiation defect production and annealing of irradiated diamonds and preliminary experiments 184
5.1.2.1. Interstitials in irradiated diamond 184
5.1.2.2. Vacancies in irradiated diamonds 188
5.1.2.3. Other defects occurring during annealing of irradiated diamond 191
5.1.2.4. Photochromism of irradiation induced defects in diamond 193
5.1.2.4. Preliminary experiments 194
5.2. Experimental 198
5.2.1. Sample description 198
5.2.2. Instrumental set-up 201
5.3. Vacancy trapping by nitrogen aggregate defects. 203
5.3.1. UV-VIS measurements 204
5.3.2. Captured fraction of vacancies by nitrogen related defects in diamond 208
5.3.3. The possible influence of platelets on the vacancy annealing kinetics of type IaA/B diamond 214
5.3.4. Annealing of type IaA/B diamond: H3 and H4 formation kinetics 215
5.4. Photo-induced changes of defects detectable in the UV-VIS and IR spectra...226
5.4.1. Influence of bleaching with monochromatic light on the UV-VIS spectrum of as-irradiated diamond 226
5.4.2. Influence of bleaching with monochromatic light on the UV-VIS spectrum of irradiated and high temperature annealed (T = 800°C) diamonds 228
5.4.3. Influence of bleaching with monochromatic light on the H1b H1c defects in the IR spectrum 230
5.4.4. Results of thermal recovery of UV illuminated diamond 232
5.5. Undocumented absorption peaks 234
5.6. Conclusion 236
5.6.1. Vacancy capture by nitrogen related defects 236
5.6.2. The influence of radiation on platelets 236
5.6.3. Photochromic changes of radiation induced defects in diamond 237
5.6.4. Photo-induced changes of the H1b, H1c defect 237

Chapter Six
Stability of defects during HPHT annealing 238
6.1. Introduction to HPHT annealing 238
6.1.1. Chapter outline 238
6.1.2. A-defect dissociation 240

6.1.3. Annealing of the hydrogen-related 3107 cm^{-1} defect. 240
6.1.4. Annealing of brown type Ia diamonds.....241
6.2. Experimental.....245
6.2.1. Samples and experimental setup.....245
6.2.2. Samples used.....247
6.2.2.1. Samples to measure the C defect concentration in natural type Ia diamonds.....247
6.2.2.2. Preliminary tests.....248
6.2.2.3. Brown type IaA diamonds.....249
6.2.2.5. Brown type IaA/B diamonds [A] < [B].....252
6.2.2.6. Brown type IaA/B diamonds [A] << [B] 253
6.2.2.7. Brown type IaB diamonds.....257
6.2.2.8. HPHT annealing of irradiated type Ia diamond 258
6.2.2.9. Samples HT and HPHT annealed at 1700°C 259
6.3. A centre dissociation.....262
6.3.1. Introduction.....262
6.3.2. Theoretical 263
6.3.3. Results and discussion 265
6.3.3.1. Analysis of published results.....265
6.3.3.2. Analysis of brown type Ia HPHT annealed diamonds 269
6.3.3.4. Determination of low concentrations of C defects in HPHT annealed diamond.....272
6.4. Influence of pressure.....274
6.5. HT annealing of irradiated pre-annealed diamonds.....276
6.5.1. Study of irradiated type I diamonds, annealed at high temperature (T ~ 1500°C) and low pressure (P << 1 GPa).....276
6.5.2. Study of irradiated and high temperature annealed (T ~ 1500°C) type I diamonds at various pressures (P up to 10 GPa).....282
6.5.3. Summary.....283
6.6. Optical study of the annealing behaviour of the 3107 cm^{-1} defect in natural diamond 284
6.6.1. Experimental.....284
6.6.2. Results and discussion 285
6.6.2.1. Aggregation-dissociation kinetics of the 3107 cm^{-1} defect.....287
6.6.2.2. Hydrogen source - nitrogen correlation.....291
6.7. Colour changes in HPHT annealed brown type Ia diamonds 292
6.7.1. Initial experiments 292
6.7.2. Correlation between the degree of the brown colour of a type Ia diamond and the created H3 concentration 297
6.7.3. H3 defect formation and dissociation including vacancy release from H3 defects and retrapping by A defects and excluding B defects.....304
6.7.4. Influence of the B/H4 defects on the H3 defect kinetics 308
6.7.5. Influence of different relative concentrations of A and B defects.....311
6.7.6. Released mono-vacancy concentration-platelet relation. 314
6.7.7. HPHT annealing of irradiated and annealed type Ia samples.....317
6.7.8. Final remarks 321
6.8. Conclusion 322
6.8.1. Dissociation of A defects in diamond.....322
6.8.2. Influence of pressure on the dissociation of A defects 323

6.8.3. High temperature annealing of irradiated type Ib diamond under varying pressure....323
6.8.4. Optical study of the annealing behaviour of the 3107 cm^{-1} defect in natural diamond....324
6.8.5. Dynamics of defects in brown type Ia diamond....324

Chapter Seven
Summary, conclusions and further work....327
7.1. Summary and Conclusions....327
7.1.1. Linear electron-phonon coupling....328
7.1.2. Annealing of brown type Ia diamond....329
7.1.2.1. Study of the capture of vacancies by nitrogen aggregates....329
7.1.2.2. Study of the dissociation of nitrogen-vacancy complexes....329
7.1.2.3. Study of the dissociation of nitrogen aggregates....330
7.1.2.4. Prefactors of the rate constants involved in all processes....330
7.1.2.5. Colour changes of brown diamond by variation of the HPHT annealing parameters....331
7.1.3. Hydrogen in diamond....332
7.2. Further work....332
7.2.1. Linear electron-phonon coupling....332
7.2.2. Photochromic effects....333
7.2.3. Vacancy capture by nitrogen aggregates in diamond....333
7.2.4. Brown colour in diamond and vacancy clusters....334
7.2.5. Crystallographic directions of plastically deformed regions in diamond....334
7.2.6. Platelet formation and destruction....334
7.2.7. Defect kinetics....335

Appendix A
Colour and colour coordinate calculation....336
A.1. Introduction....336
A.2. Colour coordinate calculation....336
A.3. Examples....340
A.4. Remarks....343

Appendix B
Alternative dissociation path of H3 defects: H3 → N + N-V....345

Appendix C
Examples of colour changes by treatments....349
C.1. Introduction....349
C.2. Irradiation....349
C.3. Irradiation and annealing (T = 800°C, 1h)....350
C.4. HPHT annealing of brown type Ia diamond....351

References....353

Table of figures

Chapter one

Figure 1.1. This figure illustrates the price of gem-diamond as a function of colour saturation. The price of the gem-diamond falls off rapidly with a higher degree of colour saturation. At a certain point, diamonds with a higher degree of colour saturation are rarer, which makes the diamond more valuable. p.42

Figure 1.2. Linear electron-phonon coupling shifts the equilibrium of the vibrational potential surface of the excited state with respect to the ground state, and lowers the energy of the excited state. p.48

Figure 1.3. The transition probability of the one to six phonon replica of the Zero Phonon Line as a function of the Huang-Rhys factor. A defect with a low Huang-Rhys factor will have no high order side band, while a defect with a high Huang-Rhys factor will have a strong side band and the maximum of the transition probability will shift away from the ZPL. p.49

Figure 1.4. The configuration coordination diagram of defects with different Huang-Rhys factor..... p.49

Figure 1.5. The configuration coordination diagram of ZPL transitions. p.50

Figure 1.6. The absorption of light promotes an electron from the ground state to the excited state. The electron rapidly thermalizes to the excited state with lowest vibronic quantum number and de-excites back to its ground state or a vibronic level above the ground state. If the de-excitation is radiative, a photon is emitted and fluorescence is generated in the defect. A typical example of absorption and emission spectra is illustrated here for the H3 defect. There is no mirror symmetry between the emission and absorption spectra because of the presence of a second state close to the excited state. p.51

Figure 1.7. The one and two-phonon density of states of the N3 defect as calculated by the procedure described in the text above (left) and of Davies (1981a) (right). The zero phonon line has been removed in the figure on the left. p.53

Figure 1.8. A schematic plot of the Jahn-Teller splitting due to linear coupling (---), quadratic coupling (—) and to linear and quadratic coupling combined (—). p.54

Figure 1.9. The configuration coordination diagram in the presence of two non-degenerate excited states. p.56

Figure 1.10. The energy level scheme of the H3 defect. A forbidden transition 16 meV above the excited state (dashed arrow) is vibronically mixed with the optically allowed transition (solid arrow), giving rise to an additional contribution in the absorption spectrum. p.57

Figure 1.11. The energy level scheme of the N3 defect. A forbidden transition 146 meV below the excited state (dashed arrow) is vibronically mixed with the optically allowed transition (solid arrow), giving rise to an additional contribution in the absorption spectrum. p.58

Figure 1.12. Diffusion of specie *C* through a unit area. The numbers N_{Ci} and N_{C-i} are the fluxes of particles in directions *i* and *–i*. The net flux J_C is N_{Ci} - N_{C-i} and is dependent on the concentration gradient, grad(*C*). p.59

Figure 1.13. The Gibbs free energy change as a function of the extent of the reaction ξ.. . ..... p.65

Figure 1.14. The model proposed by Newman (1995) for the formation of H2* in electron irradiated and quenched silicon. A vacancy diffuses to a site nearby the H2 molecule (a), the H2 is trapped by a vacancy (b). When the H2V traps a mobile interstitial (c) the H2* defect is created. p.69

Figure 1.15. The various microstates of dislocations in deformed materials upon recovery. The deformation introduces dislocations in the material, which cluster and form cells. These cell boundaries may in time lead to sub-grain formation. If all subgrains have different crystalline orientation, a polycrystalline material will be created upon recrystallisation. If all subgrains have identical crystalline orientation, a single crystal will form after recrystallisation. p.70

Figure 1.16. An end-on view of an edge dislocation. The Burgers vector is in this case perpendicular (in the plane of the paper) to the dislocation line (perpendicular to the paper). p.71

Figure 1.17. Dislocation climb by absorption of a vacancy. p.72

Figure 1.18. Dislocation networks with large diameter (a) and very small diameter (b) on a type IIa diamond surface. These structures are never seen in type I diamond. The diameter of the samples is 2.5 mm. p.73

Figure 1.19. A drawing of the inside of a BELT type HPHT press (Sumiya *et al.* 2005). The steel belt, surrounding the carbide die is not visible in this figure. The arrows in the figure of Sumiya are in the wrong places: Ti is the nitrogen getter and Cu is the TiC formation inhibitor. p.75

Figure 1.20. The inside of a HPHT cubic press at Sundance Inc (http://www.ussynthetic.com/rd/hpht.php). p.77

Figure 1.21. Emission curves of different light sources used for absorption and luminescence measurements in the ultraviolet to visible range (LOT Oriel catalogue). p.80

Figure 1.22. The path length difference between two neighbouring light rays of wavelength λ depends on the angle between the incoming ray θ_i and reflected ray θ_d with respect to the grating normal GN. p.81

Figure 1.23. The multiple beam interference for a grating with N = 5 or 20. ..... p.82

Figure 1.24. Schematic representation of the parameters influencing instrumental resolution. p.83

Figure 1.25. The additive (left) and subtractive (right) mode for triple monochromators. p.85

Figure 1.26. A schematic representation of a Michelson interferometer. The light beam comes from the left side onto a semi-reflective mirror. 50% of the light is reflected to the fixed mirror while 50% of the light is transmitted to a mobile mirror. The reflected light beams come together at the semi-reflecting mirror and lead to destructive or constructive interference, depending on the pathlength difference Δx between the interfering light beams. p.88

Figure 1.27. The dependence of the line width on the concentration of P1 defects in diamond for samples measured at the University of Ghent (open circles), data from Brozel *et al.* (1978) and from van Wyk *et al.* (1997). The solid curves were calculated with equation (1.5.16) and the values of the a and b parameters used to calculate the curves are summarised in table 1.2. ..... p.94

Figure 1.28. The K_α transition in X-ray fluorescence. p.98

Figure 1.29. The LINAC system of the University of Ghent. Irradiated samples are located at end station C0. Electrons are injected at the left side and accelerated (two yellow parts). p.100

Figure 1.30. A simulation of the kinetic energy distribution of accelerated electrons in the LINAC system used, when the kinetic energy is set for 1.5 and 4 MeV (Univ. of Ghent). p.101

Figure 1.31. The one-phonon density of states for diamond as calculated by Pavone *et al.* (1993). p.103

Figure 1.32. The various one-phonon induced absorption spectra in diamond due to single nitrogen, nitrogen aggregates and platelets. The A defect consists of two nitrogen atoms, the B defect of four nitrogen atoms around a vacancy, the D defect is platelet related. The C defect is a single substitutional nitrogen defect and the N^+

is an ionised C defect. A typical absorption spectrum of a type IaA/B diamond is the superposition of A, B, D spectra and the platelet peak. The strengths of the A and B absorptions are proportional to their concentrations in the diamond. p.105

Figure 1.33. The decomposition of the FTIR spectrum of a regular type IaA/B diamond with platelets and A, B and D components. The fitted spectrum is a least square fitting of the sum of A, B and D components. The experimental spectrum is shifted up by 2 cm^{-1} for clarity. p.106

Figure 1.34. Vacancies created during irradiation of diamond with hydrogen ions (H^+) of energy 100 keV. The largest amount of damage is created at the end of the hydrogen ion track. p.114

Figure 1.35. Phonons created during irradiation with hydrogen ions of energy 100 keV, and phonons created by host atom - recoil of the hydrogen ion interaction. p.114

Figure 1.36. The ionisation of the carbon atoms in the diamond lattice when the sample is irradiated with 100 keV hydrogen ions. p.115

Figure 1.37. The configuration coordination diagrams illustrating the four recombination enhanced diffusion mechanisms. (a) The charged state mechanism and saddle point mechanism (dashed D^- + h line has a saddle point at the D^0 maximum), (b) the energy release ("phonon kick") mechanism, (c) the electronic excitation mechanism. Figure from Lang (1982). p.117

Figure 1.38. The secondary absorption edge in type IaA diamond. The zero phonon lines at 302.8, 302 and 301.7 nm are not resolved. The sample is cooled to liquid nitrogen temperature. p.121

Figure 1.39. The UV-VIS absorption spectrum of a type Ib diamond. p.121

Chapter two

Figure 2.1. The absorption spectra of a diamonds typical of the samples studied in this chapter (bottom spectrum) and yellow-brown samples (canary type) studied by De Weerdt and Van Royen (2001) (top spectrum). Spectra were recorded with the samples at liquid nitrogen temperature. p.124

Figure 2.2. The absorption spectrum of a type IaB diamond with a detectable 490.7 nm defect at the edge of the broad band centred at 560 nm. The spectrum was recorded with the diamond at liquid nitrogen temperature. p.125

Figure 2.3. The PL spectrum of a brown type Ia diamond (broken curve), excited at 325 nm. The broad bands present in the spectrum can be visualised by subtracting a spectrum, with suitable intensities for the H3 and N3 components, to give the full

curve. The weak peaks in this resulting spectrum are due to the presence of H4, with residual H3 and N3. There are clearly two broad bands, centred at approximately 1.75 eV and another at approximately 2.39 eV. p.127

Figure 2.4. The PL spectra of two different brown type Ia diamonds, excited at 514.5 nm. There is a clear sample-dependent position of the maximum and the width of the broad band near 1.75 eV. p.128

Figure 2.5. The PL spectrum with sharp peaks at 2.152 eV (576 nm) and 2.313 eV (536 nm) (figure 2.5a) which is used in combination with a spectrum of the H3 defect (figure 2.5b) for a least squares decomposition of the background leading up to the broad band near 1.75 eV (~ 710 nm). p.129

Figure 2.6. The luminescence spectrum after subtraction of the background caused by the side bands of the emission lines at 2.152 eV (576 nm) and 2.313 eV (536 nm) and the H3 defect. In a number of cases a weak peak at 2.152 eV (576 nm) remained present after the subtraction, sometimes in the positive and sometimes in the negative sense, without significantly altering the background at energies below 2.152 eV (576 nm). p.130

Figure 2.7. Integrated intensities of (a) the 2.008 eV (617 nm) peak and (b) the 1.978 eV (626 nm) peak versus that of the 2.034 eV (609 nm) peak. The lines are least squares fits to the equation y = ax. (This is justified since fits to y = ax + b gave values of b which were 3 times smaller than the uncertainties in b.) p.131

Figure 2.8. The Arrhenius plot of the integrated intensity of the 2.034 eV peak in the temperature range 77 to 160 K. Measurements at higher temperatures are not possible because of strong broadening of the peak, making it impossible to discriminate the peak from the background. From the linear fitting of the data, an activation energy of 18 meV can be calculated. p.132

Figure 2.9. The calculated vibronic broad band (broken curve) compared with the experimental curve. The calculated spectrum does not fit perfectly to the experimental spectrum, partly because the calculated spectrum was fitted to spectra from four different samples. The inset shows the calculated one-phonon spectrum. p.132

Figure 2.10. The difference (full curve) between the experimental spectrum and the calculated spectrum (red curve). The reconstructed spectrum has been calculated up to the twelfth phonon replica. The small oscillations in the full curve are due to differences between the calculated and experimental curves. p.133

Figure 2.11. The PL spectra of the four samples after subtraction of the calculated broad band and rescaled to subtract the most suitable calculated spectrum. The residual bands have been rescaled to the same maximum intensity. p.134

Figure 2.12. A typical photoluminescence spectrum of a brown type Ia diamond with strong 490.7 nm emission and weak luminescence due to other defects (full curve). The broken curve is the same spectrum with suitable N3 background subtraction. p.135

Figure 2.13. The experimental and calculated side band spectrum of the 490.7 nm defect. The arrow indicates the region of the removed ZPL. The two additional peaks at 2.31 eV (536 nm) and 2.15 eV (576 nm) are different defects. The inset shows the one-phonon density of states as a function of the energy difference between the zero phonon line and the phonon interacting with the defect. p.136

Figure 2.14. The decomposition of a PL spectrum into a spectrum of H3, H4 and 490.7 nm defects. The peak at 2.31 eV is due to a different defect. p.136

Figure 2.15. The correlation between the scaling factor and the integrated intensity of the 490.7 nm ZPL. p.137

Figure 2.16. The temperature behaviour of 5 different samples (4 samples, and one measurement is on the same sample, but at a different location). The integrated intensity of the ZPL has been rescaled in a way that the value of the maximum of the integrated intensity is close to the theoretical temperature behaviour. p.138

Figure 2.17. The FWHM of the 490.7 nm zero phonon line as function of temperature. p.138

Chapter three

Figure 3.1. Schematic representation of the model for the sub-threshold excitation. Excitation is from a state which lies at energy $\eta\omega$, equal to the energy difference between the zero-phonon line transition and the energy of the Ar^+ laser photons (2.409 eV). p.141

Figure 3.2. Intensities of the H3 and H4 zero-phonon lines, recorded in luminescence, using excitation at 325 nm. The solid line is the calculated transition probability of the H3 centre as a function of temperature. The amplitudes of the H3 and H4 ZPLs have been rescaled to the same amplitude as that of the calculated curve at 77 K. p.145

Figure 3.3. The experimentally measured and calculated transition probabilities of the 3H centre as a function of temperature. p.147

Figure 3.4. Arrhenius plots of the integrated intensity of the H3 zero-phonon line, using sub-threshold excitation at 514.5 nm. Data in the lower plot are uncorrected for the change in transition probability with temperature; the line through the low-

temperature points is a guide to the eye. Data in the upper plot are corrected; the line is the best fit to the data. p.147

Figure 3.5. Arrhenius plot of the integrated intensity of the 3H zero-phonon line, using sub-threshold excitation at 514.5 nm. The data have been corrected for the experimentally-measured temperature dependence of the transition probability. p.149

Figure 3.6. Arrhenius plots, using sub-threshold excitation at 514.5 nm, for the integrated intensity of (a) the H3 zero-phonon line, in a diamond containing predominantly H3 centres (triangles) and a diamond containing similar concentrations of H3 and H4 centres (squares); (b) the H4 zero-phonon line, in a diamond containing predominantly H4 centres (circles) and a diamond containing similar concentrations of H3 and H4 centres (squares). The lines in figures (a) and (b) for the data from the diamond containing both H3 and H4 defects are linear extrapolations of the low-temperature behaviour. In all cases the data have been corrected for the change in transition probability with temperature. p.150

Figure 3.7. Arrhenius plot of the ratio of the integrated intensities of the H3 and H4 zero-phonon lines, using sub-threshold excitation at 514.5 nm, in a diamond containing both defects. The data are corrected for the changes in the transition probabilities with temperature. p.152

Figure 3.8. Arrhenius plots of (a) the H4 ZPL, (b) the 3H ZPL, corrected for the changes in the transition probabilities with temperature, in a diamond containing both defects. p.152

Figure 3.9. The intensity of the 637 nm zero-phonon line observed in photoluminescence, divided by $\exp[E/(k_B T)]$, (data points), following sub-threshold excitation, compared with the photoluminescence spectrum measured at 150 K, divided by ν^3. The horizontal axis shows the energy from the position of the ZPL. The diamond was held at a temperature of 150 K. The error bars for the lowest energy data points increase significantly since the intensity of the $(N\text{-}V)^-$ signal decreases rapidly as the energy between the ZPL and the laser line increases.. p.154

Figure 3.10. The UV-VIS absorption spectrum of a brown type IaA/B diamond before HPHT annealing and after HPHT annealing. The H3 absorption before annealing is very low, and the H13 peak is undetectable. After annealing there is a strong increase in the H3 absorption, and the H13 peak is weakly detectable. p.155

Figure 3.11. The H3 defect excited with different lasers and laser lines. From top to bottom: H3 excited with 325 nm HeCd laser, 351 nm, 457 nm and 488 nm laser line of an Argon-ion laser. The spectra are shifted for clarity and have not been corrected for instrument response or different laser power of each line. The 537 nm (2.308 eV) peak is not detected when the photon energy is below the higher excited state transition energy. p.155

Figure 3.12. The correlation between the intensity of the 537 nm line and the intensity of the ZPL of the H3 defect. ..... p. 156

Chapter Four

Figure 4.1. The nitrogen concentration vs. the calculated integrated area of the 3107 cm^{-1} absorption line in the IR spectrum. There is an apparent correlation between the total nitrogen concentration and the integrated area of the 3107 cm^{-1} line, however there is no one to one correspondence. p.165

Figure 4.2. The integrated area of the 3107 cm^{-1} line against the fraction of A centres (squares) and the fraction of the B centres (open circles) of the total nitrogen concentration. p.166

Figure 4.3. Typical UV-VIS-NIR spectra recorded at liquid nitrogen temperature of diamonds with predominantly A centres (a.), A and B centres, where [A] > [B] (b.) and where [B] > [A] centres (c.) as determined from the IR spectrum. p.167

Figure 4.4. Absorption spectrum of an HPHT synthetic diamond grown from ^{13}C and containing hydrogen-related features. p.168

Figure 4.5. Absorption spectrum of the hydrogen-related peaks near 3100 cm^{-1} in an HPHT synthetic diamond grown from ^{13}C. The top spectrum is the experimental spectrum and the bottom spectrum is the simulated spectrum (broken curve) and the different simulated individual peaks (solid curves)..... p.169

Figure 4.6. Absorption spectrum of the hydrogen-related peaks near 1400 cm^{-1} in an HPHT synthetic diamond grown from ^{13}C. The top spectrum is the experimental spectrum and the bottom spectrum is the simulated spectrum (broken curve) and the two different simulated individual peaks (solid curves)..... p.171

Figure 4.7. The absorption spectrum of the one-phonon A defect related absorption without the intrinsic diamond spectrum. p.174

Figure 4.8. The wavenumber correction factor R', compared with the expected factor R from equation 4.1. ..... p.174

Figure 4.9. The ratio of the ^{13}C to ^{12}C A defect peak position is set out as function of the ^{12}C percentage in the synthetic diamond. The 480 cm^{-1} peak position does not shift with different ^{12}C to ^{13}C isotopic content. The legend gives the values of the A centre maxima for natural diamond. p.176

Figure 4.10. The correlation between the integrated intensity of the platelet peak and the D component in the infrared spectrum of diamond. The error bars give an example of the magnitude of the uncertainty on the measured values. p.178

Figure 4.11. The correlation between the concentration of the B defect and the absorption coefficient at 1282 cm^{-1} due to the D component in the IR spectrum. Crosses and open circles are regular diamonds, while all other points are irregular diamonds, most of them are brown in colour. The datapoints at the origin are from 9 different samples. The data points are from the same regular and irregular samples as in figure 1.32. ..... p.179

Figure 4.12. The correlation between the 480 cm^{-1} peak in the absorption spectrum of type IaA diamond and the maximum of the absorption at 1282 cm^{-1}. The solid line is a weighted, unconstrained linear fit and the dotted line is a weighted linear fit through the origin. p.179

Chapter five

Figure 5.1. Schematic diagram of the vacancy-interstitial recombination process. The interstitial has to overcome two barriers before it can recombine with the vacancy. p.185

Figure 5.2. The isochronal (1h) annealing data of electron and gamma irradiated diamond of Iakoubovskii *et al.* (2005). p.187

Figure 5.3. The UV-VIS absorption spectrum, recorded at liquid nitrogen temperature. The 3H peak is completely bleached by annealing for 1 hour at 450°C. p.188

Figure 5.4. The isothermal annealing data in figures 3 and 7 from the paper of Collins *et al.* (2005) (left and right figure). The left figure displays the isothermal annealing data of a type IaA diamond after irradiation and the figure on the right displays the isothermal annealing data (T>900°C or 1173 K) of a type IaB diamond after irradiation. p.192

Figure 5.5. The broad band absorption in the IR spectrum of sample 1H7 (see section 2 for details). The intrinsic diamond spectrum has been subtracted from the spectrum of the sample. p.193

Figure 5.6. The change in FWHM of the GR1 ZPL of an irradiated diamond after isochronal annealing (1 h) at different temperatures. The FWHM of the as irradiated sample is the first data point (room temperature). The other data points are after annealing at 300°C (573 K) to 750°C (1023 K) in steps of 50°C. p.196

Figure 5.7. The change in integrated intensity of the H3 defect after isochronal (1 h) annealing at temperatures between 300°C (573 K) and 750°C (1023 K) in steps of 50°C. p.196

Figure 5.8. The change in the absorption spectrum of an irradiated diamond (top spectrum) after one hour annealing at temperature of 450°C (723 K) (bottom spectrum). The ZPL sharpens and decreases in strength (Collins 1999). The interstitial related absorption with a ZPL at 667 nm is almost completely removed after one hour annealing at 450°C (723 K) (see inset). Spectra were collected at liquid nitrogen temperature and have been shifted for clarity. p.197

Figure 5.9. The UV-VIS spectra of sample 7 after irradiation, irradiation and annealing at 450°C (723 K), and after additional annealing at 800°C (1073 K) for 1 hour. Spectra were recorded at liquid nitrogen temperature and shifted for clarity. .. p.201

Figure 5.10. The UV-VIS absorption spectrum of the three samples recorded at liquid nitrogen temperature after irradiation and annealing at 800°C (1073 K). The top spectrum is of sample 1H7, the spectrum in the middle is of sample 10, and the spectrum in the bottom is of sample 1. Spectra have been shifted for clarity. Only sample 1H7 has a detectable H2 absorption peak. p.203

Figure 5.11. The UV-VIS spectra of sample 3 before irradiation, after irradiation and after each annealing step. Strong absorption is detected in the UV part of the spectrum, consistent with observations of Dyer (1966) and Davies (1992), which is substantially reduced after annealing. Spectra were recorded with the samples at liquid nitrogen temperature. p.204

Figure 5.12. A more detailed view of the spectral region close to the GR1 peak in sample 3. No absorption is detected before irradiation, strong GR1 absorption is detected after irradiation. The GR1 peak is substantially reduced after annealing for 1 hour at 800 °C (1073 K), and is completely removed after annealing at 1000°C for 1 hour. The additional peaks at 1.679, 1.691 and 1.710 eV are not removed by annealing at 1000°C (1273 K). The (black) spectrum of the sample after annealing at 1000°C is shifted for clarity. p.205

Figure 5.13. Sample 1 after irradiation and after annealing at 800°C (1073 K) for 1 hour. Spectra are recorded at liquid nitrogen temperature. p.206

Figure 5.14. The PL spectrum of sample 3, recorded at liquid nitrogen temperature. The peak positions of the three peaks are almost the same as the peak positions of the peaks in the UV-VIS absorption spectrum. p.207

Figure 5.15. The [H3]/[H4] ratio as a function of the [A]/[B] ratio. The full line is a weighted least squares fit through the origin and gives a gradient of 3.85 ± 0.23, in good agreement with published data (Davies *et al.* 1992). p.210

Figure 5.16. The ratio of the nitrogen aggregate-vacancy complex to the product of the nitrogen aggregate trapping defect concentration and the vacancy concentration as function of the nitrogen trapping defect concentration itself. The data is fitted with the rhs of equation (5.3.4). Note the concentrations are the concentrations of A and B defects and not the atomic concentration of nitrogen in the A and B defects. p.212

Figure 5.17. The change of the H3 absorption as function of isothermal annealing of an irradiated type IaA diamond (Collins *et al.* 2005). p.214

Figure 5.18. The platelet peak clearly decreases in intensity when the sample 7 is irradiated. No changes occur after annealing at 450°C, and 800°C. A similar decrease in intensity was observed in sample 1 and 2 after irradiation. p.215

Figure 5.19. The formation of H3 and H4 defects; the vacancy is trapped at an A defect (a.) or B defect (b.) and the complex restructures into the H3 or H4 defect respectively defect. In each case, the number of dangling bonds of carbon atoms decreases from three to two. The red arrow indicates the direction of the dipole responsible for the optical absorption (Jones *et al.* 1994). p.216

Figure 5.20. The simulated H3 and H4 defect concentration increase with time in a type Ia diamond with equal concentrations of A and B defects, annealed at 600°C. The behaviour of H3 is equal to the H3 behaviour described by Davies *et al.* (1992). p.219

Figure 5.21. The simulated H3 and H4 defect concentration increase with time in a type Ia diamond with equal concentration of A and B defects, annealed at 800°C. . p.220

Figure 5.22. The simulated vacancy concentration decrease with time in a type Ia diamond with equal A and B defect concentration, annealed at 600°C (873 K). The decay is modelled with mixed double first order (fast and slow process) and second order decay (solid curve) and double first order decay only (broken curve). The double first order decay fits the experimental data of Davies *et al.* (1992) the best. p.221

Figure 5.23. The single first order decay model for vacancies in type IaA diamond, where vacancies are preferentially created inside the capture radius R_C. These can diffuse freely to the A defect and restructure to an H3 defect. A fraction of the vacancies created outside the capture radius (α[A(t)].[V(t)]) of these vacancies diffuses to the A defect. These vacancies outside the capture radius have to overcome an energy barrier before being trapped inside the A defect capture radius. Vacancies inside the capture radius can also overcome the energy barrier and diffuse away from the A defect. p.223

Figure 5.24. The difference between the single first order vacancy decay model with an energy barrier around the A defect and the double first order decay model. In the

single first order vacancy decay model, ~ 40% of the vacancies is located between the A defect and its energy barrier. p.224

Figure 5.25. The histogram of the distribution of distance between a vacancy and an A defect in a irradiated type IaA diamond with 7 ppm of vacancies and 296 ppm of A defects. p.225

Figure 5.26. The difference between the UV-VIS spectrum after and before illumination. There is a decrease in GR1 and an increase in ND1 absorption strength. The ratio of GR1 to ND1 absorption intensity is ~ 2. ..... p.227

Figure 5.27. The difference between the absorption spectra of sample 1 before and during illumination with UV light (370 nm LED). p.228

Figure 5.28. The difference between the absorption spectra of sample 1 before and during illumination with the 470 nm LED. p.230

Figure 5.29. IR spectra of sample 1 before (middle spectrum), and during illumination with the 370 nm LED (top spectrum) and during illumination with the 470 nm LED (bottom spectrum). p.231

Figure 5.30. The percentage change of the H1b line of sample 1, 10 and 1H7 before and after illumination with light of different wavelength. p.232

Figure 5.31. The recovery of the H1b defect by annealing at 300°C. The full curve is the single exponential decay equation (5.14) fitted to the data. p.233

Figure 5.32. The thermal recovery (T = 600°C) of the integrated intensity of the H1b line in sample 1 after illumination with UV light. The solid curve on the figure is calculated from parameters derived at lower temperature. p.234

Figure 5.33. The Arrhenius plot of the recovery process of the H1b defect..... p.234

Figure 5.34. The UV-VIS-NIR absorption spectrum, recorded with the sample at liquid nitrogen temperature of the HPHT annealed, irradiated and heat treated diamond. An undocumented peak at 805 nm is detected. p.235

Figure 5.35. The mid-IR absorption spectrum, recorded with the sample at room temperature of the HPHT annealed, irradiated and heat treated diamond. An undocumented peak at 6170 cm^{-1} is detected in this sample. p.235

Chapter six

Figure 6.1. The UV-VIS-NIR absorption spectrum of a brown type Ia diamond after HPHT annealing. A weak H2 absorption peak is detectable in the NIR spectrum.

The NIR spectrum is recorded with the Princeton Instruments spectrometer, while the UV-VIS spectrum is recorded with a Varian Cary 100 spectrometer. p.242

Figure 6.2. The IR spectrum of sample 1B2 before, after the first and second HPHT annealing. No platelet peak is detected before annealing but is present after the first and second HPHT annealing. Spectra have been displaced for clarity. p.250

Figure 6.3. The UV-VIS-NIR absorption spectrum of a light brown type IaA diamond before and after the first and second HPHT annealing at 2100°C, for 3 minutes. No N3, H3 or H2 peak was detected before annealing, but were present after every subsequent HPHT annealing. Spectra have been displaced for clarity. p.251

Figure 6.4. The N3 defect concentration of the samples 1B1, 1B2, 1B3 and 1D1 before and after two subsequent HPHT annealings. p.251

Figure 6.5. The H3 defect concentration of the samples 1B1, 1B2, 1B3 and 1D1 before and after two subsequent HPHT annealings. p.252

Figure 6.6. The $(N\text{-}V)^-$ defect concentration as function of annealing time for samples HPHT annealed at 2100°C. p.254

Figure 6.7. The $(N\text{-}V)^-$ defect concentration as function of annealing time for samples HPHT annealed at 2200°C. p.254

Figure 6.8. The N3 defect concentration, relative to the initial concentration, as a function of annealing time for samples HPHT annealed at 2100°C in steps of three minutes. p.255

Figure 6.9. The N3 defect concentration, relative to the initial concentration, as a function of annealing time for samples HPHT annealed at 2200°C in steps of three minutes. p.255

Figure 6.10. The H3 defect concentration of the samples, HPHT annealed at 2100°C in steps of three minutes. p.256

Figure 6.11. The H3 defect concentration of the samples, HPHT annealed at 2200°C in steps of three minutes. p.256

Figure 6.12. The IR spectra of a brown type IaB diamond before HPHT annealing. Note the absence of platelets in the IR spectrum. p.258

Figure 6.13. The UV-VIS absorption spectrum at room temperature of sample 6-1 before and after HPHT annealing at 2300°C..... p.259

Figure 6.14. The room temperature UV-VIS spectra of colourless type IaA diamonds (sample 7-3) before and after annealing under high vacuum for 1 hour. p.260

Figure 6.15. The UV-VIS spectrum recorded at room temperature of a colourless type IaA diamond (sample 4-1) before HPHT annealing at 1700°C for 15 minutes and for 45 additional minutes (the total annealing time was 1 hour)..... p.260

Figure 6.16. Concentration of C centres as a function of time, calculated numerically from equation 6.3.4 (continuous curve). The dashed curve is the function given in equation 6.3.5 (see text for details). p.264

Figure 6.17. The fit with equation 6.3.8 to the data in figure 6 of Brozel *et al.* (1978) for a sample annealed at T = 1950°C and P = 8.5 GPa for various periods of time. p.266

Figure 6.18. The fit with equation 6.3.8 to the data in figure 6 of Brozel *et al.* (1978) for a sample annealed at T = 2040°C and P = 8.5 GPa for various periods of time. p.266

Figure 6.19. The binding energy as derived by fitting the $\ln([A]/[C]^2)$ vs. 1000/T plot with a linear function, using data from Brozel *et al.* (1978). A value of 7.66 ± 0.6 eV is determined for the binding energy. p.267

Figure 6.20. Simulation of the concentration of C defects as function of annealing time of sample 9. ..... p.268

Figure 6.21. The UV-VIS spectrum of sample B1a after HPHT annealing at 2200°C for 6 minutes. Only very low concentrations of H3 and H4 defects are detected.... p.271

Figure 6.22. The data of the eight HPHT annealed type Ia diamonds and the one light brown type IaB diamond overlaid on the Arrhenius plot of the data of Brozel *et al* (1978). The red circles are the values from the samples of the ak series, the black open triangles are of the colourless type IaA diamonds and the blue open circle is the data point of the light brown type IaB with some A defects diamond. The error bar on the left is the uncertainty on the measurements. p.272

Figure 6.23. The absorption coefficient at 400 nm and the concentration of C defects in ppm as determined from the IR absorption spectrum. The two lowest C defect concentration data points are taken from Sumiya and Satoh (1996). The proportionality coefficient between the absorption at 400 nm and the concentration of C defects is 2.00 ± 0.04. ..... p.273

Figure 6.24. Simulation of the A and C defect concentrations of samples irradiated and annealed at 1500°C (Collins 1980) with equations 6.5.1 – 6.5.6. ..... p.279

Figure 6.25. The data of Collins (1978) on N-V and H3 defect concentrations in irradiated and annealed type Ib diamond. The data of Collins (1980) of figure 6.25 is fitted with same parameters. p.280

Figure 6.26. The simulated concentration of the A and C defect concentrations after 1 hour and 4 hours annealing at 1500°C of an irradiated type Ib diamond..... p.281

Figure 6.27. The concentrations of A and C defects in samples with 280 ppm of C defects and annealed under vacuum (0 GPa) or at 7 or 10 GPa and a temperature of 1500°C..... p.283

Figure 6.28. A change in the dissociation activation energy of the A defect does not change the kinetics of C defect aggregation at T = 1500°C. The curves have been displaced by 10 ppm for clarity..... p.283

Figure 6.29. The hydrogen-related absorption lines at 1405 and 3107 cm^{-1} before (top) and after the final (bottom) HPHT annealing. The ratio of the intensities of these lines is similar after each annealing, and both have been reduced to approximately 75% of their initial intensities after the final annealing. p.285

Figure 6.30. Two cases of interest: a) where dissociation dominates the kinetics, and b) where aggregation of the 3107 cm^{-1} defect is dominant. In each graph, the dotted curve represents the dissociation of the initial 3107 cm^{-1} concentration, the broken curve represents the aggregation and dissociation of the 3107 cm^{-1} defect and the full curve indicates the total concentration. It is assumed that the hydrogen originates from a source, which is undetectable using infrared absorption. p.289

Figure 6.31. Three examples of data points from samples annealed at 2100°C (a), and two examples of data from samples annealed at 2200°C (b), fitted with equation 6.6.9. The lower curves in figure 6.32a and 6.32b have been shifted for clarity. p.290

Figure 6.32. The factor proportional to the initial hydrogen concentration in the hydrogen source as function of the initial (a) total atomic nitrogen concentration, (b) B defect concentration and (c) A defect concentration..... p.291

Figure 6.33. A typical absorption spectrum of a brown diamond before (bottom) and after (top) HPHT annealing. Both H3 (ZPL at 503.2 nm) and N3 (ZPL at 415 nm) defect concentrations increase after HPHT annealing. Spectra have been shifted for clarity..... p.292

Figure 6.34. UV-VIS absorption spectra of the samples annealed at 1900°C (a), 2100°C (b) and 2300°C (c). Three spectra were recorded for every sample. In every set, the bottom, middle and top spectra are the pre HPHT annealing, after the first and second HPHT annealing, respectively. The spectra have been shifted for clarity. Note the change in the shape of the absorption spectra below 325 nm for the samples annealed at 2100°C and 2300°C, caused by the onset of the broad UV absorption band at 270 nm due to C defects. There is also a strong increase in the N3 absorption when the samples are annealed at 2300°C..... p.293

Figure 6.35. IR spectra of a sample prior to, after the first and second annealing at 2100°C. The platelet peak decreases in strength and a peak at 1344 cm^{-1} (see inset) appears after the second annealing. p.294

Figure 6.36. Schematic representation (not to scale) of the different processes during the HPHT annealing of type Ia brown diamond. Figure 6.36.a represents the processes, which occur when the diamond sample is annealed at relatively low temperature T ≤ 1900°C. A low concentration of mono-vacancies is created due to dissociating of a vacancy source. At higher temperatures (1900°C < T < 2200°C), the same processes occur as at low temperatures, and a low concentration of NV defects is also created; this is due either to the dissociation of H3 defects into N + NV or the dissociation of A defects into N + N and subsequent trapping of a vacancy. Because the vacancy source is depleted after a certain time, no increase of H3 should be observed after some time during the annealing (Figure 6.36.b). At high temperatures (T > 2300°C) a high concentration of NV centres is created because a large concentration of C defects is created from dissociated A defects (6.36.c), which will trap the mono-vacancies. p.295

Figure 6.37. Analysis of the samples of the preliminary annealed samples and samples of groups 1, 2 and 3 show a correlation between the increase of H3 concentration and the saturation brown colour of the sample prior to HPHT annealing. The black squares are the data points of the samples annealed at 2100°C, red circles are of the samples annealed at 2200°C and the blue triangles are data points of brown type IaA samples annealed at 2100°C..... p.298

Figure 6.38. Cathodoluminescence image of the surface of sample 2b (before annealing) Monochromatized at 530 nm. The white line indicates where the CL line scan has been done. The angle between the octahedral growth horizons with <110> direction on the nearly {100} surface and lines where the line scan is measured is ~ 23° so the lines are parallel with the <210> direction (see also figure 6.44). p.299

Figure 6.39. Cathodoluminescence image of the surface of sample 2a (after annealing) Monochromatized at 530 nm. The white horizontal line indicates where the CL line scan has been done. p.300

Figure 6.40. A CL line scan on the surface of the brown type Ia diamond (sample 2b) reveals that H3 and other defects are inhomogeneously dispersed in the diamond. Increased concentrations of H3 and 490.7 nm defects are located at lines in the diamond, which run through different growth sectors, indicating post growth formation. The step size along the line is 1 μm..... p.300

Figure 6.41. A CL line scan on the surface of the HPHT annealed brown type Ia diamond (sample 2a) reveals an overall increase of H3 defects especially around lines in the diamond. The step size along the line is 1 μm. p.301

Figure 6.42. The pole figure of the diamond 2a. The surface of the sample is close to the {100} plane because sample was not exactly cut along a plane parallel to the {100} crystallographic plane: the orientation of the surface of samples 2a and 2b is more like the red and grey surfaces in the schematic drawing bottom right. As a consequence the angle between the equivalent octahedral planes intersecting the {100} plane in the CL images are not perpendicular. p.302

Figure 6.43. The intersection of a growth horizon of an octahedral plane with the {100} plane gives a line parallel to the <110> direction. The angle between the intersection of the octahedral plane and the {211} plane intersecting a cubic surface is 22.5°..... p.302

Figure 6.44. The CL image of the surface of sample 2a, recorded over a larger area than shown in figure 6.37. The sample image is recorded with the diamond rotated over 90 degree with respect to the image of the sample in figure 6.22. Arrows point to non-luminescent lines on the surface of the diamond, which are polishing grooves.. ..... p.303

Figure 6.45. The DiamondView™ image and pole figure of one of the brown type IaA diamonds after HPHT annealing. Note the H3 defect rich lines are at 45° to one of the octahedral growth horizons intersecting the polished surface of the diamonds, so these lines cannot be parallel to an octahedral plane (the angle between octahedral planes intersecting another octahedral plane must be 60°)..... p.304

Figure 6.46. Examples of the change of H3 concentration with annealing time, fitted with equations 6.7.1-6.7.5 to the tlb and lb samples of group one and two annealed at two different temperatures (2100°C and 2200°C)..... p.307

Figure 6.47. The H3 defect concentration after successive HPHT annealing and the fit of H3 defect concentration as calculated by equations (6.7.9) - (6.7.18) to the data. The activation energies of the processes are tabulated in table 6.18..... p.311

Figure 6.48. Two examples of the H3 defect concentration change upon successive HPHT annealing at 2200°C and 2100°C when B defects are present in the diamond sample. Higher concentrations of B defects will lead to increased concentration of H4 defects and in turn lead to increased concentration of H3 defects as the H4 dissociates in two H3 defects. Samples tlb5, tlb1 and lb6 have almost equal concentration of A defects, but a different concentration of B defects and integrated intensity of the platelet peak. The examples shown here are fitted with the numerical solution of equations 6.7.9 – 6.7.18 with one set of activation energies (see table 6.18)..... p.312

Figure 6.49. The calculated maximum of H3 as function of the intensity of the band at 550 nm, typical for brown type Ia diamond. The values are grouped for diamonds with similar concentrations of A and B defects. In general a higher degree of brown coloration results in a higher concentration of H3 defects..... p.314

Figure 6.50. The released mono-vacancy concentration as function of the integrated intensity of the initial platelet peak in the IR spectrum. There is clearly a anti-correlation between the mono-vacancies available for trapping at nitrogen defects and the concentration of platelets. p.315

Figure 6.51. The integrated intensity of the platelet peaks as function of the FWHM of the platelet peak. Samples with high concentrations of released mono-vacancies have a very complicated behaviour. p.316

Figure 6.52. The FWHM of the platelet peak as a function of the position of the maximum absorption. In samples with low concentration of released mono-vacancies, the mean platelet size decreases weakly upon successive annealing. In samples with a high concentration of released mono-vacancies, the mean platelet size can grow and shrink upon successive HPHT annealing. The uncertainty for the FWHM and the peak position is 2 cm^{-1}. p.317

Figure 6.53. The UV-VIS absorption spectrum of an irradiated (6 MeV, 10^{17} e^-/cm^2) diamond after HPHT annealing at 2100°C for three minutes. The inset is a detail of the absorption spectrum, showing weak H3 absorption. p.318

Figure 6.54. Simulation of H3 defect concentration in the irradiated HPHT annealed diamond, including H3 and H4 defect formation. The H4 defect concentration (not shown here) is below the detection limit by UV-VIS absorption. H4 defect is only weakly detectable by luminescence..... p.319

Figure 6.55. The relative absorption strength of H3 and H4 defects during isochronal annealing of irradiated type IaB diamond. The point where H4 defects begin to decay is ~ 50°C lower than observed experimentally, but the gradient of the H4 decay curve is the same. The curves are renormalized with respect to the maximum defect concentration..... p.320

Figure 6.56. The relative absorption strength of a number of defects during isochronal annealing of irradiated type IaB diamond (figure 7 from Collins *et al.* (2005)). p.321

Appendix A

Figure A.1. The D65 spectrum, imitating northern daylight. p.337

Figure A.2. The colour matching functions of the eye. These reflect the response function of the eye as function of the wavelength of the light. p.338

Figure A.3. The CIE 1931 chromaticity diagrams with the approximate colour name regions (right) and the real CIE colour space (left). The black dot is the D65 reference point p.338

Figure A.4. The colour coordinate of a total transmission spectrum. p.340

Figure A.5. The colour coordinate calculation result of a total transmission spectrum with an absorption spike at 450 nm. The inset in the spectrum shows the coordinate of spectrum in the chromaticity diagram together with the D65 white point. There is almost no difference. p.341

Figure A.6. The colour coordinate calculation result of a total absorption spectrum with an emission spike at 450 nm. The red arrow indicates the dominant wavelength with respect to the D65 illuminant. p.342

Figure A.7. The colour coordinate calculation result of a brown type IaA diamond. The red arrow indicates the dominant wavelength with respect to the D65 illuminant. The black triangle indicates the calculated colour coordinate of the spectrum.. p.342

Figure A.8. The colour coordinate calculation result of a Cape Yellow diamond. The red arrow indicates the dominant wavelength with respect to the D65 illuminant. The black triangle indicates the calculated colour coordinate of the spectrum..... p.343

Figure A.9. The complementary and dominant wavelength in the 1931 CIE chromaticity diagram. p.344

Appendix B

Figure B.1. The concentration of C defects after HPHT annealing when H3 dissociates in A + V or N + N-V. p.347

Figure B.2. The simulation of the concentration of N-V defects, generated during HPHT annealing of brown type Ia diamond with [A] = 20 ppm and [B] = 300 ppm. The hatched region is where the N-V concentration is below the UV-VIS absorption detection limit. The top curve is the concentration of N-V defects when H3 dissociates into single nitrogen and N-V defect combination, the lower curve is when H3 splits into and A defect and a vacancy. The maximum concentration of N-V defects should be detected after ~ 9 minutes..... p.348

Appendix C

Figure C.1. A green diamond sample after irradiation with electrons (dose: 8 1018 e^- /cm^2, energy: 8 MeV). p.350

Figure C.2. The various colours of diamonds after irradiation (irradiation conditions unknown). From left to right: depending on the irradiation dose and energy, the diamond can be black, green or blue. p.350

Figure C.3. A diamond after irradiation and annealing at 800°C. The colour of the diamond changed from green to golden yellow. p.350

Figure C.4. The different colours of a brown type Ia diamond after HPHT annealing, and irradiation and heat treatment. After HPHT annealing the colour of the brown diamond changed into a yellow-green colour. After irradiation and annealing the colour of the diamond changes into purple-red. p.351

Figure C.5. Brilliant polished diamonds after HPHT annealing. Annealing for a shorter time or at lower temperature will give the diamond a yellow-green colour (diamonds on left and right side). Prolonged annealing or annealing at higher temperature will give the diamond a yellow to orange colour (diamond in the centre). p.351

Table of tables

Chapter one

Table 1.1. The different types of reactions and their influence on the Gibbs free energy. p.64

Table 1.2. The *a* and *b* parameters, used to calculate the curves in figure 1.27..... p.95

Table 1.3. The calibration coefficients used to determine the concentrations of the nitrogen containing defects in the one-phonon region of the FTIR spectrum... p. 106

Table 1.4. A is the integrated intensity of the zero-phonon absorption line of the defect, measured at 77K, with the absorption coefficient in cm-1 and the photon energy in meV. ..... p. 107

Chapter two

Table 2.1. The ratios of the integrated intensities of the 2.008 eV (617 nm) and the 1.978 eV (626 nm) peaks with respect to the integrated intensity of the 2.034 eV (609 nm) peak. ..... p. 130

Chapter three

Table 3.1. Details of diamonds used in this investigation..... p.143

Table 3.2. Activation energies for sub-threshold-excited photoluminescence, compared with the differences between the exciting energy and that of the corresponding zero-phonon line. All values for the activation energies are the averages of the results for all the samples. p.149

Table 3.3. Results of the analysis on samples with more than one sub-threshold-excited defect. Three samples containing both H4 and H3 centres were measured; in each case the activation energies were ill-defined and only the average activation energy derived from the ratio plots is given. Only one sample containing both H4 and 3H defects has been analysed..... p.151

Chapter four

Table 4.1. Positions, intensities and assignments of the hydrogen-related absorption peaks in natural diamond (Davies *et al.* 1984, Fritsch *et al.* 1991 and this work). The very weak component at 5555 cm^{-1} has been observed only by Fritsch *et al.* p.160

Table 4.2. The samples and their respective carbon 12 content, the peak positions and relative shift compare to natural type IaA diamond. p.175

Table 4.3. The measured and calculated (from equation 4.3) ratio of the peak position of the various A defect related absorption features of natural and ^{13}C isotopically enriched diamonds. The bracketed values in table 4.3 are the values from the least squares fit of equation 4.3 to the experimentally determined ratio. p.177

Table 4.4. The fitting parameters for an unconstrained linear fit of the data in figure 4.12. ..... p.180

Table 4.5. The fitting parameters for a constrained linear fit of the data in figure 4.13. ..... p.180

Chapter five

Table 5.1. The change in concentration and FWHM of the GR1 defect ZPL of the sample after irradiation and annealing at 450°C (723 K). The concentration of vacancies is determined as described in chapter 1, section 7. ..... p.197

Table 5.2. The concentrations of A, B, C and N^+ defects in the diamonds and the D absorption coefficient at 1282 cm^{-1}, determined from the IR spectrum of the diamonds and the concentrations of neutral and negatively charged mono-vacancies in the different samples. All samples, except sample 10 were irradiated at 20°C. p.199

Table 5.3. The concentrations of A, B, C and N^+ defects in the diamonds and the D absorption coefficient at 1282 cm^{-1}, determined from the IR spectrum of the data of the samples of K. Iakoubovskii and the concentrations of neutral and negatively charged mono-vacancies in the different samples. All samples were irradiated at room temperature. The uncertainties in the concentrations are 10% and 30 % for defects determined by IR and UV-VIS measurements respectively. ..... p. 200

Table 5.4. The peak position, integrated intensity of the peak at ~ 1.679 eV in the samples. The values for peaks for sample 3 after annealing at 800 and 1000°C are also recorded. ND stands for not detected. p.207

Table 5.5. The concentrations of the various nitrogen-vacancy aggregates in the irradiated and annealed samples. $[C_{total}]$ is the total concentration of single nitrogen defects (C and N^+ defects). The uncertainty in the H3 and H4 concentrations is 30%. The uncertainties in the ratios [A]/[B] and [H3]/[H4] are 14% and 42% respectively. The uncertainty in the other calculated ratios is 45%. p.209

Table 5.6. The integrated intensity of the zero phonon lines of the different defects in the diamonds before and after UV illumination. p.229

Table 5.7. The integrated intensity of the zero phonon lines of the different defects in the diamonds before and after blue light illumination (470 nm). p.230

Chapter six

Table 6.1. The concentrations of the different forms of nitrogen in natural, colourless and brown type IaA and brown type IaB samples. No C defect concentration could be detected. The uncertainty on the concentration of the defects, determined by IR measurements is 10%. Uncertainty on the concentration of C defects determined by EPR and UV-VIS measurements is 25 % and 27 % respectively. p.247

Table 6.2. The concentrations of the different nitrogen related defect concentrations in the 1H3, 1H5 to 1H8 and FDW1 diamonds, before annealing. The uncertainty on the defect concentration is 10%. HPHT annealed at 2300°C for 5 minutes at Sundance Inc. p.248

Table 6.3. The concentrations of the different nitrogen related defect concentrations in the ak diamonds, HPHT annealed at 2300°C. The uncertainty on the defect concentration is 10%. p.249

Table 6.4. The defect concentrations in type Ia diamonds before HPHT annealing at 2300°C. The uncertainty on the defect concentration is 10%. p.249

Table 6.5. The concentrations of the nitrogen aggregates in the brown type IaA samples before HPHT annealing. The uncertainty on the concentration of the defects, determined by IR measurements is 10%. Uncertainty on the concentration of C defects determined by EPR and UV-VIS measurements is 25 % and 27 % respectively. p.250

Table 6.6. The concentrations of the different forms of nitrogen in the samples annealed at 2300°C and 5 – 6 GPa. All concentration values have a ± 10 % uncertainty. p.252

Table 6.7. The concentrations of the different nitrogen aggregates, detected in the IR spectrum of the brown type IaA/B ([A]<<[B]) diamonds before annealing. Samples tlb-1, 3, 5, 6, 7 and lb-1, 2, 3, 5, 6 are annealed at 2100°C in steps of 3 minutes and sample tlb-4 and lb-4, 7 and 8 are annealed at 2200°C also in steps of 3 minutes. There are no values for the sample tlb-7 because of strong background absorption in the one-phonon region, making the decomposition unreliable. The uncertainty on the defect concentration is 10%. p.257

Table 6.8. The nitrogen aggregate concentration as detected by IR, EPR and UV-VIS in the type IaB diamonds before HPHT annealing at 2100°C (samples B1b and Al84b) and 2200°C (samples B1a and Al84a). The uncertainty on the defect concentration

is 10%. Uncertainty on the concentration of C defects determined by EPR and UV-VIS measurements is 25 % and 27 % respectively. p.258

Table 6.9. The concentrations of nitrogen aggregates of colourless type Ia diamonds, before irradiation and HPHT annealing. The irradiation conditions of each diamond are given in the last two columns. The uncertainty on the defect concentration is 10%. p.259

Table 6.10. The concentrations of nitrogen aggregates of colourless type IaA diamonds, after HT and HPHT annealing at 1700°C. Uncertainty on the concentration of C defects determined by EPR, IR and UV-VIS measurements is 25%, 10%and 27% respectively. p.261

Table 6.11. The calculated and experimental concentration of C defects after annealing at 2300°C. The uncertainty on the concentration of the defects, determined by IR measurements is 10%. Uncertainty on the concentration of C defects determined by EPR and UV-VIS measurements is 25 % and 27 % respectively. p.270

Table 6.12. The calculated and experimental concentration of C defects after annealing at 2200°C for 6 minutes. The sample is a type IaB diamond with low concentration of A defects before annealing (5 ppm). There is a good agreement between the calculated concentration of C defects and the measured concentration of C defects. The uncertainty on the concentration of the defects, determined by IR measurements is 10%. Uncertainty on the concentration of C defects determined by EPR is 25 %. The UV-VIS absorption spectrum is shown in figure 6.21. .. p.271

Table 6.13. The concentration of C defects of different samples after HPHT and HT annealing at 1700°C for 1 hour. Sample starting with numbers 1, 4 and 7 were cut from the same rough diamond. Sample 5-2 had too high concentration of N3 defects before annealing, making the determination of C defect concentration from the UV-VIS spectrum unreliable. The uncertainty on the concentration of the defects, determined by IR measurements is 10%. Uncertainty on the concentration of C defects determined by EPR and UV-VIS measurements is 25 % and 27 % respectively. p.276

Table 6.14. The activation energies and the vibrational pre-factors determined from the simulations of the annealing behaviour of the A, C, H3 and $(N\text{-}V)^-$ defects in irradiated and high temperature (T ~ 1500°C) annealed type Ib diamond. p.284

Table 6.15. The tables give the integrated intensity in cm^{-2} of the 3107 cm^{-1} line before (time t = 0) and after subsequent HPHT annealing (at times t = 3, 6, 9, 12 and 15 min) at 2100°C (top table) and at times t = 3, 6, 9 and 12 min at 2200°C (bottom table). The uncertainties are ± 5 %. The "br" means the sample broke during annealing. p.286

Table 6.16. The parameters used in equation 6.6.9 to fit the data points, normalized with respect to the initial integrated intensity of the 3107 cm^{-1} line. The Chi square value of is also given. p.290

Table 6.17. The parameters used in the simulation of the change with annealing time of the H3 defect concentration. p.307

Table 6.18. The vacancy cluster, H3 and H4 defect dissociation energies, which fit the change of the H3 defect dissociation data with time in all samples..... p.313

Table 6.19. The χ^2 values calculated from the fit of equations 6.7.1 – 6.7.18 to the H3 defect data of samples of group 1 (left) and 2 (right)..... p.313

Table 6.20. The C defect concentrations in the irradiated and HPHT annealed type Ia diamonds. The concentrations of C defects were measured by IR, UV-VIS and EPR absorption spectroscopy. Uncertainty on the concentration of C defects determined by EPR, IR and UV-VIS measurements is 25%, 10% and 27% respectively. p.319

Chapter One

Introduction

1.1. Introduction

Perfectly crystallized diamond without point defects is colourless because of its wide electronic bandgap (5.49 eV at 77 K) (Clark *et al.* 1964). The presence of defects in the diamond lattice can induce local states in the bandgap of diamond. An electron can be promoted from one electronic state to a higher electronic state by the absorption of a photon. The optical absorption by these defects may give the diamond a colour.

Defects in diamond can be subdivided in two classes: intrinsic and extrinsic. Examples of intrinsic defects are vacancies, dislocations, stacking faults, interstitial carbon atoms, … Examples of extrinsic defects, are nitrogen and boron both of which are substitutional defects. Other, less studied impurities are hydrogen, silicon, nickel, and cobalt. Some of the large atoms can be present as interstitials (Isoya *et al.* 1990) while others occupy a position halfway between two vacancies (Nadolinny *et al.* 1999). Both configurations are supposed to decrease the stress of the defect due to its relatively larger atomic size, compared to the carbon host lattice atom. Hydrogen is not commonly studied defect in semiconductors as it is elusive, unless bonded to a host lattice or another impurity atom.

The bonding in diamond between the carbon atoms is purely covalent and consequently there is no strong absorption in the infrared spectral region. Weak intrinsic absorption due to two and three phonon combination bands of diamond can be seen in the infrared absorption spectrum between 4000 and ~1330 wavenumbers (Lax and Burstein 1955). Substitutional defects can induce small dipole moments leading to optical absorption in the one-phonon region of diamond (Lax and Burstein 1955).

Most natural diamonds contain nitrogen as a substitutional impurity, giving rise to characteristic absorption in the one-phonon region (Kaiser and Bond 1959). The classification of diamond is based on the presence and aggregation stage of nitrogen. Diamonds with nitrogen as an impurity are called type I, while diamonds without nitrogen are called type II (Robertson *et al.* 1934). In both categories further subdivisions are made: type Ia diamond contains nitrogen aggregated in groups of two (A defects), three (N3 defects) or four nitrogen atoms (B defects) (Boyd *et al.*1995, Davies 1976), while the majority of the nitrogen atoms in type Ib diamonds is in single substitutional form (Smith *et al.* 1959, Chrenko *et al.* 1971). Most synthetic diamonds are type Ib diamonds (Dyer 1965a). Type II diamonds are also subdivided into two different classes: type IIa diamond is relatively free from extrinsic impurities, while type IIb diamond has boron as the major impurity (Lightowlers and Collins 1976). This last type of diamond is also the only natural type of diamond which is semi-conductive (p-type).

Type Ia diamonds are also called type IaA, type IaB or type IaA/B depending whether the dominant defects are A defects, B defects or a combination of A and B defects.

Many of the nitrogen-related defects are optically active in the ultra-violet and visible spectral region (UV-VIS). The so-called N3 defect consists of three nitrogen atoms around a vacancy and the typical absorption spectrum gives the diamond a pale yellow colour, also known as the Cape colour. Pure type IaA diamond does not absorb visible light but has a number of sharp absorption lines and an absorption continuum in the UV region.

Radiation induced defects also have localised states in the bandgap and optical absorption due to vacancies and interstitials can be detected in diamond after irradiation with a sufficient dose and energy (Clark *et al.* 1956a, Davies 1974a, Smith *et al.* 2004). Depending on the presence of other point defects like nitrogen or hydrogen, annealing of the primary irradiation defects at typically 800 °C induces changes in the UV-VIS absorption spectrum as single nitrogen atoms and nitrogen aggregates can trap vacancies (Davies 1974a, Lawson *et al.* 1992a). For example, the A and B defects can trap a vacancy during the annealing and these convert into an H3 and an H4 defect respectively. After high temperature annealing, at approximately

1100 °C, additional defects can also be detected in the infrared spectrum of the diamond. These defects are thought to consist of a nitrogen aggregate and a radiation damage product, the so-called 594 nm defect (Collins *et al.* 1986). Depending on the type of aggregate (A defect or a B defect), the defect created will be the H1b or H1c defect respectively. The decay of the 594 nm absorption strength and simultaneous growth of the H1b and H1c defects as a function of temperature has been studied by Collins *et al.* (1986).

In all cases, colour in diamond is caused by absorption of light by one defect or a combination of defects. The colour of a sample depends on its spectrum and can be characterised by a colour coordinate in the CIE chromaticity diagram, see appendix A. At room temperature, optical absorption spectra caused by defects consist of a broad band giving diamond a specific colour. This broad band is caused by electron-phonon coupling which is the interaction between the phonons in the lattice and the electronic levels of the defect in the bandgap (the next section will give a review of linear electron phonon coupling). As a result, the optical absorption related to the transition between two electronic levels is a sharp line (the so-called zero phonon line), plus a so-called side band. At room temperature, the line and side band are broadened because of various interactions and are in the majority of cases indistinguishable. The mono-vacancy in diamond has a zero phonon line (GR1 line) at 741 nm and a broad side band with a maximum at ~ 620 nm, giving the diamond a blue to blue-green colour. Depending on the irradiation dose and energy, additional absorption starting at 500 nm and increasing with shorter wavelength, can be detected in irradiated diamonds. The result of the combination of this increasing absorption and the GR1 band is a transmission window at ~ 500 nm in the VIS absorption spectrum, giving the diamond a green colour. Other defects like the 594 nm defect give the diamond a golden-yellow colour. H3 and H4 defects absorb light with a wavelength shorter than 500 nm and give the diamond a yellow colour. Fluorescence or emission of light of these defects peaks at 520 nm and is perceived as green. The presence of H3 and H4 defects can therefore colour the diamond yellow-green.

Naturally coloured gem diamonds have become very fashionable in recent years, and thus are very expensive because of their rarity. Colourless diamonds are also very high in price, for the same reason. The price of a diamond as a function of colour

saturation looks like the curve in figure 1.1: a diamond with a rare colour is more valuable. Colour is one of the so-called four Cs determining the price of a diamond. The other three are Clarity, Cut and Carat (weight). The points where the price changes rapidly are taken arbitrarily as this figure only serves as an illustrative example.

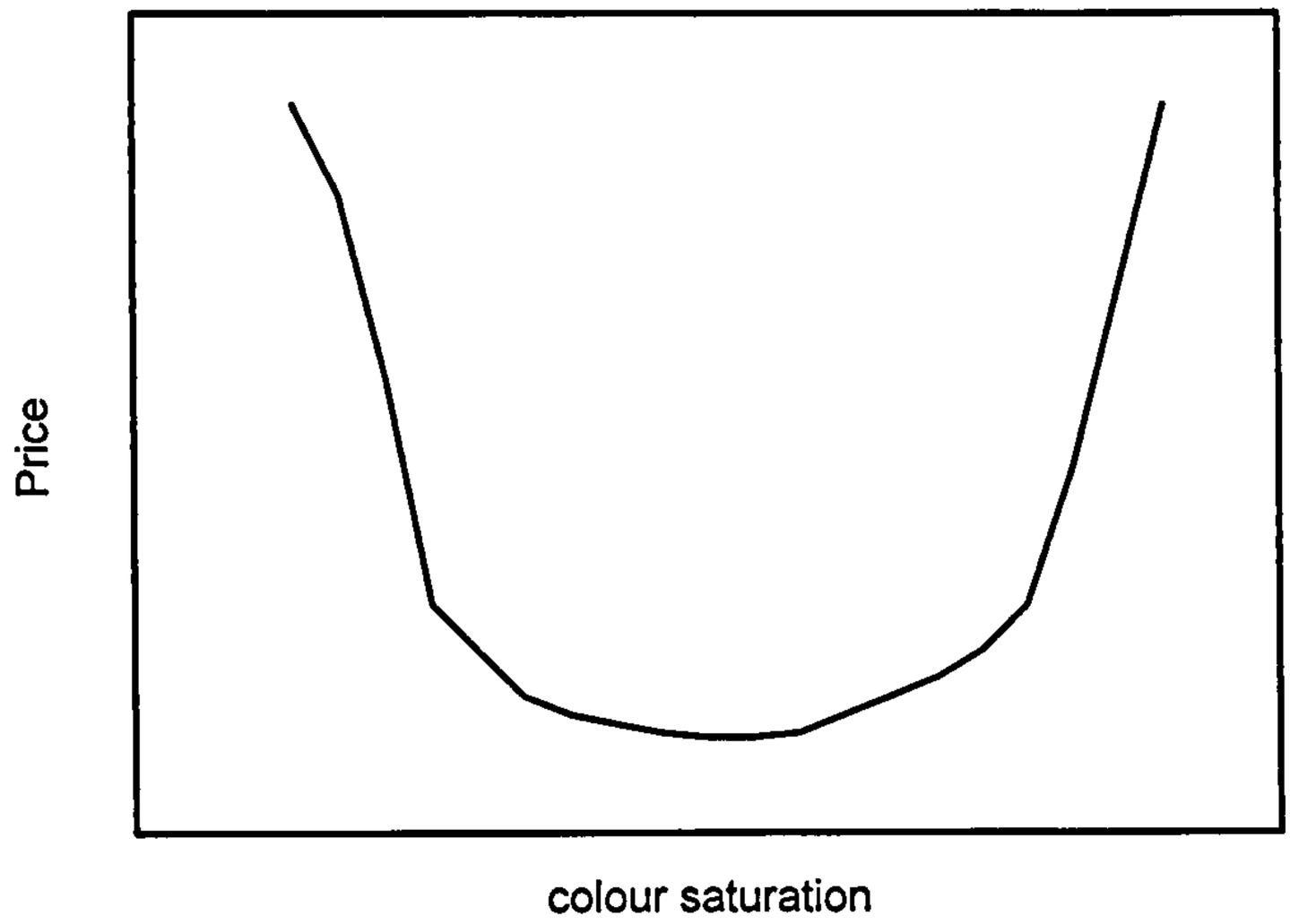

Figure 1.1. This figure illustrates the price of gem-diamond as a function of colour saturation. The price of the gem-diamond falls off rapidly with a higher degree of colour saturation. At a certain point, diamonds with a higher degree of colour saturation are more rare, which makes the diamond more valuable.

It is clear that there is a very high potential profit increase when a diamond with a low and relatively cheap colour grade can be turned into a diamond with a colour grade where the price is at a maximum of figure 1.1, i.e. colourless (left maximum) or fancy colour (right maximum). The GE-POL process aims at making colours with low colour saturation (Smith *et al.* 2000) by High Pressure High Temperature (HPHT) annealing of relatively cheap brown type IIa diamonds. The high price of fancy coloured diamond has prompted many people to try to design treatments to change the colour of an unattractive (and relatively cheap) diamond into a rare, exclusive and thus high priced coloured diamond (Templesman 1999, De Weerdt and Van Royen 2000).

In recent years, the colour treatment business has become an industry. The cheap and easy dying treatment, where the culet or the girdle of a polished gem diamond is

stained with a coloured dye, has become obsolete and more sophisticated treatments like irradiation, irradiation and heat treatment or HPHT annealing have become more fashionable, partly because of their more permanent character. High Pressure (P > 7 GPa) High Temperature (T > 2000°C) annealing mimics the temperature and pressure conditions deep in the earth and as a result the HPHT annealed diamonds are in some cases difficult to distinguish from untreated natural diamonds (Rappaport 1999, Smith *et al.* 2000). Gem laboratories need to keep up and be able to distinguish between naturally coloured and artificially coloured diamonds. Highly sophisticated techniques are used nowadays to detect these kinds of treatments. The results of these treatments are strongly dependent on the type of diamond, and the different types of diamond can be distinguished with the aid of infrared and UV-VIS spectroscopy.

Understanding how defects are created and destroyed by various treatments or combinations of treatments is the main motivation of this thesis.

The thesis is organised as follows:
Before explaining how to distinguish between the different types of diamond, this first chapter will give an introduction about the different spectroscopic techniques, and the theoretical background of the concepts, which are used throughout the whole thesis. The last section of the chapter will give an overview of the available data on defect production by irradiation, irradiation and heat treatment and high-pressure high-temperature treatment respectively.

Chapter Two will show a straightforward application of linear electron-phonon coupling theory which can be used to calculate the shape of a spectrum. The spectra under study are broad band emission and 490.7 nm emission spectra, only detected in type Ia brown diamonds.

Chapter Three will discuss the sub-threshold excitation of defects in diamond, which is a non-straightforward application of electron-phonon coupling of a defect.

Chapter Four will focus on the properties of absorption in the infrared region due to hydrogen and nitrogen in diamond. The investigation is done by isotopic substitution of carbon 12 by carbon 13. Defect vibrations are connected to the attempt-to-escape

frequency when the defect diffuses through the diamond lattice or dissociates into its components. This attempt-to-escape frequency can be illustrated by imagining two atoms, chemically bonded together. At temperatures above zero Kelvin, this molecule will vibrate and can dissociate at a certain temperature. This means the molecule can dissociate when energy is added. This dissociation can take place every time the two atoms move in opposite direction. For sake of simplicity, imagine the molecule can only vibrate with one single frequency v; then the chance to dissociate is equal to $v.\exp(-E/k_BT)$. E is the energy required to break the bond, k_B is the Boltzmann constant and T the temperature.

Chapter Five will study some of the irradiation-induced defects in the infrared and UV-VIS spectrum of diamond and the change in the absorption spectra after annealing. The capture of vacancies by nitrogen-related defects is studied in this chapter and is of importance for chapter six. Some of these defects created during the annealing of irradiated type Ia diamond, like the 594 nm, the H1b and H1c defects are not observed in HPHT annealed type Ia diamonds, while other defects like the H3, H4 and the 637 nm defect are observed. The H1b and H1c defects display sample dependent photo-induced changes of their absorption strength, which can be recovered by thermal annealing. This process is investigated, but the origin of this effect is, at present, unclear.

Chapter Six will discuss the results of HPHT annealing on the dissociation of nitrogen aggregates, on hydrogen related defects and the formation of nitrogen (aggregate)-vacancy related defects during HPHT annealing. Some of the optical centres created by HPHT annealing of brown type Ia diamonds are the same as those produced in type Ia diamonds by radiation damage and annealing at typically 800 °C. The production of the former can be understood in terms of vacancies being released during HPHT annealing. The influence of these vacancies and of pressure on the activation energy and aggregation/dissociation kinetics of the defects will also be studied.

Chapter Seven will draw the conclusions from the studies and will point to further work.

Appendix A will show the method to quantify colour of a diamond by measuring its spectrum.

Appendix B will focus on an alternative path of H3 defect dissociation.

Appendix C will show some photos of diamonds that have been artificially coloured by various methods described in this thesis.

1.2. Linear electron-phonon coupling theory and Jahn-Teller distortion

1.2.1. Linear electron-phonon coupling

An understanding of electron-phonon coupling theory is necessary as this thesis employs optical spectroscopy to characterise defects in diamond; the formation of the spectral lines and side bands in the spectra depends strongly on the electron-phonon coupling of the electrons of the defect. For example: linear electron-phonon coupling determines the broadening and intensity behaviour of the zero phonon lines (ZPL, absorption lines which do not involve phonons) with temperature, and quadratic electron-phonon coupling is responsible for the shift of the ZPL with temperature (Davies 1970, Davies 1974a, Davies 1981a). Also, it will enable us to differentiate between defects with zero phonon lines with almost the same position in the spectrum but with different electron-phonon coupling.

The origin of the electron-phonon coupling can be understood from the following intuitive example: an impurity in the diamond lattice has a different electron distribution from that of the host lattice atoms, as it has a different number of electrons or different size. The absorption of light will promote an electron from the ground state orbital to a different orbital, thereby changing the electron distribution around the defect. The lattice will relax rapidly by creating phonons and as a result the absorption is a combination of electronic and vibrational, referred to as "vibronic" processes. As stated in the previous section, this results in the appearance of a side band in the absorption and luminescence spectra and these side bands are responsible for the colour in diamond due to point defects. This is a second motivation to study the electron-phonon coupling in diamond: electron-phonon coupling will determine

whether a defect is important in diamond treatments or not: defects with strong linear electron phonon coupling will colour the diamond with low concentrations, while defects with weak electron phonon coupling will require high concentrations to reach the same colouration effect.

To illustrate the effects of linear electron-phonon coupling, we assume the electronic states of the defect in the bandgap of diamond are well separated from the valence and conduction band and only non-degenerate states are present (the presence of degenerate states can lead to splitting of the states, thereby lifting the degeneracy. This is the Jahn-Teller effect and it is discussed in the next section). The number of optical transitions and the degeneracy of the transition for a given defect which is electric dipole allowed, is imposed by the symmetry of the defect. For a given point group, the electric dipole allowed transitions can be determined by the direct product of the irreducible representation of the symmetry group with the dipole irreducible representation. The dipole irreducible representations transform as x, y or z, and fortunately these are tabulated in character tables. If Γ_{GS}, Γ_{dipole} and Γ_{ES} represent the irreducible representation of the ground state, the electric dipole and the excited state of the defect respectively, then dipole-allowed optical transitions can be found when the direct product

$$\Gamma_{GS} \otimes \Gamma_{dipole} \otimes \Gamma_{ES} \qquad (1.2.1)$$

contains the totally symmetric irreducible representation. The same restriction holds for the symmetry of the phonon which can couple to the electrons of the defect:

$$\Gamma_{GS} \otimes \Gamma_{dipole} \otimes \Gamma_{ES} \otimes \Gamma_{phonon} \supset \Gamma_{TS} \qquad (1.2.2)$$

here Γ_{phonon}, and Γ_{TS} are the irreducible representations of the phonon and the totally symmetric representation respectively. Clearly the totally symmetric phonon always couples to a defect.

In a crystalline diamond, the defect is surrounded by N atoms, with N in the order of 1.76×10^{20} carbon atoms per mm^3, giving ($3N$-6) vibrational modes. For the sake of

simplicity we assume that there is only one mode coupled to the defect, and thus the electronic ground state of the electron of the defect is in the following vibrational potential:

$$V_g = \frac{1}{2} m\omega^2 Q^2 \qquad (1.2.3),$$

here m is the mass, ω the angular frequency and Q the instantaneous displacement of the mode. If the electronic state is not coupled to the lattice, then the excited state will have an equal vibrational potential. However, if the defect has a linear coupling to the lattice, the potential has an additional term, linear in Q, say aQ:

$$V_e = E + \frac{1}{2} m\omega^2 Q^2 + aQ \equiv E + \frac{1}{2} m\omega^2 \left(Q + \frac{a}{m\omega^2} \right)^2 - \frac{a^2}{2m\omega^2} \qquad (1.2.4).$$

E is the energy difference between the electronic ground and excited state. One can clearly see the motivation for linear electron-phonon coupling: the energy of the excited states is relaxed:

$$E_R = \frac{a^2}{2m\omega^2} \qquad (1.2.5).$$

However, the equilibrium point for the excited state has now shifted from $Q = 0$ to

$$Q_0 = -\frac{a}{m\omega^2} \qquad (1.2.6)$$

.

See figure 1.2 for a schematic diagram of the effects of linear electron-phonon coupling.

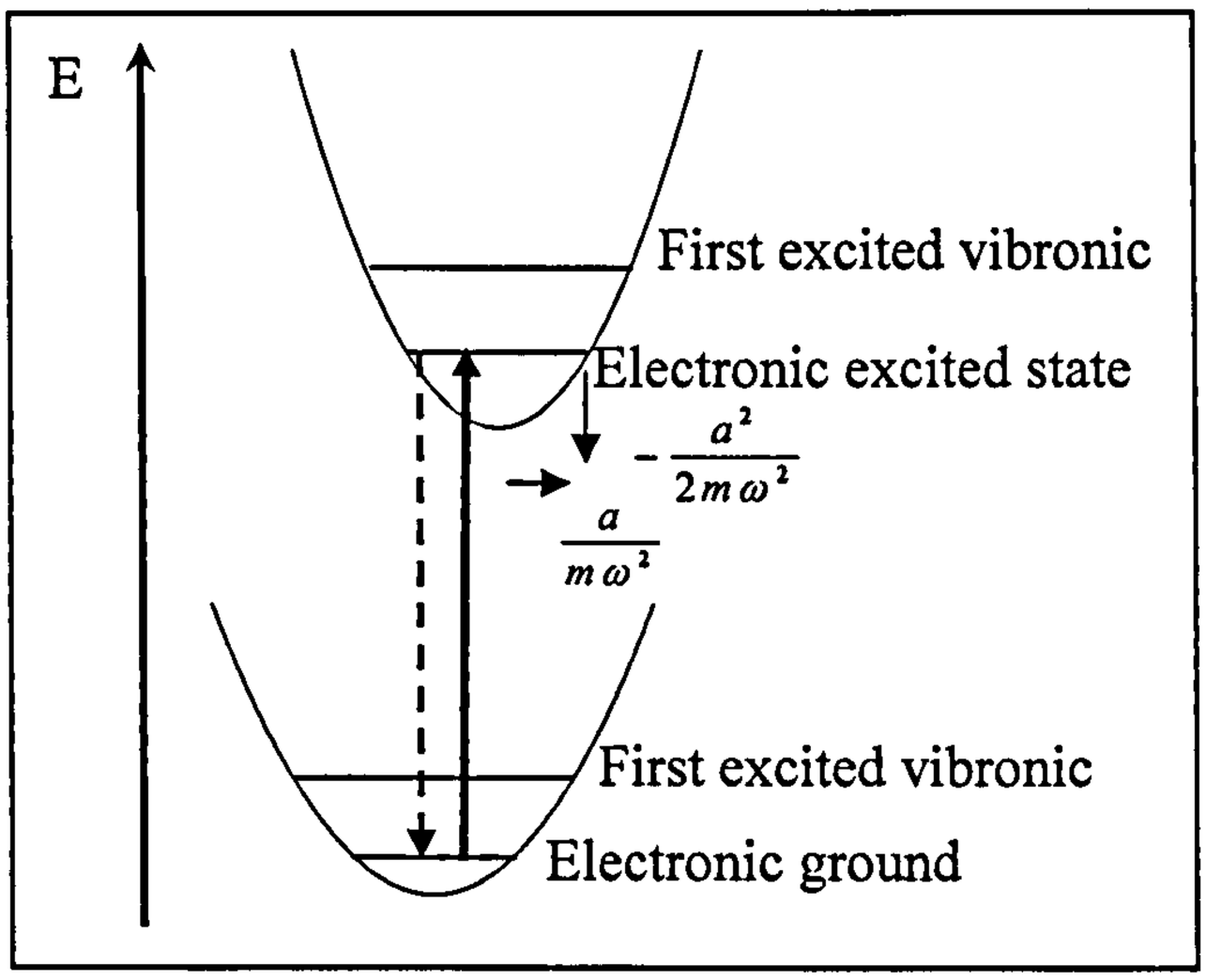

Figure 1.2. Linear electron-phonon coupling shifts the equilibrium of the vibrational potential surface of the excited state with respect to the ground state, and lowers the energy of the excited state.

The strength of the coupling is characterized by the Huang-Rhys factor *S* (Davies 1981a):

$$S = \frac{a^2}{2m\hbar\omega^3} \equiv \frac{E_R}{\hbar\omega} \qquad (1.2.7)$$

A full account of linear electron-phonon coupling is given in Davies (1981a). This will not be replicated here, but the main results, necessary to calculate and understand the temperature behaviour of the absorption/emission sidebands are summarized below.

The relative intensity I_n of the n^{th} phonon replica with respect to the ZPL transition intensity follows a Poisson distribution:

$$I_n = e^{-s}\frac{S^n}{n!} \qquad (1.2.8)$$

So the Huang-Rhys factor determines the relative intensity of the transition in the side-band (figure 1.3). As a consequence the maximum of the side band will shift to

higher energy in absorption and lower energy in emission spectra (figures 1.3 and 1.4).

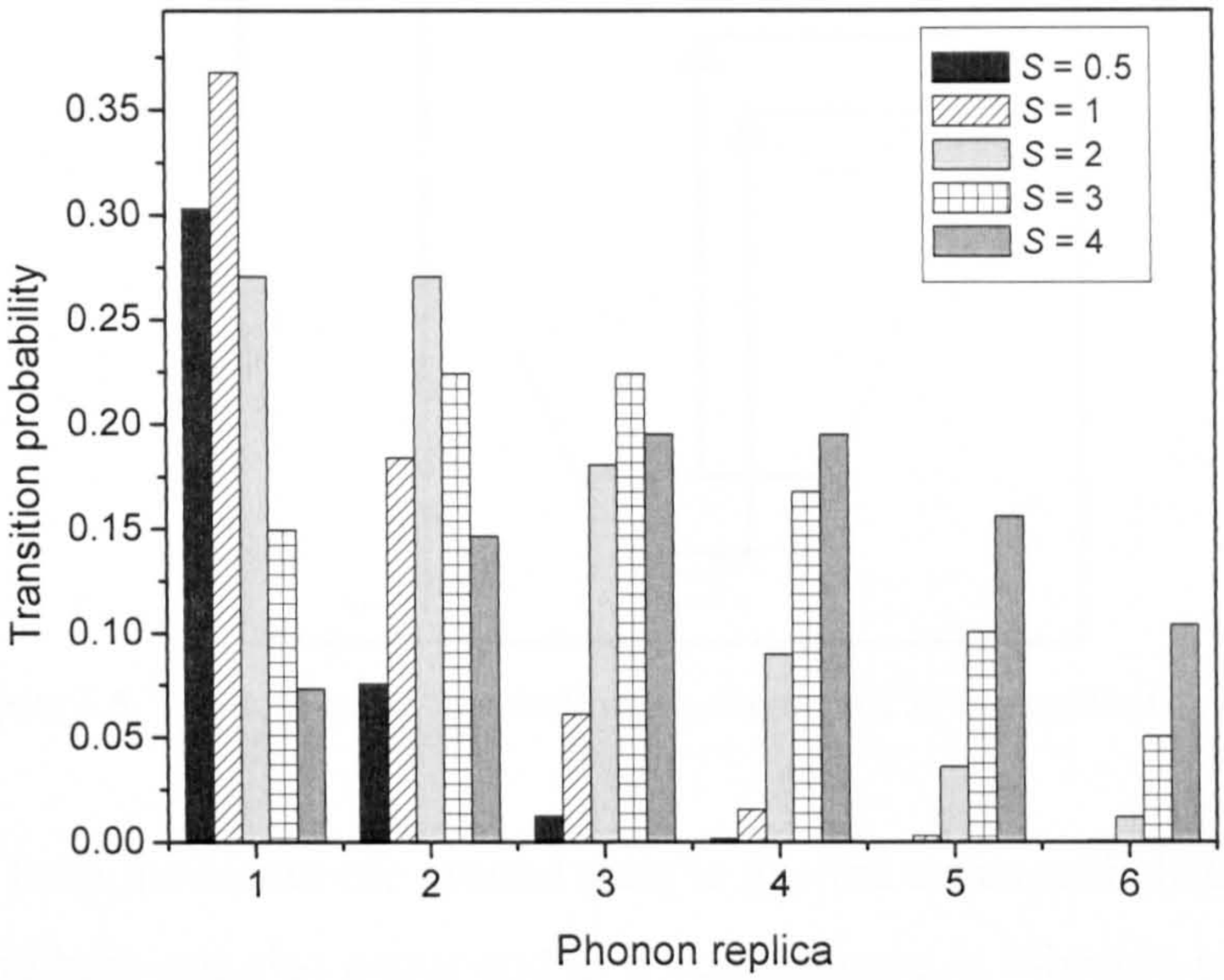

Figure 1.3. The transition probability of the one to six phonon replica of the Zero Phonon Line as a function of the Huang-Rhys factor. A defect with a low Huang-Rhys factor will have no high order side band, while a defect with a high Huang-Rhys factor will have a strong side band and the maximum of the transition probability will shift away from the ZPL.

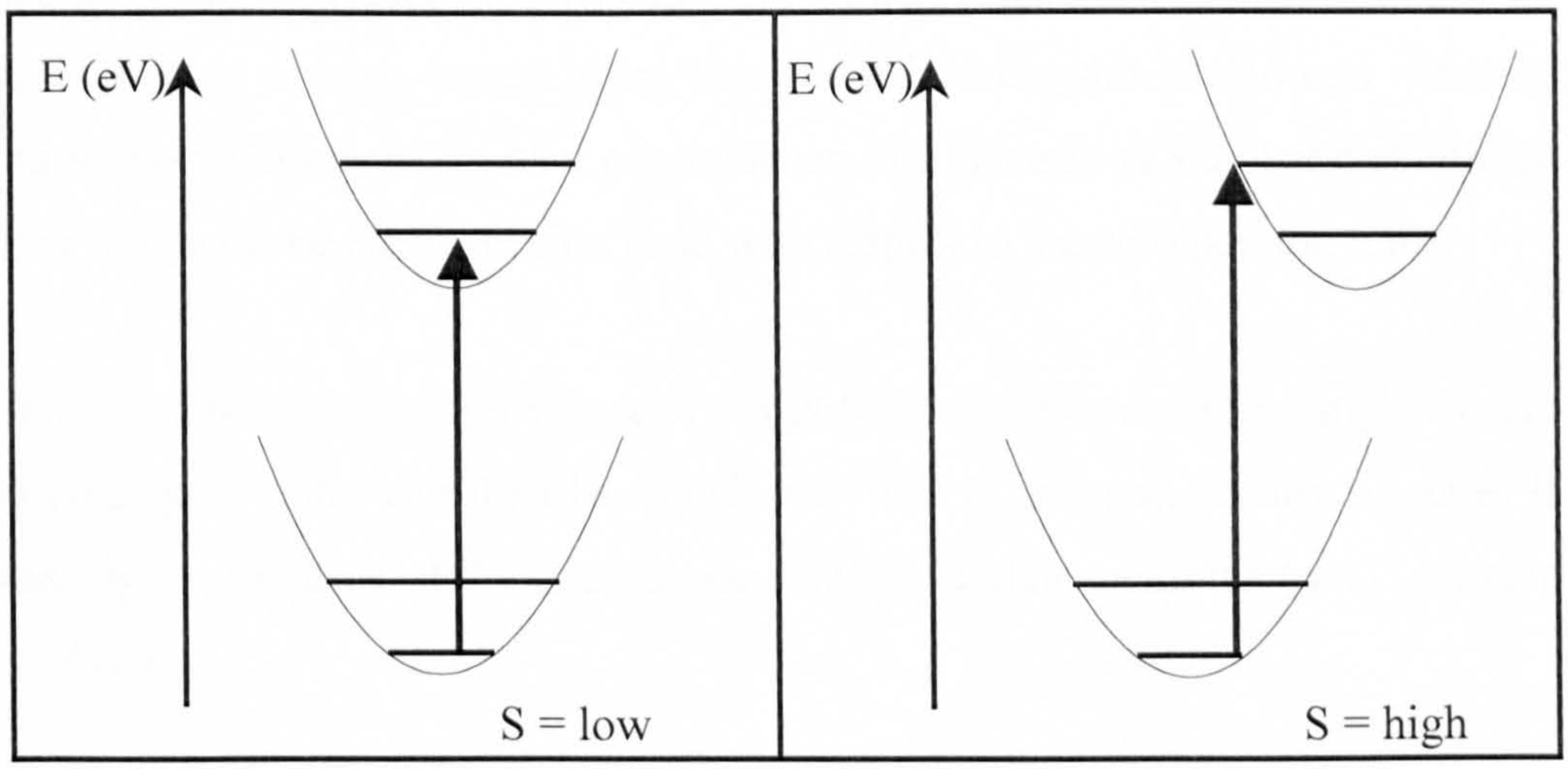

Figure 1.4. The configuration coordination diagram of defects with different Huang-Rhys factor.

The Zero Phonon Line transition includes all transitions from ground state to excited state with the same vibrational quantum number (see figure 1.5):

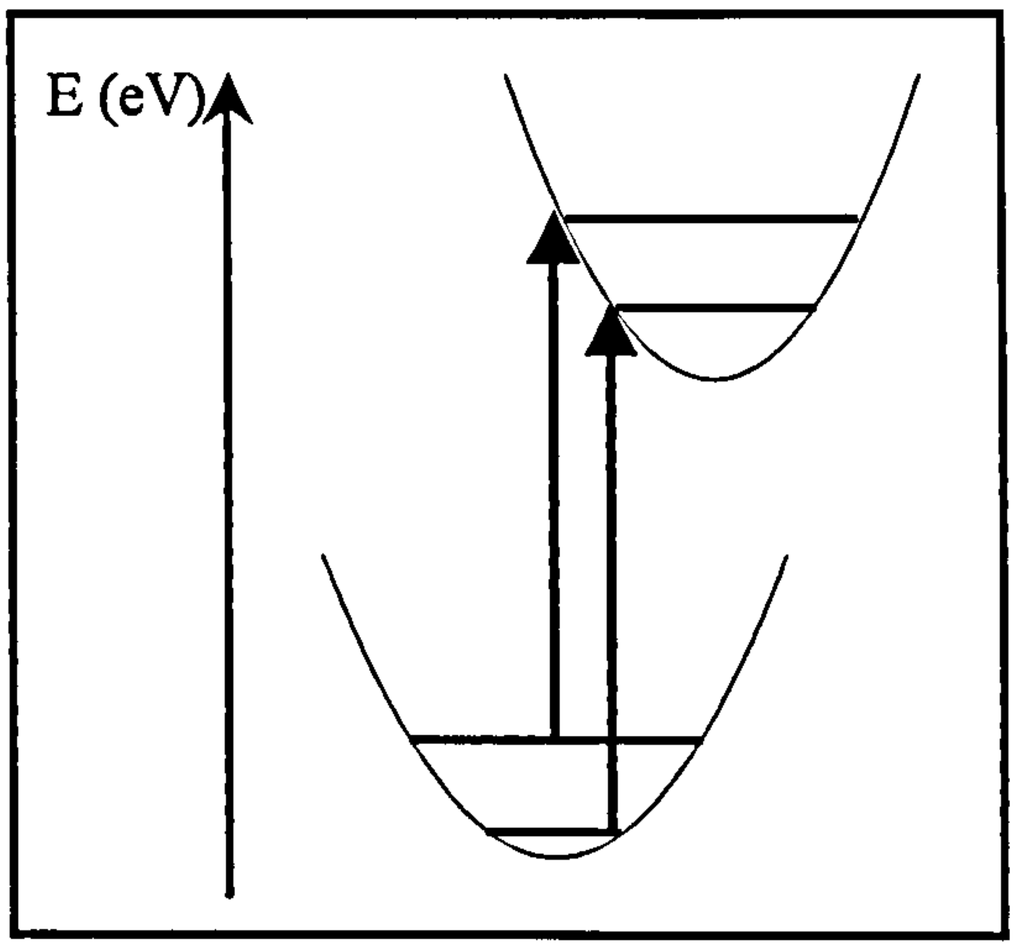

Figure 1.5. The configuration coordination diagram of ZPL transitions.

Transitions from the electronic ground state to excited states with different vibrational quantum numbers can also occur and as a consequence, a vibronic side band occurs. The excited electrons rapidly decay to the lowest excited state (with vibrational quantum number zero) and then de-excite to the electronic ground state or a vibronic level above the ground state. The de-excitation to the vibronic state with the lowest vibrational quantum number is the most probable and this is known as Kasha's Rule, proposed by professor Kasha (1950), which states that emission of a photon in the de-excitation process always occurs from the excited state with the lowest vibronic quantum number (figure 1.6). As a consequence, the absorption side band should be the mirror image of the emission side band with respect to the zero phonon line.

When the one-phonon density of states $I_1(v)$ is known, the second and higher order phonon density of states can then be calculated. The n^{th} phonon density of states is calculated by convolution of the one-phonon density of states with the $(n\text{-}1)^{th}$ phonon density of states:

$$I_n(v) = \int_0^{\omega_m} I_1(x) I_{n-1}(v-x)\,dx \qquad (1.2.9)$$

where v is the frequency of the zero phonon line, x is the frequency of the phonon and ω_m is maximum frequency of the phonon.

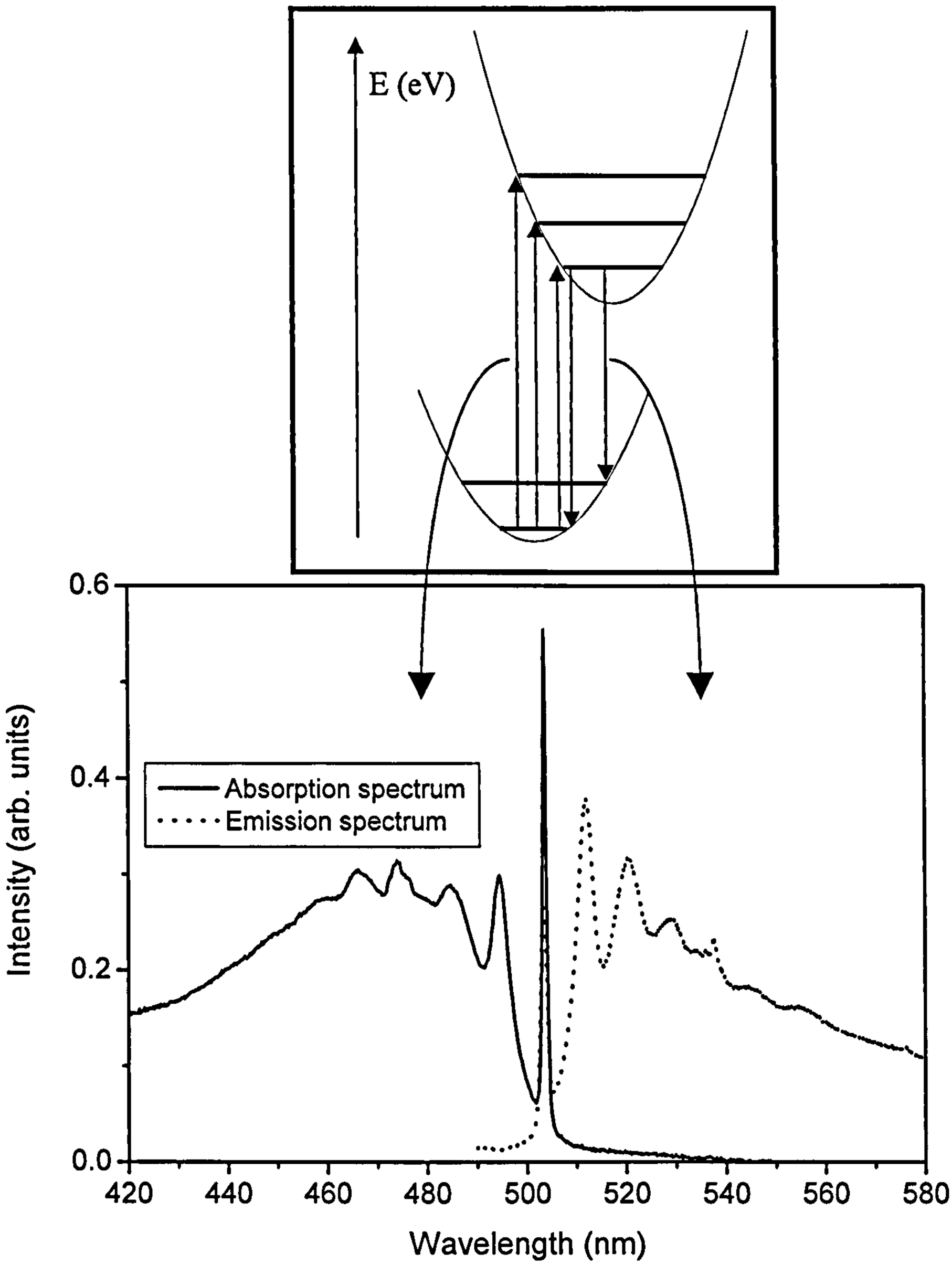

Figure 1.6. The absorption of light promotes an electron from the ground state to the excited state. The electron rapidly thermalizes to the excited state with lowest vibronic quantum number and de-excites back to its ground state or a vibronic level above the ground state. If the de-excitation is radiative, a photon is emitted and fluorescence is generated in the defect. A typical example of absorption and emission spectra is illustrated here for the H3 defect. There is no mirror symmetry between the emission and absorption spectra because of the presence of a second state close to the excited state.

In practice, a one-phonon density of states is constructed from an experimental spectrum.

A number of methods have been employed to calculate the side band due to electron-phonon coupling, some of them founded on fundamental theoretical considerations (Sangster 1972), others by semi-empirical means (Mostoller *et al.* 1971). We have adopted the procedure described by Davies (1981a).

The absorption or emission spectrum is first multiplied by the square or cube of the phonon frequency, respectively, to give the transition probability for absorption and emission of photons. The zero phonon line is fitted by a Lorentzian line and subtracted from the spectrum. In the spectrum, a baseline is drawn between the base of the ZPL and the cut-off frequency of diamond vibrations (165 meV from the ZPL) (Angress and Hall 1979). This spectrum is used as a trial one-phonon density of states.

Each higher order phonon density of states is then calculated from equation 1.2.9 and normalized in intensity according to equation 1.2.8. The difference between the experimental and calculated spectrum is then used to correct the one-phonon density of states. The whole procedure is then reiterated until a sufficient fit of the calculated spectrum to the experimental spectrum is reached. It should be noted that I_n is a transition probability and must be multiplied by the phonon frequency v to calculate an absorption spectrum and by v^3 to give a luminescence spectrum. This procedure is tested against known results from Davies (1981a) (figure 1.7).

The linear electron-phonon coupling has important consequences for the temperature behaviour of the zero phonon line: the ZPL will display a temperature dependent behaviour because more phonons will be excited in the crystal at higher temperature.

$$I_0 \propto \prod_{i=1}^{N}\left[\exp\left(-\frac{S}{N}\cosh\left(E_i/k_BT\right)\right)J_0\left(\frac{S}{N}\operatorname{csch}\left(E_i/k_BT\right)\right)\right] \qquad (1.2.10)$$

Here I_0 is the transition probability of the zero phonon line, S the Huang-Rhys factor, N the number of phonons interacting with the defect, E_i the energy of the phonon, k_B the Boltzmann constant, and T the temperature. J_0 is a Bessel function.

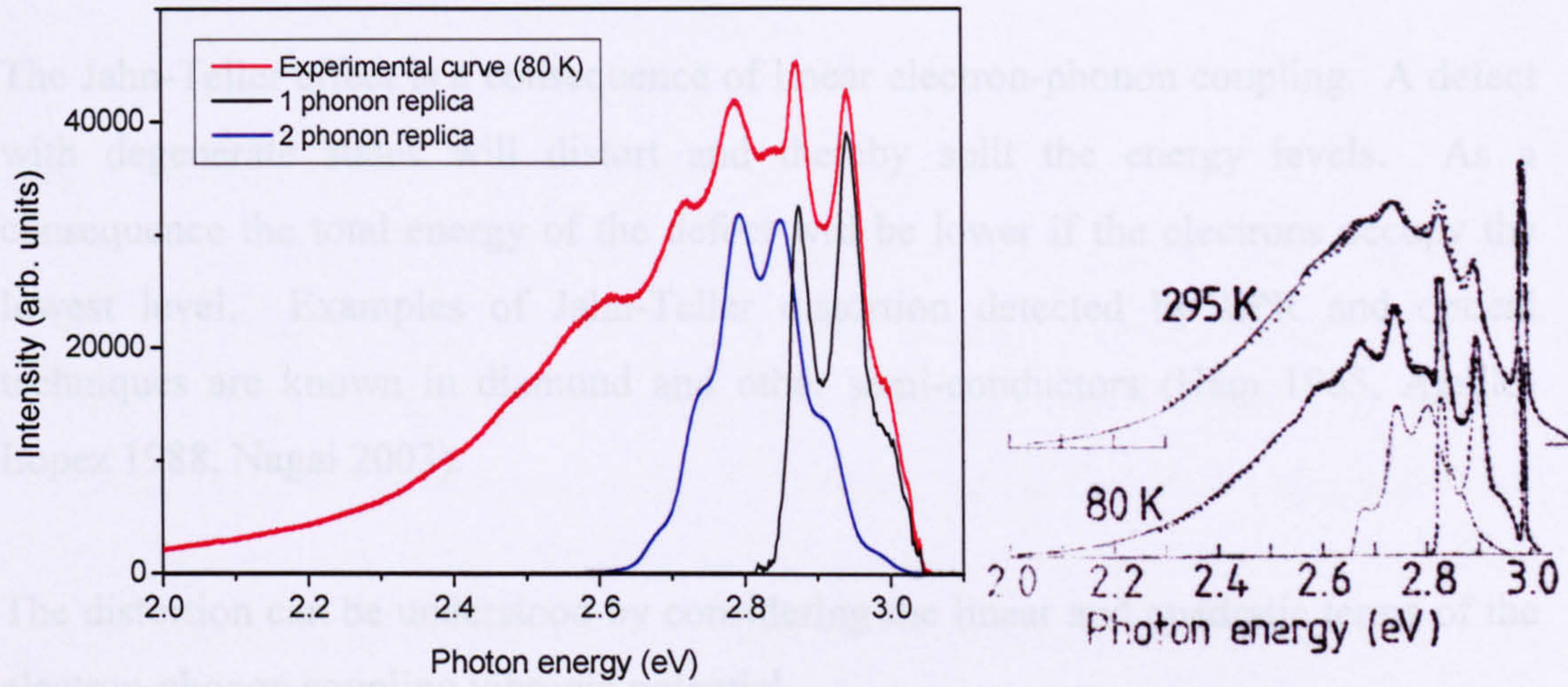

Figure 1.7. The one and two-phonon density of states of the N3 defect as calculated by the procedure described in the text above (left) and of Davies (1981a) (right). The zero phonon line has been removed in the figure on the left.

Finally, quadratic electron-phonon coupling has consequences on the ZPL: both the width W and position P of the ZPL are affected by the quadratic electron-phonon coupling (Mostoller *et al.* 1971, Davies 1981a).

$$W(T) \propto \int_0^{\omega_{\max}} [I_1(\omega)]^2 \, n(\omega)[n(\omega)+1] d\omega \qquad (1.2.11)$$

and the position P of the ZPL shifts with temperature as:

$$P(T) \propto \int_0^{\omega_{\max}} I_1(\omega) n(\omega) d\omega \qquad (1.2.12)$$

with $I_1(\omega)$ the one phonon density of states and $n(\omega)$ the Bose population term

$$n(\omega) = [\exp(\hbar\omega / k_B T) - 1]^{-1} \qquad (1.2.13)$$

1.2.2. Jahn-Teller effects

The Jahn-Teller effect is a consequence of linear electron-phonon coupling. A defect with degenerate states will distort and thereby split the energy levels. As a consequence the total energy of the defect will be lower if the electrons occupy the lowest level. Examples of Jahn-Teller distortion detected by EPR and optical techniques are known in diamond and other semi-conductors (Ham 1965, Agullo-Lopez 1988, Nagai 2003).

The distortion can be understood by considering the linear and quadratic terms of the electron-phonon coupling vibronic potential.

$$V = aQ + bQ^2 \qquad (1.2.14)$$

The energy levels depend on Q as in figure 1.8 below.

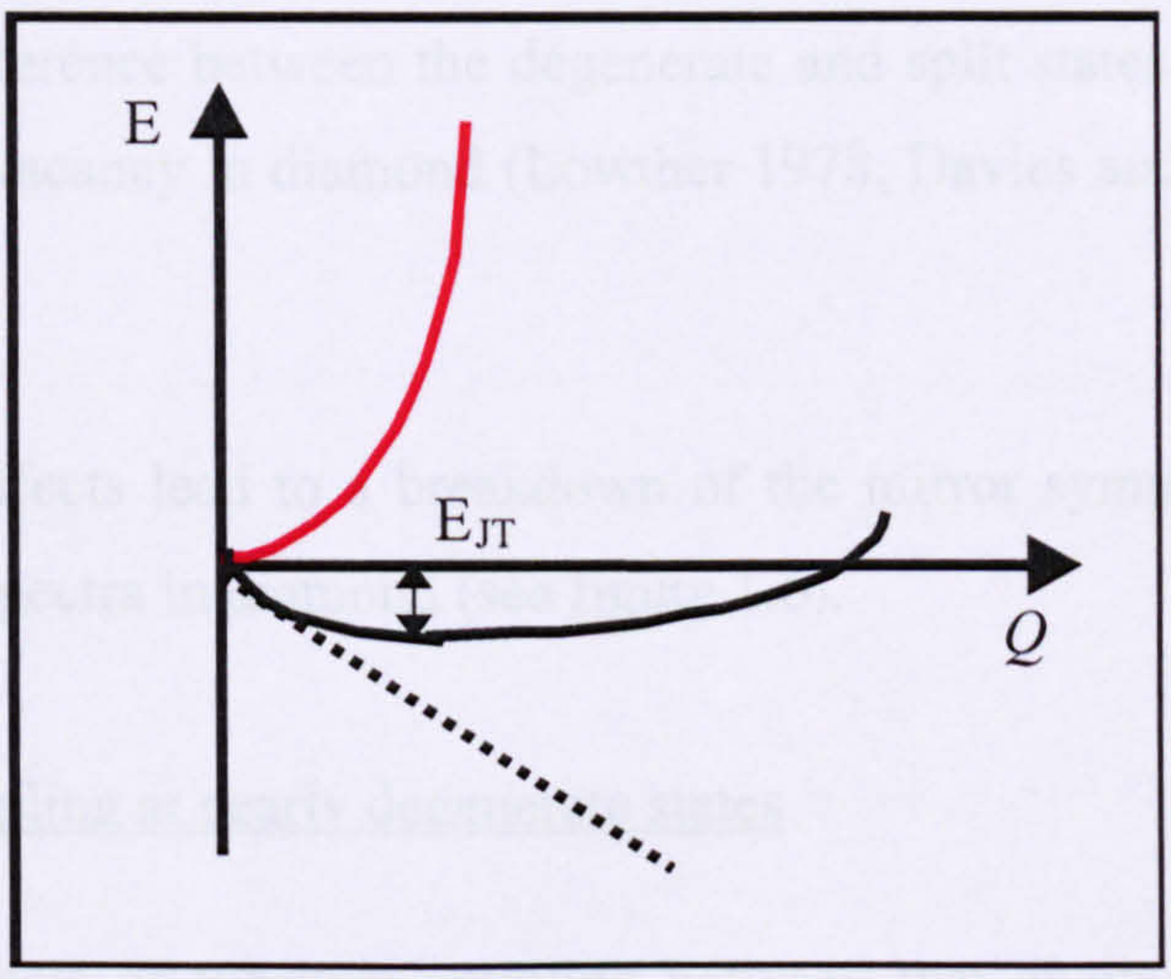

Figure 1.8. A schematic plot of the Jahn-Teller splitting due to linear coupling (---), quadratic coupling (—) and to linear and quadratic coupling combined (—).

A minimum occurs around coordinate Q_0, with an associated energy E_{JT}, the Jahn-Teller stabilization energy.

In a crystal there will be several equivalent minima as the crystal lattice is periodic in space. If the vibrational energy $\hbar\omega$ is comparable to the Jahn-Teller splitting, the different states cannot be clearly identified. This can be detected for the single

substitutional nitrogen (or P1 defect) by EPR (Loubser and van Wyk 1978, Davies 1981a, Ammerlaan and Burgemeister 1981).

One has to distinguish two types of Jahn-Teller effects:

- The static Jahn-Teller or configurational Jahn-Teller effect where the defect changes from a higher symmetry to a lower symmetry configuration (Opik and Pryce 1957). For example the single substitutional nitrogen defect changes from T_d symmetry to C_{3v} in diamond by elongation of one of the carbon-nitrogen bonds (Loubser and van Wyk 1978, Davies 1981a). As a result there are four equivalent configurations, and reorientation between these equivalent configurations requires an activation energy of 0.7 eV (Loubser and van Ryneveld 1967, Ammerlaan and Burgemeister 1981, Breuer and Briddon 1996).
- The dynamic Jahn-Teller or electronic Jahn-Teller effect where a high symmetry degenerate ground state of a defect will split into lower symmetry states (Longuet-Higgens *et al.* 1958) where the lowest state will be the lowest in energy, but the total energy difference between the degenerate and split states will be equal. An example is the vacancy in diamond (Lowther 1978, Davies and Foy 1980, Davies 1981b)

Both Jahn-Teller effects lead to a breakdown of the mirror symmetry of absorption and luminescence spectra in diamond (see figure 1.6).

1.2.3. Vibronic coupling at nearly degenerate states

A study of the effects of vibronic coupling between two excited states with small energy separation is given by Davies (1981a). No reproduction of this publication is made here, but a short recapitulation of the essentials will be given below.

Suppose we have two non-degenerate states φ_a and φ_b, separated by an energy difference W. The two states can couple through a vibrational mode with coordinate Q. This gives a deformation ΔV of the potential surface with

$$\Delta V = \tilde{O} Q \qquad (1.2.15)$$

Where $\tilde{O}$ is an operator such that the coupling C between the states is non-zero:

$$C = \int dr \varphi_a^*(r) \tilde{O} \varphi_b(r) \neq 0 \qquad (1.2.16)$$

The coupling of the two states by a totally symmetric mode (A_1 mode) will cause a quenching of the vibronic coupling itself.

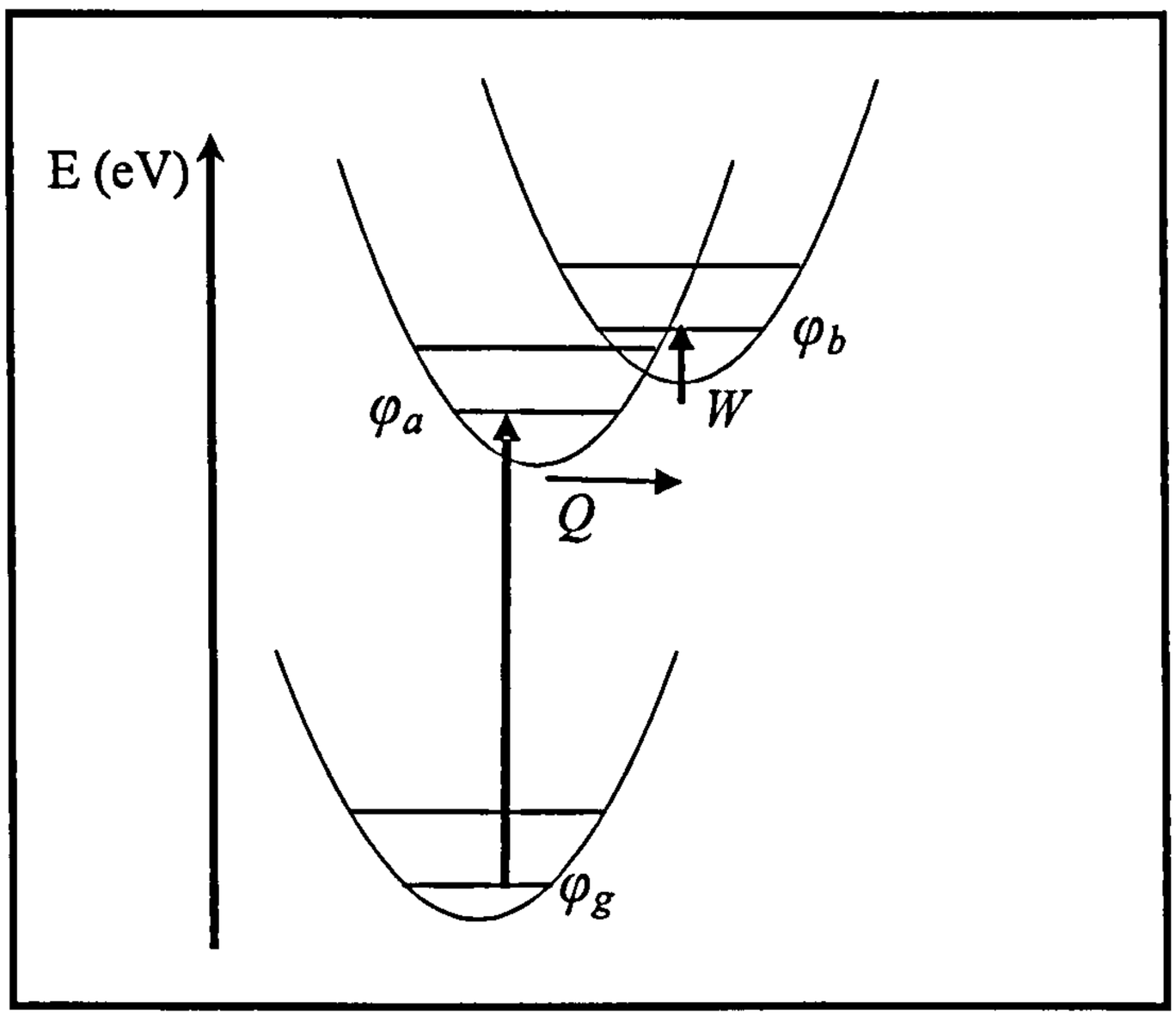

Figure 1.9. The configuration coordination diagram in the presence of two non-degenerate excited states.

Suppose now that we have a third state φ_g and transitions are allowed from the ground state φ_g to φ_a, but the transition to φ_b is not allowed. The coupling to non-totally symmetric modes will mix the states φ_a and φ_b by a phonon $\chi(Q)$, and this makes transitions possible from the state φ_g to the state $\varphi_b \chi(Q)$ but the transition to φ_b is still forbidden. However, a static distortion will mix states φ_a and φ_b and transitions from the ground state to φ_b are possible. This kind of static distortion can be induced by uniaxial stress (Davies 1976).

Examples of defects with nearly degenerate states in diamond are the H3 and the N3 defects.

In the H3 defect, the presence of an extra state at 16 meV above the first excited state induces a breakdown of mirror symmetry between the absorption and emission spectrum and uniaxial stress induces an extra zero phonon line in absorption (Davies 1981a, Davies *et al.* 1976). The optically active state induced by vibronic mixing of the two levels is ~ 150 meV above the zero phonon line. The energy level scheme is depicted in figure 1.10.

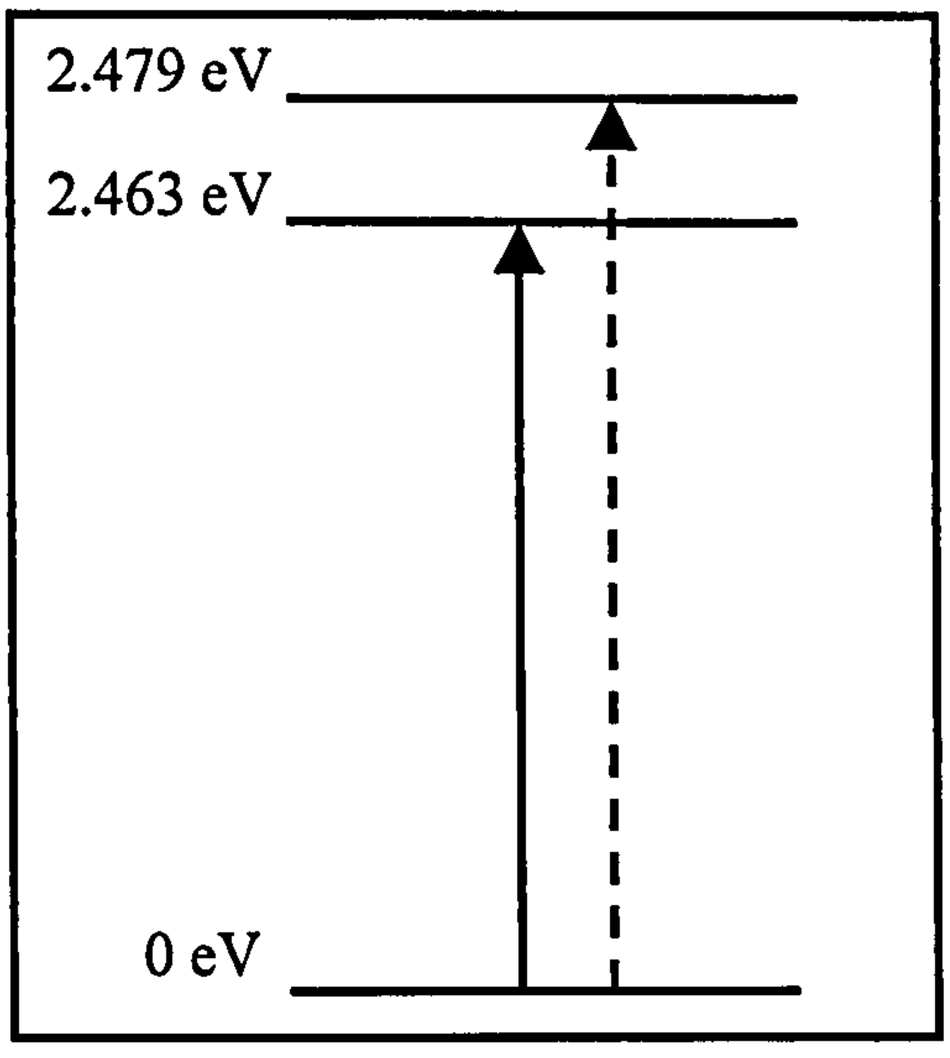

Figure 1.10. The energy level scheme of the H3 defect. A forbidden transition 16 meV above the excited state (dashed arrow) is vibronically mixed with the optically allowed transition (solid arrow), giving rise to an additional contribution in the absorption spectrum.

In the N3 defect, optical transitions between the A_1 and the E state of the defect will give the N3 ZPL at 2.986 eV (415 nm). A lower A_2 state (~147 meV below the E state) will be vibronically mixed with the lower branch of the Jahn-Teller distorted E state. This induces the "Zero-Phonon less" N2 side band starting at 2.840 eV as the ZPL with notational energy of 2.840 eV is still a forbidden optical transition (figure 1.11).

Figure 1.11 is based on Davies (1981a). However, there is now some doubt about this; our own work (De Weerdt, unpublished), and measurements by Collins (personal communication) show that diamonds which have N3 created by HPHT annealing do not show N2 proportional to N3. Iakoubovskii (personal communication) finds this is also true of some natural diamonds.

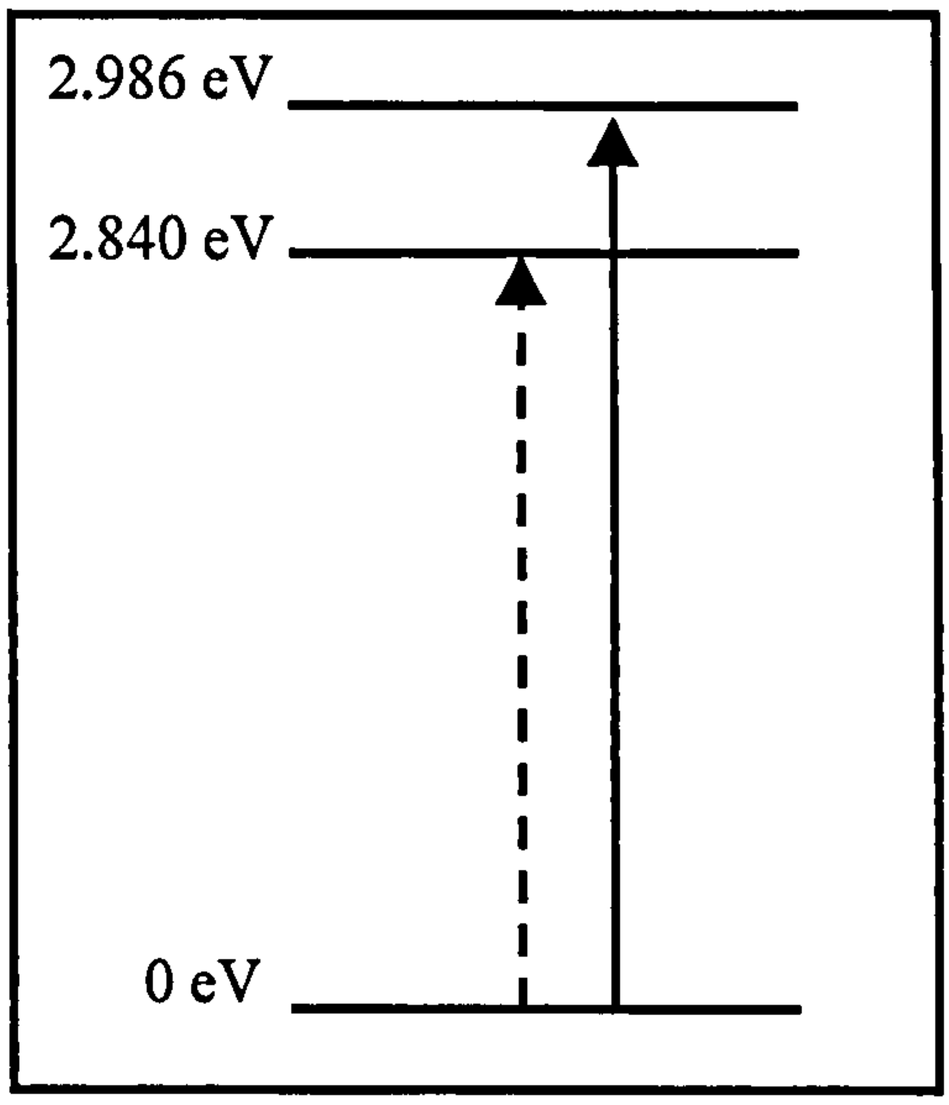

Figure 1.11. The energy level scheme of the N3 defect. A forbidden transition 146 meV below the excited state (dashed arrow) is vibronically mixed with the optically allowed transition (solid arrow), giving rise to an additional contribution in the absorption spectrum.

It is the N2 side band which is responsible for the pale yellow "Cape" colour of type Ia diamonds.

1.3. Diffusion in diamond

1.3.1. Introduction

Diffusion of impurities in solids gives rise to a change of the properties of the solid: for example nitriding of metal to increase the hardness or nitrogen diffusion and aggregation in diamond to change its colour. The impurity atoms will diffuse in the solid according to Fick's first law:

$$J_C = -D.\text{grad}(C) \qquad (1.3.1)$$

The diffusion of a specie C is proportional to the negative of the concentration gradient of the specie C. The proportionality coefficient is the diffusivity D. In three dimensions, J is a vector and D a second rank tensor, and the first law of Fick is:

$$J_{Cx} = -D_{xx}\left(\frac{\partial C}{\partial x}\right) - D_{xy}\left(\frac{\partial C}{\partial y}\right) - D_{xz}\left(\frac{\partial C}{\partial z}\right)$$

$$J_{Cy} = -D_{yx}\left(\frac{\partial C}{\partial x}\right) - D_{yy}\left(\frac{\partial C}{\partial y}\right) - D_{yz}\left(\frac{\partial C}{\partial z}\right) \qquad (1.3.2)$$

$$J_{Cz} = -D_{zx}\left(\frac{\partial C}{\partial x}\right) - D_{zy}\left(\frac{\partial C}{\partial y}\right) - D_{zz}\left(\frac{\partial C}{\partial z}\right)$$

The diffusion flux J_{Ci} is the number of specie C crossing a unit area (Kizilyalli 1999) in direction i (figure 1.12).

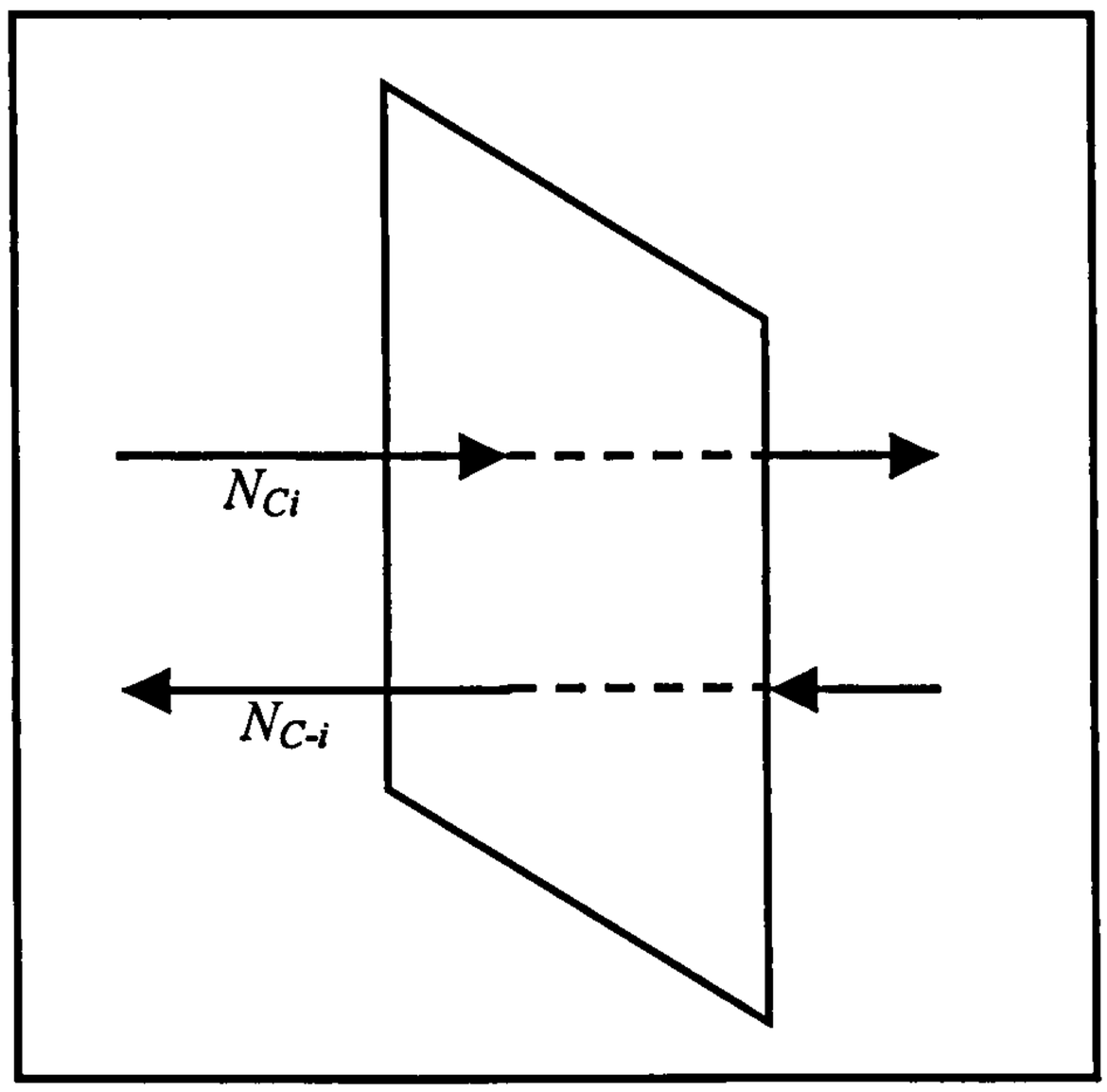

Figure 1.12. Diffusion of specie C through a unit area. The numbers N_{Ci} and N_{C-i} are the fluxes of particles in directions i and $-i$. The net flux J_C is N_{Ci} - N_{C-i} and is dependent on the concentration gradient, grad(C).

The coefficients D_{ij} with $i,j = x, y$ or z, are the diffusion coefficients of particles diffusing in direction j, through the plane perpendicular to i.

For crystalline solids, the coefficients depend on the unit cell symmetry as differences in bond strength and bond direction will influence the diffusivity tensor. The diffusivity tensor is then:

$$\begin{bmatrix} D_{xx} & D_{xy} & D_{xz} \\ D_{yx} & D_{yy} & D_{yz} \\ D_{zx} & D_{zy} & D_{zz} \end{bmatrix} \tag{1.3.3}$$

For cubic crystals like diamond silicon, copper, ... only diagonal elements of the diffusivity tensor are non-zero, and equal. The tensor is then diagonal:

$$\begin{bmatrix} D & 0 & 0 \\ 0 & D & 0 \\ 0 & 0 & D \end{bmatrix} \tag{1.3.4}$$

The diffusion coefficient is a scalar, and this makes diffusion analysis of impurities in diamond relatively easy as there is no anisotropy induced by the crystal lattice. This is not always the case. Orthorhombic crystals exhibit different bond lengths, the bond strengths along the three crystallographic axes are different for each direction, and the tensor becomes:

$$\begin{bmatrix} D_{xx} & 0 & 0 \\ 0 & D_{yy} & 0 \\ 0 & 0 & D_{zz} \end{bmatrix} \tag{1.3.5}$$

In other crystallographic systems, non-zero off-diagonal elements appear in the tensor.

In section 1.8, a review of published data of diffusion of vacancies and interstitials in diamond during and after irradiation by thermal annealing is given, and one can see that this relatively simple description of diffusion in solid state materials is inadequate; the real situation is more complicated than described in the simplified picture above.

1.3.2. Thermodynamics of diffusion

1.3.2.1. Equilibrium concentrations of defects

Thermodynamics can provide a useful theoretical framework to analyse diffusion of point defects in materials and to gain some insight in the physics of the system.

Thermodynamic potentials of any system are the internal energy U, the entropy S, the free Helmholtz energy F, the enthalpy H and the free Gibbs energy G. These are all interconnected and can be calculated from the partition function Z of the system.

$$Z = \sum_i g_i \exp\left(-\frac{E_i}{k_B T}\right) \tag{1.3.6}$$

The index i is applied to every energy level E_i in the system with degeneracy g_i. k_B is the Boltzman constant. All thermodynamic potentials depend the partition function Z.

Of special importance are the thermodynamical functions F and G and these are related to the partition function:

$$F = -k_B T \ln (Z) \tag{1.3.8}$$

$$G = F + pV \tag{1.3.9}$$

$$U = F + TS \tag{1.3.10}$$

p is the is the pressure, and V the volume of the system.

In the case of a perfect cubic crystal with N atoms, the partition function is dependent on the energy of the vibrational states with quantum numbers $n_1 \ldots n_{3N}$ with $3N$ the total number of degrees of freedom. The energy E associated with these vibrational states is:

$$E_{n_1 \ldots n_N} = \Phi + \sum_{i=1}^{3N} \left(n_i - \tfrac{1}{2}\right) \hbar \nu_i \qquad (1.3.11)$$

here Φ is the cohesive energy of the crystal lattice and ν_i the frequency of the vibrational eigenmode i. Substitution of equation 1.3.11 in 1.3.6 gives:

$$Z = \exp\left(-\frac{\Phi}{kT}\right) \prod_{i=1}^{N} \frac{\exp\left(-h\nu_i / kT\right)}{1 - \exp\left(-h\nu_i / kT\right)} \qquad (1.3.12)$$

The thermodynamic potential G is then calculated by substituting equation 1.3.12 into 1.3.8 and 1.3.9:

$$G = \Phi + \sum_{i=n_1}^{n_N} \left\{ \frac{h\nu_i}{2} + kT \ln\left[1 - \exp\left(-h\nu_i / kT\right)\right] \right\} \qquad (1.3.13)$$

The Gibbs energy depends on the ground state energy, the zero point motion of the eigenmodes, and the excitation energy of these modes weighted by the Boltzmann factor and the temperature.

In the case where n point defects are present in a crystal with N atoms, the partition function changes and can be written as:

$$Z = Z_c Z_v \qquad (1.3.14)$$

where Z_c is the configurational factor associated with the geometrical degeneracy that can be adopted for defects and can be found by combination theory, if the symmetry of the defect and the type of lattice is known). Z_v is the vibrational factor associated with the vibrational levels in the defective crystal.

The Gibbs free energy in this case is a sum of $G_0 + G_c + G_v$. Here G_0 is the Gibbs free energy of the defect-free system (a constant at constant temperature), G_c is the Gibbs free energy associated with the configurational degeneracy, and G_v is the Gibbs free energy associated with ground state vibrational levels of the defect.

For a low concentration of defects ($c = n/N$ <<1) in a monatomic crystal, with modification of the vibrational frequencies over p neighbouring atom sites, ε_d the energy required to remove the defect from the crystal, one can show that the Gibbs free energy is (Agullo-Lopez *et al.* 1988):

$$G = G_0 + N\left[c\left(\varepsilon_d - k_B T \ln\left(\frac{\nu}{\nu'}\right)^p\right) + k_B T c \ln\left(\frac{c}{\alpha}\right)\right] \qquad (1.3.15)$$

with α the combinatorial factor.

1.3.2.2. The relation between equilibrium concentrations and Gibbs free energy.

If the concentration of a set of defects changes, the Gibbs energy also changes. If one has the equilibrium reaction:

$$a_1A_1 + a_2A_2 \leftrightarrow a_1'A_1' + a_2'A_2' \qquad (1.3.16)$$

a_i stands for the stoichiometric factor of a specie (like for the reaction for water: $2H+O \rightarrow H_2O$) and A_i is the respective specie.

The reaction rate and the direction in which the reaction proceeds are determined by the difference in sums of the Gibbs free energies of the products and the reactants. From thermodynamics we know that, at low pressure ($pV << 1$), the Gibbs free energy G is the internal energy U minus the product of the temperature and the entropy, TS.

$$G = U - TS \qquad (1.3.17)$$

In a reaction at a fixed temperature, the change in Gibbs free energy is

$$\Delta G = \Delta U - T\Delta S \qquad (1.3.18)$$

If the difference in Gibbs free energy is negative, then the reaction is product favoured and will proceed to the right side of equation 1.3.16. If the difference in Gibbs free energy is positive, then the reaction is reactant favoured and the reaction will proceed to the left hand side of equation 1.3.16.

Table 1.1 summarizes the possibilities:

ΔU	ΔS	Product favour
- (exothermic)	+	Yes
- (exothermic)	-	Yes when $\Delta G < 0$ No when $\Delta G > 0$
+ (endothermic)	+	Yes when $\Delta G < 0$ No when $\Delta G > 0$
+ (endothermic)	-	No

Table 1.1. The different types of reactions and their influence on the Gibbs free energy.

Or alternatively, ξ is a measure of the extent of the reaction when the concentration of reactant B at time t during the reaction is $[B] = [B_i] - b\xi$, with b the reaction rate and $[B_i]$ the initial concentration of reactant B. During the reaction, the Gibbs free energy changes continuously until the change is zero.

We can say that the Gibbs free energy is the energy available (or which needs to be added) to make the reaction work. The Gibbs free energy changes during the reaction, and will depend on the concentration of reactants and products; the change in Gibbs free energy ΔG will become zero at thermodynamic equilibrium.

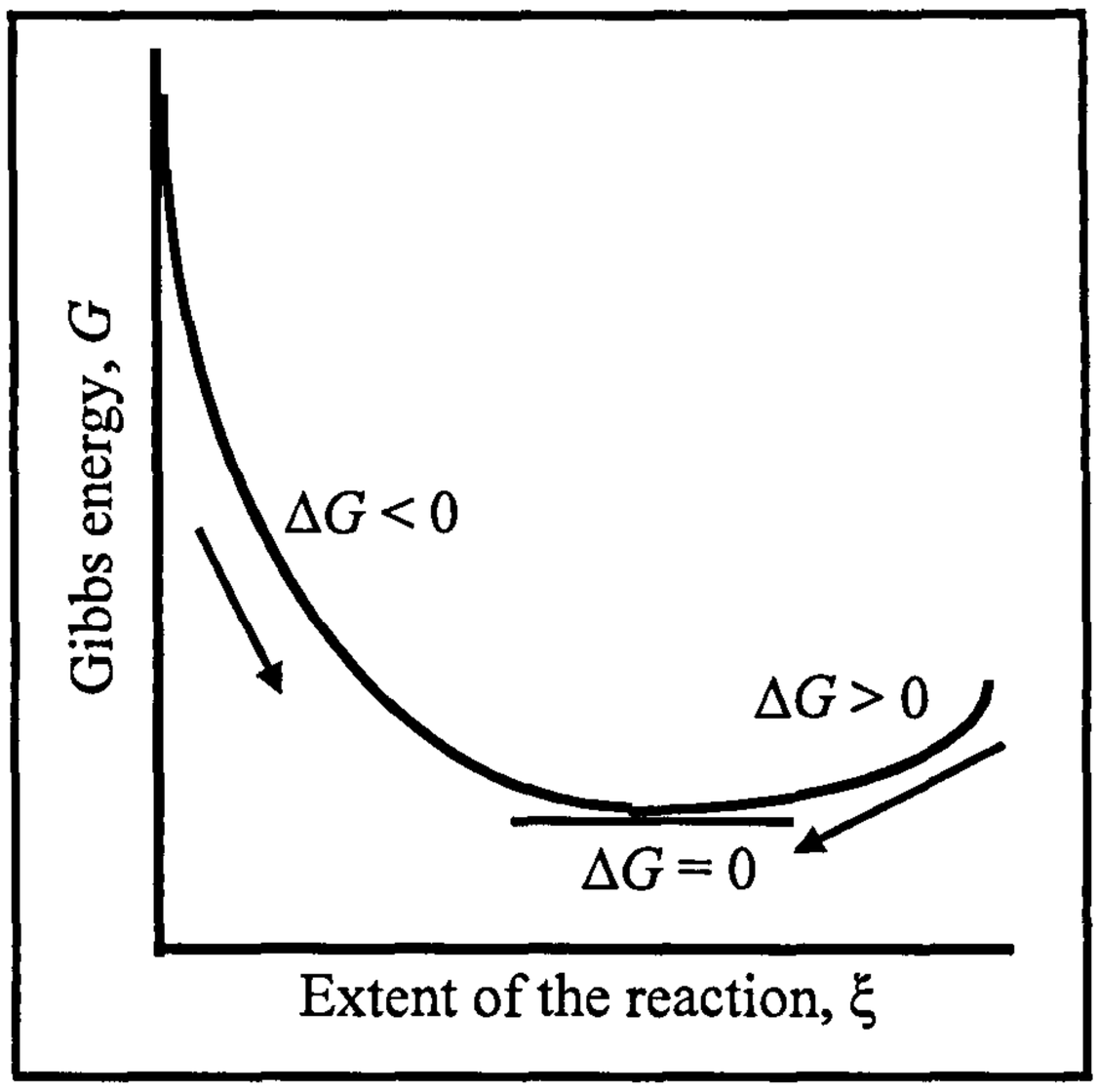

Figure 1.13. The Gibbs free energy change as a function of the extent of the reaction ξ.

The equilibrium concentration of each of the species can be calculated by setting the change of G (the sum of the Gibbs energies of each impurity) induced by the concentration change to zero:

$$\frac{\partial G(c)}{\partial c} = 0 \tag{1.3.19}$$

or by substituting equation 1.3.15 in equation 1.3.19 and with

$$g = \left(\varepsilon_d - k_B T \ln\left(\frac{\nu}{\nu'}\right)^p \right)$$

$$c_0 = \exp\left(-\frac{g}{k_B T}\right) \tag{1.3.20}$$

Equilibrium concentrations during reactions among point defects, as described by equation 1.3.16, can be calculated from the requirement:

$$\sum_j \frac{\partial G}{\partial c_j'} - \sum_i \frac{\partial G}{\partial c_i} = 0 \tag{1.3.21}$$

or

$$\frac{\prod_i (c_i')^{a_i'}}{\prod_j (c_j)^{a_j}} = \frac{\prod_j (\alpha_j)^{a_j}}{\prod_i (\alpha_i')^{a_i'}} . \exp\left(-\frac{g_r}{k_B T}\right) \qquad (1.3.22)$$

with c_i and c_j' the concentrations, α_i and α_j' the combinatorial factors of species A_i and A_j' respectively, at thermodynamic equilibrium.

g_r is the Gibbs free energy, calculated from: $g_r = \sum_i g_i' a_i' - \sum_j g_j a_j$ where g_j' and g_i are the Gibbs free energy functions of each specie.

Equation 1.3.22 is known as the law of mass action (Agullo-Lopez *et al.* 1988, Greiner *et al.* 1995).

Equation 1.3.22 can for example be used to calculate the C defect concentration generated during HPHT annealing. When an A defect splits up into two C defects, equation 1.3.16 can be rewritten as:

$$A \leftrightarrow 2\,C \qquad (1.3.23)$$

Equation (1.3.22) is then:

$$[C]^2 / [A] = cte . \exp\left(-\frac{g_r}{k_B T}\right) \qquad (1.3.24)$$

With $[C]$ and $[A]$ the C and A defect concentration after the HPHT annealing (see also Allen and Evans 1981). The constant *cte* is called the vibrational pre-constant as it is the attempt frequency for the reaction to scale the energy barrier g_r. One can interpret the reaction in a different way: a vibrating diatomic molecule can dissociate with a frequency equal to the vibrational frequency. The probability of dissociation is

proportional to the exponential of the activation energy g_r divided by the product of the temperature T and Boltzmann's constant.

1.3.2.3. Influence of pressure

There are indications that pressure can affect the activation energy of defect migration: for example in silicon, vacancy-oxygen defects disappear faster when annealed under hydrostatic pressure (Londos *et al.* 2003, Béjina *et al.* 2003). In diamond platelet destruction, and the disappearance of the associated peaks in the infrared spectrum and the X-ray spikes, take place most readily when the diamonds are subjected to annealing conditions in the graphite stable region of the carbon phase diagram (Evans *et al.* 1995). Also the nitrogen aggregation rate of irradiated type Ib diamond is lowered when pressure is increased (Kiflawi *et al.* 1997).

Pressure can be brought into equation (1.3.24) by (Béjina *et al.* 2003):

$$g = (f_C + pV_C) - (f_A + pV_A) \qquad (1.3.25)$$

with f_A and f_C the Helmholtz free energy of the A and C defect respectively, and V_A and V_C the total volume change due to the presence of A and C defects respectively.

For g_r we have:

$g = f_C - f_A + p(V_C - V_A)$ or $g_r = E_a + p(V_C - V_A)$, where E_a is the activation energy.

If the volume of the A defect is exactly twice the volume of the C defect, then there would be no influence of pressure during the reaction. If there is a volume difference, there can be an influence of the pressure. As a result, dissociation and formation of vacancy-defect complexes might have a strong influence of pressure during high temperature annealing due to the volume change involved.

Three different situations are possible:

- If the volume of the C centre is larger than the volume of one nitrogen atom of the A centre, then the term $p(V_C - V_A)$ is larger than zero, and the activation energy increases with increasing pressure (or decreases with decreasing pressure).
- If the volume of the C centre is smaller than the volume of one nitrogen atom of the A centre, then the term $p(V_C - V_A)$ is smaller than zero, and the activation energy decreases with increasing pressure (or decreases with increasing pressure).
- There is no volume difference between two C defects and the A defect, and the reaction is pressure independent.

Experimental determination of the dilatation due to nitrogen centres in diamond has been done by Lang and co-workers (Lang *et al.* 1991 and Lang and Pang 1998). They found that a C defect causes a dilatation of 1.35 ± 0.10 times a carbon atom. An A defect causes a dilatation of 1.11 times a pair of the carbon atoms. In worst case the dilatation of a nitrogen atom in the A defect causes a dilatation between 1.05 and 1.22 (Lang and Pang 1998). The total volume difference between 2 nitrogen atoms in an A defect and two separate C defects is therefore between 0.03 and 0.4 times two carbon atoms.

The pressure component of equation 1.3.25 can also be written as

$$p(V_C - V_A) = p.m.V_{Carbon}.[C] - n.V_{Carbon}.[A]) = p.\ V_{Carbon}(m.[C] - n.[A])$$

Here m and n are the dilatation coefficients of the C and A defects respectively.

The magnitude of the coefficient in the pressure dependent component is small: the total volume dilatation is a fraction of the bond length (1.5 Å or 0.15 nm) times the number of nitrogen atoms replacing the carbon atom. When the crystal is approximated as a hard sphere lattice, the volume of one carbon atom in the lattice is 1.934×10^{-30} m^3). A pressure of the order of 10000 bar or 1 GPa is an energy density of 6.242×10^{27} eV/m^3.

For 1 GPa, the energy change is equal to the fraction of the volume of a carbon atom $V_{Carbon}(m.[C] - n.[A])$, or smaller than $V_{Carbon}.p = 1.934\ 10^{-30}$ m^3 x $6.242\ 10^{27}$ eV/m^3 = 0.012 eV for a pressure change of 1 GPa. The Gibbs energy change, however,

depends on the volume change of the total system and not on the volume change of a defect and is therefore very small as the volume changes only a fraction of the total volume.

1.3.3. Other factors influencing the diffusion

The diffusion rate in solids can be increased or impaired by other defects. Vacancy diffusion can be impaired by the presence of hydrogen (Newton 2005), nitrogen diffusion can be increased by interstitials (Kiflawi *et al.* 1997 and 1998, Agullo-Lopez 1988) and vacancies (Collins 1978b, Collins 1980, Agullo-Lopez 1988). The presence of electron donors can charge a defect and thereby reduce its mobility (Davies *et al.* 1992).

In similar covalent crystals, like group IV semiconductors, hydrogen is known to increase the oxygen diffusion rate (Newman 1995). Newman (1995) also discussed the formation of H_2^* in silicon, now known as hydrogen dimers, which require the presence of a vacancy. H_2^* can form in electron irradiated silicon when a vacancy diffuses to a site nearby a H_2 molecule, already present in the as-grown silicon. The hydrogen molecule is trapped at the vacancy and when a diffusing interstitial is trapped at this site, a hydrogen dimer is created.

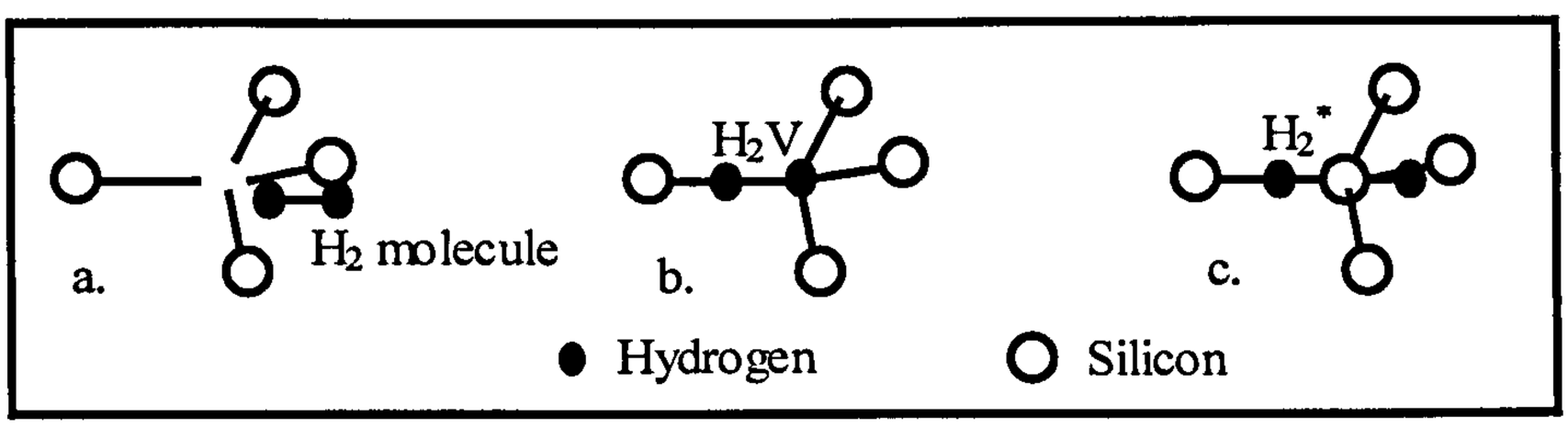

Figure 1.14. The model proposed by Newman (1995) for the formation of H_2^* in electron irradiated and quenched silicon. A vacancy diffuses to a site nearby the H_2 molecule (a), the H_2 is trapped by a vacancy (b). When the H_2V traps a mobile interstitial (c) the H_2^* defect is created.

A hydrogen dimer consists of a hydrogen atom at a bond centred position and a hydrogen atom in the anti-bonding position. In silicon, hydrogen dimers are thought to play a crucial role in hydrogen diffusion as their activation barrier for diffusion is much lower than that for molecular hydrogen (Chang and Chadi 1989).

1.3.4. Dislocation diffusion

A short discussion of dislocations and dislocation diffusion will be given here. Only concepts and properties of dislocations which are important in further chapters will be given and it will by no means be a full treatise of the properties of dislocations.

Diffusing intrinsic and extrinsic defects in a solid-state material will influence each other. An example known from metallurgy is the following: high concentrations of non-equilibrium dislocations can be introduced in materials by cold working (rolling, extrusion, ...) or irradiation, and recovery of the crystal structure can occur during subsequent annealing. This may partially restore the crystal structure, thereby changing its properties (strength, hardness, ...).

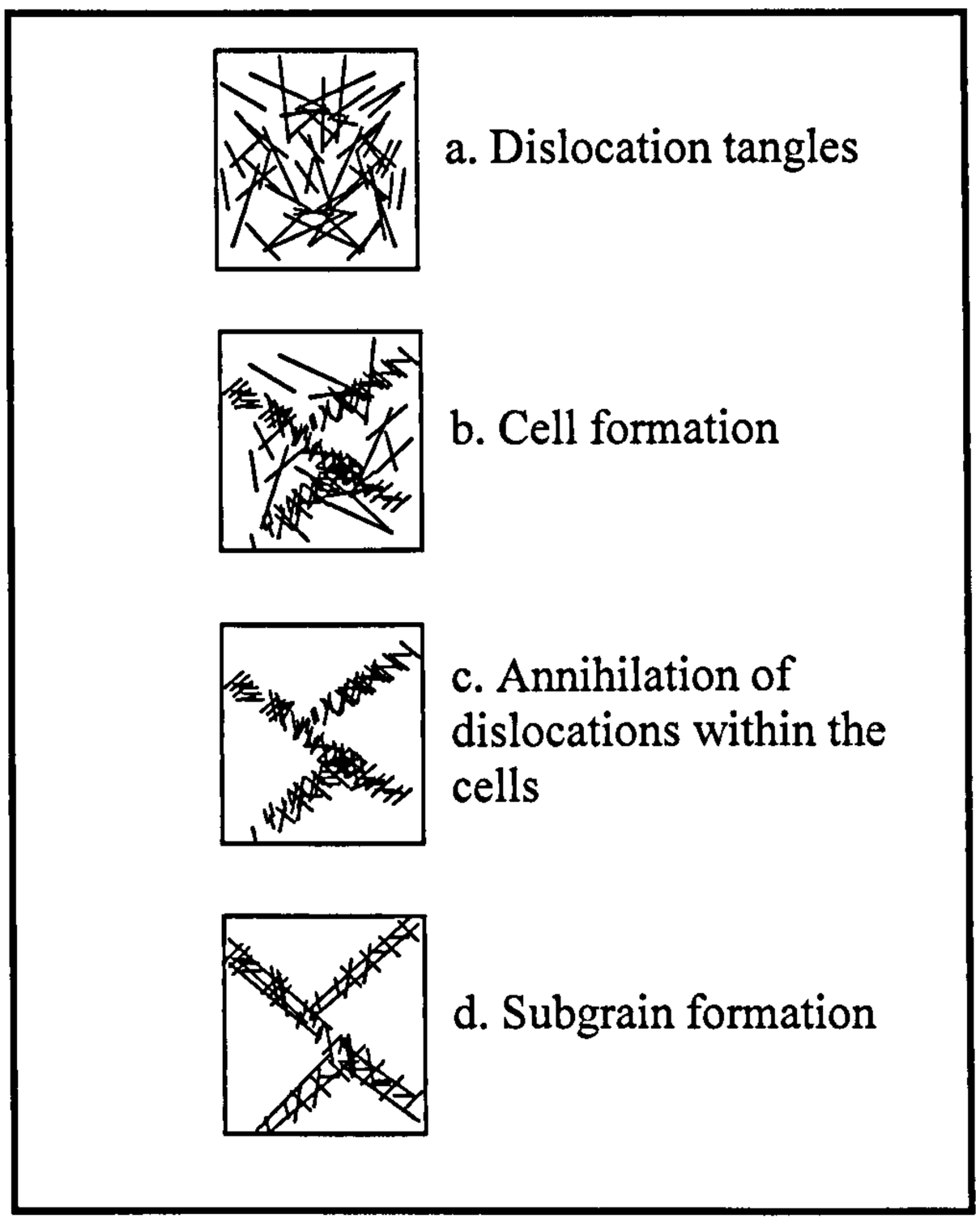

Figure 1.15. A schematic drawing of the various microstates of dislocations in deformed materials upon recovery. The deformation introduces dislocations in the material, which cluster and form cells. These cell boundaries may in time lead to sub-grain formation. If all subgrains have different crystalline orientation, a polycrystalline material will be created upon recrystallisation. If all subgrains have identical crystalline orientation, a single crystal will form after recrystallisation.

During deformation of crystalline materials, point defects and dislocations will be introduced in the crystal, and upon annealing the material will go through a series of microstates, schematically shown in figure 1.15 (Humphreys and Hatherly 1996, Nes 1995). Stress in materials could have an influence on the size and distribution of dislocation networks (Nes 1995).

The driving force behind recovery is the lowering of the internal energy stored into the dislocations (Mott 1951). The dislocation network formation is observed in a large number of materials (Rudolph 2005). The formation of cells and annihilation of dislocations within cells will recover and eventually recrystallize the material.

Before venturing into the mechanisms of dislocation diffusion, we must take a close look at dislocations and at the description of the various types of dislocations.

A dislocation itself is characterised by a Burgers vector **b**: this is the result of lattice mismatch between the part of the crystal with and without the dislocation. Any closed loop embracing the dislocation will result in the Burgers vector **b** (see figure 1.16).

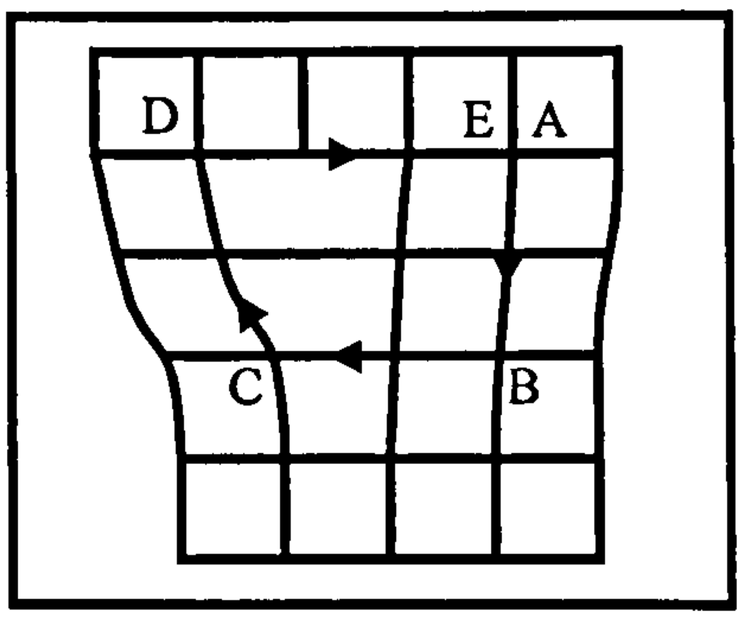

Figure 1.16. An end-on view of an edge dislocation. The Burgers vector is in this case perpendicular (in the plane of the paper) to the dislocation line (perpendicular to the paper).

Mathematically, the Burgers vector can be calculated by a loop integral:

$$\mathbf{b} = \oint \delta \mathbf{u} \qquad (1.3.26)$$

with $\delta\mathbf{u}$ the displacement vector moving along the closed loop embracing the dislocation. If **b** is parallel to the dislocation line direction, then the dislocation is a screw dislocation, and if **b** is perpendicular to the dislocation line direction, then the dislocation is an edge dislocation. Most dislocations are mixed (screw and edge type) dislocations. The Burgers vector itself is noted as a partial of the lattice parameter, and a direction. For example a dislocation with a Burgers vector of $a/2$ (111) means a displacement of the lattice in the (111) direction by half the lattice parameter a.

Dislocations can move in the crystal by two different methods: climb and glide. Movement along the Burgers vector is glide and perpendicular to the Burgers vector is climb.

Glide requires relatively low energy and can often be observed during plastic deformation of materials.

Climb of a dislocation is a non conservative motion: vacancies will need to be created or interstitials emitted during dislocation climb (figure 1.17), which requires more energy than the glide diffusion (Mott 1951). Dislocation climb can thus be an effective vacancy annihilation or generation process.

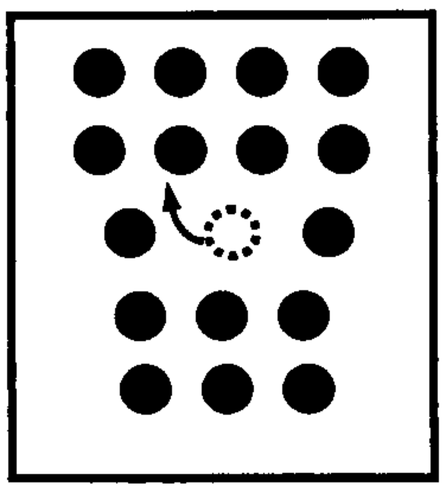

Figure 1.17. Dislocation climb by absorption of a vacancy.

During hot working or deformation of semiconductors, vacancies created during climb motion of dislocations can accumulate into vacancy aggregates (Leipner 2000, Mott 1951).

Steps in the dislocation plane are termed kinks (absorption of vacancies by an edge dislocation induces a kink in the dislocation line) and glide along with the supporting dislocation, while jogs are steps out of the plane of the dislocation. In contrast to

kinks, vacancies have to be created or taken away in order to drag jogs during dislocation glide.

Impurities have a profound influence on dislocation diffusion:

- Formation and absorption of vacancies play an essential role in the movement of dislocations.
- Point defects will influence the motion of dislocations (solute drag effect).
- Precipitates may pin dislocations (Zener pinning).

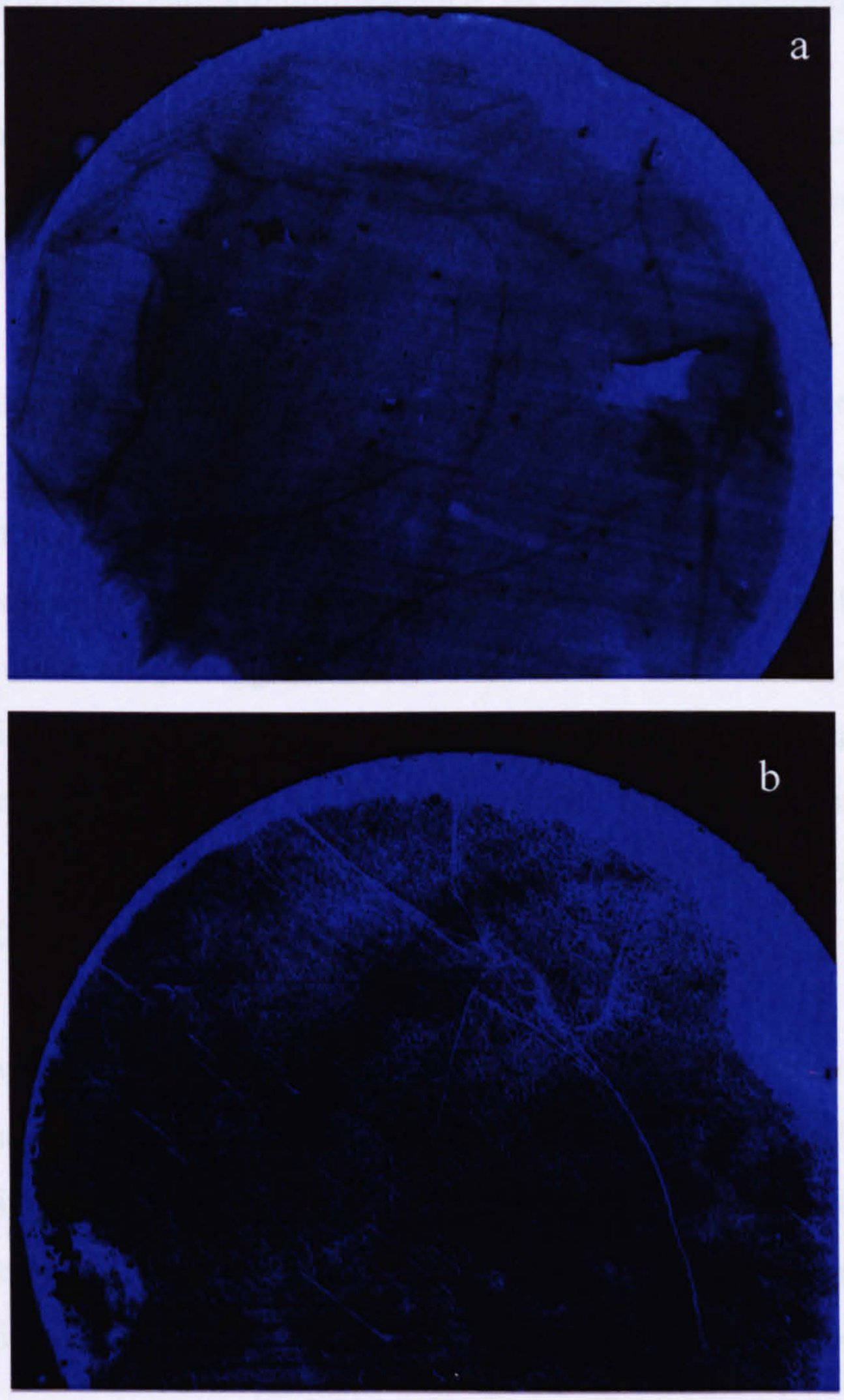

Figure 1.18. Dislocation networks with large diameter (a) and very small diameter (b) on a type IIa diamond surface. These structures are never seen in type I diamond. The diameter of the samples is 2.5 mm.

The main influence of solute drag effect on dislocation movement (Deo 2005) is pinning of the dislocation. For type Ia diamond solute drag prevents dislocation cell formation. This will not be the case in relatively pure type IIa diamond as the impurity content cell formation will be present. The cell formation in type IIa diamond is visible in cathodoluminescence (Kanda *et al.* 2005) or photoluminescence topography figures (figure 1.18a and 1.18b). Similar dislocation networks have been observed by Evans and Phaal (1962) on (111) surfaces of type IIa diamond.

Some of the polarised cathodoluminescence of type IIa diamond is thought to originate from dislocations or dislocation networks, and in type Ia diamond H3 is often found located close to the dislocations and slip bands (Hanley *et al.* 1977). It is also found that band A luminescence is weak where luminescence from dislocations is strong (Walker 1979).

According to Hirth and Lothe (1982), the activation energy for thermally activated dislocation motion is the sum of kink formation and kink migration energy. Atomic impurities might also decrease this activation energy: in silicon there is evidence that hydrogen can reduce the activation energy from 2.2 to 1.2 eV (Yamashita *et al.* 1999). Theoretical calculations by Heggie *et al.* (2000) indicate that the activation energy for dislocation motion in diamond might change from 3.3 eV (Sitch *et al.* 1997) to 1.67 eV when hydrogen is supplied to the dislocation. The mechanism of adding a hydrogen atom to the dislocation is not understood for silicon and not discussed in Heggie *et al.* (2000) for diamond.

Zener pinning will hinder the motion of the dislocation and the Zener pinning force is dependent on the precipitate volume and size (Porter and Easterling 1992). Also, the shape of precipitates (sphere, disc and needle-like) will all have a different influence in restricting the cell formation or sub-grain growth. Because of their size and shape, platelets and voidites should have a serious influence on the dislocation migration.

1.4. Synthetic diamond growth

1.4.1. Growth of synthetic diamond by HPHT

The production of synthetic diamond by High Pressure High Temperature (HPHT) has become a large-scale industry. The main product is synthetic diamond powder or grit for abrasive applications. In this process small diamond crystals are produced by spontaneous crystallisation in the HPHT cell. Larger sized diamonds can be made by growing diamond on a diamond seed (figure 1.19). A carbon source is placed at the top of the HPHT cell and carbon is transported through a solvent catalyst to the diamond seed. The diffusion of carbon from the source to the diamond seed is promoted by a temperature gradient in the HPHT cell. The carbon then precipitates on a small diamond seed, located at the bottom of the HPHT cell (figure 1.19). This results in single crystal growth of the diamond on the small seed crystal and, depending on the applied temperature and pressure, the diamond will display a different degree of octahedral and cubic growth sectors (Field 1992). A higher growth temperature will cause the diamond to grow with more octahedral shape, while a lower growth temperature will result in cubo-octahedral and cubic growth. In the grit and single crystal HPHT growth process, diamond is synthesised by dissolution of carbon from a carbon source, mainly graphite, in molten metals like iron, nickel and cobalt or alloys thereof.

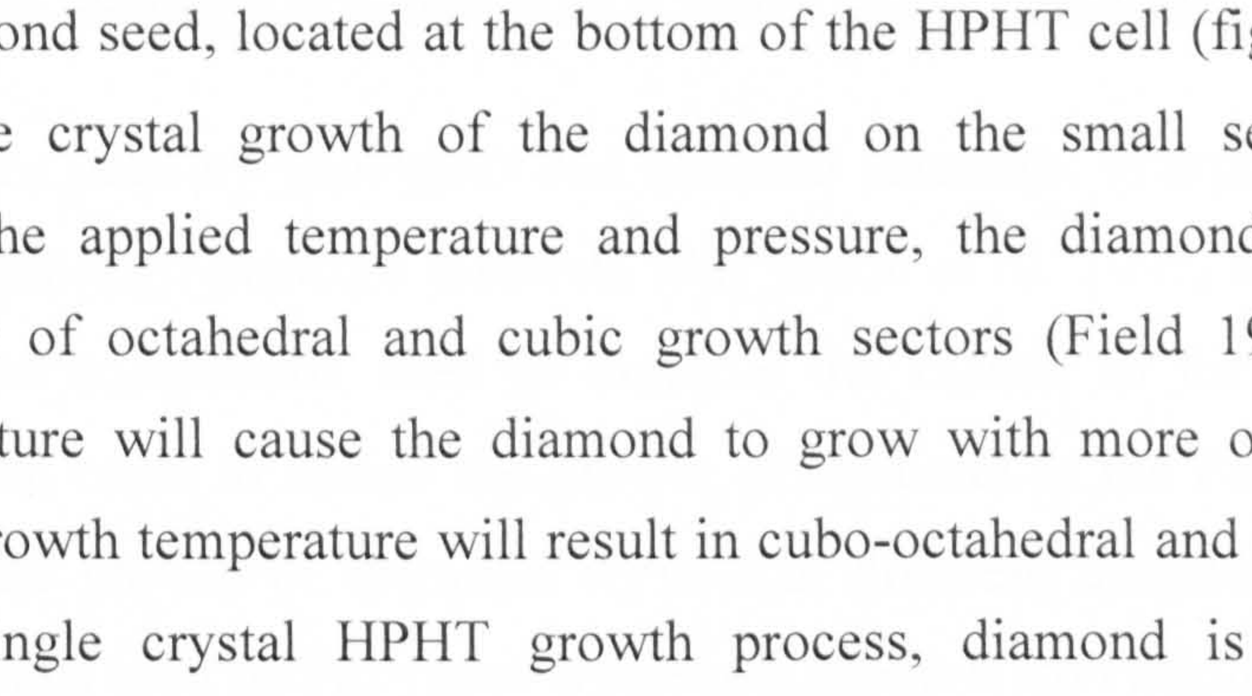

Figure 1.19. A drawing of the inside of a BELT type HPHT press (Sumiya *et al.* 2005). The steel belt, surrounding the carbide die is not visible in this figure. The arrows in the figure of Sumiya are in the wrong places: Ti is the nitrogen getter and Cu is the TiC formation inhibitor.

The synthesis of diamond by HPHT was pioneered by ASEA (Sweden) (Liander 1953), General Electric (US) (Bundy 1955) and De Beers (South Africa) (Burns and Davies 1992). The systems used by these companies are so-called belt presses, after the steel belt with a carbide die, holding the cylindrical HPHT cell (figure 1.19). Nowadays, Iljin in South Korea and Chinese companies have become the largest producers of synthetic diamond powders and these companies typically employ smaller prismatic presses.

The HPHT press which one uses to synthesize diamond can also be used for HPHT annealing.

1.4.2. Synthesis of diamond with iron nitride under HPHT conditions

HPHT presses are used by geologists and material scientists to study the growth of diamond and other high-pressure minerals (Pal'yanov *et al.* 1997, Kanda 1994). In these studies, the compounds used to dissolve the carbon in the HPHT cell are modified, in some cases to mimic the growth of diamond in the Earth, and in other cases to study the growth of diamond crystals in different chemical environments. One of the materials used by Pal'yanov's research group is iron nitride, which is made from high purity iron powder in an oven under a flow of ammonia. The diamonds made by this synthesis method are rich in hydrogen, resulting in a strong absorption peak at 3107 cm^{-1} which is thought to be hydrogen related. In chapter four, the analysis of this peak in isotopically $^{13}C/^{12}C$ mixed diamonds is studied. The model proposed by Woods and Collins (1983) is confirmed.

1.4.3. HPHT press used for HPHT treatment

The diamonds used in the study of defect dissociation and diffusion (to be described in chapters 5 and 6) were HPHT annealed at Sundance Inc. (Orem, Utah, USA) in a cubic type press (figure 1.20).

The HPHT apparatus is capable of generating pressures of 60-90 kilobars and temperatures in excess of 2500°C. The cubic press design utilizes six sintered carbide anvils mounted on hydraulically driven pistons oriented in such a way as to apply

equal pressure to the six sides of a cube. The diamond is placed inside a pressure transmitting medium which is then surrounded by a graphite tube that is used as a resistive heating element. This assembly is placed inside a cube-shaped block of pressure transmitting medium that is contacted on all sides by the press anvils. Pressure and temperature are computer controlled. Temperature accuracy is estimated to be ~50°C.

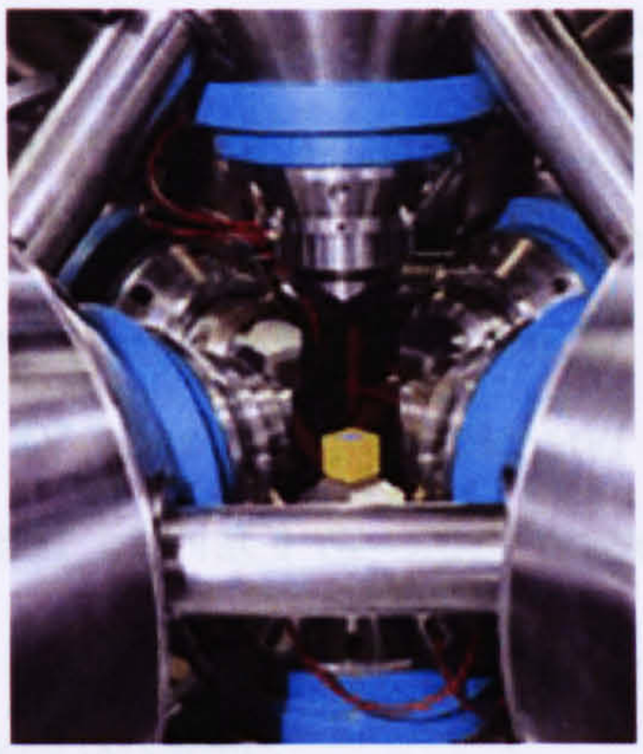

Figure 1.20. The inside of a HPHT cubic press at Sundance Inc (http://www.ussynthetic.com/rd/hpht.php).

1.4.4. Pressure and temperature measurements in HPHT presses

At this point it is appropriate to have a review of temperature and pressure measurements in HPHT presses.

1.4.4.1. Temperature measurements

Temperature is measured with a thermocouple. The thermocouple itself is a major heat leak, so the temperature inside the HPHT cell is probably different from the indication of thermocouple reading. The electromotive force (EMF) of thermocouples also changes with pressure, and this change can be considerable for certain thermocouples (Bundy 1961). Some can have a positive and some have a negative change in EMF with pressure. Evans and Qi (1982) redesigned their HPHT device and used a tungsten-iridium thermocouple for which the output was pressure corrected.

1.4.4.2. Pressure measurements

In most systems pressure is calibrated by measuring the electrical resistivity change due to phase transformations of certain materials, like Tl, Bi or Ba as they get pressurized (Decker 1972). This is called the fixed-point method. However, Jeffery *et al.* (1966) indicated that there is considerable divergence between the pressure at which transformations should take place, depending on the measurement method. Jeffery *et al.* also showed that there is considerable hysteresis in these phase transformations: they occur at different pressures in the pressurization and the depressurization of the system. Jeffrey *et al.* estimate that pressure calibration with the fixed point method over 40 kbar is unreliable and a more accurate method like measuring the lattice parameter of NaCl or other powders by diffraction should be used (Jeffery *et al.* 1966, Gierlotka *et al.* 1999, Paszkowicz *et al.* 2000). Unfortunately this is not always possible.

Most systems are pressure calibrated by the fixed-point method and temperature calibrated by measuring the known melting point of certain materials. However, the thermocouples are not corrected for change in EMF and temperature is calibrated at room pressure and pressure is calibrated at room temperature. This may give substantial systematic errors on the measured temperature and pressure.

1.5. Spectroscopic techniques

1.5.1. UV-VIS spectroscopy

In UV-VIS spectroscopy one records a spectrum by measuring the wavelength dependent absorption in the visible and ultraviolet regions of the electromagnetic spectrum. A spectrometer always consists of a stabilized light source, a dispersive element and a detector. The system is computer controlled and the computer is also used as a recorder and to calculate the spectrum from the raw data. There are different systems on the market and the main systems will be discussed below.

Most of these systems can also be used as photoluminescence or Raman spectrometers. Photoluminescence refers to the process where an electron of a defect is excited by light from a high intensity light source (e.g. a laser) and the

luminescence because of radiative decay (fluorescence) is captured and analysed by a spectrometer. Raman refers to inelastic light scattered by phonons of a crystal lattice. This is a very weak effect, and therefore needs a high intensity, monochromatic light source. A high power laser is then of course the best choice. In a UV-VIS Raman/photoluminescence system a laser is used to excite luminescence, and the luminescence spectrum is detected by the dispersive component of the system. In an UV-VIS absorption spectrometer, the light transmitted by a sample is analysed by a dispersive component. The dispersive components of the UV-VIS Raman/photoluminescence and absorption spectrometers are very similar. Therefore they are not treated in separate sections.

1.5.1.1. Light source

Lamps are used as light sources for UV-VIS absorption spectroscopy and they are subdivided in two different classes:

- Gas discharge lamps like Xenon or Deuterium lamps
- Filament lamps like Halogen light bulbs

1.5.1.1.1. Gas discharge

Gas discharge lamps have a gas inside a glass or quartz bulb and electrons are accelerated and decelerated in the gas plasma between a cathode and an anode. An arc discharge is made between the cathode and anode and the gas plasma emits light due to accelerated and decelerated electrons which are scattered by the gas molecules. Gas discharge lamps have several advantages over solid state glow lamps:

- A higher efficiency
- A smaller light emitting region
- Relatively strong emission in the UV region (see figure 1.21)

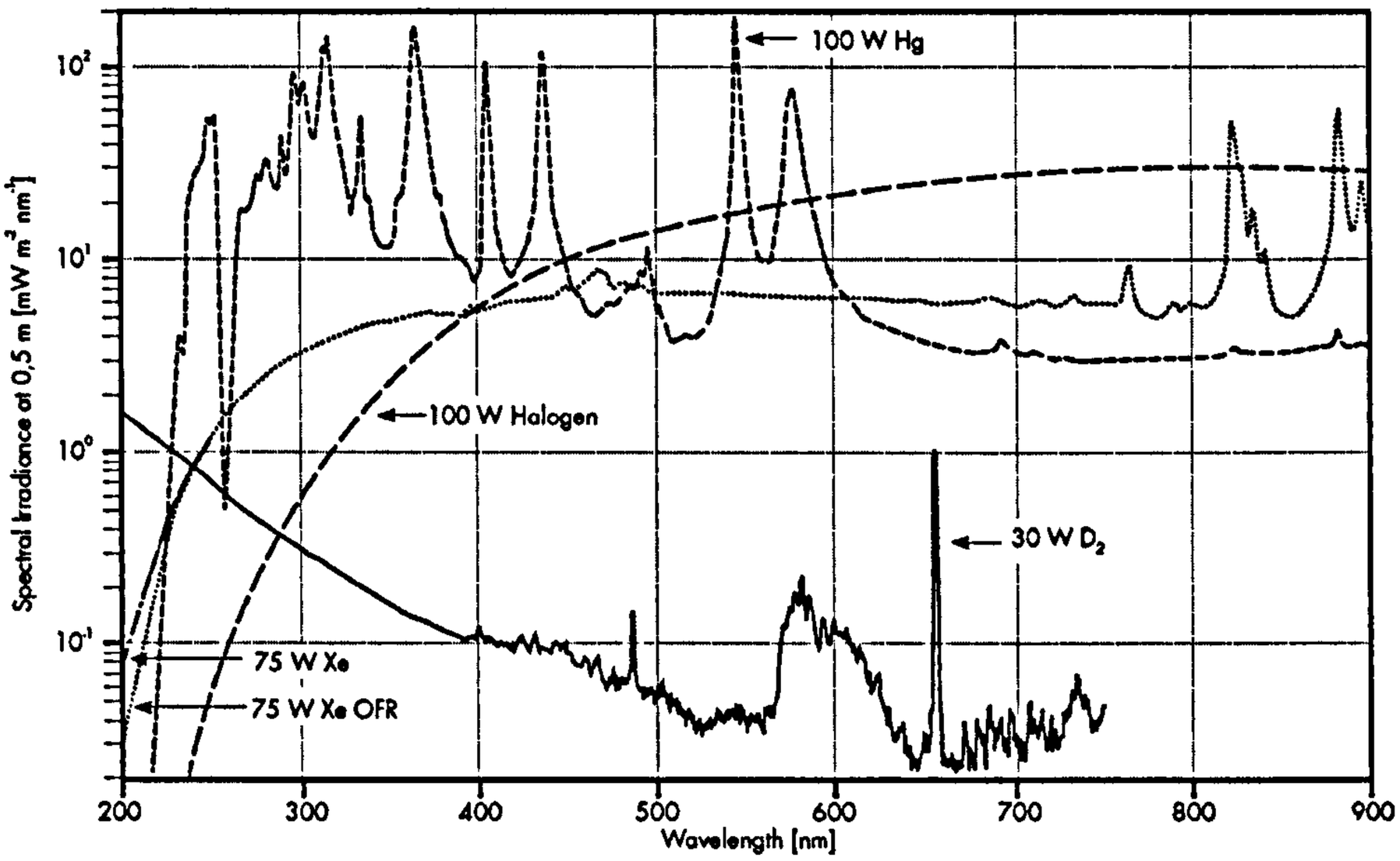

Figure 1.21. Emission curves of different light sources used for absorption and luminescence measurements in the ultraviolet to visible range (LOT Oriel catalogue).

1.5.1.1.2. Filament lamps

Light emission of filament lamps is essentially blackbody radiation. The radiation emitted per unit area into a solid angle of 1 sterradian $L(\omega)d\omega$ is given by Planck's radiation law:

$$L(\omega)d\omega = \frac{\omega^2}{8\pi^3 c_0^2} \frac{\hbar\omega d\omega}{\left[\exp\left(\hbar\omega/k_B T\right)-1\right]} \qquad (1.5.1)$$

Here ω is the frequency of the photon, T is the temperature of the blackbody, and k_B is the Boltzmann constant. c_0 is the speed of light in vacuum.

This must be multiplied by the emissivity of the tungsten filament and the transmissivity of the quartz envelope. As a result the spectrum of a Quartz halogen light bulb is a continuously rising featureless spectrum from the UV-VIS to NIR region. This makes these lamps particularly useful for UV-VIS to NIR absorption spectroscopy. The filament temperature of the lamp can be as high as 3300 K. Small

amounts of halogen gas are added to the noble gas inside the lamp, to increase the lifetime of the lamp.

1.5.1.2. Dispersive element

The dispersive element in the spectrometer is used to select the different wavelengths from the electromagnetic spectrum, hence the name monochromator. Dispersive monochromators use elements like prisms or gratings.

Only gratings will be discussed, as prisms are not used in modern spectrometers. A grating consists of a plate with grooves and is typically characterized by a number of grooves per millimetre. Each groove acts as a small mirror tilted at a certain angle with respect to the normal of the surface of the grating (figure 1.22).

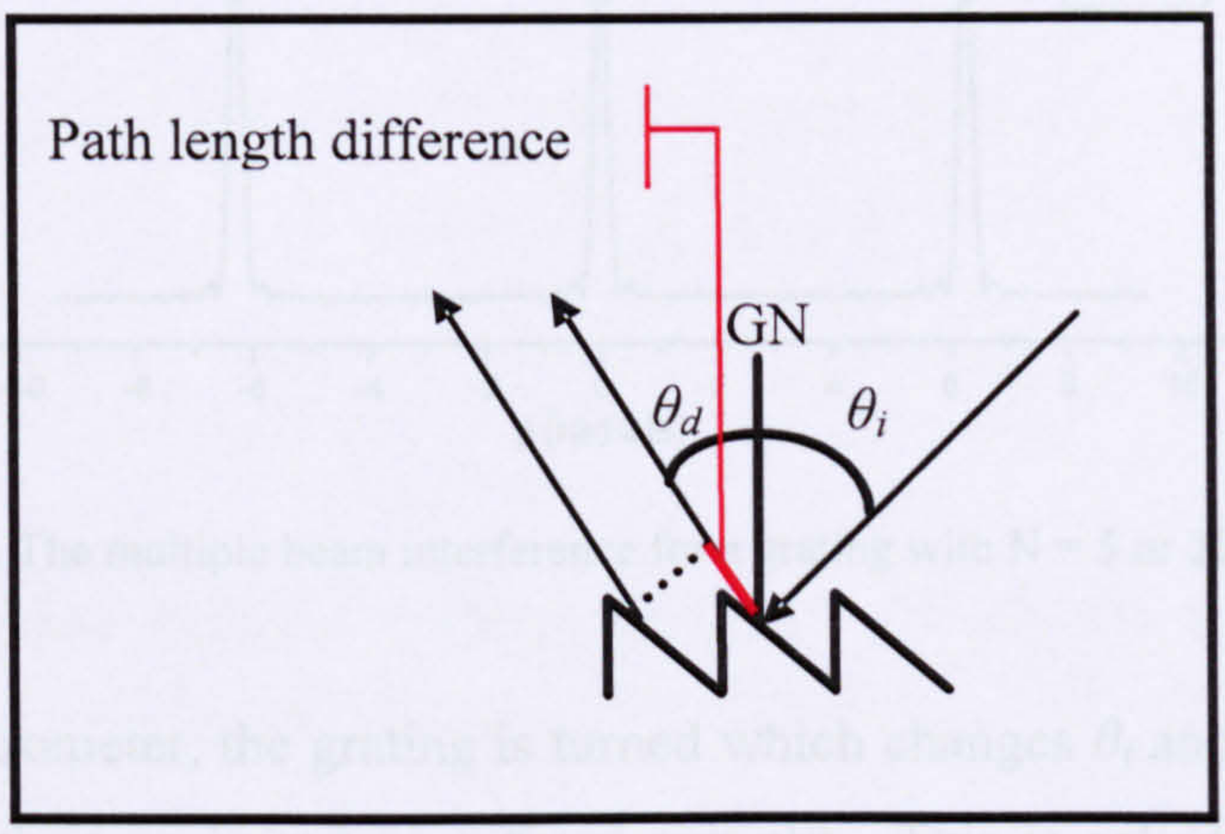

Figure 1.22. The path length difference between two neighbouring light rays of wavelength λ depends on the angle between the incoming ray θ_i and reflected ray θ_d with respect to the grating normal GN.

The resolution of the grating depends on the number of grooves per millimetre. The dispersion works by constructive and destructive interference of light of different wavelength reflected from each groove. The total intensity is:

$$I_t = RI_0 \frac{\sin^2(N\phi/2)}{\sin^2(\phi/2)} \qquad (1.5.2)$$

here R is the relative reflection of the grating, ϕ is the phase difference between beam partials, N the number of grooves per millimetre and I_0 is the intensity of the incoming light. In the directions where $\phi/2 = m\lambda$ with m an integer there is a maximum in the transmitted intensity I_t

The spectral resolution is determined by the width of the interference line. From figure 1.23 one can clearly see that this width decreases for a higher number of grooves.

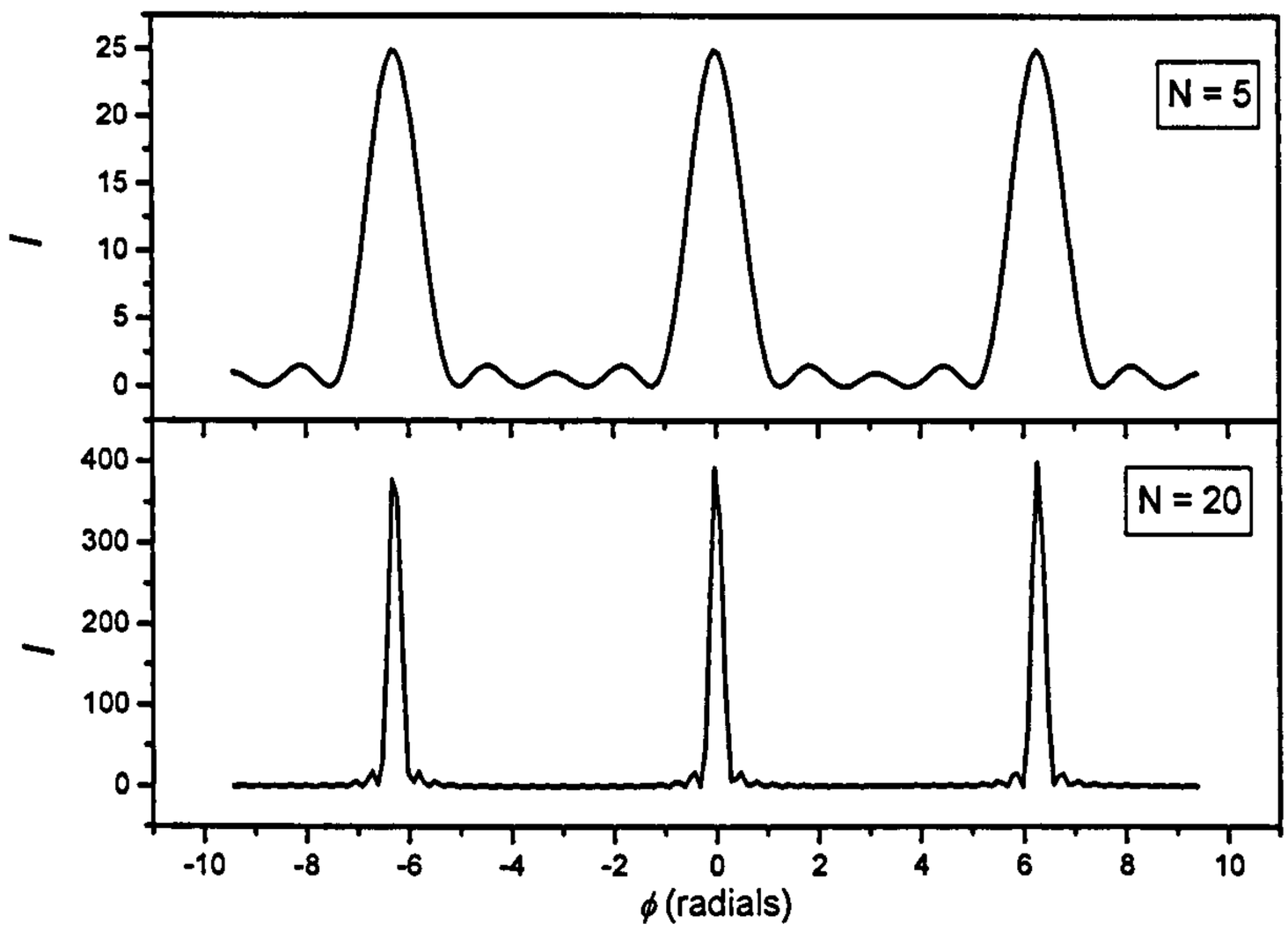

Figure 1.23. The multiple beam interference for a grating with N = 5 or 20.

In a scanning spectrometer, the grating is turned which changes θ_i and θ_d and light of different wavelength is projected on a fixed exit slit. This is called single channel scanning. In a multiple channel scanning setup, the grating is fixed and the detector is a multi channel detector like a diode array or a CCD chip.

1.5.1.3. Slit width and focal length

Two additional parameters influence the resolution of the spectrometer: the width of the entrance and exit slits placed before and after the grating and the focal length of the optical element focussing the diffracted beam on the exit slit (figure 1.24).

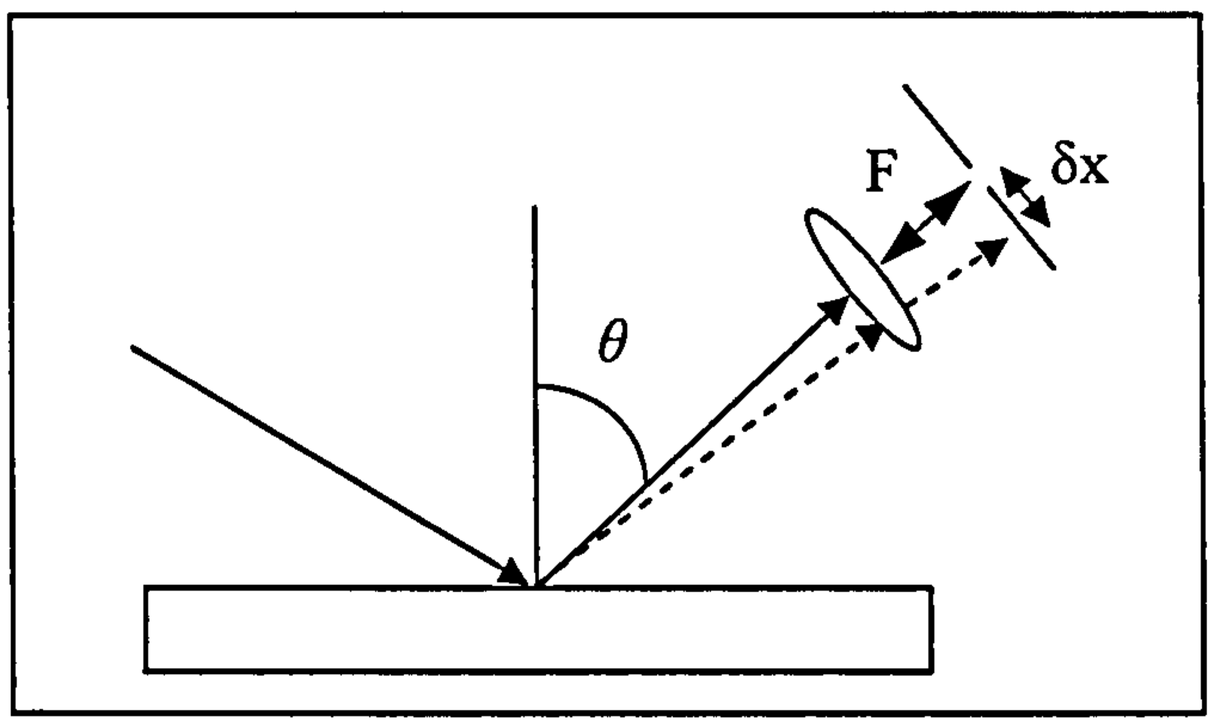

Figure 1.24. Schematic representation of the parameters influencing instrumental resolution.

The reflected light is imaged on an exit slit with a focussing optical element with focal length F. The separation δx between beams with two different wavelengths λ and $\lambda + \delta\lambda$ is $F.\delta\theta$. Resolving the two images is only possible when the width of the slit W is smaller than the separation δx or when $W < \delta x = F.\delta\theta$.

The total resolution of the system for the first order diffraction is then (Kuzmany 1998):

$$R = \lambda F/W.d.\cos\theta \qquad (1.5.3)$$

here d is the distance between different grooves. Clearly the resolution of the spectrometer is also wavelength dependent.

1.5.1.4. Detectors: multi channel systems and photomultipliers

A multi-channel detection system can be a diode array or a CCD camera. The diffracted beams are projected by the grating on the detector. This leads to defocusing at both ends of the detector, as the wave front of the diffracted light is semi-cylindrical in space, while the CCD or diode array is a flat panel. The obvious advantage of this system is speed as the entire spectrum is recorded at all wavelengths in one single measurement.

Single channel detectors like photomultipliers (PMT) or pin diodes do not suffer from defocusing, but the spectrum is recorded by turning the grating until all wavelengths

have passed the detector. These systems are slow, but there are less defocusing astigmatism and coma problems.

1.5.1.5. Single beam systems

In single beam systems, the spectrum of the light source without sample is measured and then the sample is introduced. The spectrum of the transmitted light intensity is then measured and the ratio of the two spectra gives the transmittance. There are two possible system configurations:

- The sample is illuminated with the full spectrum of the light source, and the transmitted light is then collected and dispersed in the different wavelengths. The detector is a multi-channel detector (diode array, CCD) or a scanning monochromator and a detected by a pin diode or PMT.
- In the second system, the sample is illuminated by monochromatic light and the fraction of the light transmitted by the sample is detected. The pre-monochromator then scans the entire spectrum and the transmission or absorption spectrum is recorded.

1.5.1.6. Double beam systems

In double beam systems, the spectrum is monochromated before it reaches the sample. The light is modulated by a chopper which alternatively passes the beam through the sample (sample beam) and the through a blank space (reference beam). The light is detected, typically with a photomultiplier (PMT), and this generates an alternating current. The intensity of the current is a measure of the absorbed light. The spectrum is then calculated by dividing the sample signal by the reference beam signal. Fluctuations of the intensity of the lamp are compensated, since reference and sample signals are collected almost simultaneously.

1.5.1.7 Double and triple monochromator systems

Modern high-resolution spectrometers contain two or more monochromators. These have a higher stray light rejection and a significantly higher resolution and can be

used to measure spectra close to very strong lines, for example when a spectrometer is used to measure Raman scattered light close to the laser line.

These spectrometers can be used in the additive and in the subtractive modes (figure 1.25). In the additive mode, monochromator G_1 disperses the polychromatic light and the slit $S_{1,2}$ acts as a bandpass filter, selecting the required wavelength region. All other monochromators and slits act in the same way. A high resolution is obtained by this technique as every filtered wavelength region is further dispersed by the next monochromator.

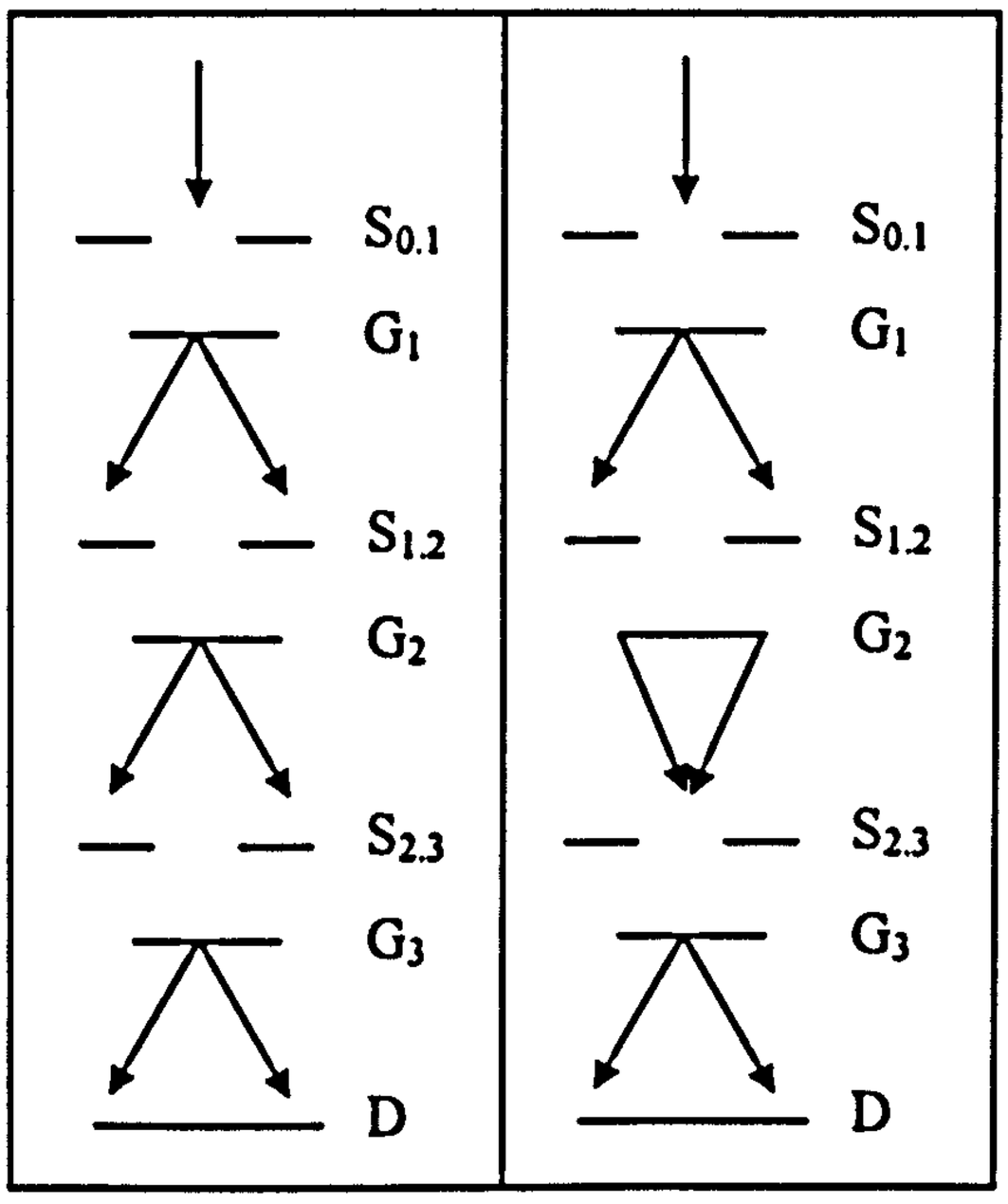

Figure 1.25. The additive (left) and subtractive (right) mode for triple monochromators.

In the subtractive mode, the slit $S_{1,2}$ acts again as a bandpass filter, but the second monochromator acts in a different way: it recombines the light and focuses it on a very narrow exit slit $S_{2,3}$ which serves as the entrance slit for monochromator G_3 which projects the spectrum on the detector D. The ultimate resolution is now of course determined by the third monochromator G_3. Excellent stray light rejection is reached due to the very narrow slit $S_{2,3}$. This arrangement is typically used in a Raman system where one has to get close to the laser line.

1.5.1.8. Systems used

The systems used in this thesis for UV-VIS absorption are a Perkin-Elmer Lambda 800 spectrometer at King's College London, capable of measuring from 900 to 200 nm, and a Varian Cary 100 at HRD Research, capable of measuring from 900 to 200 nm. Both systems are double beam systems, with a deuterium lamp for the UV region, a tungsten halogen light bulb for the visible to near-infrared region, and a photomultiplier as the detector.

The photoluminescence detection system works with a similar dispersive system, but emitted light, excited by light of a different wavelength, is analysed and detected. Different lasers are used to cover an extensive spectral emission range. Sub-threshold excitation of luminescence of defects in diamond (chapter three) and photoluminescence experiments were carried out with a Renishaw RM 2000 system, equipped with a 325 nm HeCd laser or a 514.5 nm Argon-ion laser and a 2400 g/mm grating blazed at 300 nm for the UV-VIS region or a 1800 g/mm grating blazed at 500 nm for the VIS-NIR region. The detector is a UV coated, deep depletion (NIR enhanced) CCD chip.

The samples were cooled in an Oxford Instruments MicrostatN cryostat, and an ITC601 controlled the temperature. Good thermal contact was ensured by glueing the samples to the cryostat with silver DAG. The samples were located as close as possible to the thermocouple. Before recording a PL spectrum at different temperatures, the cryostat was allowed to thermally stabilise for at least 2 minutes. Sample inhomogeneity is a major problem when working with natural diamond samples. Slight deviations from the original position of the sample due to thermal dilatation of the cryostat can give erroneous results. This problem was circumvented by repositioning the sample in the X and Y directions with respect to the origin of a thin (1 μm) laser-inscribed reference cross on the diamond's surface. After the measurement, the position of the sample was checked to ensure that no drift of the sample position had happened during the measurement. Spectra were recorded at different temperatures, held to ± 0.5 K, normally at intervals of not more than 20 K.

At King's College an XY Dilor Raman spectrometer equipped with a cooled and intensified 512-diode array multi-channel detector was used. The resolution of the spectrograph was approximately 1.3 nm at the wavelength of the zero-phonon transition of the $(N\text{-}V)^-$ defect (637 nm). The photoluminescence from the diamond sample was excited with tuneable Coherent CR-599 dye laser. Laser lines between 639.4 and 688.5 nm were produced by pumping a continuously circulating solution of DCM (4-dicyanomethylene-2-methyl-6-p-diethylaminostyryl-4-H-pyran) dye with up to 5.5 W of 532 nm radiation from a frequency-doubled Nd-YAG Coherent Verdi 5 laser. At each wavelength the intensity of the output from the dye laser was measured and used to correct the luminescence intensity afterwards.

1.5.2. FTIR spectroscopy

In modern infrared spectroscopy, a chopper does not modulate the infrared beam as in a UV-VIS spectrometer, but the beam is modulated in phase space. Fourier transformation is used to calculate the spectrum from the phase-modulated spectrum.

1.5.2.1. Light source

The light source in an FTIR spectrometer is a hot filament (SiC rod) and the emitted light has approximately a black body radiation spectrum. There are two types of sources: commonly used air cooled sources and water-cooled sources, which typically have a larger filament and thus a higher energy throughput.

Modern FTIR spectrometers can also work in the NIR spectral region by changing some parts like the beam splitter (extended KBr, CaF or quartz), detector (InGaAs, Ge, Si or PbS) and source (tungsten halogen light bulb). Special options in some spectrometers like the top range Bruker FTIR devices allow the spectrometer to scan into the visible and the UV region.

1.5.2.2. Interferometer

The heart of an FTIR system is the Michelson interferometer. This part modulates the polychromatic light of the light source, but in frequency space, by constructive and destructive interference of light propagating along different paths (figure 1.26).

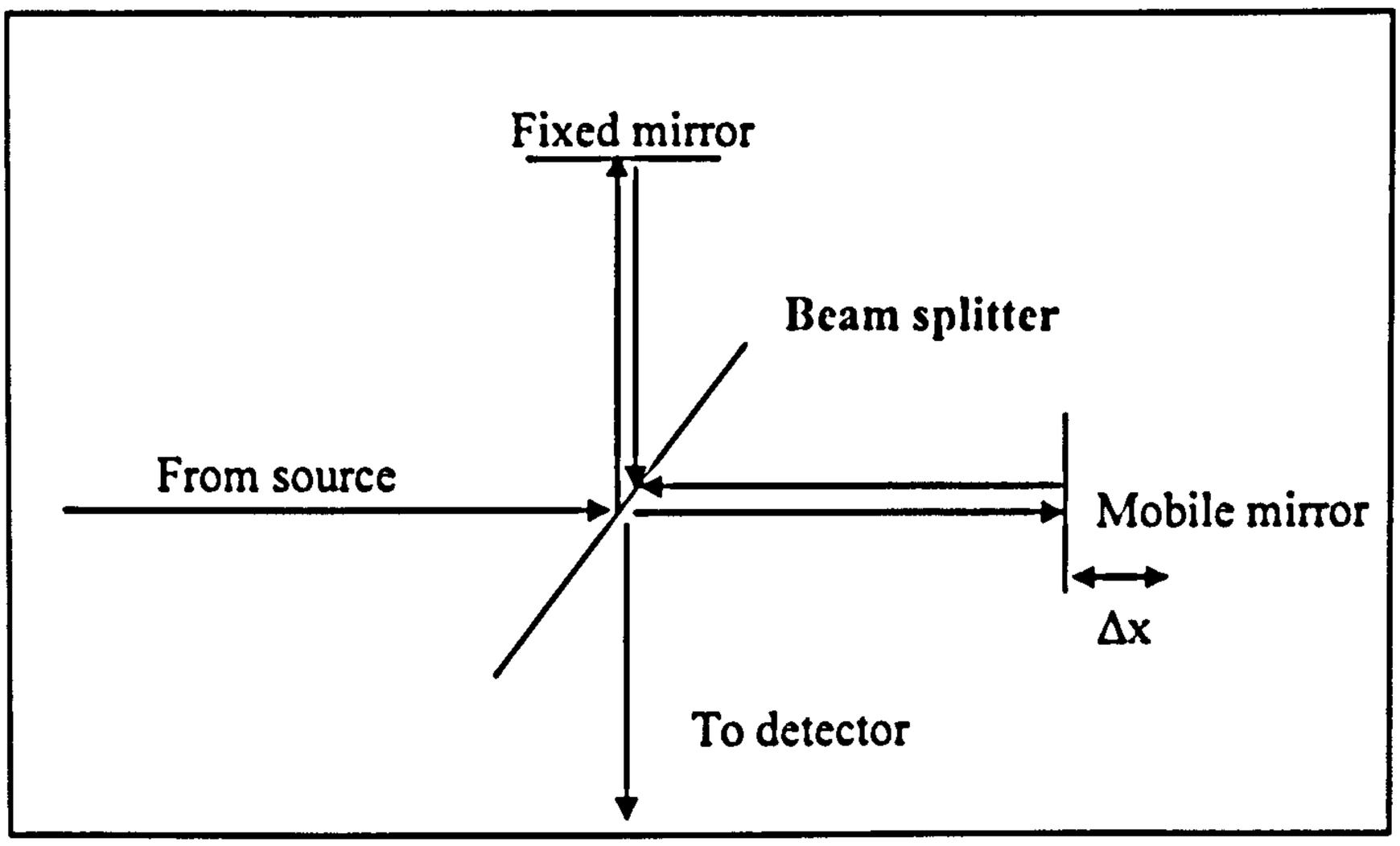

Figure 1.26. A schematic representation of a Michelson interferometer. The light beam comes from the left side onto a semi-reflective mirror. 50% of the light is reflected to the fixed mirror while 50% of the light is transmitted to a mobile mirror. The reflected light beams come together at the semi-reflecting mirror and lead to destructive or constructive interference, depending on the pathlength difference Δx between the interfering light beams.

1.5.2.3. Basic principles in FTIR spectroscopy

The Michelson interferometer is schematically shown in figure 1.26. A parallel bundle of light from the source is split by a beam splitter (half reflecting mirror). The reflected part is reflected back to the beam splitter by a fixed mirror and the transmitted part is reflected back to the beam splitter by a mobile mirror. The reflected light from the stationary and mobile mirror is combined at the beam splitter. When the mobile mirror moves over a distance Δx interference fringes develop at the detector. The intensity $I_0(\nu)$ of the light of the source with a frequency ν, described by its electrical wave vector $\mathbf{E}(\nu,t) = \varepsilon(\nu)\exp(i2\pi\nu t)$ is

$$I_0(\nu) = \langle E(\nu,t) | E(\nu,t) \rangle = \varepsilon(\nu)^2 \qquad (1.5.4)$$

The intensity at the detector is the superposition of the wave front of the beam reflected from the static and mobile mirror causing a time delay δ. The superposition of the two beams propagating along different paths causes interference fringes at the detector and the incident intensity is dependent on δ:

$$I(\nu,\delta) = \langle E(\nu,t) + E(\nu,t+\delta) | E(\nu,t) + E(\nu,t+\delta) \rangle$$
$$= \frac{1}{4}\varepsilon(\nu)^2 \left[2 + e^{-12\pi\nu\delta} + e^{12\pi\nu\delta}\right] \qquad (1.5.5.).$$
$$= \frac{1}{2} I_0(\nu)[1 + \cos(2\pi\nu\delta)]$$

For monochromatic light the output of the Michelson interferometer at the detector fluctuates sinusoidally between zero and half the source intensity.

The time delay δ is related to the displacement x of the mobile mirror from the equal displacement with respect to the beam splitter by:

$$\delta = \frac{2x}{c} \qquad (1.5.6)$$

where c is the light speed.

With this, equation (1.5.5.) becomes:

$$I(\nu,x) = \frac{1}{2} I_0(\nu)\left\{1 + \cos\left[2\pi\nu\left(\frac{2x}{c}\right)\right]\right\} \qquad (1.5.7)$$

or by using $\lambda = \nu/c$

$$I(\lambda,x) = \frac{1}{2} I_0(\lambda)\{1 + \cos[4\pi\lambda x]\} \qquad (1.5.8)$$

So the output fluctuates with $2\lambda x$. Of course in the light source, there is a distribution of intensities S(v) so the total intensity of the light source is the integral over all frequencies:

$$I_0 = \int S(v)dv \qquad (1.5.9).$$

So the total output intensity at the detector is given by:

$$I(\delta) = \frac{1}{2}\int S(v)[1+\cos(2\pi v\delta)]dv \qquad (1.5.10).$$

The equation can be rewritten as:

$$\int S(v)\cos(2\pi v\delta)dv = 2I(\delta) - I_0 \qquad (1.5.11).$$

The constant term does not provide anything about the spectrum, but the term $I(\delta)$ does. The inverse cosine Fourier transform of $I(\delta)$ in equation (1.5.11) provides the spectrum:

$$S(v) = 2\int I_0(\delta)\cos(2\pi v\delta)d\delta \qquad (1.5.12)$$

Here one sees the benefit of Fourier Transform spectrometers. The whole spectrum is recorded in one scan and the input intensity is not dispersed, making this technique very sensitive. Also, interference fringes when measuring plane parallel plates will appear as spikes in the interferogram and can easily be removed. This results in the removal of interference fringes in the spectrum.

In practice the interferogram is recorded in numeric form after the mirror has been displaced over its full range and an inverse cosine Fourier transform is performed after the collection of the spectrum. Normally several spectra are co-added to improve the signal-to-noise ratio.

1.5.2.4. Systems used

FTIR spectra of the samples have been collected with a Nicolet Nexus or a Bruker Equinox 55. When necessary, a beam condenser (in the Bruker) or a microscope (a Continuμm microscope in the Nicolet) has been used to collect spectra from small samples.

1.5.3. EPR measurements

1.5.3.1. Basic principles and setup

EPR or electron paramagnetic resonance is resonant absorption of electromagnetic radiation by unpaired electrons in a magnetic field. These electrons have different spin states and the application of a magnetic field will split these states. Resonant absorption of electromagnetic radiation will flip one state into the other. The energy required to flip the spin state is of course equal to the energy separation between the states:

$$h\nu = g\beta H \qquad (1.5.13)$$

Here h is the Planck constant, ν is the frequency of the electromagnetic radiation, g is the spectroscopic splitting factor for the free electron (g = 2.0023) and β is the Bohr magneton. We remark here that the transition is not between different electronic energy levels, in contrast to optical absorption or emission. In this study we used EPR to determine the concentration of single substitutional nitrogen or P1 defects in diamond. A review of EPR detectable defects in diamond is given in Loubser (1978) and Newton (1994).

For EPR investigation a defect in a solid is usually described by an effective Hamiltonian $\hat{H}$.

$$\hat{H} = \beta H.g.S + S.D.S + S.A.I \qquad (1.5.14)$$

Here the first term represents the Zeeman interaction (electron-magnetic field), the second term is the zero field splitting (surrounding crystal field-electron interaction) and the third term is the magnetic hyperfine interaction. The terms S and I are operators describing electron spin and nuclear spin respectively, while the g, D and A terms are tensors: the g tensor, the zero field splitting tensor D and the hyperfine tensor A respectively.

Details on the information one can extract from the different tensors can be found elsewhere (Spaeth *et al.* 1992) and a review of the essential data will be given below.

The Zeeman term or the g tensor will give information about the symmetry of the defect and consists of a symmetrical and an asymmetrical part.

The zero field splitting term or D tensor, arises because of the presence of other paramagnetic defects (spin-spin interaction, or spin-orbit coupling, ...) and in diamond the dominant interaction will be the dipole-dipole interaction between different unpaired electrons. The term is important to determine the symmetry of the system and will be a measure of the dimension of the defect (Spaeth *et al.* 1992).

The hyperfine parameter or A term describes the interaction between the unpaired electron and the nuclear spin of atoms near the defect. If the nucleus has zero spin there will be no interaction. This parameter can be used to determine the orbital character of the defect (more s or p character), see Lannoo and Bourgoin (1983).

The EPR spectrometer consists of a klystron which produces monochromatic microwave radiation which is guided by a microwave guide through an attenuator into a resonant metal cavity. The cavity is located in the magnetic field and the magnetic field is perpendicular to the microwave field. The impedance of the cavity at resonance is (Loubser and van Wyk 1978):

$$Z_R = R\left(1 + 4\pi\eta Q\chi''\right) + i4\pi L_0\omega\chi' \qquad (1.5.15)$$

where χ'' and χ' are the imaginary and real parts of the magnetic susceptibility. Q is the quality factor and η is the filling factor since only part of the cavity is filled with the sample. The impedance will go through a maximum when resonance is reached and this will change the amount of microwave power reflected by the cavity. This signal is then measured by a detector.

The microwave field is modulated with a high frequency modulation (100 kHz) while the large steady field is swept slowly through the magnetic resonance which is known from the reflected microwave power. When the modulation amplitude is smaller than the width of the EPR line, the spectrum is the derivative of the magnetic susceptibility of the defect with respect to the magnetic field.

1.5.3.2. Experimental procedure to determine the concentration of P1 defects

The diamonds were measured with a Varian CW spectrometer in the field range where the central P1 line is detectable. The P1 spectrum is due to single substitutional nitrogen atoms (Loubser 1978). The measurements were done in three days, and to eliminate drift in the spectra, a reference sample was measured every day. This reference sample is a plate of synthetic diamond grown by Sumitomo (without nickel, detectable by absorption spectroscopy), cut from a single growth sector. The concentration of the reference sample was determined by deconvolution of the one-phonon absorption in the FTIR spectra.

The central line of the P1 spectrum is at ~ 3394.5 G, with a microwave field frequency of ~ 9.51 GHz. The field sweep range was done over 20 G to eliminate the background and 5 G to determine the peak-to-peak width in the derivative spectrum. The spectra were normalized with respect to resonance frequency, and signal gain. The square of maximum to minimum separation multiplied with the signal intensity in the derivative 5 G spectrum is taken as a measure of the integrated intensity. The resolution of the spectra is 0.1 G, which is probably inadequate for the low concentration samples. In the paper of van Wyk (1997) the resolution is set to less than 20% of the peak to peak width, ensuring a correct measurement of the line shape. This procedure was not adopted here which might lead to substantial broadening of the line for low concentration of P1 defects. However, increasing the resolution by

decreasing the modulation frequency by 50% did not significantly change the peak-to-peak width of samples with low concentration of single substitutional nitrogen (~ 120 ppb). The noise increased substantially without a decrease of the peak-to-peak width (the peak width changed from 20.9 to 19.7 G) so the procedure of van Wyk was not adopted as this would take too long before results could be produced.

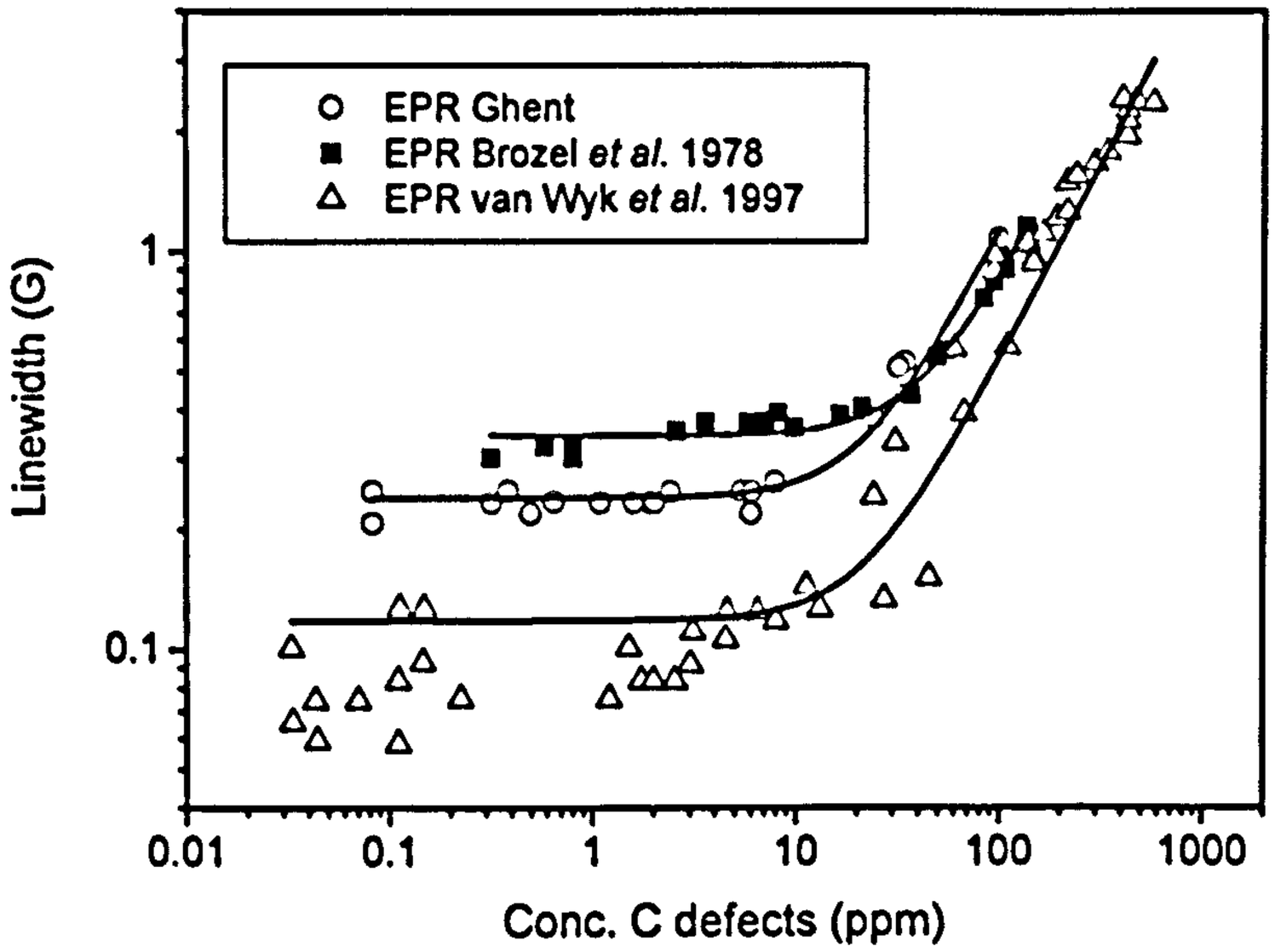

Figure 1.27. The dependence of the line width on the concentration of P1 defects in diamond for samples measured at the University of Ghent (open circles), data from Brozel et al. (1978) and from van Wyk et al. (1997). The solid curves were calculated with equation (1.5.16) and the values of the a and b parameters used to calculate the curves are summarised in table 1.2.

The concentration of P1 defects is determined by the following procedure: the relative signal intensity of each sample is calculated by comparing it with the reference sample. The intensity is corrected for the different weight (and thus volume) of the sample. As a check, the width of the P1 line is compared with the concentration calculated from the ESR signal intensity. The data (figure 1.27) is fitted with the equation 1.5.17 (van Wyk *et al.* 1997), which includes line broadening because of dipole-dipole interaction between spins with the same (P1-P1 defect interaction) and with different Larmor frequency (P1-^{13}C nuclear spin interaction):

$$y = \left(a + bx^2\right)^{1/2} \qquad (1.5.16)$$

The data of Brozel *et al.* (1978) and Van Wyk *et al.* (1997) are superimposed on the data of the samples, measured in this investigation at the University of Ghent.

The free parameters *a* and *b* for the different datasets are tabulated below.

Sample set	a	b
Univ. of Ghent	$5.8\ 10^{-2} \pm 0.4\ 10^{-2}$	$1.2\ 10^{-4} \pm 6.5\ 10^{-6}$
Brozel *et al.* (1978)	$1.2\ 10^{-1} \pm 0.1\ 10^{-2}$	$0.7\ 10^{-4} \pm 2.0\ 10^{-6}$
Van Wyk *et al.* (1997)	$1.4\ 10^{-2}$	$1.2\ 10^{-4}$
Zhang *et al.* (1994)	$6.4\ 10^{-4}$	$1.2\ 10^{-4}$

Table 1.2. The *a* and *b* parameters, used to calculate the curves in figure 1.27.

One can see significant differences between the different parameters from different investigations. The sample used by Zhang 1994 was a synthetic type IIa diamond with a ^{13}C content of 0.05% (GE isopure HPHT synthetic diamond). As the *a* parameter depends rather strongly on the actual ^{13}C content, changes of this parameter are expected. Other parameters which could lead to differences between the results of van Wyk *et al.* (1997) and the results presented here are sample inhomogeneity, insufficient spectral resolution and magnetic field inhomogeneity. The total EPR P1 signal in our samples would then be the sum of Gaussian absorption lines, with different widths, corresponding to locally different concentrations of P1 defects in the samples. Small samples in the study of van Wyk *et al.* were cut from a single growth sector of synthetic diamonds, ensuring better sample and magnetic field homogeneity.

In summary, the concentrations of C defects can accurately be measured when above 20 ppm. In that case the measured concentrations would not differ significantly when measured by different techniques. However, measurements of concentrations of C defects below 10 ppm should be treated with caution.

1.5.4. Cathodoluminescence spectroscopy

1.5.4.1. Basic principles and setup

Cathodoluminescence (CL) is the emission of light from a material under electron bombardment. The luminescent properties are dependent on the material and the defects in the material. In contrast to photoluminescence, cathodoluminescence will lead to light emission of all possible radiative channels in the sample. However, some defects are not excited using the CL technique. These defects are the negatively charged defects like ND1 or $(N\text{-}V)^-$. Low energy electrons have a limited penetration depth, and variation in the energy of the electrons can lead to probing of depth dependent characteristics.

A CL system typically consists of an electron source, a movable sample stage and a spectrometer. To avoid energy loss of the electrons, the sample stage is evacuated. If the sample is not coated with a conductive layer, a low vacuum is used to avoid charging of the sample (since most diamonds are electrically non-conductive). This charge build up would reduce the CL emission efficiency. In high vacuum systems like scanning electron microscopes, the sample needs to be coated by a sputtered thin gold or carbon layer. In some scanning electron microscopy (SEM) systems simultaneous detection of CL and X-ray Fluorescence (XRF) (see section 1.5.5. of this chapter) emission is an additional advantage.

The irradiating electrons will create a non-equilibrium concentration of electrons and holes in the sample. Recombination of electrons and holes can be radiative and non-radiative. Radiative electron-hole defects in diamond can be divided in two classes: a) intrinsic or fundamental and b) extrinsic or impurity dependent.

Intrinsic emission is due to interband transitions of electrons in the bandgap. Diamond is an indirect-gap material, and therefore free excitons will not have an energy E_g close to the bandgap energy, but somewhat smaller, because the electron-hole recombination must be accompanied by the creation of a phonon (Kittel 1996). As a result, free exciton emission will be weaker in indirect-gap materials than in direct gap materials (Petrov 1996).

Extrinsic emission is due to impurities in the material, and the defect can lead to excitonic emission (bound excitons) or other luminescence. Many of the vibronic centres are readily excited using CL.

The shape of the excitation volume in a bulk object depends on the atomic number of the material: the excitation volume of a low atomic number material will have a pear shape, while for 15 < atomic number < 40, the volume is spherical. It is hemispherical for larger atomic number materials (Petrov 1996).

Polarization of CL emission has sometimes been observed. For example, in diamonds of type IIb, blue CL from linear defects oriented in the <110> direction has been observed with the E vector polarized along the same direction. This emission has been identified as originating at dislocations (Kiflawi and Lang 1976).

1.5.4.2. Systems used

Micro-cathodoluminescence (CL) was recorded with a Topcon 350 scanning electron microscope at NIRIM in Tsukuba, Japan. Here, the luminescence is produced by an electron beam (20 kV, 4 μA), and focussed by a mirror on the entrance slit of a 32 cm Photon Design PDP320 monochromator fitted with a 300 g/mm grating. Monochromatized light is detected by a Hamamatsu R928 photomultiplier for scanning and a Roper LN/CCD 400-EB-GI camera for imaging. The sample is cooled to liquid nitrogen temperature with a VG cold stage. The sample stage is motorized and can be moved in steps of 1 micrometer or larger, and spectra are recorded along a line with steps of 1 micrometer. All CL spectra were recorded with samples at ~80 K.

1.5.5. Energy Dispersive X-ray Fluorescence (EDXRF)

1.5.5.1. Basic principles and setup

Chemical analysis of the atomic impurities is carried out with Energy Dispersive X-ray Fluorescence or EDXRF. The basic working principle of EDXRF is the following: an X-ray from an X-ray source ionises an electron from an inner shell of an atom. This induces instability in the electronic configuration of the atom, and

electrons from a higher orbital shell will fall back into this lower shell. The energy difference between the electron of the higher and lower orbital will be emitted as an X-ray. The X-ray has an atom-dependent energy, since the energy difference depends on the energy difference between the inner shells, and on the atomic mass of the nucleus. If an electron falls back from one orbital above the ionised orbital, the transition is an alpha transition, if it falls back from the second orbital above the ionised orbital, the transition is a beta transition and so on. The ionised shell gives the name of the transition, see figure 1.28.

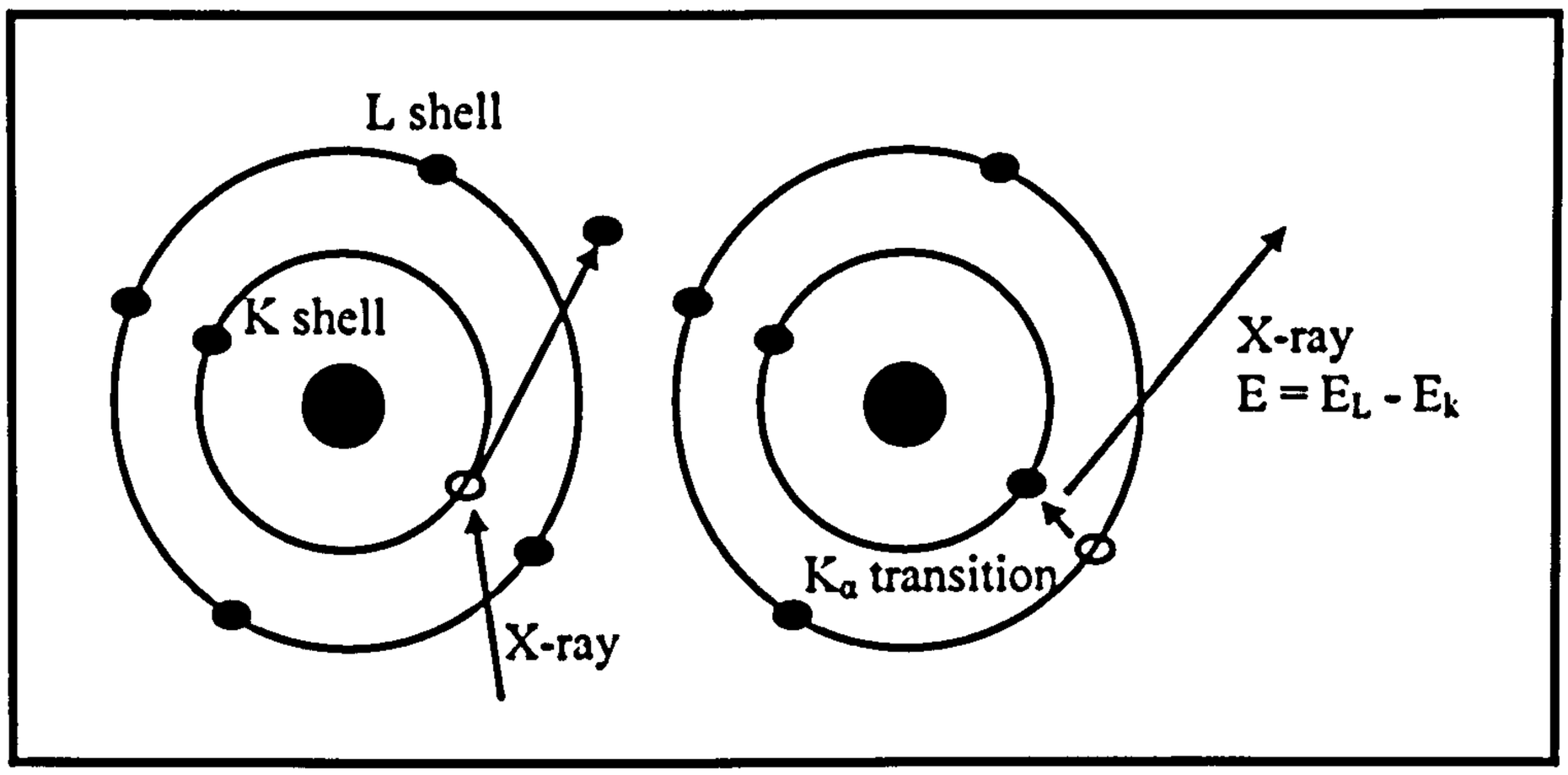

Figure 1.28. The K_α transition in X-ray fluorescence.

Since the inner electrons are not influenced by binding to other atoms, one can identify the trace elements in the sample.

The sample is illuminated with pulsed X-rays and the fluorescence is recorded. As this fluorescence decays in time, a time window is set in which the fluorescence is detected to eliminate fluorescence of overlapping excitation peaks. The energy of the X-ray is determined with a liquid nitrogen cooled silicon-lithium drift detector.

EDXRF measurements were carried out with an Oxford Instruments ED2000 system.

Quantitative XRF measurements cannot be carried out, partly because adequate calibration standards are not available and partly due to inhomogeneities of the samples. However, to estimate the concentrations in a semi-quantitative way, pellets

were made of carbon powder with nickel in well-determined quantities (10.0, 1.0 and 0.1 ppm) at Tessenderlo Chemie at Tessenderlo, Belgium. The signatures were first measured on a calibrated Wavelength Dispersive X Ray Fluorescence (Siemens WDXRF) system to set up a calibration curve. A synthetic diamond sample was measured with the WDXRF system and the intensities of the nickel peaks, measured with both the Oxford Instruments ED2000 and the Siemens systems were then compared. From this routine, an estimate of the lower detection limits can be given. This limit is not a constant for each of the atom, but it is estimated to be between 1 and 0.1 ppm for the Oxford Instruments ED2000 system.

1.5.6. Irradiation by with a linear electron accelerator (LINAC)

1.5.6.1. Basic principles and setup

A LINAC is a linear accelerator capable of accelerating nuclear particles like electrons or protons to high speed. The kinetic energy of the electron is expressed in kilo electron volts (keV) or mega electron volts (MeV). Electrons are generated by an electron gun, and inserted in the linear accelerator. The electron is injected into a high vacuum tube and accelerated in a high frequency RF electric field. The electron is accelerated in the negative half cycle of the RF wave and shielded by a copper tube when it is in the positive half cycle of the RF wave. The length of the shielding tubes increases along the path of the electron, to keep up with the pace of the electron (Burcham and Jobes 1995).

Electrons impinge on the diamond sample, which is cooled by running water at 19°C, and they lose their energy. There are three basic processes by which the electron can lose energy:

- Interaction of the electron with the electrons of the lattice, where the electron generates phonons, locally heating the sample.
- Direct momentum transfer of the electron with an atom in the lattice, displacing the atom out of its lattice site.
- At high energies (> 1 MeV) Brehmsstrahlung radiation becomes important as an energy loss mechanism.

In theory low energy irradiation will give a closely spaced vacancy-interstitial pair. Higher energy irradiation will transfer more energy to the knocked out atom, which can displace a neighbouring atom, pushing this atom into an interstitial position. If this atom has sufficient energy, a next atom can be displaced and so on. This will lead to a well-separated vacancy-interstitial pair. When the momentum transfer is higher, one particle can induce multiple vacancies and the closeness of the vacancies and interstitials will lead to significant ZPL broadening.

1.5.6.2. System used

The system used is a LINAC system at the University of Ghent, Belgium. The system is capable of accelerating electrons with energies between 2 and 10 MeV (theoretically 15 MeV can be reached).

There are four beam stations (figure 1.29), two (C0 and C2) of which are used for irradiation with electrons and two (C1 and CT) for generation of high energy X-rays. For irradiation with electrons with kinetic energy below 2 MeV, a set of metal filters is used to decelerate the electrons. However, the deceleration of the electrons makes the beam less mono-energetic and Gamma and high energy X-rays can also be created. The energy of the accelerated electrons is not mono-energetic (see figure 1.30).

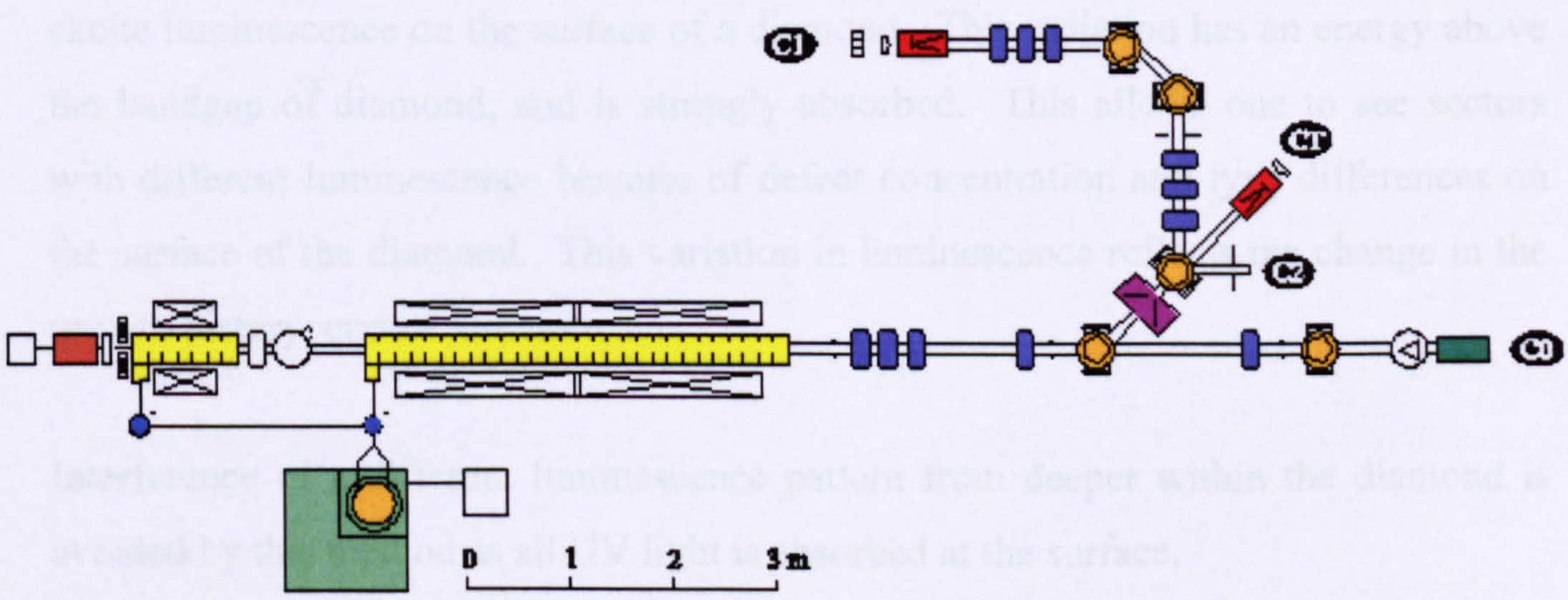

Figure 1. 29. The LINAC system of the University of Ghent. Irradiated samples are located at end station C0. Electrons are injected at the left side and accelerated (two yellow parts).

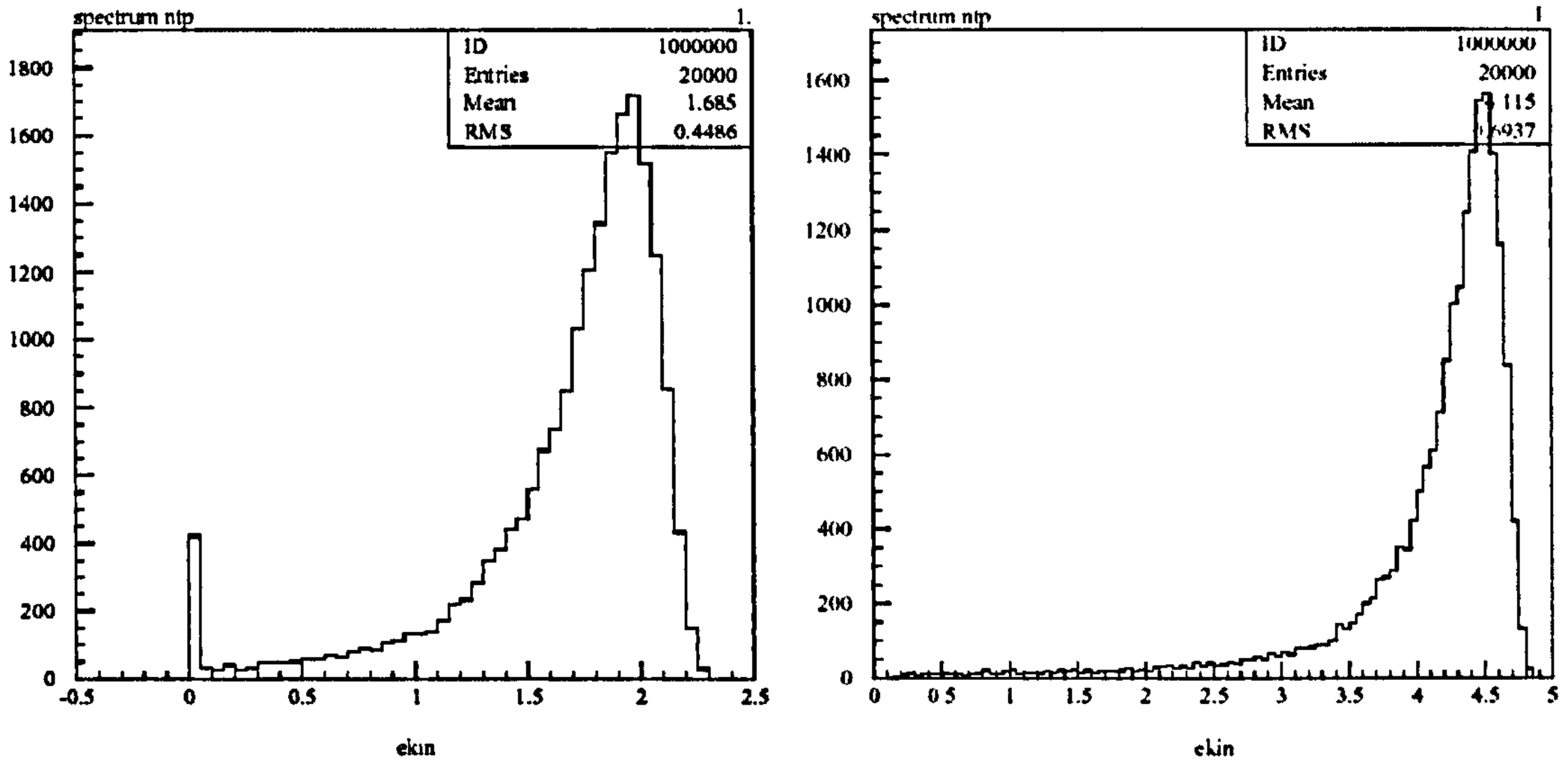

Figure 1.30. A simulation of the kinetic energy distribution of accelerated electrons in the LINAC system used, when the kinetic energy is set for 1.5 and 4 MeV (Univ. of Ghent).

All samples were turned 180° halfway through the irradiation process to induce a homogeneous vacancy concentration.

1.5.7. The DiamondView™ Instrument

1.5.7.1. Basic principle and setup

The DiamondView™ device uses short-wave UV light (wavelength < 225 nm) to excite luminescence on the surface of a diamond. This radiation has an energy above the bandgap of diamond, and is strongly absorbed. This allows one to see sectors with different luminescence because of defect concentration and type differences on the surface of the diamond. This variation in luminescence reflects the change in the growth history, crystal structure, …

Interference of a different luminescence pattern from deeper within the diamond is avoided by this method as all UV light is absorbed at the surface.

1.5.7.2. Device used

The short-wave UV topographic observations were performed using the DTC DiamondView™ instrument. The sample is put on a suction cup of a vacuum tweezer when inserted in the instrument. The generated luminescence is captured by a colour CCD camera and displayed on a computer screen.

1.6 Sample cleaning

The diamonds were cleaned by boiling in acids and in by immersion in acetone and an ultrasonic bath. This removes absorption and luminescence peaks because of grease from fingers, dirt, …

1.7. The concentration of infrared-active nitrogen-related defects in diamond

1.7.1. Defect induced infrared absorption

Pure diamond, like crystalline silicon and germanium, is a crystal with covalent interatomic bonds. As a result, infrared absorption is mainly due to two and three phonon absorption (Bilz 1966). Another way to understand this is by looking at the symmetry of the crystal: diamond has O_h symmetry, so the lowest symmetry is two-fold. One-phonon absorption is thus impossible and can only be introduced by breaking the crystal symmetry locally: i.e. by distortion of the lattice by intrinsic or extrinsic impurities.

A prerequisite for one-phonon infrared absorption is that the defect can induce an electric dipole. This depends on the symmetry of the defect which can be found in character tables (see section 1.2.1. of this chapter). The theory of defect activated infrared absorption has been used by Lax and Burstein (1955) to explain the infrared absorption in type I diamond. Later Dawber and Elliot (1963), and Elliot (1966) calculated absorption spectra of impurities in silicon by Green function techniques (for an introduction on the use of Green functions to calculate absorption spectra, see Yu and Cardona (2003)). If the symmetry of the substitutional defect is the same as that of the host lattice, the defect induced one-phonon infrared absorption can be

calculated from Elliot (1966) and the theory shows that the absorption is then composed of two parts:

- The first part is due to localized vibrational modes, where frequencies have no analogue with the frequencies of the lattice modes.
- The second part is due to the activation of lattice modes and the frequency dependence of the absorption is the one-phonon density of states (DOS) of a perfect crystal, modified by a smoothly varying frequency dependent function. As a result the one-phonon absorption due to defects will show maxima and shoulders in the absorption spectrum at critical points in the DOS.

The one-phonon density of states for diamond is shown in figure 1.31 and one can observe deviations from the one-phonon density of states measured by inelastic neutron scattering (Bilz and Kress 1979). A significant feature in the calculated DOS is the sharp peak at the Raman frequency (1332 cm^{-1}) and the non-zero density of states at frequencies above the Raman frequency (Pavone *et al.* 1993). This is due to the overbending of the [100] LO phonon, which is also experimentally observed (Kulda *et al.* 1996). This overbending of the LO phonon has been used to explain the anomalous shape of the second order Raman peak (Kulda *et al.* 2002, Windl *et al. 1993*).

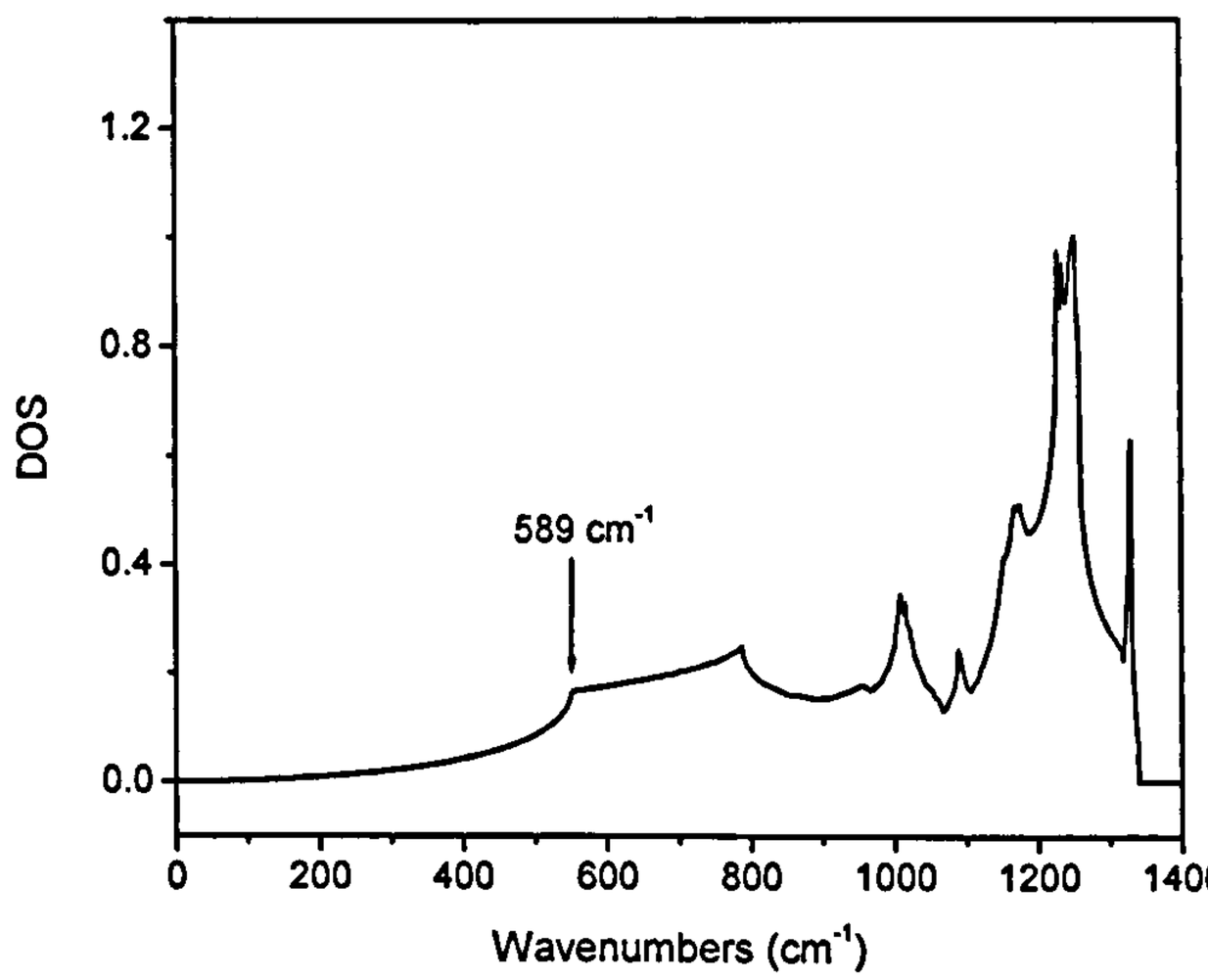

Figure 1.31. The one-phonon density of states for diamond as calculated by Pavone *et al.* (1993).

For A defects, which involve two nitrogen atoms, the effect of the off-diagonal elements is to induce a shift, dependent on the change in bond strength between the

nitrogen-carbon (748 kJ/mol), the carbon-carbon (610 kJ/mol) and nitrogen-nitrogen bonds (945 kJ/mol) (Weast 1989). Since the change in bond strength between the nitrogen-nitrogen bonds is the largest compared to the carbon-carbon bond, one can expect a significant shift of nitrogen-nitrogen vibrations with respect to critical points in the DOS. Indeed the first critical point in the vibrational DOS is at 73 meV or 589 cm^{-1} (figure 1.31), while the lowest frequency absorption due to the A defect in diamond is observed at 480 cm^{-1} (or 60 meV).

As stated in the introduction, nitrogen in type I diamonds can be present as a single substitutional atom or in aggregated form. Aggregates of 2 nitrogen atoms are called A defects and have C_{3v} symmetry (Davies 1976), while aggregates of 4 nitrogen atoms around a vacancy are called a B defects and have T_d symmetry. Both defects have a distinctive absorption spectrum in the IR (figure 1.32).

Groups of three nitrogen atoms around a vacancy also exist, but these defects are not detected in the infrared spectrum of the diamond: the presence of these defects is only detectable in the UV-VIS absorption spectrum. Single substitutional nitrogen defects are called C centres. Another defect which is frequently detected in the infrared spectrum of type Ia diamonds is the platelet. Platelets are thought to consist of planes of interstitial carbon atoms (Goss 2003), and they have a distinctive peak outside the one phonon region of diamond, around 1365 cm^{-1}. Platelets are known to correlate with D defects in diamond (Woods 1986). D defects have a relatively featureless absorption spectrum, in the same region where the A and B defects have their strongest absorption. Woods (1986) showed a correlation between the integrated intensity of the platelet (B') peak and the D absorption at 1282 cm^{-1} and also, for most diamonds, between the integrated intensity of the B' peak and the B defect absorption. Diamonds showing this relation are called regular diamonds. Some diamonds deviate from the relation between the B component and the integrated intensity of the platelet peak. These are called irregular diamonds. Positively charged single substitutional nitrogen can also be detected in the infrared spectrum of diamond. This defect has T_d symmetry and its spectrum is substantially different from the C defect absorption spectrum (figure 1.32) (Lawson *et al.* 1998). This reflects the different symmetry of the defect.

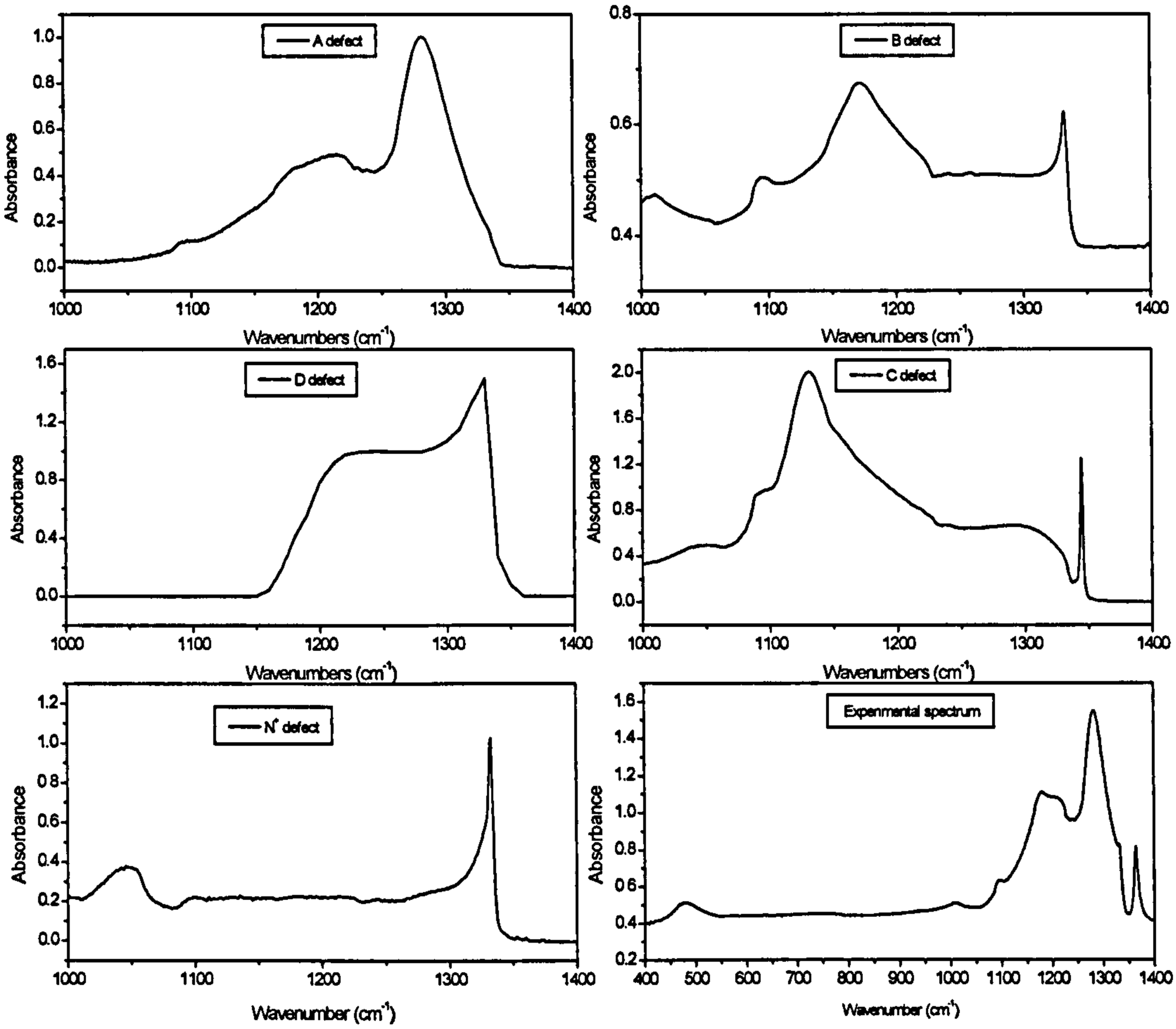

Figure 1.32. The various one-phonon induced absorption spectra in diamond due to single nitrogen, nitrogen aggregates and platelets. The A defect consists of two nitrogen atoms, the B defect of four nitrogen atoms around a vacancy, the D defect is platelet related. The C defect is a single substitutional nitrogen defect and the N^+ is an ionised C defect. A typical absorption spectrum of a type IaA/B diamond is the superposition of A, B, D spectra and the platelet peak. The strengths of the A and B absorptions are proportional to their concentrations in the diamond.

The C defect has a sharp absorption maximum at 1344 cm^{-1}, a frequency outside the range of lattice frequencies. The peak position does shift with ^{13}C isotopic subtitution in synthetic diamond, but does not shift when ^{14}N is substituted by ^{15}N, proving it is a localised mode (Collins *et al.* 1987, Collins *et al.* 1988).

1.7.2. Concentration determination procedure

The concentration of nitrogen in the defects detectable by infrared spectroscopy can be calculated by using the procedure described in Boyd *et al.* (1994, 1995), Lawson *et*

al. (1998) and Kiflawi *et al.* (1994). All FTIR spectra are first baselined and renormalized for a pathlength of 1 cm^{-1} absorption (or absorption coefficient) and then decomposed into the A, B and/or C, N^+ centres respectively. The strength of the absorption at specific wavenumbers is then multiplied with the parameters of table 1.3. An example of the decomposition of the FTIR spectrum of a type Ia diamond with A, B, D and platelets is shown in figure 1.33.

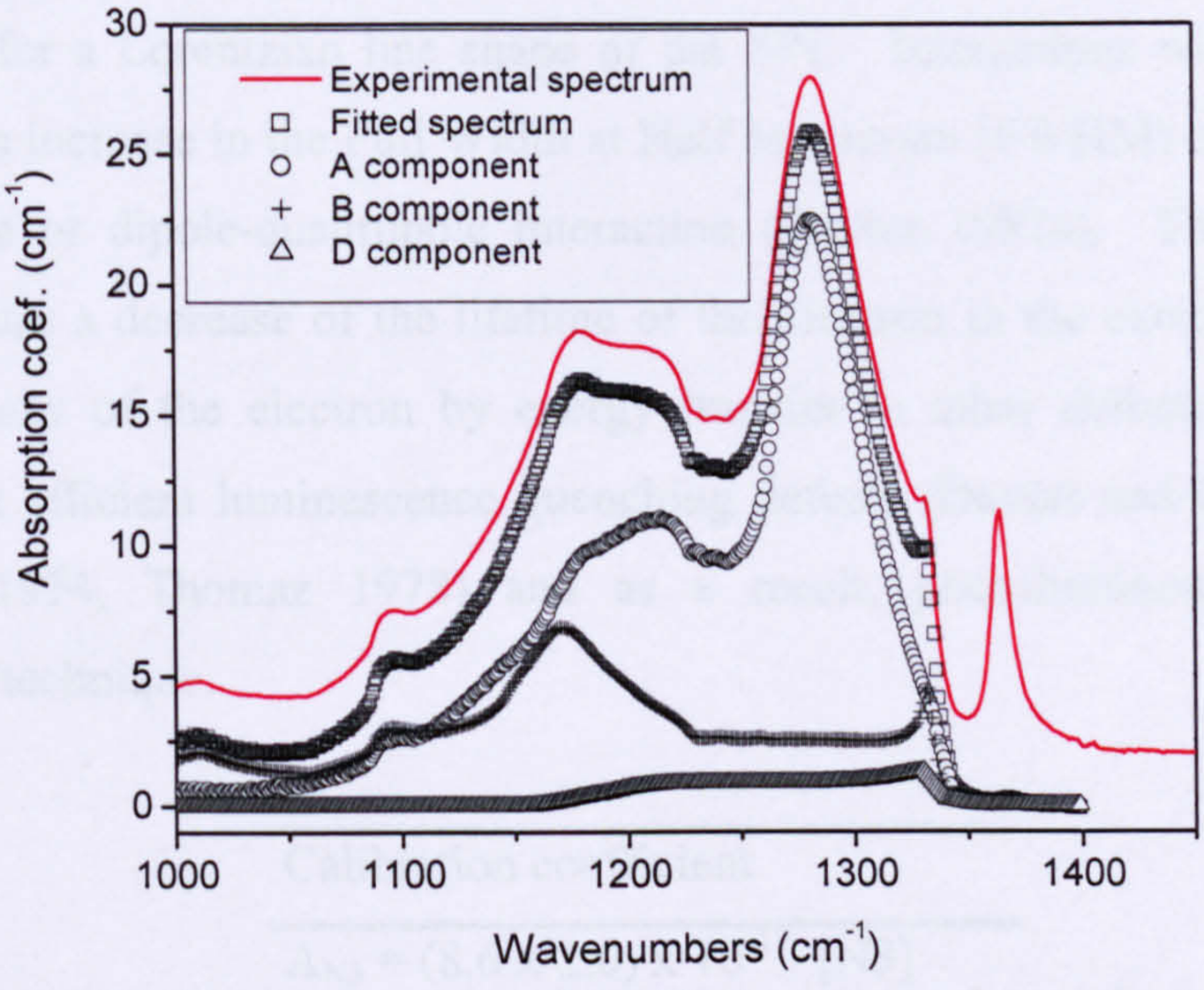

Figure 1.33. The decomposition of the FTIR spectrum of a regular type IaA/B diamond with platelets and A, B and D components. The fitted spectrum is a least square fitting of the sum of A, B and D components. The experimental spectrum is shifted up by 2 cm^{-1} for clarity.

Nitrogen conc. (at. ppm)	Abs. coef.
$[N^0] = (25.0 \pm 2)$	at 1130 cm^{-1}
$[N^+] = (5.5 \pm 1)$	at 1332 cm^{-1}
$[N_A] = (16.5 \pm 1)$	at 1282 cm^{-1}
$[N_B] = (79.4 \pm 8)$	at 1282 cm^{-1}

Table 1.3. The calibration coefficients used to determine the concentrations of the nitrogen containing defects in the one-phonon region of the FTIR spectrum.

1.8. The concentrations of defects determined by UV-VIS absorption spectroscopy

Because of the large bandgap of diamond (5.5 eV) (Clark 1964) defects can have localised states in the bandgap, and optical transitions can occur between the different energy levels. This leads to a Zero Phonon Line transition and a side band due to electron-phonon coupling. Random stress and the electron-phonon coupling are responsible for a Lorentzian line shape of the ZPL. Interactions with other defects will cause an increase in the Full Width at Half Maximum (FWHM) of the line due to dipole-dipole or dipole-quadrupole interaction (Davies 1981a). These interactions will also cause a decrease of the lifetime of the electron in the excited state or non-radiative decay of the electron by energy transfer to other defects. A defects in diamond are efficient luminescence quenching defects (Davies and Crossfield 1973, Crossfield 1974, Thomaz 1978) and as a result, photoluminescence is not a quantitative technique.

Calibration coefficient
$A_{N3} = (8.6 \pm 2.0) \times 10^{-17}$ [N3]
$A_{ND1} = (3.9 \pm 1.0) \times 10^{-16}$ [V^-]
$A_{ND1} = (4.8 \pm 0.2) \times 10^{-16}$ [V^-]
$A_{GR1} = (1.2 \pm 0.3) \times 10^{-16}$ [V^0]
$A_{NV} = (1.4 \pm 0.35) \times 10^{-16}$ [N-V]
$A_{H3} = (1.0 \pm 0.35) \times 10^{-16}$ [H3]
$A_{H4} = (1.0 \pm 0.35) \times 10^{-16}$ [H4]
$A_{1.859} = (1.0 \pm 0.2) \times 10^{-17}$ [R2]

Table 1.4. A is the integrated intensity of the zero-phonon absorption line of the defect, measured at 77K, with the absorption coefficient in cm^{-1} and the photon energy in meV.

The concentration of a particular defect with absorption in the UV-VIS spectrum is calculated by multiplying the area under the curve of a Lorentz function fitted to the experimental curve, with an appropriate calibration factor. The abscissa of the spectrum needs to be in meV or another energy unit as absorption is proportional to the amount of energy absorbed by a defect.

The coefficients are known from Davies (1999) and are summarised in table 1.4.

1.9. Defect properties

In this thesis a number of defects, detectable in UV-VIS absorption, photoluminescence and infrared measurements will be encountered. This section will summarize properties of these defects, to prevent unnecessary repeating of their properties in all the following chapters. In the next section, a more elaborate explanation will be given about the correlation between the different defects, defect production and the correlation between some absorption lines in IR and UV-VIS spectra.

1.9.1. Table of electronic transitions

Zero Phonon line	Symmetry	Transition	Composition and remarks
ND1 (393 nm)	T_d	A to T	Negatively charged vacancy (Davies 1977) S = 3.18 Phonon interaction: 76, 80 meV Dynamic Jahn-Teller distortion (Lowther 1978)
N3 (415 nm)	C_{3v}	A_1 to E	3N around a vacancy (van Wyk 1982, van Wyk 1993) S = 2.45 Phonon interaction: 93, 165 meV In absorption, vibronic coupling to an A_2 state gives rise to the N2 side band (Davies 1981a), however there are doubts about this (see section 1.2.3) and N2 absorption might be independent of N3 absorption.

490.7 nm	Monoclinic I	A' to A'	Unknown composition, thought to be related to plastic deformation (Collins *et al.* 2000, Nazare *et al.* 1992) S = 2.8 Phonon interaction: 80, 106, 143 meV
H4 (496 nm)	C_{1h}	Unknown	B defect + vacancy (Davies 1977, Clark and Davey 1984) S = 3 Phonon interaction: 40, 154 meV
H3 (503.2 nm)	C_{2v}	A_1 to B_1	$(N\text{-}V\text{-}N)^0$, A defect + vacancy (Davies 1977, Clark and Davey 1984) Nearly degenerate excited state S = 3 Phonon interaction: 41 and 152 meV Higher excited states between 3.2 and 3.6 eV (Collins 1983). Vibronic mixing with a second B1 state 16 meV above the 2.463 eV (503.2 nm) state (Davies *et al.* 1976)
3H (503.5 nm)	Rhombic-I	Unknown	Interstitial related (Twitchen 2001) S ~ 0.8 Phonon interaction: 67 meV
$(N\text{-}V)^0$ (575 nm)	C_{3v}	A_1 to E	Neutral N-V defect (Mita 1993) S = 3.3 Phonon interaction: 46 meV

594 nm	D_{3d}	E to E	Unknown composition, radiation damage related defect in nitrogen-containing diamond S = 2.1 Phonon interaction: 75, 165 meV
$(N\text{-}V)^-$ (637 nm)	C_{3v}	A_1 to E	Negatively charged N-V defect S = 3.65 Phonon interaction: 65 meV
GR1 (741 and 744 nm)	T_d	A to T (744 nm) E to T (741 nm)	Vacancy [Clark 1956a] Dynamic Jahn-Teller distortion (Lowther 1978, Davies and Foy 1980, Davies 1981b), S = 3.7 Phonon interaction: 41, 93 meV Higher excited states (GR2-8) between 2.88 and 3.01 eV (Collins 1978a).
H2 (986 nm)	C_{2v}	B_1 to A_1	$(N\text{-}V\text{-}N)^-$, Negatively charged H3 defect (Lawson *et al.* 1992a, Mita 1990) S = 3.35 (Lawson *et al.* 1992a) Phonon interaction: 65 meV, local mode at 167 meV above ZPL (Lawson *et al.* 1992a)
H1b (2024 nm)	Monoclinic-I	Unknown	A defect + 594 nm defect (Collins *et al.* 1986) S = 0.1 Phonon interaction: Unknown

H1c (1934 nm)	Monoclinic-I	Unknown	B defect + 594 nm defect (Collins *et al.* 1986) S = 0.1 Phonon interaction: Unknown

1.9.2. Table of vibrational transitions

Defect	Symmetry	Peaks (cm^{-1})	Composition and remarks
A	C_{3v}	1282 1214 1095 480	Two nearest neighbour substitutional nitrogen atoms (Davies 1976)
B	T_d	1331 1075 1094 1010	Four nitrogen atoms around a vacancy (Jones *et al.* 1992)
C	C_{3v}	1344 1134	Single substitutional nitrogen atom (Kiflawi *et al.* 1994,Woods *et al.* 1990) Static Jahn-Teller effect (Loubser and van Wyk 1978, Davies 1981a)
D and B' (platelet)	C_{1h}	1360-1370	Platelet absorption Planar structure of interstitial carbon atoms on {001} planes (Goss *et al.* 2003)
N^+	T_d	1332	Ionised single substitutional nitrogen atom (Lawson *et al.*1998)

3107 cm^{-1}	trigonal	3107 1405	Hydrogen related absorption peak. A to A transition (Newton 2006) 3107 cm^{-1} peak: stretch vibration 1405 cm^{-1} peak: bend vibration Overtones at 2786, 4169, 4499, 5889, 6070 cm^{-1}.

1.9.3. Defect production and correlations

1.9.3.1 General aspects of defects production by irradiation

Various types of high-energy irradiation have been used to induce radiation damage in diamond and in materials in general. These are electron, gamma ray and nuclear particle (alpha, proton, neutron, ...) irradiation. The mechanism of defect production is different for each type of radiation (Agullo-Lopez *et al.* 1988): neutrons generate vacancies in the lattice by direct momentum transmission (neutron-atom collision) while charged particles will lose energy by electronic excitation of the lattice, thereby generating non-equilibrium excitons. As the charged particle moves through the lattice along certain crystalline direction, it will loose energy by Brehmsstrahlung. As a result intense X-ray emission can be observed when the incident particle beam is oriented along certain crystalline directions (Derry *et al.* 1982, Agullo-Lopez *et al.* 1988). Charged particles will push an atom out of its position because the Coulomb force between the equal charges of the atom and the impinging particle exceeds the binding energy of the atom to the rest of the lattice.

In order to displace an atom from its position in the lattice, a minimum energy is required; the displacement energy E_D. For diamond the displacement energy is 30 eV (Campbell and Mainwood 2000).

For electron irradiation, the differential cross section depends on the incident angle, the energy transferred, and the energy of the incident electron (Mott 1929, 1932, McKinley and Feshbach 1948, Agullo-Lopez *et al.* 1988). Multiple vacancy creation can occur when the transferred energy exceeds $2E_D$. Replacement collisions (where the primary displaced atom replaces a neighbouring atom) can lead to well separated

Frenkel pairs (vacancy-interstitial pairs) which are more stable than closely separated pairs. The maximum lattice damage depth and lattice damage profile of electrons, as a function of initial electron energy has been calculated by Campbell *et al.* (2002). The lattice damage profile has a sharp cut-off and the maximum depth is ~1.5 mm/MeV (Campbell *et al.* 2002).

In ion beam irradiation an intense beam of ionised particles such as protons or alpha particles is used. Understanding radiation-induced damage in solids is very complicated; for example one needs to take into account screening of the nuclear cell by surrounding electrons. For a classical two-particle collision, one knows the maximum energy E_{max} transferred to the atom in the lattice with mass M_1 by a particle with mass M_2 (Agullo-Lopez *et al.* 1988):

$$E_{\max} = \frac{4M_1M_2}{(M_1+M_2)^2} E_{kin} \qquad (1.9.1)$$

Here E_{kin} is the kinetic energy of the ion. This of course does not take Coulomb screening into account, but one can see that the transferred energy is maximal when the ion and lattice atom mass are equal. Free programs, available on the internet (www.srim.org), have been tested extensively and are used to simulate radiation damage by ions in materials, taking limited quantum mechanical processes (exchange and correlation terms) into account. The SRIM (Stopping Range of Ions in Materials) program is such an example and is educative as it gives an idea of the vacancy and interstitial profile, the generation of phonons, lateral deviations of the ion track because of Coulomb screening, ... However, it must be said that these programs neglect crystalline direction or additional processes like channelling of non-standard materials, like diamond. In the program, diamond is modelled as closely packed carbon atoms with a density of 3.52 and a displacement energy of 30 or 40 eV. The damage profile of 100 keV protons, calculated by SRIM is shown in figure 1.34. From the calculated phonon creation profile (fig 1.35), one can see that the generation of phonons is a significant energy loss process and the sample is substantially heated.

The SRIM calculation differentiates between different phonon creation mechanisms:

1. by the Coulomb interaction between the lattice electrons and the hydrogen ion,
2. and the knock on of the hydrogen ion without displacing the carbon atom from its lattice site (figure 1.35). The carbon atom will then jump back into the correct lattice site and the kinetic energy transferred by the recoil from the hydrogen ion energy to the carbon atom is dispersed in the lattice by phonons.
3. Also, Coulomb interaction between the ion and lattice electrons will ionise some of the lattice atoms (figure 1.36) as calculated by SRIM.

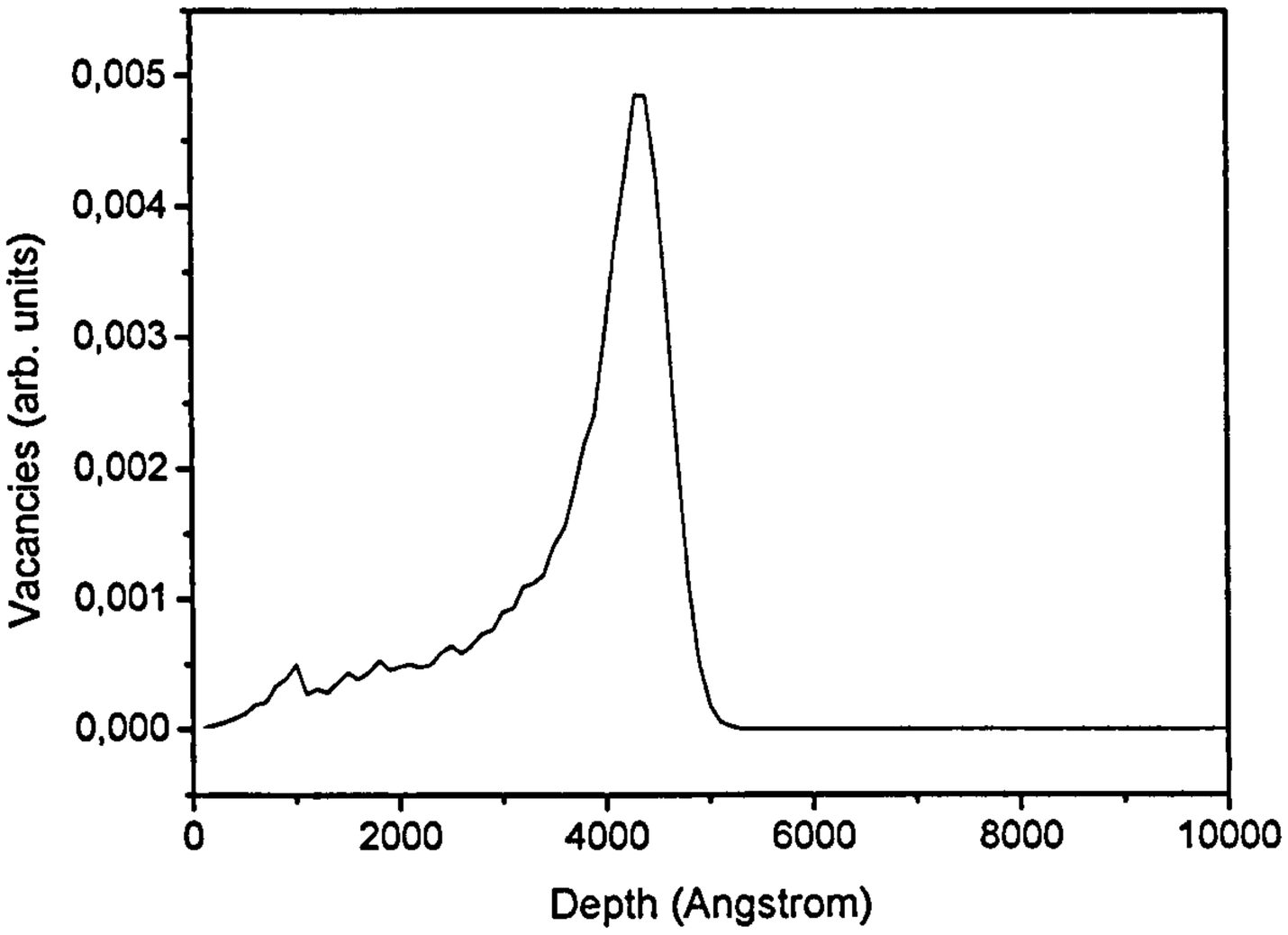

Figure 1.34. Vacancies created during irradiation of diamond with hydrogen ions (H^+) of energy 100 keV. The largest amount of damage is created at the end of the hydrogen ion track.

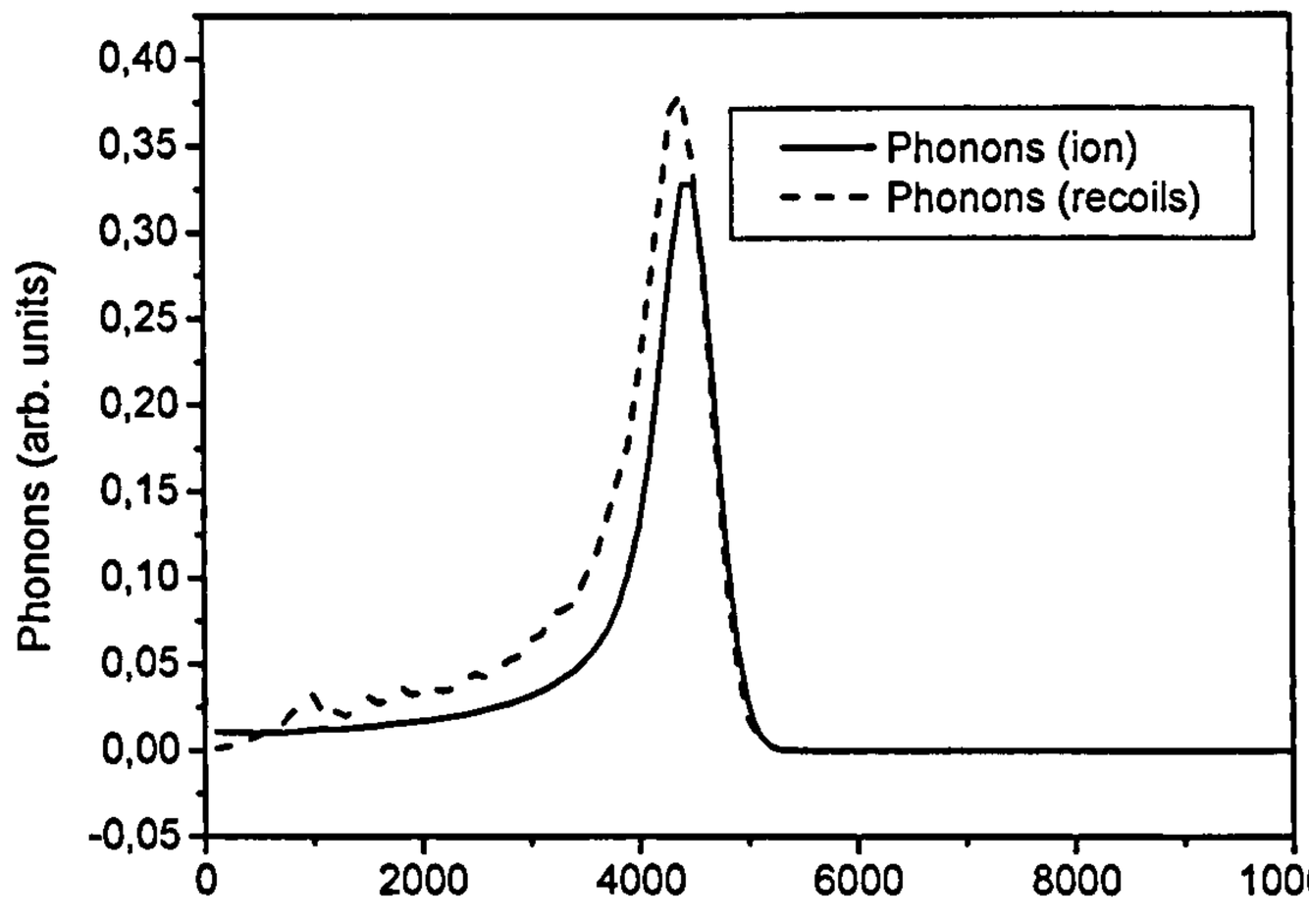

Figure 1.35. Phonons created during irradiation with hydrogen ions of energy 100 keV, and phonons created by host atom - recoil of the hydrogen ion interaction.

Multiple vacancy creation can occur as the lattice atom can have sufficient energy to create secondary damage which should be much more effective for heavy mass ions because energy transfer is much more efficient. Multiple vacancy creation can occur as the lattice atom can have sufficient energy to create secondary damage which should be much more effective for heavy mass ions because energy transfer is much more efficient.

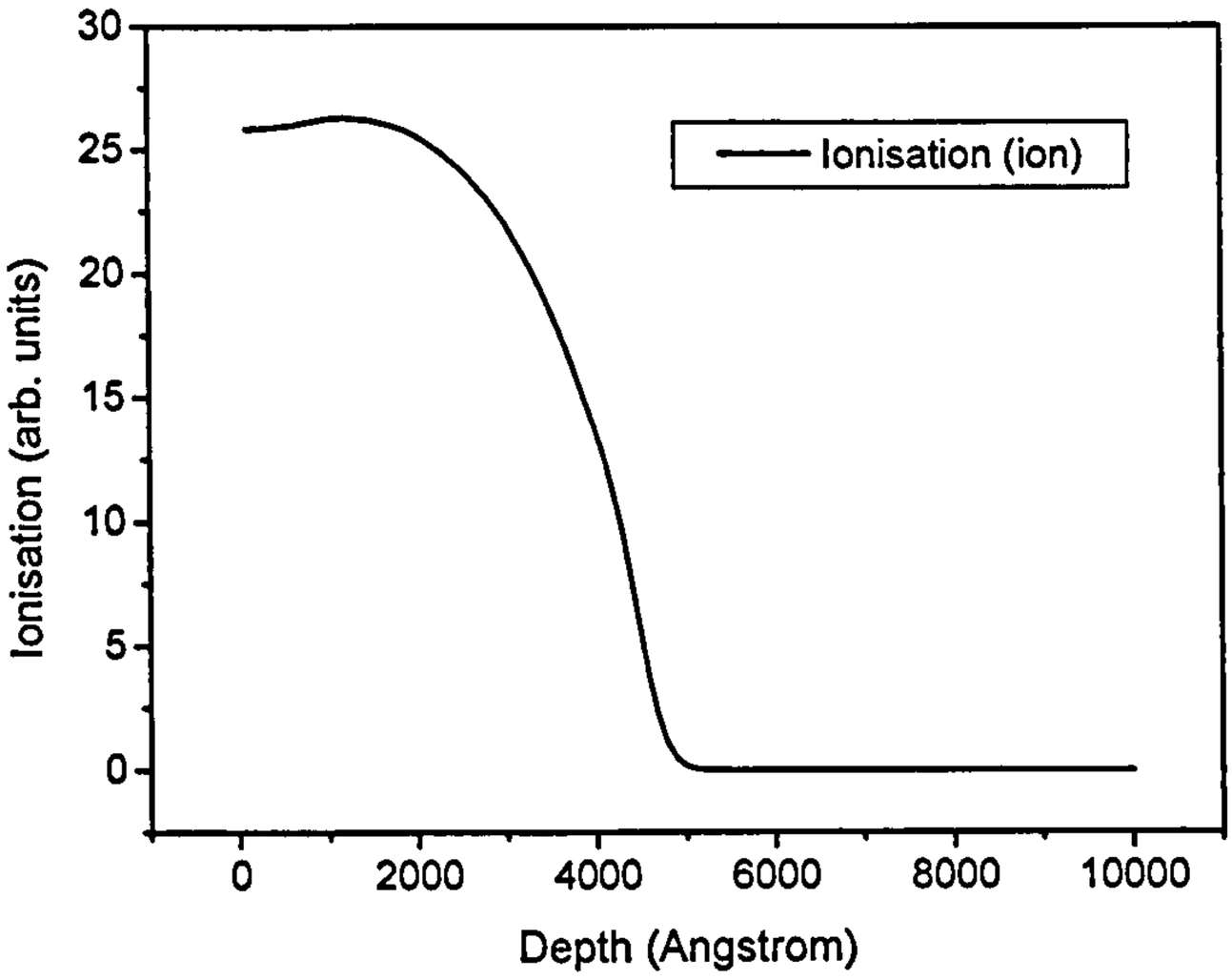

Figure 1.36. The ionisation of the carbon atoms in the diamond lattice when the sample is irradiated with 100 keV hydrogen ions.

Vacancy generation by neutron irradiation is different from other processes as the vacancy is generated by displacement of the lattice atom after direct knock-on by the neutron (hard sphere collision). Also the neutron can be captured by the nucleus of the atom and nuclear reactions can happen. The by-product of nuclear reactions can be alpha particles, which in turn can cause radiation damage.

Gamma irradiation is a highly inefficient vacancy creation process as radiation damage occurs through the creation of a Compton electron, and if the electron has energy above the displacement energy E_D, it can create a vacancy in the diamond lattice. Gamma rays are electrically neutral and can penetrate deep in the crystal lattice, as they have no interaction with lattice electrons.

During irradiation with electrons or ions, a non-equilibrium concentration of excitons is created and recombination enhanced reactions can occur (Lang 1982) and host lattice atoms can ionize. This can enhance diffusion of certain defects. Electron-

phonon coupling and charge trapping are the physical mechanisms underlying all these phenomena. We will illustrate these with the aid of configuration coordination (CC) diagrams from Lang (1982) (figure 1.37). The electron-phonon coupling must be strong and be significantly different for different charged states. Three different charge states are considered: the neutral state of the defect (D^0), the defect plus a delocalized electron hole (D^0 + e+ h), and the defect in the negative charge state plus a hole (D^- + h, where the electron is trapped at the defect). The energy barrier to diffusion is different for each state (E^- for D^-, E^0 for D^0). Four processes are known (Lang 1982) and are discussed below:

- Charge state mechanism: energy barrier for diffusion of the defect in the neutral state from one minimum in the CC diagram Q^0 to another (Q^0 + a, i.e. an equivalent lattice position separated by the lattice constant a) is different for the neutral and the charged defect ($E^- < E^0$). By trapping an electron, the defect can overcome the lower energy barrier in the negative charge state by the aid of a phonon (figure 1.37a).
- Saddle point (Bourgoin) mechanism: this is the extreme case of the charged state and has a saddle point in the CC diagram $E^- = 0$; there might also be an energy barrier at another point in the charged state CC diagram. In this an equal ratio of the charged defects will go to neighbouring lattice sites. This gives rise to athermal diffusion by multiple trapping of charge from excitons (figure 1.37a).
- Energy release ("phonon kick") mechanism: in this situation, the D^- + h state has enough energy to surmount the barrier to diffusion by assistance of a phonon: the D^0 + e + h captures the electron from the exciton and the energy difference between the minimum of the D^- + h state and the D^0 state ($\Delta E = E_R - E^0$) is small enough to be overcome by the assistance of a phonon (figure 1.37b).
- Electronic excitation mechanism: the electronically excited state of the negative defect can have a smaller diffusion barrier E^{*-} than the ground states of D^0 and D^-. This is somewhat analogous to the charged state mechanism, with the difference that electronic excitation is necessary (illumination) (figure 1.37c).

From this, it is clear that one can expect differences in defects created when diamond is irradiated with ions, electrons, gamma rays and neutrons. One can also expect differences when irradiation is continuous or pulsed: in the latter case the local

heating of the sample can efficiently be removed by cooling, while this is more difficult with the former method. Efficient cooling or heating during irradiation is known to induce differences (Newton 2002) in the relative concentrations of defects.

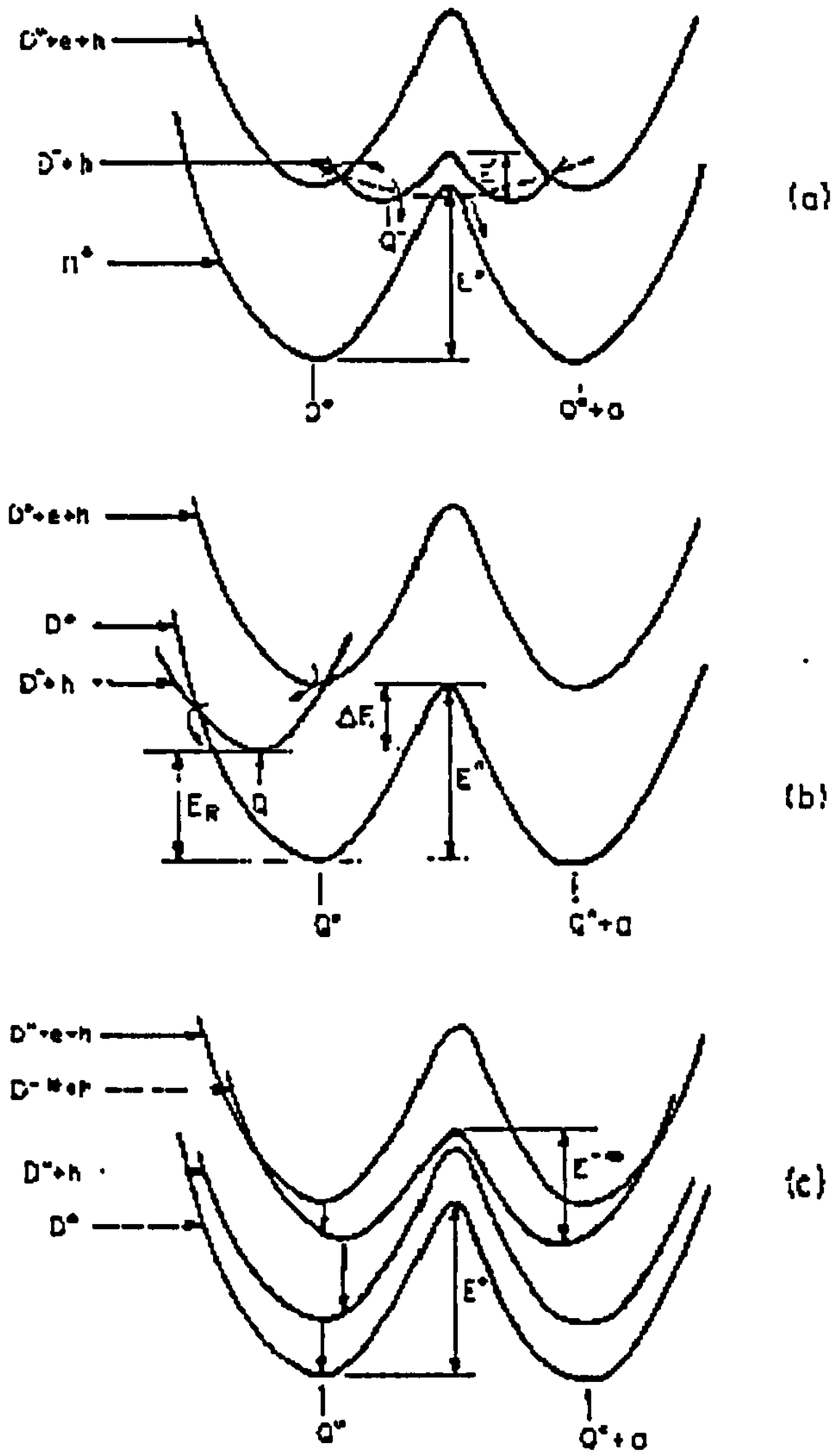

Figure 1.37. The configuration coordination diagrams illustrating the four recombination enhanced diffusion mechanisms. (a) The charged state mechanism and saddle point mechanism (dashed $D^- + h$ line has a saddle point at the D^0 maximum), (b) the energy release ("phonon kick") mechanism, (c) the electronic excitation mechanism. Figure from Lang (1982).

In indirect semi-conductors, the generated non-equilibrium charges can recombine through intermediate defects. This theory has been developed by Shockley and Read (1952) and Hall (1952) when radiative recombination is absent (SRH theory). The theory is widely used in computer simulations for photovoltaic cells. Additions have

been made to the theory to include radiative transitions (Beaucarne and Green 2003). The impurity recombination as described by SRH is important as it may reduce recombination enhanced diffusion of interstitials when the interstitial-vacancy pair is created close to or far from a nitrogen or nitrogen aggregate impurity (see chapter five). The detailed investigation of SRH in diamond is beyond the scope of this thesis, but should be investigated.

1.9.3.2. Defect production by HPHT annealing of type Ia diamond

Some defect aggregates can form during High Pressure High Temperature (HPHT) annealing, for example the concentration of H3 defects is substantially increased when brown type Ia diamonds are subjected to HPHT annealing (De Weerdt and Van Royen 2000, Collins *et al.* 2000). Minor increases of N3 defect concentrations are also detectable (Kanda 2004). Nitrogen A aggregates can be created by HPHT annealing of synthetic and natural type Ib diamond (Chrenko *et al.* 1977). This process is a second order process as it involves two moving nitrogen atoms (Chrenko *et al.* 1977). It is unclear at the moment how B defects form, but they can be created by HPHT annealing at high temperatures ($T > 2600°C$). Platelets also form during the HPHT annealing, and the diamond becomes a regular type IaA/B diamond (Kiflawi 2001). Further annealing at temperatures above 2500 to 2700°C makes the diamond an irregular type IaA/B diamond: platelets are destroyed (Evans and Rainey 1975, Evans and Qi 1982, Evans *et al.* 1995). This upsets the relation between B defect concentration and the integrated platelet absorption in the FTIR spectra of type Ia diamonds (Evans *et al.* 1995). The temperature at which this process occurs is dependent on the pressure, the lower end of the annealing temperature when the diamond is in the graphite stable region and the higher end of the temperature interval when the diamond is annealed in the diamond stable region of the carbon phase diagram (Evans 1995). Other structural changes are also detectable when the diamond becomes irregular: platelets convert into dislocation loops and voidites (Evans *et al.* 1995, Kiflawi and Bruley 2000).

Almost all natural Cape colour diamonds are regular, while a lot of fancy coloured diamonds are irregular or have additional absorption peaks (De Weerdt and Van Royen 2001).

Defects can also dissociate during the HPHT annealing: A defects will dissociate and split up into two C defects (Brozel *et al.* 1978) with an activation energy of 7.3 ± 0.6 eV (De Weerdt and Collins 2003, see also chapter 5), in agreement with the calculations of Mainwood (1994).

Other defects are detectable in the UV-VIS-NIR spectrum of HPHT annealed brown type Ia diamond. The most prominent are H3 and H4 defects. The dissociation of A defects into C defects will lead to the creation of N-V defects and their negatively charged counterparts: the $(N\text{-}V)^-$ and negatively charged H3 defects (the H2 defects). In some cases when a large concentration of C defects (a few ppm) is created, a C defect absorption spectrum can be detected by FTIR spectroscopy.

In chapter six, a detailed account will also be given of the stability of A, H3 and H4 defects, in HPHT annealed brown type Ia diamonds.

1.9.3.3. Defects in type Ia brown diamonds

A number of optical and EPR defects are very specific for brown type Ia diamonds. All these defects are thought to be related to plastic deformation.

In photoluminescence and cathodoluminescence spectra of a large number of brown type Ia diamonds, a defect can be seen with a ZPL at 490.7 nm (Collins *et al.* 2000). This defect is associated with plastic deformation of the diamond lattice as it can be produced by indentation (Brookes *et al.* 1993); CL studies have shown that the luminescence is polarized with the E vector along the slip line (Collins and Woods 1982). This defect is strongly reduced or removed upon HPHT annealing (Collins *et al.* 2000, De Weerdt 2001). From examinations of CL images (Kaneko and Lang 1993), it appears that luminescence of H3 defects is also pinned at the slip bands which cross different growth layers.

Newton and Baker (1992a, 1992b) analysed EPR measurements of various nitrogen related defects in brown type Ia diamonds and suggested that some of these defects are formed during plastic deformation: the N4 and the W7. Both defects are di-

nitrogen defects and are not homogeneously distributed in the diamond. There is axial symmetry of the hyperfine parameters along a preferential (111) direction. The authors have speculated that the defect is formed by distortion of the A defect with a Burgers vector of $a/\sqrt{2}$ in the $(\bar{1}10)$ direction in the <111> plane, combined with ionisation of the defect.

The origin of brown colour in diamond is unknown, but high-pressure experiments of Mao and Bell (1978) have indicated that tips of diamond anvils sometimes turn brown at a pressure close to 1.7 Mbar. This colouration is reversible as it disappears after release of the pressure. Flow deformation was observed on the diamond surface (Mao and Bell 1978). Research of Weidner *et al.* (1994) and Brookes *et al.* (1999) has indicated that plastic flow can be initiated at lower pressures when the temperature is increased or different slip systems can be activated at high temperature.

1.9.4. Correlations between different absorption lines due to one defect

A number of defects absorb light in the mid-infrared region and also in the UV-VIS spectrum of diamond. Defects can sometimes not be detected, because of overlap of the absorption band by absorption bands of other defects and in this case cross referencing between the strengths of the absorption peaks in different parts of the electromagnetic spectrum can be useful. In other cases different zero phonon lines of defects can almost coincide and the occurrence of associated peaks, for example due to the presence of higher excited states, will aid in the identification of the nature of the defect. Below we will give a number of examples of defects with absorption in different parts of the electromagnetic spectrum.

1.9.4.1. The A defect

The A defect in diamond not only absorbs light in the infrared spectrum, but also in the UV region. Sharp zero phonon lines can be detected at 330.0 nm, 317.8 nm, 315.7 nm, 302.8 nm, 302.0 nm, 301.7 nm (Davies 1979) (figure 1.38).

These diamonds also display n-type photo-conductivity with an ionisation energy of 4.04 eV (Denham 1967). The very strong absorption at energies above ~ 4 eV is

therefore also called the secondary absorption edge of type IaA diamonds (Davies 1979).

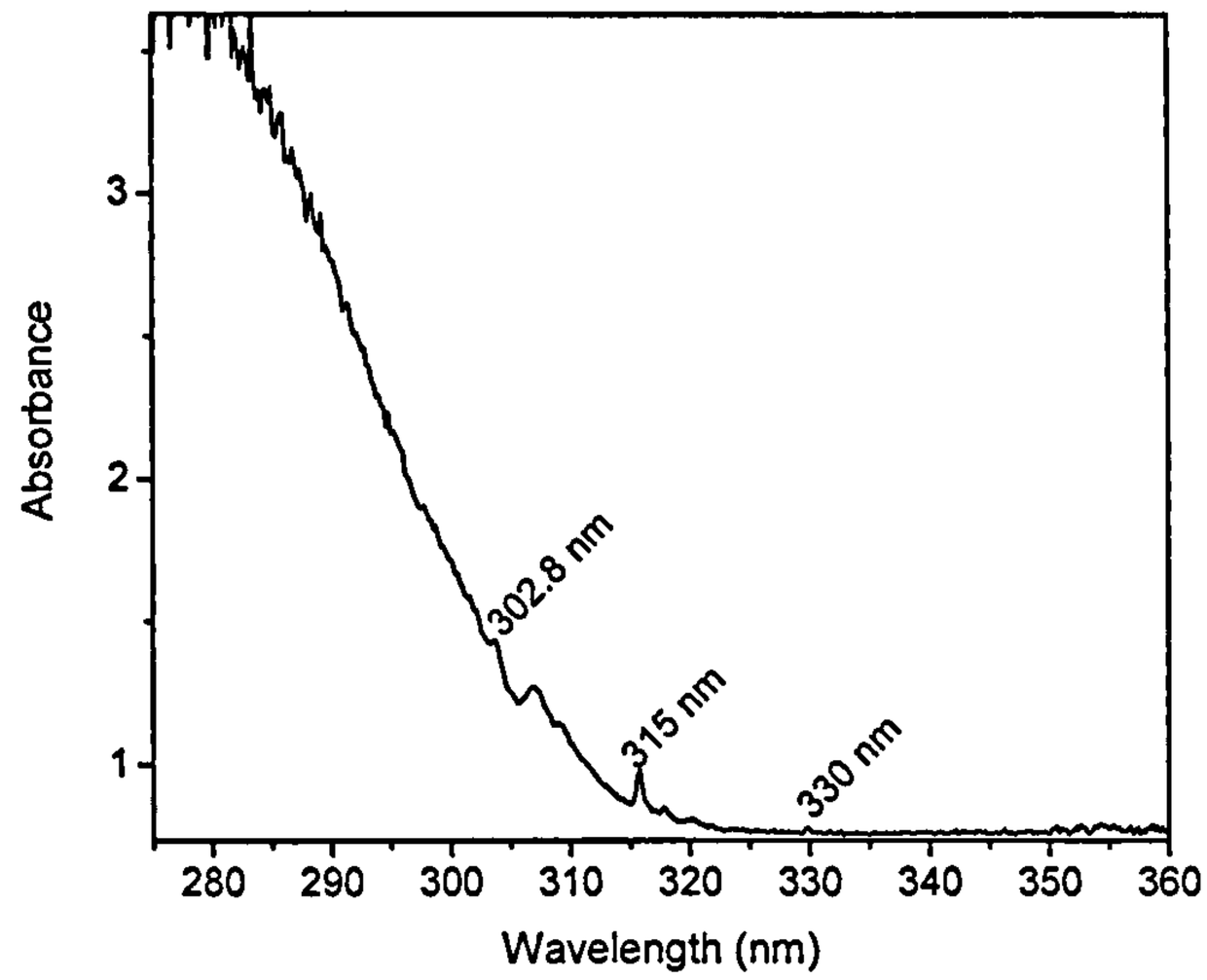

Figure 1.38. The secondary absorption edge in type IaA diamond. The zero phonon lines at 302.8, 302 and 301.7 nm are not resolved. The sample is cooled to liquid nitrogen temperature.

1.9.4.2. The C defect

The C defect in diamond absorbs light in the visible region and also in the UV region of the electromagnetic spectrum (figure 1.38). The C defect is a deep donor (1.7 eV) (Farrer and Vermeulen 1972) and absorption of light with energy larger than 1.7 eV gives this type of diamond its characteristic yellow colour (Dyer *et al.* 1965a).

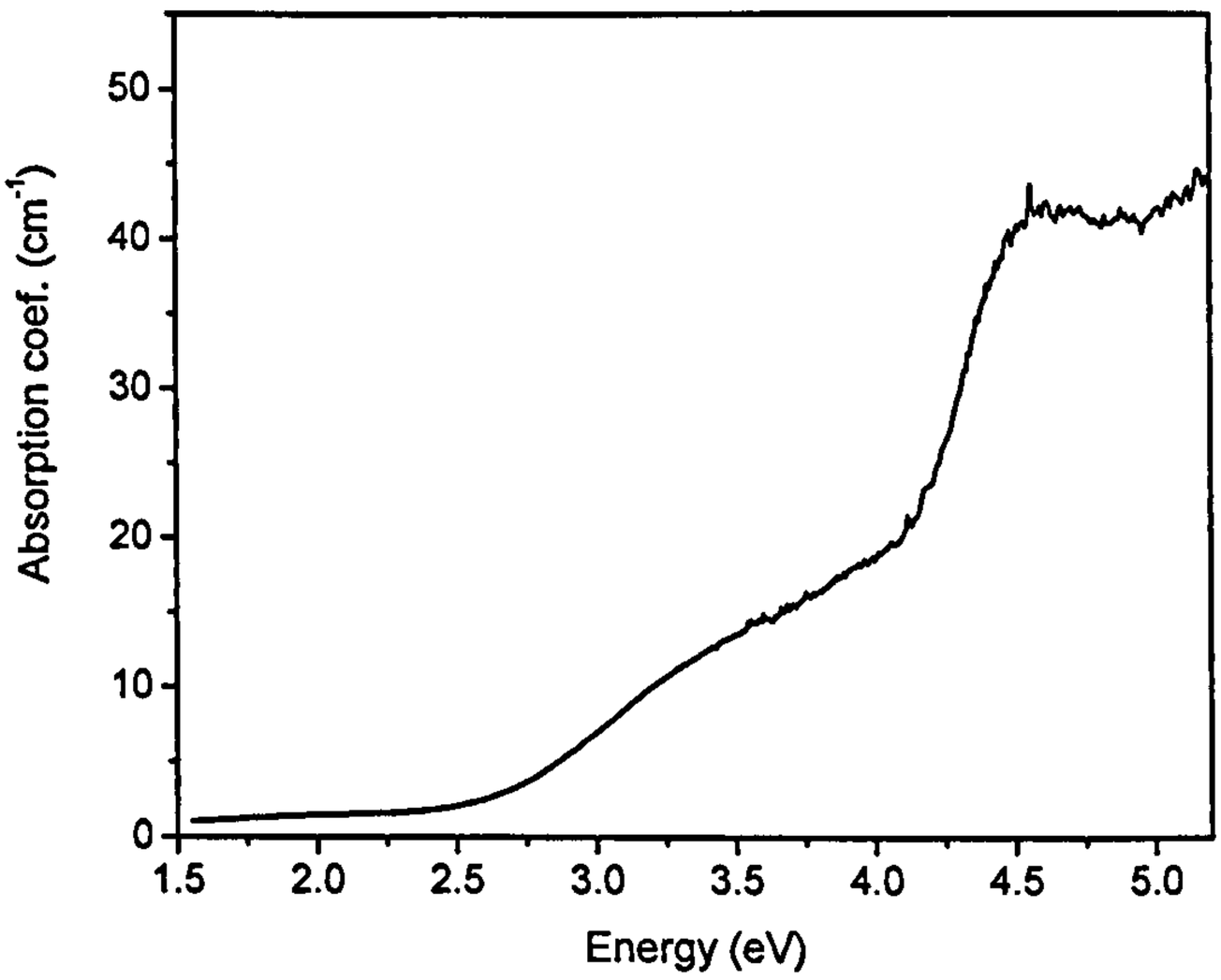

Figure 1.39. The UV-VIS absorption spectrum of a type Ib diamond.

The broad absorption band, centred at 270 nm (4.590 eV) (figure 1.39), was used by Sumiya and Satoh (1996) to estimate the concentration of single substitutional nitrogen in nitrogen gettered synthetic diamonds with C defect concentrations in the order of 100 ppb. Sumiya and Satoh (1996) derived a proportionality coefficient of 0.56 between the absorption coefficient at 270 nm and the concentration of C defects.

This absorption band at 270 nm is not always detectable in HPHT annealed natural type Ia or Ib diamonds because of the presence of A defects, with strong absorption in the UV.

Chapter Two

Luminescence spectra of defects specific to brown type Ia diamonds.

2.1. Introduction

2.1.1. Chapter outline

This chapter deals with the characterisation of two defects, frequently and exclusively encountered in brown type Ia diamonds. Both defects are destroyed during HPHT annealing (Collins *et al.* 2000). The first defect causes a broad vibronic band in the PL spectrum with a maximum near 1.75 eV (~ 710 nm), and we will show this is caused by strong electron-phonon coupling. The second defect is the so-called 490.7 nm defect because of its ZPL position in the UV-VIS spectrum. The defect is thought to correlate with slip planes in plastically deformed diamond (Collins and Woods 1982).

2.1.2. Broad band luminescence

The broad-band luminescence around 700 nm can be encountered in type Ia diamonds and there is only scattered information and analysis about this in the literature (Collins and Mohammed 1982, Nazaré *et al.* (1985a, 1985b), Pereira and Jorge 1987). In literature a number of diamonds with brown colour have been described with broad band absorption and luminescence, but with different absorption and luminescence spectra. These can be divided in roughly two types of brown diamonds.

One group of diamonds exhibiting such luminescence also display broad-band absorption (figure 2.1, top spectrum), and nitrogen atoms are present in unaggregated and aggregated states, i.e. the diamonds are a mixture of type Ib and type Ia material (De Weerdt and Van Royen 2001). The resulting colour of these diamonds is orangy-

yellow to brown-yellow and they display yellow luminescence when illuminated with light in the 340 – 460 nm region, and red luminescence when illuminated with light in the 440 – 540 nm region (Collins and Mohammed 1982). These diamonds were described by De Weerdt and Van Royen (2001) as Canary colour and were also studied by Collins and Mohammed (1982), Nazaré *et al.* (1985a, 1985b) and Pereira and Jorge (1987). These diamonds do not show evidence of strong plastic deformation when held between crossed polarizers. This type of diamond is not the subject of the research in this chapter.

The second group of diamonds described in this chapter are brown and a typical example of the absorption spectra is illustrated in figure 2.1 (bottom spectrum); the origin of the colour is thought to be due to plastic deformation.. The colour of the diamond is due to a number of overlapping broad absorption bands, with increasing absorption at shorter wavelengths. The strain produced by the plastic deformation in samples of this second group is clearly visible when the diamonds are held between crossed polarizers. This group of diamonds is more common than the so-called yellow-brown types of diamonds of group one.

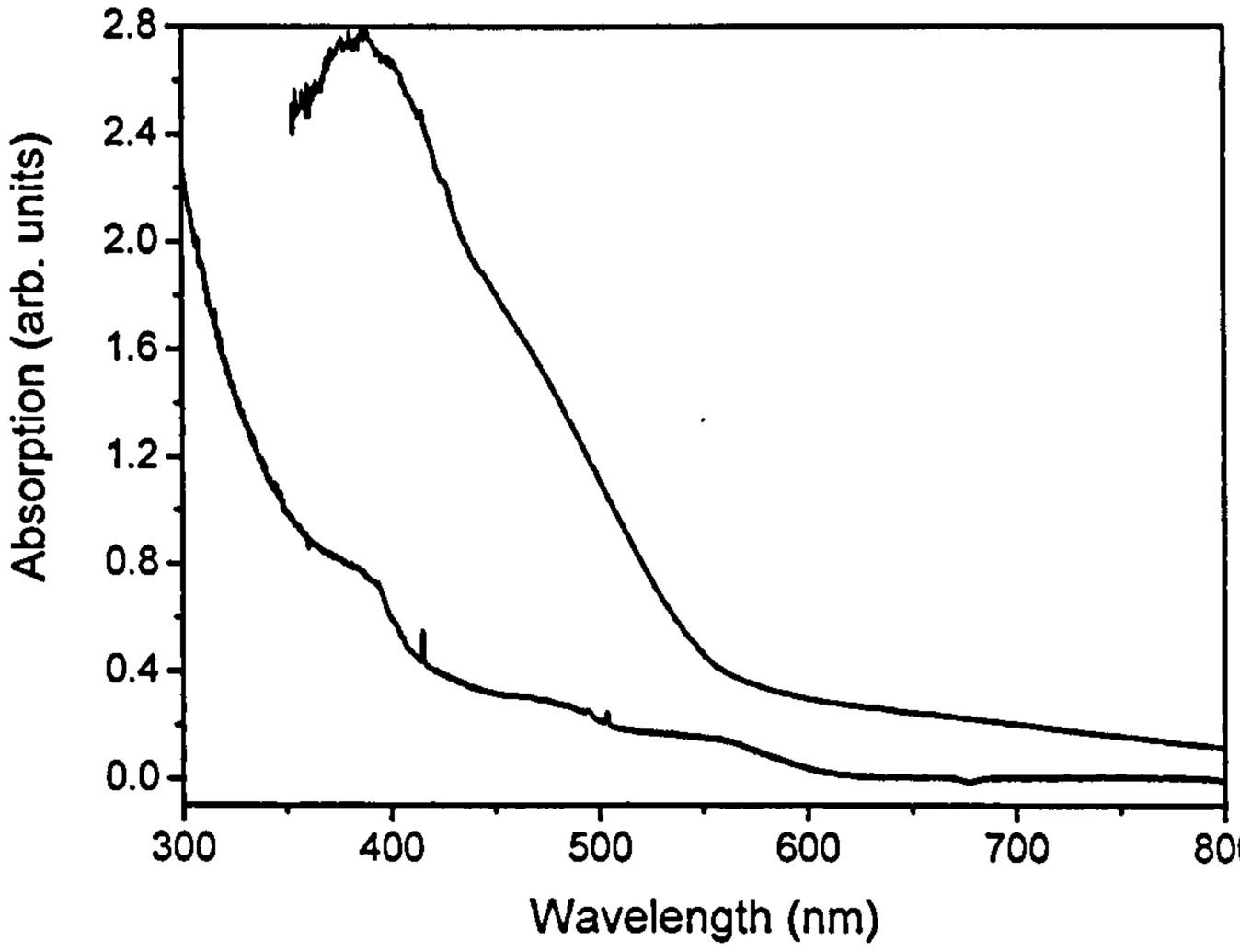

Figure 2.1. The absorption spectra of a diamonds typical of the samples studied in this chapter (bottom spectrum) and yellow-brown samples (canary type) studied by De Weerdt and Van Royen (2001) (top spectrum). Spectra were recorded with the samples at liquid nitrogen temperature.

When excited with the 514.5 nm Ar-ion laser line, the luminescence spectra are dominated by a broad band with a maximum near 1.75 eV (~ 710 nm). The exact position of the maximum is sample-dependent, suggesting that the luminescence band consists of at least two sub-bands. We will show that the spectrum can be decomposed into two or possibly more broad bands, one of which shows temperature-dependent structure on the high-energy side. From an analysis of this structure we have determined the Huang-Rhys factor and the one-phonon density of states for the defect giving rise to the luminescence. The low frequencies (17 meV and 44 meV) determined in the density of states spectrum suggest that a heavy impurity atom may be involved, but none has been detected above the detection limit of the X-ray fluorescence (XRF) techniques applied.

2.1.3. The 490.7 nm defect

Another defect frequently encountered in natural brown type Ia diamonds and related to strong plastic deformation has a zero phonon line at 490.7 nm (see chapter 1, section 1.8.3.4.). The defect is easily detectable, showing intense photoluminescence, but the absorption is very weak; (figure 2.2) shows a rarely seen example.

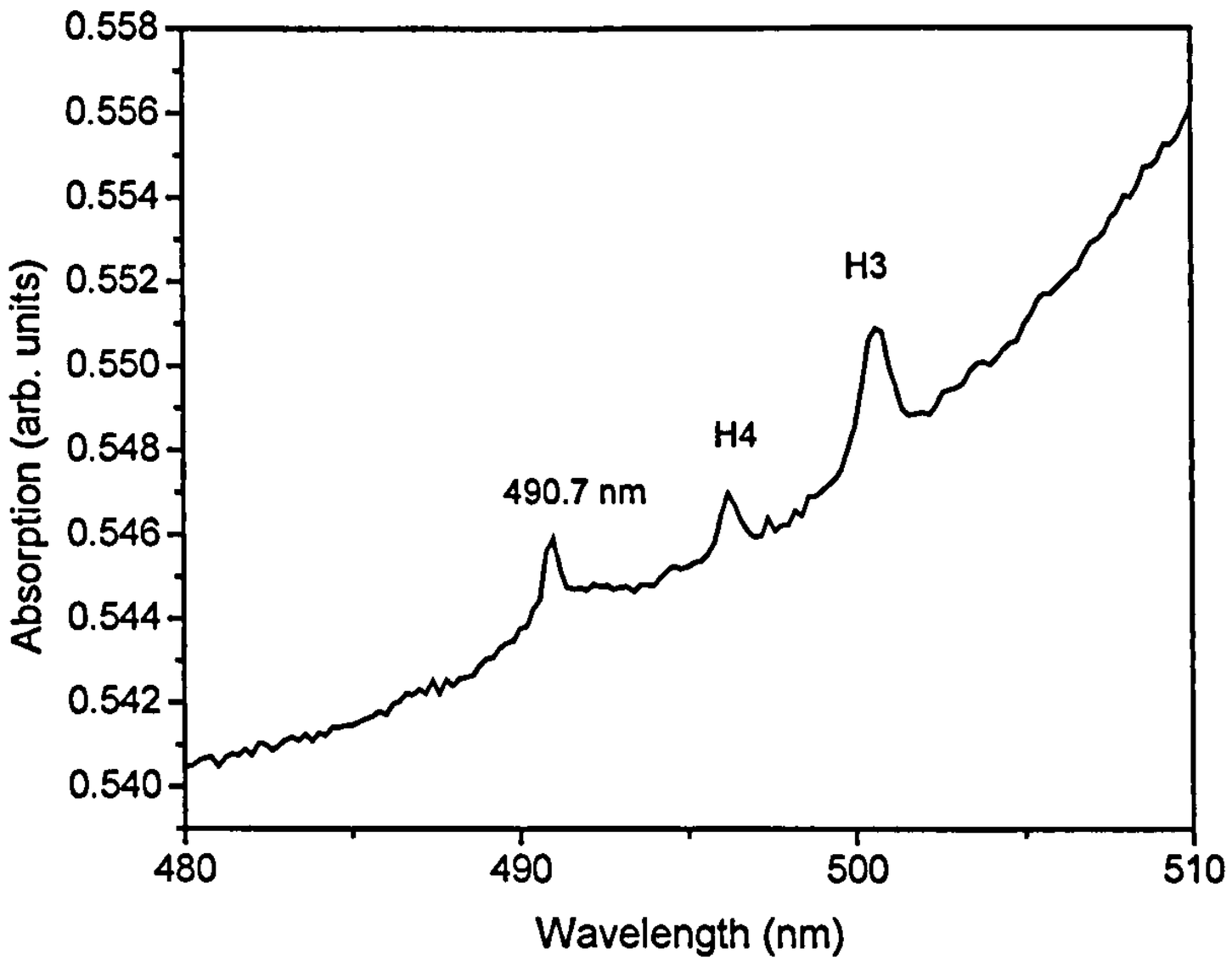

Figure 2.2. The absorption spectrum of a type IaB diamond with a detectable 490.7 nm defect at the edge of the broad band centred at 560 nm. The spectrum was recorded with the diamond at liquid nitrogen temperature.

2.2. Experimental

A Renishaw RM 2000 instrument was employed for the luminescence experiments, using excitation by the 514.5 nm line of an Ar-ion laser or with the 325 nm line of a HeCd laser. Suitable neutral density filters were used when the luminescence intensity was above the linear response region of the CCD detector. The samples were cooled in a MicrostatN cryostat, allowing measurements to be made, in principle, at temperatures between 77 and 500 K. However, dilatation of the copper sample holder above 180 to 200 K is too large to ensure reproducible positioning of the sample. The inhomogeneity of defects in the samples, combined with this large dilatation, gives a non-reproducible variation in the intensities of the spectra at temperatures above 200 K. This problem was circumvented by marking the samples with a cross, laser inscribed on the surface of the diamond. The lines of this marker were approximately 1 μm thick, allowing repositioning of the samples with an error of less than 2 μm. The sampled region is an ellipse with dimensions of approximately 100 μm x 150 μm. By this method, measurements can be performed at different temperatures up to 250 K.

Absorption measurements were carried out with a Varian Cary 100 UV-VIS absorption spectrometer, equipped with a home made cryostat. XRF measurements were carried out with an Oxford Instruments ED2000 system.

Four out of ten samples were clear type Ia diamonds from the Argyle production in Western Australia, with various concentrations of A and B defects. We have confirmed that the broad-band luminescence is not present in type IIa diamonds or type IaA diamonds.

2.3. Results and discussion

2.3.1. Broad band luminescence

2.3.1.1. Photoluminescence data

Figure 2.3 (experimental spectrum) shows a typical luminescence spectrum of a brown type Ia diamond when excited by a 325 nm laser and with the sample at 77 K. The broad-band luminescence in this case is masked by the vibronic luminescence side bands of the H3 and N3 defects. However, the broad band luminescence can be visualised (figure 2.3, corrected spectrum) by subtraction of a spectrum, with suitable intensities for the H3 and N3 components. When using excitation at 514.5 nm (figure 2.4), the broad-band luminescence is not masked by the luminescence of nitrogen-vacancy centres like H3, H4 and N3. From the spectra, obtained from two different diamonds, it is apparent that the position of the maximum intensity and the width of the broad band are sample-dependent. This suggests that there are at least two bands present, superimposed on each other.

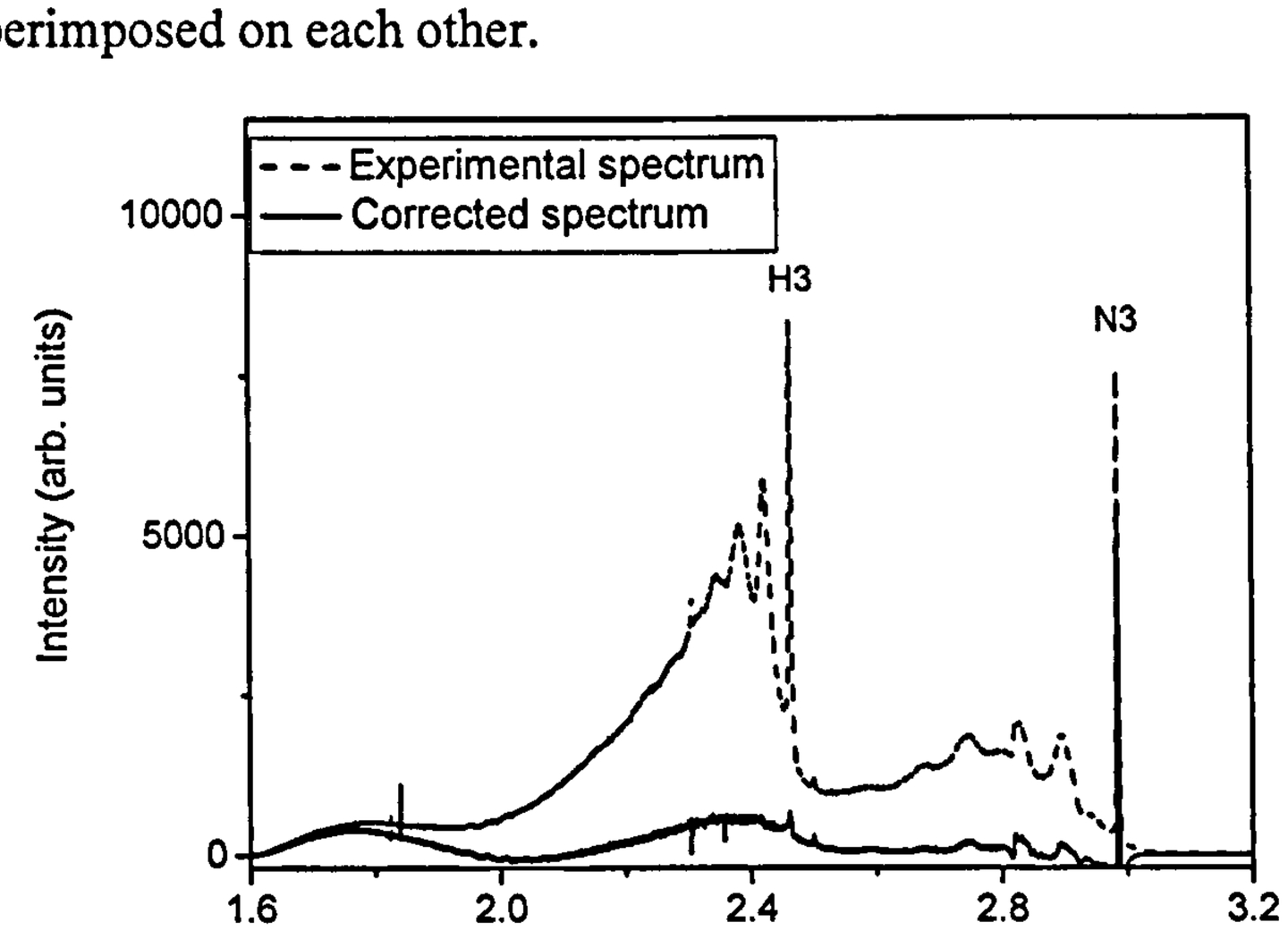

Figure 2.3. The PL spectrum of a brown type Ia diamond (broken curve), excited at 325 nm. The broad bands present in the spectrum can be visualised by subtracting a spectrum, with suitable intensities for the H3 and N3 components, to give the full curve. The weak peaks in this resulting spectrum are due to the presence of H4, with residual H3 and N3. There are clearly two broad bands, centred at approximately 1.75 eV and another at approximately 2.39 eV.

The upper spectrum in figure 2.4 consists of a broad band, with a maximum near 1.75 eV (~ 710 nm) together with weak peaks on the high energy side of the band starting at 2.034 eV (609 nm). Additional sharp lines are detectable. The well-known H3 defect is formed when a vacancy is trapped at the A form of nitrogen to produce the N-V-N structure. The zero-phonon line (ZPL) is on the high-energy side of the laser line, and the luminescence results from a sub-threshold excitation mechanism (Iakoubovskii 2001, De Weerdt and Collins 2005). The mechanism of sub-threshold excitation will be described in chapter three. The emission lines at 2.152 eV (576 nm) and 2.313 eV (536 nm) have been observed previously in some natural brown diamonds, and can also be produced in diamonds containing nitrogen mainly in the B form by radiation damage and annealing at high temperature (typically 1600 °C) (Collins 2001, Collins *et al.* 2005). We will show in the present investigation that the intensities of these two lines are unrelated to the intensities of the peaks between 1.920 eV (646 nm) and 2.034 eV (609 nm).

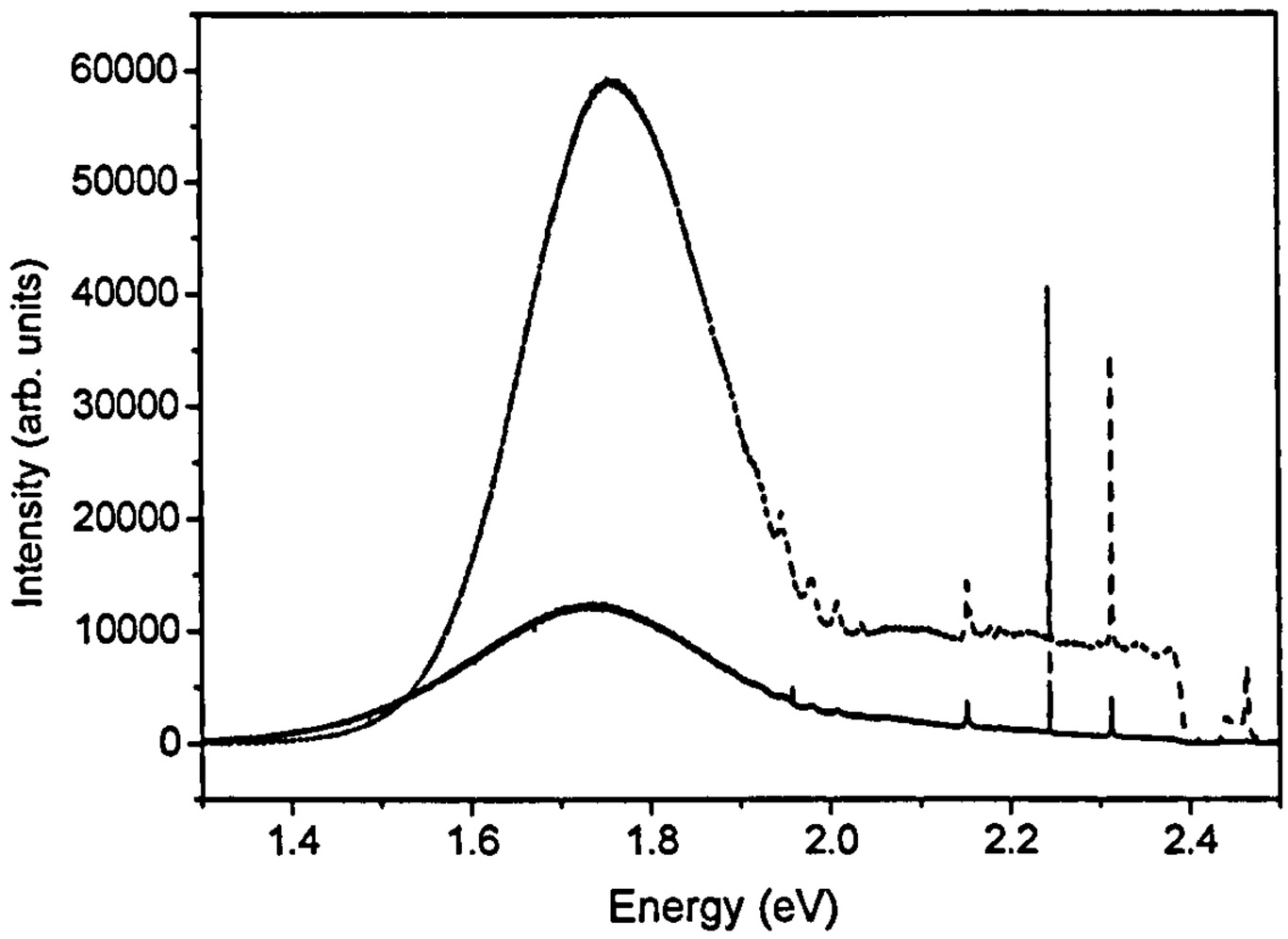

Figure 2.4. The PL spectra of two different brown type Ia diamonds, excited at 514.5 nm. There is a clear sample-dependent position of the maximum and the width of the broad band near 1.75 eV.

Even using excitation at 514.5 nm (figure 2.4), the broad-band luminescence cannot be analysed without subtracting the background caused by the side bands of the 2.152 (576 nm), 2.313 (536 nm) and 2.463 eV (H3) luminescence spectra. The shape of this background was determined by using a spectrum containing only the 2.152 (576 nm) and 2.313 eV (536 nm) lines (figure 2.5a) and a second spectrum, containing only the

2.463 eV (H3) spectrum (figure 2.5b). These two spectra were used in a least squares fitting routine to make the spectral region between 2.05 (605 nm) and 2.45 eV (506 nm) as close to zero as possible (figure 2.6). In a number of cases, the peak at 2.152 eV (576 nm) was positive and in other cases it was negative, without significantly altering the background of the corrected broad band luminescence spectrum. This indicates that the intensity of the side band of the 2.152 eV (576 nm) defect is small, and does not change the shape of the broad band in the corrected spectrum. Furthermore, the small linewidth of the 2.152 eV (576 nm) and 2.313 (536 nm) lines suggest a very small Huang-Rhys coupling and consequently a weak side band, which should have negligible influence on the emission spectrum of the broad band at 1.75 eV (710 nm).

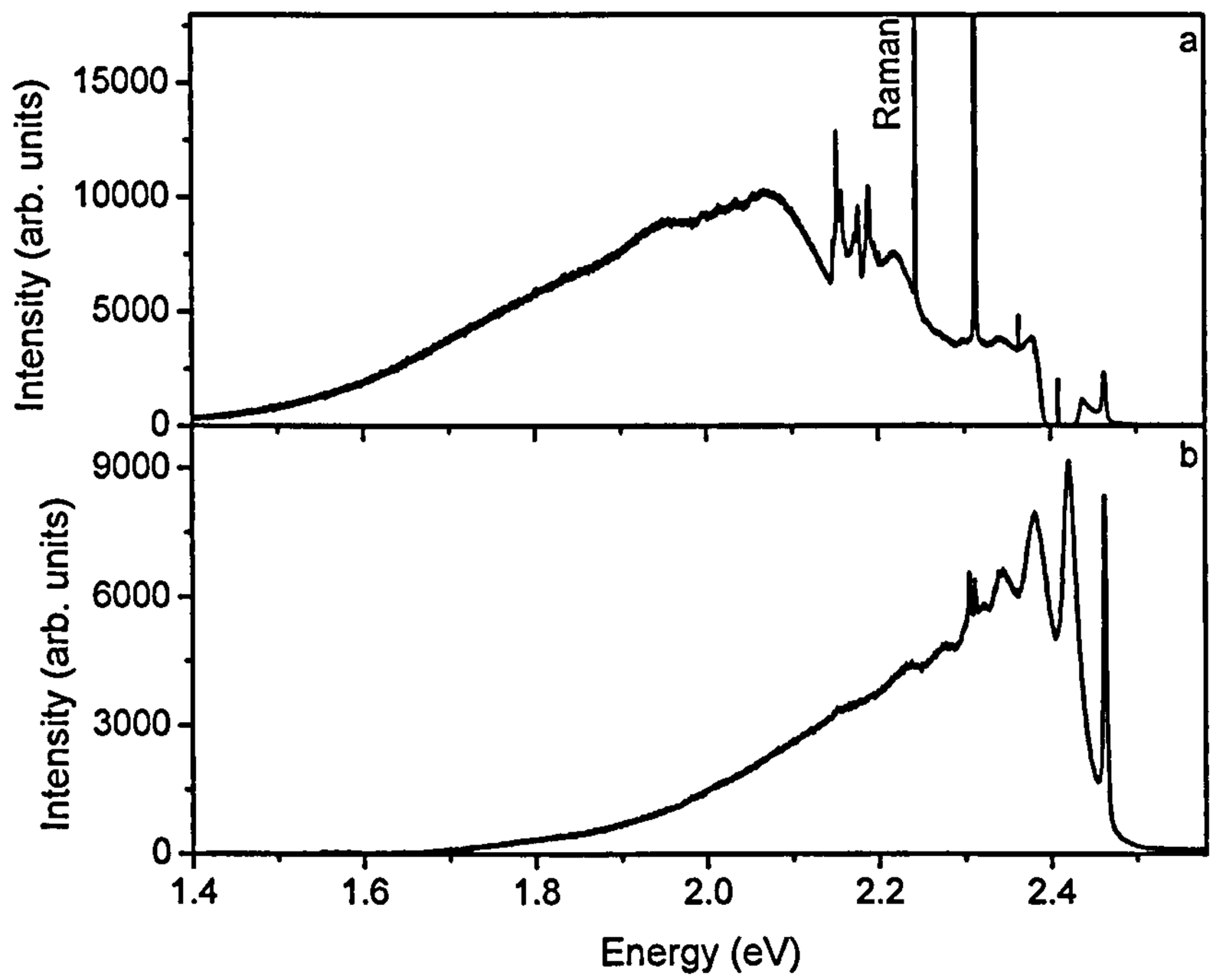

Figure 2.5. The PL spectrum with sharp peaks at 2.152 eV (576 nm) and 2.313 eV (536 nm) (figure 2.5a) which is used in combination with a spectrum of the H3 defect (figure 2.5b) for a least squares decomposition of the background leading up to the broad band near 1.75 eV (~ 710 nm).

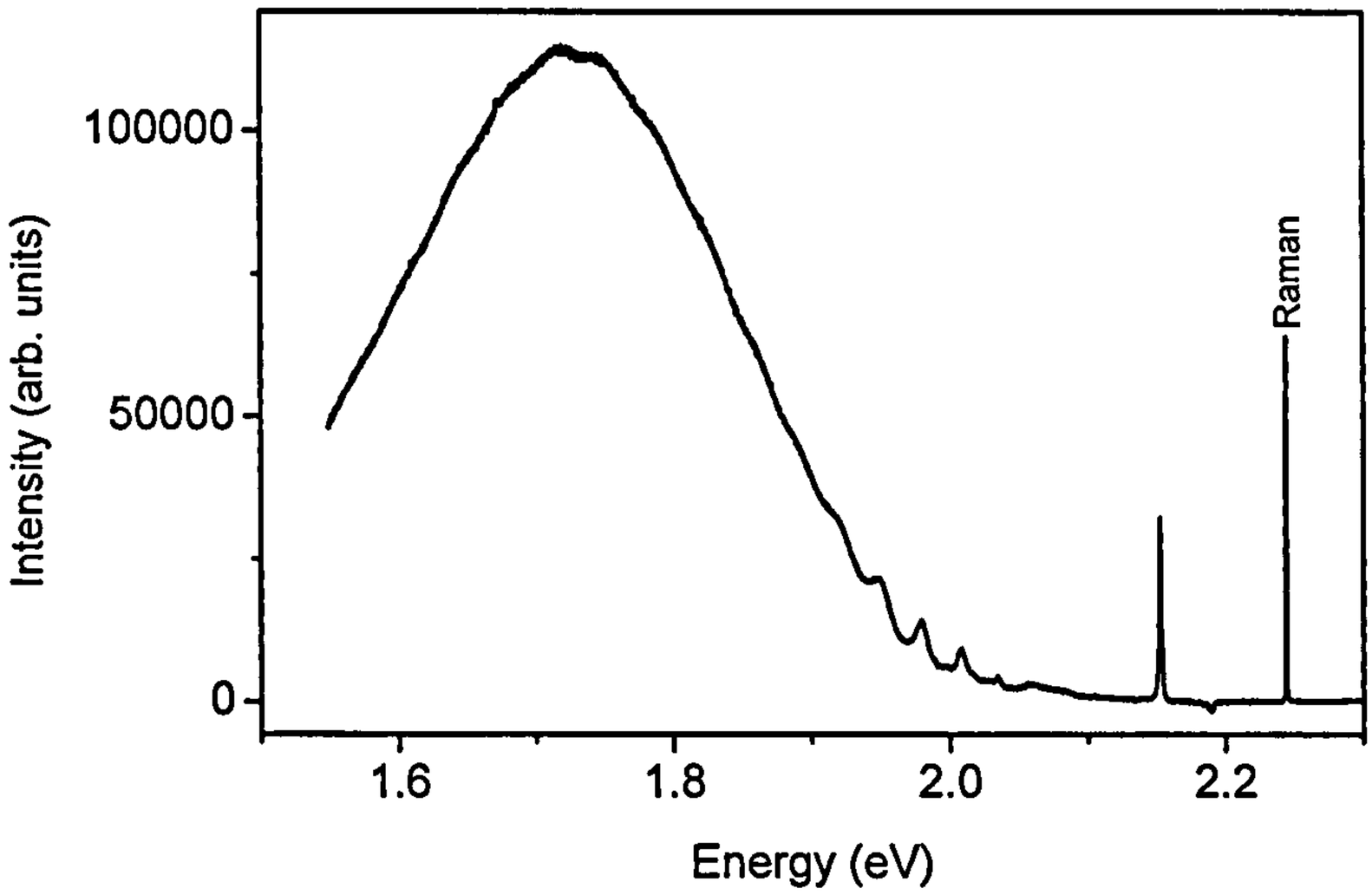

Figure 2.6. The luminescence spectrum after subtraction of the background caused by the side bands of the emission lines at 2.152 eV (576 nm) and 2.313 eV (536 nm) and the H3 defect. In a number of cases a weak peak at 2.152 eV (576 nm) remained present after the subtraction, sometimes in the positive and sometimes in the negative sense, without significantly altering the background at energies below 2.152 eV (576 nm).

Sample no.	I(2.008 eV)/I(2.034 eV)	I(1.978 eV)/I(2.034 eV)
1	2.72 ± 0.21	4.70 ± 0.32
2	2.52 ± 0.30	4.90 ± 0.32
3	2.48 ± 0.22	4.72 ± 0.33
4	2.43 ± 0.22	4.70 ± 0.33

Table 2.1. The ratios of the integrated intensities of the 2.008 eV (617 nm) and the 1.978 eV (626 nm) peaks with respect to the integrated intensity of the 2.034 eV (609 nm) peak.

As noted above, a number of peaks are observed on the high energy side of the broad band at 2.034 eV (609 nm), 2.008 eV (617 nm), 1.978 eV (626 nm), 1.949 eV (636 nm) and 1.920 eV (646 nm). Weaker structure can also be observed at even lower energies. Some of the former features appear to be correlated in intensity. Using Grams/32 and Origin software, each of these peaks was fitted with a Lorentzian function, together with a quadratic baseline correction to account for the underlying part of the background from the broad band. The ratios of the integrated intensities of the peaks at 2.008 eV (617 nm) and 1.978 eV (626 nm) were calculated with respect to the 2.034 eV (609 nm) peak. These ratios shown in table 2.1 and figure 2.7. appear

to be constant for 4 different samples so they are correlated in strength and this suggests they originate from the same defect.

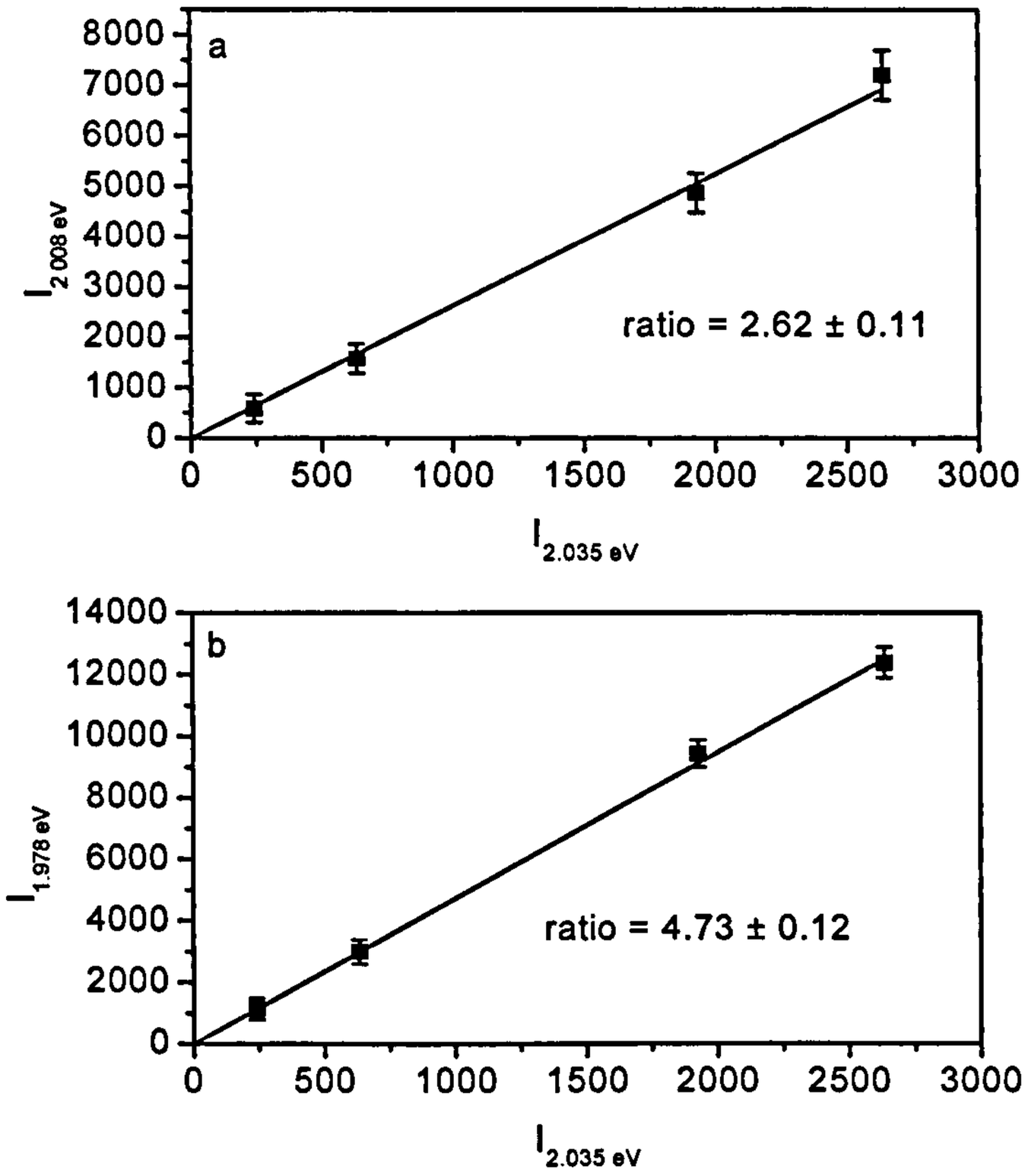

Figure 2.7. Integrated intensities of (a) the 2.008 eV (617 nm) peak and (b) the 1.978 eV (626 nm) peak versus that of the 2.034 eV (609 nm) peak. The lines are least squares fits to the equation $y = ax$. (This is justified since fits to $y = ax + b$ gave values of b which were 3 times smaller than the uncertainties in b.)

The integrated intensity of the 2.034 eV (609 nm) peak was calculated from spectra recorded at different temperatures, and increases with increasing temperature. This indicates that the 2.034 eV (609 nm) line is not a zero-phonon line, since the integrated intensity of a ZPL decreases with temperature because the transition probabilities shift in the higher vibronic states (Davies 1981a). From the Arrhenius plot of the data (figure 2.8) an activation energy of 18 ± 1.6 meV can be calculated.

We conclude that these correlated peaks on the high energy side of the broad band are part of a vibronic band, and we have determined the one-phonon density of states, and the Huang-Rhys factor S, by fitting a calculated vibronic band to the experimental broad band. The vibronic band is calculated by the procedure described in chapter 1,

section 1.2. The structure can be fitted with S = 8.0 ± 0.5 and a one-phonon density of states with 2 maxima at 17 and 44 meV (figure 2.9). Because of the strong coupling (S = 8.0) the ZPL is too small to be easily detectable at liquid nitrogen temperature.

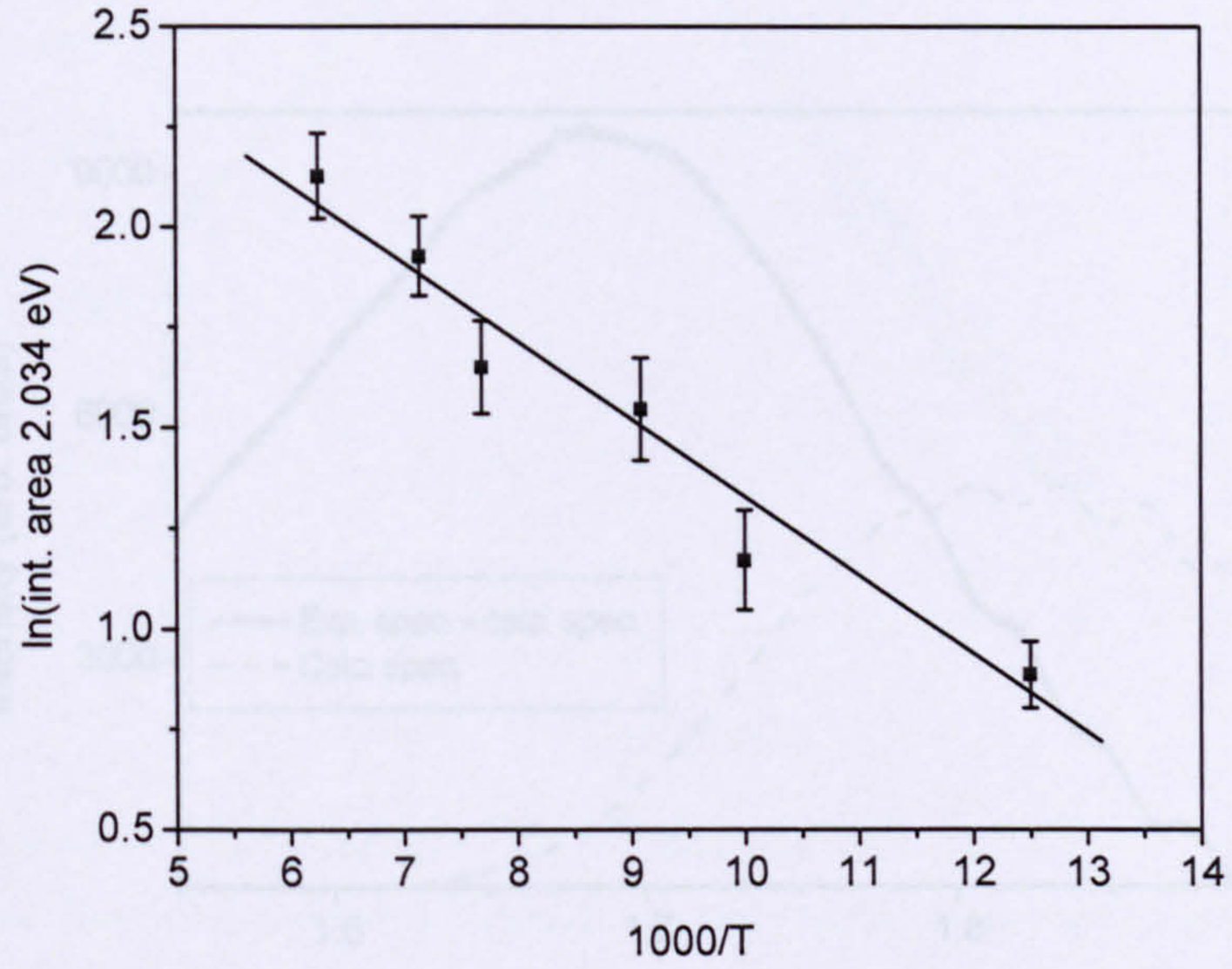

Figure 2.8. The Arrhenius plot of the integrated intensity of the 2.034 eV peak in the temperature range 77 to 160 K. Measurements at higher temperatures are not possible because of strong broadening of the peak, making it impossible to discriminate the peak from the background. From the linear fitting of the data, an activation energy of 18 meV can be calculated.

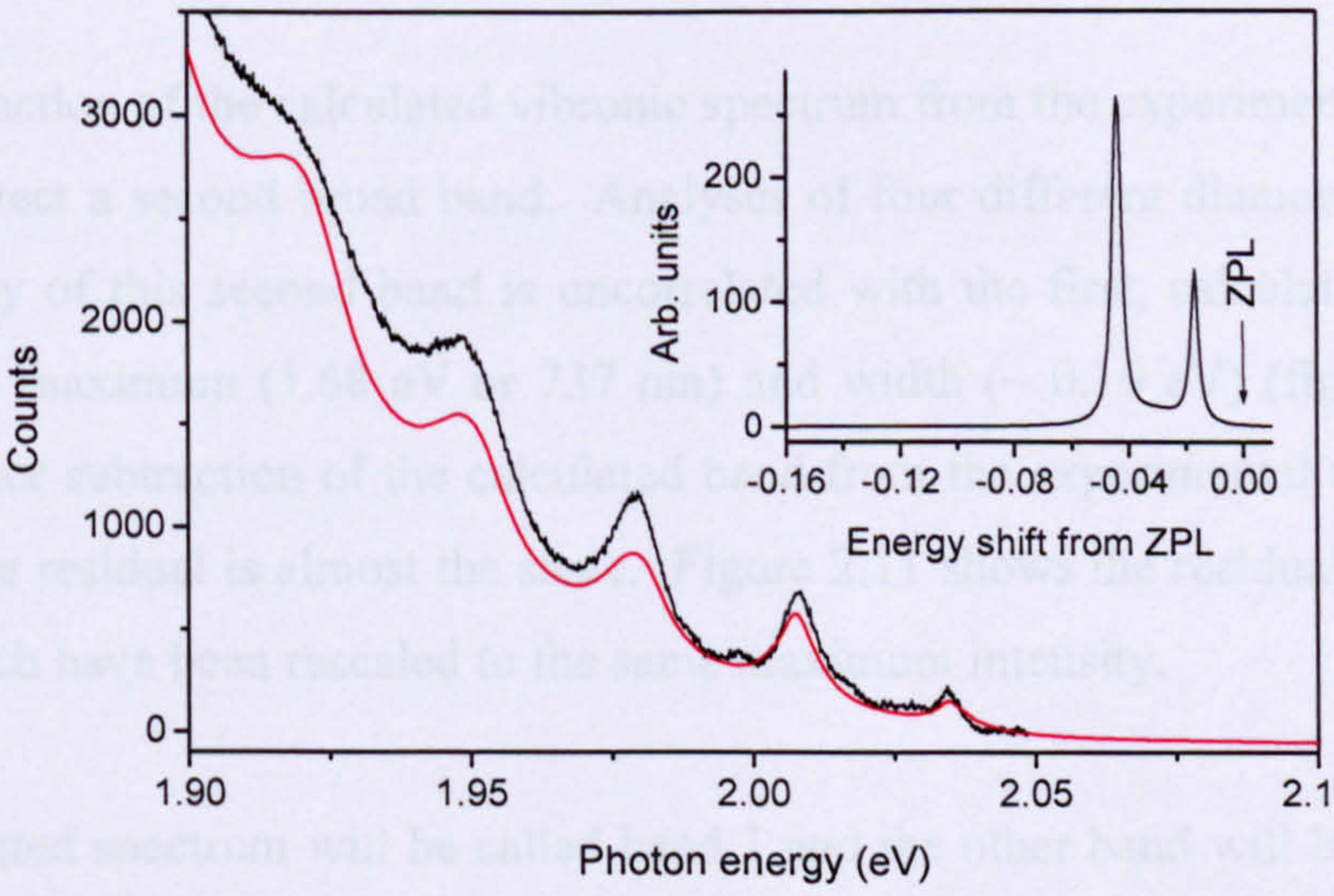

Figure 2.9. The calculated vibronic broad band (red curve) compared with the experimental curve. The calculated spectrum does not fit perfectly to the experimental spectrum, partly because the calculated spectrum was fitted to spectra from four different samples. The inset shows the calculated one-phonon spectrum.

We infer that the peak at 2.304 eV (609 nm) is the first maximum of the one-phonon replica in the vibronic band and will be 17 meV from the ZPL. This energy separation between the ZPL and the first one-phonon maximum, nicely correlates with the 18 ± 1.6 meV activation energy for the increase of the 2.034 eV (609 nm) peak.

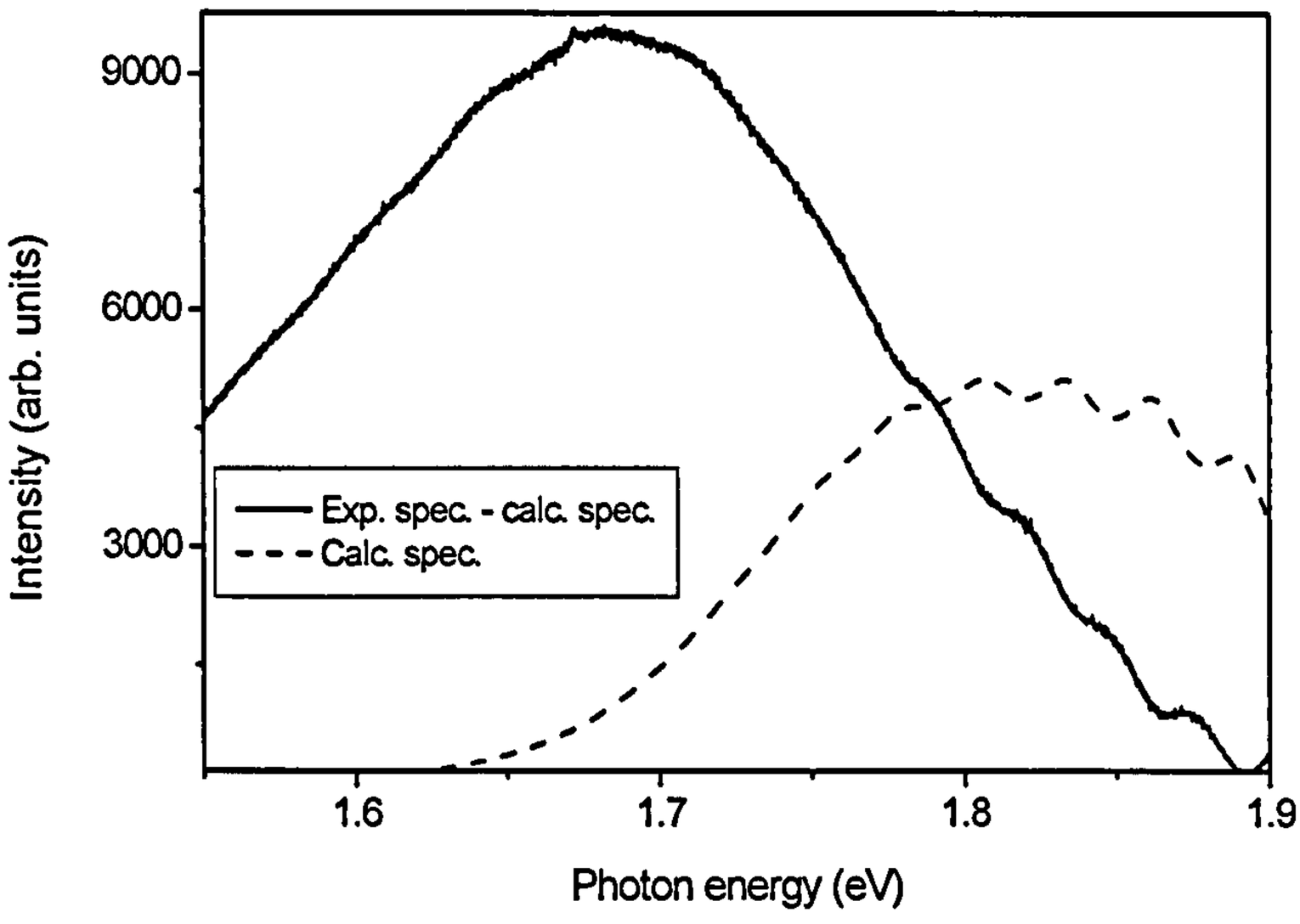

Figure 2.10. The difference (full curve) between the experimental spectrum and the calculated spectrum (broken curve). The reconstructed spectrum has been calculated up to the twelfth phonon replica. The small oscillations in the full curve are due to differences between the calculated and experimental curves.

After subtraction of the calculated vibronic spectrum from the experimental spectrum, one can detect a second broad band. Analyses of four different diamonds show that the intensity of this second band is uncorrelated with the first, calculated, band and has a fixed maximum (1.68 eV or 737 nm) and width (~ 0.19 eV) (figure 2.10 and 2.11). After subtraction of the calculated band from the experimental spectrum, the shape of the residual is almost the same. Figure 2.11 shows the residual of the broad bands, which have been rescaled to the same maximum intensity.

The calculated spectrum will be called band 1 and the other band will be called band 2. The weak, oscillating structure on the high energy side of band 2 is due to discrepancies between the experimental and calculated spectrum. These differences arise, in part, from the fact that the calculated band was optimised to fit to more than one experimental spectrum.

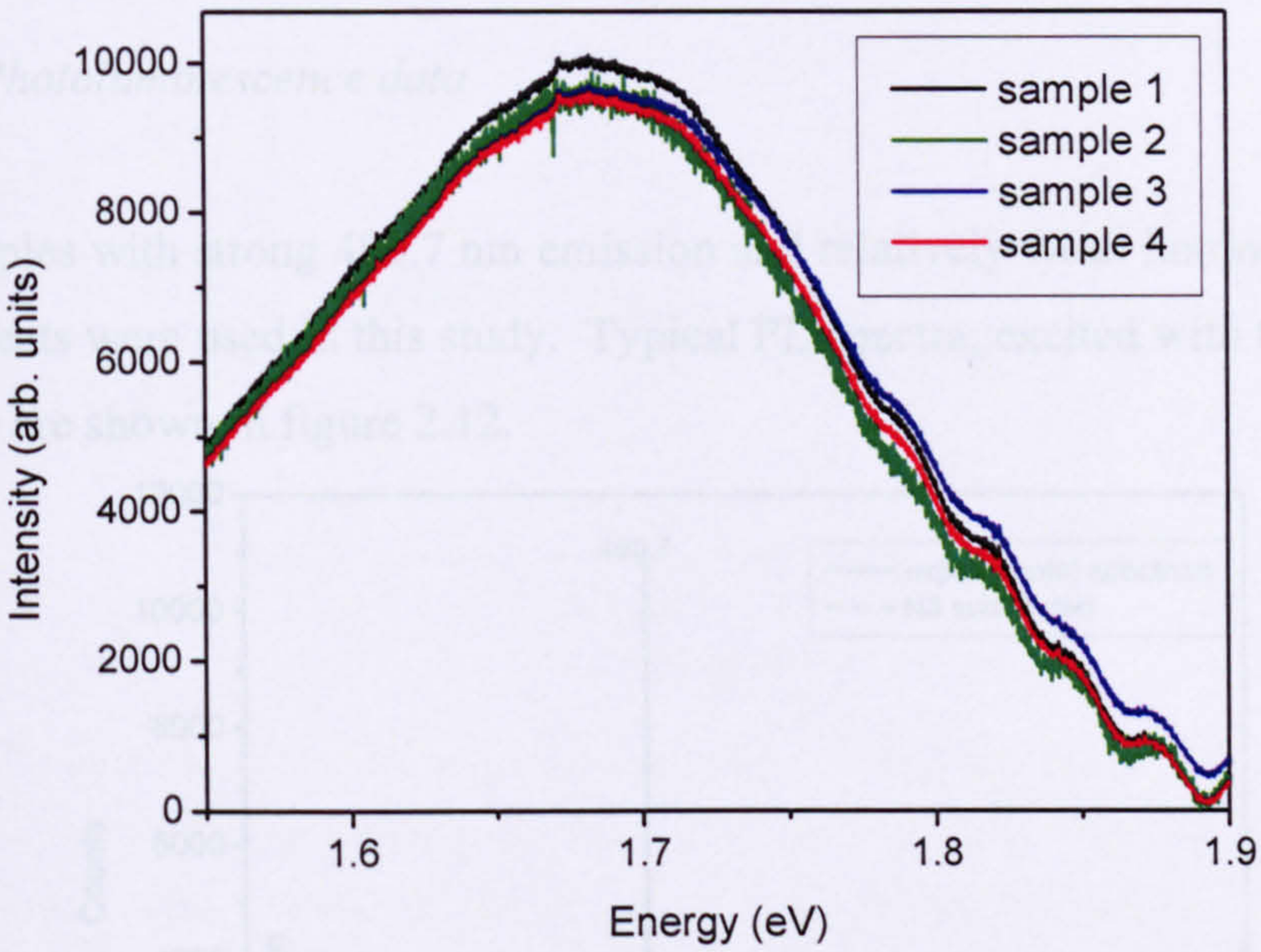

Figure 2.11. The PL spectra of the four samples after subtraction of the calculated broad band and rescaled to subtract the most suitable calculated spectrum. The residual bands have been rescaled to the same maximum intensity.

The procedure adopted here is not rigorously correct, because the spectra have not been corrected for the optical transfer function of the luminescence spectrometer. The analysis is only strictly valid if the data are plotted as photons per unit energy interval versus energy (Collins and Mohammed 1982). Over the small energy interval used to determine S, and the one-phonon density of states, this will be approximately true, but over the wider energy range covered by the whole band some discrepancy between the calculated and measured spectra is not surprising.

2.3.1.2. X-Ray fluorescence data

The X-ray fluorescence measurements were carried out using two different methods. One method is optimised for atomic impurities with high nuclear mass like tungsten, lead, etc., and the other method is optimised for detection of atomic impurities of lower nuclear mass like nickel, iron and cobalt. None of the measurements indicated the presence of impurities with a concentration greater than the limiting sensitivity of the instrument (0.1 to 1.0 ppm).

2.3.2. The 490.7 nm defect

2.3.2.1. Photoluminescence data

Five samples with strong 490.7 nm emission and relatively weak luminescence due to other defects were used in this study. Typical PL spectra, excited with the HeCd laser (325 nm) are shown in figure 2.12.

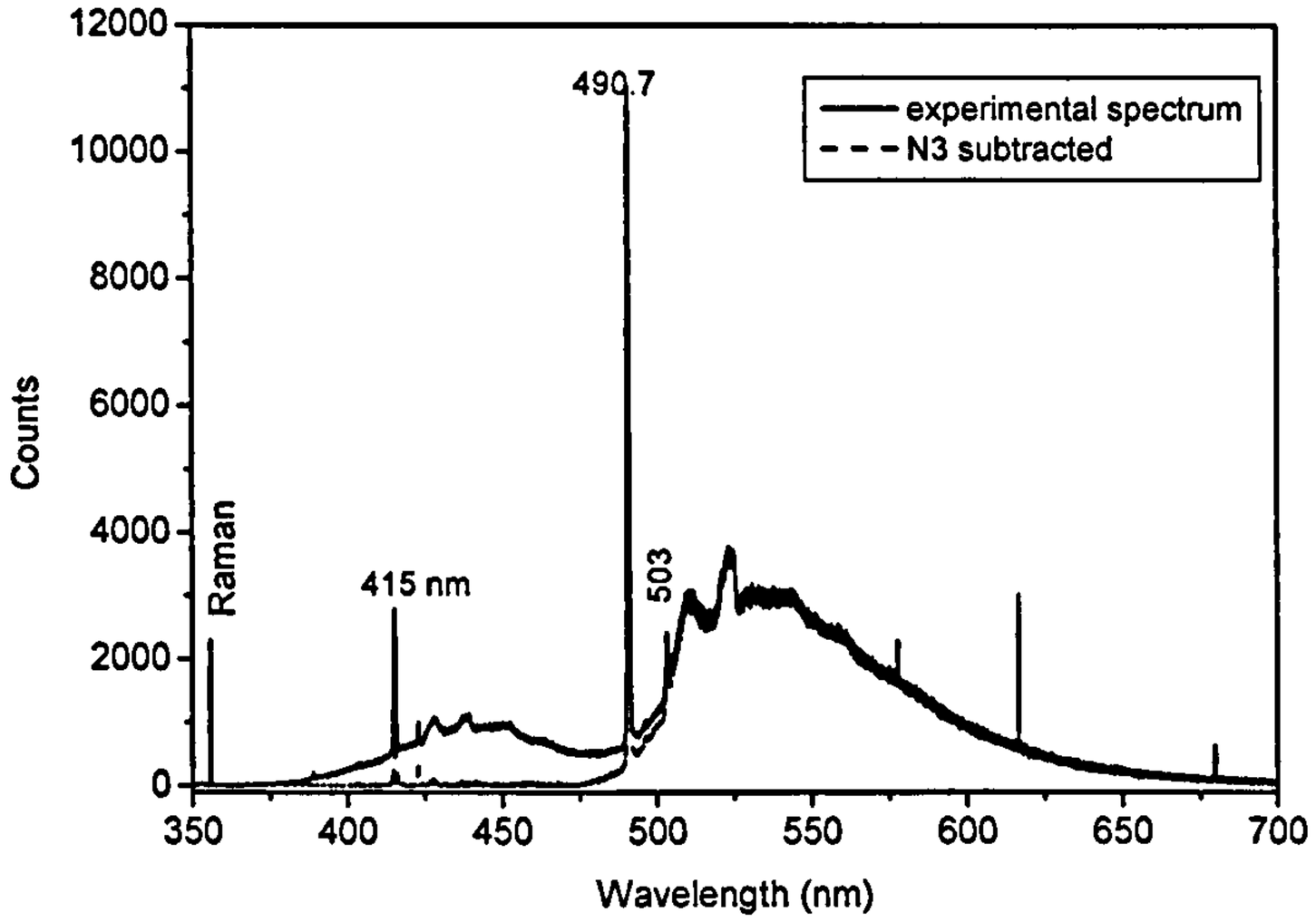

Figure 2.12. A typical photoluminescence spectrum of a brown type Ia diamond with strong 490.7 nm emission and weak luminescence due to other defects (full curve). The broken curve is the same spectrum with suitable N3 background subtraction.

Again the one-phonon spectrum was calculated by the procedure described in chapter 1, section 1.2. The calculated spectrum can be fitted to the experimental spectrum with a one-phonon spectrum with maxima at 153.8 and 89.6, two shoulders at 122 and 62 meV and a Huang-Rhys factor of 2.8 (figure 2.13), in good agreement with already published data (Zaitsev 2001).

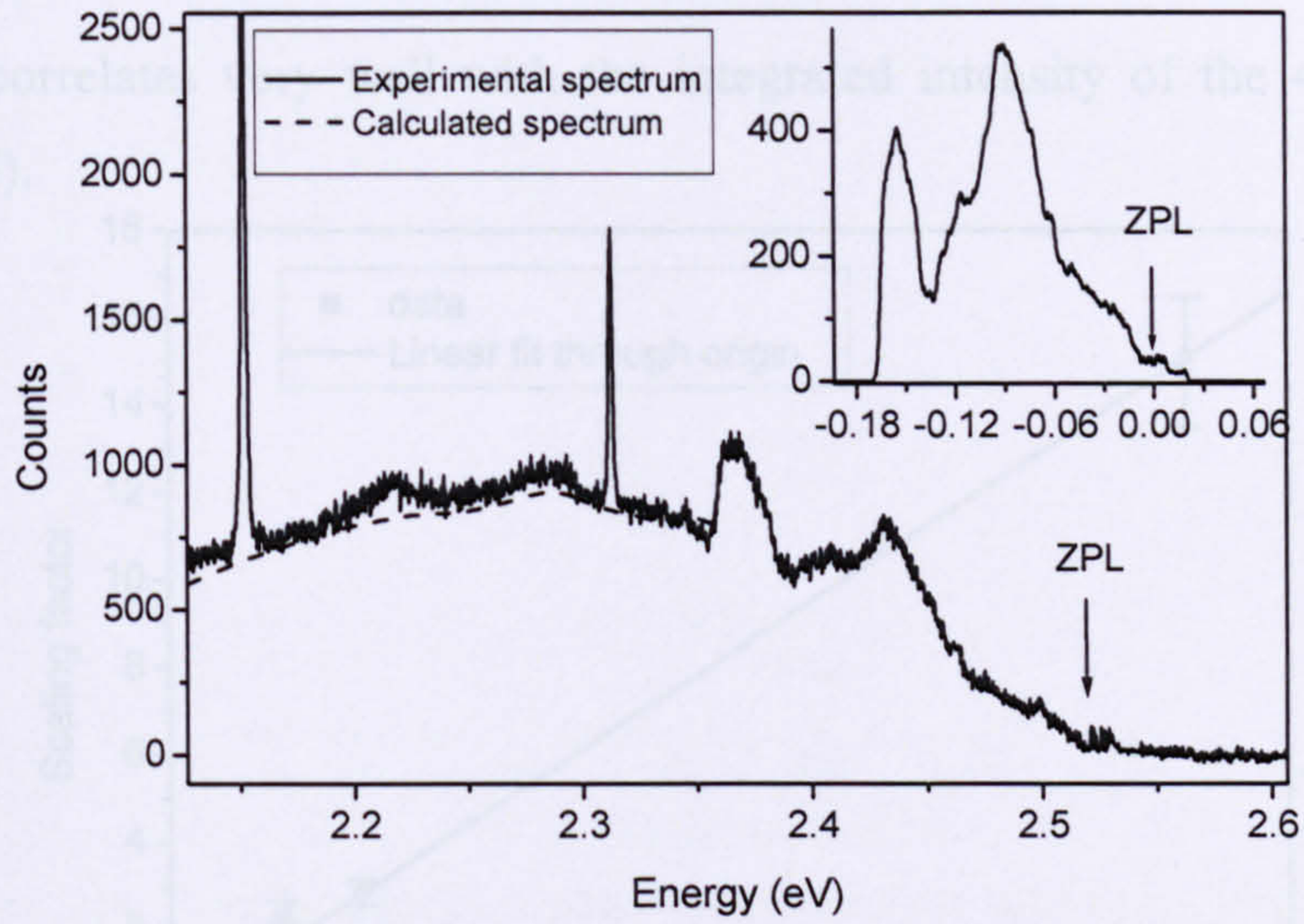

Figure 2.13. The experimental and calculated side band spectrum of the 490.7 nm defect. The arrow indicates the region of the removed ZPL. The two additional peaks at 2.31 eV (536 nm) and 2.15 eV (576 nm) are different defects. The inset shows the one-phonon density of states as a function of the energy difference between the zero phonon line and the phonon interacting with the defect.

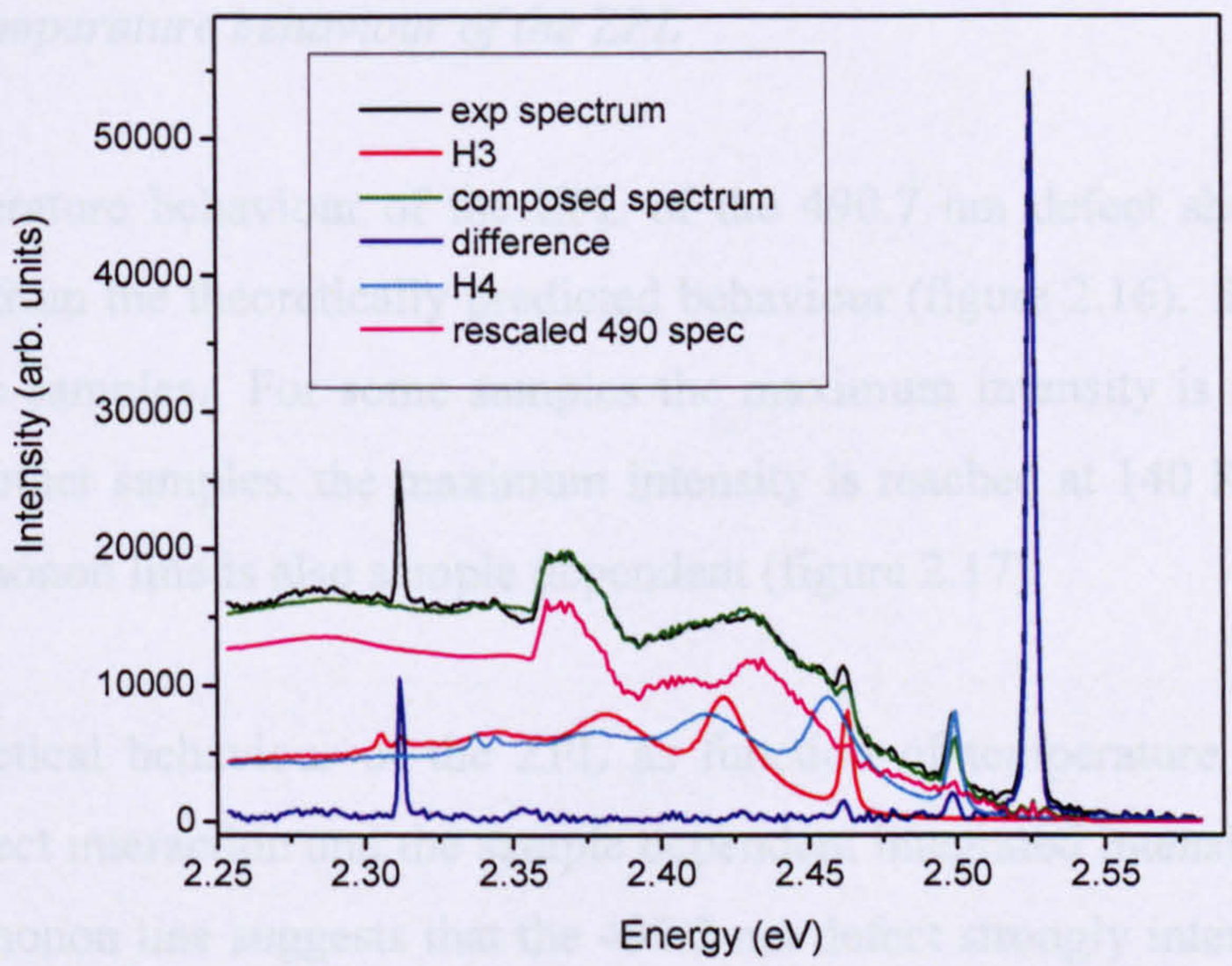

Figure 2.14. The decomposition of a PL spectrum into a spectrum of H3, H4 and 490.7 nm defects. The peak at 2.31 eV is due to a different defect

The rigidity of the adopted procedure and the correctness of the calculated spectrum is verified by decomposing the spectra of all samples into a sum of H3, H4 and calculated side band of the 490.7 nm defect spectra by a least squares fitting procedure (figure 2.14). All spectra could be fitted by this procedure and the factor used to scale the calculated 490.7 nm defect side band spectrum in this fitting

procedure correlates very well with the integrated intensity of the 490.7 nm peak (figure 2.15).

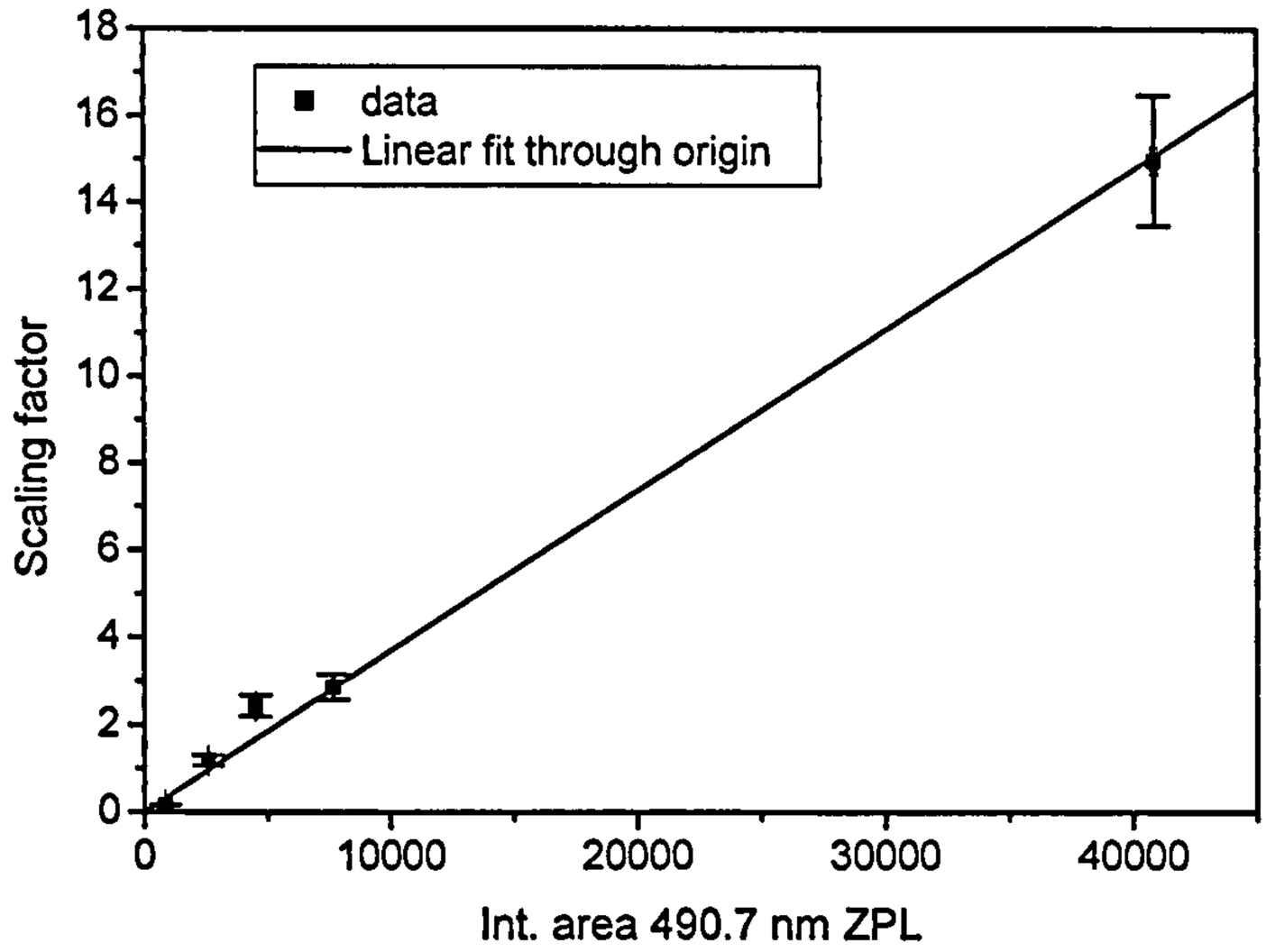

Figure 2.15. The correlation between the scaling factor and the integrated intensity of the 490.7 nm ZPL.

2.3.2.2. Temperature behaviour of the ZPL

The temperature behaviour of the ZPL of the 490.7 nm defect shows a remarkable deviation from the theoretically predicted behaviour (figure 2.16). It is even different for all five samples. For some samples the maximum intensity is reached at 100 K, while for other samples, the maximum intensity is reached at 140 K. The FWHM of the zero phonon line is also sample dependent (figure 2.17).

The theoretical behaviour of the ZPL as function of temperature does not include defect-defect interaction and the sample dependent integrated intensity and FWHM of the zero phonon line suggests that the 490.7 nm defect strongly interacts with another defect, which leads to the observed ZPL integrated intensity and FWHM behaviour.

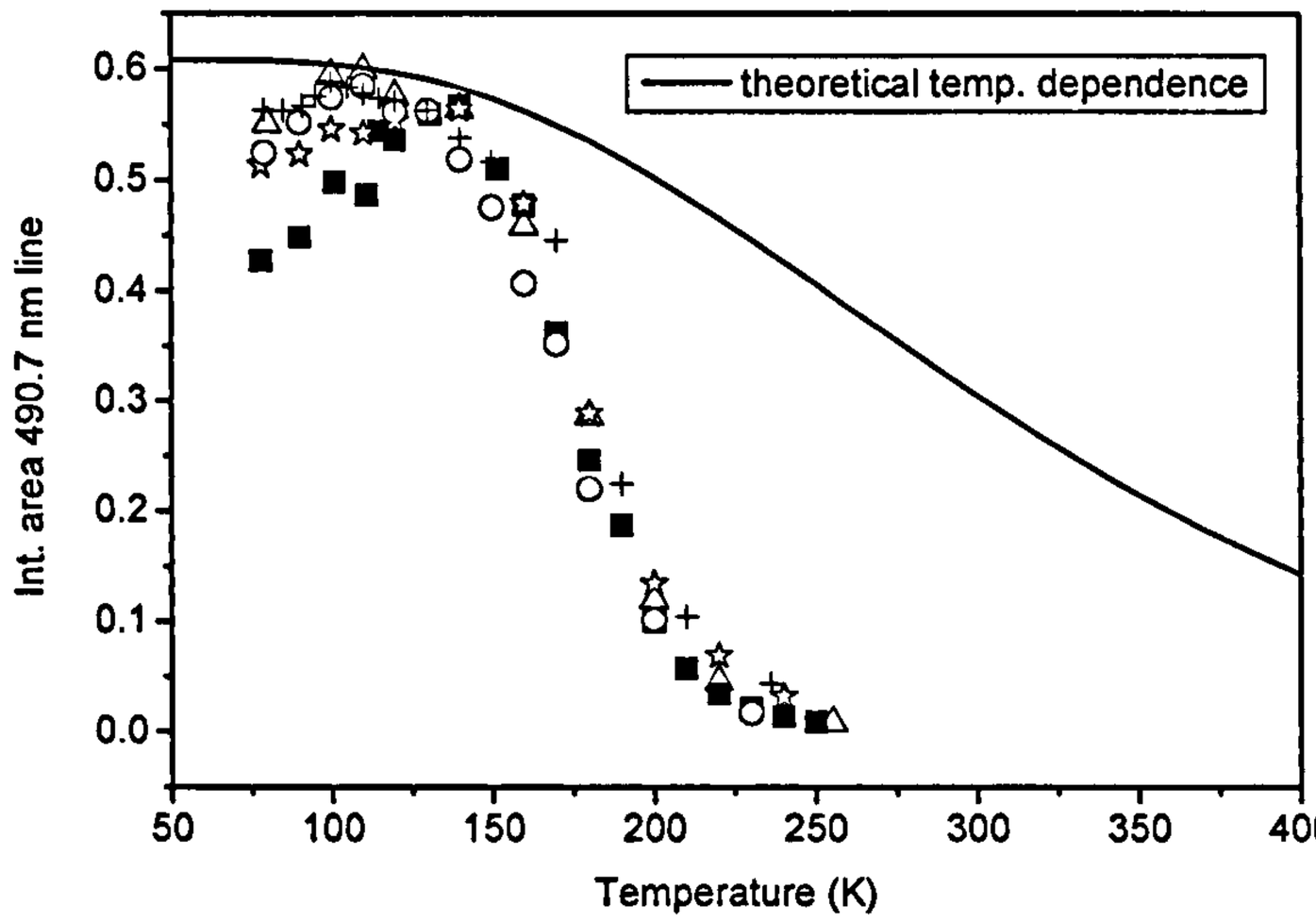

Figure 2.16. The temperature behaviour of 5 different samples (4 samples, and one measurement is on the same sample, but at a different location). The integrated intensity of the ZPL has been rescaled in a way that the value of the maximum of the integrated intensity is close to the theoretical temperature behaviour.

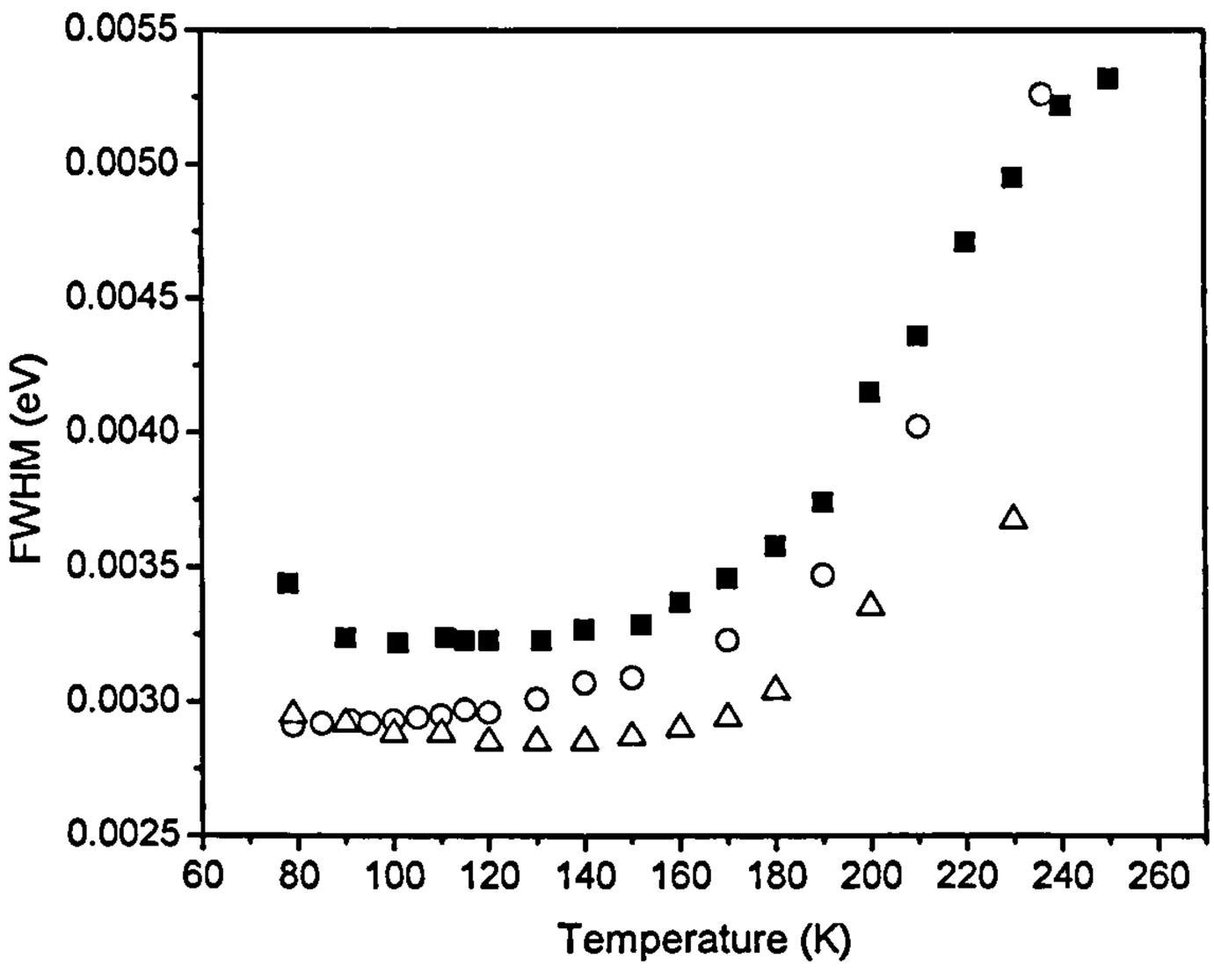

Figure 2.17. The FWHM of the 490.7 nm zero phonon line as function of temperature.

4. Conclusion

4.1. Broad band luminescence

The broad band luminescence with a maximum at 1.75 eV (~ 710 nm) observed in plastically deformed brown type Ia diamonds is composed of two broad bands

superimposed on each other. Band 1 has peaks at 2.034 eV (609 nm), 2.008 eV (617 nm), 1.978 eV (626 nm), 1.949 eV (636 nm) and 1.920 eV (646 nm).

The structure of band 1 was analysed in the theoretical framework of linear electron-phonon coupling and it is concluded that the band arises from a transition at a defect with an relatively high Huang-Rhys factor of S = 8.0 ± 0.5. The one-phonon density of states for the defect has maxima at 17 meV and 44 meV.

The maximum of band 2 is at 1.68 eV and the width is ~ 0.19 eV. It is possible that this band consists of more than one component.

A coupling to low energy phonons would be typical for impurities with high atomic mass with respect to carbon; however, no significant concentrations of impurities could be detected in the samples. The observation that the luminescence bands studied are observed in natural brown, plastically deformed, type Ia diamonds containing predominantly nitrogen in the form of B aggregates leads us to conclude that the optical transitions occur at defects which involve the B-form of nitrogen, perhaps in combination with an intrinsic impurity (vacancy or carbon interstitial) or a structural defect.

2.4.2. The 490.7 nm defect

The 490.7 nm defect is frequently detected in brown type Ia diamonds, and is thought to originate from decorated slip bands in plastically deformed diamonds (Collins and Woods 1982). The temperature behaviour of the ZPL of the defect is atypical, and deviates from the predicted behaviour for linear-electron phonon coupling. The sample dependent integrated intensity and the FWHM behaviour of the ZPL line of defect suggests a strong interaction with another defect or these phenomena may be due to strain in the plastically deformed diamond. This clearly needs further investigation.

Chapter three

Sub-threshold excitation of luminescence of defects in diamond

3.1. Introduction

The work reported here has been carried out to understand the mechanism by which optical centres in diamond can be excited with photons having a lower energy than that of the zero-phonon line (ZPL). We refer to this process as "sub-threshold excitation". Previous work has shown that luminescence can be observed from the 3H, H3, H4 and TR12 centres with sub-threshold excitation (Iakoubovskii 2001, Vlasov 2001). Each of these optical centres has a sharp ZPL with a vibronic absorption band to higher energies, and a vibronic luminescence band to lower energies.

A possible explanation for the observed phenomenon has been given by Iakoubovskii (2001), who suggested that the photons ionise the negatively charged counterpart of the centre, which then converts into an excited neutral centre. In that model, the subsequent de-excitation of the neutral centre gives rise to the observed photoluminescence. Vlasov (2001), on the other hand, argued that the process is thermally activated, although his result showed a deviation from Arrhenius behaviour at low temperatures (Vlasov 2001).

In our more extensive investigations on the H3, H4, $(N–V)^-$ and 3H centres we confirm that the thermally-activated mechanism is the correct interpretation. For these defects the electronic ground and excited states are non-degenerate and can couple to the lattice by linear electron-phonon coupling. The strength of the electron-phonon coupling is characterised by the Huang-Rhys factor S. For a given centre, the zero-phonon transition probability $P_{ZPL}(T)$ at temperature T is determined by the Huang-Rhys factor and the one-phonon density of states, and, in all cases, increases at lower temperatures (Davies 1974, 1981).

A schematic representation of the proposed sub-threshold excitation process is given in figure 3.1. The excitation occurs from thermally populated levels in the phonon density of states associated with the ground state. If E is the difference between the zero-phonon energy and the energy of the exciting light (2.409 eV in this case), the excitation requires the absorption of one or more phonons having a total energy of $\hbar\omega = E$.

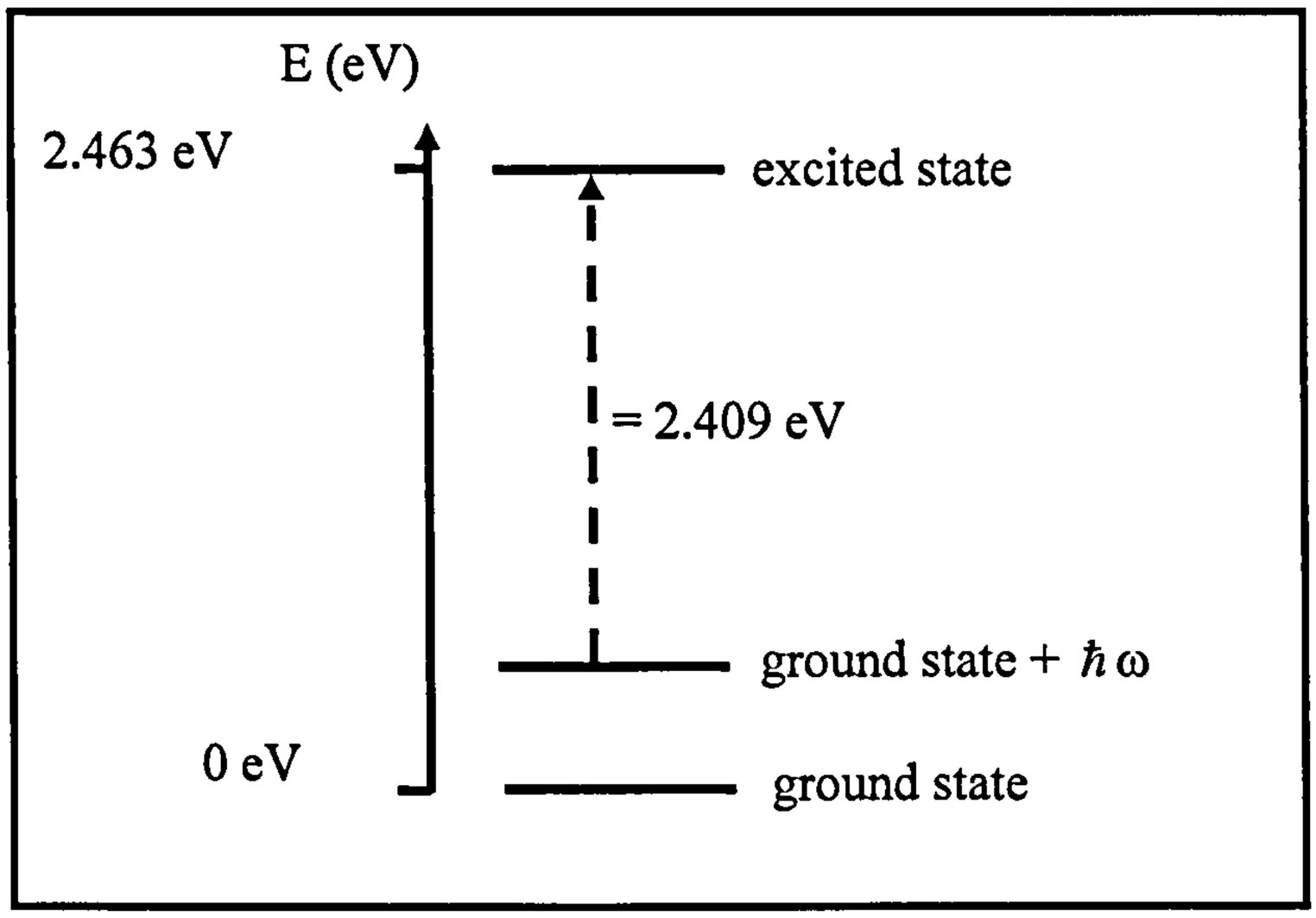

Figure 3.1. Schematic representation of the model for the sub-threshold excitation. Excitation is from a state which lies at energy $\hbar\omega$, equal to the energy difference between the zero-phonon line transition and the energy of the Ar^+ laser photons (2.409 eV).

If we assume a Boltzmann distribution for the population of the phonon states then the probability of absorbing one phonon of energy E will be given approximately by

$$C_1\, g(E) \exp[-E/(k_B T)] \qquad (3.1.1),$$

where g(E) is the phonon density of states and k_B is the Boltzmann constant. Similarly, the probability of absorbing two phonons, with energies E_1 and E_2, and with $E_1 + E_2 = E$, is

$$C_2\, g(E_1) \exp[-E_1/(k_B T)]\, g(E_2) \exp[-E_2/(k_B T)] = C_2\, g(E_1)\, g(E_2) \exp[-E/(k_B T)] \qquad (3.1.2).$$

The constants C_1 and C_2 describe the relative probabilities of the one- and two-phonon processes and E is the sum of E_1 and E_2. Transitions involving the absorption of three or more phonons are also possible. Once the centre has been excited, then, provided there are no non-radiative recombination paths, we expect the intensity of the luminescence, following relaxation to the ground state, to be given by

$$I(E,T) \propto G(E) \exp[-E/(k_B T)] P_{ZPL}(T) \qquad (3.1.3).$$

Here G(E) represents the appropriate combination of multi-phonon processes, and will be discussed further in section 3.3.3.

There are two ways in which this model can be verified. Using a fixed-wavelength laser to excite the luminescence, and varying the temperature, should give a variation in the intensity of the luminescence proportional to $\exp[-E/(k_B T)] P_{ZPL}(T)$. Alternatively, using a tuneable laser, with the specimen at constant temperature, measuring the integrated intensity of the ZPL at different excitation wavelengths should map out the multi-phonon function G(E) multiplied by $\exp[-E/(k_B T)]$

3.2. Experimental

Measurements have been made on 11 different diamonds, initially selected using absorption and/or luminescence spectroscopy. Important characteristics of these specimens are summarised in table 3.1.

3.2.1. Specimen details

Five samples with relatively strong H3 absorption were studied. One (sample 0337) was an irradiated and annealed specimen for which the details of the irradiation and heat-treatment are unknown. Another (sample 2b) was a brown type Ia diamond that had been colour-enhanced using annealing for 20 h at high temperature (1900 °C) and high pressure (7 GPa). Samples W1a and HRD1 are brown type Ia samples with naturally-occurring H3 defects.

Three type Ia samples (Sample 1, sample 3, sample 10), with different concentrations of nitrogen in the A and B aggregate forms, were irradiated and annealed at 800°C for 2 h, producing H3 and H4 centres. Samples 1 and 3 had been irradiated with 8-MeV electrons, and Sample 10 with 4-MeV electrons. See chapter four for more details.

Sample name	Defect creation	Defect studied by sub-threshold excitation
0337	Irradiation and annealing Conditions: Unknown	H3
W1a	Naturally occurring	H3
HRD1	Naturally occurring	H3
2b	HPHT annealing of a brown type Ia diamond Conditions: 1900°C, 7 GPa, 20 h	H3
R1 (2 measurements)	Naturally occurring	3H
H4-1 (3 measurements)	Irradiation and annealing Conditions: 2 MeV e^- + 800°C (2 h)	H4
Sample 1	Irradiation and annealing Conditions: 8 MeV e^- + 800°C (2 h)	H3 and H4
Sample 3	Irradiation and annealing Conditions: 8 MeV e^- + 800°C (2 h)	H3 and H4
Sample 10	Irradiation and annealing Conditions: 4 MeV + 800°C (2 h)	H3 and H4
Edu1	Naturally occurring	3H and H4
Type Ib sample	Irradiation and annealing Conditions: 2 MeV e^- + 800°C (2 h)	$(N–V)^-$

Table 3.1. Details of diamonds used in this investigation.

Diamond R1 was a type Ia specimen with naturally occurring 3H centres present. Diamond Edu1, exhibited naturally-occurring luminescence from the 3H and H4 centres, and diamond H4-1 was a type IaB specimen that had been irradiated with 2-MeV electrons and annealed at 800 °C for 2 hours to produce H4 centres. Because

only one specimen of each of these three examples of diamond was available, measurements were taken at more than one location on each diamond's surface.

Nitrogen-vacancy centres, $(N–V)^-$, were produced by 2-MeV electron irradiation and annealing for 2h at 800 °C in a low-nitrogen diamond grown by high-pressure, high-temperature synthesis.

3.2.2. Photoluminescence as a function of temperature

For almost all the sub-threshold measurements a Renishaw RM 2000 system is used. For the measurements where the laser wavelength is varied, a XY Dilor Raman spectrometer setup is used. See chapter 1, section 1.5.1. for a detailed description of the apparatus.

3.2.3. Photoluminescence as a function of exciting energy

The instruments are described in chapter 1, section 1.5.1. and additional procedures are as follows: the diamond sample was placed on a cold stage at a temperature of 150 K in a constant flow of dry nitrogen, held at a pressure slightly above atmospheric to eliminate water vapour and keep the sample surface free of ice. Indium was used to mount the sample and this was then bonded to the cooling element, ensuring good thermal contact. The indium was also moulded to mask the diamond, and select a reasonably homogenous region.

The temperature chosen (150 K) was sufficiently low that there was only a small amount of thermal broadening of the ZPL of the $(N–V)^-$ centre, but also sufficiently high that the luminescence intensity did not decrease too rapidly with increasing energy separation between the ZPL and the laser line (see equation 3.1.1). The temperature was stabilised for twenty minutes before measurements were taken; the temperature stability was estimated to be better than ± 1 K.

3.3. Results and discussion

All the results presented involve measuring the integrated area of the zero-phonon line. For each defect, the ZPL was least-squares-fitted with Lorentzian curve and a suitable quadratic background was subtracted.

3.3.1. Measurement of the transition probability

The integrated areas of the H3, H4 and 3H zero-phonon lines were measured as a function of temperature from 77 to 240 K, using excitation at 325 nm. Data for the H3 and H4 ZPLs, together with the calculated curve for the H3 transition probability, are shown in figure 3.2.

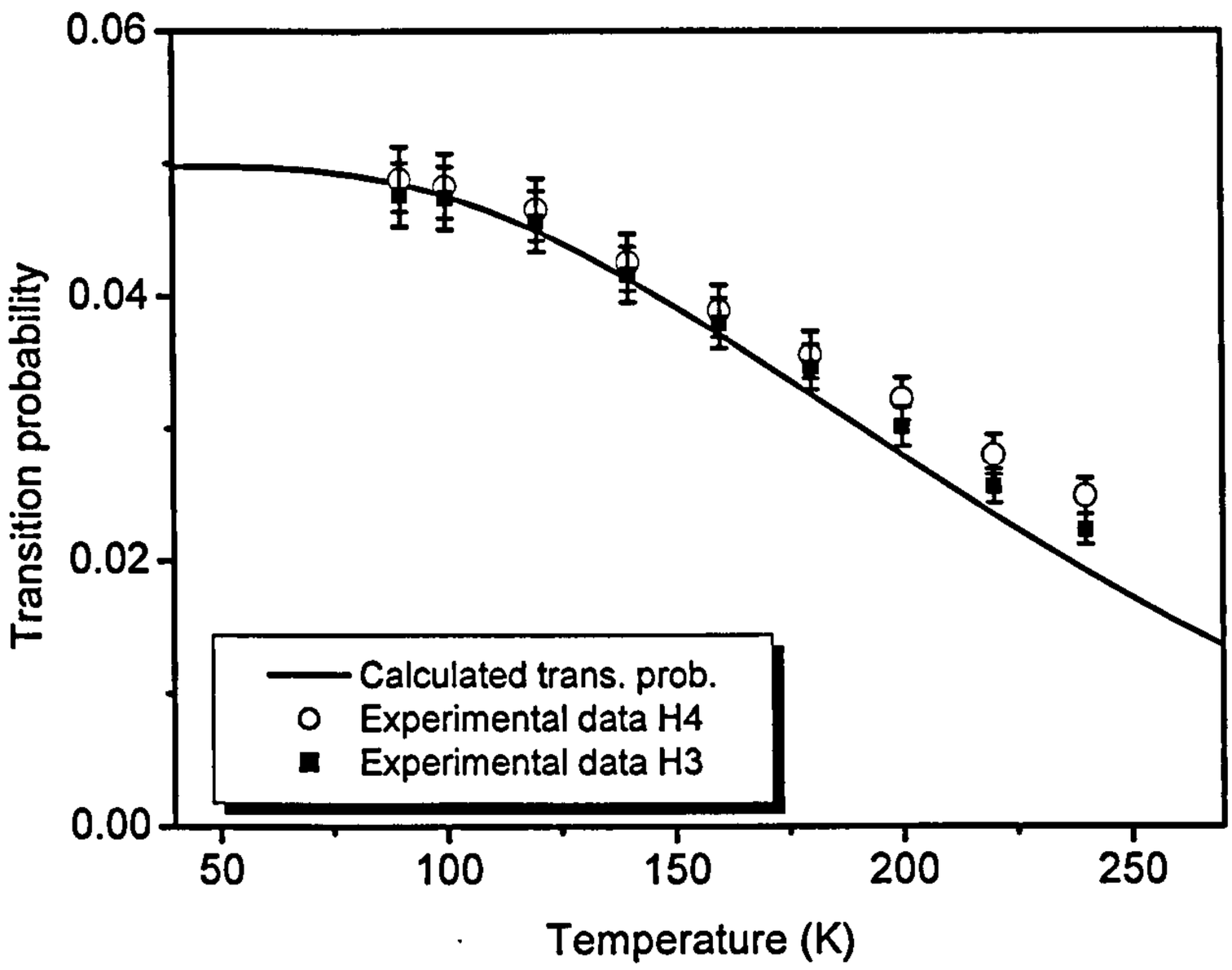

Figure 3.2. Intensities of the H3 and H4 zero-phonon lines, recorded in luminescence, using excitation at 325 nm. The solid line is the calculated transition probability of the H3 centre as a function of temperature. The amplitudes of the H3 and H4 ZPLs have been rescaled to the same amplitude as that of the calculated curve at 77 K.

The calculated curve is given by equation 1.2.10 of chapter one (Davies 1981a). Two modes were taken into account, one at 41 meV and one at 152 meV, together with a Huang-Rhys factor of S = 3 (Davies 1981a, Zaitsev 2001).

A curve was also calculated for the H4 ZPL, using two modes at 40 meV and 154 meV, with S = 3 (Davies 1981a, Zaitsev 2001). Not surprisingly, because of the similarity of the parameters used, this curve was almost indistinguishable from that for the H3 centre. In both cases the experimental data in figure 3.2 diverge somewhat from the calculated curves at higher temperature.

Data in figure 3.2 for the H3 ZPL were obtained from a type IaA diamond in which [H3] >> [H4] and data for the H4 ZPL were obtained from a type IaB diamond in which [H4] >> [H3]. Here the quantities in square brackets indicate the concentrations of the corresponding defect. However, very similar data were obtained from type IaA/B diamonds containing similar concentrations of H3 and H4 centres.

The transition probability for luminescence from the 3H centre was calculated with a single mode in the one-phonon spectrum at 67 meV and a Huang-Rhys factor S ~ 0.8 (Zaitsev 2001). However, as shown in figure 3.3, the experimental data from sample R1 do not follow the calculated curve well, indicating the presence of non-radiative decay channels. For that reason the experimentally-measured transition probabilities were used to correct the sub-threshold data for the 3H centre.

3.3.2. Sub-threshold excitation as a function of temperature

3.3.2.1. Diamonds containing one type of defect excited by sub-threshold excitation

Figure 3.4 shows the logarithm of the integrated area of the H3 zero-phonon line, plotted against the reciprocal of temperature, using excitation at 514.5 nm. Similar data were obtained from all the diamonds in which the H3 centre was the dominant defect. The lower plot shows the data without being corrected for the transition probability. A line to guide the eye has been drawn through the points at low temperature, and the data points at high temperature clearly diverge from this line. When the data points are corrected for the transition probability, as in the upper plot, all the points lie on a straight line, as expected from equation 3.1.1, and the gradient of this line, $-E/k_B$, gives an energy equal, within the experimental uncertainties, to the energy separation between the zero-phonon transition and the energy of the laser.

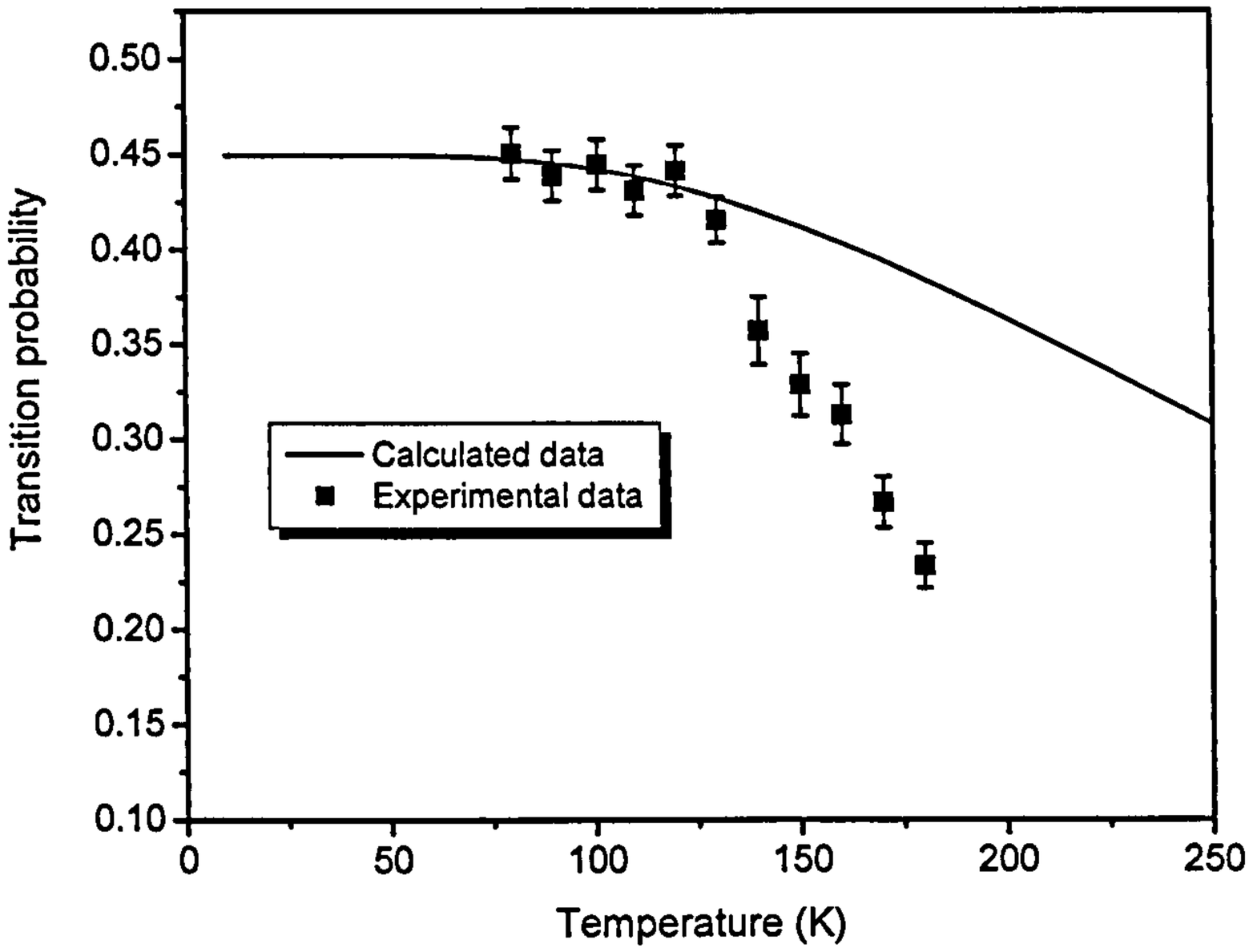

Figure 3.3. The experimentally measured and calculated transition probabilities of the 3H centre as a function of temperature.

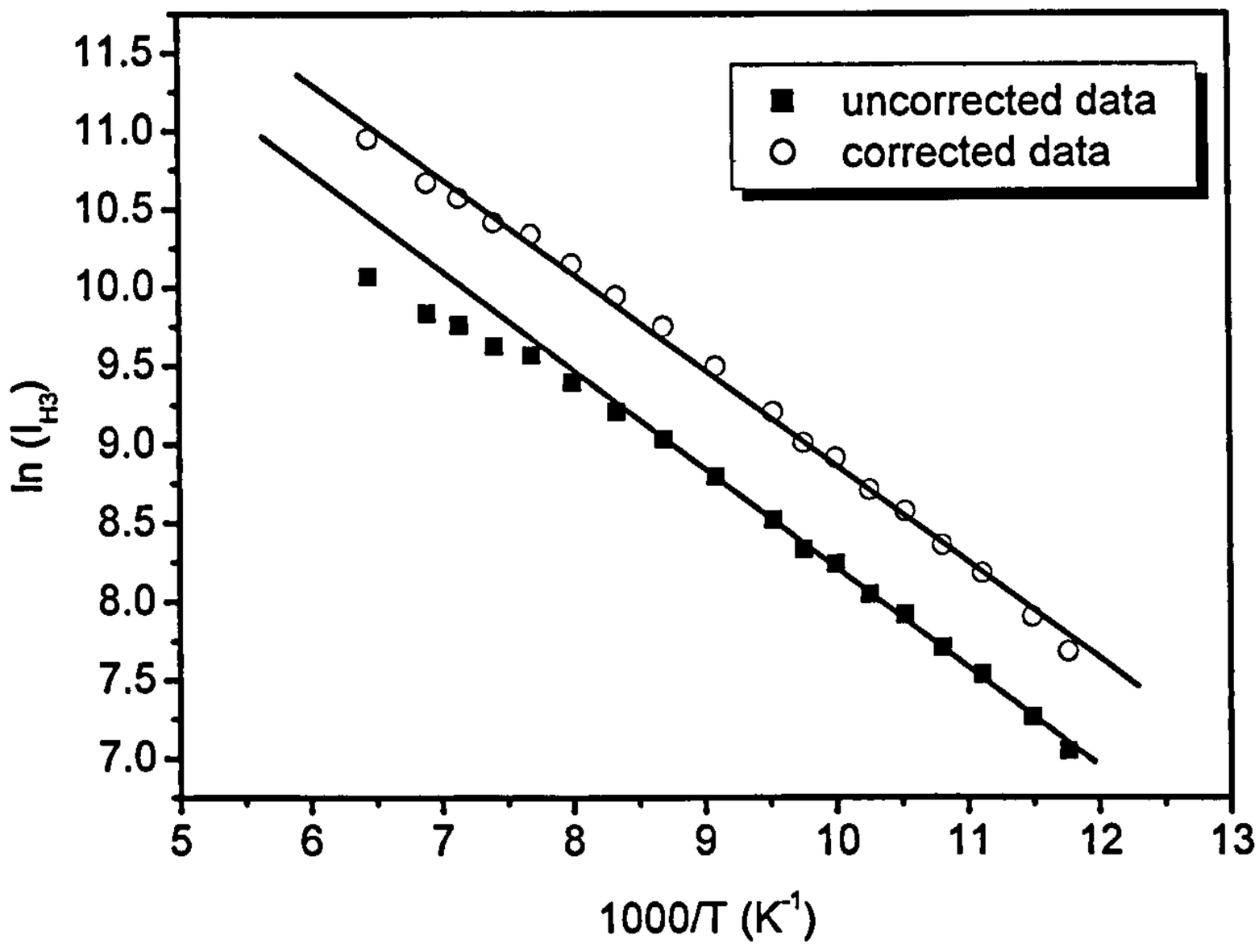

Figure 3.4. Arrhenius plots of the integrated intensity of the H3 zero-phonon line, using sub-threshold excitation at 514.5 nm. Data in the lower plot are uncorrected for the change in transition probability with temperature; the line through the low-temperature points is a guide to the eye. Data in the upper plot are corrected; the line is the best fit to the data.

Similar data were obtained from the diamond in which the H4 centre was the dominant defect, and for diamond R1 in which the 3H centre was the major defect giving rise to luminescence in the vicinity of 2.46 eV. Figure 3.5 demonstrates that

the Arrhenius plot for the 3H centre is an excellent straight line, once the raw data have been corrected for the experimentally-measured transition probability.

In each case the activation energies for the H3, H4 and 3H defects, summarised in table 3.2, are close to those expected.

3.3.2.2. Diamonds containing more than one type of defect

In diamonds exhibiting H3 and H4 luminescence with a comparable intensity (when excited at 325 nm) the integrated intensities of the sub-threshold-excited ZPLs deviate from Arrhenius behaviour at higher temperatures. Figure 3.6(a) shows data for the H3 centre in a diamond containing predominantly H3 centres and a diamond containing similar concentrations of H3 and H4 centres. Figure 3.6(b) shows a similar comparison for the H4 centre. For the diamond containing predominantly H4 centres the Arrhenius plot is linear up to at least 240 K, whereas, when H4 and H3 centres are present together, the data are not strictly exponential. Furthermore the gradient at lower temperatures is smaller than the gradient observed for diamonds containing only H4 centres. For specimens containing mainly H3 centres (figure 3.6(a)) the plot is linear up to at least 240 K (although the high-temperature data are not shown here) whereas, for a diamond containing both H3 and H4 centres the data deviate from a linear plot at high temperatures. This deviation is opposite in sign for the two defects; at high temperatures the H4 intensity always increases, while the H3 intensity always decreases, relative to the linear extrapolations of the low-temperature data. Interestingly, the Arrhenius plot of the *ratio* of the H3 and H4 integrated intensities is a good straight line, giving an activation energy which is close to the energy difference between the zero-phonon lines (figure 3.7 and table 3.3).

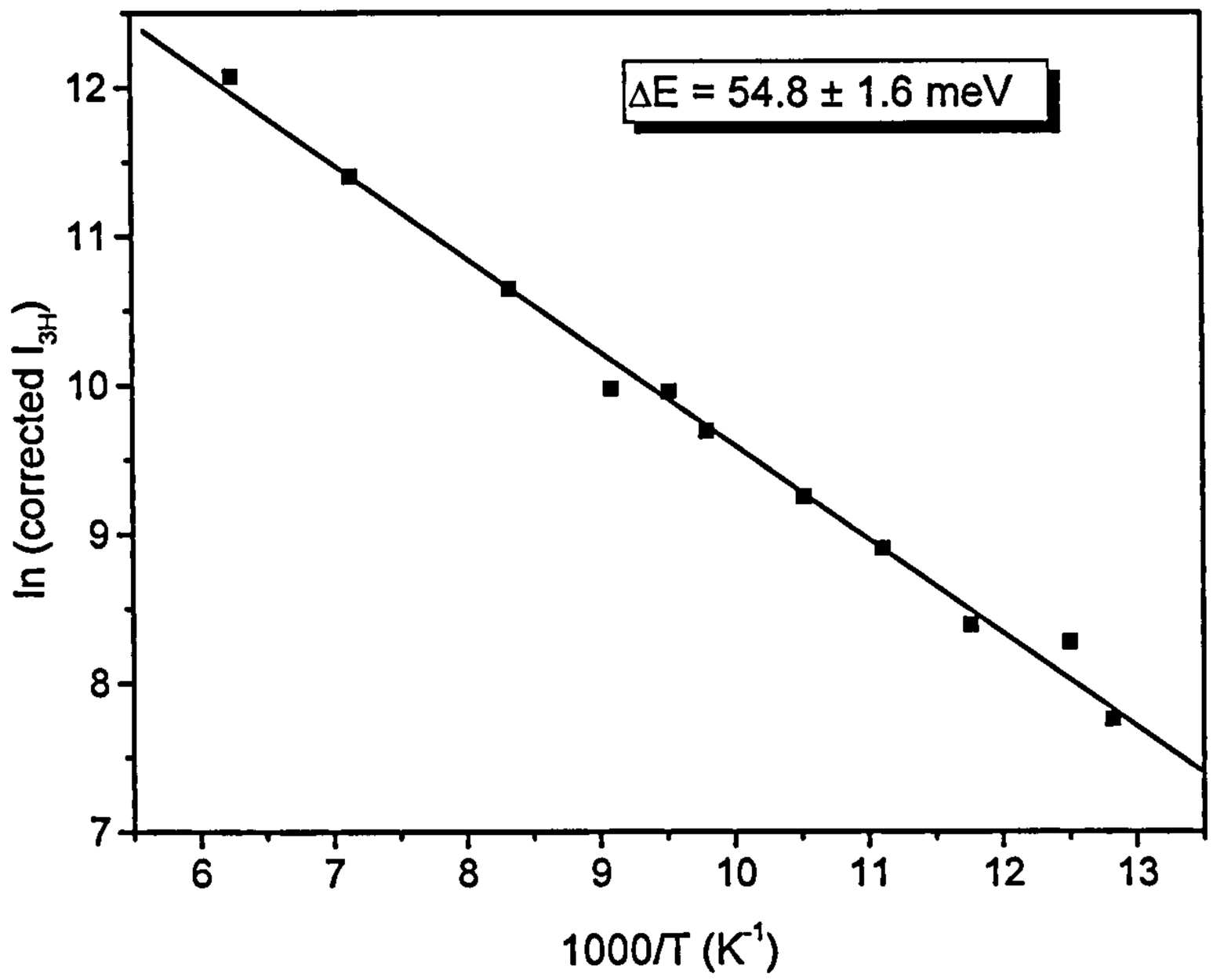

Figure 3.5. Arrhenius plot of the integrated intensity of the 3H zero-phonon line, using sub-threshold excitation at 514.5 nm. The data have been corrected for the experimentally-measured temperature dependence of the transition probability.

ZPL position (eV)	Number of samples	Energy difference between ZPL and excitation (meV)	Activation energy (meV)
2.463 (H3)	5	53.9	55.8 ± 4.6
2.499 (H4)	3*	89.9	83.5 ± 1.1
2.462 (3H)	2°	52.9	55.0 ± 4.5

* Three measurements at different locations on the same sample

° Two measurements at different locations on the same sample

Table 3.2. Activation energies for sub-threshold-excited photoluminescence, compared with the differences between the exciting energy and that of the corresponding zero-phonon line. All values for the activation energies are the averages of the results for all the samples.

However, when H4 and 3H centres are present together, there is no deviation from Arrhenius behaviour of either the H4 luminescence or the 3H luminescence. Figure 3.8 shows plots for these two defects, present in the same diamond, and both sets of data lie on good straight lines. The results are summarised in table 3.3 which shows that the activation energies agree with the spectroscopic difference in energy between the laser line and the corresponding ZPL.

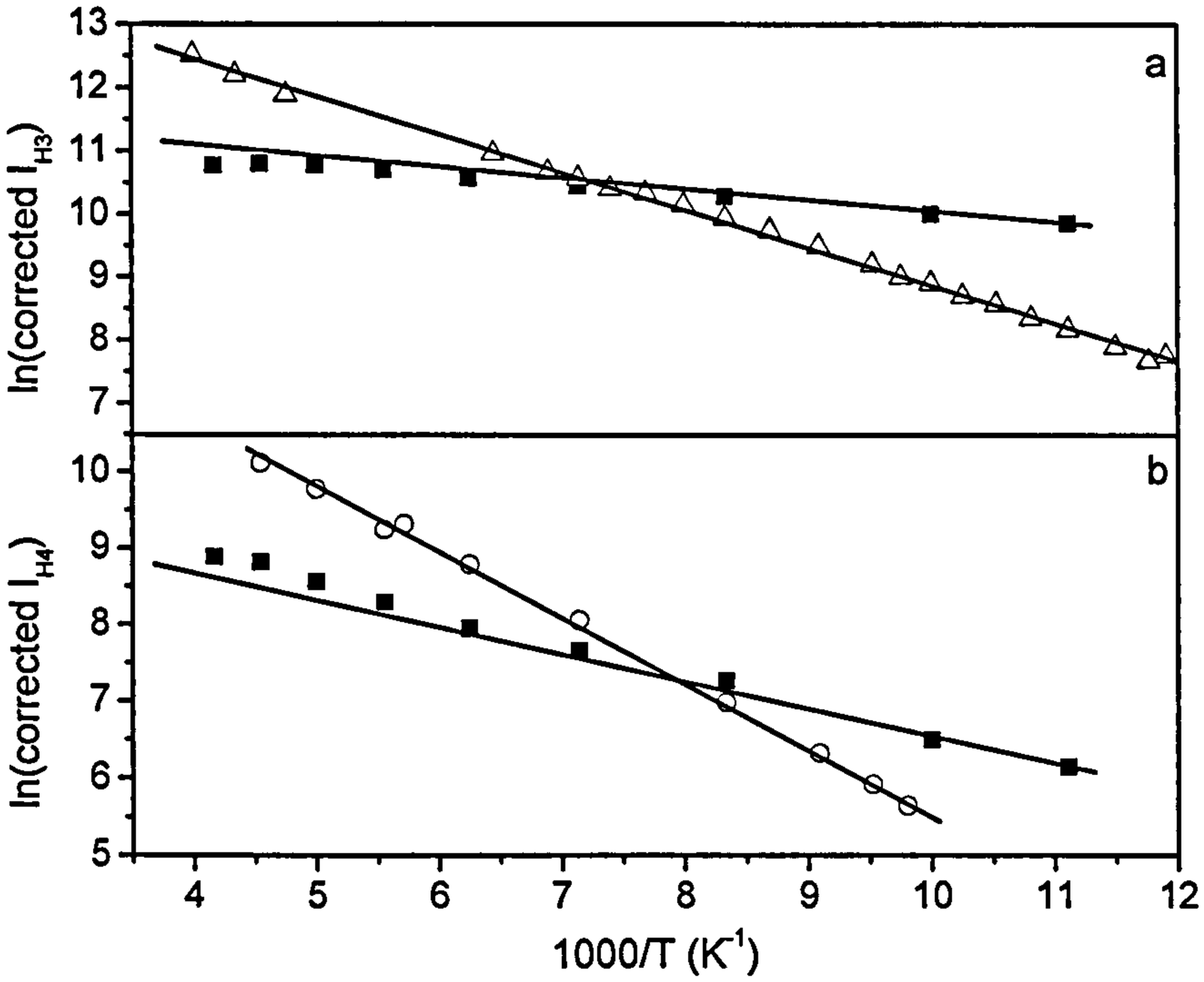

Figure 3.6. Arrhenius plots, using sub-threshold excitation at 514.5 nm, for the integrated intensity of (a) the H3 zero-phonon line, in a diamond containing predominantly H3 centres (triangles) and a diamond containing similar concentrations of H3 and H4 centres (squares); (b) the H4 zero-phonon line, in a diamond containing predominantly H4 centres (circles) and a diamond containing similar concentrations of H3 and H4 centres (squares). The lines in figures (a) and (b) for the data from the diamond containing both H3 and H4 defects are linear extrapolations of the low-temperature behaviour. In all cases the data have been corrected for the change in transition probability with temperature.

A number of possible mechanisms have been considered to account for the behaviour observed when H3 and H4 centres are present in the same diamond. We consider first whether H4 PL can be reabsorbed and generate additional H3 luminescence with a temperature-dependence that would lead to the behaviour shown in figure 3.6. In a diamond containing similar concentrations of H3 and H4 centres, the relative intensities of the H4 and H3 emissions produced by sub-threshold excitation will be $I_{H4} / I_{H3} \sim 0.01$ at 90 K and ~ 0.1 at 180 K. (We assume here – see equation 3.1.1 – that $g_1(E)$ at 514.5 nm and $P_{ZPL}(T)$ are similar for both centres.) Only a small fraction of the H4 photons, in the energy range where the H4 luminescence band overlaps with the H3 absorption band, can potentially excite H3 luminescence. Furthermore, because of the confocal geometry used, only those H4 photons absorbed within the small volume of the diamond sampled by the microscope have any significance. Following absorption of H4 photons, it is only those H3 centres which emit in a

direction that can be collected by the numerical aperture of the microscope which will be detected. It is clear that the intensity of such a signal will be completely negligible compared with that from the H3 centres excited by sub-threshold illumination at 514.5 nm. H3 absorption competing with the H4 absorption is not a possible explanation for the following reasons: (i) different relative concentrations of H3 and H4 defects cause deviations from Arrhenius behaviour in the same sense; (ii) in some specimens the absorption coefficients are very small; (iii) there is no deviation of Arrhenius behaviour in diamonds containing both the 3H and H4 defects. A possible explanation for the behaviour shown in figure 3.6 is that there is a thermally-activated energy exchange between the H4 and H3 centres, and the data in figure 3.7 are consistent with such a proposal.

Defect combination	Activation energy (meV)	Activation energy (meV) from ratio plots
H4 + H3	Not well-defined	31.0 ± 1.7
H4 + 3H	H4: 87.1 ± 0.5 3H: 54.8 ± 1.6	----------

Table 3.3. Results of the analysis on samples with more than one sub-threshold-excited defect. Three samples containing both H4 and H3 centres were measured; in each case the activation energies were ill-defined and only the average activation energy derived from the ratio plots is given. Only one sample containing both H4 and 3H defects has been analysed.

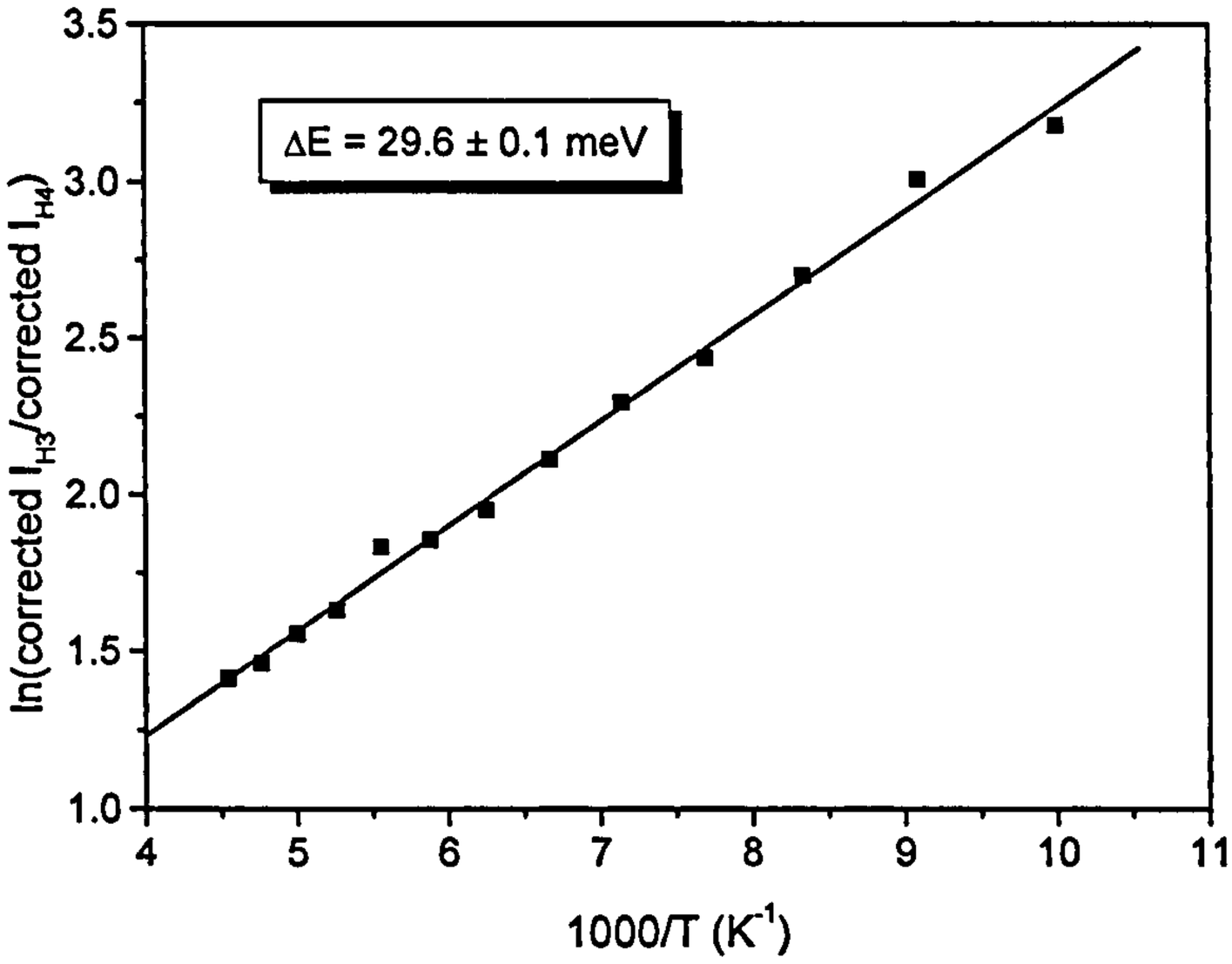

Figure 3.7. Arrhenius plot of the ratio of the integrated intensities of the H3 and H4 zero-phonon lines, using sub-threshold excitation at 514.5 nm, in a diamond containing both defects. The data are corrected for the changes in the transition probabilities with temperature.

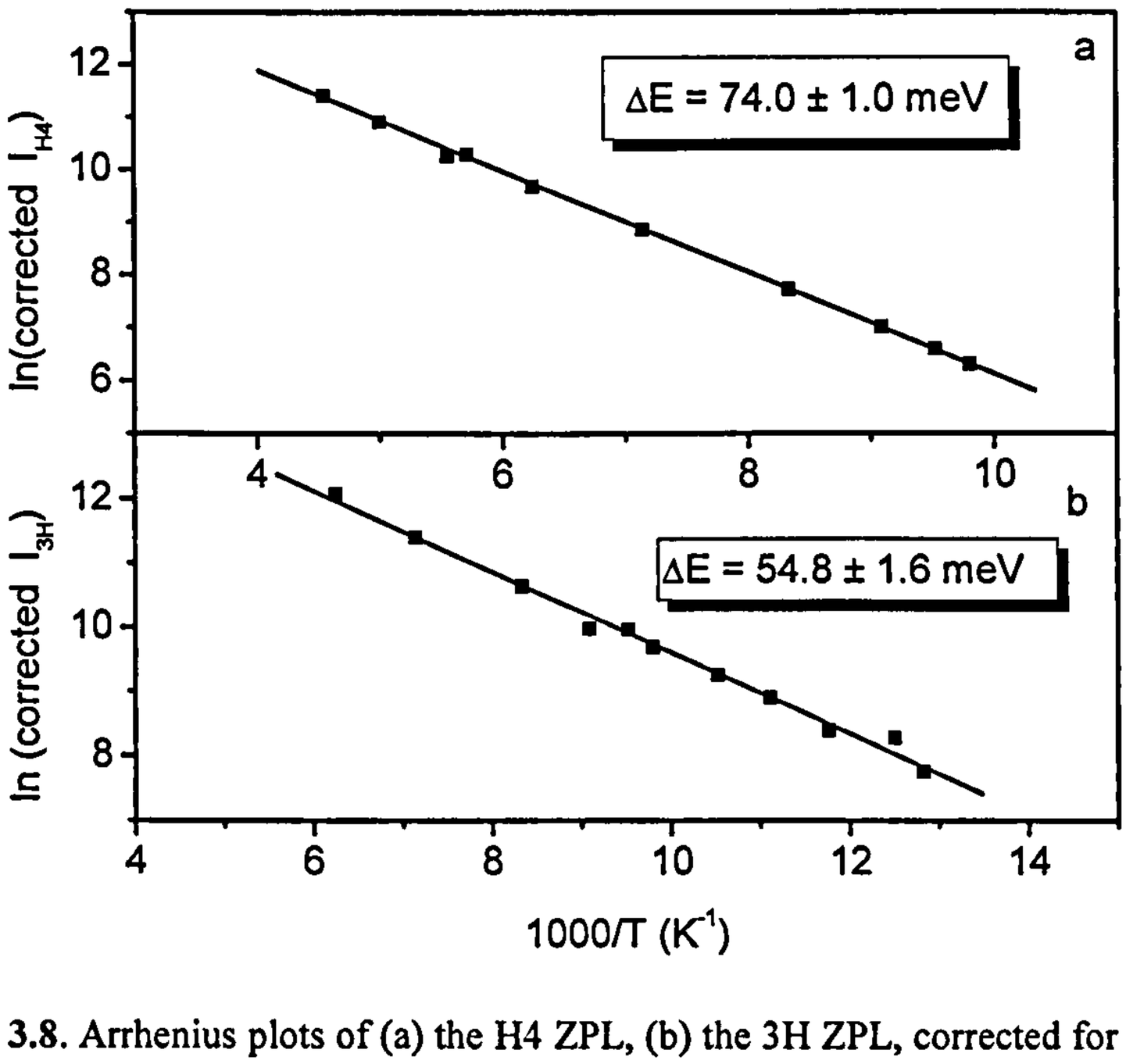

Figure 3.8. Arrhenius plots of (a) the H4 ZPL, (b) the 3H ZPL, corrected for the changes in the transition probabilities with temperature, in a diamond containing both defects.

3.3.3. Sub-threshold excitation as a function of energy

Equation 3.1.1 shows that, at constant temperature, following sub-threshold excitation, the intensity of the ZPL in photoluminescence should be proportional to

G(E) multiplied by $\exp[-\Delta E/(k_B T)]$. G(E) here is the multi-phonon transition probability for the absorption of ground-state phonons. This can be derived from the photoluminescence vibronic band which is produced by the coupling between the electronic transition and ground-state phonons.

If the one-phonon density of states $I_1(\nu)$ is known, (where ν is the frequency) the second $I_2(\nu)$, third $I_3(\nu)$, ... phonon replicas can be calculated by convolution of the one-phonon spectrum with itself, then with $I_2(\nu)$, ... as in equation 3.1.3.

$$I_n(\nu) = \int_0^{\omega_m} I_1(x) I_{n-1}(\nu - x)\, dx \qquad (3.3.1).$$

Here ω_m is the cut-off frequency of the one-phonon spectrum (165 meV).

The square of the integrated intensity of the I_n curve is proportional to

$$|I_n|^2 \sim S^n \frac{e^{-S}}{n!} \qquad (3.3.2),$$

where S is the Huang-Rhys factor and n is the index of the n^{th}-phonon replica. (Davies 1981a). The sum of all the phonon replicas, with the appropriate amplitudes from equation 3.1.3, is equivalent to G(E). To obtain the shape of the photoluminescence vibronic band this function is multiplied by ν^3 (Davies 1981a).

It follows that G(E) may be obtained from a PL spectrum, plotted as photons per unit energy interval, by dividing every point in the PL spectrum by ν^3.

Figure 3.9 shows the intensity of the $(N\text{–}V)^-$ ZPL at 637 nm, divided by $\exp[-E/(k_B T)]$, plotted against E at T = 150 K, where E is the energy separation between the ZPL and the laser line. The experimental points are compared with the photoluminescence vibronic band, measured at 150 K, divided by ν^3, and it can be seen that a tolerable agreement has been obtained. Unfortunately the sensitivity of this technique drops off rapidly with increasing ΔE.

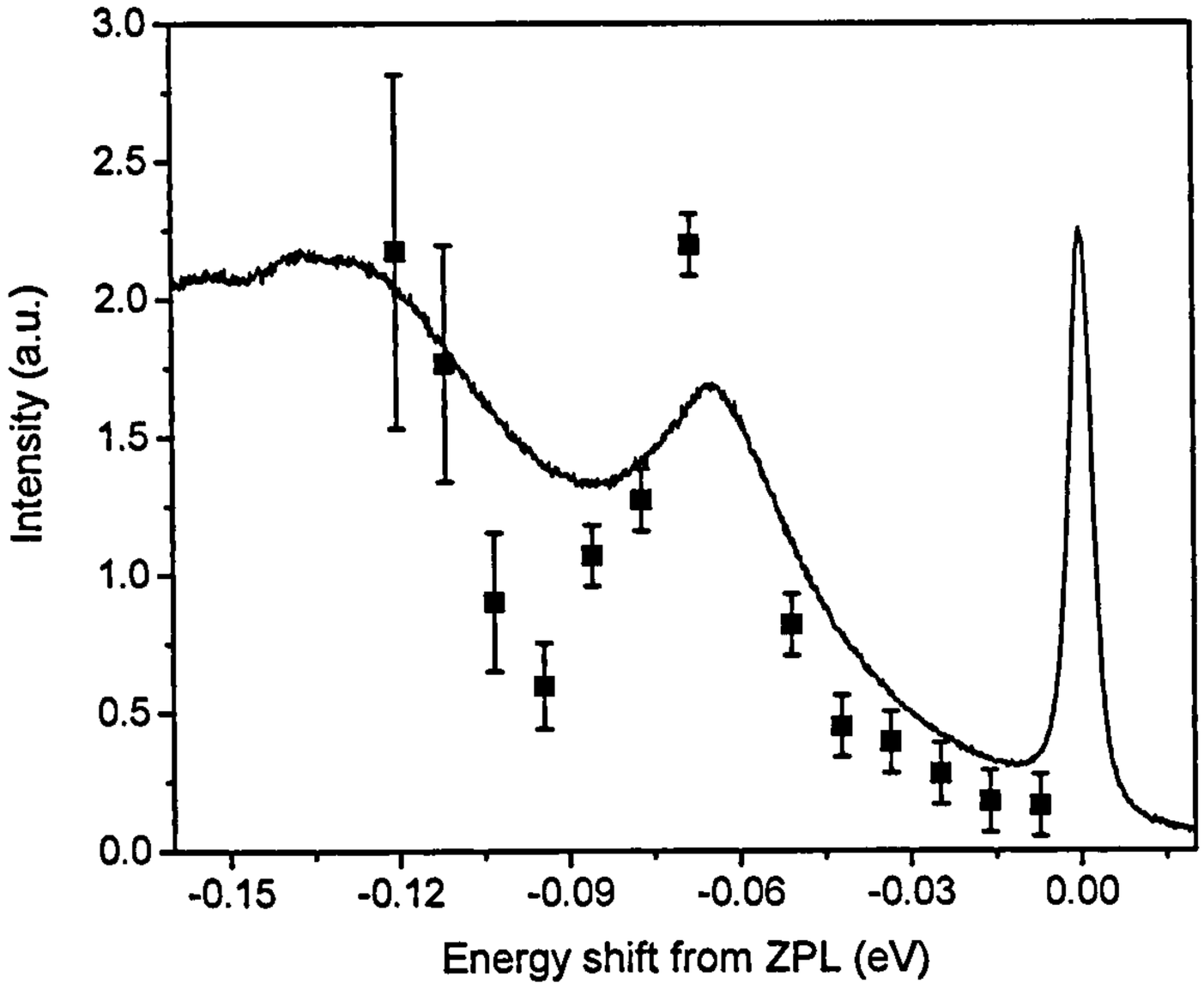

Figure 3.9. The intensity of the 637 nm zero-phonon line observed in photoluminescence, divided by $\exp[-E/(k_BT)$, (data points), following sub-threshold excitation, compared with the photoluminescence spectrum measured at 150 K, divided by ν^3. The horizontal axis shows the energy from the position of the ZPL. The diamond was held at a temperature of 150 K. The error bars for the lowest energy data points increase significantly since the intensity of the $(N-V)^-$ signal decreases rapidly as the energy between the ZPL and the laser line increases.

The PL spectrum used to calculate G(E) was not corrected for the response function of the spectroscopic equipment. Nevertheless, over the small energy range covered the shape of G(E) has been determined with sufficient accuracy for comparing with the data obtained using sub-threshold excitation.

3.3.4. Higher excited states of the H3 defect

The defect has a not only a zero phonon line at 2.463 eV (503.2 nm) but also transitions to higher excited states in the UV between 3.2 and 3.6 eV with a zero phonon line at ~3.35 eV (370 nm) (see figure 3.10), the H13 line (Collins 1983). As a consequence the H3 defect can be efficiently excited by UV light: the absorbed photon will promote an electron from the ground state to the higher excited state from where it relaxes to its lowest excited state. The electron then de-excites by emission of a photon. Excitation of luminescence in this region also induces an extra emission line at 537 nm and the line is the most intense when excited in cathodoluminescence.

The 537 nm (2.308 eV) line is not detected when luminescence is excited with visible light (figure 3.11) or by the sub-threshold mechanism and line correlates in intensity with the H3 line when excited with short wave UV light (figure 3.12).

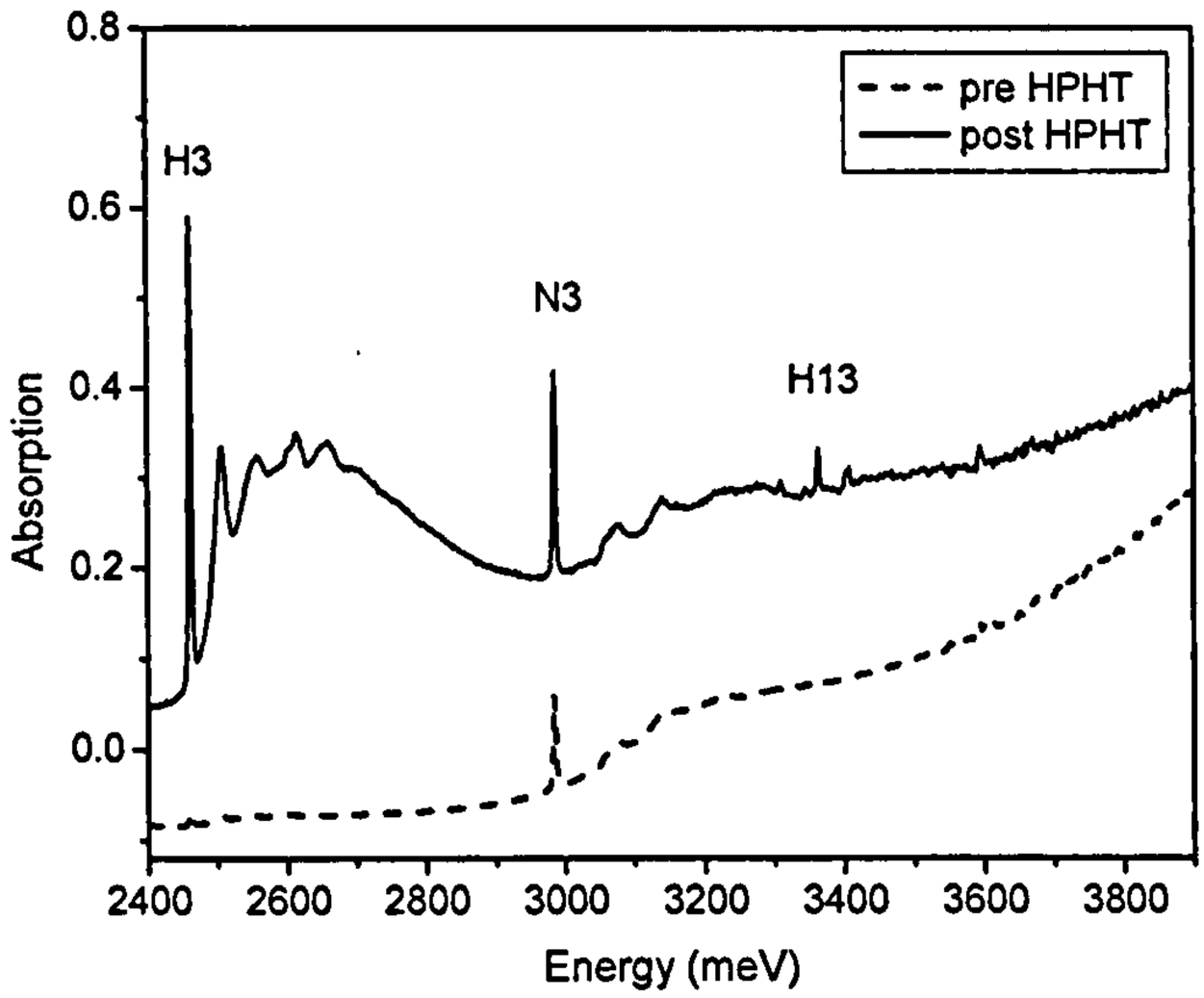

Figure 3.10. The UV-VIS absorption spectrum of a brown type IaA/B diamond before HPHT annealing and after HPHT annealing. The H3 absorption before annealing is very low, and the H13 peak is undetectable. After annealing there is a strong increase in the H3 absorption, and the H13 peak is weakly detectable.

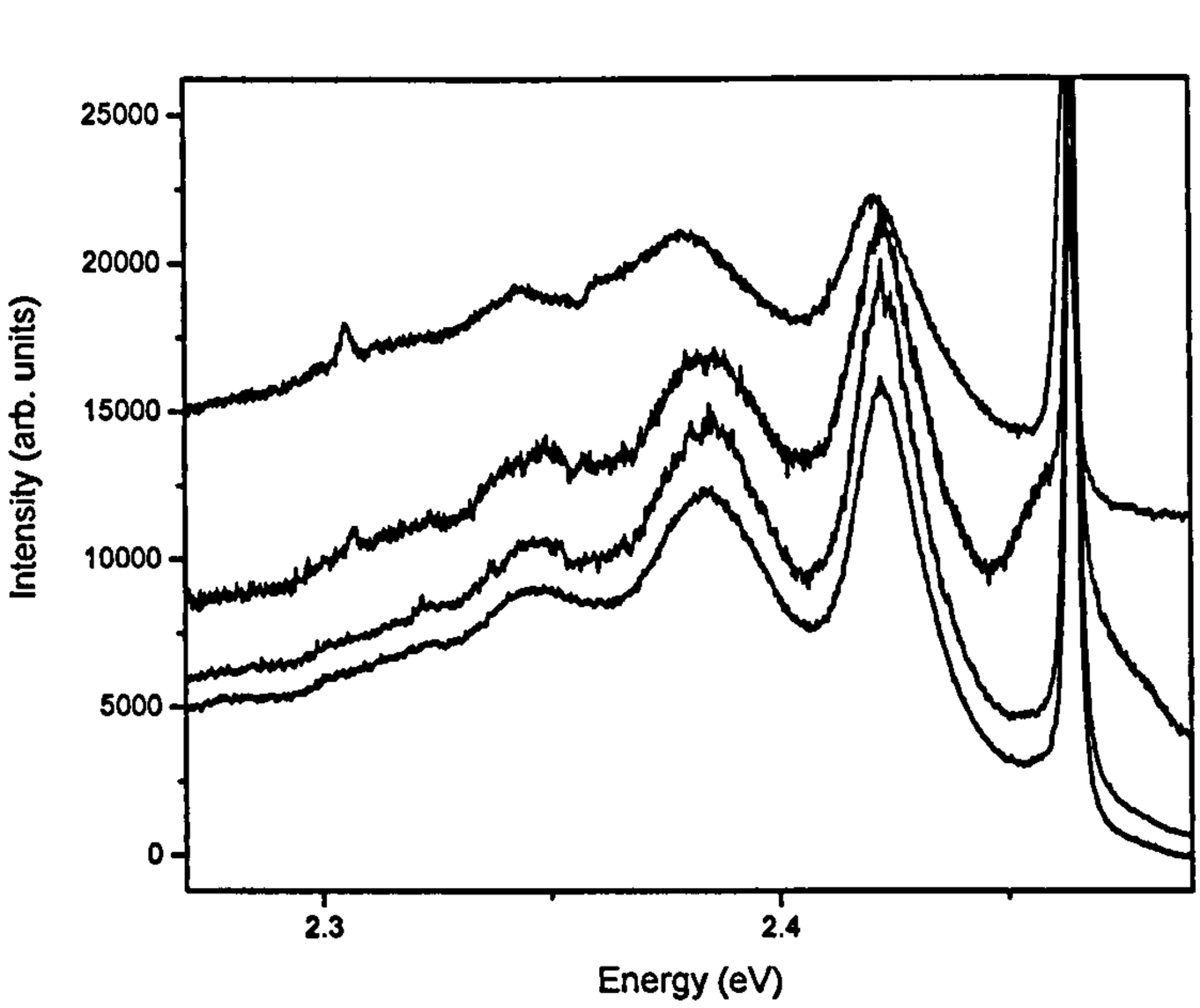

Figure 3.11. The H3 defect excited with different lasers and laser lines. From top to bottom: H3 excited with 325 nm HeCd laser, 351 nm, 457 nm and 488 nm laser line of an Argon-ion laser. The spectra are shifted for clarity and have not been corrected for instrument response or different laser power of each line. The 537 nm (2.308 eV) peak is not detected when the photon energy is below the higher excited state transition energy.

The ZPL of the H3 defect almost coincides with a zero phonon line of two other defects: the 3H defect has a ZPL at 503.5 nm and the nickel related S1 defect has a ZPL at 503.2 nm (Zaitsev 2001). However, all three defects have a very different vibronic side band, which allows clear identification of the defect.

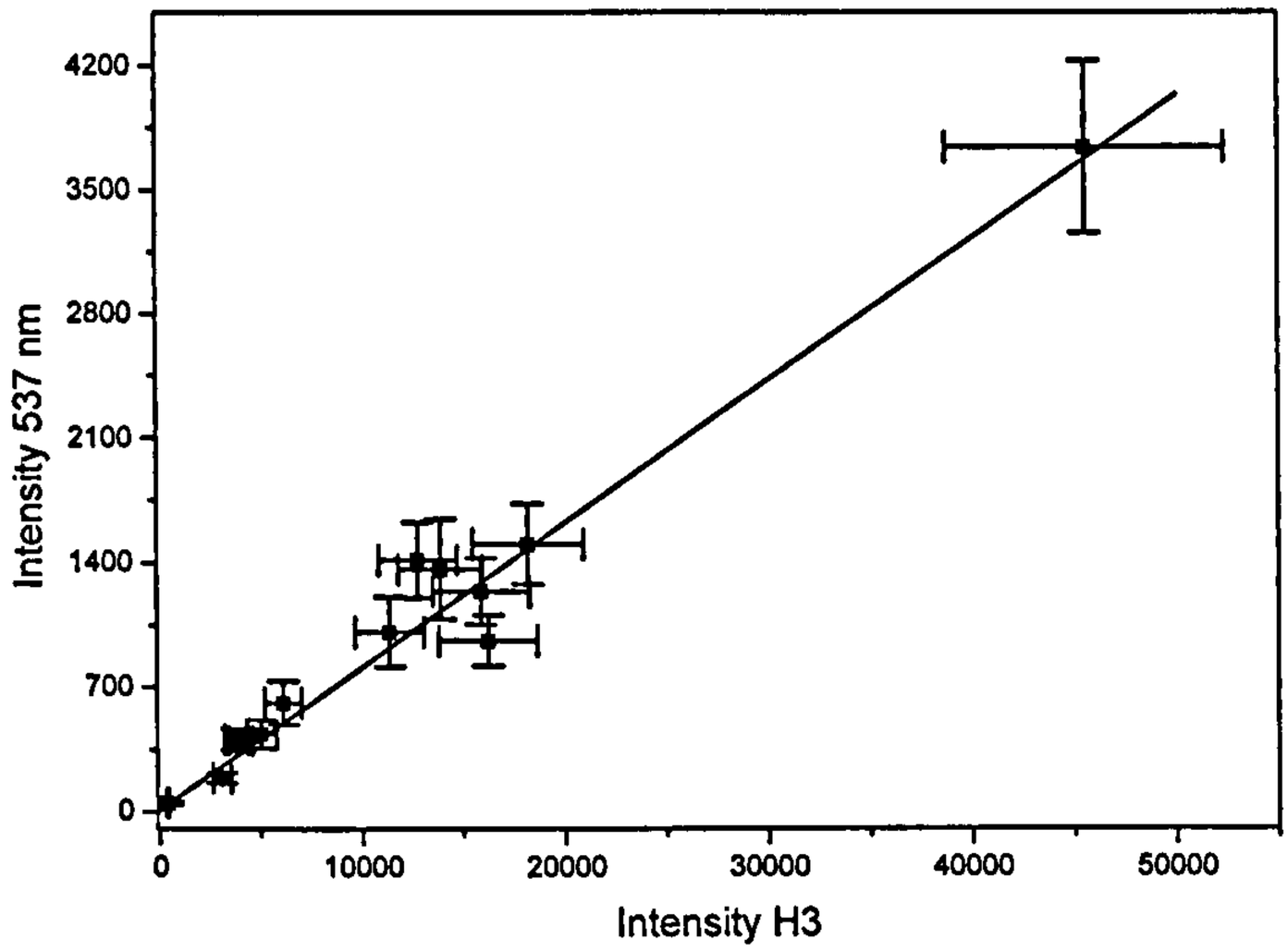

Figure 3.12. The correlation between the intensity of the 537 nm line and the intensity of the ZPL of the H3 defect.

3.4. Conclusions

Diamonds containing predominantly H3 or H4 centres, illuminated with a laser having an energy slightly less than that of the zero-phonon transition, exhibit luminescence due to sub-threshold excitation. Both types of centre show the same behaviour with temperature; the excitation process is thermally activated with an activation energy equal to the energy difference between the laser photons and the energy of the corresponding zero-phonon transition. The same phenomenon is also observed in diamonds containing 3H centres. This conclusion contrasts with that of Iakoubovskii et al (2001) who found that the intensity of the zero-phonon line for sub-threshold-excited H3 luminescence was almost temperature-independent. However, they made measurements only at 120 and 300 K, and did not correct the intensity of the luminescence for the large change in transition probability.

In diamonds that contain similar concentrations of H3 and H4 centres the sub-threshold excitation of both defects shows a deviation from Arrhenius behaviour.

However, an Arrhenius plot of the ratio of the H3 and H4 integrated intensities, yields an activation energy which is close to the energy difference between the zero-phonon lines. This may indicate that there is a thermally-activated energy transfer between the H3 and H4 centres.

The $(N–V)^-$ centre also exhibits sub-threshold excitation, and varying the excitation energy with the diamond at a fixed temperature maps out the phonon distribution derived from the PL spectrum, in further confirmation of the proposed model.

Chapter four

IR properties of impurities in diamond

4.1. Introduction

There are two topics in this chapter:

- The first part of this chapter investigates the properties of hydrogen related absorption in diamond.
- The second part investigates the nature of the nitrogen A aggregate in diamond by isotopic substitution of ^{12}C by ^{13}C.

4.1.1. Hydrogen in diamond.

As stated in the introduction, the two most common defects in diamond are nitrogen and hydrogen and both impurities have been detected in diamond in relatively high concentrations (> 1000 ppm).

Sharp absorption lines at 1405 and 3107 cm^{-1} in the infrared absorption spectra of natural diamond were tentatively attributed to hydrogen by Charette (1961) and have subsequently been studied by several researchers. Recently the role of hydrogen in diamond has acquired a technological importance; it is frequently incorporated in diamond grown by chemical vapour deposition (CVD) and it can passivate boron acceptors in doped material (Chevallier *et al.* 1998, Zeisel *et al.* 1999, Uzan-Saguy *et al.* 2001). In the present investigation we have studied the absorption spectra associated with hydrogen, in diamond produced from ^{13}C by high-pressure, high-temperature (HPHT) synthesis, in order to obtain a better understanding of the defects involved.

Runciman and Carter (1971) found that the absorption peaks at 1405 and 3107 cm^{-1} correlated in intensity, and assigned them, respectively, to the bending and stretching modes of either N–H or C–H bonds. Woods and Collins (1983) drew attention to a

very weak shoulder that is always present near the base of the 3107 cm^{-1} peak. A manual deconvolution of this feature showed that it had the correct position (3098 cm^{-1}) and approximately the correct intensity (1.4 %) to be associated with the stretching of ^{13}C–H. In reaching this conclusion Woods and Collins assumed that the main peak was due to ^{12}C–H, and that the ratio of the vibration frequencies could be calculated by treating the C-H as an isolated diatomic molecule (the natural abundance of ^{13}C is 1.1 %).

When the intensity of the 3107 cm^{-1} peak is moderately high (~ 10 cm^{-1}), two additional minor features at 2786 and 3237 cm^{-1} are easily observed on either side of the main peak. The intensity of the 3107 cm^{-1} peak correlates reasonably well with that of the 2786 cm^{-1} peak (Davies *et al.* 1984) but there is no correlation with the 3237 cm^{-1} peak (Woods and Collins 1983). Other, even weaker, peaks have been found which correlate with the main peaks, and are listed in table 4.1. These have been attributed (Davies *et al.* 1984, Fritsch *et al.* 1991) to overtones and combinations of the fundamental vibrational modes. The frequencies at which such peaks are observed are slightly lower than those given by the arithmetic sums of the fundamental frequencies because of slight anharmonicity in the vibrations (Davies *et al.* 1984). The combinations at 5555, 5889 and 6070 cm^{-1} were not detected by Davies *et al.* (1984), but can be seen (Fritsch *et al.* 1991) in specimens with very strong hydrogen-related absorption, using the more sensitive technique of Fourier transform infrared (FTIR) spectroscopy. We have confirmed in the present investigation, by comparing absorption spectra for three separate diamonds, that the peaks at 5889 and 6070 cm^{-1} are indeed correlated with the other peaks listed. However, we were not able to detect the peak at 5555 cm^{-1} observed by Fritsch *et al.* (1991).

Some diamonds, particularly those in which the H-related absorption is very strong, exhibit many additional peaks in the vicinity of the 3107 cm^{-1} peak. Woods and Collins (1983) show some of these, and attribute them to N–H vibrations.

Line position (cm^{-1})	Relative peak height	Assignment
1405	400	$\hbar\omega_b$
2786	34	$2\hbar\omega_b$
3107	1000	$\hbar\omega_s$
4169	4	$3\hbar\omega_b$
4499	29	$\hbar\omega_s + \hbar\omega_b$
5555	~0.1	$4\hbar\omega_b$
5889	~0.6	$\hbar\omega_s + 2\hbar\omega_b$
6070	~1.2	$2\hbar\omega_s$

Table 4.1. Positions, intensities and assignments of the hydrogen-related absorption peaks in natural diamond (Davies *et al.* 1984, Fritsch *et al.* 1991 and this work). The very weak component at 5555 cm^{-1} has been observed only by Fritsch *et al.* ω_s and ω_b are the of C-H bend and stretch vibrations modes respectively.

Although the measurements of Woods and Collins appeared to be consistent with the interpretation that the 3107 cm^{-1} peak, and the correlated features listed in table 4.1, are due to C–H vibrations, they were unable to detect these absorption features in type IIa (nitrogen-free) diamonds, although the features were present in all but one of the 50 type Ia diamonds they investigated. (Type Ia diamonds contain nitrogen in aggregated forms). Later Mendelssohn *et al.* (1986) obtained two-dimensional maps of the infrared absorption spectra from a polished slice of type Ia diamond that also exhibited strong hydrogen-related absorption. The distribution of nitrogen in the diamond they studied was very inhomogeneous, and the measurements showed that, although there was no one-to-one correlation, the intensity of the 3107 cm^{-1} peak varied in sympathy with the concentration of the A aggregate of nitrogen.

Diamond grown by HPHT synthesis from a metal solvent-catalyst, at typically 1400 °C may contain nitrogen in isolated substitutional positions at an average typical concentration of 200 ppm. No hydrogen-related absorption is observed in such specimens. However, if the diamonds are annealed at > 2100 °C, a substantial fraction of the nitrogen forms A aggregates, and in some cases hydrogen-related absorption is

also observed (Kiflawi *et al.* 1996). To maximise the amount of hydrogen-related absorption, Kiflawi *et al.* annealed their specimens at 2650 °C for 5 hours. For a diamond grown by HPHT synthesis the concentrations of nitrogen are very different in the different growth sectors, and vary within each growth sector, depending on the growth conditions. From a two-dimensional infrared absorption map of a hydrogen-containing specimen, Kiflawi *et al.* (1996) showed that the intensity of the 3107 cm^{-1} peak correlated approximately with the concentration of the A aggregate of nitrogen. The origin of the hydrogen in these diamonds that exhibited this absorption was not known.

Borzdov et al. (2002) showed that it is possible to grow diamonds by HPHT synthesis using Fe_3N as the solvent-catalyst. Typical growth conditions use a temperature of 1700 °C and a pressure of 7 GPa maintained for 20 hours. The use of a nitride results in a much higher nitrogen concentration (up to 3300 ppm) in the specimens, compared with the typical 200 ppm in commercial synthetic diamonds grown using a metal solvent-catalyst. The higher nitrogen concentration, combined with the high temperature and long growth time, results in most of the nitrogen being present in the form of A aggregates in the as-grown material. Furthermore, many of the specimens show the hydrogen-related absorption peaks at 1405 and 3107 cm^{-1}. Measurements on different diamonds, from the same growth run, but containing different nitrogen concentrations, showed that the intensity of the 3107 cm^{-1} peak increased as the nitrogen concentration increased. The source of the hydrogen in these diamonds is assumed to be the Fe_3N solvent-catalyst which itself was synthesised using NH_3 gas (Borzdov et al. 2002).

Kiflawi et al. (1996), faced with the apparent nitrogen-dependence of the 3107 cm^{-1} peak, examined this feature in high-temperature-annealed synthetic diamonds doped with ^{15}N, but found no shift of the peak. They therefore concluded that the absorption is not due to N–H centres. Instead they proposed that the conditions that produce the A aggregate of nitrogen also favour the formation of C–H centres. However, Chevallier et al. (2002) correctly point out that the absence of an isotope shift of the line does not disprove that the centre producing the line contains nitrogen. They give examples known in Si and GaP where changing the isotope of an impurity does not

result in a change of the vibrational frequency. They could also have drawn attention to the lack of an isotope shift of the sharp 1344 cm^{-1} line in diamond. This absorption arises at a localised vibrational mode produced by the presence of single substitutional nitrogen, but shows no detectable shift in diamonds grown using ^{15}N (Collins and Woods 1982b). Chevallier *et al.* therefore propose that the centre producing the 3107 cm^{-1} absorption is a H–C••• N complex containing at least one nitrogen atom. Since the 3107 cm^{-1} system is only seen in type Ia diamonds, the H–C••• N complex would probably contain two or more nitrogen atoms.

To date the only evidence that the 3107 cm^{-1} peak is due to a C–H vibration comes from the work of Woods and Collins (1983), based on an extremely weak feature of relative intensity ~ 1 % at the base of the 3107 cm^{-1} peak and believed to be due to ^{13}C. In the present investigation we have therefore examined the hydrogen-related absorption in diamonds with a high nitrogen concentration grown from ^{13}C.

It has been demonstrated by nuclear techniques that there is no correlation between the total hydrogen content in diamond and the concentration of IR active hydrogen (Sweeney 1999, Field 1992).

4.1.2. Vibrational properties of the A defect in diamond.

Theoretical calculations of Jones *et al.* (1992) and Briddon and Jones (1993) have shown different components in the calculated IR absorption spectrum of diamond. The calculated maxima in the absorption spectrum are at 543, 1064, 1182 and 1293 cm^{-1} while the measured peaks are at 480, 1093, 1203 and 1282 cm^{-1} respectively. Some of the measured values coincide with maxima in the vibrational density of states, but the lowest one does not. The calculated maximum with the lowest wavenumber is at 543 cm^{-1}, which is due to in phase N-N vibration, and is close to the experimentally observed maximum of 480 cm^{-1}. However, from the difference in binding energy between the nitrogen-nitrogen or carbon-nitrogen bond compared with the carbon-carbon bond (see chapter 1, section 1.6) we would expect a larger shift (more than 125 cm^{-1}).

Collins *et al.* (1987) measured infrared absorption spectra of synthetic HPHT annealed diamonds where virtually all the single nitrogen was aggregated. Approximately 65 to 70 % of the ^{14}N nitrogen was substituted by ^{15}N and the 1282 cm^{-1} peak of the A defect absorption shifted to lower wavenumbers by 7 cm^{-1}.

Jones *et al.* (1992) assigned the calculated absorption features at 543, 1064, 1182 and 1293 cm^{-1} in the infrared spectrum of diamond to vibrations with the following character

- The maximum at 543 cm^{-1} is due to in phase motion of nitrogen atoms along the high symmetry axis. The closest maximum in the IR spectrum of natural type IaA diamond is at 480 cm^{-1}.
- The maximum at 1064 cm^{-1} is due to vibrations of carbon atoms. The closest maximum in IR spectrum of natural type IaA diamond at 1094.
- A maximum at 1182 cm^{-1}. This is a carbon – nitrogen vibration. The closest maximum in the IR spectrum of natural type IaA diamond is at 1212 cm^{-1}.
- A maximum at 1293 cm^{-1} due to vibrations of carbon atoms. The closest maximum in the IR spectrum of natural type IaA diamond is at 1282 cm^{-1}. Following Jones, Briddon and Öberg, this must mainly be due to carbon atoms; however Collins *et al.* (1987) clearly observed a relatively large shift of the 1282 cm^{-1} peak in ^{15}N doped samples.

To date there is no experimental data on the character of the vibrations connected to A defect absorption in diamond.

4.2. Experimental

All UV-VIS and NIR spectra were recorded at liquid nitrogen temperature with a Princeton Instruments diode array detector, fitted with a 300 g/mm grating and a 25 μm slit. This gives a spectral resolution of approximately 0.5 nm. IR spectra were recorded at room temperature with a Bio-Rad FTS-40 spectrophotometer in the range of 7000 to 400 cm^{-1} with a resolution of 4 cm^{-1}. Rough and polished samples were measured with a DRIFT accessory. High resolution scans with 1 cm^{-1} resolution were recorded when C centres were suspected to be present. This enables us to estimate the

concentration of C centres from the 1344 cm^{-1} line when other features of the C centres are masked by the presence of A and B centres and/or platelets.

To study the correlation with various nitrogen aggregates in diamond, the IR and UV-VIS spectra of approximately 60 type Ia diamonds have been recorded for this study. The nitrogen aggregate signature in the one-phonon region absorption spectrum is decomposed into the A, B, C and D components, by using the procedure described in chapter one. The integrated area of the 3107 cm^{-1} line is then calculated by first subtracting the underlying intrinsic diamond absorption spectrum and then fitting the line with a Lorentzian curve.

To study the shift and splitting of the 3107 cm^{-1} line as function of the carbon 13 to carbon 12 isotope ratio, synthetic single crystal diamond was made by the HPHT method by Yuri Pal'yanov's research group in Novosibirsk (Russia). Amorphous carbon powder, isotopically enriched to 98 – 99 % ^{13}C, was placed into a Pt ampoule and partially graphitised by heating to 1400°C under a pressure of 5 GPa, using a split-sphere-type multi-anvil apparatus or BARS press (Pal'yanov *et al.* 1997). This carbon powder was used as the source material to grow diamonds from a Fe_3N solvent-catalyst, as described by Borzdov *et al.* (2002). The diamond growth time was 20.5 h, with a pressure fixed at 7 GPa and a temperature of 1850 °C. A few spontaneously nucleated diamonds of sufficient size (approximately 100 μm across) and clarity to carry out infrared absorption measurements were recovered from the growth run. To study the shift of A defect absorption peaks, other diamonds were synthesized in the same system but in an iron-nickel solvent catalyst.

Specimens were moulded in indium and placed at the focus of a 5 × beam condenser in a Bruker Equinox 55 FTIR spectrometer. Spectra were obtained at a resolution of 0.5 cm^{-1} over the range 400 to 4750 cm^{-1}. Closely spaced peaks were deconvoluted into Lorentzian sub-components using the Grams/32 software. Deconvolution is carried out using either a linear or a quadratic baseline correction; for a given peak the calculated intensities were the same for both backgrounds, within the experimental uncertainty.

Raman spectra were recorded with a Renishaw 2000 Raman spectrophotometer, with an uncertainty in the Raman shift of ± 2 cm^{-1}. The 514.5 nm line of an Ar-ion laser was used with the sample mounted in a near-normal backscattering geometry. Shifting of the Raman line due to laser-induced heating of the sample was prevented by mounting the sample on a copper heat sink.

4.3. Results and discussion

4.3.1. Correlation of the 3107 cm^{-1} with nitrogen and nitrogen aggregates

The results clearly show that the 3107 cm^{-1} line tends to increase when the total nitrogen concentration increases (figure 4.1.). However, there is no one to one correspondence between the concentration of defects causing the 3107 cm^{-1} line and the total nitrogen concentration. The line is found in type Ia diamonds with a small concentration of C defects (Woods and Collins 1983); however, this study indicates that at least 20 % of the nitrogen must be present as A aggregates before the 3107 cm^{-1} line appears in the IR spectrum.

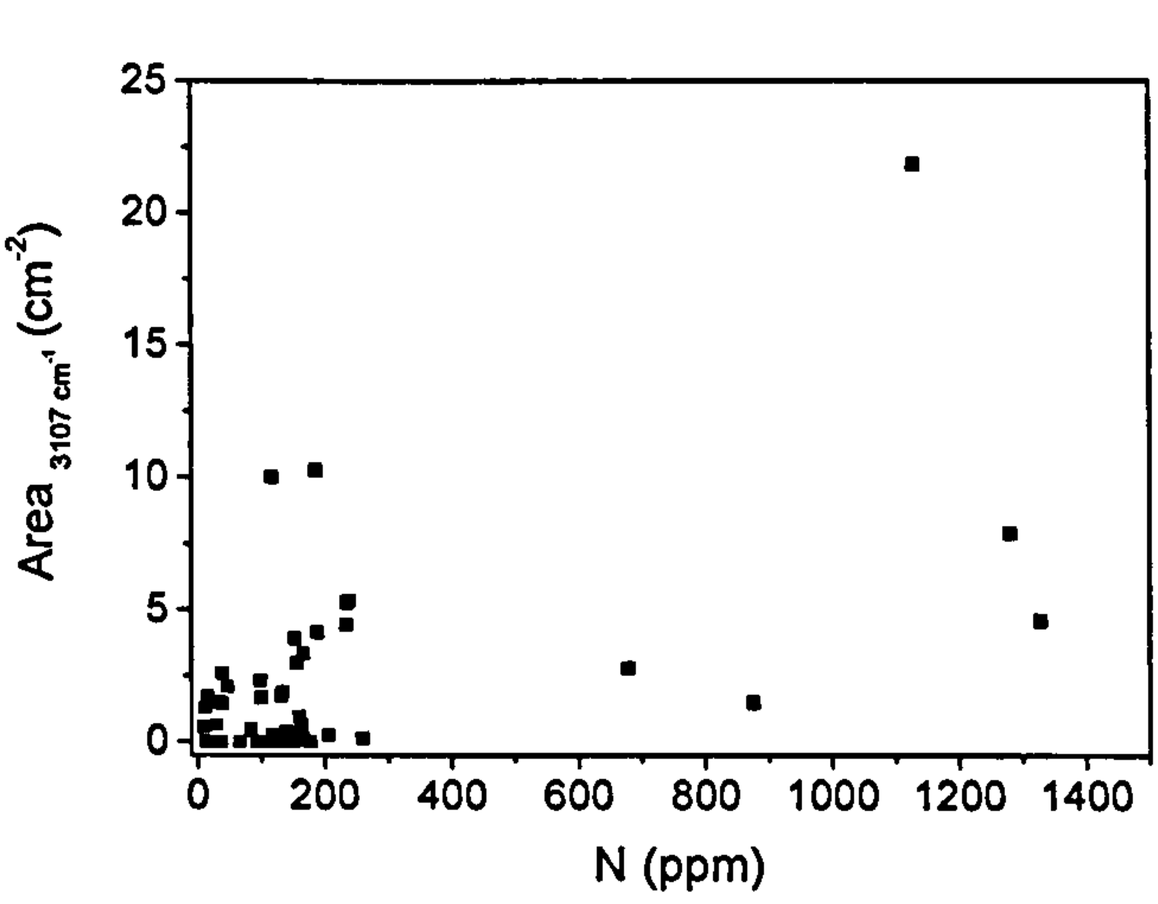

Figure 4.1. The nitrogen concentration vs. the calculated integrated area of the 3107 cm^{-1} absorption line in the IR spectrum. There is an apparent correlation between the total nitrogen concentration and the integrated area of the 3107 cm^{-1} line, however there is no one to one correspondence.

The fraction of A and B centres with respect to the total nitrogen concentration is also determined, and again there is no correlation between the integrated area of the 3107 cm^{-1} line and the fraction of the A and B nitrogen aggregates (figures 4.2.a., 4.2.b.).

The IR spectra of 20 natural type IIa diamonds and 10 natural type Ib diamonds were recorded and none of the spectra displayed substantial 3107 cm^{-1} absorption.

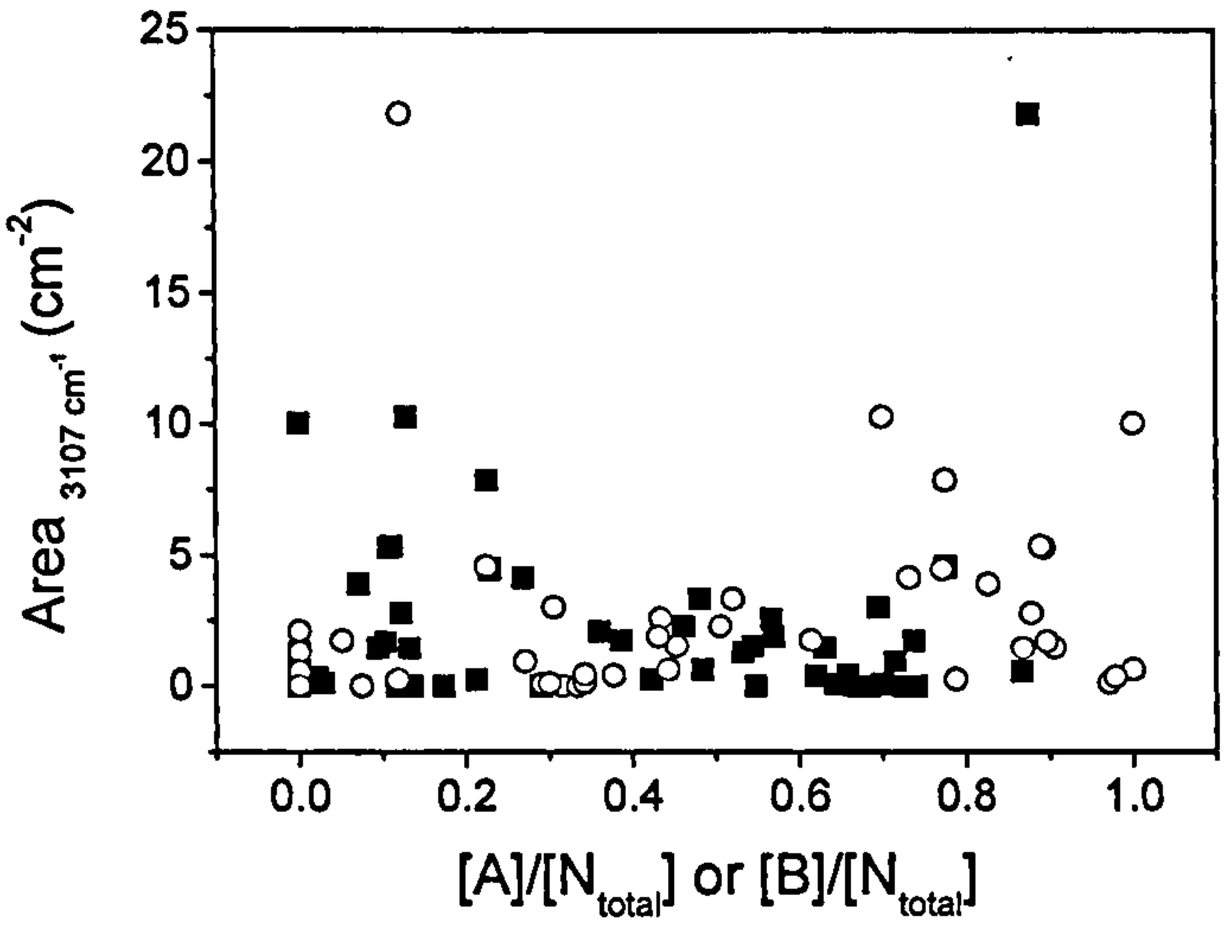

Figure 4.2. The integrated area of the 3107 cm^{-1} line against the fraction of A centres (squares) and the fraction of the B centres (open circles) of the total nitrogen concentration.

Spectroscopic investigation indicates that diamonds with predominantly A centres and very high concentrations of IR active hydrogen (absorption coefficient of the 3107 cm^{-1} line in excess of 2 cm^{-1}) have similar UV-VIS and NIR absorption characteristics. This also holds for diamonds with high IR active hydrogen concentrations and with predominantly B centres in the IR spectrum and diamonds with A as well as B centres in the IR spectrum (see figures 4.3.a.-4.3.c.).

Diamonds with predominantly A centres may have absorption lines at 545, 792, 845, 945, 968, 974 and 978 nm. Diamonds with A and B centres in the IR spectrum can display more lines: 545, 563, 618, 630, 656, 672, 687, 792, 824, 945, 942, 968, 974, 978, 990 and 998 nm and the 415 nm line. Diamonds with predominantly B centres display apart from the typical "Cape" absorption lines, an additional set of absorption lines at 545, 564, 614, 893, 954, 968, 978, 986, 990, 992 and 998 nm. Broad bands cantered at 735, 775, 803 826, 836 and 842 nm are also typical for these diamonds.

The 3107 cm^{-1} line is detected in type I diamonds, but not in type II diamonds. This indicates that nitrogen may play a role in the formation of the 3107 cm^{-1} defect.

However, as stated earlier, Kiflawi *et al.* (1996) showed by isotopic substitution of ^{14}N by 50 - 66 % ^{15}N that nitrogen is not directly involved in the 3107 cm^{-1} defect.

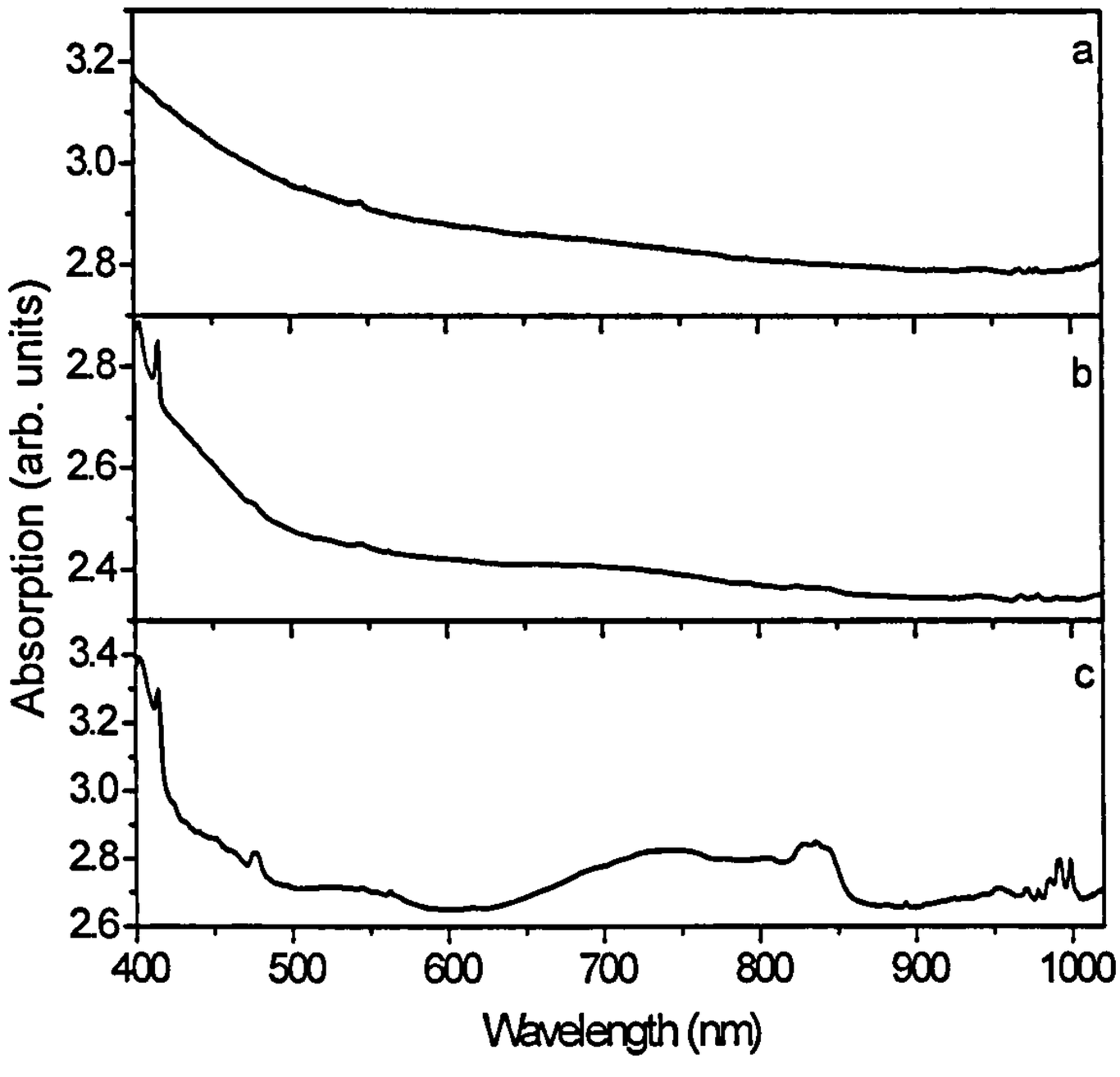

Figure 4.3. Typical UV-VIS-NIR spectra recorded at liquid nitrogen temperature of diamonds with predominantly A centres (a.), A and B centres, where [A] > [B] (b.) and where [B] > [A] centres (c.) as determined from the IR spectrum.

The absence of one to one correspondence can be explained by considering a number of possibilities:

- The 3107 cm^{-1} line does not correlate with the hydrogen concentration of diamond.
- The 3107 cm^{-1} line can be created or destroyed during HPHT annealing, which the diamond experiences during its stay deep in the Earth.
- The activation energy for the creation of the 3107 cm^{-1} defect will probably not be the same as for the A centre formation.

So there may be a correlation between the total nitrogen and an undetectable hydrogen concentration in diamond, while the nitrogen concentration and the 3107 cm^{-1} defect may only show the same trend.

4.3.2. Observations of the 3107 cm^{-1} line in isotopically $^{12}C/^{13}C$ mixed HPHT synthetic diamonds.

The full IR absorption spectrum is shown in figure 4.4. The shape of the one-phonon absorption indicates that virtually all of the nitrogen is present in the A-aggregate form at an approximate concentration of 800 ppm. It is also clear that there is hydrogen-related absorption present at ~ 1400 cm^{-1} and at ~ 3100 cm^{-1}. Various features in the spectrum are considered in more detail below.

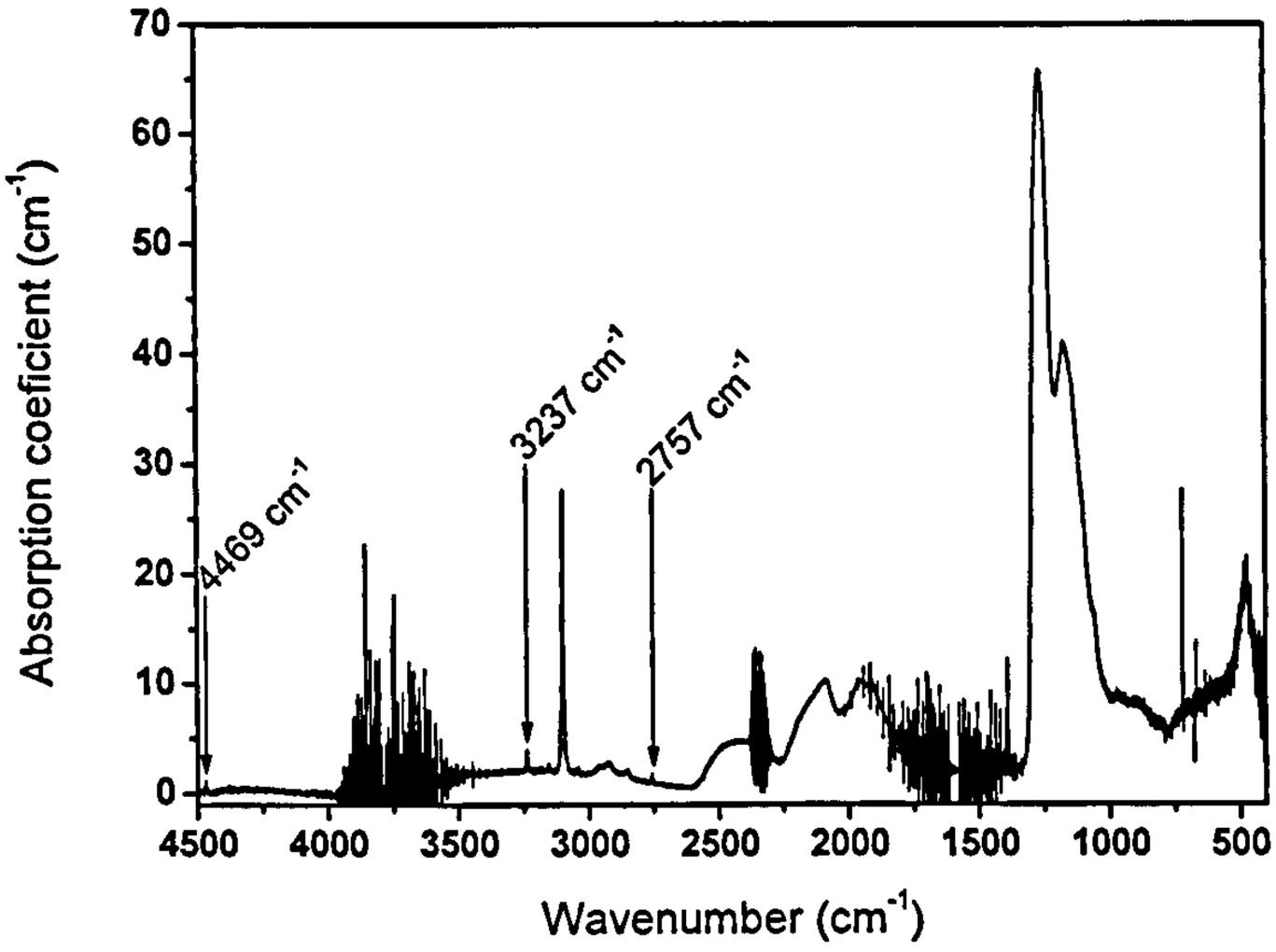

Figure 4.4. Absorption spectrum of an HPHT synthetic diamond grown from ^{13}C and containing hydrogen-related features.

4.3.2.1 Absorption near 3100 cm^{-1}.

Figure 4.5 shows that the absorption near 3100 cm^{-1} is composed of two peaks, at 3098 and 3107 cm^{-1}, together with some minor features which are just above the noise level. The two major components are at the identical frequencies determined by Woods and Collins (1983), but now the 3098 cm^{-1} peak is dominant. This confirms beyond doubt that the absorption is produced by the vibration of a C–H structure. Because the frequencies are more than twice that of the maximum vibrational frequency of the diamond lattice (1332.5 cm^{-1}), the stretching vibration of the bond is highly localised, and there is an insignificant coupling to the lattice modes.

Considering only the 3107 and 3098 cm^{-1} peaks, the former, due to the ^{12}C–H vibration, comprises (11.4 ± 0.3) % of the total absorption, whereas the starting material contained only 1 – 2 % ^{12}C. We attribute this difference to the diffusion of carbon into the growth capsule from the graphite heater rod. We show below that the relative intensities of the two absorption peaks are consistent with the isotopic composition of the diamond.

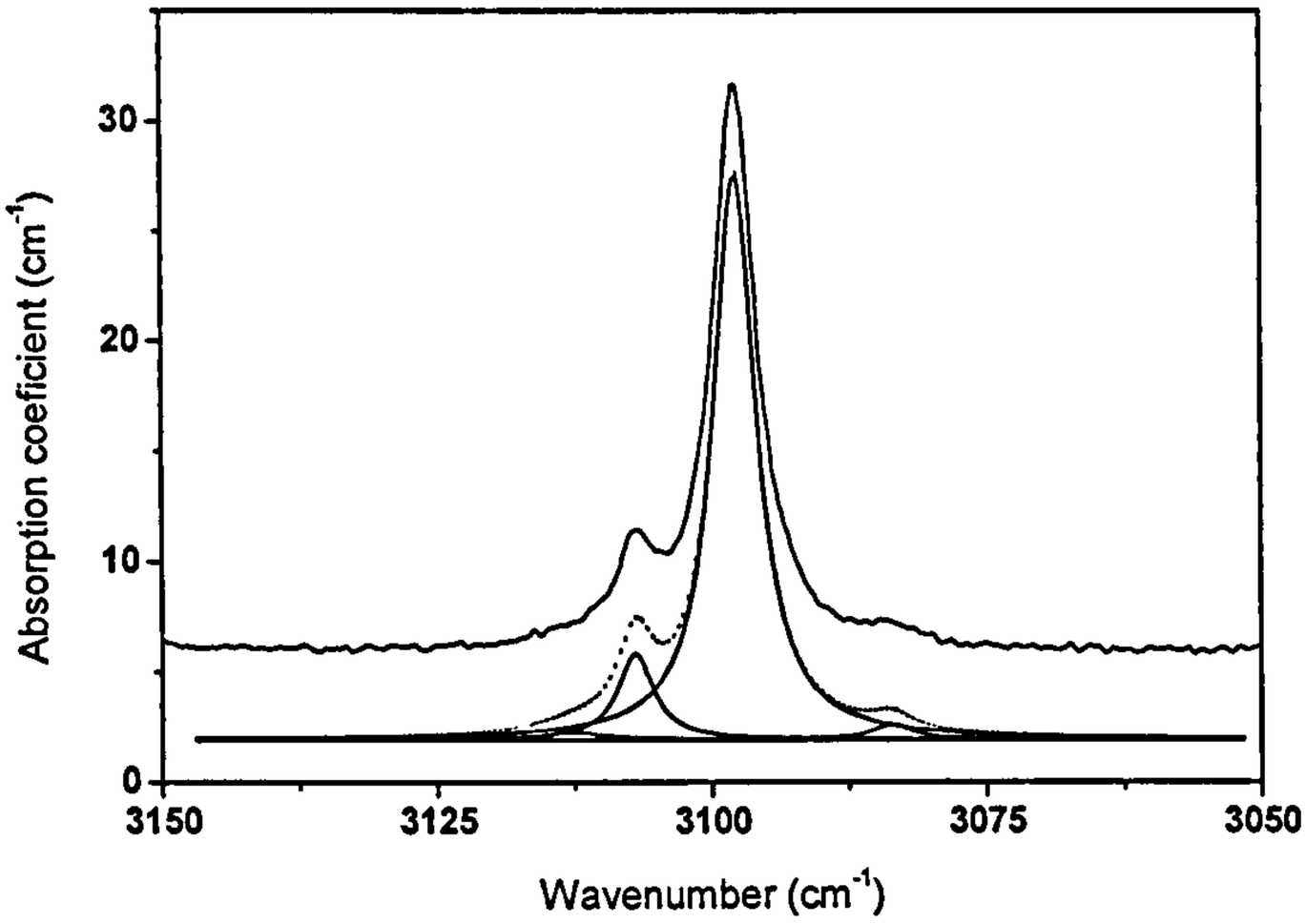

Figure 4.5. Absorption spectrum of the hydrogen-related peaks near 3100 cm^{-1} in an HPHT synthetic diamond grown from ^{13}C. The top spectrum is the experimental spectrum and the bottom spectrum is the simulated spectrum (broken curve) and the different simulated individual peaks (solid curves).

4.3.2.2. Intrinsic two-phonon absorption.

The absorption bands between approximately 1400 and 2600 cm^{-1} (figure 4.4) represent the two-phonon combination bands. These are made up of frequencies which propagate through the diamond lattice. Consequently, when we have a mixture of ^{12}C and ^{13}C atoms, we can assume, to a good approximation, that the frequencies of sharp features in the spectrum are inversely proportional to the square root of the average mass. In natural diamond there are two sharp spikes in the two-phonon spectrum at 1977 and 2158 cm^{-1}. In the synthetic diamonds investigated here these features are less sharp, but, from the spectrum in figure 4.4, can be located at 1909 ± 3 and 2087 ± 4 cm^{-1}, respectively. The ratios of corresponding frequencies in the diamonds grown from ^{13}C, to those in natural diamond, are 0.9656 ± 0.0015 and

0.9671 ± 0.0019, respectively. If P is the percentage of ^{12}C in the synthetic diamonds, then we expect the ratio, R, to be given by

$$R = \left(\frac{(98.9 \times 12) + (1.1 \times 13.00335)}{(P \times 12) + [(100 - P) \times 13.00335]} \right)^{1/2} \qquad (4.3.1)$$

Using a weighted average of $R = 0.9662 \pm 0.0012$ gives $P = (13.7 \pm 3.2)$ % in good agreement with the value inferred from the relative amplitudes of the peaks in figure 4.5.

4.3.2.3. Raman measurements.

The samples were pressed in indium attached to a copper heat sink, thus minimizing local heating of the sample under the laser beam.

The Raman line in natural type IIa diamonds, where the natural abundance of ^{13}C is 1.1 %, is at 1332.5 cm^{-1}. The change in atomic mass when ^{12}C is substituted by ^{13}C induces a shift and an asymmetric broadening of the first order Raman line (Hass *et al.* 1992, Ruf *et al.* 1998). From the shift, one can calculate the isotopic composition of the diamond from the relation (Vogelgesang *et al.* 1996):

$$\omega_0 = 1332.82 - 34.77\, x - 16.98\, x^2 \qquad (4.3.2)$$

In this equation, x is the fraction of ^{13}C, and ω_0 is the position of the Raman line which, in this case, is at 1290 ± 2 cm^{-1}. This gives the fraction of ^{12}C as (13.4 ± 3.1) %, in excellent agreement with the previously calculated values.

4.3.2.4. Absorption near 1400 cm^{-1}.

The 1405 cm^{-1} C–H bending vibration in natural diamond is close to the maximum one-phonon frequency (1332.5 cm^{-1}). The high-frequency limit of the one-phonon band decreases by approximately 50 cm^{-1}, on substituting ^{12}C by ^{13}C. Because of weak interaction with the one-phonon modes, the C–H frequency is pulled somewhat

lower than that predicted by the isotope shift for an isolated C–H defect. The vibration is still sufficiently localised that, in our diamond with mixed isotopes, the individual ^{12}C–H and ^{13}C–H peaks are seen at 1396 and 1391 cm^{-1} respectively (figure 4.6). The separation of these two peaks is 20 % larger than that calculated for the stretching vibration of an isolated diatomic molecule, and the intensity of the component due to ^{12}C is (36 ± 6) %, compared with 11.4 % derived from figure 4.5. The latter figure was shown to be consistent with the isotopic composition of the diamond. We infer that the simplistic analysis which worked well for the highly localised stretching vibrations near 3100 cm^{-1} is less appropriate for the partially localised bending vibrations near 1400 cm^{-1}.

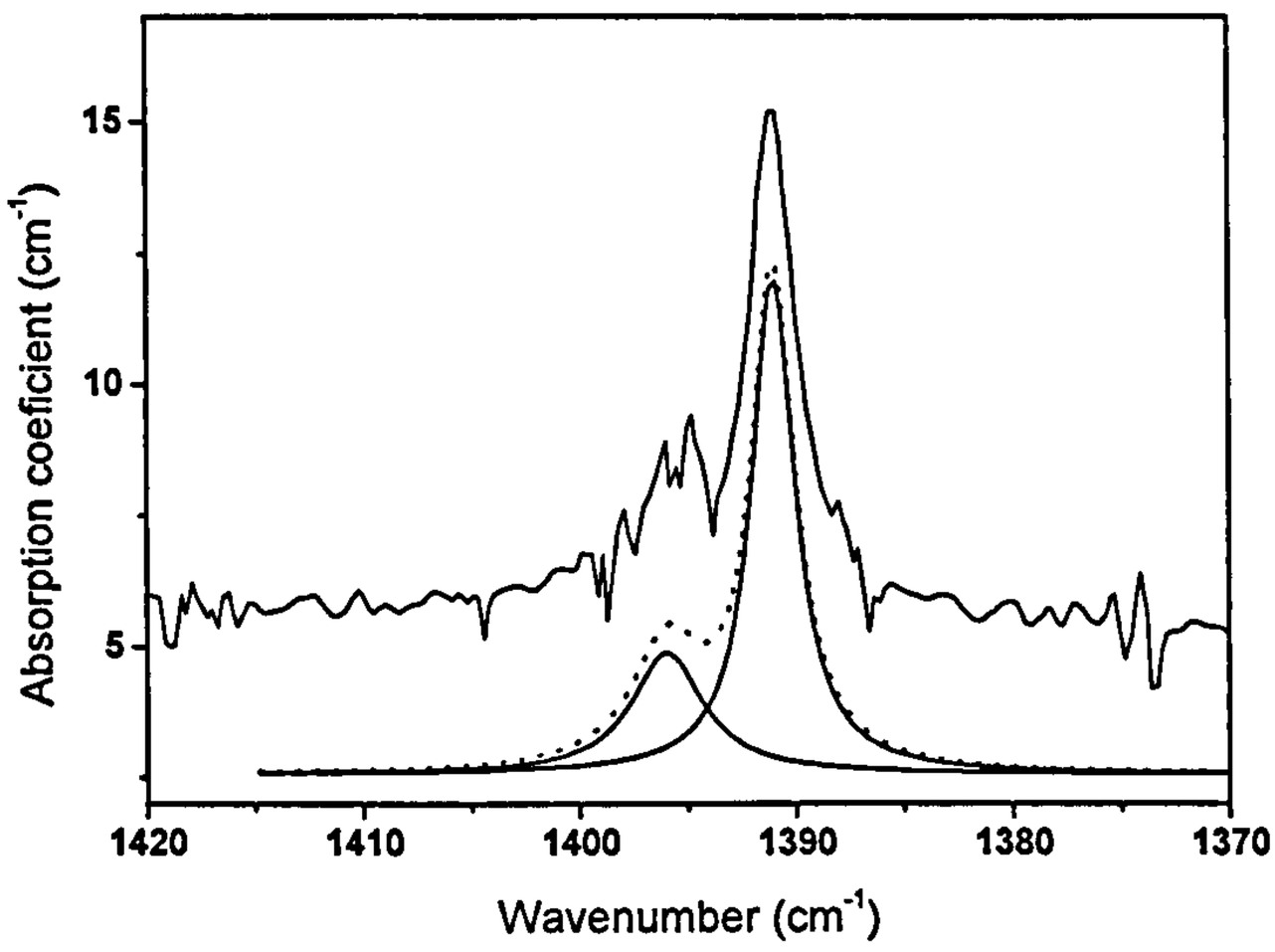

Figure 4.6. Absorption spectrum of the hydrogen-related peaks near 1400 cm^{-1} in an HPHT synthetic diamond grown from ^{13}C. The top spectrum is the experimental spectrum and the bottom spectrum is the simulated spectrum (broken curve) and the two different simulated individual peaks (solid curves).

4.3.2.5. One-phonon absorption.

The major absorption peak associated with A aggregates of nitrogen occurs at 1282 cm^{-1} in the defect-induced one-phonon region of natural diamond. There is no straightforward method of calculating the position of this peak in ^{13}C diamond. We see from figure 4.4 that in our diamond containing approximately 88 % ^{13}C the maximum absorption occurs at 1260 cm^{-1}. The isotope shift is comparable with, but rather smaller than, the 32 cm^{-1} shift observed (Collins *et al.* 1988) for the peak

associated with isolated substitutional nitrogen which, in natural diamond, is located at 1130 cm^{-1}.

4.3.2.6. Combination bands

Three weak peaks at 2757, 3237 and 4469 cm^{-1} can be observed in figure 4.4. By analogy with natural diamond (table 4.1), we attribute the 2757 cm^{-1} peak to the combination $2\hbar\omega_b$ (2 × 1391 cm^{-1}) and the 4469 cm^{-1} peak to $\hbar\omega_s + \hbar\omega_b$ (1391 + 3098 cm^{-1}). As in natural diamond, because of slight anharmonicity, the positions of the combination bands are at slightly lower frequencies than those given by the arithmetic sums. Since the diamonds contain mainly ^{13}C, combinations involving ^{12}C with ^{13}C (and especially ^{12}C with ^{12}C) will be too weak to detect in these specimens.

The feature at 3237 cm^{-1} occurs at the same frequency as in natural diamond. Woods and Collins (1983) noted that this peak did not correlate in intensity with those attributed to C–H vibrations, and suggested that it was due to an N–H vibration. That proposal is not inconsistent with the absence of an isotope shift, observed here in diamonds grown from ^{13}C.

Because of the small sizes of the synthetic diamonds, and their relatively weak hydrogen-related absorption, the counterparts of the extremely weak combination bands seen in natural diamonds (table 4.1) could not be detected.

4.3.3. The shift of the A defect absorption peaks in isotopically $^{12}C/^{13}C$ mixed HPHT synthetic diamonds

4.3.3.1. Sample details

A number of samples descibed in section 4.3.2. of this chapter are used for this study, and a number of additional samples were synthesized by the HPHT method by Pal'yanov's research group by using spontaneous crystallisation in a BARS press with isotopically mixed $^{12}C/^{13}C$ powder as carbon source. Some other samples were on

loan from I. Kiflawi (samples H441R, H439rt, h667b2, h667a2). The isotopic ^{13}C content of the diamonds varied between 98 and 1%.

4.3.3.2. Raman measurements

An accurate ^{12}C isotopic fraction for each of the synthetic diamonds was determined by Raman measurements using the procedure described in this chapter, section 4.3.2.3.

4.3.3.3. Infrared measurements

The ^{12}C content of the synthetic diamonds was determined from the peak shift of the two phonon intrinsic diamond absorption by same procedure as in section 4.3.2.2. The peak positions of the nitrogen related absorption in the one-phonon absorption region of diamond was determined after subtraction of the intrinsic diamond spectrum. The intrinsic diamond spectrum of a $^{12}C/^{13}C$ isotope enriched diamond was constructed by shifting the frequencies of the intrinsic spectrum of a natural type IIa diamond by a ratio R' determined from a least squares fitting of the intrinsic diamond spectrum of the natural type IIa diamond and a synthetic isotope enriched diamond. This procedure removes the background absorption under the one-phonon nitrogen related absorption (see figure 4.7).

To check the consistency with other measurements, the ratio R is calculated from equation 4.3.1. with P the concentration of ^{12}C as determined by the peak position of the Raman measurements and two phonon absorption peaks and compared with the factor R' (see figure 4.8).

The peak positions of the A defect related absorptions are summarized in table 4.2 and the relative shift with respect to A defect absorption peaks in natural diamond (figure 4.9).

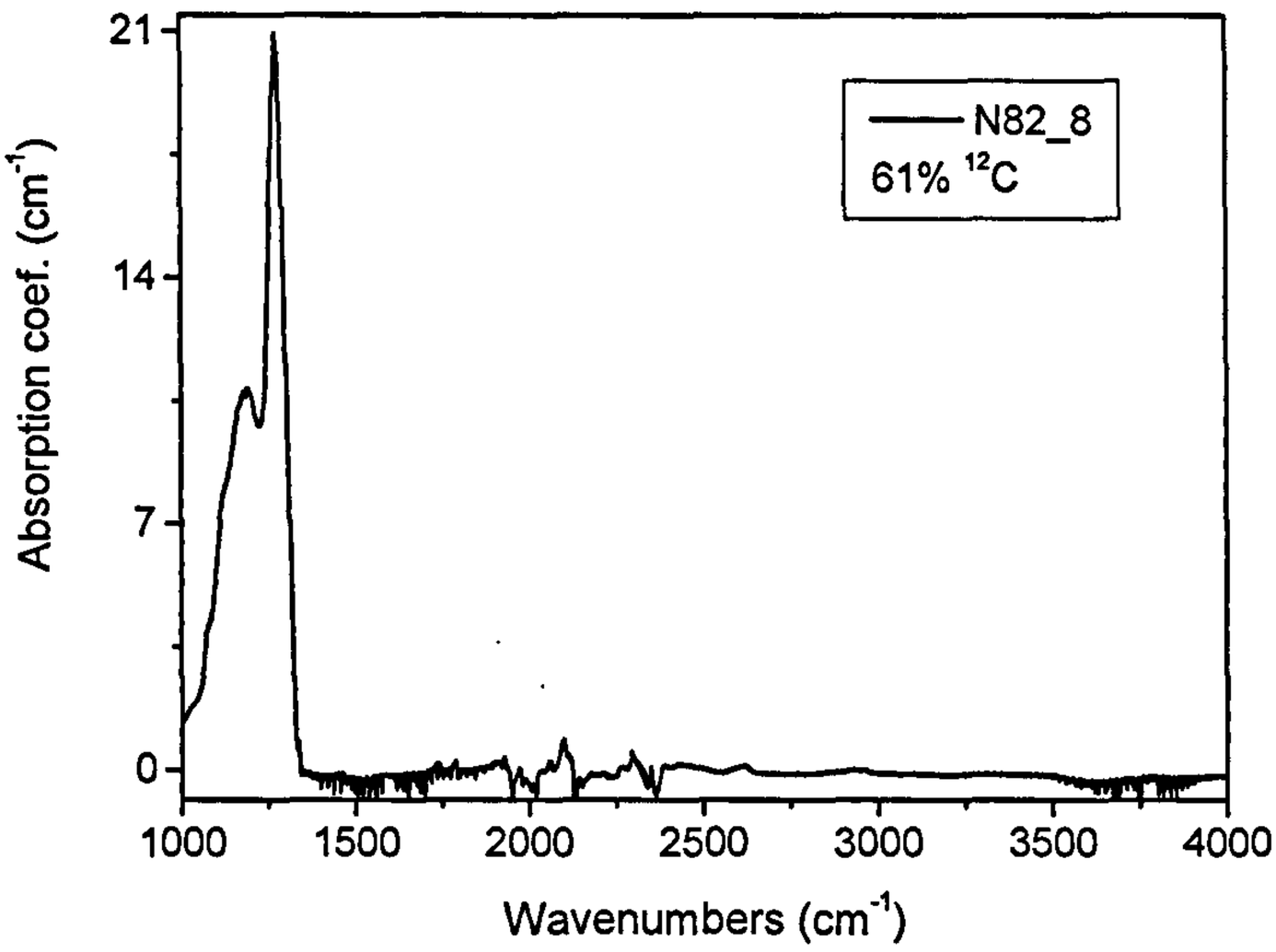

Figure 4.7. The absorption spectrum of the one-phonon A defect related absorption without the intrinsic diamond spectrum.

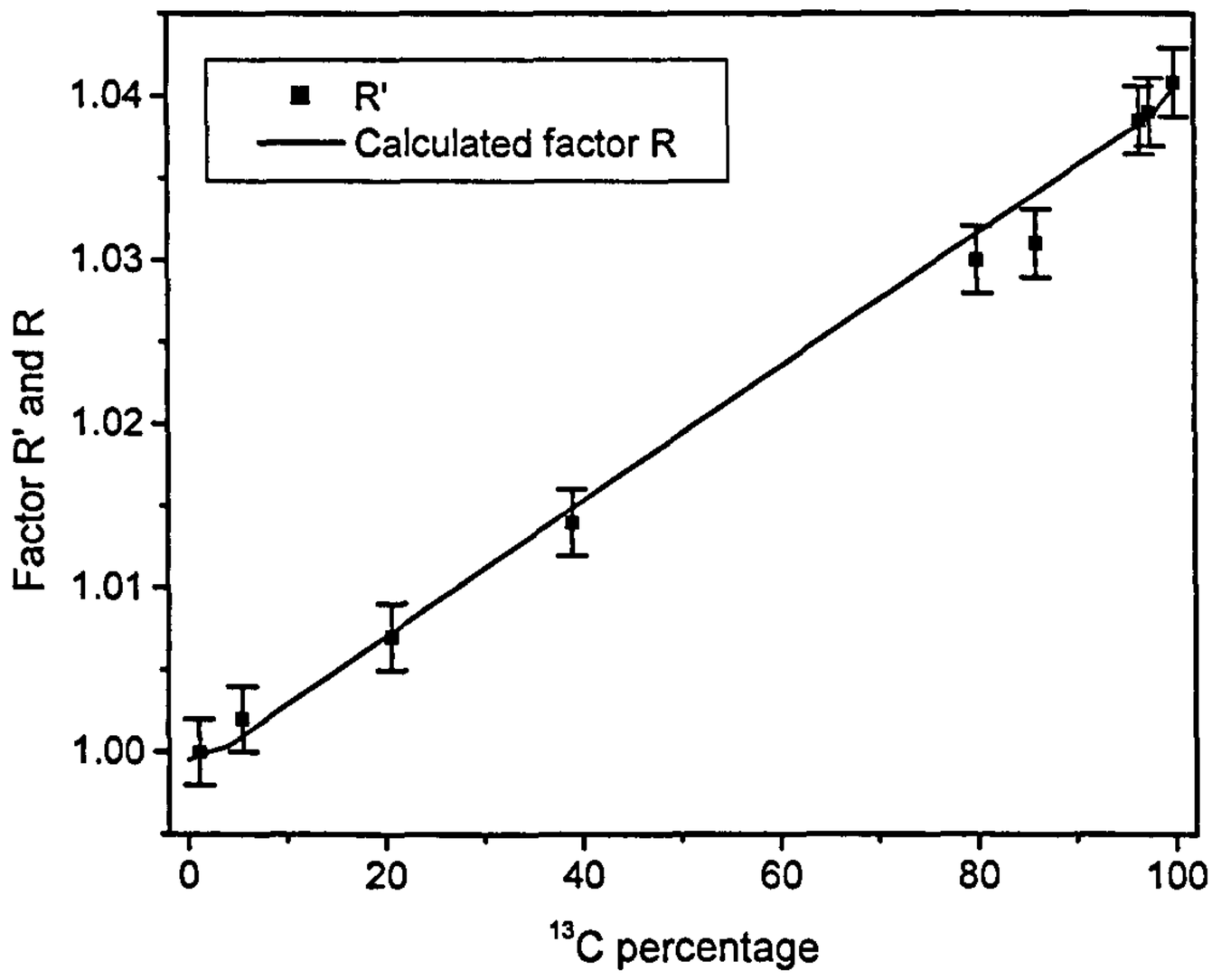

Figure 4.8. The wavenumber correction factor R', compared with the expected factor R from equation 4.3.1.

Sample	% ^{12}C	1282 cm^{-1}	1212 cm^{-1}	1094 cm^{-1}	480 cm^{-1}
H441R	2	1261 (-21)	1170 (-42)	1055 (-39)	480 (0)
H439rt	8	1261 (-21)	1170 (-42)	1055 (-39)	480 (0)
F1	14	1260 (-22)	1170 (-42)	1057 (-37)	480 (0)
F3	20	1260 (-22)	1170 (-42)	1057 (-37)	480 (0)
h667b2	25	1265 (-17)	1178 (-34)	1066 (-28)	480 (0)
F4	40	1266 (-16)	1168 (-44)	1069 (-25)	480 (0)
82_8	61	1271 (-11)	1191 (-21)	1076 (-18)	480 (0)
h667a2	82	1274 (-8)	1205 (-7)	1083 (-11)	480 (0)
98_8	94	1282 (0)	1212 (0)	1094 (0)	480 (0)
Natural	98.9	1282 (0)	1212 (0)	1094 (0)	480 (0)

Table 4.2. The samples and their respective carbon 12 content, the peak positions and shift compared to natural type IaA diamond.

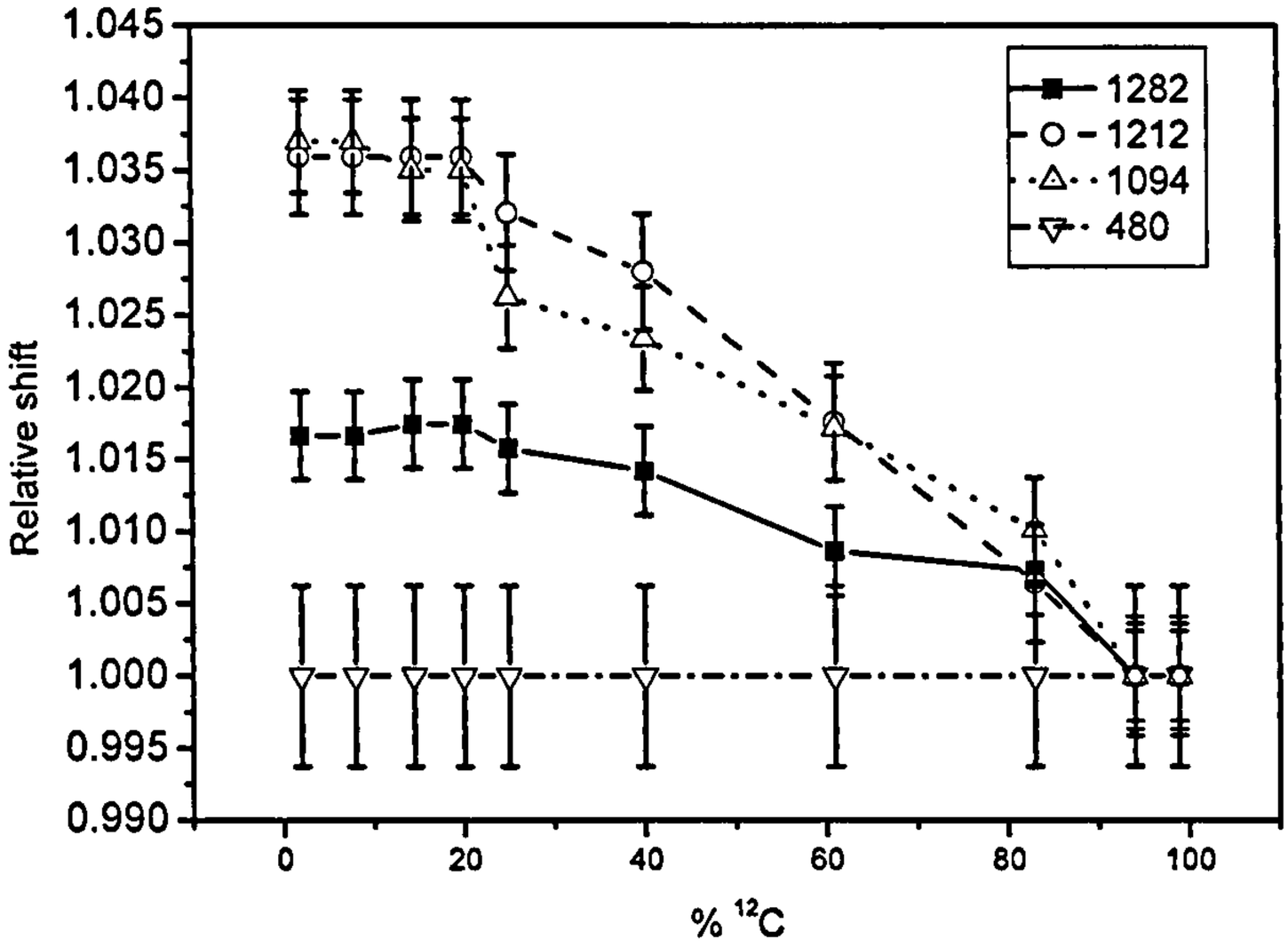

Figure 4.9. The ratio of the ^{13}C to ^{12}C A defect peak position is set out as a function of the ^{12}C percentage in the synthetic diamond. The 480 cm^{-1} peak position does not shift with different ^{12}C to ^{13}C isotopic content. The legend gives the values of the A centre maxima for natural diamond.

4.3.2.4. The peak position shift of the A defect in ^{13}C enriched diamond when assuming harmonic coupling to nearest neighbours only.

If we assume that bond strength is not affected by replacing the carbon 12 atom by its isotope carbon 13, then we can expect the ratio of the peak positions of the A defect of natural and 100% ^{13}C isotope enriched diamond to be given by:

$$\text{Peak shift} = \sqrt{\frac{n*14+m*13.00335}{n*14*m*13.00335}} \Big/ \sqrt{\frac{n*14+m*12}{n*14*m*12}} \qquad (4.3.3)$$

With n and m the number of nitrogen and carbon atoms respectively. This is correct when there is no anharmonic coupling between the atoms and only nearest neighbour interaction occurs. Table 4.3 summarises the relative shift of the A defect related peak positions sample H411R (2% ^{12}C).

Peak pos. Natural	Meas. ratio	Calc. ratio	n Nitrogen	m Carbon
1282	0.9836	0.9830	2 (1.91)	3 (3.06)
1212	0.9653	0.9726	2 (1.99)	0 (0.31)
1094	0.9635	0.9726	2 (2.00)	0 (0.18)
480	1.0000	1.0000	2	0

Table 4.3. The measured and calculated (from equation 4.3.3) ratio of the peak position of the various A defect related absorption features of natural and ^{13}C isotopically enriched diamonds. The bracketed values in table 4.3 are the values from the least squares fit of equation 4.3.3 to the experimentally determined ratio.

Note that the ratios of the last two peaks are close to the $\sqrt{(12/13)} = 0.9607$, but in all cases, the measured ratios are higher, so more than one nitrogen/carbon atom is involved in the vibration. This is no surprise as the wavelength of the vibration is by a factor of $\sim 10^4$ longer than the length of a few lattice sites, so the vibration will involve next nearest neighbours and more carbon atoms.

Theoretical calculations of the frequencies of vibrations of A defects in isotopically $^{12}C/^{13}C$ mixed diamond could aid in the understanding of observed change of the vibrational frequency of the A defects as function of ^{12}C isotopic fraction. This is not attempted here as it is outside the scope of this thesis.

4.3.4. Correlation between spectral features in the IR spectra of nitrogen aggregates.

As stated in the introduction (chapter 1), there is a relation between the D absorption coefficient and the integrated intensity of the platelet peak (Woods 1986). This is also observed in the samples studied here (figures 4.10 and 4.11), consistent with Woods (1986). An abnormally large number of brown and pink type Ia, and colourless, pure type IaB (no A defects) diamonds from the western Australian Argyle diamond mine are irregular diamonds.

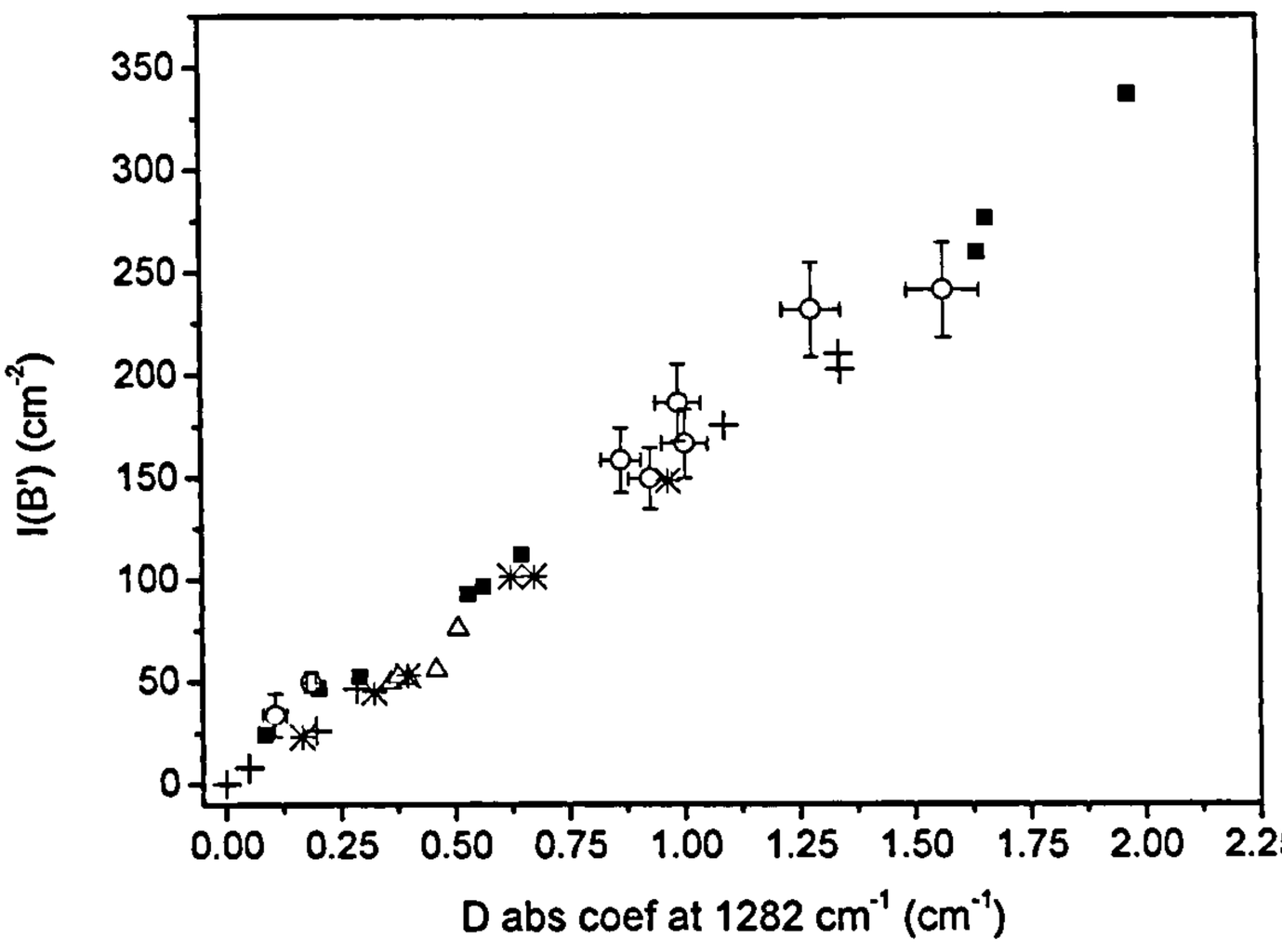

Figure 4.10. The correlation between the integrated intensity of the platelet peak and the D component in the infrared spectrum of diamond. The error bars give an example of the magnitude of the uncertainty on the measured values. Open circles and squares are data points from regular diamonds, while other data points are from irregular brown type Ia diamonds.

Luyten (1994), Evans *et al.* (1995) and Kiflawi and Bruley (2000) investigated the annealing behaviour of nitrogen aggregates in samples subjected to extreme HPHT conditions and found that platelets are destroyed during HPHT annealing. That behaviour is also observed in this study (see chapters 1 and 6 for more information).

The one phonon absorption spectrum around 1282 cm^{-1} of some type IaA diamonds is saturated and the concentration of the A defect was determined by the absorption coefficient of the A defect at 480 cm^{-1}. The correlation factor between the A defect absorption at 480 cm^{-1} and 1282 cm^{-1} has been determined for 7 colourless samples with different A defect concentrations without a detectable platelet absorption. The spectra were renormalized and the intrinsic spectrum was subtracted from the experimental spectrum. Then the absorption coefficients at 480 cm^{-1} and 1282 cm^{-1} were recorded and a linear correlation is found (figure 4.12).

The data has been fitted with a weighted linear fit (function: $y = E + F.x$, with E and F free parameters) without constraints and a linear fit with the constraint that the linear fit must go through 0 at the origin (function: $y = F.x$, with F a free parameter).

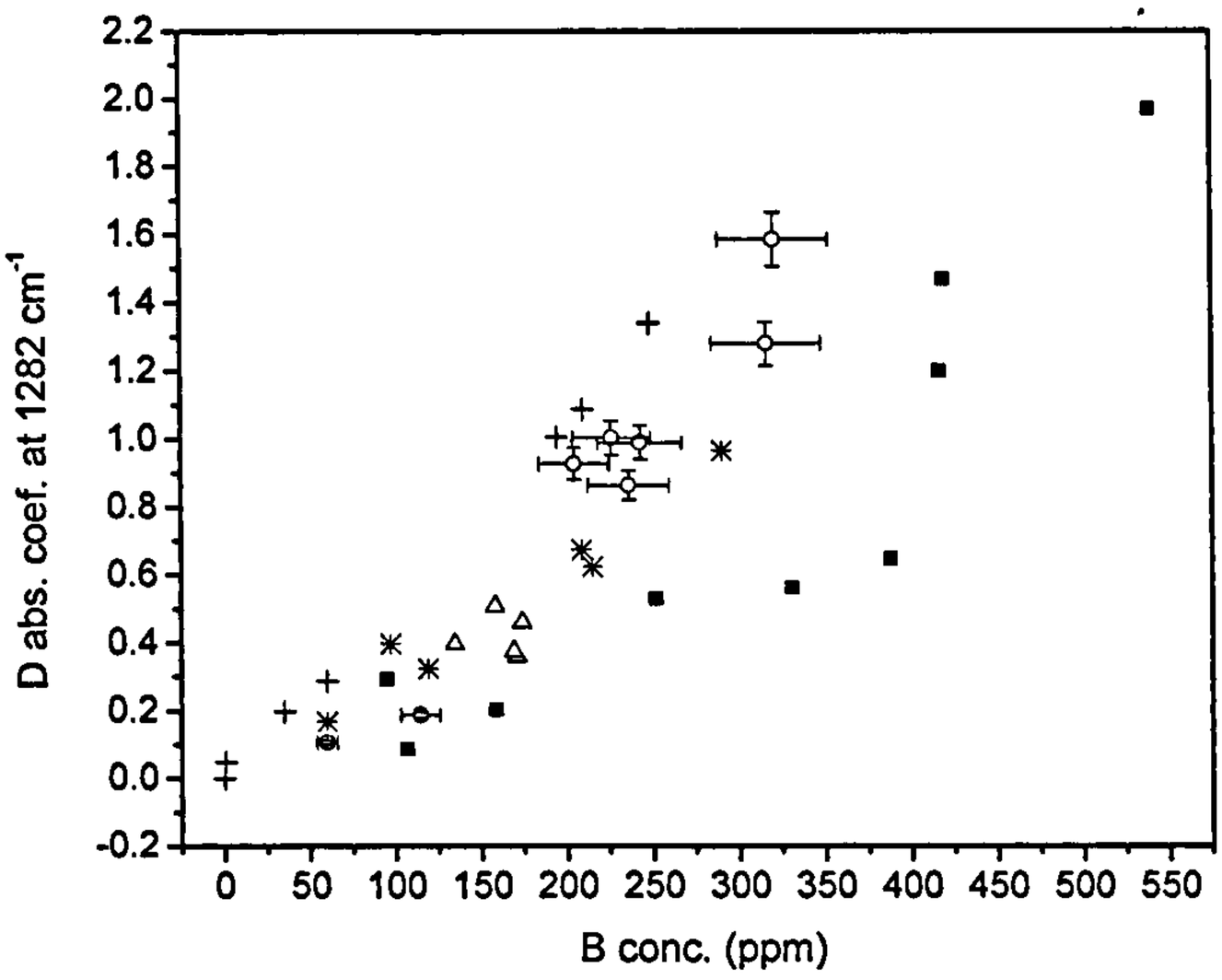

Figure 4.11. The correlation between the concentration of the B defect and the absorption coefficient at 1282 cm^{-1} due to the D component in the IR spectrum. Crosses and open circles are regular diamonds, while all other points are irregular diamonds, most of them are brown in colour. The data points at the origin are from 9 different samples. The data points are from the same regular and irregular samples as in figure 4.10.

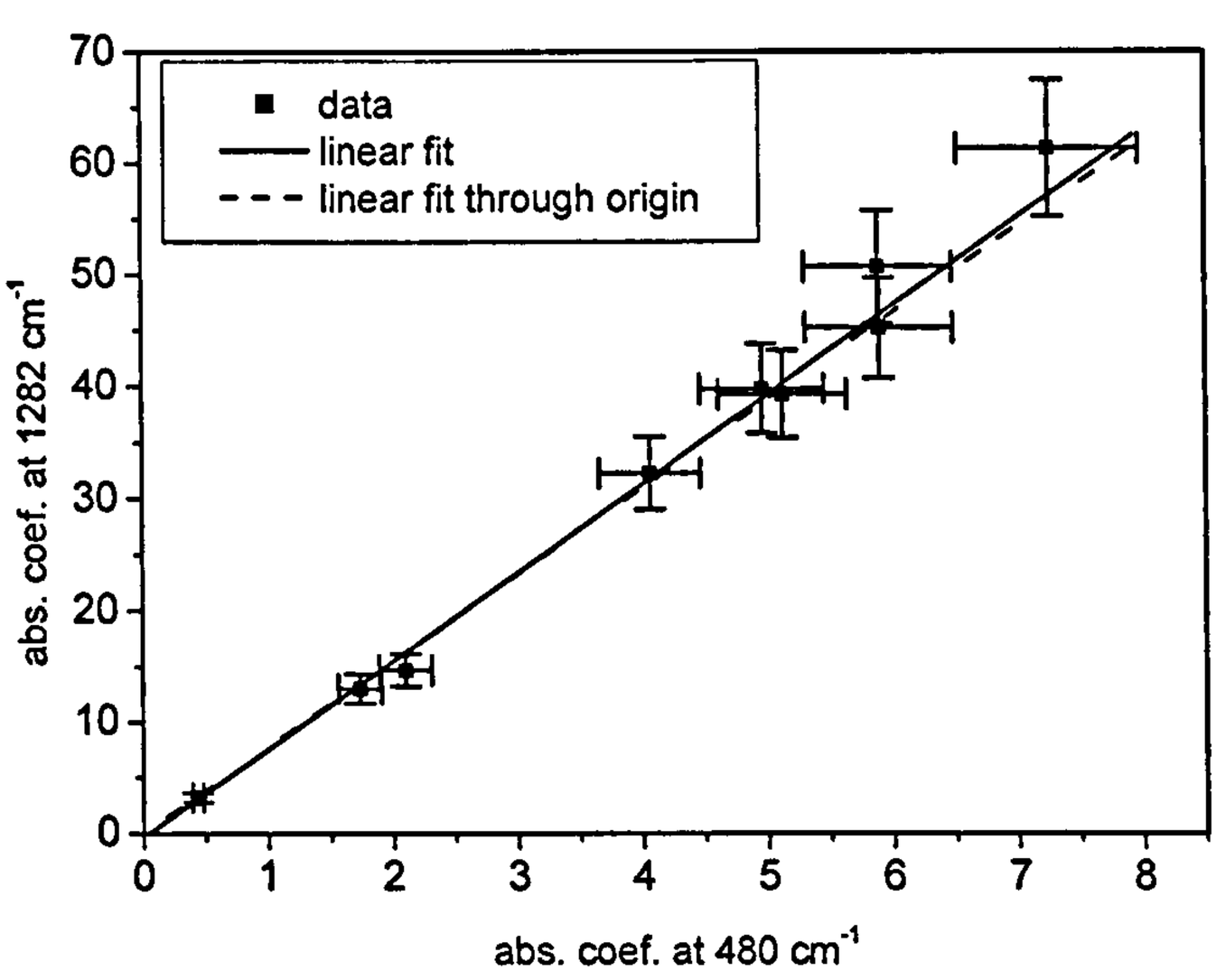

Figure 4.12. The correlation between the 480 cm^{-1} peak in the absorption spectrum of type IaA diamond and the maximum of the absorption at 1282 cm^{-1}. The solid line is a weighted, unconstrained linear fit and the dotted line is a weighted linear fit through the origin.

For the unconstrained fit, the parameters are:

Parameter	Value	Error
E	-0.39	0.30
F	7.93	0.21

Table 4.4. The fitting parameters for an unconstrained linear fit of the data in figure 4.12.

For the fit with the additional requirement y = 0 at x = 0:

Parameter	Value	Error
F	7.76	0.17

Table 4.5. The fitting parameters for an constrained linear fit of the data in figure 4.12.

The correlation between the absorption at 480 cm^{-1} and 1282 cm^{-1} can be used to determine the absorption coefficient at 1282 cm^{-1} for samples where the 1282 cm^{-1} region is saturated. The concentration of A defects can then be determined by multiplying with the appropriate coefficient from table 1.3 in chapter one.

4.4. Conclusion

4.4.1. Correlation of the 3107 cm^{-1} line with nitrogen and nitrogen aggregates.

The fact that the 3107 cm^{-1} line only occurs in type I diamond leads us to believe that nitrogen has an influence on the formation of the 3107 cm^{-1} line in the IR spectrum.

It is possible that nitrogen aggregate - hydrogen complex centres have vibronic transitions in the UV-VIS-NIR spectrum which give rise to additional absorption lines in the "Cape-Yellow" spectrum of type Ia diamonds.

4.4.2. Results related to the 3107 cm^{-1} line in isotopically $^{12}C/^{13}C$ mixed HPHT synthetic diamonds.

We have studied hydrogen-related absorption peaks in diamonds grown from ^{13}C and which contain approximately 800 ppm nitrogen in the A-aggregate form. The results show unambiguously that the absorption peaks at 3107 and 3098 cm^{-1} are due to the stretching vibrations of a C–H bond. The relative intensities of the two components are consistent with the isotopic composition of the diamond, determined from the shift of sharp features in the intrinsic two-phonon absorption band, and from the shift of the Raman peak. The isotopic splitting for the bending vibration is close to that calculated for isolated diatomic molecules comprised of ^{12}C–H and ^{13}C–H, but both components are pulled to lower frequency because of weak coupling to the one-phonon lattice vibrations. The relative intensity of the ^{12}C–H peak, calculated using a simple model, is higher than expected from the isotopic composition. The first overtone of the bend vibration, $2\hbar\omega_b$, and the combination band $\hbar\omega_s + \hbar\omega_b$ have been detected; as in natural diamond the frequencies are slightly lower than those calculated from the arithmetic sum of the frequencies. The position of a feature at 3237 cm^{-1} has been shown to be independent of the isotopic composition of the diamond, and this is not inconsistent with the proposal that this feature is due to an N–H vibration.

4.4.3. Results related to the A defect in isotopically $^{12}C/^{13}C$ mixed HPHT synthetic diamonds.

From our limited data set, the following conclusions can be drawn: the 480 cm^{-1} vibration is probably a vibration along the nitrogen-nitrogen axis of the A defect. The 1094 and 1212 cm^{-1} vibrations involve only carbon atoms. The 1282 cm^{-1} vibration is a vibration of a nitrogen-carbon complex.

It is not clear why the 1282 cm^{-1} vibration has a different frequency change to that of the 1094 and 1212 cm^{-1} vibrations when the ^{12}C isotopic content is changed.

Theoretical calculations could give further insight in the change of the vibrational frequency as function of the isotopic ^{12}C content in diamond.

4.4.4. Correlation between spectral features in the IR spectra of nitrogen aggregates.

The correlation between the integrated absorption coefficient of the platelet peak and the D defect absorption spectrum for regular diamonds found by Woods (1986) is confirmed in this study.

The A defect concentration can be determined from the absorption strength of the 480 cm^{-1} peak in cases where the A defect absorption is very intense and the absorption at 1282 cm^{-1} is saturated. This can be done by multiplying the absorption coefficient at 480 cm^{-1} by 7.8 ± 0.2, to calculate the absorption coefficient of the A defect peak at 1282 cm^{-1}, and then by 16.5 ± 1.0 to determine the concentration of A defects.

Chapter Five

Vacancy capture by nitrogen aggregates and photo-induced changes of the H1b and H1c defect

5.1. Introduction

5.1.1. Chapter outline and motivation

There are two main topics in this chapter:

- The capture of vacancies by nitrogen aggregates in diamond.
- Photo-induced changes of the H1b and H1c defect.

The first part of this chapter studies the kinetics of the decay of vacancies and the formation of nitrogen-vacancy complexes in irradiated diamonds when subjected to annealing. The defect formation and dissociation kinetics will play a crucial role in chapter six, where the formation and dissociation of nitrogen-vacancy aggregates during the HPHT annealing of type Ia brown diamond will be studied. Simultaneous dissociation of these defects during HPHT annealing will make the study difficult. A study the formation of the nitrogen vacancy complexes in a more controlled way can be done by eliminating the dissociation processes. This is done by electron irradiation and annealing (T ~ 800°C) of type Ia diamond and study of data in literature on irradiated diamonds, annealed up to 1750°C.

The second part describes photo-induced changes of the H1b and H1c defects in the infrared spectrum of irradiated and annealed diamonds. This will illustrate the importance of illumination and thermal history of a sample with respect to detectability and strength of absorption peaks.

5.1.2. Radiation defect production and annealing of irradiated diamonds and preliminary experiments

Vacancies and interstitials can be produced by high energy irradiation with electrons, gamma rays and nuclear particles (neutrons, protons, alpha particles, ...) (Campbell *et al.* 2000, Davies *et al.* 2001). Production rates of neutral vacancies and interstitials when type IIa diamond is irradiated with 2 MeV electrons have been published (Newton *et al.* 2002, Davies *et al.* 1992). Newton *et al.* found that the total concentration of neutral vacancies per cubic centimetre produced in the process is 1.4 times the total dose in electrons per square centimetre. However, for thin samples, Davies *et al.* (1992) deduced a different vacancy production factor of 0.075 cm^{-1} for samples irradiated with a dose of $3x10^{17}$, 2 MeV electrons/cm^{-2} at room temperature. In the same study, Davies *et al.* also found that for type Ia diamond, the vacancy production factor is 1.6 ± 0.1 times higher than for type IIa diamond. Irradiation of type Ia diamond produces negatively charged and neutral vacancy defects, while the neutral vacancy is predominant in relatively pure type IIa diamonds (Davies 1974b). The relative concentrations of the neutral and negatively charged vacancy in type Ia diamond are dependent on measurement conditions and history as photochromic processes occur (Dyer 1965b). Photochromic processes or photo-induced changes appear to be common in irradiated diamonds (Mita *et al.* 1990, Iakoubovskii *et al.* 2000, Kupriyanov *et al.* 2000, Vlasov *et al.* 2001, Vlasov *et al.* 2002).

Vacancies and interstitials can be mobilised by thermal annealing with different activation energies. Below a summary is given of the most relevant points on the current knowledge of interstitials and vacancies and some preliminary experiments on irradiated samples.

5.1.2.1. Interstitials in irradiated diamond

Newton *et al.* (2002), Smith *et al.* (2004) and Davies *et al.* (2000) identified the neutral interstitial by EPR (the R2 defect) and optical absorption measurements (the 1.859/1.685 eV or 666.7/735.6 nm defects). Annealing measurements and irradiation at different temperatures lead Newton *et al.* (2002) to the conclusion that there are two equal energy barriers to vacancy-interstitial recombination: there is a barrier at an annihilation radius where the interstitial is bound to recombine with the vacancy and

an energy barrier at a larger capture radius. To cross each radius, the interstitial must overcome the energy barrier (see figure 5.1).

At a low annealing temperature (T < -123°C (150 K)), the interstitial is not mobile. At a higher temperature (-123°C (150 K) < T < 277°C (550 K)) the interstitial concentration decreases strongly, but does not anneal out. This is because the interstitials outside the capture radius can anneal out to traps or to the surface, but the interstitial between the capture and recombination barrier cannot overcome the capture nor recombination barrier and this would account for the interstitials which remain after irradiation at temperatures between 150 and 550 K. The interstitials inside the annihilation radius recombine and this accounts for the decrease of the vacancy concentration at relatively low annealing temperature. At temperatures above 550 K (277°C), the interstitial can overcome the energy barrier to recombine or escape from the vacancy capture radius.

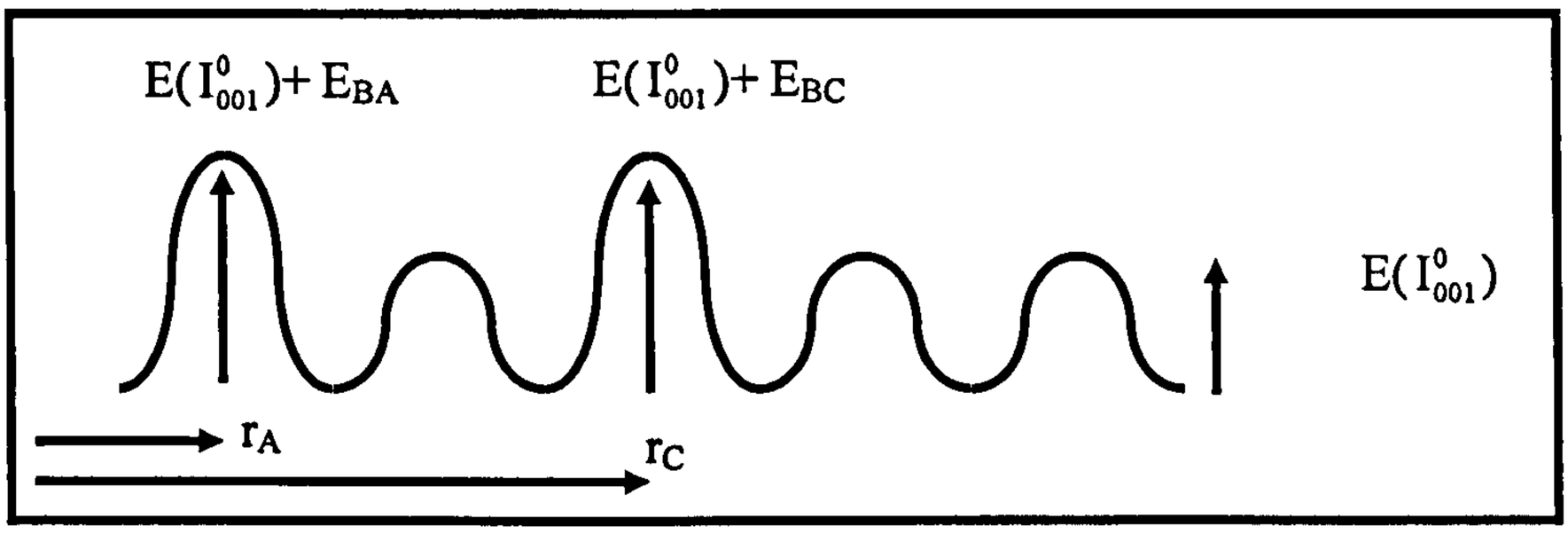

Figure 5.1. Schematic diagram of the vacancy-interstitial recombination process. The interstitial has to overcome two barriers before it can recombine with the vacancy.

During the electron irradiation excess, non-equilibrium excitons will be created and electrons or holes can be captured by the neutral <001> self-split interstitial (I_{001}) and convert it into a relatively more mobile interstitial I^* with unknown charge. The Bourgoin-Corbett mechanism requires differently charged interstitials to occupy different sites in the crystal lattice and the neutral interstitial could then diffuse through the lattice during irradiation by trapping and release of charge: $I_{001} \rightarrow I^* \rightarrow I_{001} \rightarrow I^*$ etc; this non-thermal diffusion process would be responsible for the "recombination enhanced diffusion of self interstitial atoms" in diamond (Newton *et al.* 2005). As a remark we note that interstitial related defects typically have a low

Huang-Rhys factor, while recombination enhanced diffusion requires a high Huang-Rhys factor (see chapter 1, section 1.8).

An EPR study of the R1 defect in type IIa synthetic diamond by Twitchen *et al.* (2001) identified this defect as the nearest neighbour di-<100>-split interstitial. Isothermal and isochronal annealing studies of the R1 defect indicated it is possibly linked to the 3H defect. The defect anneals out with a very low activation energy (0.6 eV), and a very low attempt-to-escape frequency (10^3 Hz).

The annealing behaviours of other interstitial related defects have been studied by Collins *et al.* (1993) and Allers *et al.* (1998). The 5RL band with a ZPL at 4.582 eV (270.5 nm) is thought to be a pair of interstitial carbon atoms. However, the defect is stable up to 800°C (1073 K), which casts some doubts on its interstitial character. The R1 defect anneals out at a temperature in the range of 620 K (347°C) – 670 K (397°C) (Twitchen *et al.* 2001). The 1.859 eV (666.7 nm) and the R11 (311 nm) systems, are attributed to the single neutral interstitial, and anneal out at temperatures below the temperature where the vacancy becomes mobile (420 – 540°C or 694 – 814 K) and are thought to be responsible for the initial rapid decay of the GR1 peak, observed by Davies *et al.* (1992). The activation energy for the process is 1.68 ± 0.15 eV (Allers *et al.* 1998, Twitchen *et al.* 2001).

Goss *et al.* (2006) studied different configurations of closely separated, negatively charged Frenkel pairs by theoretical calculations. Their study pointed to different configurations of the Frenkel pair, with different symmetries, similar to a number of defects detected in irradiated type Ib diamond. The symmetries and hyperfine parameters are consistent with the W11 – W14 centres. Key point here is the capture of an electron by the Frenkel pair, giving the defect a total spin of 3/2. Conversion can then happen between different configurations. The energy barriers to change from one configuration into another are low (~ 0.2 eV). During thermal annealing, a closely spaced Frenkel pair could oscillate several times between different configurations before recombining, making the recombination process slower than anticipated from the interstitial diffusion energy alone. There is experimental evidence for the conversion between W11 and W13 defects in irradiated type Ib diamonds (Iakoubovskii *et al.* 2005) when subjected to temperatures above 200°C

(473 K) as shown in figure 5.2. Theoretical calculations of the stabilities of different configurations of neutral Frenkel pairs, which should be present in type IIa and type Ia diamond, have not been carried out as yet, but if a neutral Frenkel pair can have several geometrical configurations, and similar calculations indicate these are stable, then some aspects of the annealing behaviour of vacancies in irradiated diamonds at relatively low temperature (300°C < T < 500°C or 573 K < T < 773 K) could be explained: if one configuration would be particularly stable, the concentration of interstitials would decrease upon annealing like the data obtained experimentally by Newton *et al.* (2002).

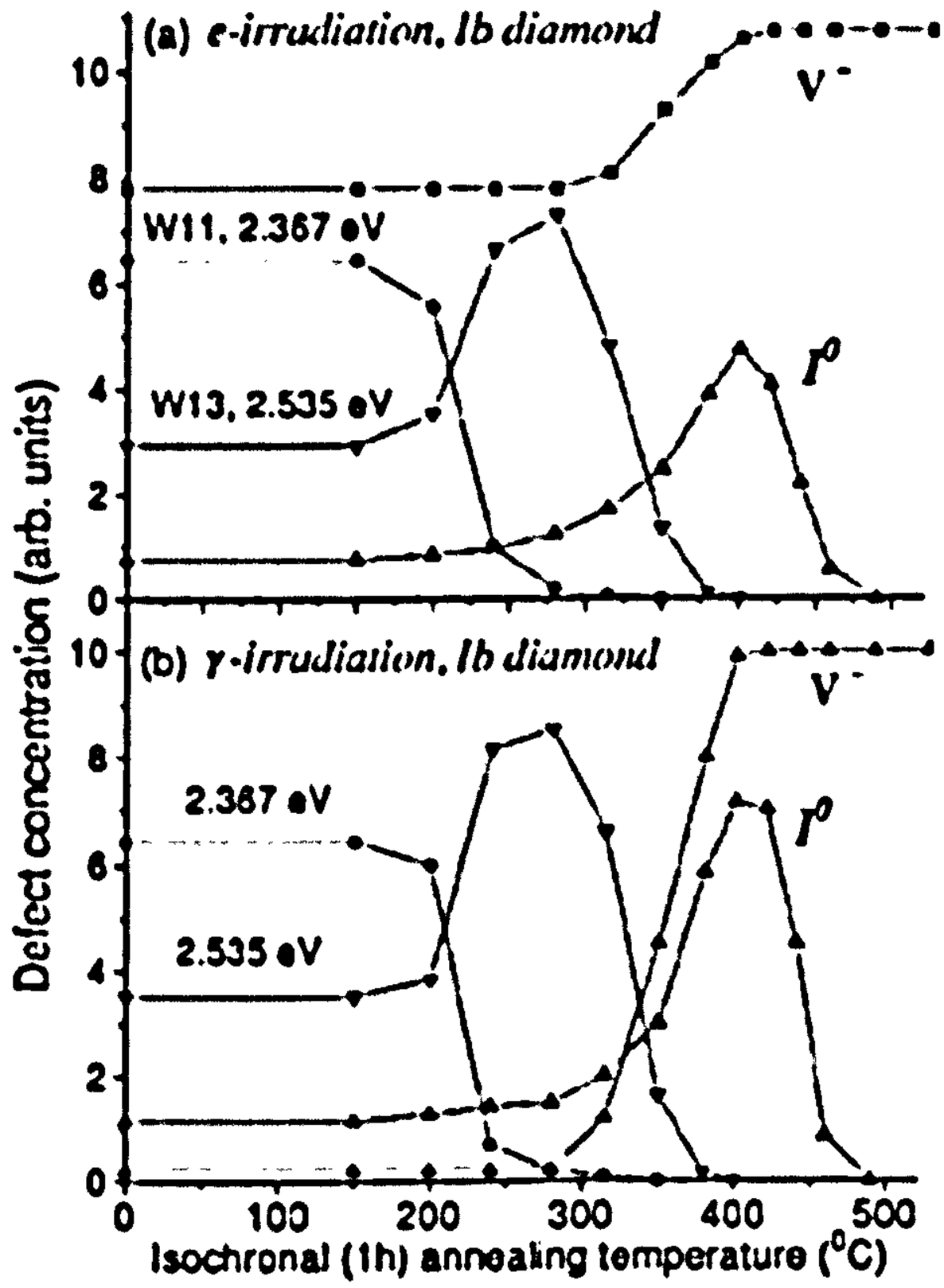

Figure 5.2. The isochronal (1h) annealing data of electron and gamma irradiated diamond of Iakoubovskii *et al.* (2005).

The 3H defect is readily detected in the UV-VIS absorption and emission spectrum (ZPL at 503.5 nm) after irradiation and is bleached by annealing at 450°C (723 K) (see figure 5.3); it is thought to be interstitial related (Steeds *et al.* 1999). The 3H defect can also be bleached by UV illumination (Vlasov *et al.* 2001, Vlasov *et al.*

2002). After annealing the absorption can be recovered by X-ray or UV illumination of the sample (Walker 1979), even after annealing at T ~ 800°C (1073 K) (Iakoubovskii *et al.* 2003). No recovery of the absorption of the 3H defect has been attempted in the work presented in this thesis.

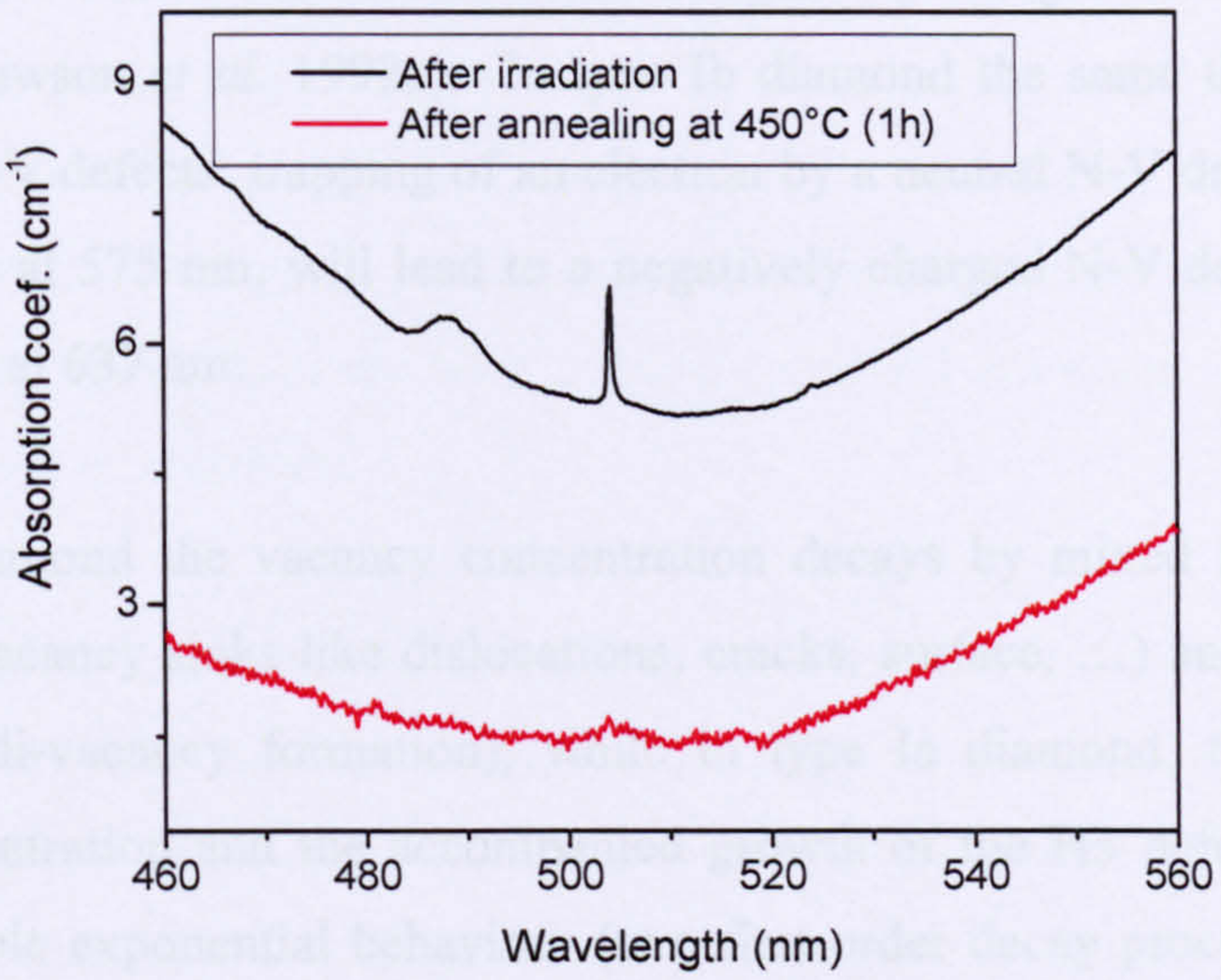

Figure 5.3. The UV-VIS absorption spectrum, recorded at liquid nitrogen temperature. The 3H peak is completely bleached by annealing for 1 hour at 450°C.

5.1.2.2. Vacancies in irradiated diamonds

Annealing of irradiated samples at temperatures over 600°C (873 K) will make the vacancy mobile, and detailed investigations of Davies *et al.* (1992) and Lawson *et al.* (1992b) on annealing of irradiation damage in type IIa, IaA, IaB and Ib diamonds, identified a slow and fast annealing component of the radiation damage in type IaA. The decrease of the vacancies by the fast and slow processes and the growth of H3 in the diamonds correlate very well (Davies *et al.* 1992, Lawson *et al.* 1992b). The slow rate is ~ 12x lower than the fast rate and both processes have, within experimental uncertainty, the same activation energy of 2.3 ± 0.2 eV. In type Ib diamond, nitrogen vacancy (N-V) defects will be formed (Clark and Norris 1971, Davies and Hamer 1976, Mita 1993), while in type IaA/B diamond, the vacancy trapped at an A defect will give rise to H3 defects, and trapping by B defects will give rise to H4 defects (Davies 1977, Clark and Davey 1984). Davies (1977) and Clark and Davey (1984) observed a proportionality between the ratio of the A and B defect concentration and

the H3 and H4 defect concentration proving H3 is a vacancy trapped at and A defect and H4 is a vacancy trapped by a B defect.

If C defects or other electron donors are present in the diamond, an electron can be trapped by the H3 defect and convert it into a negatively charged defect: the H2 defect (Mita 1990, Lawson *et al.* 1992a). In type Ib diamond the same thing can happen with neutral N-V defects: trapping of an electron by a neutral N-V defect, with a ZPL absorption line at 575 nm, will lead to a negatively charged N-V defect with a ZPL absorption line at 637 nm.

In type IIa diamond the vacancy concentration decays by mixed first order decay (diffusion to vacancy sinks like dislocations, cracks, surface, ...) and a weak second order decay (di-vacancy formation), while in type Ia diamond, the decay of the vacancy concentration and the accompanied growth of the H3 defect concentration follows a double exponential behaviour (two first order decay processes): Davies *et al.* did not model the decay of the vacancy concentration by two first and second order processes, but by two first order processes only as the nitrogen defect concentration was two orders of magnitude higher than the vacancy concentration. Vacancy trapping by nitrogen aggregates and dislocations are thus the dominant processes and di-vacancy formation is negligible when the trapping defect concentration is much larger than the vacancy concentration. Single substitutional nitrogen defects appear to be much more effective vacancy traps (see section 5.3 of this chapter).

Lawson *et al.* (1992b) observed a change in the Full Width at Half Maximum (FWHM) of the GR1 peak after annealing at 600°C (873 K), where the peak width slowly changed from 4 to 3.26 meV. However, experiments carried out and described in this chapter will show that the FWHM of the GR1 line changes even at lower temperature. Lawson *et al.* (1992) considered three explanations for the decrease of the FWHM of the GR1 line in type Ia diamonds, which appeared to be correlated with the fast decay component only:

- Annihilation of closely spaced vacancy V^0 interstitial C_i pairs.
- Rapid trapping of vacancies in regions with high density of A defects and slower trapping of vacancies in regions with lower A defect density.

- Fast annealing because of preferential creation of vacancies close to the nitrogen aggregate.

The first option was ruled out because the increase of the H3 concentration correlated with the decrease of the vacancy concentration diffusing by the fast process. The second option was also ruled out because H3 zero phonon line narrowing is not observed when the H3 defect concentration increases during annealing. This should happen as the H3 defect created in the region with high A defect concentration has a large FWHM because of strain generated by other A defects near the H3 defect and the H3 ZPL line should become more narrow when H3 is created in regions with a low concentration of A defects.

A remark must be made here (see Chapter 1, section 1.8 for more details): irradiation with gamma rays and electron irradiation at different energies will give different results: high energy irradiation will give well separated vacancy-interstitial pairs, while gamma irradiation will give closely separated vacancy-interstitial pairs. Additionally, increasing the energy during electron irradiation will create increased concentrations of non-equilibrium excitons, increasing the rate of recombination enhanced diffusion during irradiation. Detailed investigation of irradiation conditions used in literature shows that they are different in energy, irradiation dose and type (gamma, electron, neutron, ...) making comparison of published results very difficult.

Modelling vacancy migration data in irradiated type IIa diamonds is best fitted with mixed first and second order kinetics (Davies *et al.* 1992). The first order process dominates, indicating that dislocations might be an effective vacancy trap. EPR measurements identified the W29 defect as a di-vacancy (Kirui *et al.* 1999) and positron lifetime experiments tentatively identified a defect with a ZPL at 488 nm as a di-vacancy (Pu *at al.* 2001). Both processes will also take place during annealing of type I diamond, and in principle, an accurate model will need to take this into account. However, we will show in this chapter that di-vacancy formation is negligible in type Ia diamond with a well detectable concentration of nitrogen aggregates, consistent with the findings of Davies *et al.* (1992).

5.1.2.3. Other defects occurring during annealing of irradiated diamond

Another defect created during irradiation of type Ia diamond is the "594 nm" defect, with a ZPL at 594 nm in the absorption spectrum. The absorption strength of the line increases when the diamond is annealed at relatively low temperature (~ 400°C or 673 K) and disappears after annealing at a high temperature (T > 1000°C or 1273 K) (figure 5.4). The structure of the 594 nm defect is unknown. However, since the defect is detected after irradiation at room temperature and increases in strength after annealing at temperatures where the vacancy is immobile and since the defect only appears in type Ia diamond (Collins 1999), it is probable that the defect involves interstitials and nitrogen. In mixed type IaA/B diamond, the formation of two defects, H1b (ZPL at 0.6124 eV or 4940 cm^{-1}) and H1c (ZPL at 0.6408 eV or 5170 cm^{-1}) correlates with the destruction of the 594 nm defect by annealing at temperatures over 700°C (973 K) (Collins *et al.* 1986). Collins *et al.* (1986) also found that [H1b]/[H1c] ~ [H3]/[H4] when the samples are annealed between 700 and 1200°C (973 – 1473 K), which implies that some or all of the 594 nm defects are trapped at A and B defects to form H1b and H1c respectively.

The intensity of the H1b defect grows after annealing up to 1200°C (1473 K), and then decreases (figure 5.4). Annealing of irradiated type IaB diamond at temperatures above 1500°C (1773 K) destroys H4. When H4 breaks up, H3 defects are created (Collins *et al.* 2005). Annealing above 1700°C (1873 K) also destroys the H3 defects. The absorption intensity associated with the H1b centre grows in intensity after annealing up to 1200°C (1473 K) (figure 5.4). Annealing above this temperature destroys the H1b and H1c defects. In irradiated and annealed type IaA diamond, destruction of the H1b centre is accompanied by an increase in the concentration of H2 centres. The H2 defect, (negatively charged H3 defect (Mita *et al.* 1990, Lawson *et al.* 1992)), is detectable in irradiated type Ia diamond after annealing at 1200°C, and grows as the H1b and H1c defects are destroyed. In irradiated diamond, the H2 defect is destroyed after annealing at ~ 1700°C (1973 K) as the H3 defect is also destroyed at these temperatures (Collins *et al.* 2005) (figure 5.4).

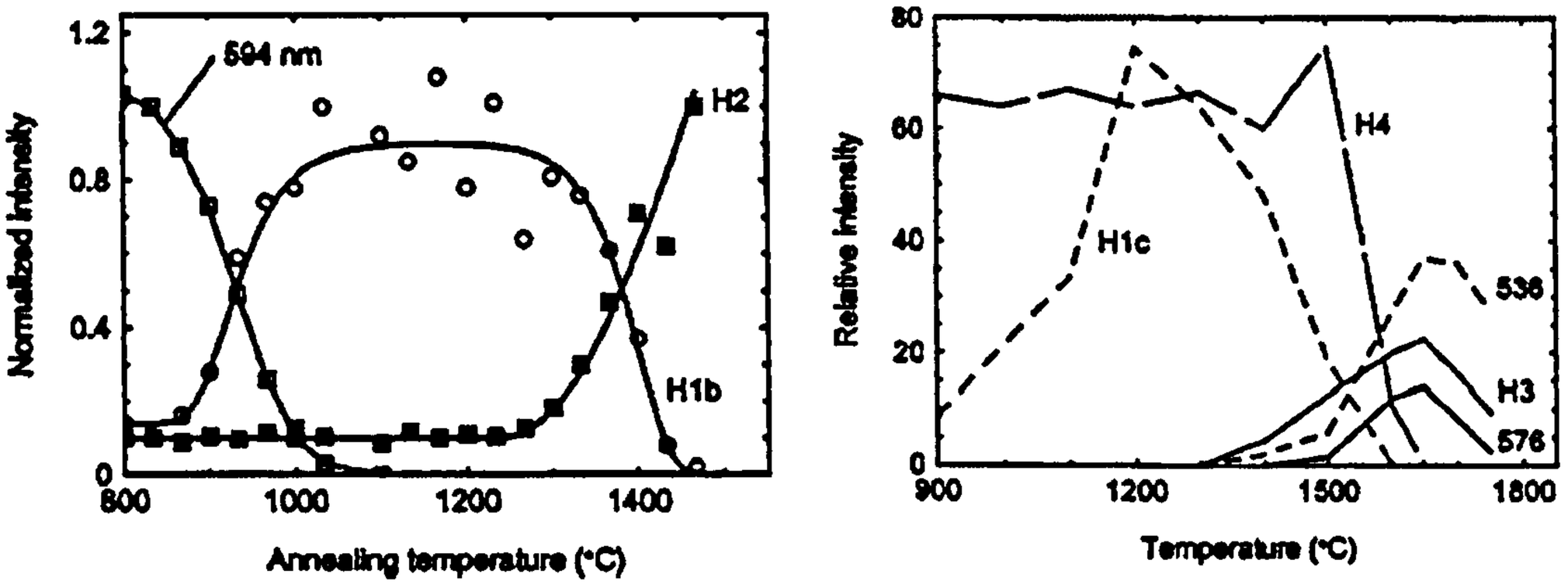

Figure 5.4. The isothermal annealing data in figures 3 and 7 from the paper of Collins *et al.* (2005) (left and right figure). The left figure displays the isothermal annealing data of a type IaA diamond after irradiation and the figure on the right displays the isothermal annealing data (T>900°C or 1173 K) of a type IaB diamond after irradiation.

Data from Collins (1978b, 1980, 1982) suggest the H3 defect splits up into an A defect and a vacancy. A detailed investigation of this process will be presented in this chapter and chapter six.

Additional absorption lines and a broad band with a maximum at 3094 - 3110 cm^{-1} can be detected in the infrared absorption spectrum, of type Ia diamonds electron irradiated with a high dose. This broad band anneals out at ~ 1000°C (1273 K) and additional sharp absorption lines appear. These lines are called the H1d (2678 cm^{-1}), H1e (2917 cm^{-1}), H1f (4400 cm^{-1}) and H1g (4437 cm^{-1}) lines (Kiflawi *et al.* 1999). The H1d and H1g pair and the H1e and H1f pair show the same isochronal annealing behaviour. All lines are electronic transitions (Kiflawi *et al.* 1999).

Figure 5.5 shows the IR spectrum of a type Ia diamond irradiated at room temperature with a 8.10^{18} e^-/cm^2 at 8 MeV (see section 5.2 of this chapter for more details on this sample).

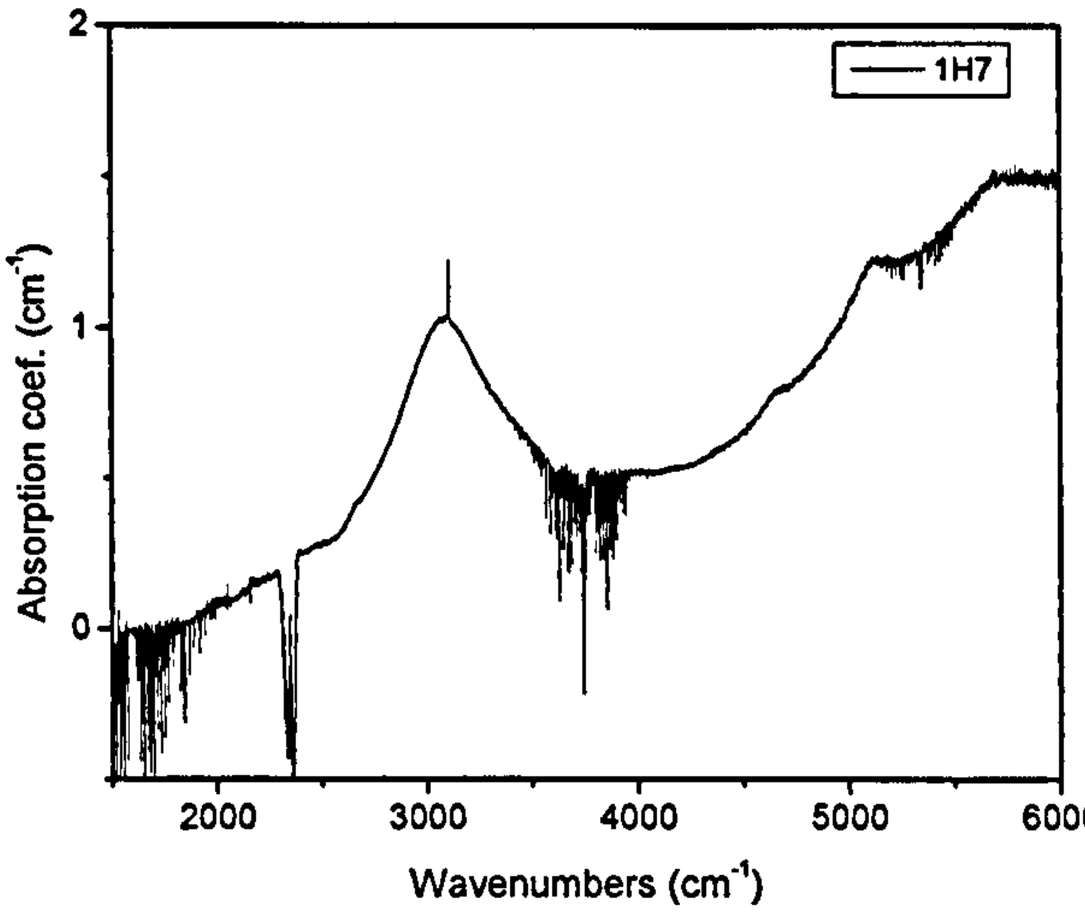

Figure 5.5. The broad band absorption in the IR spectrum of sample 1H7 (see section 5.2 for details). The intrinsic diamond spectrum has been subtracted from the spectrum of the sample.

Mita (1997) also found sharp, additional absorption lines at 4066, 4113, 4139 and 4168 cm^{-1} and a broad band at 2916 cm^{-1} in the infrared spectrum of a neutron irradiated (7.10^{17} cm^{-2}) synthetic type IIa diamond, HPHT annealed (from T = 1400°C (1673 K) to 1700°C (1973 K) at 6 GPa). All peaks appear on annealing at 1400°C (1673 K) and are stable up to 1700°C (1973 K). The broad band at 2916 cm^{-1} is probably not the broad band observed by Kiflawi *et al.* (1999), as the latter disappears after annealing at 1000°C (1273 K).

5.1.2.4. Photochromism of irradiation induced defects in diamond

It has been noticed that a large number of point defects created by irradiation, or irradiation with subsequent annealing at moderate temperatures around 1000 K, are photo chromic or have photo-induced changes in their absorption strength (Dyer and du Preez 1965, Davies 1974b, Collins and Rafique 1979, Mita *et al.* 1990, Mita 1993, Iakoubovskii *et al.* 2000, Kupriyanov *et al.* 2000, Vlasov *et al.* 2001 and 2002, Shareef and Collins 2003, Gaillou *et al.* 2005).

Of special importance to this chapter is the work of Shareef and Collins (2003) and Gaillou *et al.* (2005). Both describe phenomena similar to observations in this chapter: the bleaching/enhancement of the H1b, H1c defects with visible light and UV

illumination respectively. The absorption of both defects can be restored to its original intensity by heating to moderate temperatures (500°C (773 K) to 600°C (873 K) for 1 hour) and Shareef and Collins (2003) also determined the activation energy for the recovery process, after bleaching by green light to be 770 ± 210 meV.

The bleaching and recovery process of H1b and H1c defects after illumination with light of different wavelengths is investigated further in this chapter.

5.1.2.4. Preliminary experiments

Initial experiments were carried out for the following reasons:

- basic understanding of the annealing behaviour of irradiation induced defects in diamond and how these relate to results published in literature.
- to determine optimal annealing conditions for the annealing experiments.

In the first initial annealing experiment, a rough naturally irradiated diamond (irradiation conditions unknown) was isochronally (1 h) annealed at temperatures between 300°C (573 K) and 750°C (1023 K) in steps of 50°C. The sample was cleaved and micro PL measurements on the cleaved surface indicated the presence of GR1 at the centre of the diamond. The FWHM of the GR1 zero phonon line was determined from photoluminescence spectra as it was not possible to measure a good absorption spectrum through the irregularly shaped rough faces of the diamond. To avoid errors due to the inhomogeneity of the sample, the spectra were recorded at a well recognisable mark on the rough surface of the diamond. It is clear from figure 5.6 that the FWHM of the GR1 already changes at 300°C (573 K), and possibly at even lower temperature. However, one can see from figure 5.7 that the there is no substantial increase of the H3 defect concentration while the FWHM of the GR1 line decreases by a factor of ~ 2 after 400°C (673 K) annealing. The decrease of the FWHM also seems to level out at slightly higher temperature, and then decreases again after annealing above 600°C (873 K) where the vacancy becomes mobile and is trapped at nitrogen aggregates. This sample was probably exposed to γ ray irradiation in Nature as this is consistent with the presence of GR1 in the body of the diamond and the large FWHM of the GR1 line typical for γ irradiated diamond (Clark *et al.* 1956a, Clark *et al.* 1956b). The change in FWHM of the GR1 peak by annealing at

relatively low temperature (T < 300°C or 573 K) would then be associated not with interstitial-vacancy recombination, but following the model of Newton *et al.* (2002), interstitials outside the vacancy capture radius would diffuse to form aggregates or find their way to sinks. They will not recombine with vacancies. Newton *et al.* (2002) also observed a second fall in interstitial concentration after annealing or irradiating the sample held at 550 K (276°C) which is associated with interstitials escaping the capture radius or interstitial-vacancy recombination. The data on the FWHM of the GR1 defect presented here is consistent with this model and furthermore, combined with the data on the H3 defect, the indications are that the interstitial is indeed the mobile specie as no significant increase of H3 concentration is observed after annealing for 1 h at 550°C (824 K). The increase of H3 defect concentration is only observed after annealing at 600°C (873 K) and similar results have been observed for room temperature electron irradiated diamond (3 MeV, $2x10^{18}$ e/cm^2) (Iakoubovskii *et al.* 2003). To conclude: the FWHM change of the GR1 peak during low temperature annealing (T << 600°C or 873 K) is associated with interstitials diffusing away from the vacancy to sinks or the surface. The fast FWHM change of the GR1 peak during high temperature annealing (T > 600°C (873 K) immediately after irradiation) must thus be associated with vacancy-interstitial recombination. This also explains the very fast drop of the initial absorption strength of the GR1 peak when a type IaA diamond is subjected to annealing at 600°C (873 K) after irradiation (Davies *et al.* 1992) when the annealing of the sample at temperatures below 600°C (873 K) is skipped.

It appears that the FWHM of the GR1 line as function of annealing temperature, of the presumably gamma irradiated type Ia diamond, is similar to the behaviour of an electron irradiated diamond (Newton *et al.* 2002).

Another type Ia diamond was irradiated with 8 MeV electrons with a dose of 8.10^{18} e^-/cm^2, with the sample kept at room temperature, and annealed at 450°C (723 K) for one hour. One can see a decrease of the FWHM of the GR1 line and a decrease of the absorption intensity (see table 5.1, figure 5.8). The 3H peak disappears completely and there is a weak increase in the absorption strength of the 594 nm. The interstitial related peak at 667 nm also disappeared almost completely.

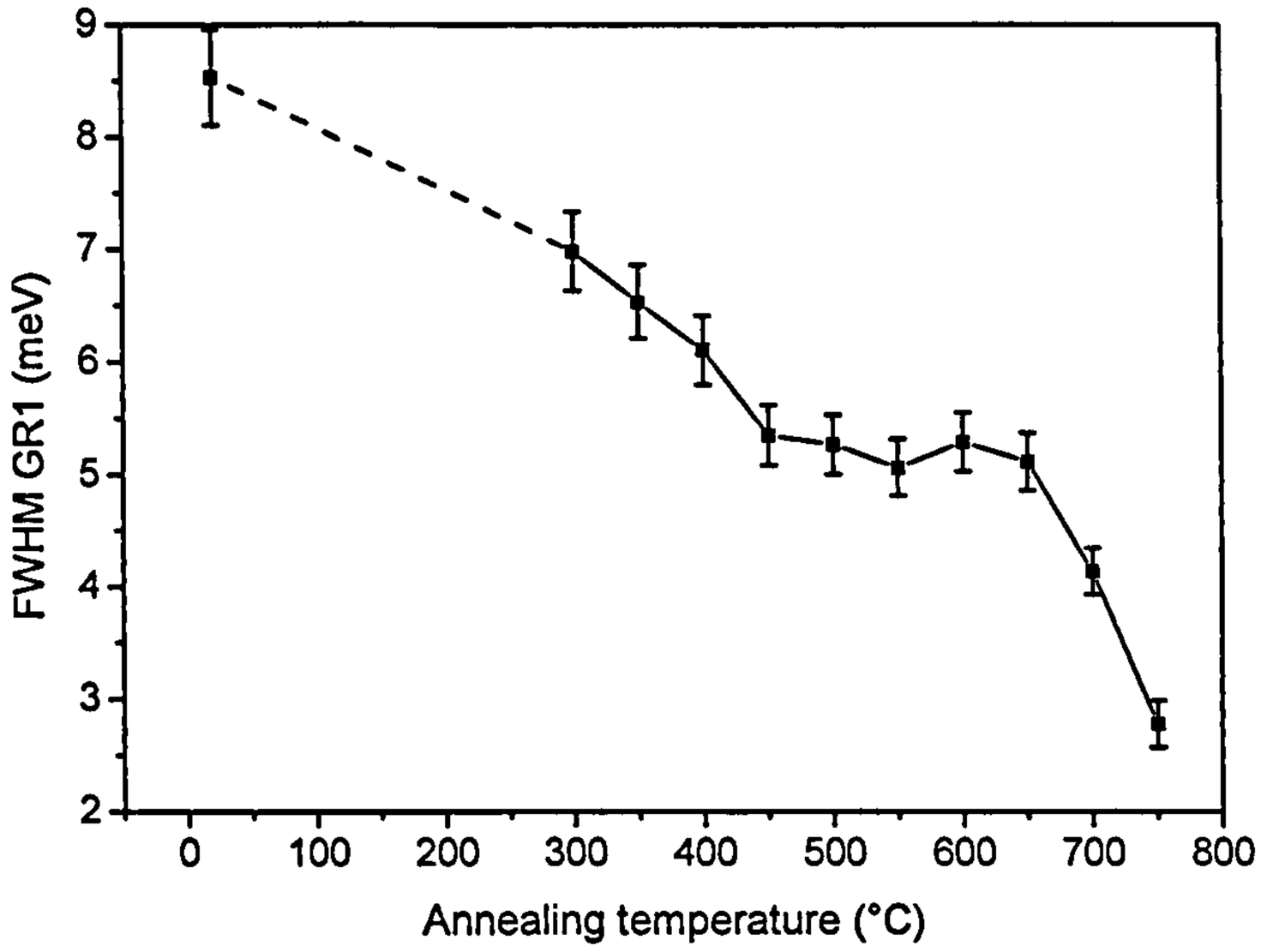

Figure 5.6. The change in FWHM of the GR1 ZPL of an irradiated diamond after isochronal annealing (1 h) at different temperatures. The FWHM of the as irradiated sample is the first data point (room temperature). The other data points are after annealing at 300°C (573 K) to 750°C (1023 K) in steps of 50°C.

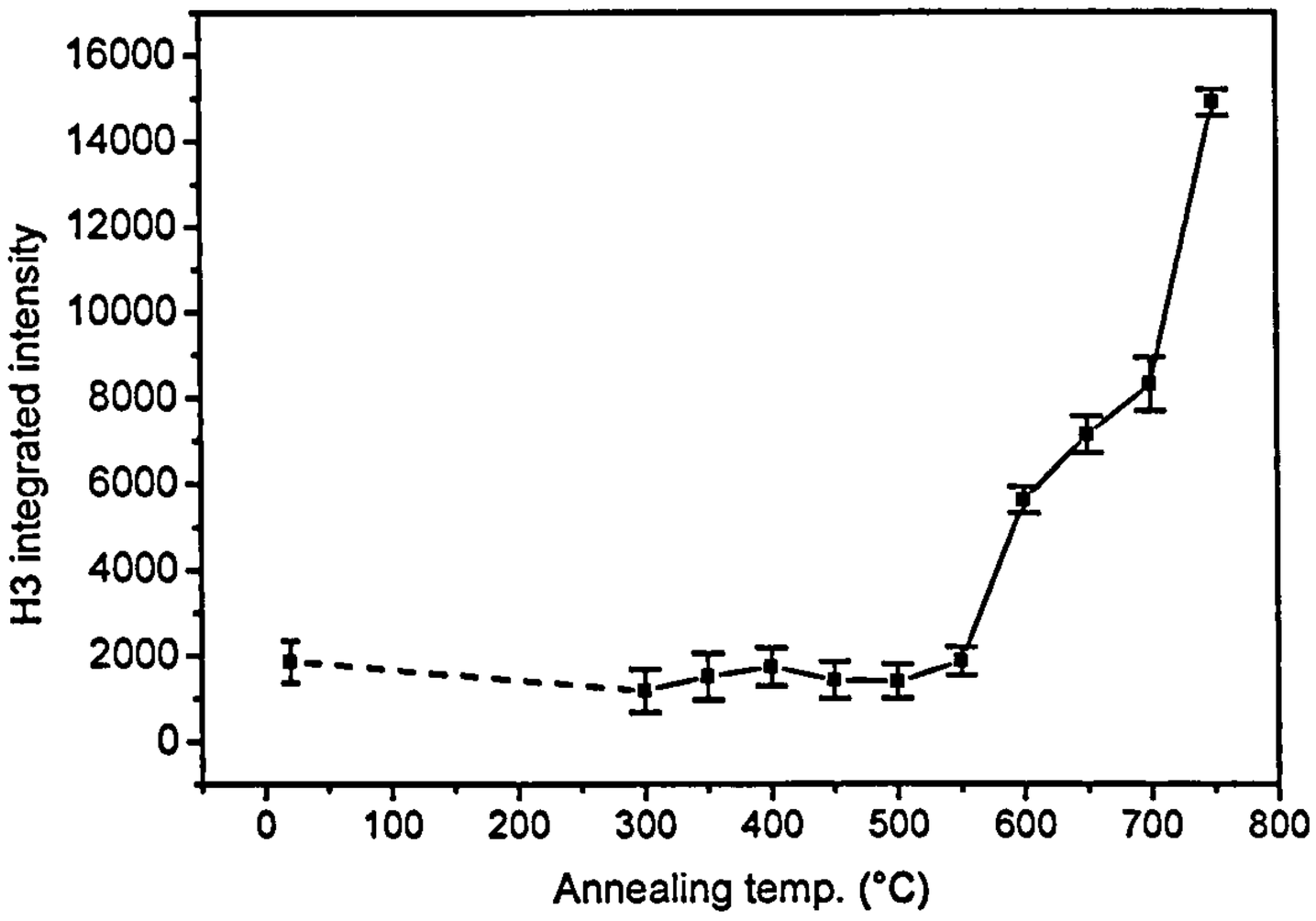

Figure 5.7. The change in integrated intensity of the H3 defect after isochronal (1 h) annealing at temperatures between 300°C (573 K) and 750°C (1023 K) in steps of 50°C.

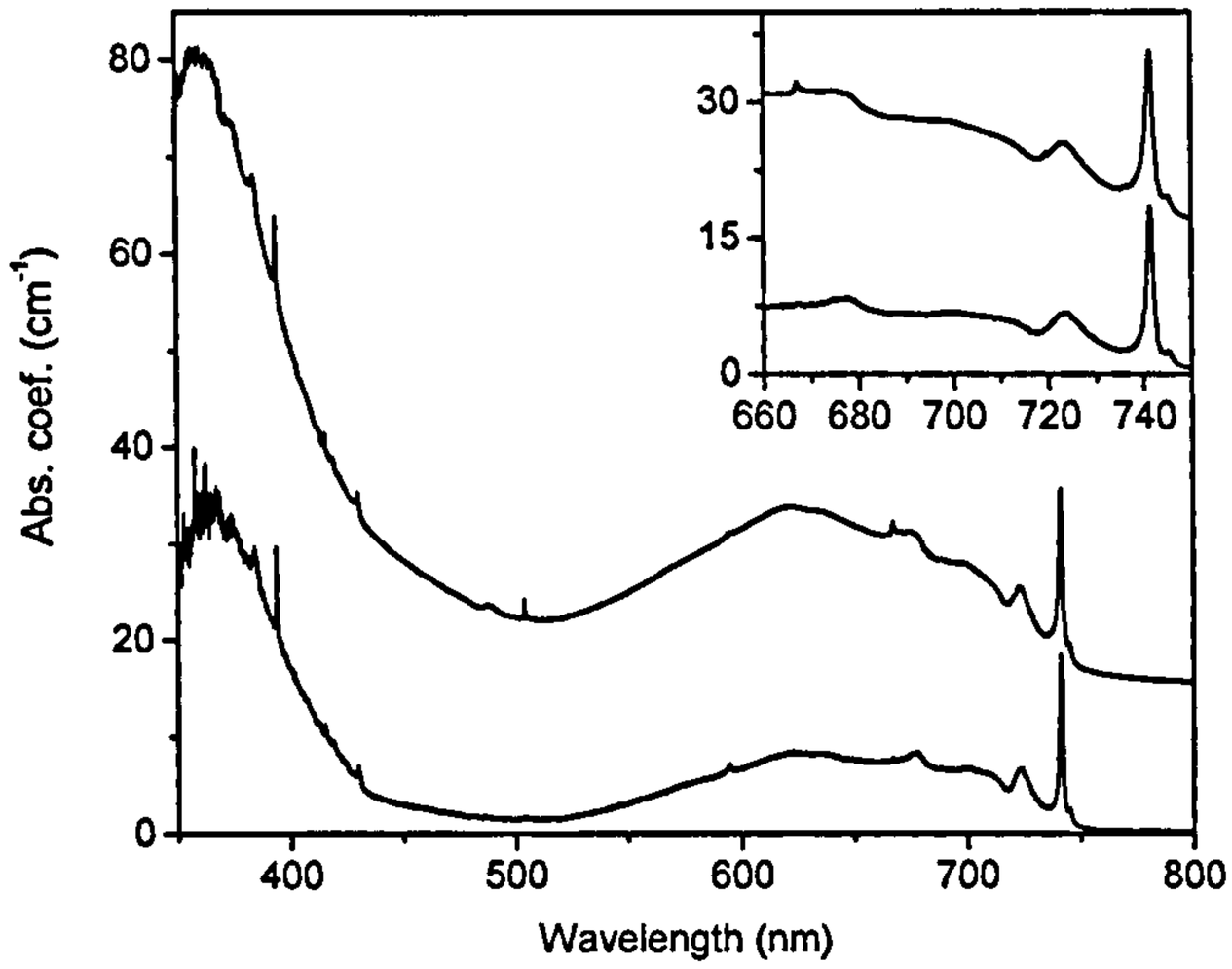

Figure 5.8. The change in the absorption spectrum of an irradiated diamond (top spectrum) after one hour annealing at temperature of 450°C (723 K) (bottom spectrum). The ZPL sharpens and decreases in strength (Collins 1999). The interstitial related absorption with a ZPL at 667 nm is almost completely removed after one hour annealing at 450°C (723 K) (see inset). Spectra were collected at liquid nitrogen temperature and have been shifted for clarity.

Treatment	$[V]^0$ (ppm)	FWHM (meV)
As irradiated	5.1 ± 1.5	3.66 ± 0.25
After 450°C, 1 hour	4.1 ± 1.2	3.29 ± 0.20

Table 5.1. The change in concentration and FWHM of the GR1 defect ZPL of the sample after irradiation and annealing at 450°C (723 K). The concentration of vacancies is determined as described in chapter 1, section 1.7.

In a second type Ia sample, irradiated and annealed at similar conditions, the FWHM of the GR1 line changed from 5.93 to 4.90 meV with an integrated intensity change from 110 to 88 meV cm^{-1} (vacancy concentration change from 5.20 ppm to 4.17 ppm). The uncertainty on all values is equal to these of the previous sample. Upon annealing, the 3H, 594 nm and 667 nm peaks in this sample behaved in an identical manner to their behaviour in the previous sample.

The results on these two samples confirms the approximately 20% loss of vacancies when an electron irradiated diamond is annealed at T ~ 450°C (673 K) (Iakoubovskii *et al.* 2003) and the results between the two samples are consistent.

5.2. Experimental

5.2.1. Sample description

Samples 1, 2, 3, 4-2 and 6-1 were electron irradiated with a dose of 8.10^{18} e^-/cm^2 and an energy of 8 MeV. The irradiation dose of sample 14 was 1.10^{17} e^-/cm^2 at 6 MeV. These samples were mounted on a water-cooled (20 °C) copper block. Samples 1 and 3 were annealed at 800°C (1073 K) for 1 hour under argon flow and sample 3 was then annealed at 1000°C (1273 K) for 1 hour in high vacuum ($P < 10^{-6}$ mbar). Samples 2, 4-2, 6-1 and 14 were annealed under HPHT conditions after irradiation. These results are reported in chapter six.

Sample 7 was electron irradiated with a dose of 1.10^{18} with an energy of 2 MeV. The sample was heated to 450°C (723 K) for 1 hour to remove the interstitials, and then annealed to 800°C (1073 K) for 1 hour to generate H3 and H4.

Sample 10 was electron irradiated with a dose of 1.10^{18} e^-/cm^2 (8 MeV). The colour of the diamond is orange yellow with strong H3 absorption because the sample was accidentally not cooled during irradiation.

Sample 1H7 is a type IaA/B diamond, HPHT annealed prior to irradiation (see chapter 6), and then irradiated (dose : 8.10^{18} e^-/cm^2, 8 MeV) and annealed at 900°C (1173 K) for 1 hour in a flow of argon.

Samples 1H7, 3, 4-2, 6-1 and sample 10 do not display platelet absorption in the IR.

Concentrations of A, B C, N^+ defects and the intensity of the D component were determined by the procedure as described in chapter 1, section 1.6 and are summarized in table 5.2.

Sample	A (ppm)	B (ppm)	D (cm^{-1})	C (ppm)	N^+ (ppm)	Irr dose (e^-/cm^2)	Irr energy (MeV)	GR1 (ppm)	ND1 (ppm)
Sample 1	613	212	0.84	0	0	8.10^{18}	8	6.8	1.9
Sample 2	660	243	0.99	0	0	8.10^{18}	8	7.4	1.8
Sample 3	0	2	0.00	0	0	8.10^{18}	8	4.1	$6.2\ 10^{-2}$
Sample 4-2	973	53	0.00	0	0	8.10^{18}	8	4.6	1.2
Sample 6-1	552	89	0.00	0	0	8.10^{18}	8	4.4	1.1
Sample 7	311	320	1.59	0	0	1.10^{18}	2	2.7	0.6
Sample 7 450°C	311	320	1.59	0	0	1.10^{18}	2	2.3	0.6
Sample 10	634	51	0.00	0	0	1.10^{18}	4	-----	-----
Sample 14	107	60	0.11	0	0	1.10^{17}	6	2.3	0.2
Sample 1H7	24	149	0.00	17	5	8.10^{18}	8	0.5	Saturation

Table 5.2. The concentrations of A, B, C and N^+ defects in the diamonds and the D absorption coefficient at 1282 cm^{-1}, determined from the IR spectrum of the diamonds and the concentrations of neutral and negatively charged mono-vacancies in the different samples. All samples, except sample 10 were irradiated at 20°C.

The uncertainty on the concentration of the concentration of defects determined by IR absorption measurements is 10%. The concentration of GR1 and ND1 defects is determined by the procedure outlined in Chapter 1, section 1.7, with an uncertainty of 30%.

Data on four further samples was kindly provided by K. Iakoubovskii from AIST institute, Japan. All samples were irradiated with electrons (1.10^{18} e^-/cm^2) and annealed isothermally up to 800°C or 720°C. Sample details are given in table 5.3. Sample K1 is a single growth sector of a synthetic type Ib diamond with [C] = 160 ± 20 ppm. After annealing at 720°C, a weak GR1 peak (neutral vacancy concentration of ~ 0.2 ppm) and a well detectable ND1 peak (negatively charged vacancy concentration of 1.0 ± 0.3 ppm) could be detected together with 8.2 ± 2.5 ppm of negatively charged N-V defects. After annealing at 1500°C for 1 hour, this N-V defect concentration did not change significantly ($[N\text{-}V]^-$ = 8.2 ppm). Sample details after 4 hour annealing is given in table 5.3. Sample K2 is a type IaA diamond with

[A] = 140 ± 14 ppm. After annealing at 800°C, 7.0 ± 2.1 ppm of H3 defects could be detected. Sample K3 is a type IaA/B diamond with [B] = 532 ± 53 ppm and [A] = 29 ± 3 ppm. After annealing at 800°C, 1.8 ± 0.5 ppm of H3 and 8.0 ± 2.4 ppm of H4 was detectable. Sample K4 is a type IaA diamond with ~ 1100 ppm of nitrogen in A defects.

Sample	A (ppm)	B (ppm)	D (cm^{-1})	C (ppm)	N^+ (ppm)	Irr dose (e^-/cm^2)	Irr energy (MeV)	GR1 (ppm)	ND1 (ppm)
Sample K1 irradiated	0	0	0	150	10	1.10^{18}	3	0.1	10
Sample K1 720°C	0	0	0	160	1			0.2	1
Sample K1 1500°C 1h	15	0	0	136	8			0	0
Sample K1 1500°C, 4h	48	0	0	125	7			0	0
Sample K2 irradiated	140	0	0	0	0	1.10^{18}	3	6.9	3.3
Sample K2 800°C	140	0	0	0	0			0	0
Sample K3 irradiated	29	532	2.46	0	0	1.10^{18}	3	7.8	4.3
Sample K3 800°C	29	532	2.46	0	0			0	0
Sample K4 irradiated	1077	0	0	0	0	2.10^{18}	3	8.8	7.4
Sample K4 760°C	1077	0	0	0	0			0	0

Table 5.3. The concentrations of A, B, C and N^+ defects in the diamonds and the D absorption coefficient at 1282 cm^{-1}, determined from the IR spectrum of the data of the samples of K. Iakoubovskii and the concentrations of neutral and negatively charged mono-vacancies in the different samples. All samples were irradiated at room temperature. The uncertainties in the concentrations are 10% and 30 % for defects determined by IR and UV-VIS measurements respectively.

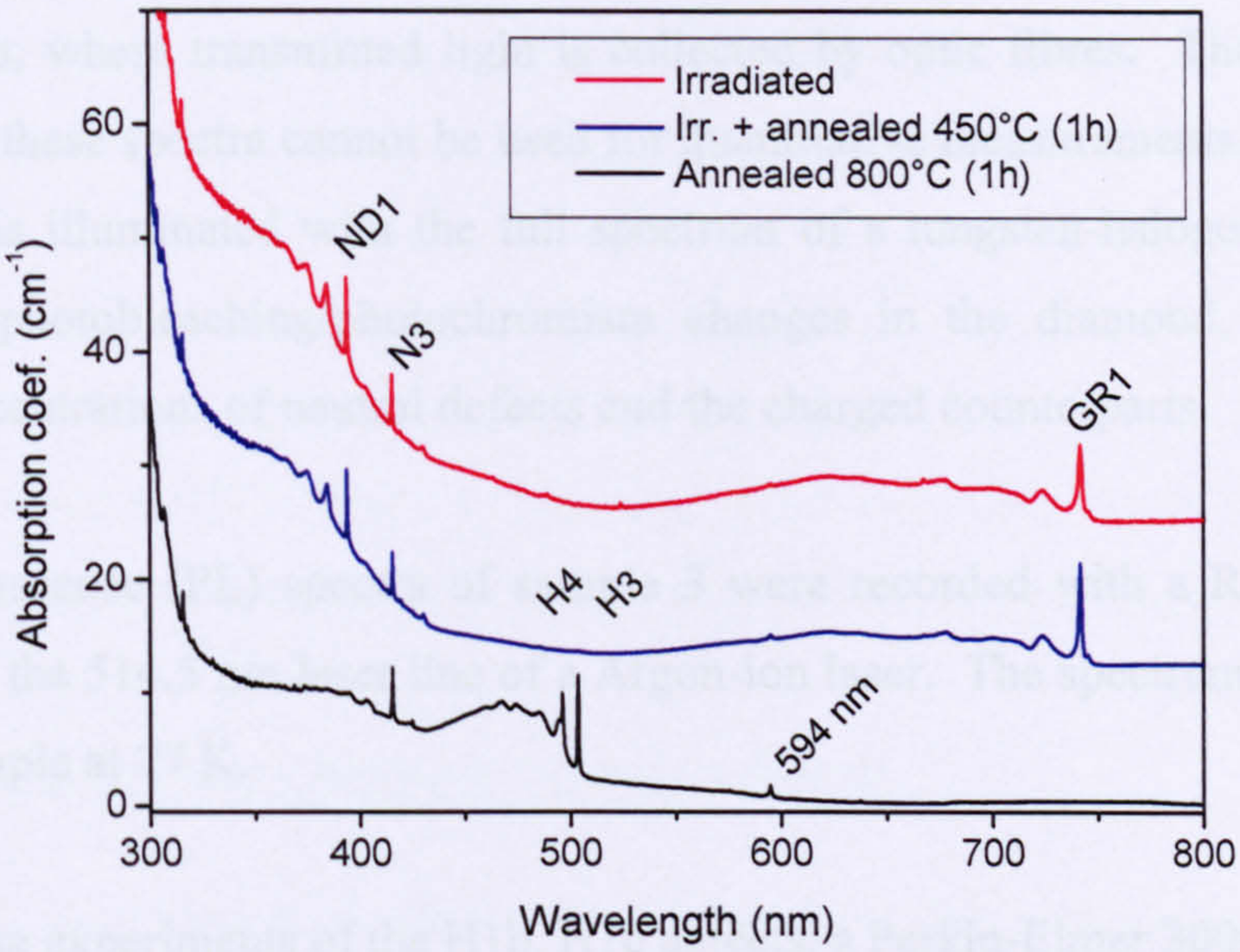

Figure 5.9. The UV-VIS spectra of sample 7 after irradiation, irradiation and annealing at 450°C (723 K), and after additional annealing at 800°C (1073 K) for 1 hour. Spectra were recorded at liquid nitrogen temperature and shifted for clarity.

5.2.2. Instrumental set-up

IR spectra were measured with a Bruker Equinox 55, equipped with a 5x beam condenser.

As already remarked in previous chapters, sample inhomogeneity is a problem when using diamonds. This can lead to confusing and incorrect results, especially when the sample must be taken out and reinserted in the IR beam. In order to place the sample in the IR beam as reproducibly as possible, it was moulded in indium, located in the sample holder of the beam condenser. Before recording the first spectrum, the peak value of the interferogram was recorded. The negative print of the sample in the indium was used to relocate the sample in the holder. The sample holder was then positioned in the x and y directions, perpendicular to the IR beam, with micrometer screws, until the same interferogram peak value was reached. This procedure ensured the best, reproducible repositioning of the sample.

UV-VIS-NIR absorption measurements from 220 nm to 900 nm were recorded with a Varian Cary 100 double beam spectrometer with 0.2 nm resolution. NIR

measurements (1000 - 800 nm) were recorded with the Princeton Instruments single beam system, where transmitted light is collected by optic fibres. The resolution is 0.5 nm, and these spectra cannot be used for quantitative measurements: in this set-up the sample is illuminated with the full spectrum of a tungsten-halogen lamp which may cause photobleaching/photochromism changes in the diamond, changing the relative concentrations of neutral defects and the charged counterparts.

Photoluminescence (PL) spectra of sample 3 were recorded with a Renishaw 2000 system with the 514.5 nm laser line of a Argon-ion laser. The spectrum was recorded with the sample at 77 K.

For bleaching experiments of the H1b, H1c defects, a Perkin-Elmer 3000 fluorescence spectrometer was used. The light source used was a 7 W Xenon flash lamp, and monochromatic light was selected by a 1200 g/mm grating and a slit, giving a spectral band width of the light on the sample of 5 nm. In situ illumination of the sample in the cryostat of the UV-VIS spectrometer and in the FTIR machine was done with commercially available light emitting diodes (LED), with maxima at 470 and 370 nm. After a few preliminary experiments, a thermal treatment at 500°C (773 K) for one hour was found to be the most efficient way to recover the peak intensity without the risk of surface etching after a large number of subsequent thermal treatments. The time required to saturate the bleaching effect depends strongly on the intensity of the light source: illumination with the intense light of a LED saturates the bleaching effect in a few minutes, while it was also found that it takes 30 minutes illumination of the sample with the Perkin-Elmer 3000 to saturate the bleaching. Selecting a smaller slit width (spectral band with of 2.5 nm) resulted in a few hours of illumination before the bleaching effect reached its saturation point. 30 minutes illumination with a spectral band width of 5 nm was chosen as a balance between sufficiently short experiment time and spectral resolution.

Samples were annealed at 800°C (1073 K) or 900°C (1173 K) under argon flow in a gas washing tube to avoid surface oxidization. The avoidance of surface oxidization eliminates the need to repolish the etched diamond surfaces and thereby reduced measurement errors. The outlet of the sample tube is guided through a gas washing bottle, filled with oil to prevent in-diffusion of oxygen. As a result the whole system

is at a slight overpressure which prevents in diffusion of oxygen. After annealing at 800°C or 900°C, the samples were cooled while remaining under argon flow and after one minute, the tube was opened and the samples were quenched in water at 20°C.

Samples annealed at 1000°C (1273 K) were inserted in a quartz tube under high vacuum ($P < 10^{-6}$ mbar) placed in a tubular furnace at the University of Antwerp. The furnace heated up to 1000°C in ~ 13 minutes. After annealing, the tube was retracted from the furnace and cooled in air to room temperature in ~ 10 minutes.

5.3. Vacancy trapping by nitrogen aggregate defects.

Prior to all illumination experiments discussed in later sections, the UV-VIS absorption spectra of every sample were measured. Example spectra of samples 1, 10 and 1H7 are shown in figure 5.9. To reduce errors due to photochromic behaviour of the defects, the UV-VIS measurements were halted as soon as total absorption in the UV region was reached (~ 300 nm). The influence of intense illumination/bleaching with light of different wavelengths will be investigated in later sections.

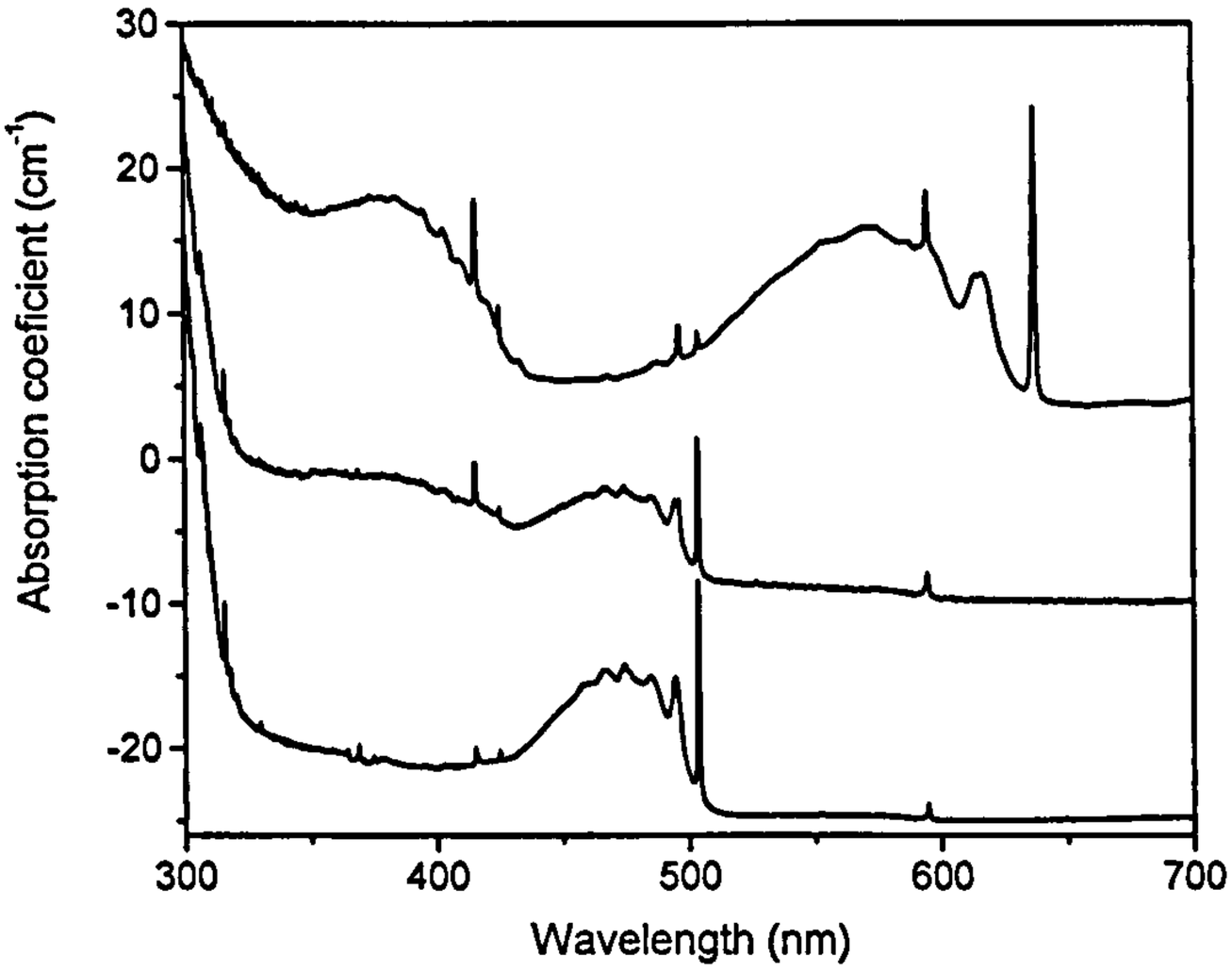

Figure 5.10. The UV-VIS absorption spectrum of the three samples recorded at liquid nitrogen temperature after irradiation and annealing at 800°C (1073 K). The top spectrum is of sample 1H7, the spectrum in the middle is of sample 10, and the spectrum in the bottom is of sample 1. Spectra have been shifted for clarity. Only sample 1H7 has a detectable H2 absorption peak.

5.3.1. UV-VIS measurements

After annealing, the GR1 absorption peak in the samples was decreased or destroyed and various nitrogen-vacancy or nitrogen aggregate-vacancy related peaks were detected (figure 5.10). In all cases we see additional absorption in the UV increasing with shorter wavelengths, which reduces when vacancies are mobile consistent with Davies (1992) (see figure 5.11).

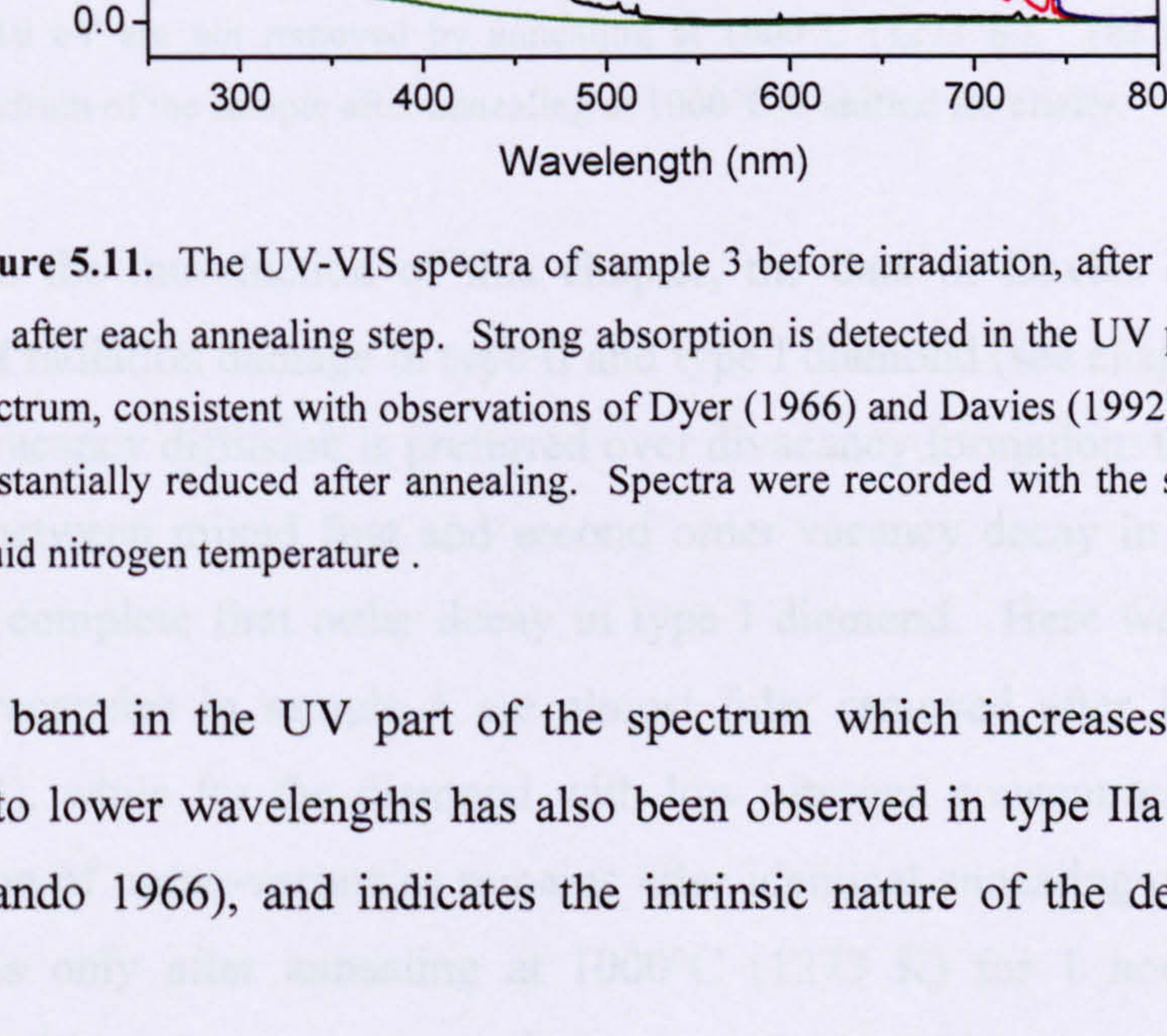

Figure 5.11. The UV-VIS spectra of sample 3 before irradiation, after irradiation and after each annealing step. Strong absorption is detected in the UV part of the spectrum, consistent with observations of Dyer (1966) and Davies (1992), which is substantially reduced after annealing. Spectra were recorded with the samples at liquid nitrogen temperature .

This broad band in the UV part of the spectrum which increases with increasing absorption to lower wavelengths has also been observed in type IIa diamonds (Dyer and Ferdinando 1966), and indicates the intrinsic nature of the defect causing the absorption.

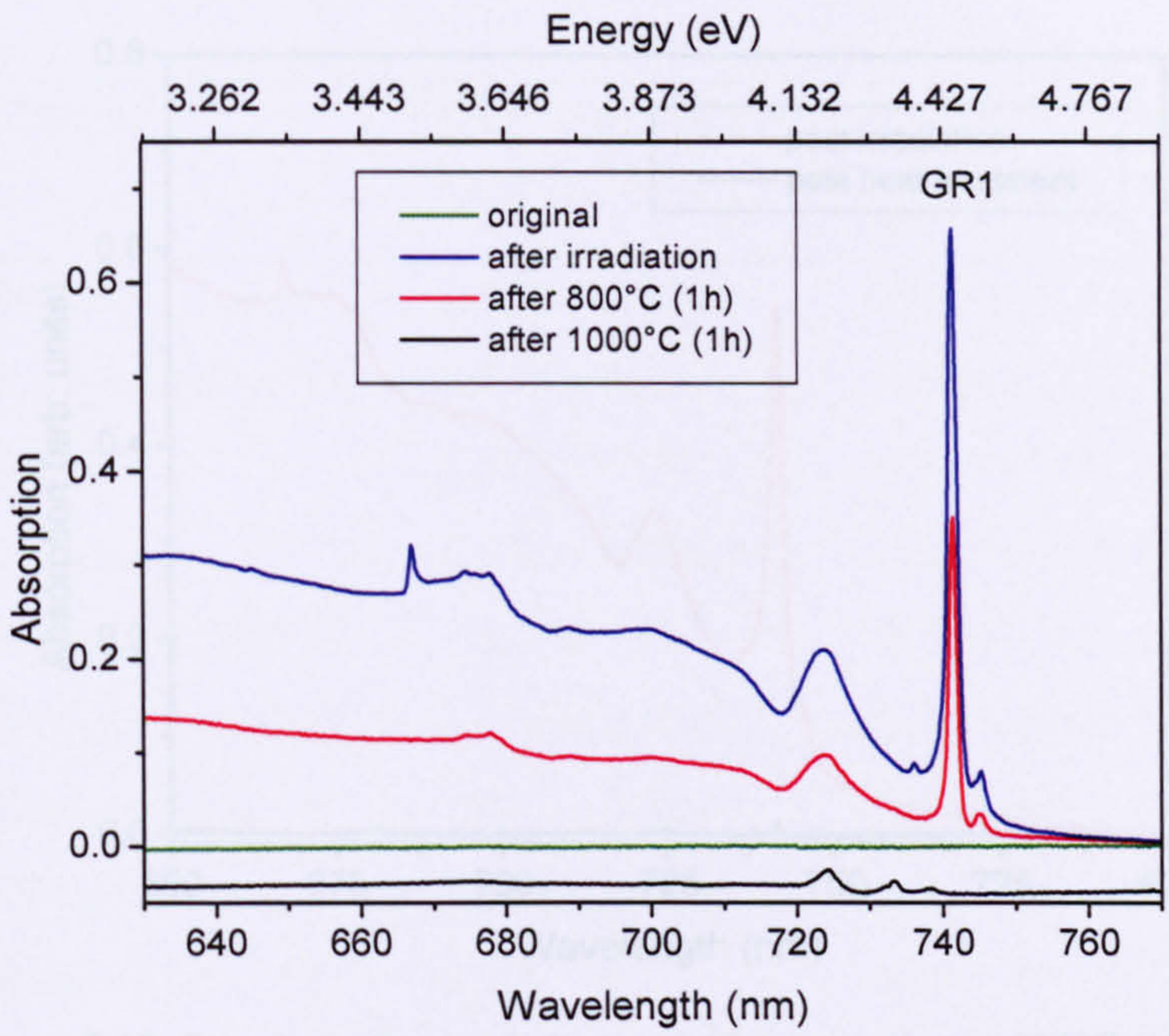

Figure 5.12. A more detailed view of the spectral region close to the GR1 peak in sample 3. No absorption is detected before irradiation, strong GR1 absorption is detected after irradiation. The GR1 peak is substantially reduced after annealing for 1 hour at 800 °C (1073 K), and is completely removed after annealing at 1000°C for 1 hour. The additional peaks at 1.679, 1.691 and 1.710 eV are not removed by annealing at 1000°C (1273 K). The (black) spectrum of the sample after annealing at 1000°C is shifted for clarity.

As stated in the introduction of this chapter, the data of Davies *et al.* (1992) on annealing of radiation damage in type II and type I diamond (see chapter one) indicate that mono-vacancy diffusion is preferred over divacancy formation: there is almost no difference between mixed first and second order vacancy decay in type II diamond and almost complete first order decay in type I diamond. Here we observe similar facts: the vacancies in sample 1 are almost fully removed after 1 hour annealing (figure 5.13), while for the diamond with low nitrogen concentration (sample 3) a large fraction of mono-vacancies remains after identical annealing conditions (figure 5.12). It is only after annealing at 1000°C (1273 K) for 1 hour that complete destruction of the vacancy concentration occurs (figure 5.12).

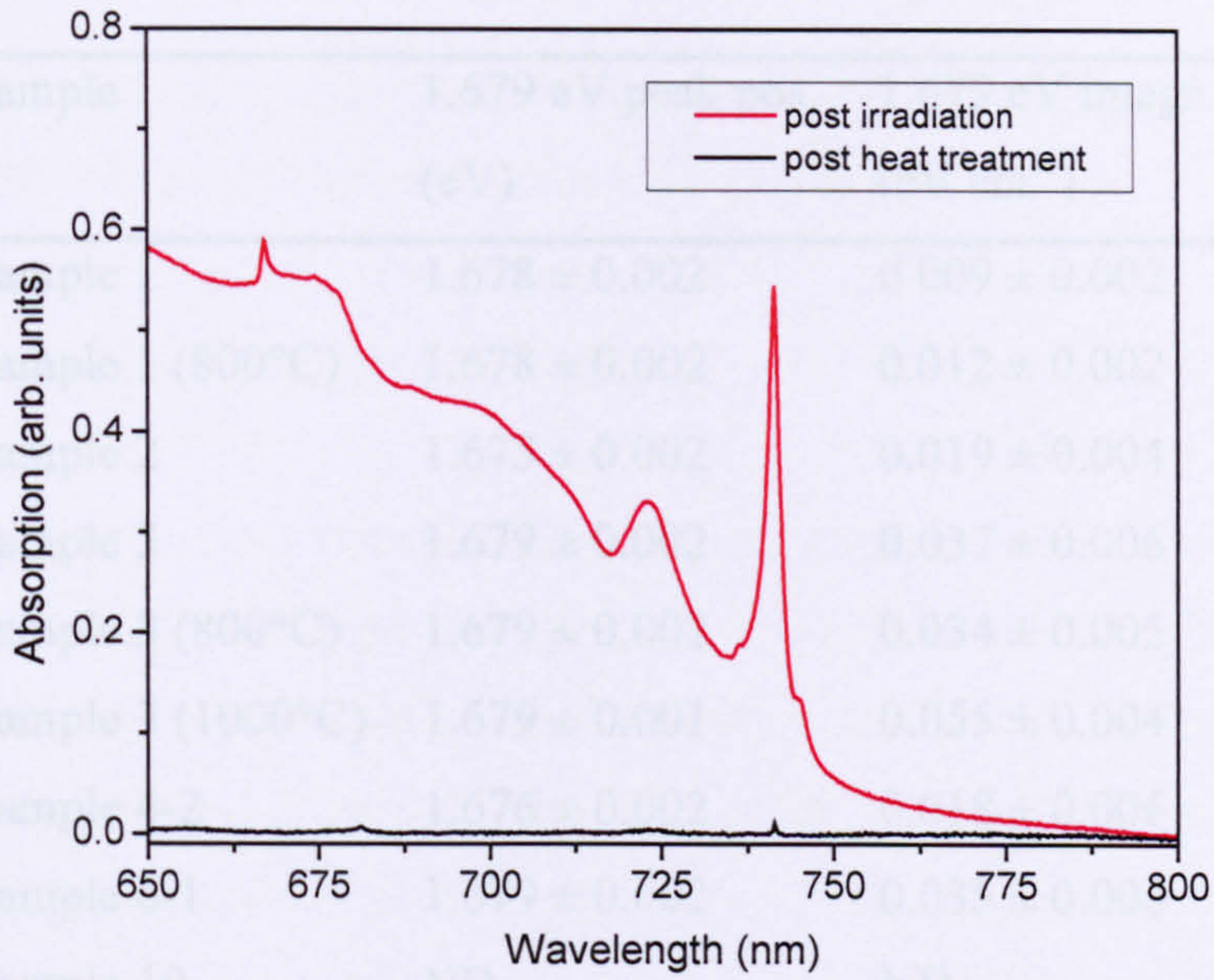

Figure 5.13. Sample 1 after irradiation and after annealing at 800°C (1073 K) for 1 hour. Spectra are recorded at liquid nitrogen temperature.

Davies (1974b) noticed additional structure in the side band of the GR1 spectrum at 1.685 eV (735.6 nm) and 1.665 eV line (744.4 nm). The line at 1.685 eV (735.6 nm) is now known to originate from self-interstitials. Davies (1982) showed the 744 nm peak originates from Jahn-Teller splitting of the ground level of the vacancy.

In this work additional peaks are noted at ~ 1.679, ~ 1.691 and ~ 1.710 eV and these peaks are still detectable after annealing at 1000°C (figure 5.12). The peaks are also detectable in the other samples before annealing, as the GR1/744nm peak pair cannot be deconvoluted properly by 2 Lorentzian peaks and proper baseline subtraction. An additional peak at ~ 1.679 eV is always needed to have proper peak fitting of the GR1/744 nm peak pair.

The exact position of the 1.679 eV peak is sample dependent (see table 5.4), indicating that this peak is probably the envelope of two peaks (Kiflawi *et al.* 2005).

Furthermore, the same peaks can be detected in the PL spectrum of sample 3 (figure 5.14) after annealing at 1000°C (1273 K), at almost exactly the same peak positions, suggesting these peaks are zero phonon lines.

Sample	1.679 eV peak pos. (eV)	1.679 eV integr. int. ($eV.cm^{-1}$)
Sample 1	1.678 ± 0.002	0.009 ± 0.002
Sample 1 (800°C)	1.678 ± 0.002	0.012 ± 0.002
Sample 2	1.675 ± 0.002	0.019 ± 0.004
Sample 3	1.679 ± 0.002	0.037 ± 0.006
Sample 3 (800°C)	1.679 ± 0.002	0.034 ± 0.005
Sample 3 (1000°C)	1.679 ± 0.001	0.055 ± 0.004
Sample 4-2	1.676 ± 0.002	0.018 ± 0.006
Sample 6-1	1.679 ± 0.002	0.035 ± 0.006
Sample 10	ND	ND
Sample 14	1.674 ± 0.002	0.100 ± 0.004
Sample 1H7	1.675 ± 0.002	0.006 ± 0.004

Table 5.4. The peak position, integrated intensity of the peak at ~ 1.679 eV in the samples. The values for peaks for sample 3 after annealing at 800 and 1000°C are also recorded. ND stands for not detected.

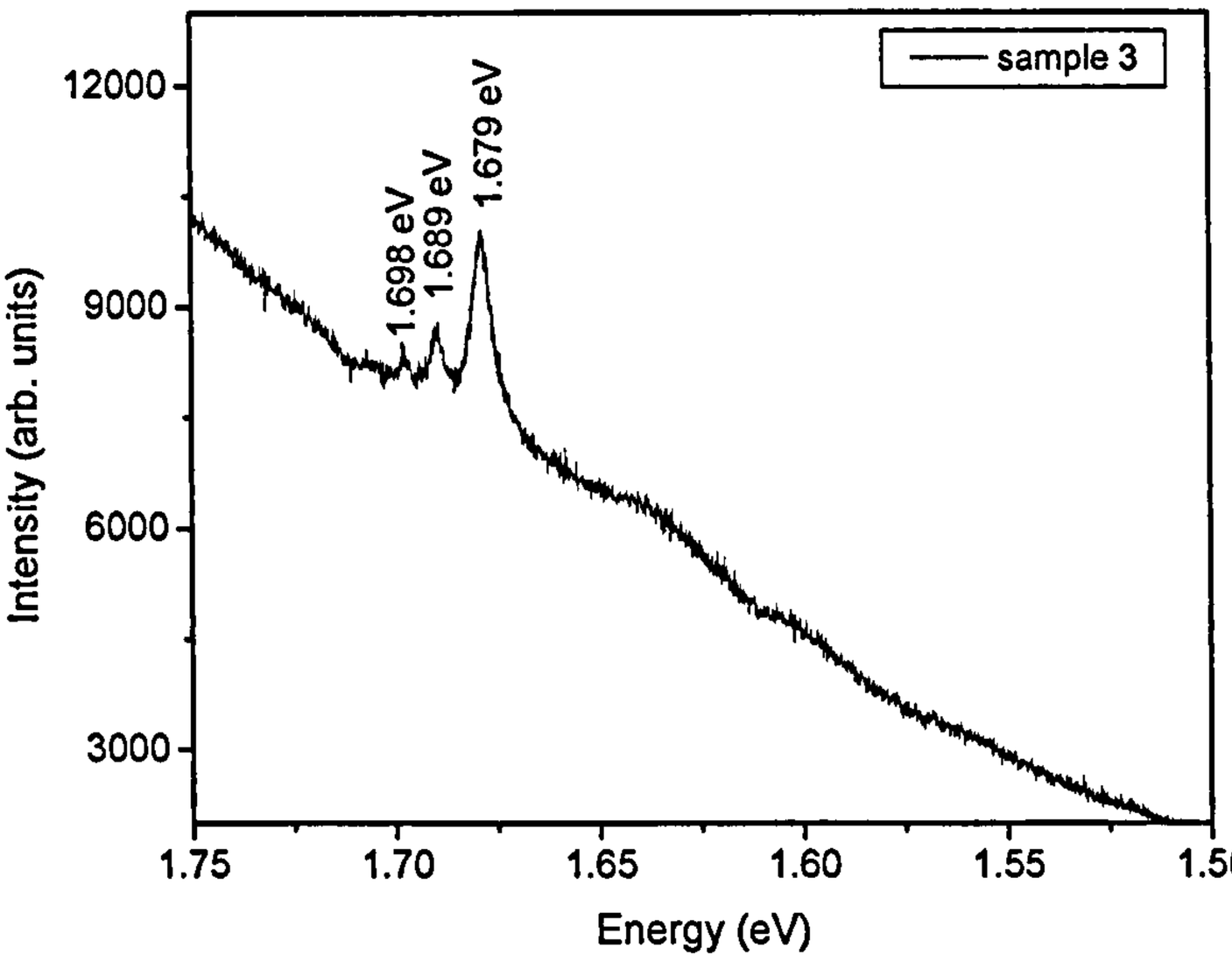

Figure 5.14. The PL spectrum of sample 3, recorded at liquid nitrogen temperature. The peak positions of the three peaks are almost the same as the peak positions of the peaks in the UV-VIS absorption spectrum.

Also, note that the relative intensities of the three peaks, detected in PL, are reversed compared to the absorption spectrum (figure 5.12 and 5.14):

- In PL: $I_{1.679\ eV} > I_{1.689\ eV} > I_{1.698\ eV}$
- In absorption: $I_{1.679\ eV} < I_{1.691\ eV} < I_{1.710\ eV}$

If the lines originate from the same defect, thermalization between different energy levels of the defect should be detectable by recording the PL spectrum with the sample at different temperatures. Unfortunately, at elevated temperatures, broad underlying background luminescence appears in the PL spectrum under the different lines, making the deconvolution of the peaks unreliable.

There is one marked difference between the peaks detected here and the peaks described by Kiflawi *et al.* (2006): in this study, the peaks are found to be stable up to 1000°C, while the peaks studied by Kiflawi *et al.* (2006) anneal out at 390°C after several hours. Therefore it is possible that peaks disappear upon annealing at 390°C and other peaks at the same position appear after annealing at 1000°C. Further research should clarify this point.

5.3.2. Captured fraction of vacancies by nitrogen related defects in diamond.

The vacancy capture of the various nitrogen aggregates is now investigated. Davies (1972), Clark and Davey (1984), Woods *et al.* (1990) and Lawson *et al.* (1992) studied the annealing behaviour of vacancies in type Ia diamonds and Davies *et al.* (1992) found that

$$[H3]/[H4] = 4\ [A]/[B] \qquad (5.3.1).$$

This relation is confirmed for the samples under study (figure 5.15), as long as no C defects are present. In that case, a relatively high negatively charged N-V defect concentration is detected. Sample 1H7 has 17 ppm of C defects and 5 ppm of positively charge C defects. This correlates very well with the detected concentration of $[N\text{-}V]^-$ defects of 4.5 ppm (see table 5.5). The sample also displays well detectable H2 absorption; taking the results at face value, this could be responsible for

discrepancy of the remaining 0.5 ppm of positively charged C defects. The total concentration of N-V-N defects is then 0.9 ppm and the ([H3]+[H2])/[H4] ratio is 0.8, if we suppose that 0.5 ppm of N^+ is compensated completely by the formation of H2 defects. In that case the ([H3]+[H2])/[H4] ratio of sample 1H7 would correlate very well with that of the other samples. However, once the uncertainties indicated in table 5.5 are taken into account, it is clear that this approach must be treated with caution. Also, as we shall see later (section 5.4.1), the calibration factors used to convert the areas of zero-phonon lines to concentrations of defects are still open to question.

Sample	[H3] (ppm)	[H4] (ppm)	$[N\text{-}V]^-$ (ppm)	[A]/[B]	[H3]/[H4]	$\frac{[H3]}{[A][V]}$	$\frac{[H4]}{[B][V]}$	$\frac{[637]}{[C_{total}][V]}$
Sample 1	3.3	0.3	-----	2.89	10.36	0.0016	0.0047	-----
Sample 3	0.00*	0.00*	-----	-----	-----	-----	-----	-----
Sample 7	2.6	1.0	-----	0.97	3.7	0.0032	0.0031	-----
Sample 10	2.3	0.1	-----	12.43	44.03	-----	-----	-----
Sample K1	-----	-----	8.2	-----	-----	-----	-----	0.0051
Sample K2	7.0	0.0	-----	-----	-----	0.0049	-----	-----
Sample K3	1.8	8.0	-----	0.05	0.23	0.0310	0.0015	-----
Sample K4	14.1	-----	-----	-----	-----	0.0009	-----	-----
Sample 1H7	0.40	1.12	4.5	0.16	0.36	-----	-----	-----

*In these cases, no H3 or H4 absorption could be detected.

Table 5.5. The concentrations of the various nitrogen-vacancy aggregates in the irradiated and annealed samples. $[C_{total}]$ is the total concentration of single nitrogen defects (C and N^+ defects). The uncertainty in the H3 and H4 concentrations is 30%. The uncertainties in the ratios [A]/[B] and [H3]/[H4] are 14% and 42% respectively. The uncertainty in the other calculated ratios is 45%.

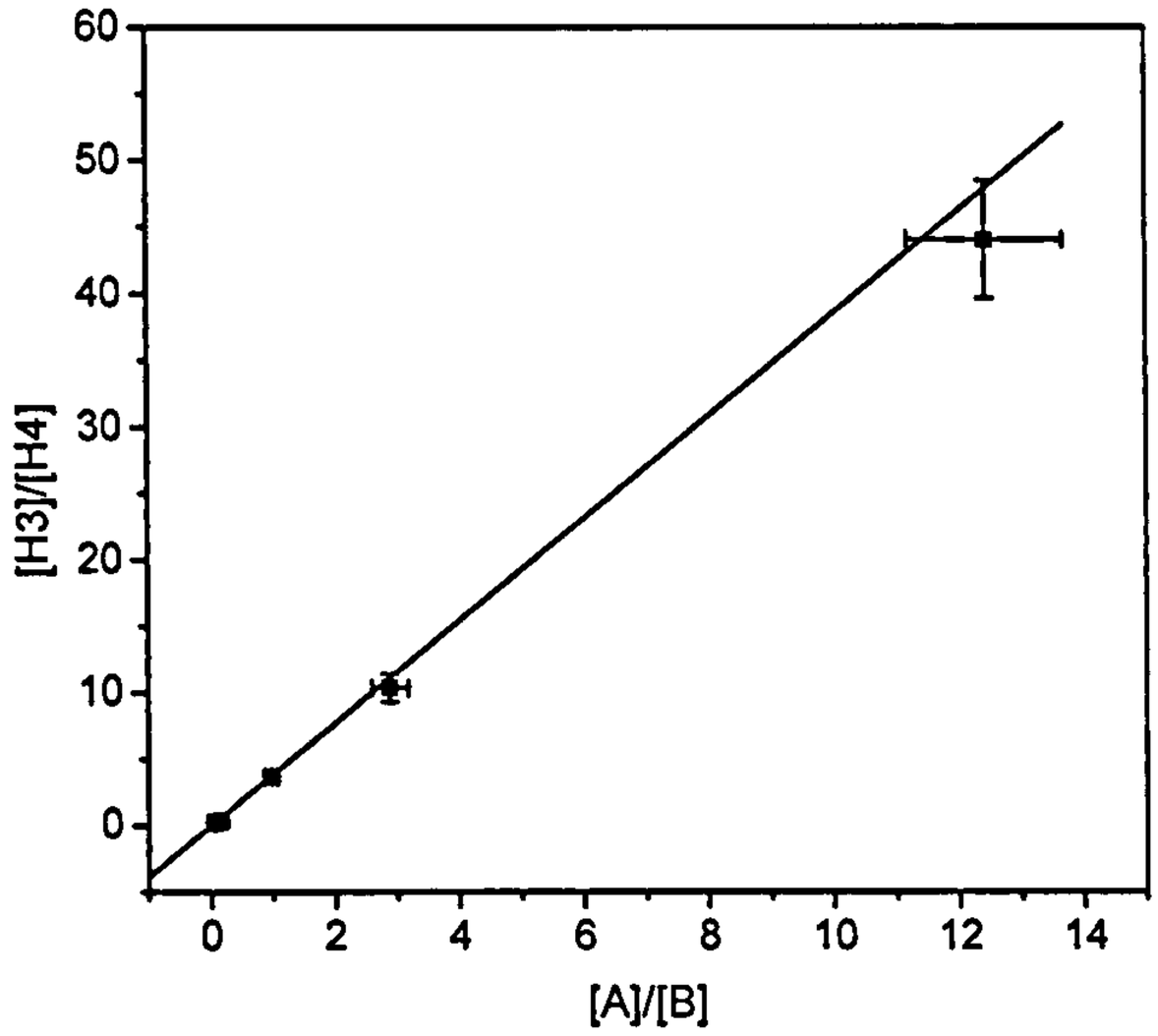

Figure 5.15. The [H3]/[H4] ratio as a function of the [A]/[B] ratio. The full line is a weighted least squares fit through the origin and gives a gradient of 3.85 ± 0.23, in good agreement with published data (Davies *et al.* 1992).

From the data of sample K1 and 1H7 (table 5.2 and 5.3), one can notice that C defects are very efficient trapping defects. Data in the literature (Collins 1980, Davies *et al.* (1992)) confirm the C defect to be a very efficient vacancy sink; this may be due to the absence of a vacancy barrier for N-V formation (Mainwood 1994).

The concentration of H3 (or H4) defects is proportional with the A defect and vacancy concentration (or B defect and vacancy concentration). The proportionality coefficient can be determined by dividing the H3 defect concentration by the A defect and vacancy concentration. When type Ia diamond is irradiated, the vacancy concentration is in most cases smaller than the A or B defect concentration and as a consequence, the proportionality factor should increase with decreasing A (or B) defect concentration when normalised to the vacancy concentration.

$$[H3]=\alpha[V][A] \text{ and } [H4]=\beta[V][B]$$

If all vacancies are trapped at nitrogen aggregates and in the absence of C defects, then the proportionality factor should be equal to the reciprocal value of the concentration of the nitrogen aggregate trapping defect:

$$\frac{[H3]}{[A]([V]-[H4])}=\alpha=\frac{1}{[A]} \qquad (5.3.2)$$

and

$$\frac{[H4]}{[B]([V]-[H3])}=\beta=\frac{1}{[B]} \qquad (5.3.3)$$

Because all vacancies are trapped at either A or B defects to form H3 or H4 defects, the difference between the total vacancy concentration and the H3 defect concentration should be equal to the H4 defect concentration: [V]-[H3] = [H4]

However, if not all vacancies are trapped then part of [V] in equations (5.3.2 and 5.3.3) is the concentration of vacancies trapped at H3 (or H4) and the concentration of vacancies lost to various other traps in the diamond (dislocations, surface, ...). In that case the concentration of vacancies minus the concentration of H3 must be larger than the concentration of H4, i.e. [V] – [H3] > [H4]. The same relation is found for the H3 defect concentration i.e. [V] – [H4] > [H3]. Equations 5.3.2 and 5.3.3 become:

$$\frac{[H3]}{[A]([V]-[H4])}=\alpha=\frac{1}{a[A]} \qquad (5.3.4)$$

and

$$\frac{[H4]}{[B]([V]-[H3])}=\beta=\frac{1}{b[B]} \qquad (5.3.5)$$

with a and b > 1; a and b are the multiple of H3 or H4 defect concentrations in the diamond which traps vacancies but is not detectable. So (a-1)[H3] or (b-1)[H4] is the total concentration of vacancy lost in optically undetectable sinks.

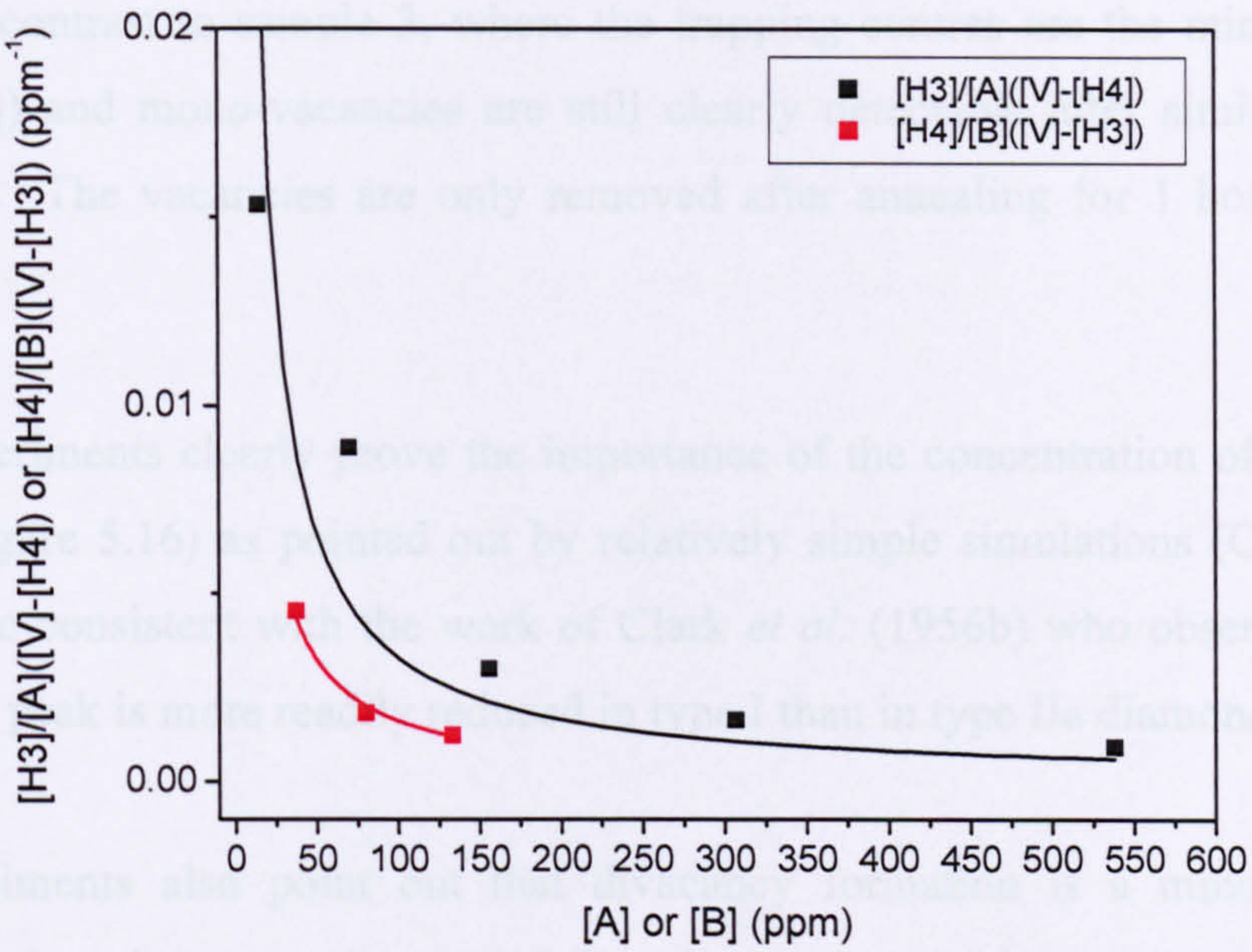

Figure 5.16. The ratio of the nitrogen aggregate-vacancy complex to the product of the nitrogen aggregate trapping defect concentration and the vacancy concentration as function of the nitrogen trapping defect concentration itself. The data is fitted with the rhs of equation (5.3.4). Note the concentrations are the concentrations of A and B defects and not the atomic concentration of nitrogen in the A and B defects.

Fitting of the datapoints calculated by formulas above gives for the datapoints a factor $a = 3.3 \pm 1.5$ and $b = 6.5 \pm 2.9$.

Checking the correctness of the values can be done very easily because the total concentration of vacancies before and after annealing must be identical.

$$[H3] + [H4] + (a-1)[H3] = [V] = [H3] + [H4] + (b-1)[H4] \qquad (5.3.6)$$

A very close fit of relation (5.3.6) to the experimental data can be reached when $a = 2.1 \pm 1.2$ and $b = 6.5 \pm 3.0$ equal to the factors a and b obtained by a reciprocal fit of the experimental data (figure 5.16) within experimental error. However, the errors are too large to allow a reasonable estimate of the number of vacancies lost to optically undetectable traps.

Note also that sample 1, with A and B defects as major trapping defects ([A] and [B] > [V]), only about 50% of the total vacancy concentration is trapped by annealing at 800°C for 1 hour, but no mono-vacancies are detected in the experimental spectrum.

This is in contrast to sample 3, where the trapping centres are the minority defects ([B] < [V]) and mono-vacancies are still clearly detectable after similar annealing conditions. The vacancies are only removed after annealing for 1 hour at 1000°C (1273 K).

These experiments clearly prove the importance of the concentration of the trapping defects (figure 5.16) as pointed out by relatively simple simulations (Collins 1998). This is also consistent with the work of Clark *et al.* (1956b) who observed the GR1 absorption peak is more readily reduced in type I than in type IIa diamond.

The experiments also point out that divacancy formation is a minor process in diamond; otherwise vacancies should then disappear at high rate, irrespective of the trapping defect concentration. This is in contradiction to the data for sample 3 and is further substantiated by the fact that

- Irradiated high purity CVD diamond must be annealed above 1000°C to remove the vacancies (Collins, personal communication).
- The vacancy concentration decrease by annealing of irradiated type Ia diamond with elevated concentration of nitrogen, follows first order kinetics.
- ~ 20% of the vacancies is lost by vacancy-interstitial recombination when diamonds are annealed at temperatures above 400°C (673 K). In type Ia diamond, almost all remaining vacancies are trapped at nitrogen aggregates, and almost no vacancies are lost to dislocations, divacancies or other optically inactive traps.
- The di-vacancy related TH5 band is under the H3 defect absorption side band making it hard to identify the TH5 band. Positron annihilation experiments indicate divacancies are stable up to 1100°C (Dannefaer, pers. comm.). However, no substantial decrease of the H3 absorption side band is detected when irradiated type Ia diamond is annealed at temperatures over 900°C (Collins *et al.* 2005). Also, Clark *et al.* (1956b) did not observe the TH5 band in irradiated and annealed diamonds.
- When divacancies or optically undetectable vacancy traps dissociate, the released mono-vacancies would be trapped at nitrogen aggregates, thereby increasing the absorption of H3 or/and H4 defects. However, there is no substantial rise in the

absorption strength of the H3 defect spectrum of an irradiated type IaA diamond when annealed (Collins *et al.* 2005) above 1000°C (figure 5.17).

For these reasons, divacancy formation and dissociation is neglected in all further simulations in this and further chapters.

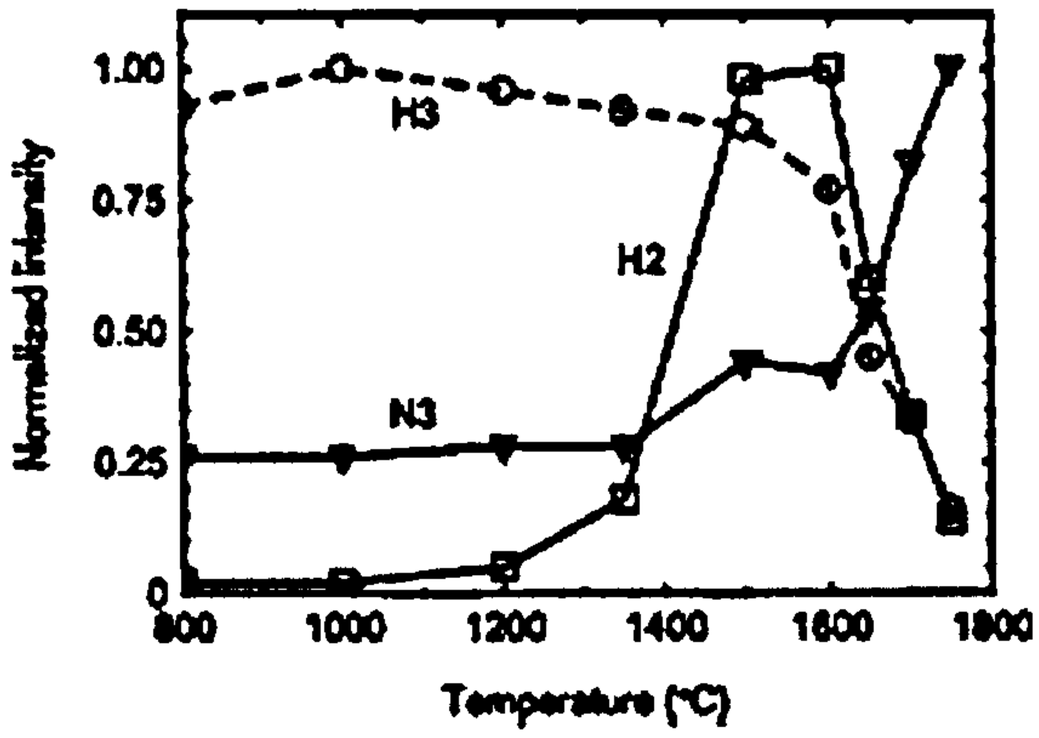

Figure 5.17. The change of the H3 absorption as function of isothermal annealing of an irradiated type IaA diamond (Collins *et al.* 2005).

5.3.3. The possible influence of platelets on the vacancy annealing kinetics of type IaA/B diamond

Because platelets are extended defects and consist of a layer of carbon interstitials, it is possible that platelets trap significant concentrations of vacancies during annealing of irradiated type IaA/B diamond. Vacancies can be absorbed by the platelet and interstitial atoms would then move into a regular lattice position.

The most significant change in platelet absorption is observed immediately after irradiation (figure 5.18.) and not when interstitials are mobile (at 450°C (723 K)) or when vacancies are mobile (at 800°C (1073 K)). Clearly, the platelets do not significantly change during annealing, and it is possible that the concentrations of interstitials and vacancies trapped by the platelets after irradiation and annealing is too small to detect a change in platelet properties. The experimental data presented here is on a limited sample set and further tests should be carried out.

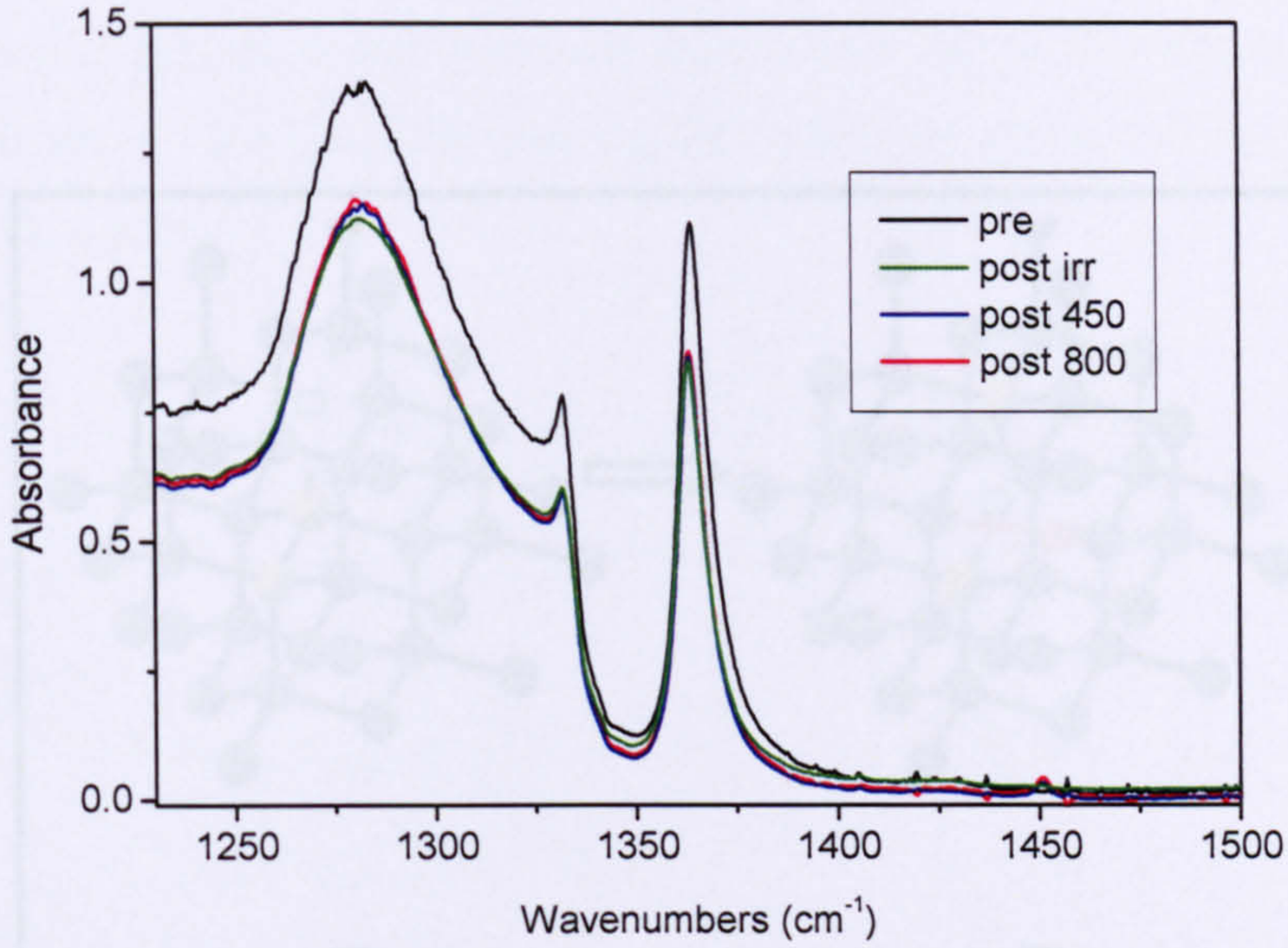

Figure 5.18. The platelet peak clearly decreases in intensity when the sample 7 is irradiated. No changes occur after annealing at 450°C, and 800°C. A similar decrease in intensity was observed in sample 1 and 2 after irradiation.

The decrease of intensity of the platelet peak is accompanied by a similar decrease in intensity of the D absorption component.

5.3.4. Annealing of type IaA/B diamond: H3 and H4 formation kinetics

Experimental and theoretical studies of Davies *et al.* (1992), Mainwood (1994) and Prins (2001) point towards a possible explanation of the relatively different capture efficiency between A and B defects and the slow and fast component of vacancy trapping by A defects in diamond: the vacancy has to overcome an energy barrier, greater than the vacancy diffusion energy, before being trapped at the defect itself. The origin of this barrier may be the energy required to restructure the defect from a N-N-V configuration into a N-V-N configuration: the A defect has D_{3d} symmetry and the H3 has C_{2v} symmetry, which is not a sub-group of D_{3d}, so the N-N + V configuration cannot simply restructure into a H3 defect configuration (see figure 5.19). These energy barriers are not equal for each vacancy aggregate or defect (Mainwood 1994): theoretical calculations predict there is no barrier for the formation of N-V defects, a barrier of 5.1 eV for H3 defects and 6.5 eV for H4 defects. However, Davies (1992) concluded that the barrier should be smaller than or equal to the uncertainty on the activation energy for vacancy diffusion.

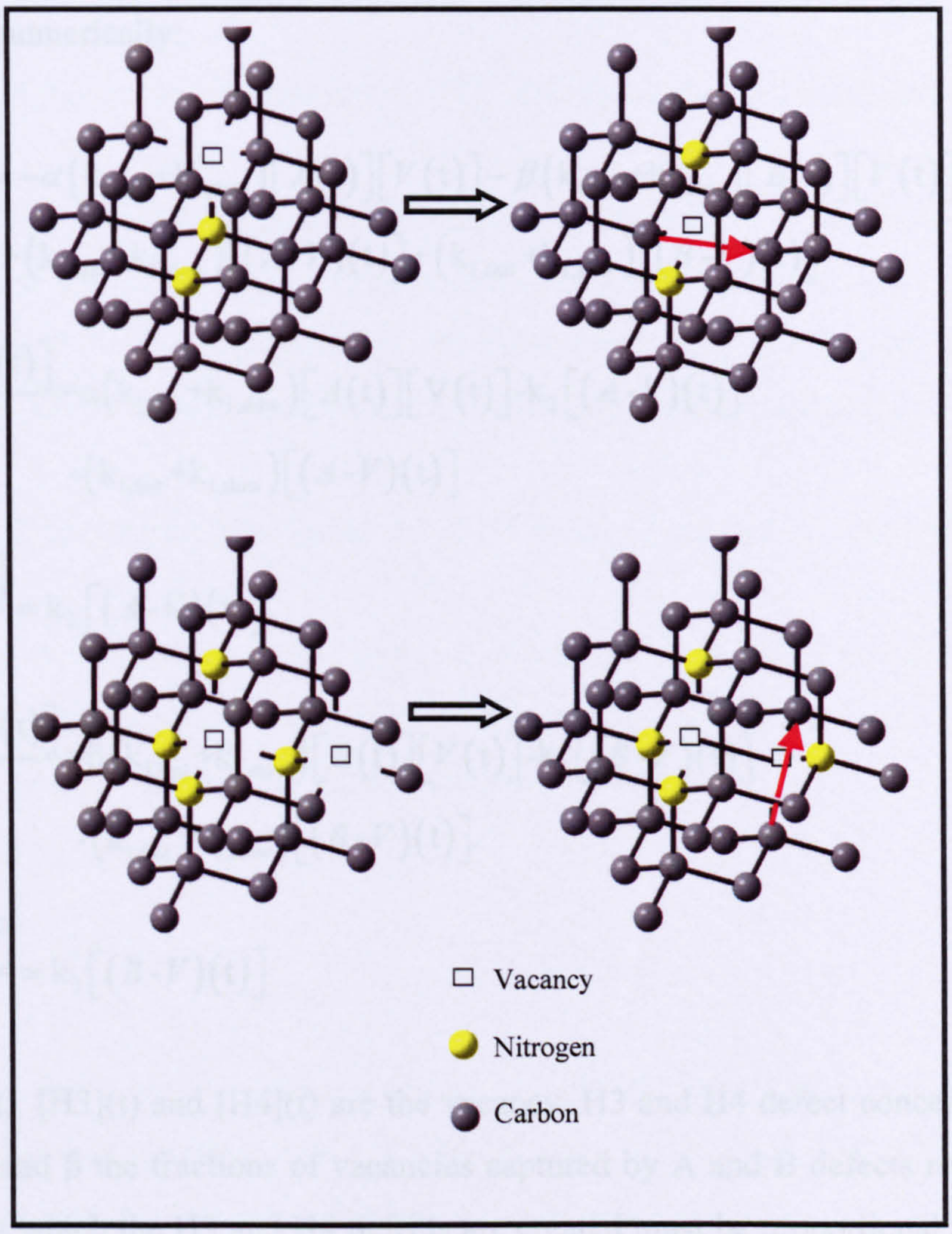

Figure 5.19. The formation of H3 and H4 defects; the vacancy is trapped at an A defect (a.) or B defect (b.) and the complex restructures into the H3 or H4 defect respectively defect. In each case, the number of dangling bonds of carbon atoms decreases from three to two. The red arrow indicates the direction of the dipole responsible for the optical absorption (Jones *et al.* 1994).

In the vacancy diffusion and trapping by nitrogen aggregates model presented below, the vacancy can diffuse through the diamond lattice until it encounters a nitrogen aggregate. An A-V complex is created and, provided there is enough energy, the vacancy can now overcome the energy barrier and restructure into a H3 defect or it cannot overcome the energy barrier and diffuses away from the A defect.

Equal concentrations of A and B defects should give rise to four times more H3 than H4 and this can be simulated by solving the following differential equations, which are solved numerically:

$$\frac{d[V(t)]}{dt} = -\alpha\left(k_{1,fast}+k_{1,slow}\right)[A(t)][V(t)] - \beta\left(k_{1,fast}+k_{1,slow}\right)[B(t)][V(t)] + \left(k_{1,fast}+k_{1,slow}\right)[(A-V)(t)] + \left(k_{1,fast}+k_{1,slow}\right)[(B-V)(t)] \quad (5.3.7)$$

$$\frac{d[(A-V)(t)]}{dt} = \alpha\left(k_{1,fast}+k_{1,slow}\right)[A(t)][V(t)] - k_2[(A-V)(t)] - \left(k_{1,fast}+k_{1,slow}\right)[(A-V)(t)] \quad (5.3.8)$$

$$\frac{d[H3(t)]}{dt} = k_2[(A-V)(t)] \quad (5.3.9)$$

$$\frac{d[(B-V)(t)]}{dt} = \beta\left(k_{1,fast}+k_{1,slow}\right)[B(t)][V(t)] - k_3[(B-V)(t)] - \left(k_{1,fast}+k_{1,slow}\right)[(B-V)(t)] \quad (5.3.10)$$

$$\frac{d[H4(t)]}{dt} = k_3[(B-V)(t)] \quad (5.3.11)$$

Here [V](t), [H3](t) and [H4](t) are the vacancy, H3 and H4 defect concentrations at time t, α and β the fractions of vacancies captured by A and B defects respectively. The rate at which the H3 and H4 defects are created must be proportional to the total concentration of trapping centres (Collins 1998) and the trapping cross sections (factors α and β).

The r.h.s. of equation 5.3.7 describes the loss of vacancies by first order kinetics when trapped by A (first term) and B defects (second term). The third and fourth terms describe the generation of vacancies when the vacancy diffuses away from the A-V configuration or the B-V configuration respectively.

The right hand side of equation 5.3.8 describes the capture of vacancies by the A defect by the fast and slow diffusion mechanism (first term), the formation of H3

from the A-V configuration (the second term) and the loss of the A-V combination when the vacancy diffuses away (third term).

Equation 5.3.9 describes the formation of H3 defects for the A-V configuration.

The right hand side of equation 5.3.10 describes the capture of vacancies by the B defect by fast and slow diffusion mechanism (first term), the formation of H4 due to restructuring of the B-V configuration into H4 (second term) and the loss of vacancies when the vacancy diffuses away from the B-V configuration (third term).

Equation 5.3.11 describes the formation of H4 defects from the B-V configuration.

$k_{1,fast}$, $k_{1,slow}$, k_2 and k_3 the are the fast and slow vacancy diffusion rate constants, the H3 formation rate constant, and the H4 formation rate constant respectively. The rate constants depend exponentially on the activation energy:

$$k_i = \nu_i . \exp\left(E_i / k_B T\right) \qquad (5.3.12)$$

with ν_i the vibrational pre-exponential factor, E_i the activation energy of the process, k_B the Boltzmann constant and T the temperature in Kelvin. The vibrational pre-factors have been determined by Davies *et al.* (1992).

Pre-exponential factors for the slow and fast vacancy diffusion processes are:

$$\nu_{1,slow} = (2.4 \times 10^{-8}\ s)^{-1},\ \nu_{1,fast} = (1.4 \times 10^{-9}\ s)^{-1} \qquad (5.3.13)$$

The pre-exponential factors for the rate constant to scale the energy barrier to H3 and H4 formation should be in the order of the vibrational frequency of the vacancy ($\sim 10^{13}$ Hz). However, since the experimentally determined pre-constant for vacancy diffusion is smaller, the highest experimentally determined pre-factor is used (the fast process).

$$\nu_2 = \nu_3 = (1.4 \times 10^{-9}\ s)^{-1} \qquad (5.3.14)$$

Using the slow component pre-exponential factors gives a slow initial rise of the H3 defect concentration and thus cannot account for the experimental data.

If there is no energy barrier, equal concentrations of A and B defects would give equal concentrations of H3 and H4 defects as there is no preferential trapping of vacancies at A or B defects. The energy barrier must be smaller than the experimental error on the vacancy diffusion energy (0.2 eV), and the simulated H3 increase during annealing must fit the data of Davies *et al.* (1992). This can be done if we introduce an energy barrier, of 2.50 eV and 2.61 eV (0.20 and 0.31 eV above the vacancy migration energy of 2.3 ± 0.2 eV respectively) for A-V to H3 and B-V to H4 restructuring respectively. The ratio of H3 to H4 defect concentration compared to A to B defect concentration for an annealing temperature of 800°C (1073 K) is then always different by a factor 4.

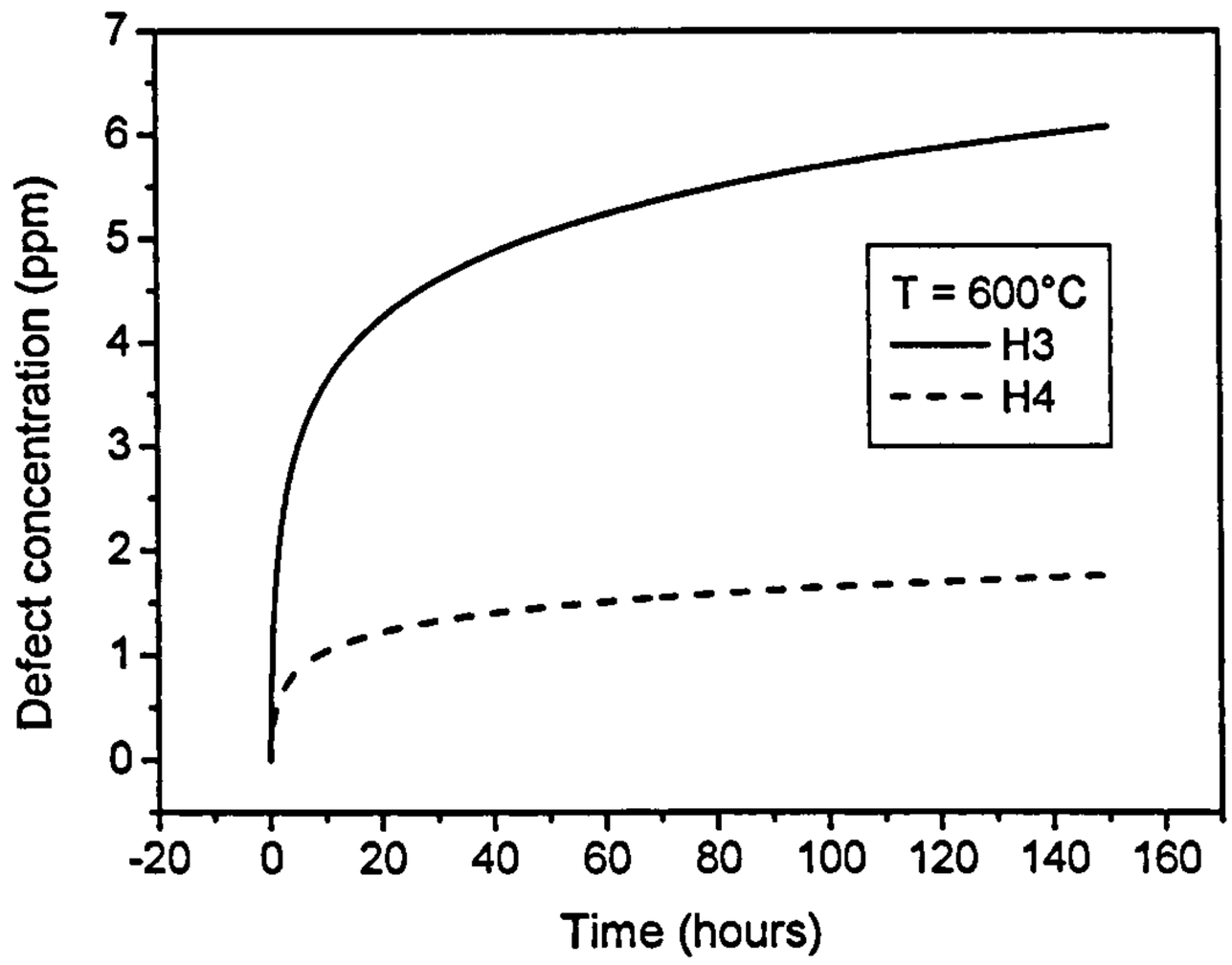

Figure 5.20. The simulated H3 and H4 defect concentration increase with time in a type Ia diamond with equal concentrations of A and B defects, annealed at 600°C. The behaviour of H3 is equal to the H3 behaviour described by Davies *et al.* (1992)

Simulation of the H3 and H4 defect concentration evolution with time with the parameters above an annealing temperature of 600°C can simulate the double exponential rise of the H3 defect concentration described by Davies *et al.* (1992) very

well (figure 5.20). For the simulations a vacancy concentration of 7 ppm is used, and the B defect concentration is set equal to the A defect concentration (296 ppm).

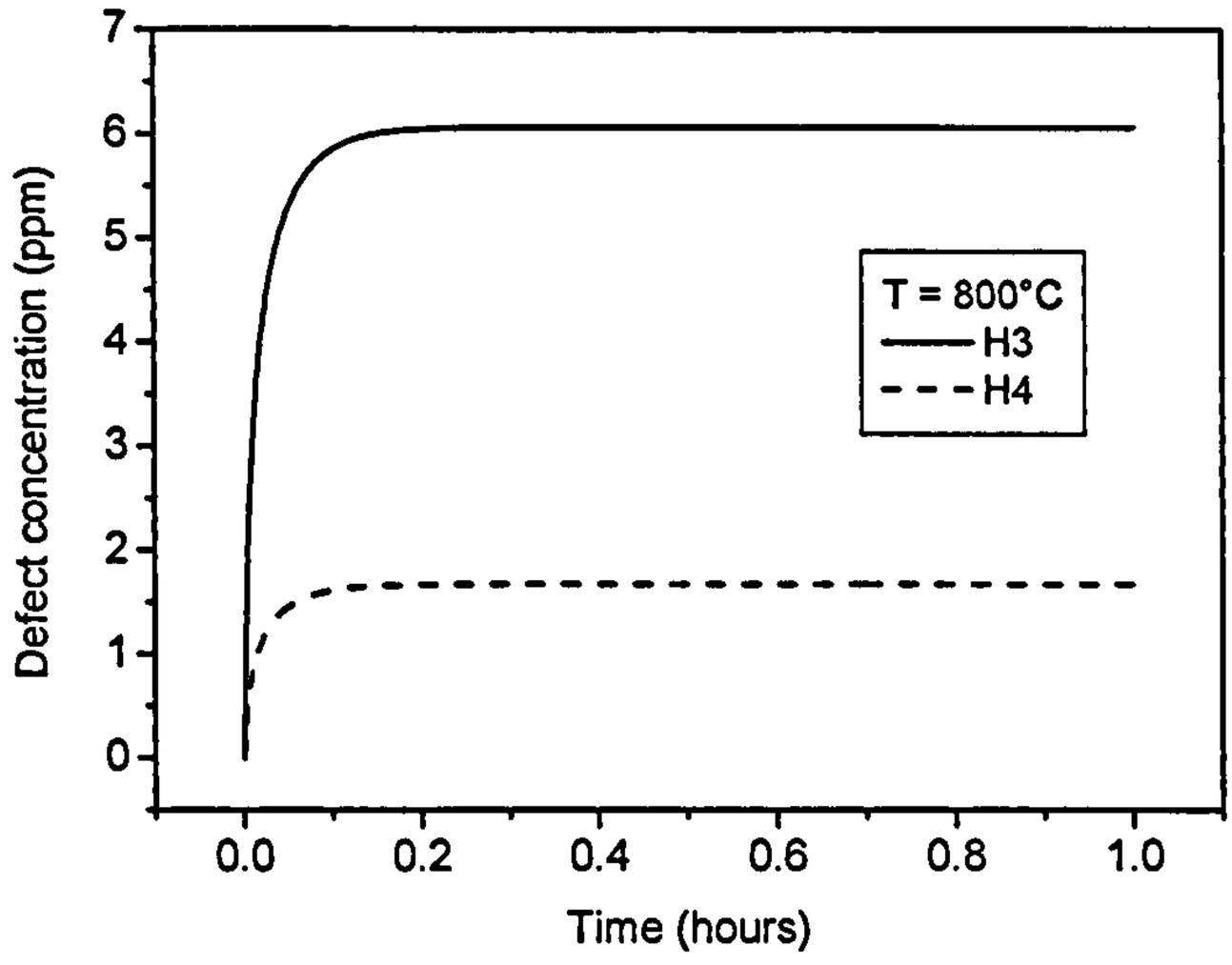

Figure 5.21. The simulated H3 and H4 defect concentration increase with time in a type Ia diamond with equal concentration of A and B defects, annealed at 800°C.

Simulation of the H3 and H4 defect concentration evolution with time for an annealing temperature of 800°C (1073 K) shows that all H3 and H4 is formed in less than 1 h annealing (figure 5.21), and only a very low concentration of GR1 should be detectable. This is indeed observed (figure 5.10).

In Davies *et al.* (1992), the vacancy decay in type IaA diamond is described by a double exponential, and neglecting the formation of di-vacancies as the concentration of trapping centres is larger than the vacancy concentration by two orders of magnitude; the vacancy decay could be described by a double first order decay. A mixed double first and second order decay cannot describe the time evolution of the vacancies as this would induce a very fast initial decrease in vacancy concentration which is not observed (see figure 5.22).

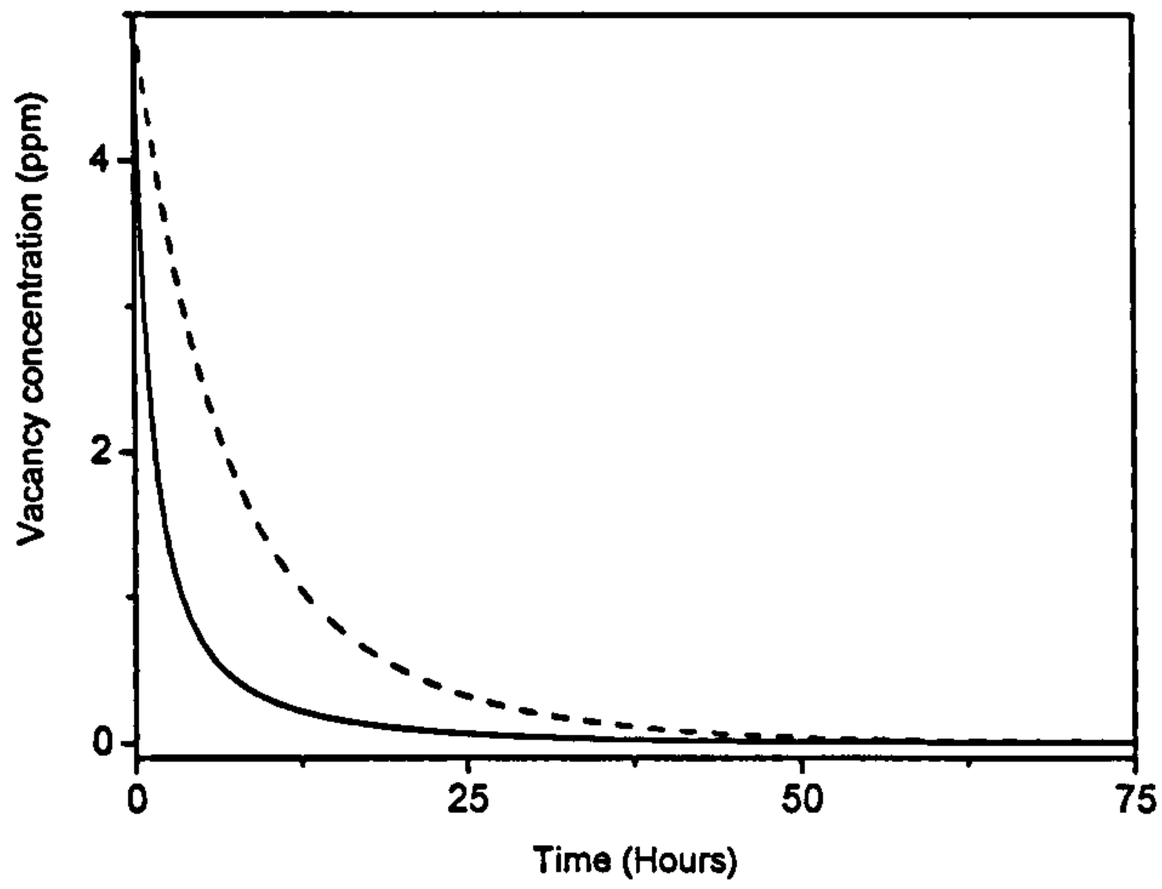

Figure 5.22. The simulated vacancy concentration decrease with time in a type Ia diamond with equal A and B defect concentration, annealed at 600°C (873 K). The decay is modelled with mixed double first order (fast and slow process) and second order decay (solid curve) and double first order decay only (broken curve). The double first order decay fits the experimental data of Davies *et al.* (1992) the best.

Here we propose an alternative model which needs only one diffusion rate for the vacancy and gives a possible explanation for the decrease in fast fraction when irradiated samples are annealed at higher temperatures.

In this model, all vacancies diffuse with the same diffusion rate but the vibrational pre-factor in the diffusion rate constant is different ($\nu \sim (0.6\ 10^{-9}\ s)^{-1}$) from the values used by Davies *et al.* (1992). To account for the results in the literature, we introduce an energy barrier around, but not at the A and B defect, with slightly higher activation energy for vacancy diffusion (2.5 and 2.6 eV for the A and B defect respectively). The differential equations describing this model are the following:

$$\frac{d[V(t)]}{dt} = -\alpha k_1[A(t)][V(t)] - \beta k_1[B(t)][V(t)] - k_1[V(t)] - k_1[V(t)]^2 + k_1[A_{barrier}(t)] + k_1[B_{barrier}(t)] \quad (5.3.15)$$

$$\frac{d[A_{barrier}(t)]}{dt} = \alpha k_1[A(t)][V(t)] - k_2[A_{barrier}(t)] - k_1[A_{barrier}(t)] \quad (5.3.16)$$

$$\frac{d\left[(A\text{-}V)(\mathrm{t})\right]}{d\mathrm{t}} = -\mathrm{k}_1\left[(A\text{-}V)(\mathrm{t})\right] - \mathrm{k}_1\left[(A\text{-}V)(\mathrm{t})\right]^2 + \mathrm{k}_2\left[A_{barrier}(\mathrm{t})\right] - \mathrm{k}_2\left[(A\text{-}V)(\mathrm{t})\right] \quad (5.3.17)$$

$$\frac{d\left[H3(\mathrm{t})\right]}{d\mathrm{t}} = \mathrm{k}_1\left[(A\text{-}V)(\mathrm{t})\right] \quad (5.3.18)$$

$$\frac{d\left[B_{barrier}(\mathrm{t})\right]}{d\mathrm{t}} = \beta\mathrm{k}_1\left[V(\mathrm{t})\right] - \mathrm{k}_3\left[B_{barrier}(\mathrm{t})\right] - \mathrm{k}_1\left[B_{barrier}(\mathrm{t})\right] \quad (5.3.19)$$

$$\frac{d\left[(B\text{-}V)(\mathrm{t})\right]}{d\mathrm{t}} = -\mathrm{k}_1\left[(B\text{-}V)(\mathrm{t})\right] - \mathrm{k}_1\left[(B\text{-}V)(\mathrm{t})\right]^2 + \mathrm{k}_3\left[B_{barrier}(\mathrm{t})\right] - \mathrm{k}_1\left[(B\text{-}V)(\mathrm{t})\right] \quad (5.3.20)$$

$$\frac{d\left[H4(\mathrm{t})\right]}{d\mathrm{t}} = \mathrm{k}_3\left[(B\text{-}V)(\mathrm{t})\right] \quad (5.3.21)$$

In this model vacancies are created by irradiation in and outside the capture radius around the A and B defect (figure 5.23). When vacancies start to diffuse at 600°C (873 K), the vacancies within the capture radius can freely diffuse to the A or B defect and create an H3 or H4 defect. This will account for the fast diffusion rate of vacancies and the equally fast formation rate of H3. The vacancies outside the capture radius have to scale the energy barrier before they can enter the capture radius. This will slow down the formation of H3 and H4 defects, accounting for the slow diffusion rate of vacancies and slow creation of H3 defects. Small changes in the diffusion energy of the vacancy are possibly caused by changes in electron distribution when the vacancy approaches the A or B defect. Dilatation of the vacancy and A defect cause a deviation from ideal sp^3 charge distribution of the surrounding carbon atoms. When the vacancy approaches the A defect or B defect, the delocalised electrons of the distorted sp^3 configurations will interact, causing a change in the diffusion energy. Because the distortion of the A defect and B defect is different, their perturbation on the vacancy diffusion energy will be different. Theoretical calculations indicate a

weak change in the vacancy diffusion energy when it approaches the A or B defect, but the changes are too small (J. Goss, personal communication) to differentiate.

The difference in barrier height at the A and B defect will result in a different ratio for H3/H4 compared to [A]/[B] ratio. As the difference between the energy barrier and the vacancy diffusion energy is small, annealing at higher temperatures will appear to happen with the fast diffusion rate only. However, the fast fraction should increase with increasing nitrogen concentration, which is not observed (Davies *et al.* 1992). Similar accuracy in fitting the experimental data of Davies *et al.* (1992) as with the double first order decay model can be reached with slightly different vibrational pre-factors (figure 5.24) and with a barrier height of 0.2 eV and 0.3 eV for the A and the B defect respectively.

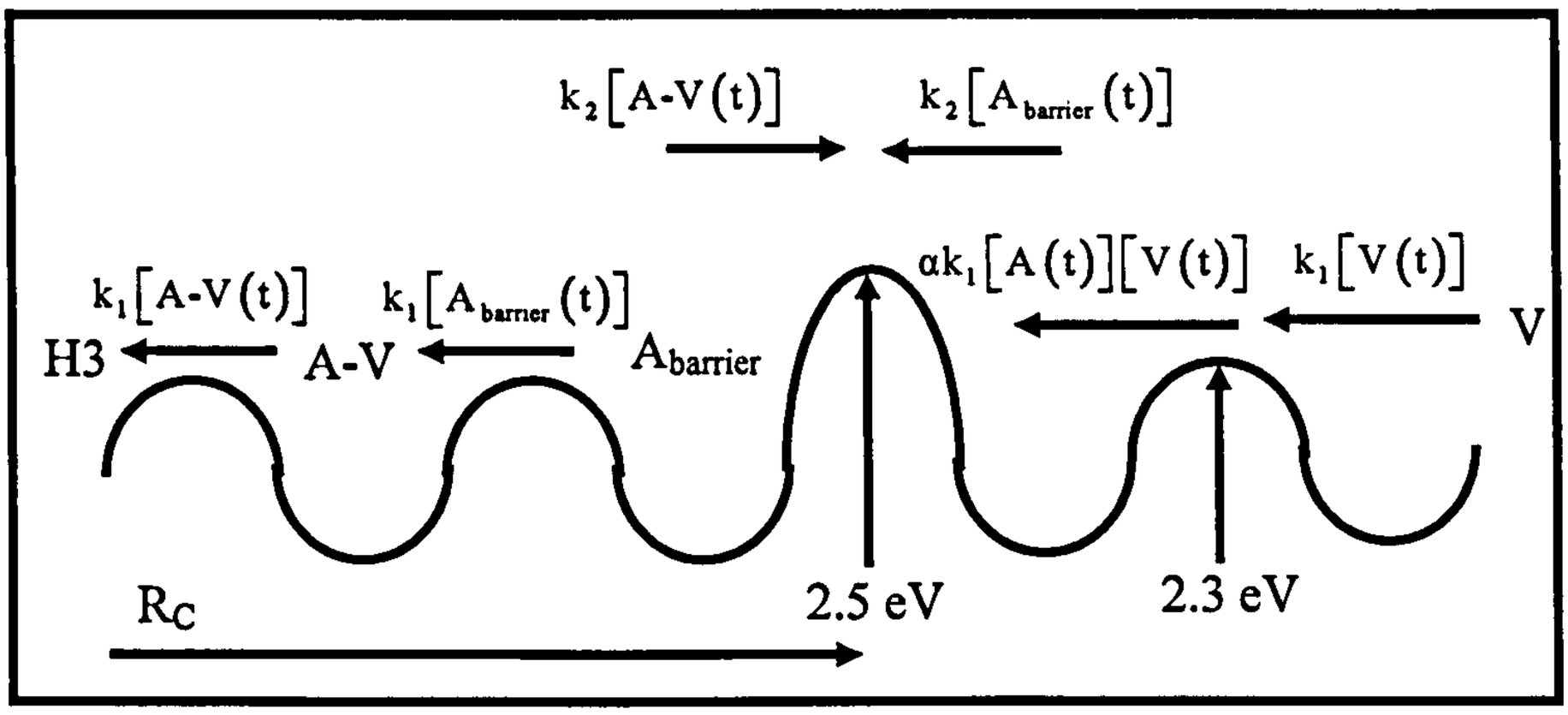

Figure 5.23. The single first order decay model for vacancies in type IaA diamond, where vacancies are preferentially created inside the capture radius R_C. These can diffuse freely to the A defect and restructure to an H3 defect. A fraction of the vacancies created outside the capture radius (α[A(t)].[V(t)]) of these vacancies diffuses to the A defect. These vacancies outside the capture radius have to overcome an energy barrier before being trapped inside the A defect capture radius. Vacancies inside the capture radius can also overcome the energy barrier and diffuse away from the A defect.

As temperature increases, the barrier height will become insignificant and the increase of the H3 defect concentration will appear to be single first order as experimentally observed by Davies *et al.* (1992).

To account for the relatively high concentration of the perturbed charged vacancies, 40% of the vacancies must be created close to the nitrogen aggregates (Davies *et al.* 1992), which will be within the capture radius. This also means that the concentration of vacancies is proportional to the concentration of nitrogen.

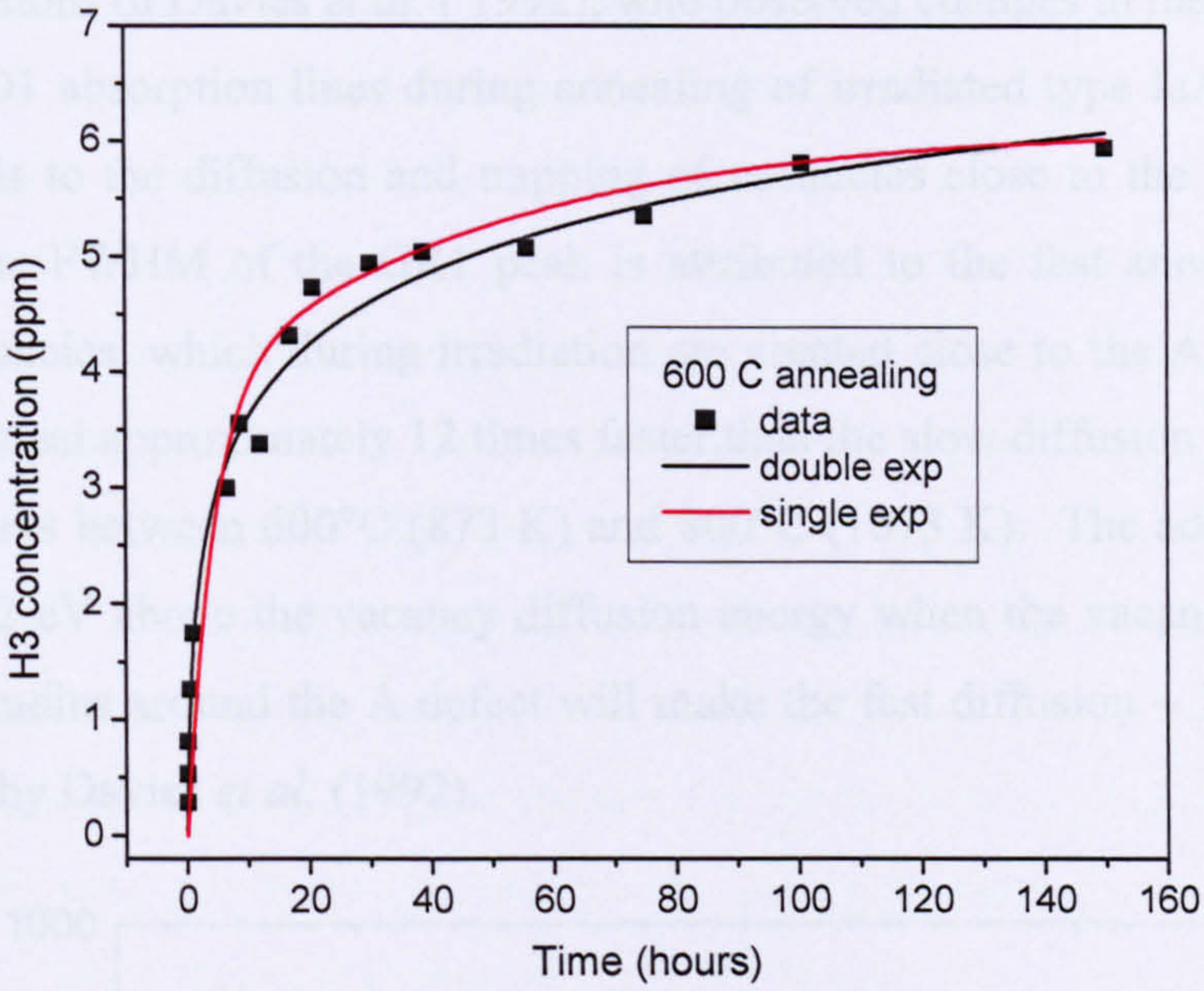

Figure 5.24. The difference between the single first order vacancy decay model with an energy barrier around the A defect and the double first order decay model. In the single first order vacancy decay model, ~ 40% of the vacancies is located between the A defect and its energy barrier.

This 40% of vacancies is created within a few atomic lattice spacing from the nitrogen aggregates: if one simulates the distance distribution for the concentrations of vacancies (7 ppm) and A defects (296 ppm), with defects positioned randomly on microscopic level but homogeneously at macroscopic level, then the average distance between the A defect and a vacancy is 9.7 atomic nearest neighbour distances (figure 5.25). About 50% of the vacancies are created within 10 atomic nearest neighbour distances. If 40% of the vacancies is created within 3 to 4 units of nearest neighbour distance, then the proximity of the A defect must promote the formation of vacancies or prevent vacancy-interstitial recombination. This can be caused by reduction of the interstitial recombination enhanced diffusion by the presence of the A defect close to the nitrogen aggregate. Vacancy-interstitial recombination would be reduced close to the A defect because of reduced interstitial enhanced diffusion compared to the bulk, where the interstitial can diffuse more easily during irradiation and recombine. The

net result is an apparently higher concentration of strained vacancies because of the presence of the A defect (and possibly also the interstitial), consistent with the observations of Davies *et al.* (1992). These vacancies are also the first to anneal out as they are very close to either a nitrogen atom or an interstitial. This is consistent with observations of Davies *et al.* (1992), who observed changes in the FWHM of the GR1 and ND1 absorption lines during annealing of irradiated type IaA diamond and attributed this to the diffusion and trapping of vacancies close to the A defect. The change in the FWHM of the GR1 peak is attributed to the fast annealing of these stressed vacancies, which during irradiation are created close to the A defect. These vacancies anneal approximately 12 times faster than the slow diffusion when annealed at temperatures between 600°C (873 K) and 800°C (1073 K). The additional energy barrier of 0.2 eV above the vacancy diffusion energy when the vacancy has to cross the capture radius around the A defect will make the fast diffusion ~ 12 times faster, as observed by Davies *et al.* (1992).

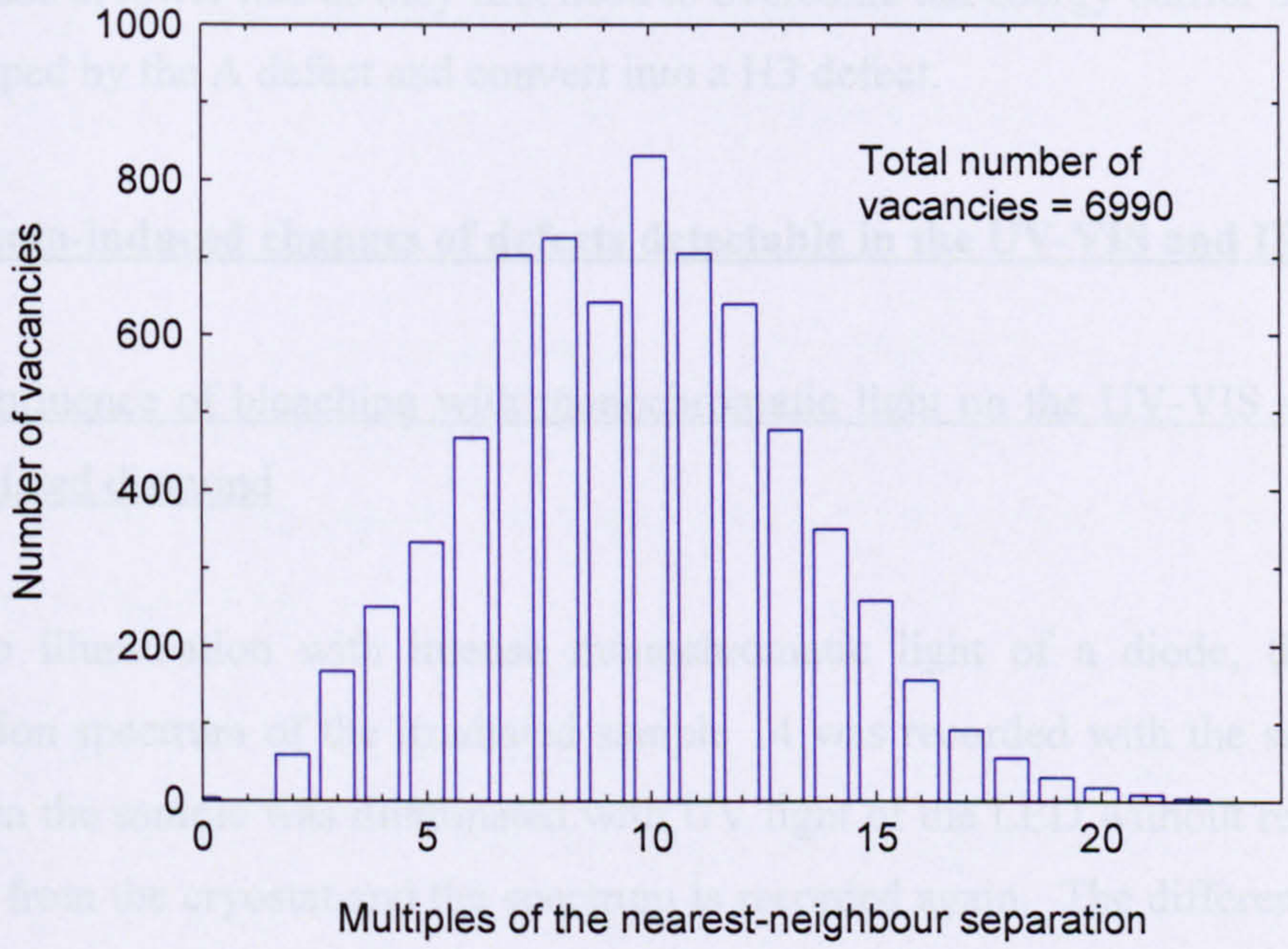

Figure 5.25. The histogram of the distribution of distance between a vacancy and an A defect in a irradiated type IaA diamond with 7 ppm of vacancies and 296 ppm of A defects.

Note that our alternative model does not include an energy barrier for restructuring of the A-V configuration into the N-V-N structure. Theoretical calculations of Jones *et al.* (1994) found the A-V structure to be highly unstable, so this assumption is not

unreasonable. Furthermore the constants α, β and γ will be proportional to the inverse of the trapping concentration, making equation sets 5.3.7 – 5.3.11 and 5.3.15 – 5.3.21 independent of the concentration of trapping defects.

It appears that neither of the two models is entirely appropriate to describe H3 formation and vacancy removal by trapping at nitrogen aggregates: it is hard to think of a physical mechanism which would allow two different diffusion rates, as described by the model of Davies *et al.* (1992). Of the two alternative models for vacancy-nitrogen complex formation presented in this section:

- The first model has the two different diffusion rates which is unphysical.
- The second model solves the problem of the two diffusion rates and can account for the fast loss of strained vacancies as these are the vacancies created within the energy barrier around the A and B defects. These can diffuse at normal rate while the unstrained vacancies, created outside the barrier around an A or B defect will diffuse at lower rate as they first need to overcome the energy barrier before being trapped by the A defect and convert into a H3 defect.

5.4. Photo-induced changes of defects detectable in the UV-VIS and IR spectra.

5.4.1. Influence of bleaching with monochromatic light on the UV-VIS spectrum of as-irradiated diamond

Prior to illumination with intense monochromatic light of a diode, the UV-VIS absorption spectrum of the irradiated sample 14 was recorded with the sample at 80 K. Then the sample was illuminated with UV light of the LED without removing the sample from the cryostat and the spectrum is recorded again. The difference between the spectrum before and after illumination is given in figure 5.26. The decrease of the GR1 peak is compensated by an increase in ND1.

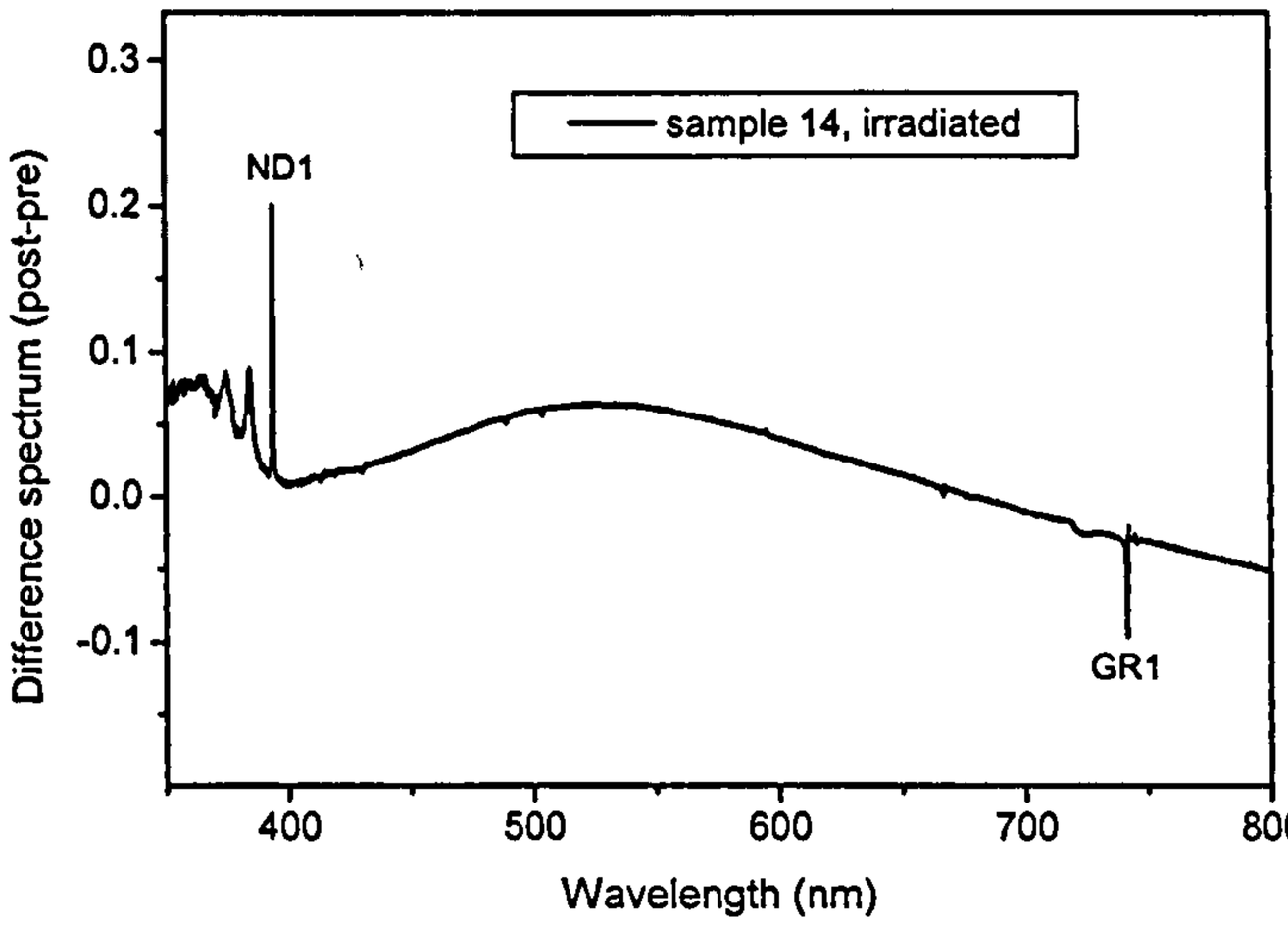

Figure 5.26. The difference between the UV-VIS spectrum after and before illumination. There is a decrease in GR1 and an increase in ND1 absorption strength. The ratio of GR1 to ND1 absorption intensity is ~ 2.

Since conversion between GR1 and ND1 must involve equal concentrations of GR1 and ND1 defects, the ratio of integrated intensity of the absorption peaks of the GR1 and ND1 peak is equal to the ratio in absorption cross section of the defects themselves.

Low resolution absorption measurements of Dyer and du Preez (1965b) indicated a ratio of the oscillator strengths of 5.5 - 10, while Davies *et al.* (1992) derived a value of 4.0 ± 0.2 by charge transfer analysis and absorption analysis of irradiated type Ib and type IaA diamonds.

Here, the ratio of the absorption strength of the ND1 over GR1 peak is 2.0 ± 0.3. The absorption cross section is larger for negatively charged defects than for neutral defects, a fact which is also detected for H3 and H2 defects (Mita *et al.* 1990). Iakoubovskii *et al.* (2003) observed a ratio in the change of GR1 and ND1 absorption strength of 8, again different from the values obtained in this study and the values of Davies *et al.* (1992). This difference in oscillator strength has significant consequences for the proportionality coefficient between the integrated intensity of the ZPL peak and the defect concentration. Twitchen *et al.* (1999) determined the oscillator strength of the ND1 defect by correlation between EPR and optical absorption data. To determined the oscillator strength of the GR1 defect, they used

the factor 4, determined by Davies (1992). The oscillator strength of the H3 and H4 and $(N\text{-}V)^-$ defects have been determined from the oscillator strength of the GR1 peak. In view of the data presented here and the data of Iakoubovskii *et al* (2003), the oscillator strength of the GR1 peak might differ from the value determined by a factor of 2: i.e. the actual concentration of neutral vacancies might be twice as large or twice as small. Clearly, this point needs further investigation. To relate the data presented in this work to other, already published work, we use the factor 4 for the ratio f_{GR1}/f_{NDI} and keep in mind that the concentration of neutral vacancies, H3, H4 and $(N\text{-}V)^-$ might be twice as large or twice as small.

Finally note the weak decrease in the absorption strength of the 3H defect peak upon UV illumination (figure 5.26).

5.4.2. Influence of bleaching with monochromatic light on the UV-VIS spectrum of irradiated and high temperature annealed (T = 800°C) diamonds

Prior to illumination with intense light of specific wavelength, the UV-VIS absorption spectrum of sample 1 after annealing was recorded with the sample at 80 K.

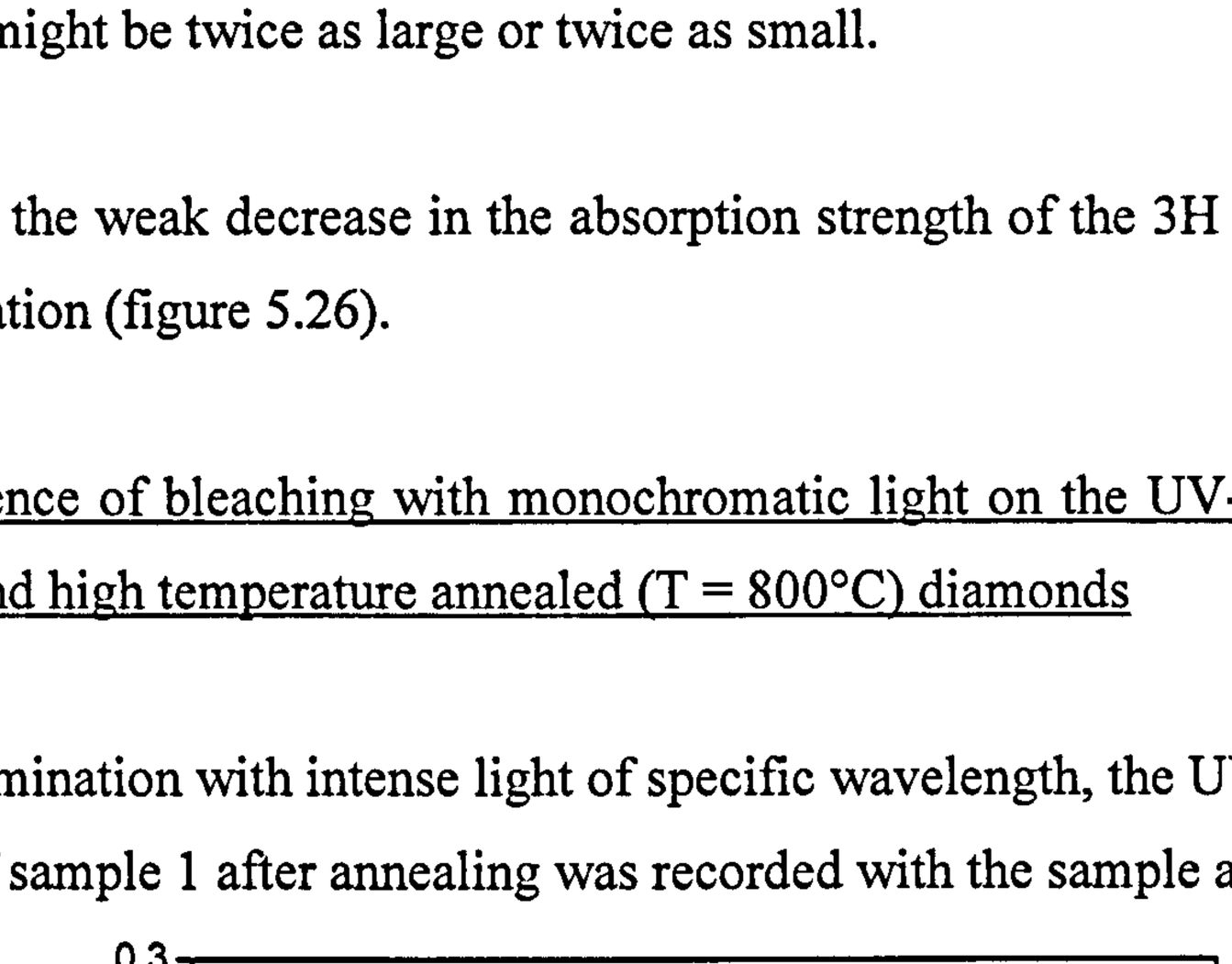

Figure 5.27. The difference between the absorption spectra of sample 1 before and during illumination with UV light (370 nm LED).

Then the sample was illuminated with UV light from a LED (peak at 370 nm) for 20 minutes before starting the measurement, through the optical window of the cryostat

without removing the sample and keeping the sample at 77 K (-196°C). The spectrum was recorded again while the sample was illuminated.

By subtracting the two spectra, a clear increase in absorption of H3 and a decrease of absorption of the 594 nm (2.087 eV) defect is observed (see figure 5.27, table 5.6). N3 does not seem to be affected by the UV illumination. The background changes also.

Defect	Pre illumination (meV cm^{-1})	Post illumination (meV cm^{-1})	Change
594 nm	5.62 ± 0.19	4.93 ± 0.39	-12.3 ± 0.5 %
H3	21.99 ± 0.40	24.79 ± 0.15	12.7 ± 0.2 %
H4	3.88 ± 0.04	6.96 ± 0.10	79.4 ± 0.5 %

Table 5.6. The integrated intensity of the zero phonon lines of the different defects in the diamonds before and after UV illumination.

The integrated intensities of the defects before and after illumination are given in the table below.

The sample was annealed at 500°C (773 K) for 1 hour to bring all peak intensities back to their original value. The sample was placed in the cryostat and the absorption spectrum was recorded with the sample at 77 K (-196°C). Then the procedure described above was repeated but this time the sample was illuminated with a blue LED (max. at 470 nm) for 20 minutes. Again differences in the absorption spectrum are observed (figure 5.28, table 5.7).

The changes of the H3 and H4 and 594 nm absorption intensities are in this case insignificant (table 5.7).

Defect	Pre illumination (meV cm^{-1})	Post illumination (meV cm^{-1})	Change
594 nm	6.28 ± 0.16	6.60 ± 0.13	5.0 ± 0.5 %
H3	27.01 ± 0.08	27.73 ± 0.08	2.7 ± 0.1 %
H4	3.10 ± 0.01	3.01 ± 0.10	3.0 ± 0.1%

Table 5.7. The integrated intensity of the zero phonon lines of the different defects in the diamonds before and after blue light illumination (470 nm).

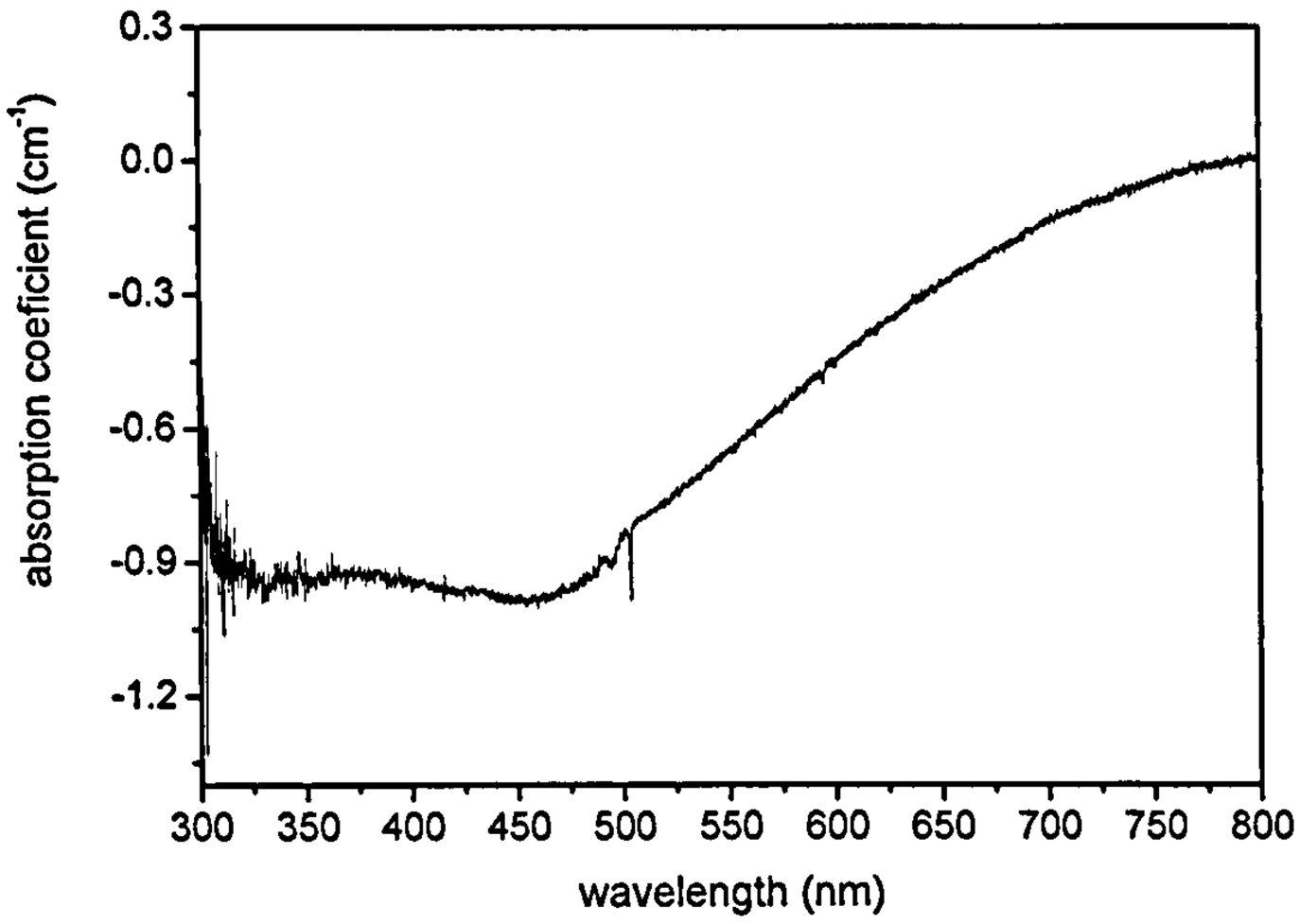

Figure 5.28. The difference between the absorption spectra of sample 1 before and during illumination with the 470 nm LED.

5.4.3. Influence of bleaching with monochromatic light on the H1b H1c defects in the IR spectrum

Prior to illumination the IR spectra of samples 1, 10 and 1H7 were recorded. After every illumination, each sample was heated to 500°C (773 K) for 1 hour to recover the intensity of the peak to its original intensity. Leaving the samples in the dark after illumination, even for 48 hours, did not change the increased absorption strength of the H1b and H1c peaks. The intensities of the peaks can be changed again by white light illumination, so special care was taken not to expose the sample to light during transport from the furnace and when mounting the sample in the IR sample holder.

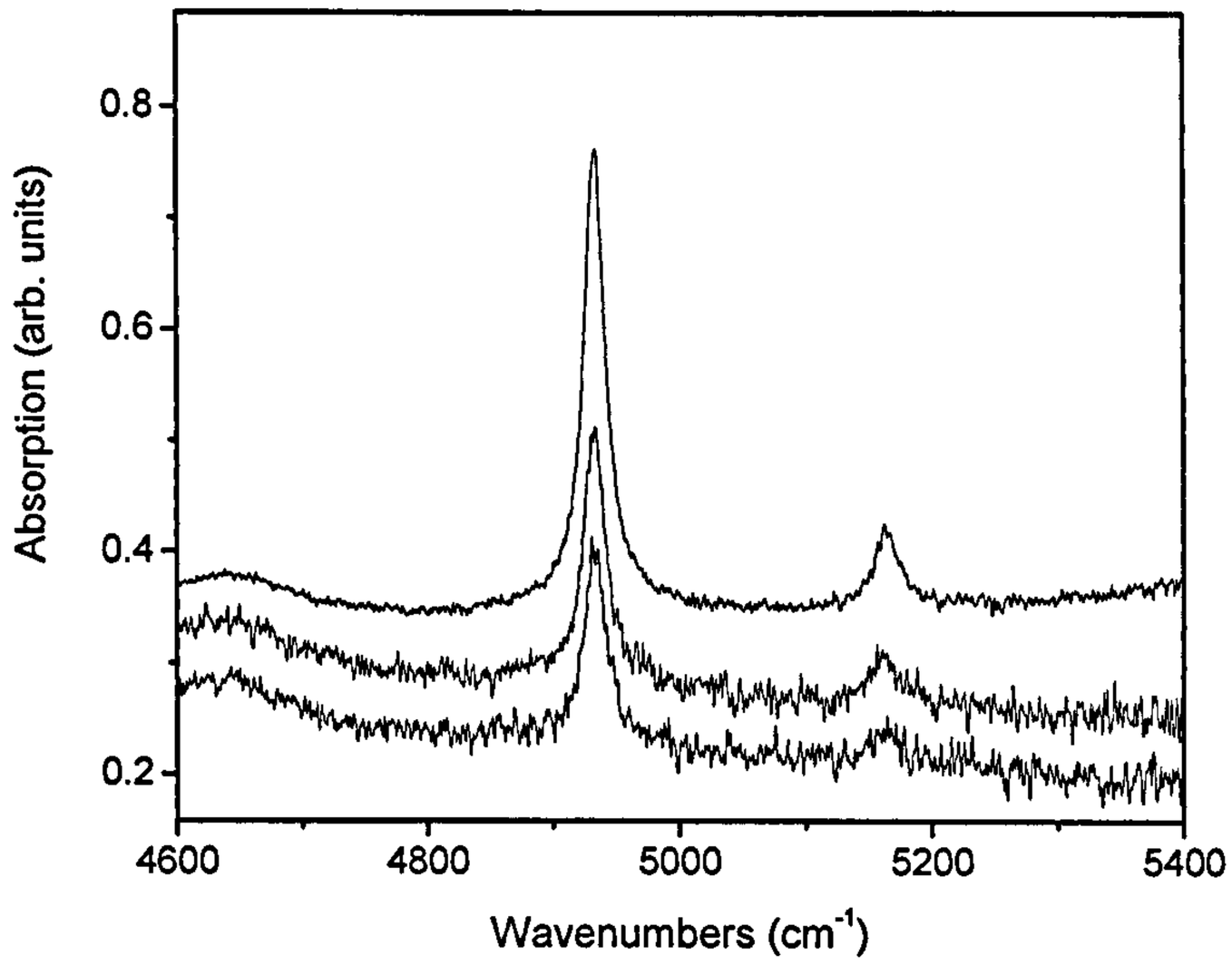

Figure 5.29. IR spectra of sample 1 before (middle spectrum), and during illumination with the 370 nm LED (top spectrum) and during illumination with the 470 nm LED (bottom spectrum).

For sample 1, in situ illumination with UV light (370 nm) doubles the intensities of the H1b and H1c peaks, while illumination with blue light (470 nm) decreases the intensity of the H1b and H1c peaks (figure 5.29). It is found that the H1b and H1c lines behave similarly under monochromatic light illumination and thermal recovery in all samples.

The H1b and H1c lines in samples 1H7 and 10 display a similar behaviour when illuminated with the blue LED (470 nm), but a sample dependent behaviour when illuminated with the UV LED (370 nm) (figure 5.30).

The photo induced change of the H1b line was measured as function of the wavelength of the light, bleaching the defect by changing the wavelength of the light with steps of 10 nm. The sample was left in the light beam for more than 30 minutes. A sample dependent bleaching behaviour is observed and the reason for this is not clear.

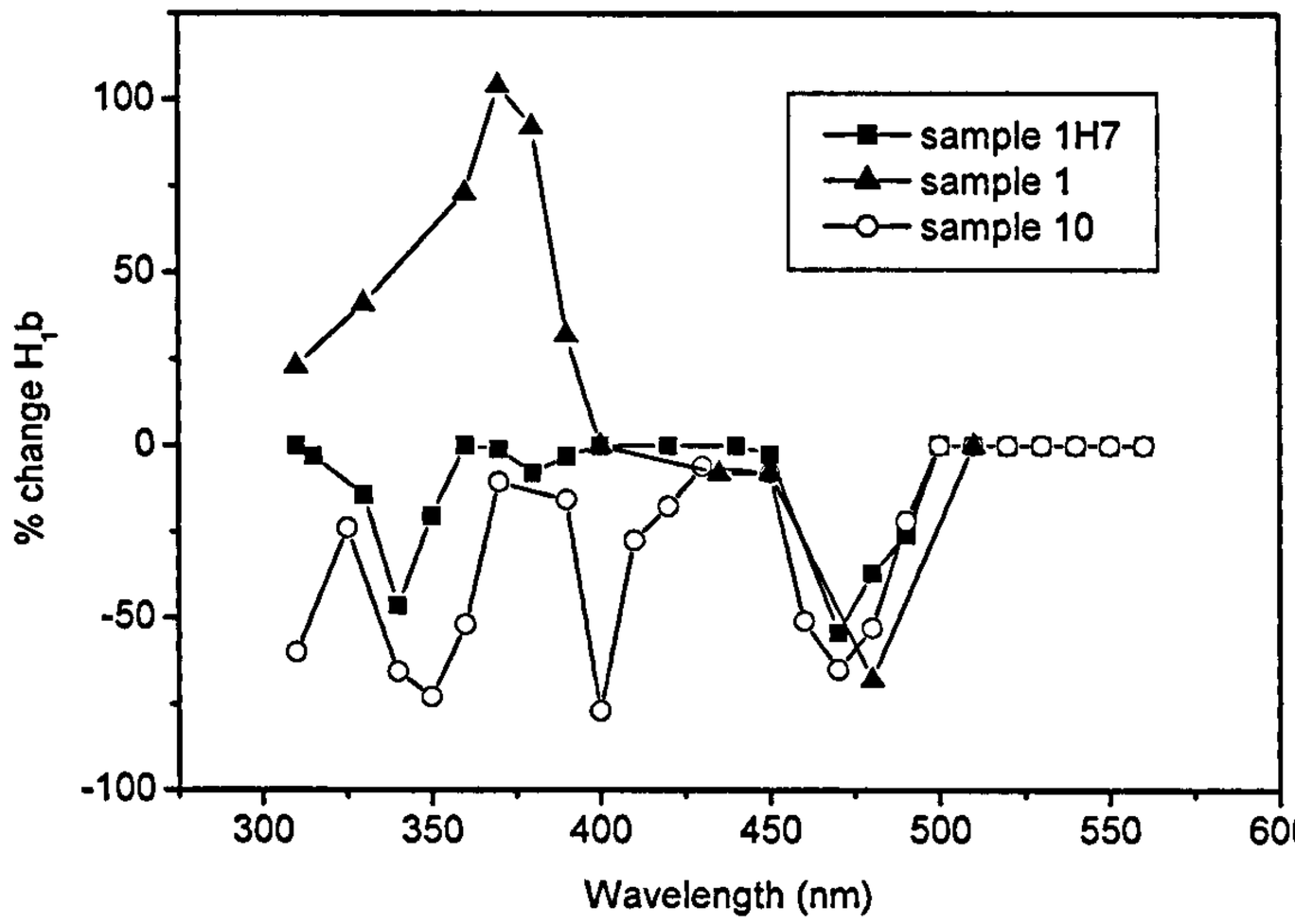

Figure 5.30. The percentage change of the H1b line of sample 1, 10 and 1H7 before and after illumination with light of different wavelength.

The wavelength dependent changes of the H1b and H1c lines appear to be strongly sample dependent (figure 5.29) and do not correlate with the change in absorption strength of other defects. No conclusion about the origin of this process can be made at this point.

5.4.4. Results of thermal recovery of UV illuminated diamond

When samples have been bleached with green (~ 500 nm) light the original intensity of the H1b and H1c lines can be recovered by thermal annealing, with an activation energy of 770 meV (Shareef and Collins 2003). Since the same, but stronger effect is reached by illumination with 470 nm in the present work, the recovery activation energy has not been calculated. Instead we focus on the changes induced by UV illumination.

The spectrum of the sample 1 was recorded before and after illumination at 370 nm, and the sample was then annealed at 300°C (573 K) in steps of 30 minutes. In between each annealing step the spectrum of the sample was recorded and again care was taken not to expose the sample to visible light during transport from the furnace to the IR spectrometer.

The same procedure as described above was followed with annealing at 300°C (573 K) (figure 5.31), 400°C (673 K), 500°C (773 K) and 600°C (873 K). However, the recovery of the H1b absorption at 600°C was too rapid to yield meaningful results: the recovery happens in less than 2 minutes (figure 5.32).

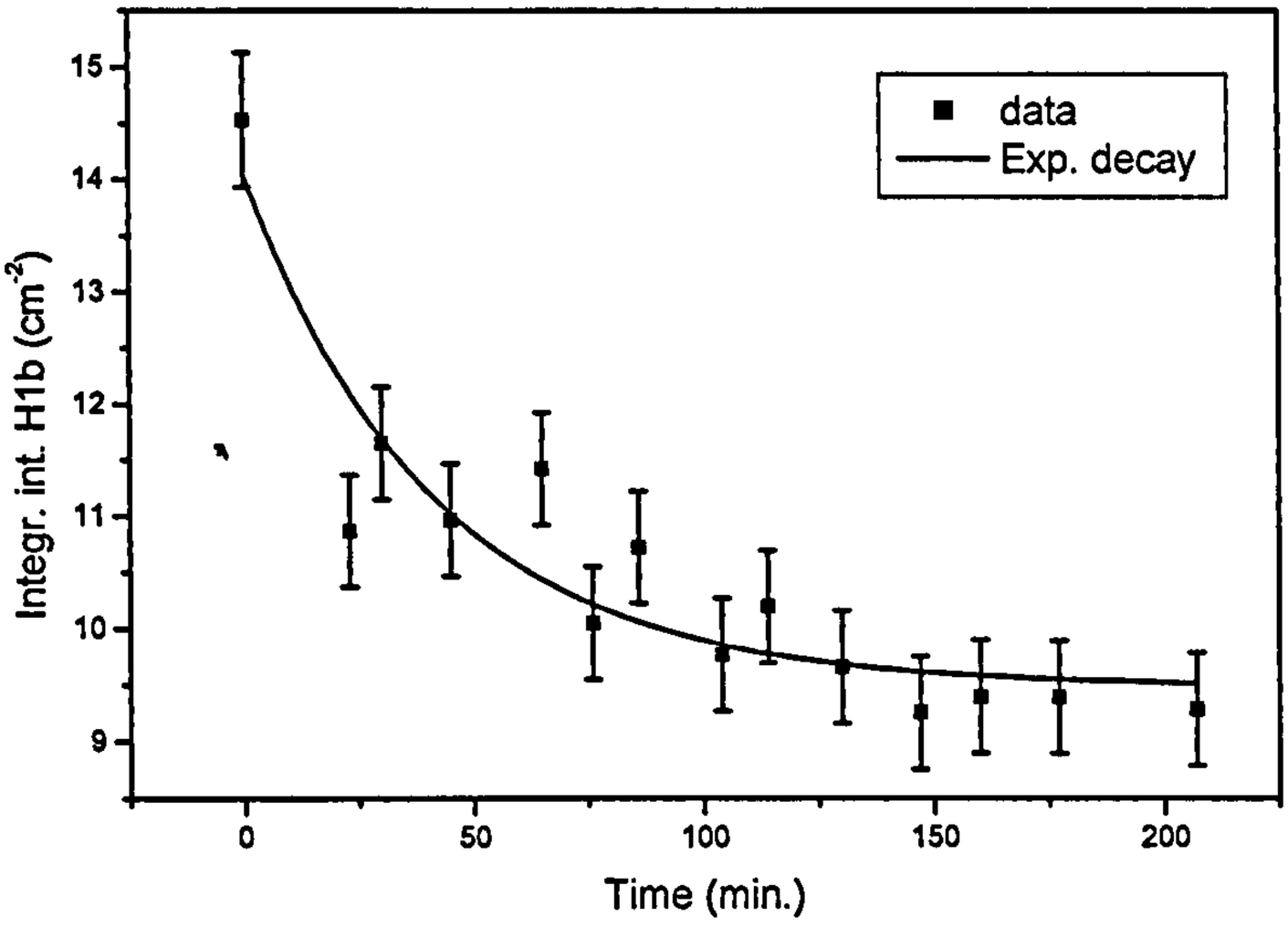

Figure 5.31. The recovery of the H1b defect by annealing at 300°C. The full curve is the single exponential decay equation (5.14) fitted to the data.

In all cases the decay is exponential, indicating that the recovery process is thermally activated. The time dependent equation describing the recovery of the H1b defect is:

$$[H1b](t) = A + B.\exp\left(-t/\tau\right) \qquad (5.4.1)$$

with τ the decay constant, A and B constants and t the time.

The activation energy for the process is then found by an Arrhenius plot of the decay constant when the sample is annealed at different temperatures.

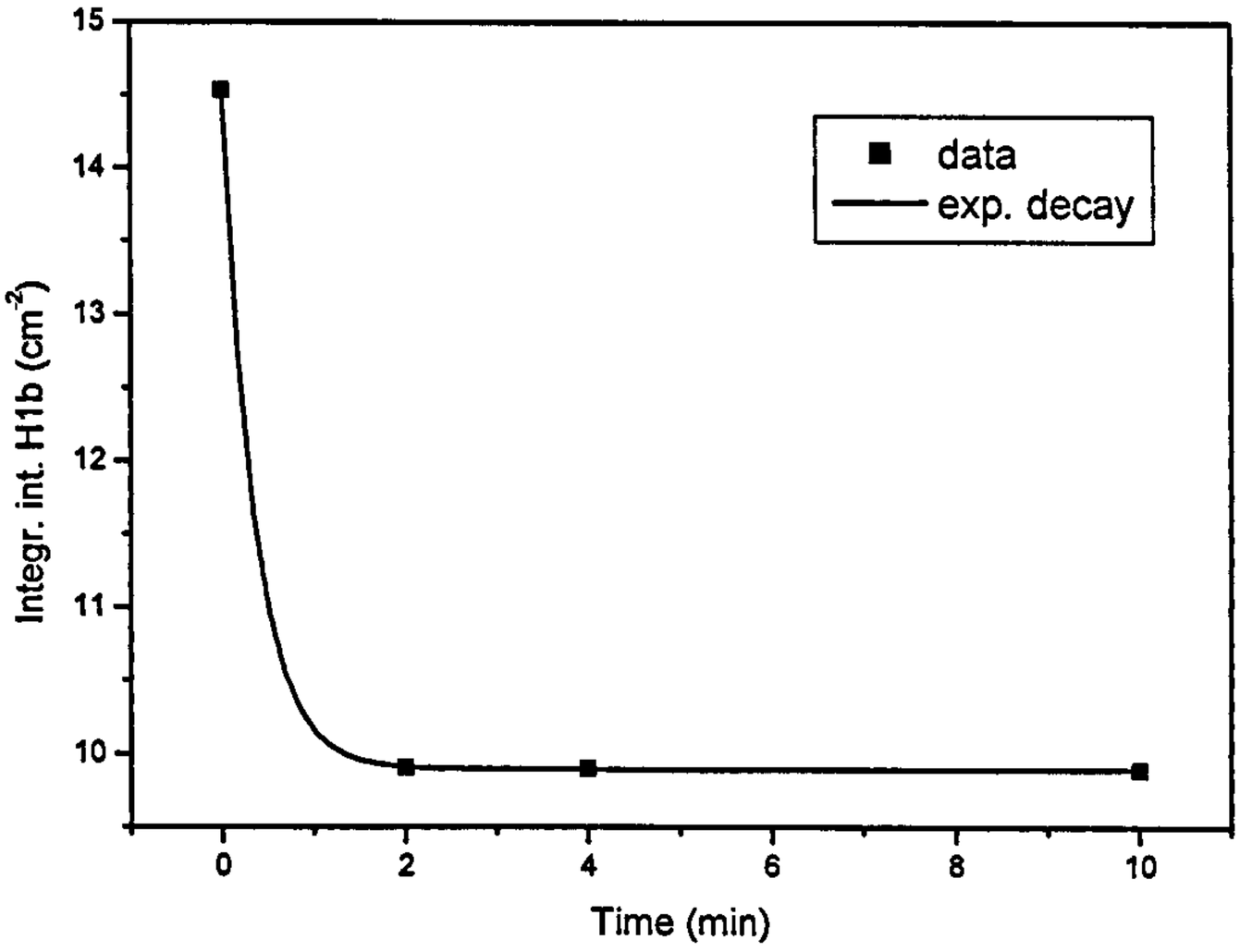

Figure 5.32. The thermal recovery (T = 600°C) of the integrated intensity of the H1b line in sample 1 after illumination with UV light. The solid curve on the figure is calculated from parameters derived at lower temperature.

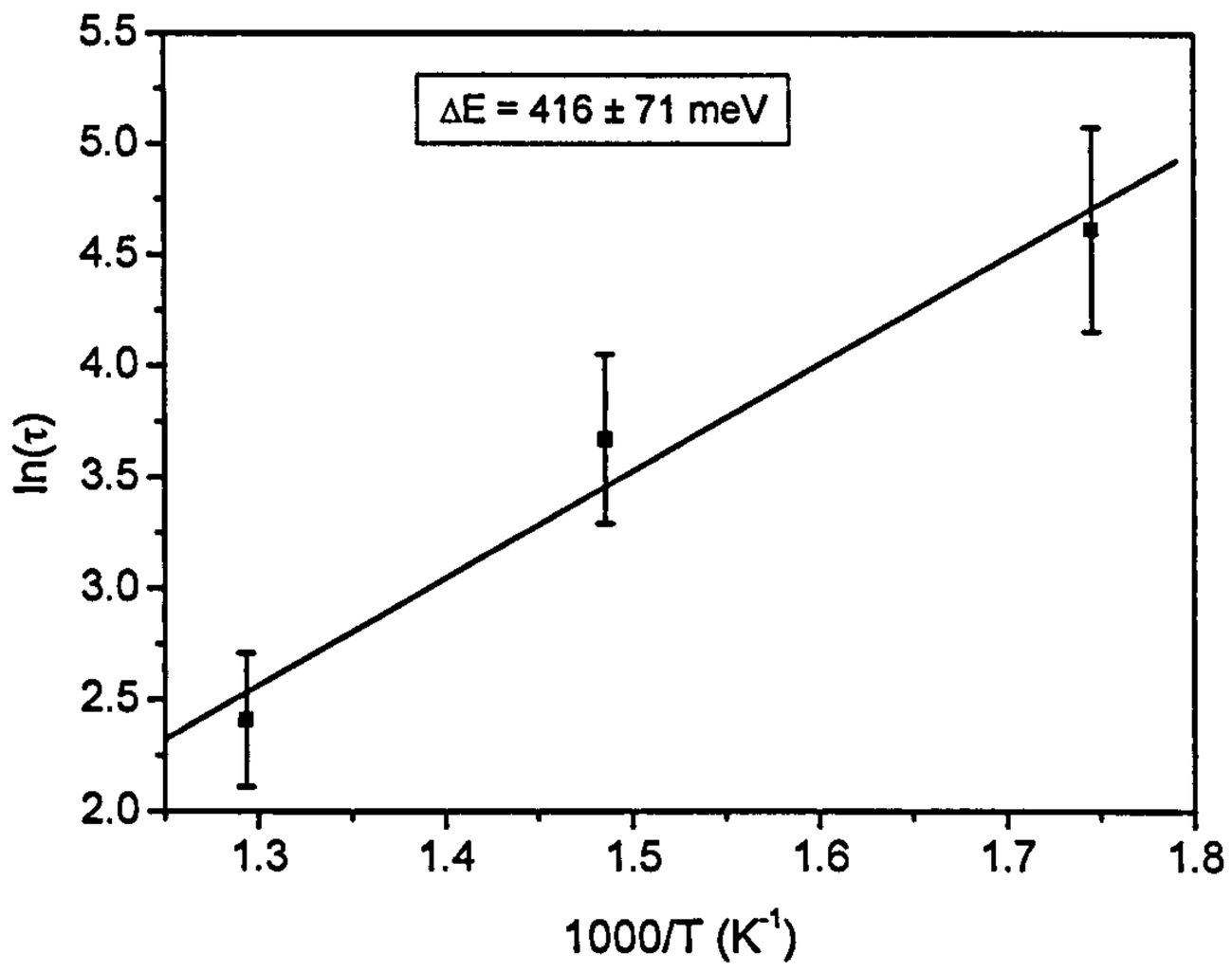

Figure 5.33. The Arrhenius plot of the recovery process of the H1b defect.

The linear fit p + q.x of the Arrhenius plot (figure 5.33) gives the following values for the A and B parameters: p = -3.70 ± 1.24 and q = 4.82 ± 0.81, giving an activation energy of 0.416 ± 0.071eV.

5.5. Undocumented absorption peaks

In a sample which was HPHT annealed prior to irradiation and heat treatment peaks appear in the NIR spectrum at 805 nm (figure 5.34) and mid-IR spectrum at 6170 cm^{-1} (figure 5.35) which have not been documented before.

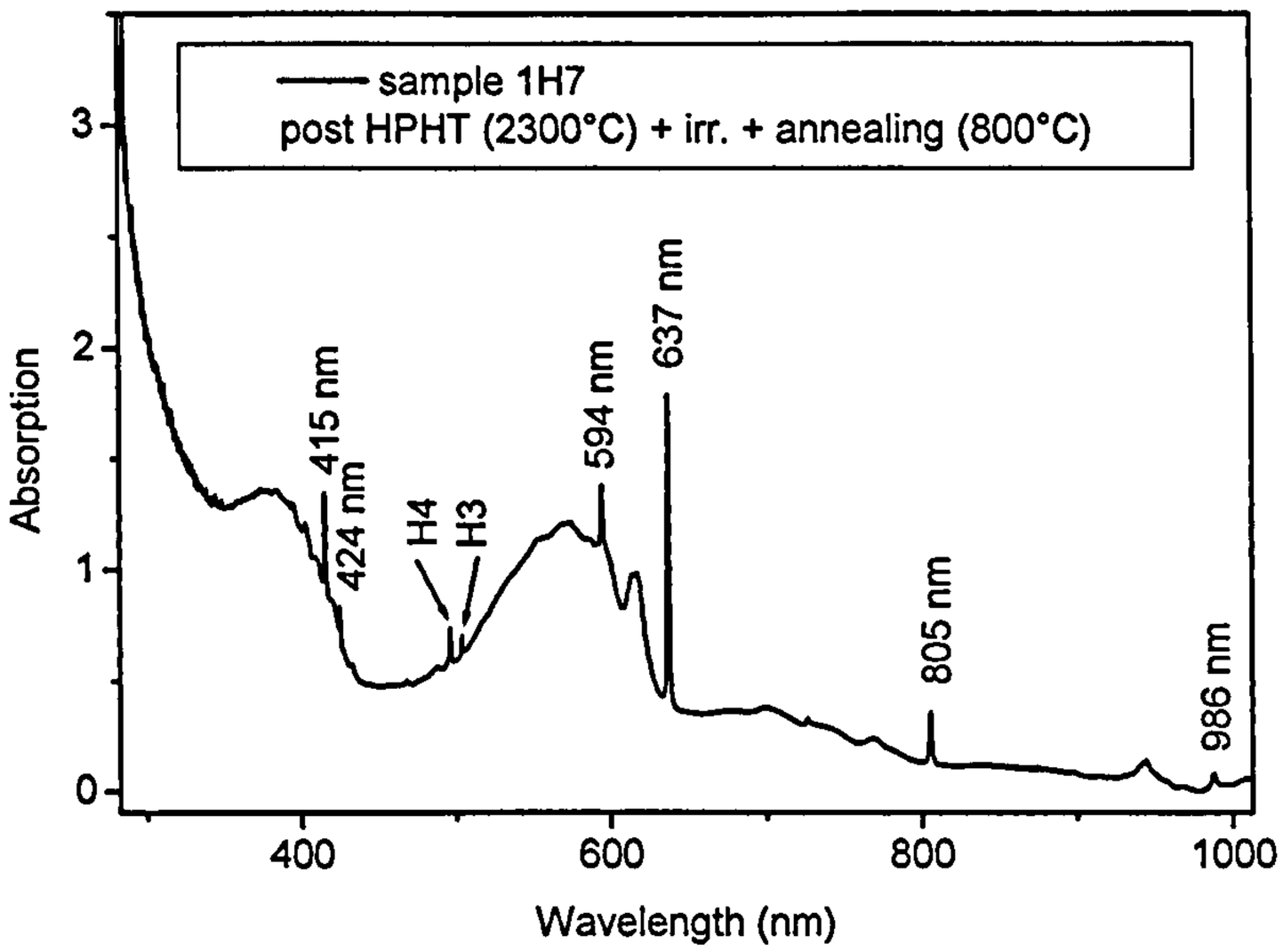

Figure 5.34. The UV-VIS-NIR absorption spectrum, recorded with the sample at liquid nitrogen temperature of the HPHT annealed, irradiated and heat treated diamond. An undocumented peak at 805 nm is detected.

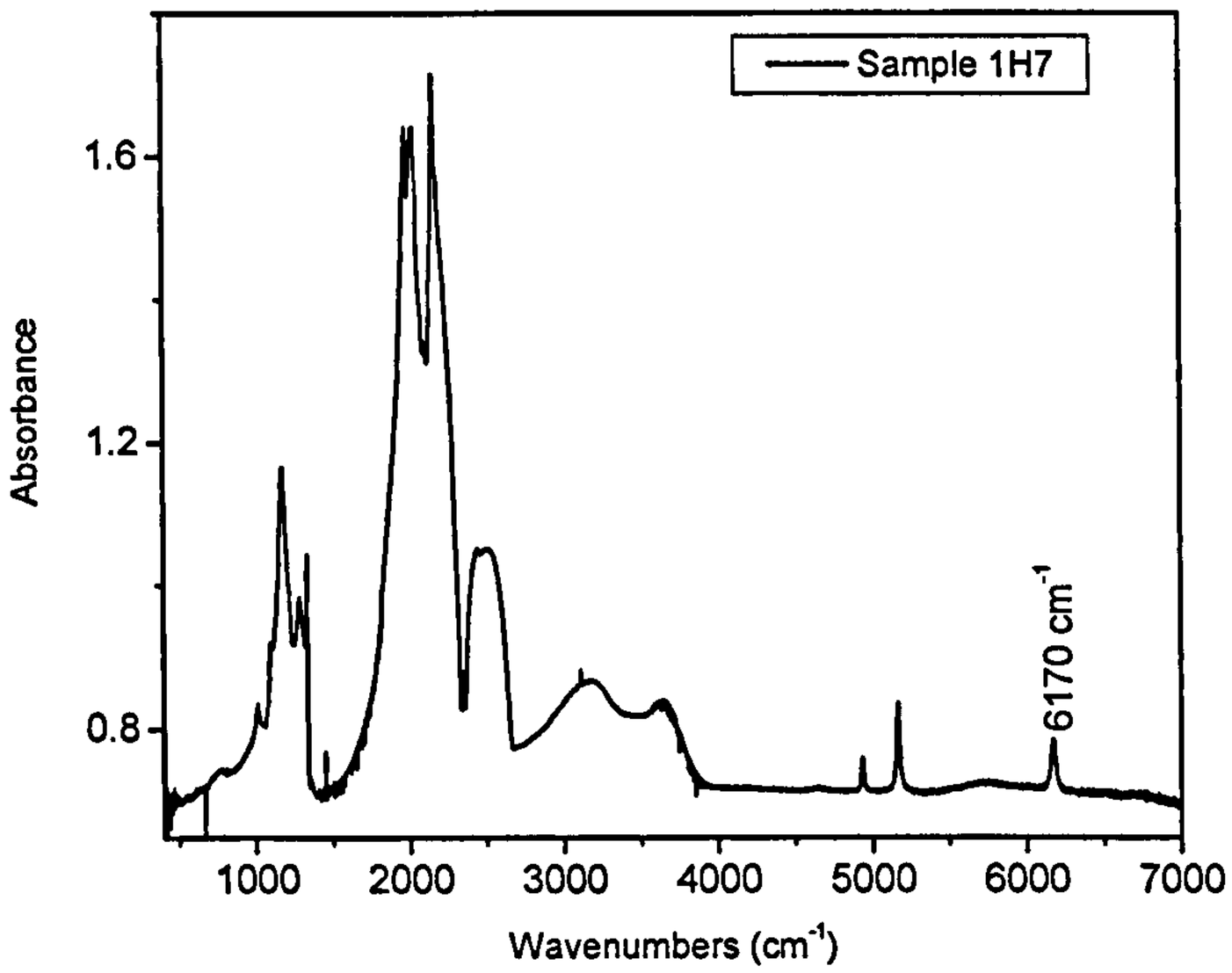

Figure 5.35. The mid-IR absorption spectrum, recorded with the sample at room temperature of the HPHT annealed, irradiated and heat treated diamond. An undocumented peak at 6170 cm^{-1} is detected in this sample.

These peaks are also detectable in colour treated type Ia diamonds which are commercially available (Wang *et al.* 2006). The peaks are not detectable in HPHT annealed type Ia diamonds or in irradiated and annealed diamonds (De Weerdt and Anthonis 2004); they are only detectable in diamonds which have been HPHT annealed, irradiated and annealed at a temperature sufficiently high to make vacancies mobile.

5.6. Conclusion

5.6.1. Vacancy capture by nitrogen related defects

The capture efficiency of nitrogen aggregates, in the absence of single substitutional nitrogen defects, is very low: only a few tenths of a percent. It seems that the capture efficiency of single substitutional nitrogen atoms is very large compared to A and B defects. There is a dependence of the captured fraction of vacancies on the concentration of the trapping defect when the irradiated diamond is subjected to annealing at temperatures over 600°C (873 K). The study of the literature data and the annealing behaviour of sample 3 indicates divacancy formation is negligibly small when an irradiated type Ia diamond is annealed to high temperature. Other vacancy traps like dislocations, cracks and nitrogen aggregates are more important than divacancy formation. It should be remarked that vacancies disappear completely by high temperature annealing at temperatures above 600°C. Not all these vacancies are trapped at nitrogen aggregates but in optically undetectable traps. These traps do not release vacancies when the diamonds are annealed to temperatures far above 600°C (Collins *et al.* 2005).

The kinetics of vacancy capture has been modelled in two different ways. In the first model, the A (or B) defect-vacancy complexes need to overcome an energy barrier before they can restructure into the N-V-N (or 4N-2V) complex, i.e. the H3 (or H4) defect. The vacancy diffuses in the bulk of the diamond with two different diffusion rates.

The second model proposed in this chapter eliminates the need for two different diffusion rates for vacancies in type I irradiated diamond. It also accounts for the fast loss of strained vacancies.

5.6.2. The influence of radiation on platelets

The study of irradiation induced changes of the platelet peak is not only paramount to the understanding on the nature of platelets themselves but also on the results of

irradiation of type Ia diamond. Clearly the concentrations of interstitials and vacancies captured by platelets do not result in a detectable change of the properties of the platelet peak. Irradiation of type Ia diamond with higher dose or multiple irradiation and annealing steps to accumulate the effects of vacancy and interstitial capture would be highly desirable.

5.6.3. Photochromic changes of radiation induced defects in diamond

Photochromic changes occur in diamond when illuminated with UV light and the measurements reveal a two times larger absorption cross section for ND1 than for GR1. This appears to be common for negatively charged defects as it is also observed for H2 and H3 defects, although the effect is not as strong as with the ND1 and GR1 defects. Data in literature has given different ratios of the oscillator strength of the GR1 and ND1 defect, being 4 (Davies *et al.* 1992) and 8 (Iakoubovskii *et al.* 2003). It is important to carry out further research as the ratio of the oscillator strength of the GR1 and ND1 peak plays a crucial role in the determination of the proportionality coefficients between the H3, H4 and $(N\text{-}V)^-$ defect concentration and integrated intensity of the zero phonon line of the defect. Ideally, the concentration of $(N\text{-}V)^-$ and H2 should be determined independently by EPR and correlated with the oscillator strength determined by Davies *et al.* (1992). However, for reasons that are not understood, H2 is not detected using EPR (Mark Newton, personal communication).

5.6.4. Photo-induced changes of the H1b, H1c defect

The H1b and H1c defects can be bleached or intensified by illumination with light of a suitable wavelength. The activation energy for the recovery of the defect after illumination with UV light is 416 ± 71 meV. It is unclear why the bleaching or enhancement of the H1b and H1c defects is sample dependent.

Chapter Six

Stability of defects during HPHT annealing

6.1. Introduction to HPHT annealing

6.1.1. Chapter outline

In this chapter, colour changes in brown type Ia diamond upon high-pressure, high-temperature (HPHT) annealing are discussed. Depending on the most abundant defects and the concentration of defects present in the diamond, the colour of the diamond can change drastically from brown to yellow-green, yellow or even colourless.

The problem of understanding colour changes of HPHT annealed brown type Ia diamond can be separated in a number of partial processes:

- A-defects can dissociate into two single substitutional nitrogen atoms. The reaction is reversible and some single nitrogen atoms can re-aggregate. The formation of the single substitutional nitrogen defects (C defects) is important; these defects are electron donors and thereby can change the mobility of other defects (Davies *et al.* 1992).
- H3 defects are created during HPHT annealing of brown type Ia diamond, but large concentrations of mono-vacancies are not detected before annealing. Thus vacancies are released from unknown defects and get trapped at various nitrogen aggregates. The vacancy trapping process by various nitrogen aggregates has been investigated in chapter five on annealing of radiation damage and this model will be extended here to include the dissociation of such defects at relatively low annealing temperature (T ~ 1500°C) as observed by Collins (1980) and Collins *et al.* (2005).

- Other nitrogen-vacancy aggregates (H4, $(N\text{-}V)^-$, $(N\text{-}V)^0$) can also dissociate into various components during HPHT annealing, thus releasing vacancies and an accurate model should include this process.

Colour changes are thus related to formation and dissociation of defects in diamond during annealing. The investigation presented here will start with the basic types of processes. In the first part this chapter, a description is given of the theoretical framework of relatively simple defect aggregation-dissociation mechanisms and this is illustrated by two examples:

- A-centre dissociation and re-aggregation is modelled by a combination of first order (dissociation) and second order (re-aggregation) processes. The model is then extended to include additional factors influencing the A and C defect concentrations created during HPHT annealing. These additional factors are pressure change and the presence of vacancies introduced by irradiation before HPHT annealing. The results of Chrenko *et al.* (1977), Brozel *et al.* (1978), Kiflawi *et al.* (1997), Collins *et al.* (2005) and Collins (1980) are analysed within this framework. Additionally, these modelled results are then tested by HPHT annealing of colourless type IaA diamonds.
- In the second example, the annealing behaviour of the hydrogen-related 3107 cm^{-1} defect is studied. This will serve as an example of the annealing behaviour of a defect, which is simultaneously created and destroyed, both by first order processes. This is in contrast to A defect generation and dissociation of A defects into C defects which follow mixed first and second order kinetics.

The next part of the chapter focuses on the source of the vacancies in brown type Ia diamond and the various aggregation-dissociation mechanisms activated by the HPHT process and their influence on the colour of the diamond. This will combine the knowledge gained from the first parts of this chapter and chapter 5.

6.1.2. A-defect dissociation

Since most of the substitutional point defects in diamond are very stable, HPHT annealing offers a way of studying the kinetics of defects on laboratory timescales. Until now, most of the attention has been directed at defect aggregation (Chrenko *et al.* 1977, Evans and Qi 1982, Kiflawi *et al.* 1997, Kiflawi and Bruley 2000), but only

a few articles have paid attention to defect dissociation (Evans *et al.* 1995, Brozel *et al.* 1978) and some mention dissociation as a remark (Davies *et al.* 1997). Brozel *et al.* (1978) and Evans *et al.* (1995) studied the dissociation of A centres, B centres and B' (platelets) defects. This change is accompanied by an increase of C centres (Evans *et al.* 1995).

6.1.3. Annealing of the hydrogen-related 3107 cm^{-1} defect.

Hydrogen is a common impurity in natural diamond, and it can be present in large concentrations (Hudson and Tsong 1977, Sellschop 1992). Sharp absorption lines in the mid-infrared spectrum of natural diamonds have been attributed to bend (1405 cm^{-1}) and stretch modes (3107 cm^{-1}) of C-H vibrations (Woods and Collins 1983, see also chapter 4). It has been shown that these absorptions can be introduced by HPHT annealing in natural diamond (De Weerdt and Kupriyanov 2002), as well as in some synthetic HPHT diamond (Kiflawi *et al.* 1996), and in diamond grown by chemical vapour deposition (CVD) (Charles *et al.* 2004). However, the strength of the absorption lines can also be decreased by HPHT annealing (De Weerdt and Kupriyanov 2002).

Here we investigate the complex behaviour of the 3107 cm^{-1} defect in natural diamond when subjected to HPHT annealing with temperature over 2000°C. Microscopic nuclear measurements have shown that there is no correlation between the total hydrogen content and the strength of the 3107 cm^{-1} absorption (Sweeney *et al.* 1999). Theoretical calculations have indicated that optically inactive hydrogen may reside in the diamond lattice as hydrogen platelets or di-hydrogen molecules, similar to the behaviour in silicon (Martsinovich *et al.* 2003, Newman 1995, Jones 1995). Calculations have also indicated that hydrogen can be trapped at other defects as hydrogen dimers, or in dislocations (Goss 2003, Heggie *et al.* 2000, Heggie *et al.* 2002). EPR measurements have indicated that grain boundaries and other defects like, for example, the N-V defect, can trap hydrogen (Goss *et al.* 2003, Zhou *et al.* 1996, Glover *et al.* 2003). In CVD diamond, hydrogen-related absorption peaks in the NIR region, observed in the as-grown material, disappear after HPHT annealing, while the 3107 cm^{-1} defect is formed (Newton 2005b). This indicates that the 3107 cm^{-1} defect is more stable than other hydrogen-containing defects in as-grown CVD

diamond. In all types of diamond any hydrogen-related defect can, in principle, act as a hydrogen source for the formation of the 3107 cm^{-1} defect, so it is expected that the strength of the 3107 cm^{-1} line can have an initial increase and a subsequent decrease when the sample is subjected to multiple HPHT annealing.

6.1.4. Annealing of brown type Ia diamonds

Recent ab-initio calculations of Hounsome *et al.* (2005a, b) indicated that vacancy clusters or disks could be the defects responsible for the brown colour of natural diamonds. During plastic deformation, mobile dislocations can leave vacancy trails, which can cluster (Leipner *et al.* 2000). These clusters can evaporate by releasing mono-vacancies during HPHT annealing. In type Ia diamonds, this induces a colour change: the released vacancies are trapped by A or B defects, which convert to H3 and H4 defects respectively and this will colour the diamond yellow. Green fluorescence due to presence of H3 or H4 defects in the samples will give the diamond an overall yellow-green colour (De Weerdt and Van Royen 2000). In practice, the concentration of H4 defects in annealed diamonds is very small (Collins *et al.* 2005). C defects, created by dissociation of A defects, act as electron donors and negatively charged defects are detected. By trapping of an electron, the neutral $(N\text{-}V)^0$ and H3 centres change into the negatively charged counterparts $(N\text{-}V)^-$ and H2. These negatively charged defects are frequently detected in HPHT annealed type Ia diamonds (see figure 6.1).

The calculations of Hounsome *et al.* (2005a) show that the formation energy, per vacancy, of vacancy clusters or disks decreases with cluster size and levels out for clusters larger than 14 atoms. Two saddle points are found for clusters of 6 and 10 vacancies respectively, without well defined formation energy maxima for clusters of 5, 7, 9 or 11 vacancies: the formation energy for clusters of 5 and 6 vacancies differ in energy by ~ 0.6 eV. The calculated total formation energy difference between clusters of 14 vacancies and divacancies is ~ 2.5 eV (Hounsome *et al.* 2005a). Clusters larger than ~ 200 vacancies are unstable and collapse into dislocation loops (Hounsome 2005b, 2006). The presence of vacancy clusters has been determined experimentally using positron annihilation by Mäki *et al.* (2005) and Avalos and Dannefaer (2003).

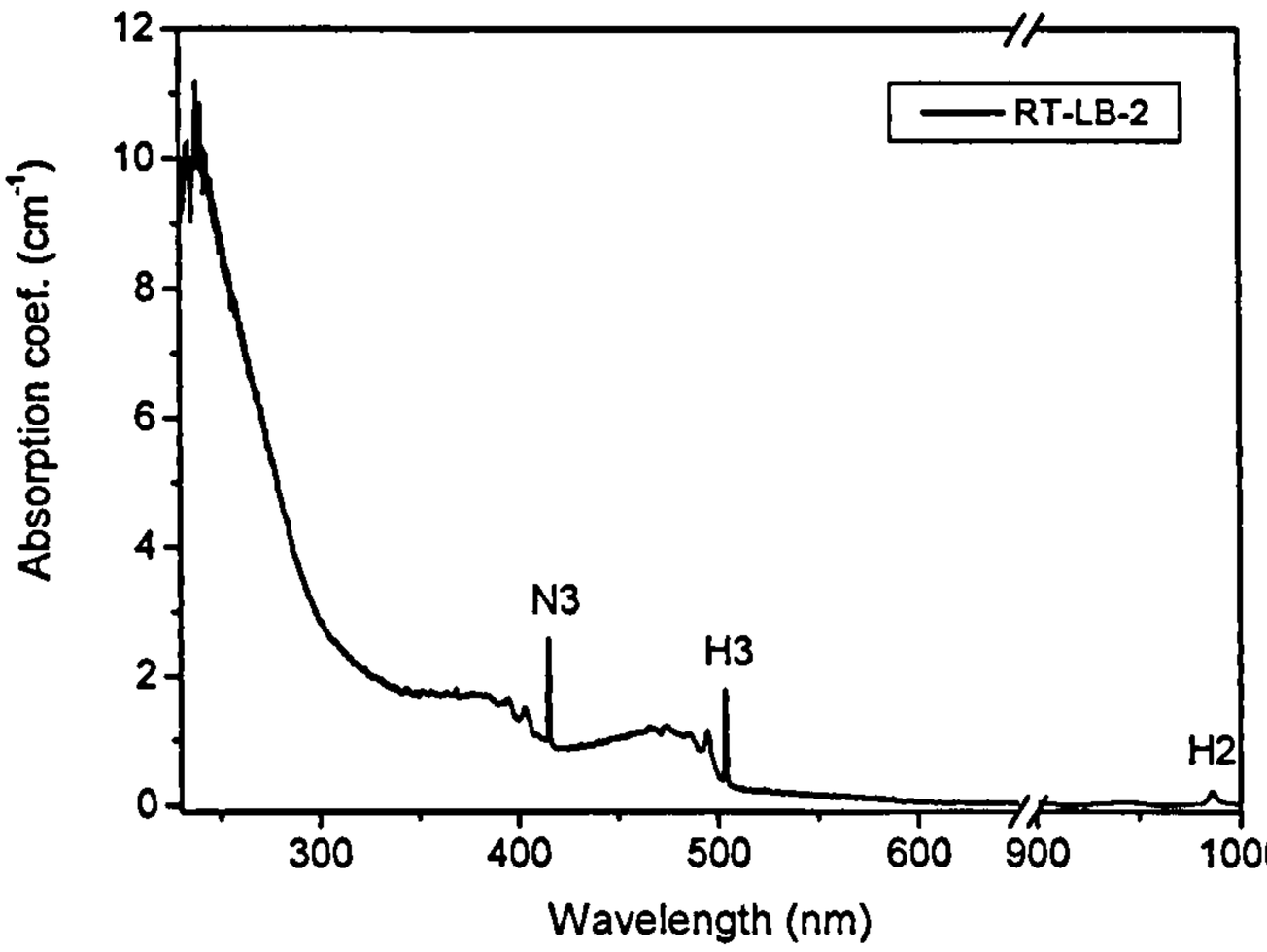

Figure 6.1. The UV-VIS-NIR absorption spectrum of a brown type Ia diamond after HPHT annealing. A weak H2 absorption peak is detectable in the NIR spectrum. The NIR spectrum is recorded with the Princeton Instruments spectrometer, while the UV-VIS spectrum is recorded with a Varian Cary 100 spectrometer.

These vacancy clusters are believed to be created during plastic deformation. Large concentrations of vacancies are created during the plastic deformation and precipitate into vacancy clusters. Large vacancy clusters grow in size at the expense of smaller clusters. This process is known as Ostwald ripening.

Ostwald ripening has been studied by Lifshitz and Slyozov (1961) and Wagner (1961), and that work has been extended and enhanced by several authors (Marsh and Glicksman 1997, Carlow *et al.* 1998, Olive *et al.* 1996, Madras and McCoy 2003, Madras and McCoy 2004, Gusak *et al.* 2006). It is an important process as this describes for example the segregation of different solid state phases, condensation, epitaxial crystal growth, … The Lifshitz-Slyozov-Wagner (LSW) theory describes the time dependent asymptotic distribution of cluster size and mass. This process relates surface curvature to vapour pressure and chemical potential and requires any particle to grow faster than any smaller particle or, put differently, the growth of larger clusters from smaller clusters with a higher solubility (IUPAC 1997). The physical driving force is the decrease of supersaturation of the vacancies. Thus the mean cluster size will grow with increasing temperature for a given period of annealing. The mean cluster size can only shrink when sufficient traps for particles evaporating

from the clusters are present, for example the surface of the sample (Colombeau *et al.* 2003). Thus during HPHT annealing of brown type Ia diamond, small vacancy clusters dissociate and large clusters will form as these are the most stable and grow at the expense of small clusters. During HPHT annealing, these large clusters may keep growing until they collapse into dislocation loops (Hounsome *et al.* 2005b) or become unstable. In due course, vacancies will be removed (evaporate) from the small clusters to feed large clusters and occasionally get trapped at nitrogen aggregates, forming H3 and H4 defects.

To summarize, the fate of vacancies evaporated from vacancy clusters can be the following:

- They will migrate to the surface or cracks, dislocations, … This will probably be the dominant process in relatively nitrogen free type II diamond.
- If the diamond is type Ia, vacancies will be trapped by nitrogen aggregates, giving rise to H3 and H4 defects.

If vacancy clusters are present in brown type Ia diamond, the vacancy source is finite and will be depleted after some time when the diamond is subjected to HPHT annealing as the large clusters will collapse into dislocation loops and small clusters will dissolve.

An alternative vacancy source could come from dislocations with climb diffusion (chapter 1, section 1.3.4). This should keep producing and absorbing vacancies as long as the dislocation is not immobilised or annihilated by a certain (unknown) process or reaches the surface. In the absence of vacancy trapping defects, the number of generated and absorbed vacancies is equal. Electron microscopy images reveal similar densities of dislocations in pre and post annealed type IIa samples (Willems *et al.* 2006), indicating the loss of dislocations is insignificant. So if this process occurs, vacancies are constantly generated and absorbed during HPHT annealing and the concentration of H3 defects evolves to an equilibrium level. Dislocations are also present in all types of natural diamonds (Lang 1967) and climb of dislocations during HPHT annealing in colourless type IaA diamonds should also generate some low concentration of H3 defects. This is not observed and this strongly

indicates that vacancy release from dislocation climb will not be responsible for the strong increase of H3 defects in HPHT annealed brown type Ia diamond.

Platelets are another type of defect, which changes dramatically during HPHT annealing of brown type Ia diamond. Platelets consist of planes of interstitial carbon atoms and the integrated intensity of the platelet peak correlates with the B defect concentration in regular diamonds (Woods 1986, Goss *et al.* 2003). Therefore it was thought that interstitials ejected during the formation of B and N3 defects form platelets. This cannot be correct for several reasons:

- B defect formation has very high activation energy and in Nature this type of defect will be created at a slow rate. On the other hand, nucleation and precipitation of interstitials into platelets requires supersaturation, but interstitials will diffuse out rapidly as the activation energy for interstitial motion is very low (~ 1.6 eV), so supersaturation will never be reached.
- Some diamonds with low concentrations of nitrogen contain large ('giant') platelets. The low concentrations of nitrogen would be responsible for a low concentration of B defects and thus a low concentration of interstitials and small platelets. This is in contradiction with the view that B defects are the interstitial source for platelets.

It is therefore more suitable to think of B defects as nucleation sites for platelets. This explains the correlation of the integrated intensity of the platelet peak with B defects and the giant platelets: regions with low nucleation density and supersaturated with interstitials will lead to the growth of large platelets. This hypothesis is supported by the fact that platelets are not detected in type IaA diamonds nor in irradiated, HPHT annealed type IIa diamond (Allen and Evans 1981).

For regular diamonds, Woods (1986) observed a correlation between the platelet FWHM and the peak position: a platelet peak with a smaller FWHM has a peak position maximum at lower wavenumbers. Also, the peak appears to become more symmetrical when shifted to lower wavenumbers (Woods 1986). It is also known that the peak position of the platelet peak is correlated with the size of the platelet: the position shifts to lower wavenumbers when the average size of the platelet increases

(Clackson *et al.* 1990). It is therefore more suitable to think of the platelet peak as the envelope of a distribution of absorption peaks with different maxima because platelets differ in size. The growth and destruction of the platelet is then similar to growth of vacancy clusters: platelets grow by capturing interstitials at the expense of smaller clusters and are destroyed when they convert into dislocation loops (Evans *et al.* 1995, Hirsh *et al.* 1986). Alternatively platelets can, in principle, be destroyed when they trap a large number of vacancies (Goss *et al.* 2003). Platelets should be very efficient vacancy sinks because of their large size. However, as shown in chapter five, there is no evidence for this when an irradiated ([V] ~ 8 ppm) type Ia diamond is annealed at ~ 800 °C. A reduction of the platelet peak and D defect absorption is only observed after room temperature irradiation.

6.2. Experimental

6.2.1. Samples and experimental setup

All samples except A12, A14, A17 and the samples with the name starting with ak (see below for a description of the samples), were HPHT annealed at Sundance Inc. at various temperatures, from 1700°C to 2300°C. The samples with the name starting with ak were on loan from professor H. Kanda of the NIMS institute in Japan. These samples were HPHT annealed in a BELT type press at 2300°C for five minutes. Sample details before annealing are given in tables 6.1 to 6.10 below. The A12, A14 and A17 samples have been HPHT annealed at the NovaDiamond Inc. facility at temperatures of app. 2300°C and pressures of 5 - 6 GPa. All samples show only octahedral growth sectors and the original colour was brown. The total annealing time when the temperature goes from 20°C to 2300°C is about 2 to 5 minutes after which the power of the electrical heater is turned off, and the HPHT cell is quickly cooled to room temperature. Four colourless type IaA diamonds (samples 1-1, 4-3, 6-2 and 7-3) were annealed at high temperature at the DTC Research Centre in a furnace under high vacuum ($P < 10^{-6}$ mbar) at 1700°C for 1 hour and quickly quenched after annealing.

A number of preliminary tests have been carried out to characterise natural diamonds of the type used in this study and to determine which annealing conditions are the

most suitable for this study. The results of these samples (1H3, 1H5, 1H6, 1H7, 1H8 and FDW1) and the characteristics of the samples before any irradiation or annealing is given in tables below (table 6.1 to 6.10).

Infrared spectra of the A12, A14 and A17 samples have been measured with a Bio-Rad FTS-40 system. IR measurements on other samples were carried out with a Bruker Equinox 55 or a Nicolet Nexus IR spectrometer.

The UV-VIS-NIR spectra in the range of 400 to 1000 nm of the A12, A14 and A17 samples were measured using a Princeton Instruments single beam spectrometer. The spectra of this instrument cannot be used for quantitative measurements. UV-VIS measurements of all other samples were carried out with a Perkin-Elmer Lambda 800 or a Varian Cary 100 with a resolution of 0.2 nm. The samples were cooled to liquid nitrogen temperature with a homemade cryostat.

The concentrations of different defects before and after every HPHT annealing were determined from the IR and UV-VIS spectra as explained in chapter one. All samples are type Ia diamonds with various concentrations of A, B, C and D defects. The concentrations of the A, B and C forms of nitrogen were determined from IR measurements by the procedure described in chapter 1, section 1.6. The procedure for the determination of the concentration of C defects by UV-VIS and EPR spectroscopy is given in section 6.3.3.4 of this chapter and in section 1.5.3.2 of chapter 1 respectively.

Measurements were carried out after each HPHT annealing. For the analysis in which values of the concentrations of different nitrogen aggregates from the article of Brozel *et al.* (1978) are used, the nitrogen concentrations have been corrected to reflect the newer values of the calibration coefficients.

6.2.2. Samples used

6.2.2.1. Samples to measure the C defect concentration in natural type Ia diamonds

A number of samples were measured by IR, EPR and UV-VIS spectroscopy to determine the concentration of C defects in natural, colourless and brown type IaA and brown type IaB samples. The concentrations of various nitrogen defects are given in table 6.1.

Sample	[*C*] (ppm) UV-VIS	[*C*] (ppm) EPR	[*C*] (ppm) IR	[*A*] (ppm)	[*B*] (ppm)
Sample 8-1	0	0	0	1003	0
Sample 8-2	0	0	0	913	41
Sample 8-3	0	0	0	271	228
Sample 2-1	0	0	0	176	4
1D1	0	0	0	66	8
1B1	0	0	0	113	0
1B2	0	0	0	129	0
1B3	0	0	0	141	15
B1b	0	0	0	8	116
A184b	0	0	0	0	203

Table 6.1. The concentrations of the different forms of nitrogen in natural, colourless and brown type IaA and brown type IaB samples. No C defect concentration could be detected. The uncertainty in the concentration of the defects, determined by IR measurements is 10%. Uncertainty in the concentration of C defects determined by EPR and UV-VIS measurements is 25 % and 27 % respectively.

As one can see, none of the measurements revealed detectable concentrations of single substitutional nitrogen defects before annealing. To determine low concentrations of single substitutional nitrogen a correlation has been determined between the absorption coefficient at 400 nm in the UV-VIS spectrum and the concentration of C defects as determined by analysis of the IR spectrum and the

concentration of C defects as determined by EPR measurements. This investigation is carried out in section 6.3 of this chapter.

6.2.2.2. Preliminary tests

Preliminary HPHT experiments on brown type IaA/B diamonds with $[A] << [B]$ were carried out on six samples 1H3, 1H5, 1H6, 1H7 and 1H8. They were cut from one piece of rough diamond, and an additional sample FDW1 was cut from a different piece of rough diamond. The optical windows were polished on the samples, taking care that different growth layers were as perpendicular as possible to the optical beam path of the spectrometers. The annealing temperature of samples FDW1 and 1H3 was 1900°C, of samples 1H5 and 1H6 was 2100°C, and of samples 1H7 and 1H8 was 2300°C. The concentrations of nitrogen defects before annealing are summarized in table 6.2. No C defects were detected after any HPHT annealing at 1900°C.

Sample	$[C]$ (ppm)	$[N^+]$ (ppm)	$[A]$ (ppm)	$[B]$ (ppm)	Integr. Int. Platelet (cm^{-2})
FDW1	0	0	20	60	23
1H3	0	0	45	215	95
1H5	0	0	45	208	106
1H6	0	0	42	97	44
1H7	0	0	49	118	51
1H8	0	0	49	312	160

Table 6.2. The concentrations of the different nitrogen related defect concentrations in the 1H3, 1H5 to 1H8 and FDW1 diamonds, before annealing. The uncertainty in the defect concentration is 10%. HPHT annealed at 2300°C for 5 minutes at Sundance Inc.

These samples (FDW1, 1H3 and 1H5 – 1H8) were annealed twice at Sundance Inc., every time for 5 min. Absorption measurements were carried out on the samples after every annealing.

Three relatively colourless type Ia diamonds (ak928a8, ak929a1 and ak9252a1) were annealed for 5 minutes at 2300°C in the Belt press at NIMS, and were used to study the A defect dissociation.

The samples annealed at NIMS were three light yellow type Ia diamonds with [*A*] >> [*B*]. The concentrations of the different nitrogen aggregates are given in tables 6.3 and 6.4.

Sample	[*C*] (ppm)	[N^+] (ppm)	[*A*] (ppm)	[*B*] (ppm)
ak928a8	47	0	441	148
ak929a1	44	0	553	138
ak9252a1	15	0	164	640

Table 6.3. The concentrations of the different nitrogen related defect concentrations in the ak diamonds, HPHT annealed at 2300°C. The uncertainty in the defect concentration is 10%.

No H3 was detected in the ak series of HPHT annealed diamonds. Three (nearly) type IaA samples were HPHT annealed at 2300°C for 3 minutes to generate C defects nitrogen.

Sample	[*C*] (ppm)	[N^+] (ppm)	[*A*] (ppm)	[*B*] (ppm)
Sample 2-2	0	0	176	5
Sample 9	0	0	526	35
Sample 10	0	0	551	84

Table 6.4. The defect concentrations in type Ia diamonds before HPHT annealing at 2300°C. The uncertainty in the defect concentration is 10%.

6.2.2.3. Brown type IaA diamonds

Four brown type IaA diamonds were HPHT annealed twice at 2100°C. In each annealing run the diamond is at 2100°C for three minutes. Increased absorption of H3

defects was detected after the first annealing. No B defects or platelets were observed prior to annealing, and after the first and second annealing, a weak platelet peak is observed (figure 6.2). Weak H2 absorption was also detected after HPHT annealing (see figure 6.3). The absorption strength of both defects decreased after the second annealing. The concentration of the nitrogen related defects as detected in the IR spectrum is given in table 6.5 and the changes of the H3 and N3 concentrations are given in figures 6.4 and 6.5.

Sample	[*C*] (ppm) UV-VIS	[*C*] (ppm) IR	[*A*] (ppm)	[*B*] (ppm)	Integr. int. platelets (cm^{-2})
1D1	0	0	66	8	0
1B1	0	0	113	0	0
1B2	0	0	129	0	0
1B3	0	0	108	0	0

Table 6.5. The concentrations of the nitrogen aggregates in the brown type IaA samples before HPHT annealing. The uncertainty in the concentration of the defects, determined by IR measurements is 10%. Uncertainty in the concentration of C defects determined by EPR and UV-VIS measurements is 25 % and 27 % respectively.

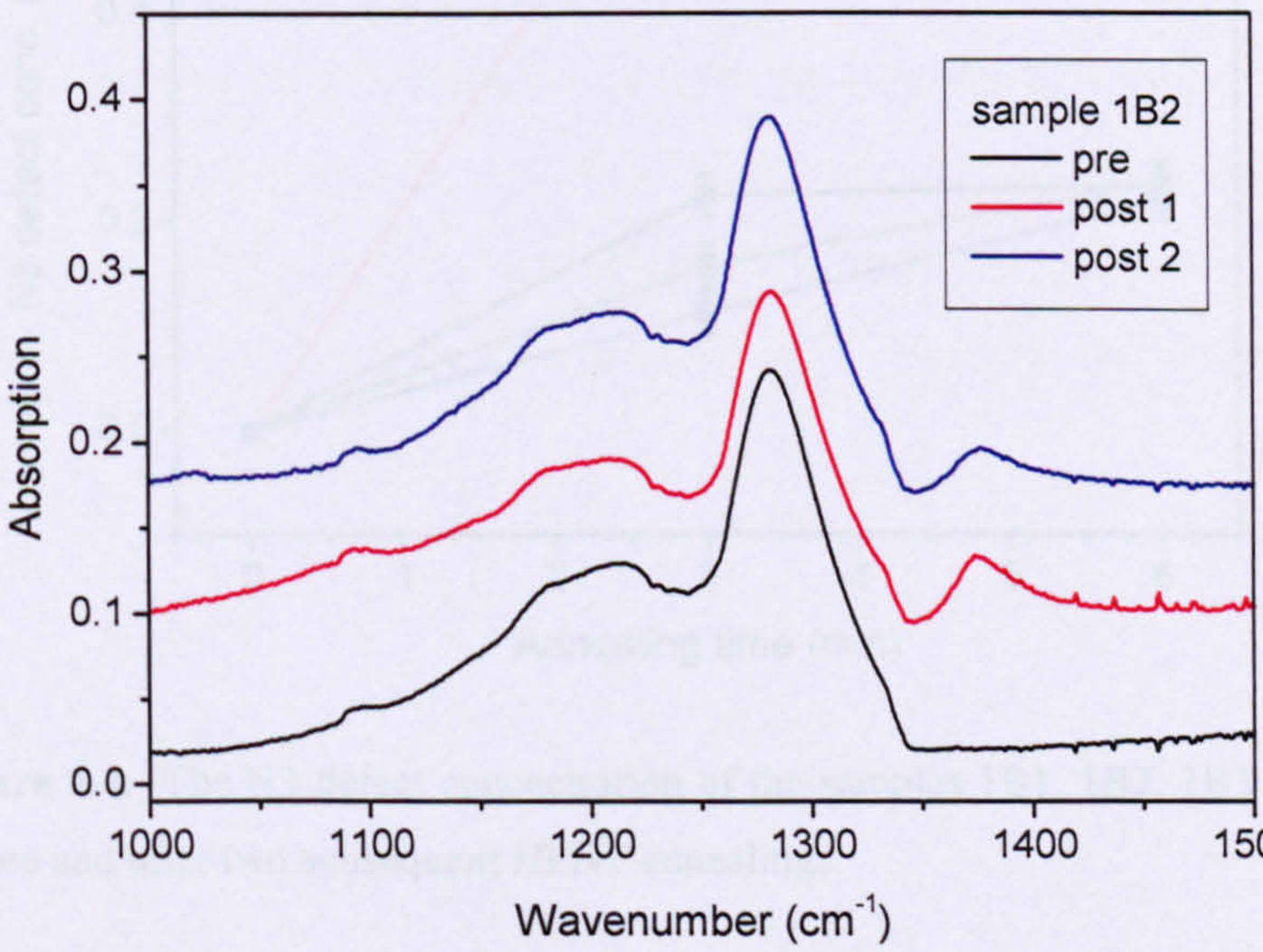

Figure 6.2. The IR spectrum of sample 1B2 before, after the first and second HPHT annealing. No platelet peak is detected before annealing but is present after the first and second HPHT annealing. Spectra have been displaced for clarity.

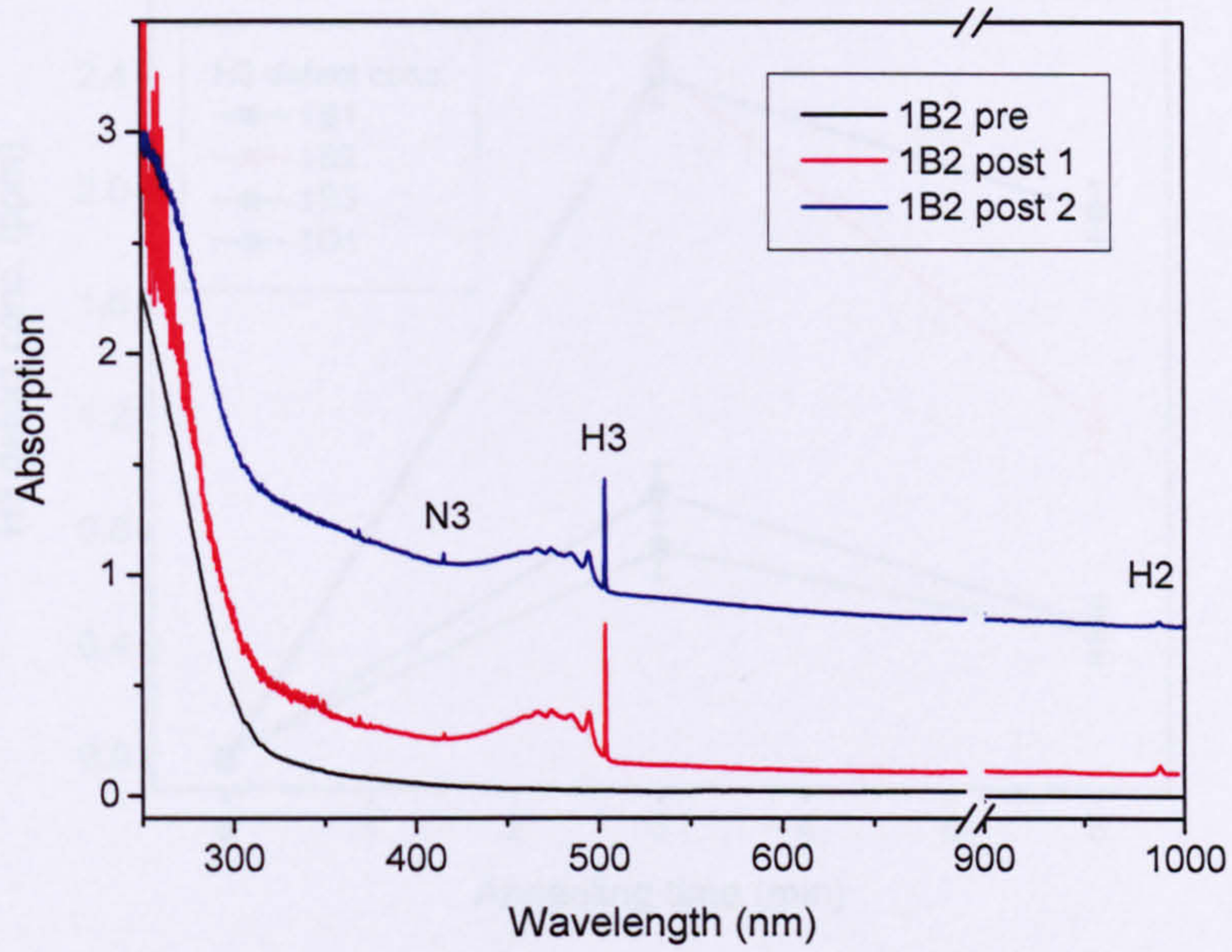

Figure 6.3. The UV-VIS-NIR absorption spectrum of a light brown type IaA diamond before and after the first and second HPHT annealing at 2100°C, for 3 minutes. No N3, H3 or H2 peak was detected before annealing, but were present after every subsequent HPHT annealing. Spectra have been displaced for clarity.

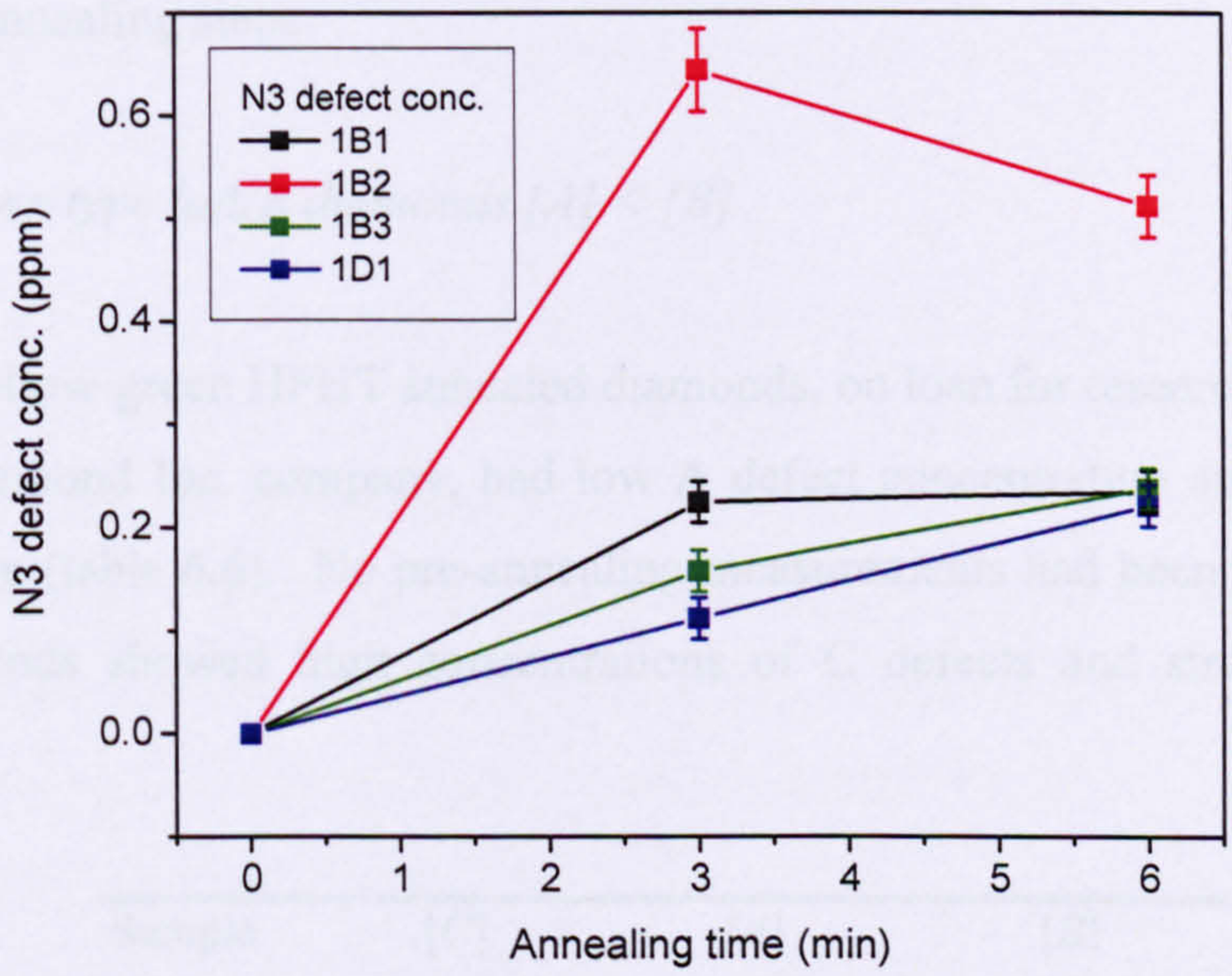

Figure 6.4. The N3 defect concentration of the samples 1B1, 1B2, 1B3 and 1D1 before and after two subsequent HPHT annealings.

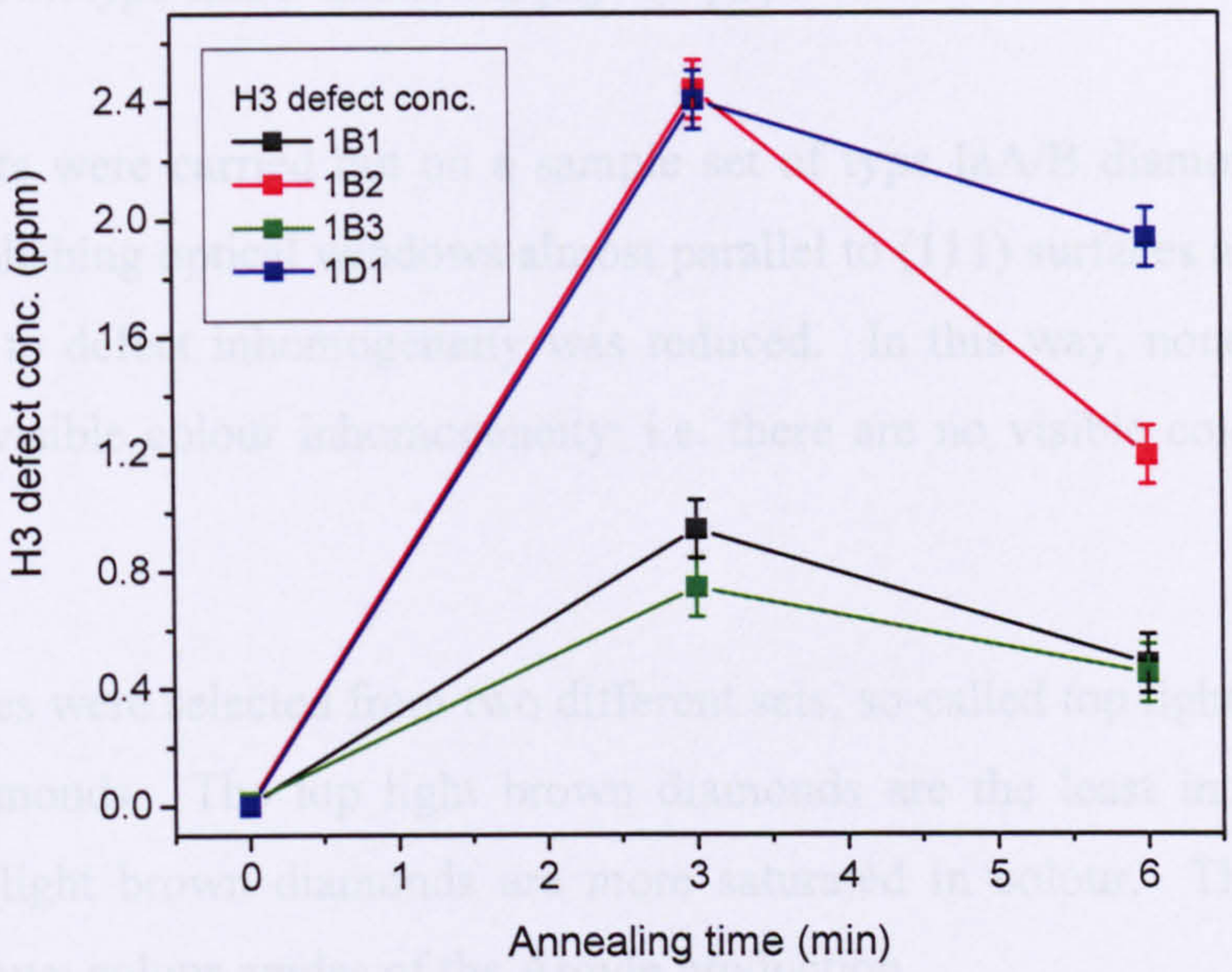

Figure 6.5. The H3 defect concentration of the samples 1B1, 1B2, 1B3 and 1D1 before and after two subsequent HPHT annealings.

No N-V defects could be detected in the UV-VIS absorption spectra after the two successive annealing steps.

6.2.2.5. Brown type IaA/B diamonds [A] < [B]

The three yellow-green HPHT annealed diamonds, on loan for research purposes from the NovaDiamond Inc. company, had low A defect concentration and high B defect concentration (table 6.6). No pre-annealing measurements had been carried out. All these diamonds showed high concentrations of C defects and strong H3 and H2 absorption.

Sample	[C] (ppm)	[A] (ppm)	[B] (ppm)
A12	9.6	13.2	83.7
A14	19.8	69.5	145.2
A17	24.7	48.0	115.7

Table 6.6. The concentrations of the different forms of nitrogen in the samples annealed at 2300°C and 5 – 6 GPa. All concentration values have a ± 10 % uncertainty.

6.2.2.6. Brown type IaA/B diamonds [A] << [B]

Further tests were carried out on a sample set of type IaA/B diamonds with [*A*] << [*B*]. By polishing optical windows almost parallel to (111) surfaces a reduction of the errors due to defect inhomogeneity was reduced. In this way, none of the samples displayed visible colour inhomogeneity; i.e. there are no visible colour bands in the diamond.

The samples were selected from two different sets, so-called top light brown and light brown diamonds. The top light brown diamonds are the least intensely coloured, while the light brown diamonds are more saturated in colour. These are the two lightest brown colour grades of the Argyle production.

This sample set is divided in two groups: one group (samples tlb-1, 3, 5, 6, 7 and lb-1, 2, 3, 5 6) and the second group (tlb-2, 4 and lb-4, 7, 8). The first sample set was subjected to a series of 3 minute anneals at 2100°C. The second sample set was similarly subjected to a series of 3 minute anneals at 2200°C. Sample tlb-2 broke after the first annealing.

The variation of the $(N\text{-}V)^-$ defect concentration with time is given in figures 6.6 and 6.7. The concentration of $(N\text{-}V)^-$ defects is only detectable after long annealing at 2100°C and relatively shorter annealing time at 2200°C. The change of N3 defect concentration appears to be strongly sample dependent (figures 6.8 and 6.9). The H3 defect concentration increases strongly and then decreases at longer annealing time (figures 6.10 and 6.11) and is clearly a transient defect. H4 defects were not observed in any of the absorption measurements.

The concentrations of the nitrogen related defects, as determined from the IR spectrum are given in table 6.7. Sample tlb-7 has additional absorption, starting under the nitrogen one-phonon part and up to ~ 1480 cm^{-1}; as a consequence the concentrations of nitrogen aggregates and the integrated intensity of the platelet peak could not be determined accurately and this sample is not used for analysis of the IR results.

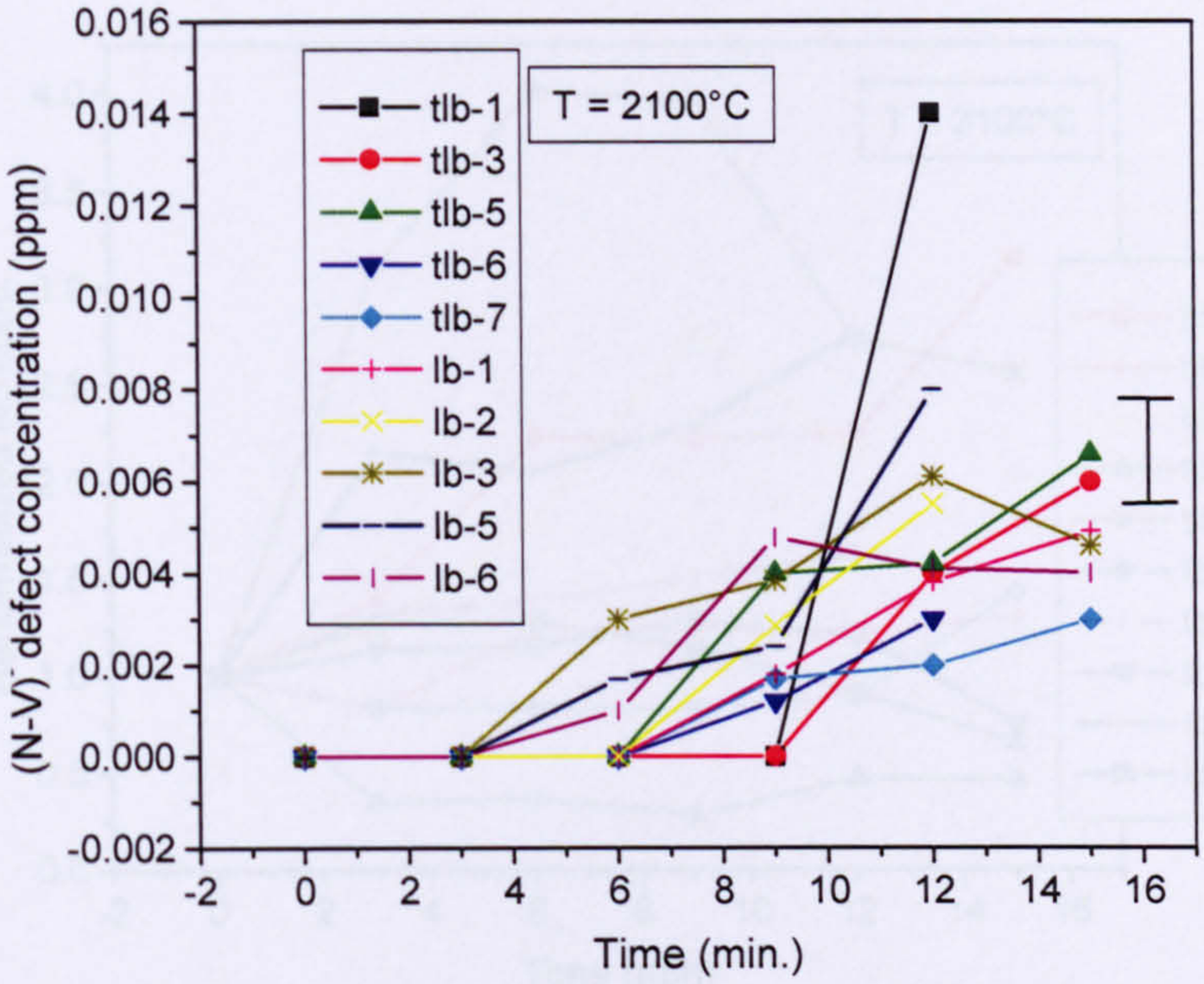

Figure 6.6. The $(N\text{-}V)^-$ defect concentration as function of annealing time for samples HPHT annealed at 2100°C.

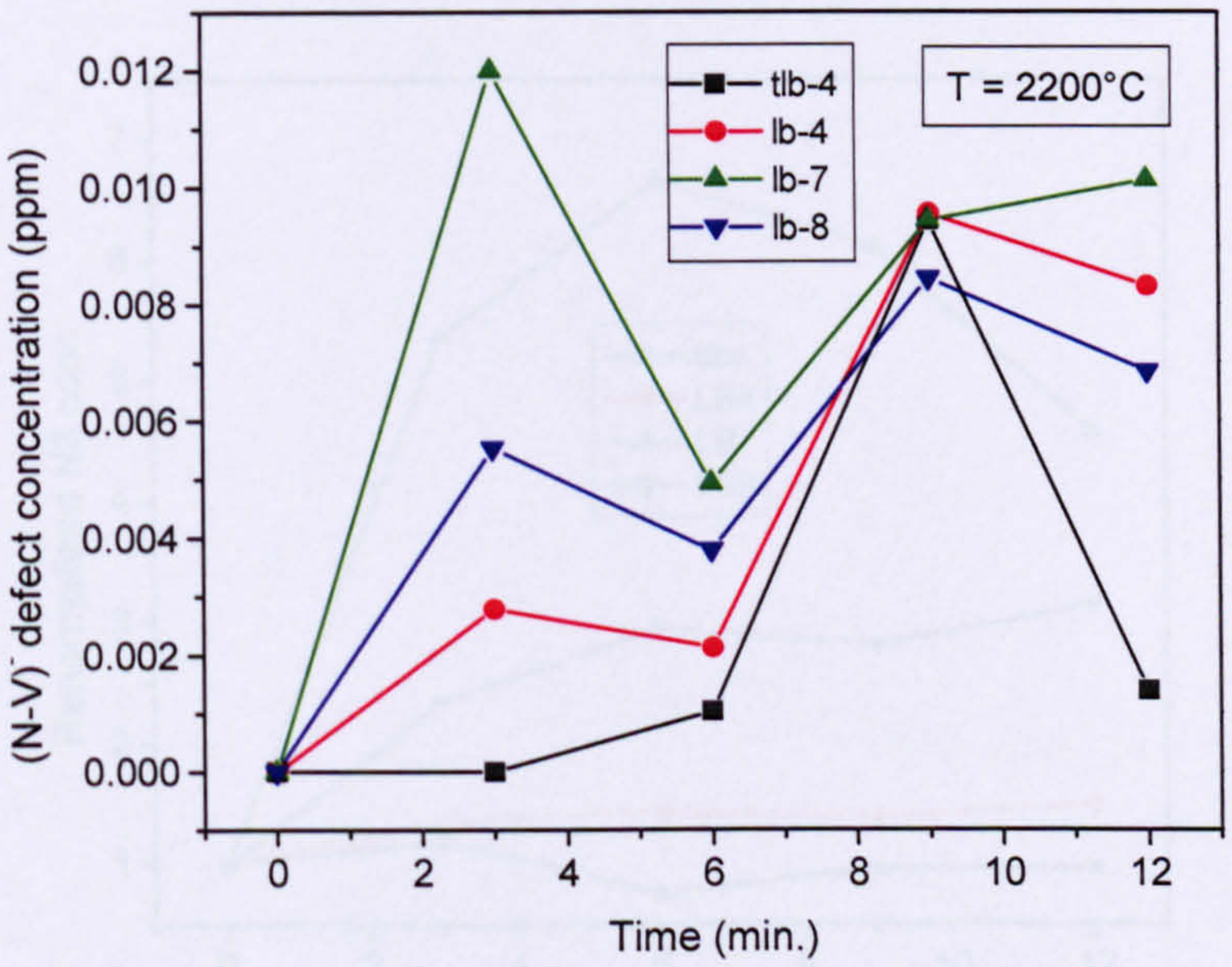

Figure 6.7. The $(N\text{-}V)^-$ defect concentration as function of annealing time for samples HPHT annealed at 2200°C.

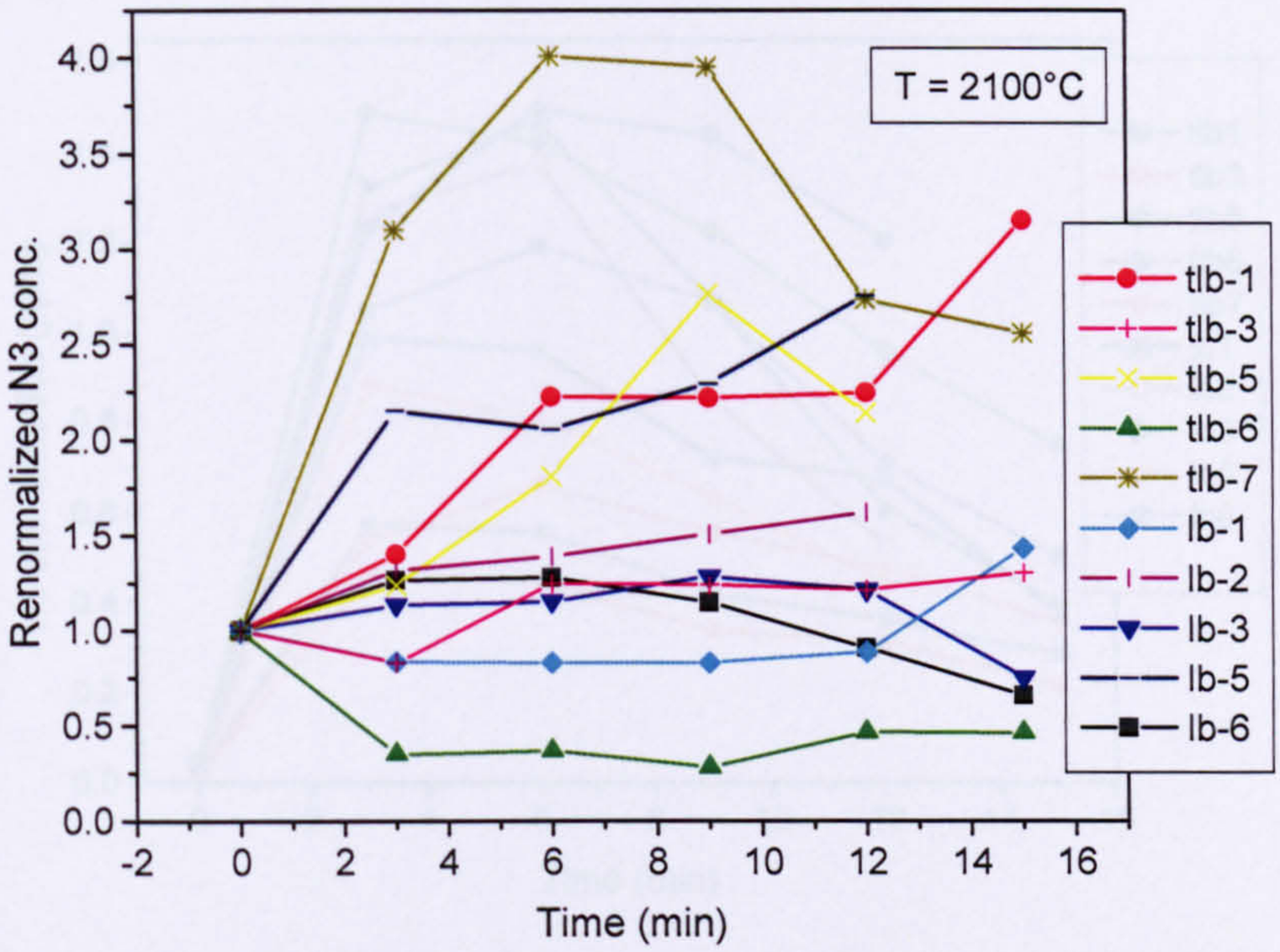

Figure 6.8. The N3 defect concentration, relative to the initial concentration, as a function of annealing time for samples HPHT annealed at 2100°C in steps of three minutes.

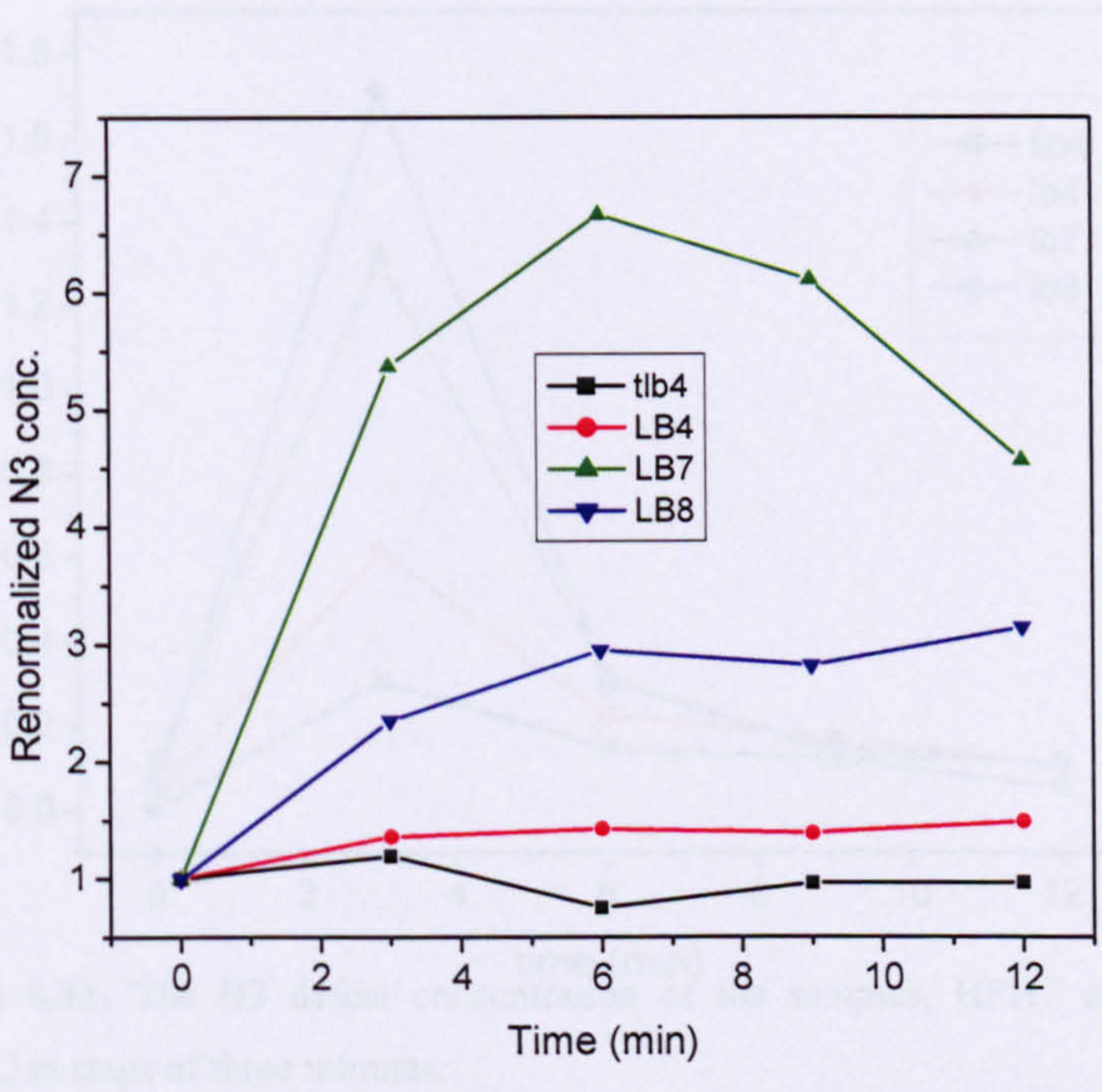

Figure 6.9. The N3 defect concentration, relative to the initial concentration, as a function of annealing time for samples HPHT annealed at 2200°C in steps of three minutes.

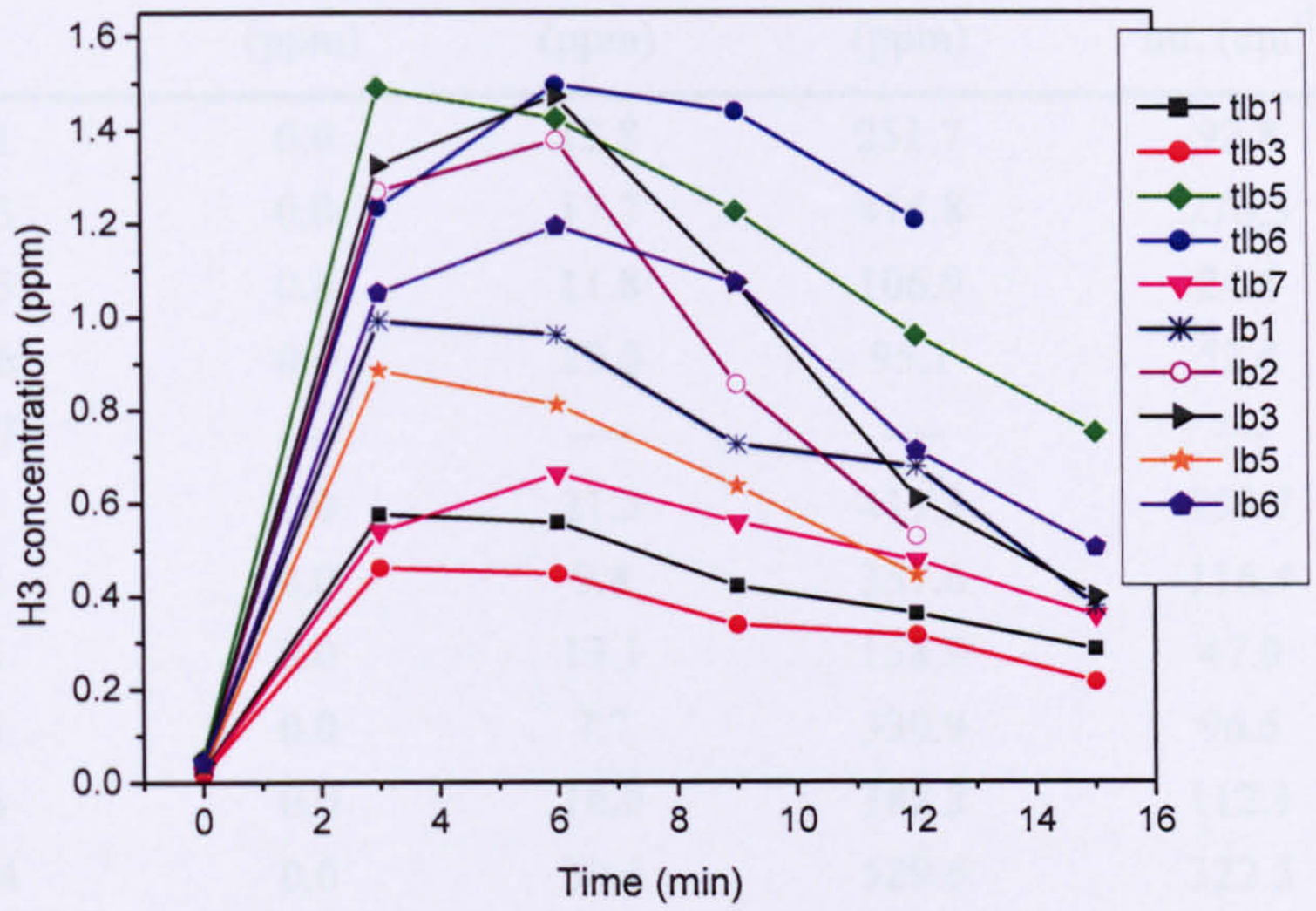

Figure 6.10. The H3 defect concentration of the samples, HPHT annealed at 2100°C in steps of three minutes.

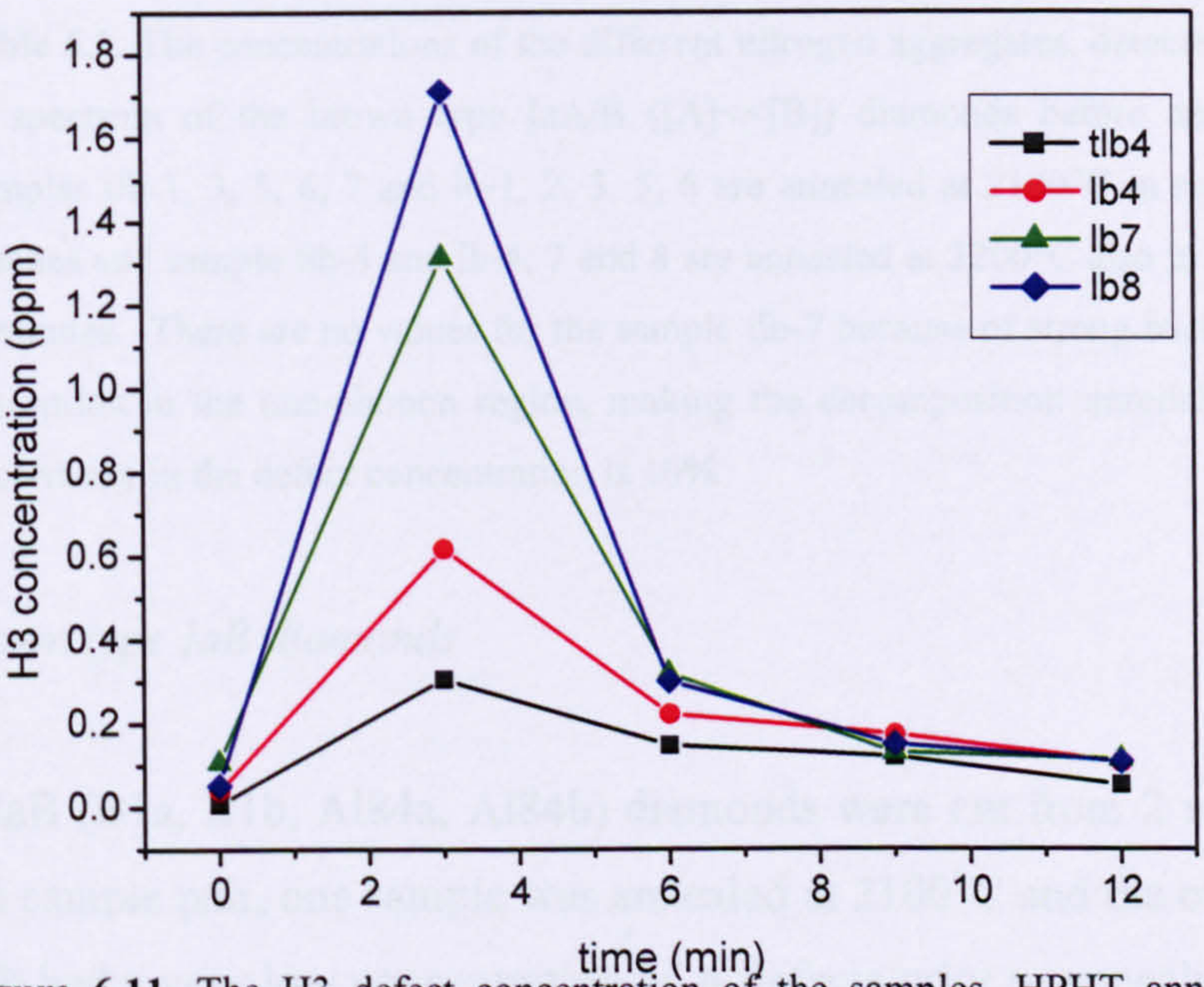

Figure 6.11. The H3 defect concentration of the samples, HPHT annealed at 2200°C in steps of three minutes.

Sample	[*C*] (ppm)	[*A*] (ppm)	[*B*] (ppm)	Platelet Integr. Int. (cm^{-2})
tlb-1	0.0	12.8	251.7	92.8
tlb-3	0.0	17.7	416.8	276.3
tlb-5	0.0	11.8	106.9	24.6
tlb-6	0.0	29.8	95.1	52.4
tlb-7	----	----	----	----
lb-1	0.0	21.5	419.3	259.7
lb-2	0.0	9.8	357.6	116.4
lb-3	0.0	13.1	158.9	47.0
lb-5	0.0	7.7	330.9	96.5
lb-6	0.0	10.9	388.3	112.1
tlb-4	0.0	30.4	529.6	322.5
lb-4	0.0	14.1	345.7	98.3
lb-7	0.0	14.8	55.3	22.7
lb-8	0.0	30.4	137.9	56.6

Table 6.7. The concentrations of the different nitrogen aggregates, detected in the IR spectrum of the brown type IaA/B ([A]<<[B]) diamonds before annealing. Samples tlb-1, 3, 5, 6, 7 and lb-1, 2, 3, 5, 6 are annealed at 2100°C in steps of 3 minutes and sample tlb-4 and lb-4, 7 and 8 are annealed at 2200°C also in steps of 3 minutes. There are no values for the sample tlb-7 because of strong background absorption in the one-phonon region, making the decomposition unreliable. The uncertainty in the defect concentration is 10%.

6.2.2.7. Brown type IaB diamonds

Four type IaB (B1a, B1b, Al84a, Al84b) diamonds were cut from 2 rough diamonds and of each sample pair, one sample was annealed at 2100°C and the other at 2200°C. Sample B1b had a very low concentration of A defects prior to annealing (8 ± 1 ppm) and turned yellow after HPHT annealing at 2200°C. The UV-VIS and IR absorption spectrum clearly identified the presence of C defects (5 ± 1 ppm). Very weak H4 defect absorption was detected in the UV-VIS absorption spectrum of all samples and was comparable with the intensity of the H3 absorption. None of the samples displayed platelet absorption in the IR spectrum (figure 6.12).

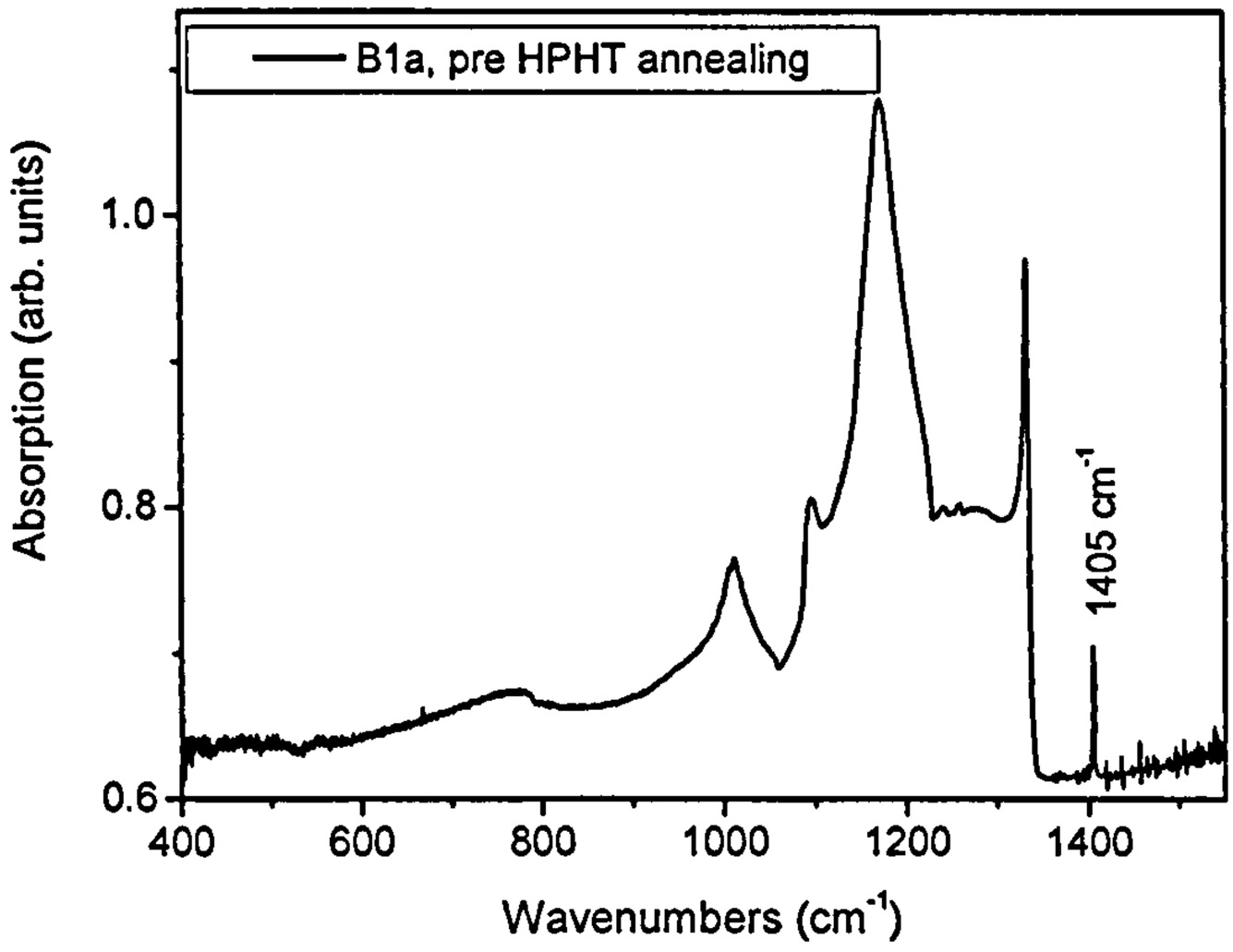

Figure 6.12. The IR spectra of a brown type IaB diamond before HPHT annealing. Note the absence of a platelet peak in the IR spectrum.

Sample	[C] (ppm) UV-VIS	[C] (ppm) EPR	[C] (ppm) IR	[A] (ppm) IR	[B] (ppm) IR
B1b	0	0	0	8	116
Al84b	0	0	0	0	203
B1a	0	0	0	0	183
Al84a	0	0	0	0	199

Table 6.8. The nitrogen aggregate concentration as detected by IR, EPR and UV-VIS in the type IaB diamonds before HPHT annealing at 2100°C (samples B1b and Al84b) and 2200°C (samples B1a and Al84a). The uncertainty in the defect concentration is 10%. Uncertainty in the concentration of C defects determined by EPR and UV-VIS measurements is 25 % and 27 % respectively.

6.2.2.8. HPHT annealing of irradiated type Ia diamond

Four irradiated type Ia diamonds (6 MeV, 1.10^{17} e^-/cm^2 or 8 MeV, 8.10^{18} e^-/cm^2) were HPHT annealed at 2100°C (sample 14), 2200°C (sample 2) and 2 samples at 2300°C (samples 6-1 and 4-2) respectively. Each sample was annealed for three minutes. The irradiation conditions and the concentrations of A and B defects are given in table 6.9 below.

Sample	[C] (ppm)	[A] (ppm)	[B] (ppm)	Irr. energy (MeV)	Irr. dose (e^-/cm^2)
Sample 2	0	660	243	6	1.10^{17}
Sample 14	0	107	60	8	8.10^{18}
Sample 4-2	0	973	53	8	8.10^{18}
Sample 6-1	0	552	89	8	8.10^{18}

Table 6.9. The concentrations of nitrogen aggregates of colourless type Ia diamonds, before irradiation and HPHT annealing. The irradiation conditions of each diamond are given in the last two columns. The uncertainty in the defect concentration is 10%.

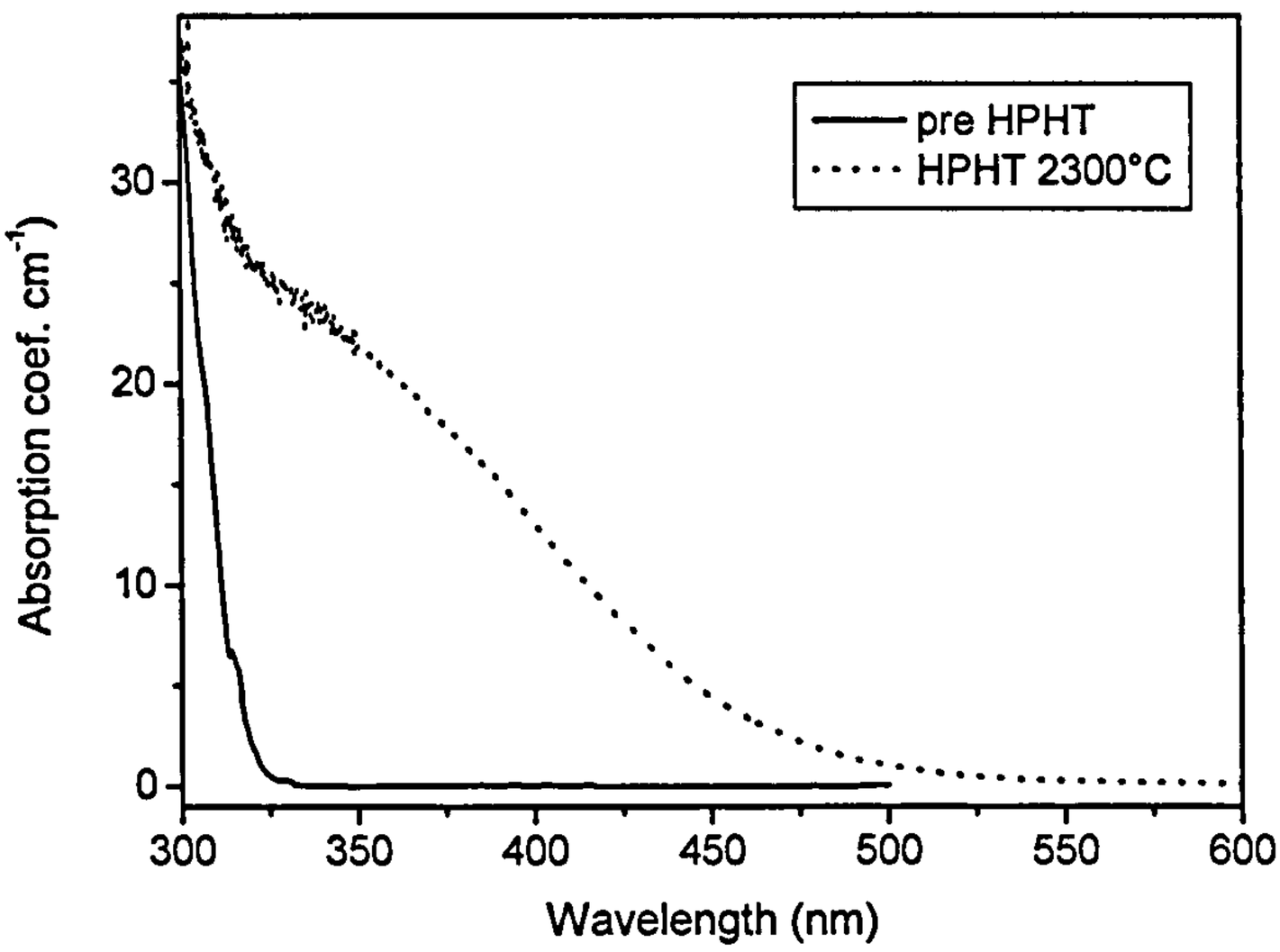

Figure 6.13. The UV-VIS absorption spectrum at room temperature of sample 6-1 before and after HPHT annealing at 2300°C.

These are the same samples as in chapter five. After HPHT annealing, only sample 14 showed weak H3 absorption. The samples annealed at temperatures above 2100°C have a spectrum similar to one shown in figure 6.13.

6.2.2.9. Samples HT and HPHT annealed at 1700°C

To study the influence of pressure on the dissociation of A defects, four colourless type IaA diamonds were annealed at 1700°C under vacuum and five colourless type IaA diamonds at 1700°C but under stabilizing pressure of 7.5 GPa.

The samples annealed at 1700°C for one hour under vacuum were graphitised on the surface and had to be repolished and the thickness of two samples was reduced by 20 μm, while the thickness reduction of two other samples was 170 and 200 μm respectively on a total sample thickness of ~ 3 mm. There is a comparable thickness loss when the diamond is HPHT annealed. One sample broke during annealing. EPR measurements were only carried out after annealing. A slight increase in the UV-VIS absorption of the samples was detected after annealing (figure 6.14).

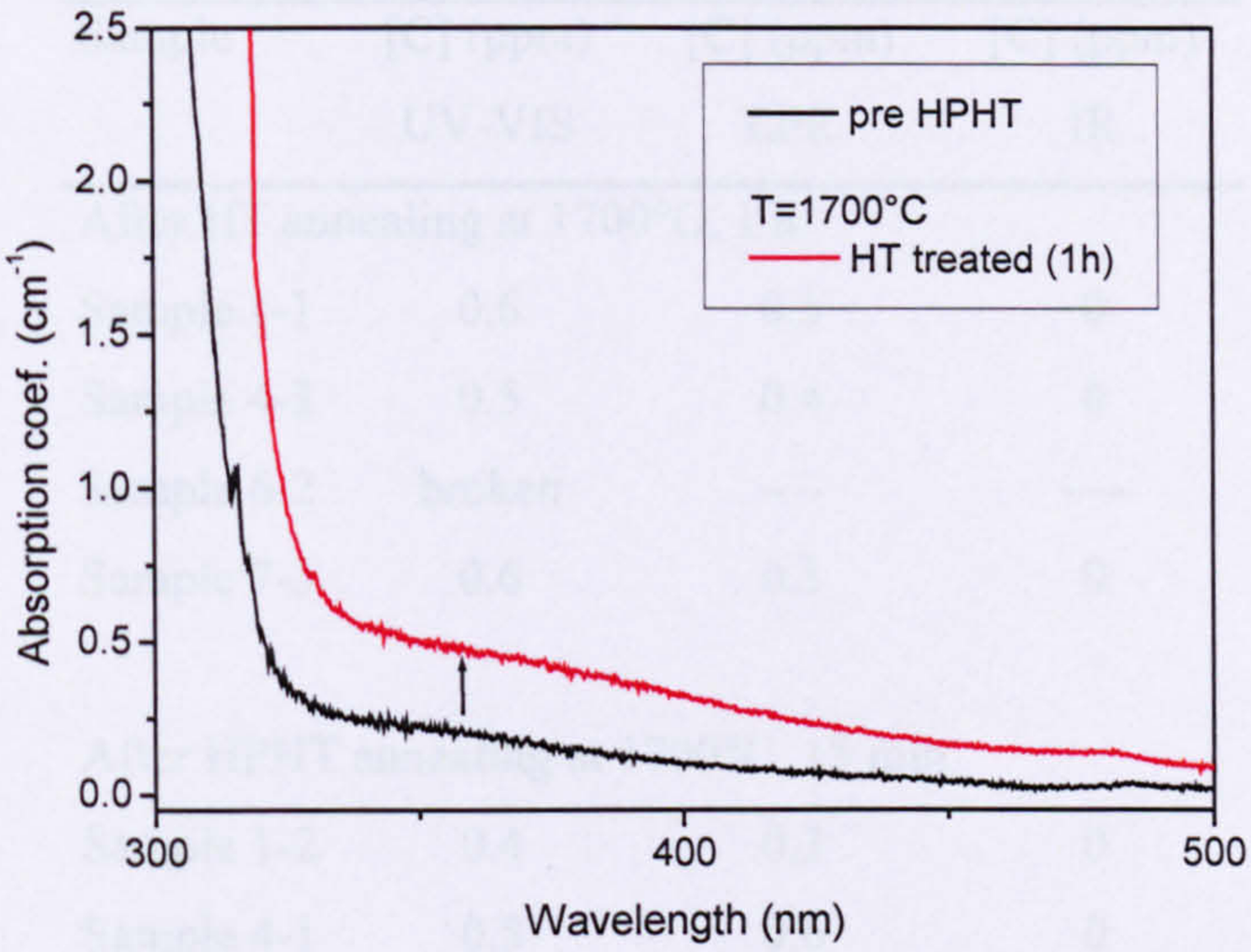

Figure 6.14. The room temperature UV-VIS spectra of colourless type IaA diamonds (sample 7-3) before and after annealing under high vacuum for 1 hour.

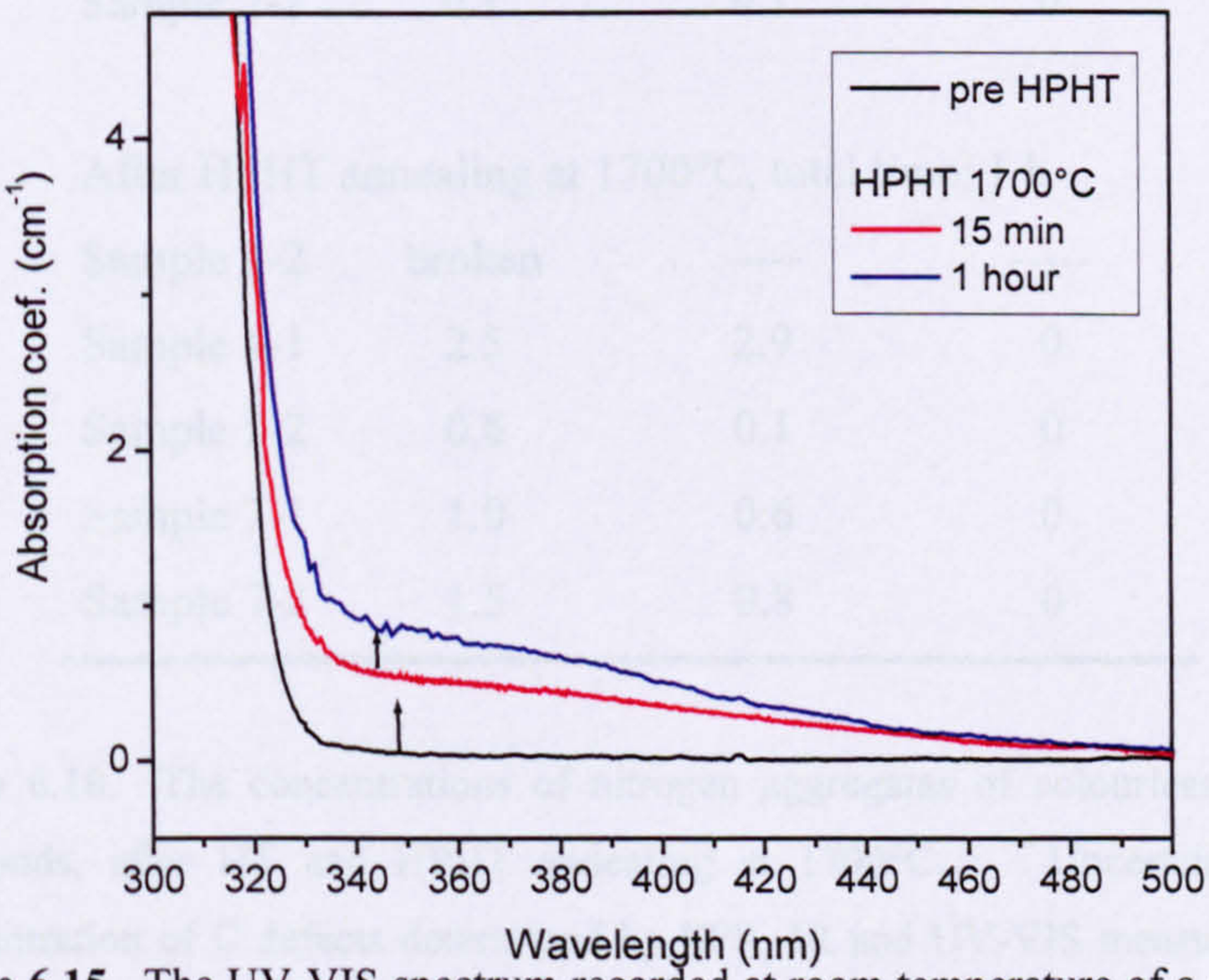

Figure 6.15. The UV-VIS spectrum recorded at room temperature of a colourless type IaA diamond (sample 4-1) before HPHT annealing at 1700°C for 15 minutes and for 45 additional minutes (the total annealing time was 1 hour).

The samples annealed at 1700°C under stabilizing pressure of 7.5 GPa were annealed for 15 minutes and additionally annealed for 45 minutes, making the total annealing time also one hour. The UV-VIS spectra are shown in figure 6.15. EPR measurements were carried out after the first and second HPHT annealing (see section 6.4 of this chapter).

The concentrations of nitrogen related defects are given in table 6.10 below.

Sample	[C] (ppm) UV-VIS	[C] (ppm) EPR	[C] (ppm) IR
After HT annealing at 1700°C, 1 h			
Sample 1-1	0.6	0.5	0
Sample 4-3	0.5	0.4	0
Sample 6-2	broken	----	----
Sample 7-3	0.6	0.3	0
After HPHT annealing at 1700°C, 15 min			
Sample 1-2	0.4	0.3	0
Sample 4-1	0.5	0.6	0
Sample 5-2	0.0	0.0	0
Sample 7-1	0.2	0.2	0
Sample 7-2	0.1	0.1	0
After HPHT annealing at 1700°C, total time: 1 h			
Sample 1-2	broken	-----	-----
Sample 4-1	2.5	2.9	0
Sample 5-2	0.8	0.1	0
Sample 7-1	1.0	0.6	0
Sample 7-2	1.5	0.8	0

Table 6.10. The concentrations of nitrogen aggregates of colourless type IaA diamonds, after HT and HPHT annealing at 1700°C. Uncertainty in the concentration of C defects determined by EPR, IR and UV-VIS measurements is 25%, 10% and 27% respectively.

A final note: none of the non-irradiated, colourless samples annealed at 1700°C under pressure or in vacuum or higher temperatures displays detectable concentrations of nitrogen-vacancy defects.

6.3. A centre dissociation

6.3.1. Introduction

When type I diamonds are subjected to HPHT annealing at moderate temperature (T ~ 1500 to 1800°C), C defects will be mobile and can aggregate as A defects. The reaction describing this process is:

$$C + C \leftrightarrow A \tag{6.3.1}$$

Annealing at moderate temperature will favour the forward reaction (Woods 1994), and the reaction has been modelled by Chrenko *et al.* (1977) and Kiflawi *et al.* (1997) as a second order reaction:

$$\frac{d[C(t)]}{dt} = -k[C(t)]^2 \tag{6.3.2}$$

with $[C(t)]$ the concentration of C defects after time t and k the rate constant. The solution of this differential equation is:

$$\frac{1}{[C(t)]} - \frac{1}{[C(0)]} = kt \tag{6.3.3}$$

Kiflawi *et al.* (1997) carefully investigated the $1/[C(t)]$ behaviour and confirmed the second order reaction of C defect aggregation in the temperature range they used to anneal the diamonds, consistent with the result of Chrenko *et al.* (1977). They were very careful to eliminate errors due to sample inhomogeneities. From their study, they determined an activation energy for nitrogen aggregation of 5.5 ± 0.7 eV. Exponential pre-constants were sample dependent and are linked to other impurities in

the synthetic diamond sample. Their influence is significant: the rate constant can differ by a factor of 10 (Kiflawi *et al.* 1997). Curiously enough, neither of the pre-constants (1.19 10^{10} Hz or 0.4 cm^{-1} and 1.59 10^{11} Hz or 5.3 cm^{-1}) is a resonant vibration frequency of C defects in diamond.

Brozel *et al.* (1978) also detected C defects after annealing of natural type Ia diamond at temperatures in excess of 1900°C. Annealing at higher temperature clearly activates the backward reaction in equation 6.3.1. The C defect concentration is thus determined by mixed first order (dissociation) and second order (aggregation) kinetics. The purpose of this section is to investigate the single substitutional nitrogen concentration produced by mixed first order aggregation and second order dissociation kinetics of the reaction.

6.3.2. Theoretical

The equation describing the kinetics is the separable first order differential equation

$$\frac{d[C(t)]}{dt} = -K_1[C(t)]^2 + 2K_2([C(0)]-[C(t)]) \qquad (6.3.4)$$

$[C(t)]$ is the concentration of C centres, $(C(0) - C(t))/2$ is the concentration of A centres. The first term on the right-hand side describes the aggregation of single substitutional nitrogen atoms into A centres. The second term describes the dissociation of A centres into C centres. K_1 and K_2 are the rate constants for aggregation and dissociation respectively. The solution of the equation describes a complicated behaviour of C as a function of time, aggregation and dissociation coefficients. The equation can be substantially simplified by keeping in mind that the concentration of C centres in our analysis is low, so the complicated C-dependent part can be approximated by the constant and linear terms of the appropriate Taylor series. The solution is then:

$$[C(t)] = f - f.\exp(-kt) \qquad (6.3.5)$$

Where f and k are constants and t is the annealing time. The constant k is equal to

$$\sqrt{4K_2^2 + 8K_1K_2[C(0)]} \qquad (6.3.6)$$

To demonstrate the validity of equation 6.3.5, the variation of [C(t)] with time has been calculated numerically from equation 6.3.4, using the plausible values [C(0)] = 100 ppm, $K_1 = 10^{-4}$ (ppm)$^{-1}$ s^{-1} and $2K_2 = 10^{-3}$ s^{-1}. The values obtained are shown by the continuous curve in figure 6.16. The dashed curve has been calculated from equation 6.3.5, where f has been chosen so that both curves have the same final amplitude and k has been adjusted so that both curves pass through the point f (1 – 1/e). It can be seen that there is a negligible difference between the two curves in figure 6.13, and this is true over a wide range of the parameters [C(0)], K_1 and K_2. The value of k used for the dashed curve in figure 6.13 is 4.63×10^{-3} s^{-1}; because of the approximations made, this differs somewhat from the value 6.40×10^{-3} s^{-1} calculated from equation 6.3.6.

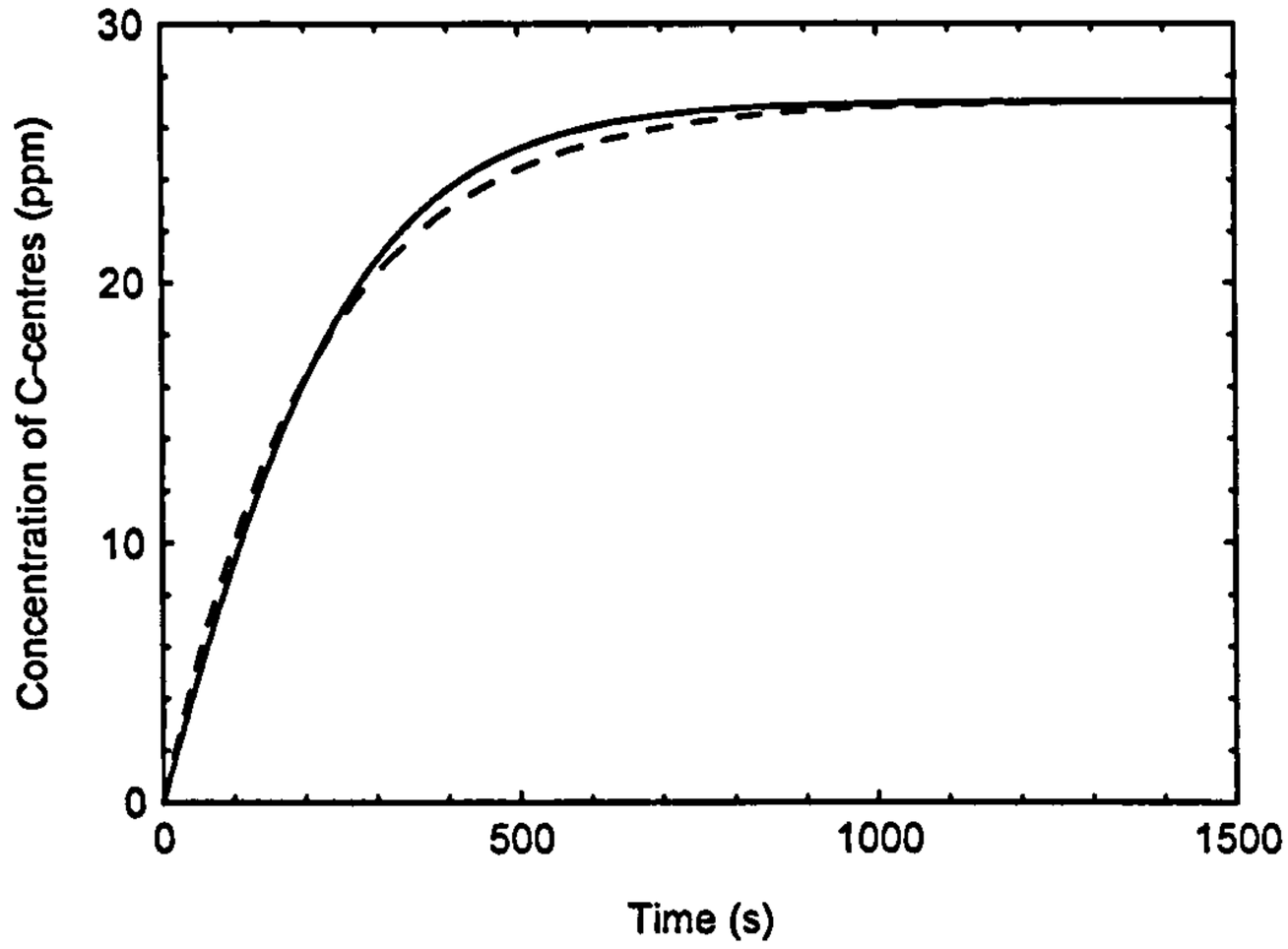

Figure 6.16. Concentration of C centres as a function of time, calculated numerically from equation 6.3.4 (continuous curve). The dashed curve is the function given in equation 6.3.5 (see text for details).

The binding energy of the nitrogen atoms in the A centres can be calculated from the equation (Allen and Evans 1981, see also chapter 1, section 1.3.2):

$$\frac{[A]_{eq}}{[C]_{eq}^2} = g.\exp\left(\Delta H / k_B T\right) \qquad (6.3.7)$$

Here the $[A]_{eq}$ is the A centre concentration in ppm, $[C]_{eq}$ is the C centre concentration in ppm at equilibrium, g is a constant, ΔH is the binding energy of the A centre, k_B is the Boltzmann constant and T is the temperature in Kelvin.

6.3.3. Results and discussion

6.3.3.1. Analysis of published results

First the results of Brozel *et al.* (1978) are analysed. In that work the C centre concentration was measured before and after HPHT annealing. The annealing was carried out at different temperatures and figure 6 in the article of Brozel *et al.* (1978) displays the results of the annealing as a function of annealing time. Here those data are fitted with a function with three different, independent parameters:

$$C = P - Q\exp(-Rt) \qquad (6.3.8)$$

A close fit to the data can be reached (see figure 6.17 and figure 6.18) and in each case the parameters P and Q are equal within the uncertainty. The parameters P and Q are then constrained to be equal. In the first seconds to minutes, when the high temperature is reached during the HPHT annealing, only dissociation occurs because of the lack of C centres; consequently the reaction is close to first order kinetics. The dissociation rate constant can then be calculated and the Arrhenius plot indicates a value of 5.6 ± 1.4 eV for the activation energy. This activation energy is effectively the binding energy of the A aggregate.

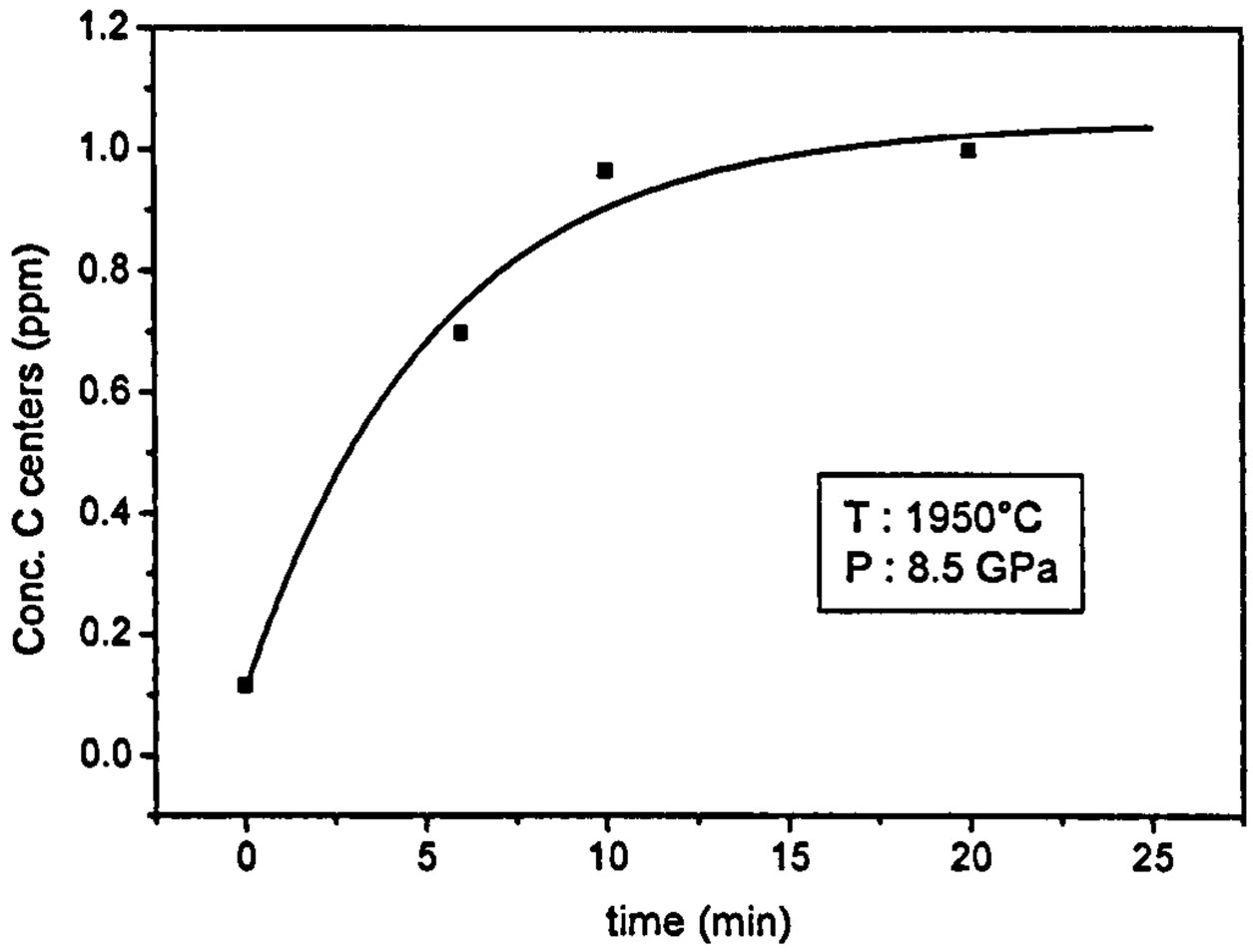

Figure 6.17. The fit with equation 6.3.8 to the data in figure 6 of Brozel *et al.* (1978) for a sample annealed at T = 1950°C and P = 8.5 GPa for various periods of time.

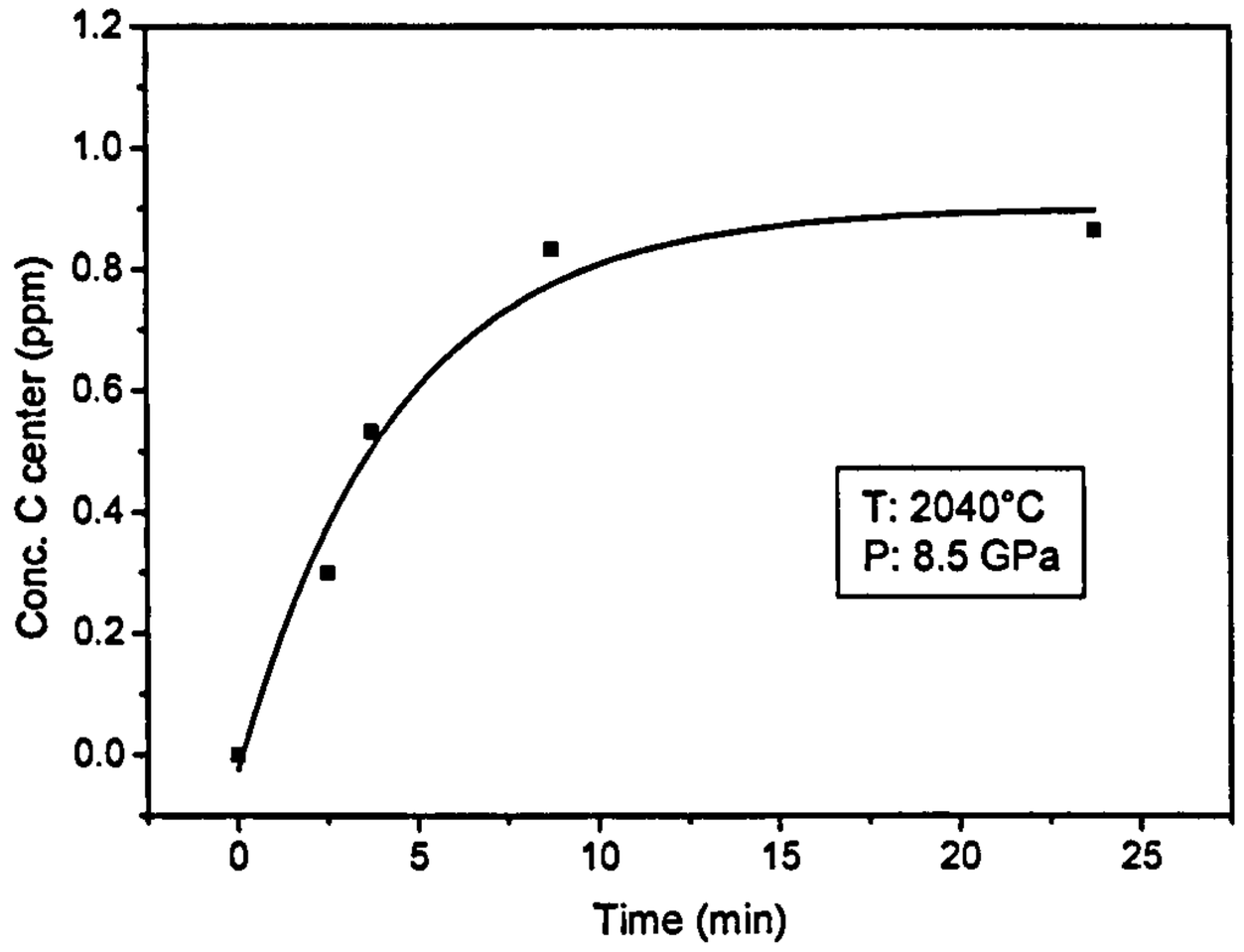

Figure 6.18. The fit with equation 6.3.8 to the data in figure 6 of Brozel *et al.* (1978) for a sample annealed at T = 2040°C and P = 8.5 GPa for various periods of time.

The binding energy can also be found by plotting $\ln([A]/[C]^2)$ versus 1000/T and fitting the data by a linear function. From these data a value of 7.66 ± 0.6 eV is determined (see figure 6.19). This is in agreement (within the standard deviations) with the value of 5.6 ± 1.4 eV, calculated above, for the dissociation of the A centre.

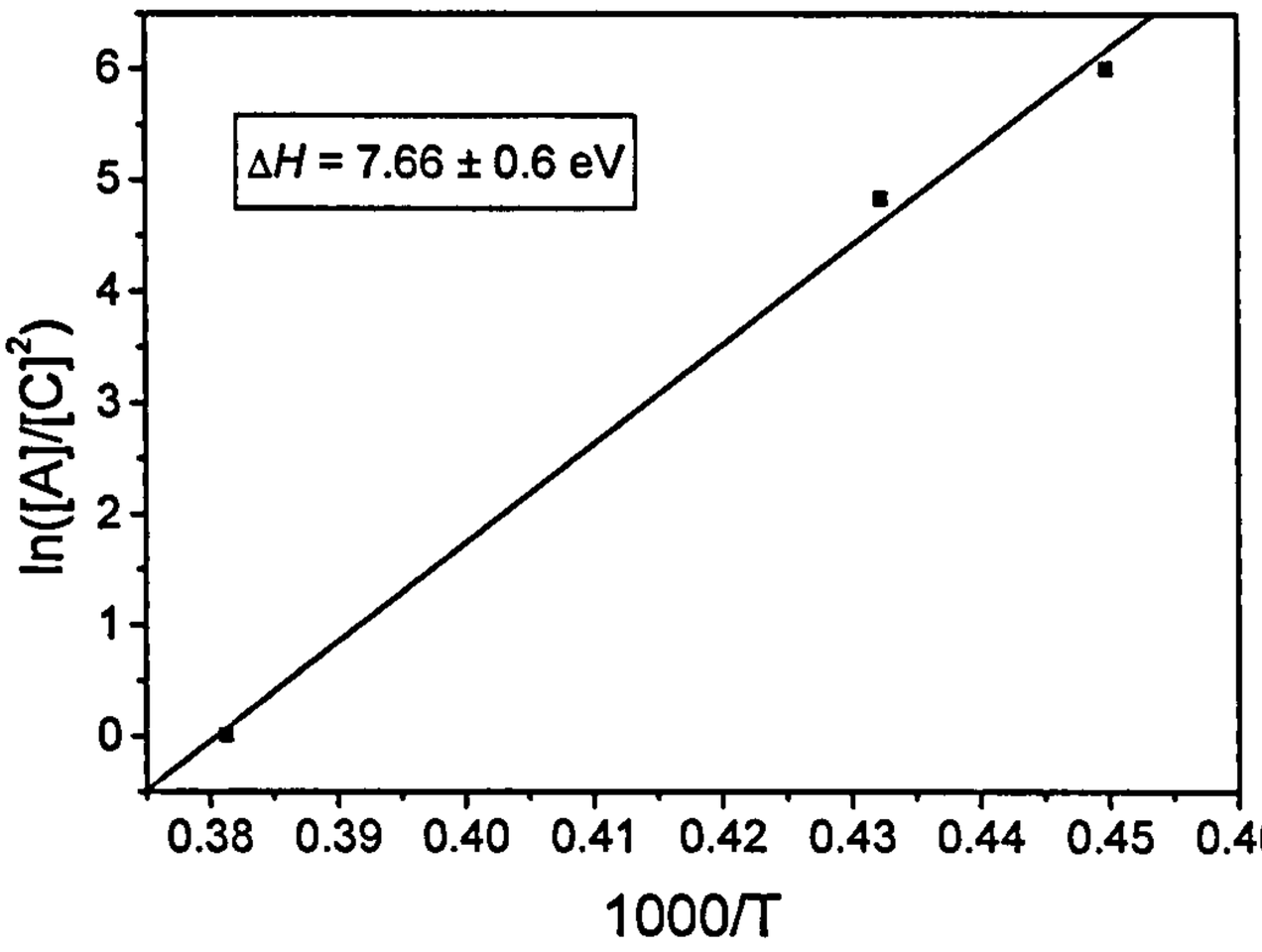

Figure 6.19. The binding energy as derived by fitting the ln([A]/[C]^2) vs. 1000/T plot with a linear function, using data from Brozel *et al.* (1978). A value of 7.66 ± 0.6 eV is determined for the binding energy.

In the experiments of Brozel *et al.* (1978) the concentrations of C centres did not change significantly for heating times longer than approximately 10 to 15 minutes and the values for the calculation of the binding energy are taken from concentration measurements after HPHT annealing in such timescales. The values of the C centre concentrations after annealing in timescales of a few minutes, which were used for the calculation of the activation energy fitted by a first order dissociation process, are more dependent on the experimental parameters like the sizes of the samples, the exact annealing conditions, heating and cooling rate, etc. Consequently the activation energy determined from figures 6.17 and 6.18 has a larger uncertainty than that for the binding energy derived from figure 6.19. The weighted average of these two values, 7.3 ± 0.6 eV, is in agreement with the theoretically calculated value of 7 – 8 eV (Mainwood 1994). The pre-constant is $e^{33.84 \pm 2.30}$ Hz/ppm. The pre-constant for the aggregation rate constant is $e^{23.85 \pm 1}$ Hz, deduced from average values of Kiflawi *et al.* (1997) and Chrenko *et al.* (1977). Deviations from the second order behaviour was not observed by Kiflawi *et al.* (1997), so the values should be reasonably accurate, but caution should still be given to these values as they are deduced for synthetic diamonds where nickel and cobalt could enhance the aggregation rate (Kiflawi *et al.* 1998).

To check the validity of the determined activation energy and vibrational pre-constant, further tests were carried out by HPHT annealing of colourless type IaA

diamond at 2300°C for 3 minutes. Simulation of the created C defect concentration with time indicates that the equilibrium concentration is reached after ~ 30 s annealing (see figure 6.20), so the concentration of C defects in the HPHT annealed diamonds are the equilibrium concentrations. The correspondence between the predicted and experimental concentrations of C defects is reasonably good, considering the relatively large uncertainty on the applied temperature, pressure and sample inhomogeneity (table 6.11 and 6.12).

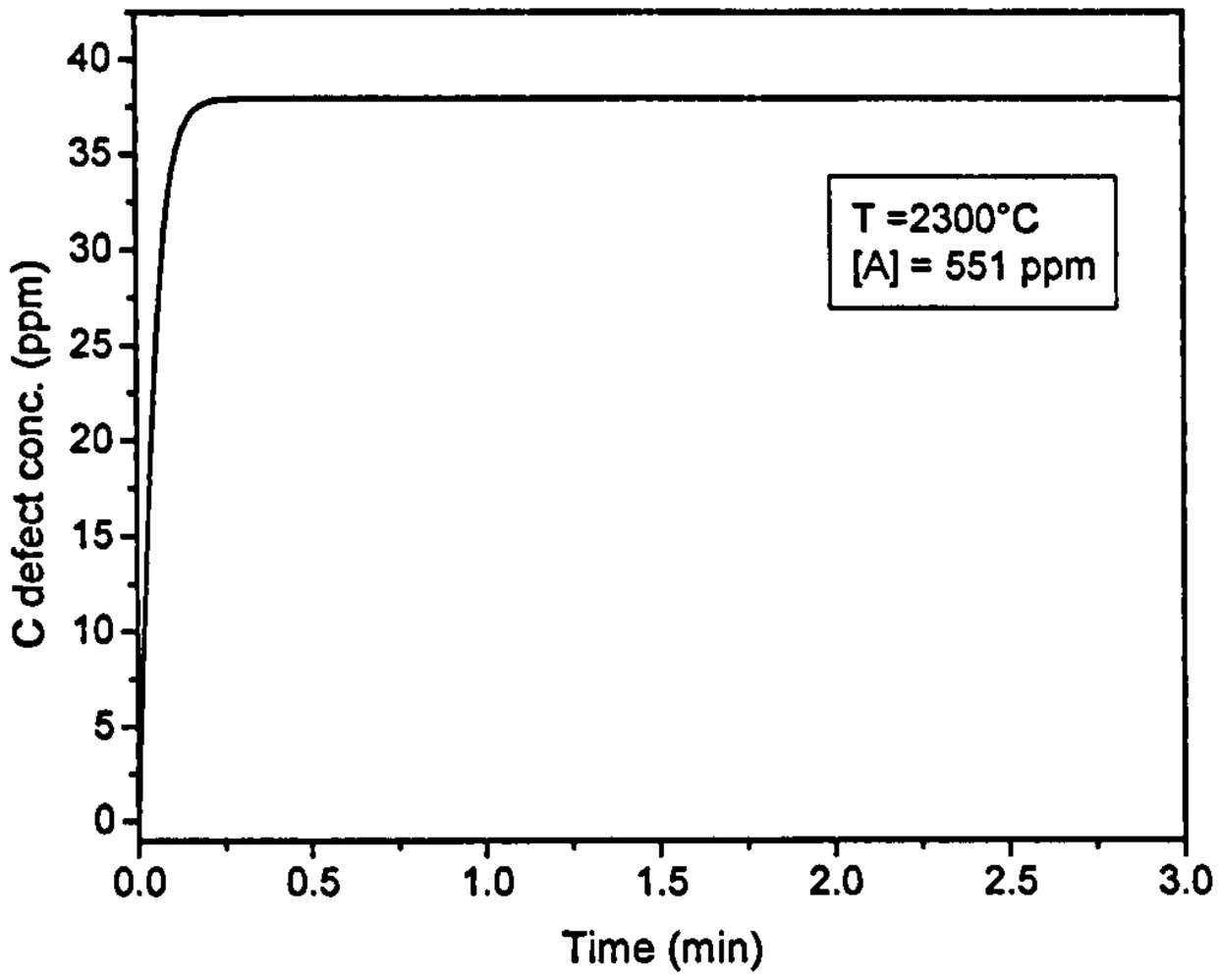

Figure 6.20. Simulation of the concentration of C defects as function of annealing time of sample 9.

The concentration of C defects and A defects at various times of samples annealed at 2300°C can be simulated numerically by the following equations, which couple the C and A defect concentration as function of time.

$$\frac{d[C(t)]}{dt} = -k_{aggr}[C(t)]^2 + 2k_{diss}[A(t)] \qquad (6.3.9)$$

$$\frac{d[A(t)]}{dt} = \tfrac{1}{2} k_{aggr}[C(t)]^2 - k_{diss}[A(t)] \qquad (6.3.10)$$

with k_{aggr} and k_{diss} the aggregation and dissociation rate constant. The rate constants depend exponentially on the activation energy for the process:

$$k_{aggr} = e^{\left(23.85 - \frac{E_{aggr}}{k_B T}\right)} \tag{6.3.11}$$

$$k_{diss} = e^{\left(33.84 - \frac{E_{diss}}{k_B T}\right)} \tag{6.3.12}$$

All parameters can be deduced from the data of Kiflawi *et al.* (1997) and De Weerdt and Collins (2003): the activation energies E_{aggr} and E_{diss} are equal to 5.5 ± 0.7 eV and 7.3 ± 0.6 eV respectively. k_B is the Boltzmann constant and T is the temperature in Kelvin.

B defect formation is left out of the equation, as B defect formation only occurs at higher temperatures (T > 2500°C); the results from Brozel *et al.* (1978) and Evans *et al.* (1995) show that well detectable B defect dissociation requires temperatures of at least 2500°C. Also, the temperatures and timescales used in the experiments are also too low for B centre formation. The influence of pressure and vacancies on the total C defect concentration generated during HPHT annealing will be discussed in next sections.

6.3.3.2. Analysis of brown type Ia HPHT annealed diamonds

No pre-annealing measurements were preformed on the three additionally studied diamonds A12, A14 and A17. However from data collected of hundreds of brown type Ia diamonds which were used as starting material for these samples, it is expected that the C centre concentration is well below 1 ppm since there is no detectable trace of it in the infrared spectrum. The samples were annealed for a few minutes at conditions below the diamond-graphite equilibrium line and the HPHT cell probably did not reach thermal equilibrium in this timescale. When comparing the C centre concentrations in samples A12, A14 and A17 with those in the samples used by Brozel *et al.* (1978), we see that a concentration approximately 5 times larger has been produced in half the annealing time (table 6.6). So annealing at lower pressure enhances the dissociation rate roughly by a factor of 10. A potential error in the analysis lies in the fact that the temperature is not precisely known within ± 100°C and a higher temperature would give rise to a higher dissociation rate and thus to a

higher concentration of C centres. In order to be certain that pressure is the influencing factor, we extrapolated the analysis of the results of Brozel *et al.* to a 100°C higher. The dissociation rate would then increase roughly by a factor of 4 and so we are certain that the relatively large uncertainty of the temperature is not the cause of the higher dissociation rate of A centres in the NovaDiamond annealed samples. The higher dissociation rate may be caused by a pressure-dependent change of the pre-factor in the Arrhenius equation or a pressure dependent change of the binding energy of the A centre. At this stage, there are insufficient experimental data to determine which parameter is influenced by the lower pressure used in the NovaDiamond HPHT annealing. The influence of pressure is investigated in section 6.4 of this chapter.

Sample	Annealing time (min)	[C] (ppm) UV-VIS	[C] (ppm) IR	[N^+] (ppm) IR	Predicted [C] (ppm)
Sample 2-2	3	30	29	0	21
Sample 4-2	3	54	52	0	47
Sample 6-1	3	60	59	0	38
Sample 9	3	42	46	0	37
Sample 10	3	40	41	0	38
ak928a8	5	-----	47	0	42
ak929a1	5	-----	46	0	45
ak9252a1	5	-----	15	0	21
Sample 6-1	broken	-----	-----	-----	-----
Sample 9	6	45	48	0	37
Sample 10	6	48	42	0	38

Table 6.11. The calculated and experimental concentration of C defects after annealing at 2300°C. The uncertainty in the concentration of the defects, determined by IR measurements is 10%. Uncertainty in the concentration of C defects determined by EPR and UV-VIS measurements is 25 % and 27 % respectively.

6.3.3.3. Analysis of the colourless and near colourless type Ia HPHT diamonds

Five colourless type IaA diamonds (samples 2-2, 4-2, 6-1, 9 and 10) and three near-colourless type Ia diamonds have been HPHT annealed at 2300°C and at a pressure of 8 GPa. The five colourless diamonds were annealed by Sundance in a cubic press and the three near-colourless diamonds were HPHT annealed at NIMS in a BELT press. Samples 6-1, 9 and 10 were annealed a second time to check if the C defect concentration had reached the equilibrium value. The C defect concentrations did not change significantly after the second HPHT annealing (table 6.11).

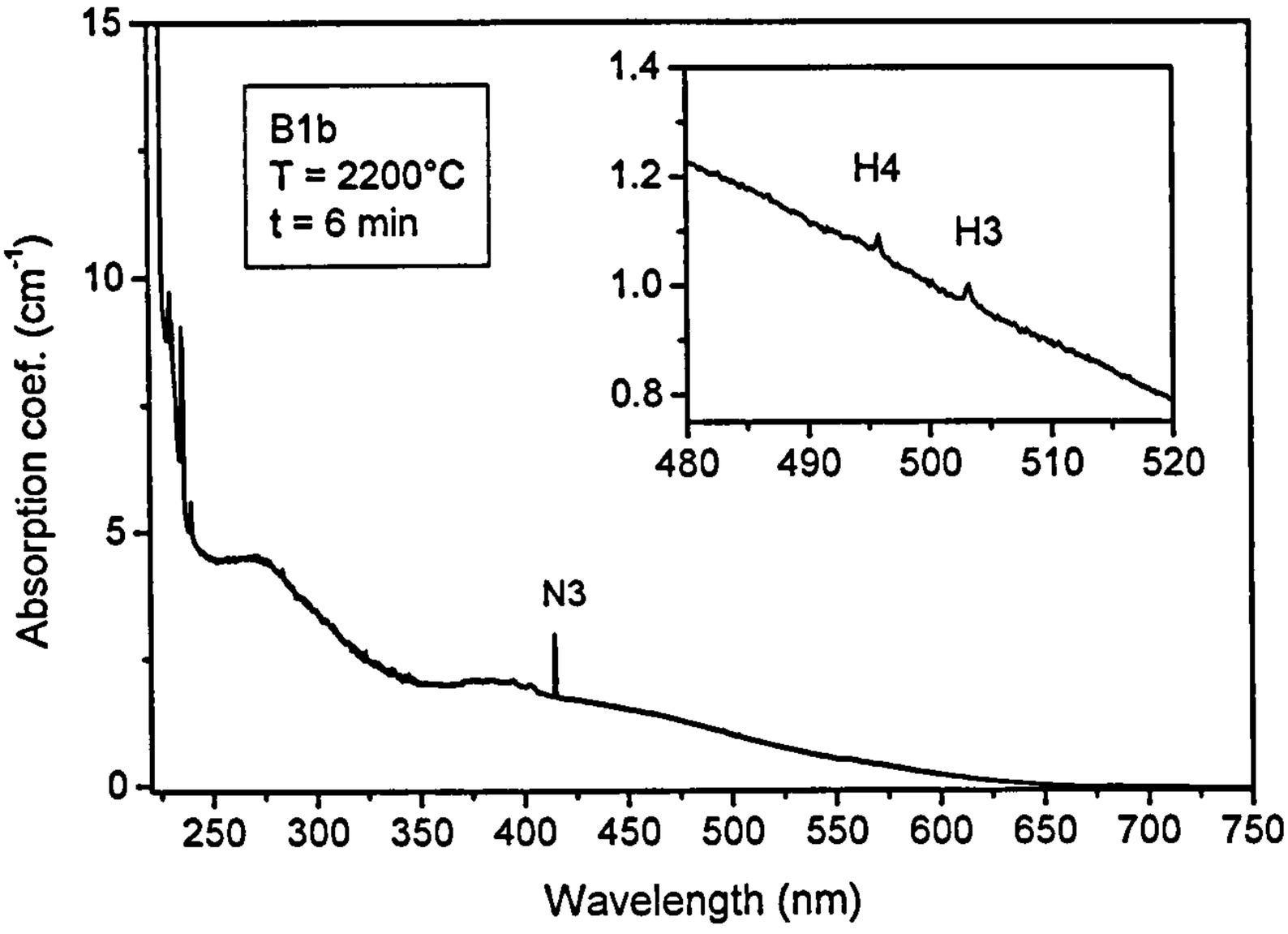

Figure 6.21. The UV-VIS spectrum of sample B1a after HPHT annealing at 2200°C for 6 minutes. Only very low concentrations of H3 and H4 defects are detected.

Sample	Annealing time (min)	[C] (ppm) EPR	[C] (ppm) IR	[N^+] (ppm) IR	Predicted [C] (ppm)
B1a	6	7	5	0	5

Table 6.12. The calculated and experimental concentration of C defects after annealing at 2200°C for 6 minutes. The sample is a type IaB diamond with low concentration of A defects before annealing (5 ppm). There is a good agreement between the calculated concentration of C defects and the measured concentration of C defects. The uncertainty in the concentration of the defects, determined by IR measurements is 10%. Uncertainty in the concentration of C defects determined by EPR is 25 %. The UV-VIS absorption spectrum is shown in figure 6.21.

For every sample, the $\ln([A]/[C]^2)$ value has been calculated and compared with the data of Brozel *et al.* (figure 6.22).

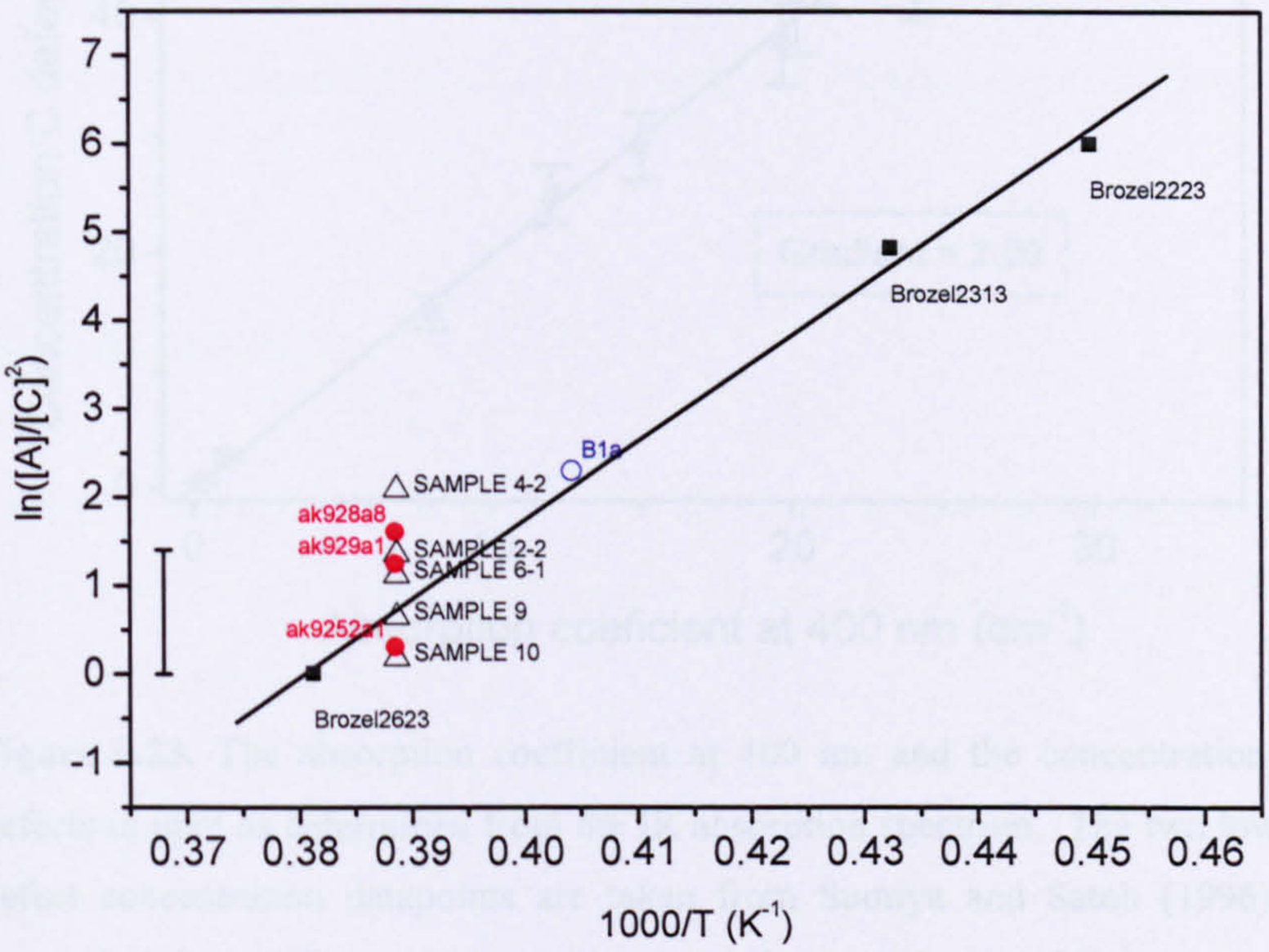

Figure 6.22. The data of the eight HPHT annealed type Ia diamonds and the one light brown type IaB diamond overlaid on the Arrhenius plot of the data of Brozel *et al* (1978). The red circles are the values from the samples of the ak series, the black open triangles are of the colourless type IaA diamonds and the blue open circle is the datapoints of the light brown type IaB with some A defects diamond. The error bar on the left is the uncertainty on the measurements.

6.3.3.4. Determination of low concentrations of C defects in HPHT annealed diamond.

Samples were annealed at 1700°C in vacuum (HT) and under stabilizing pressure of 7 GPa (HPHT) to study the influence of pressure on the aggregation of C defects and dissociation of A defects in diamond (see next section). This lower temperature will also cause a lower C defect equilibrium concentration, which cannot be determined from IR measurements. This is because of the relatively low sensitivity of IR measurements. Therefore, a correlation has been made between the concentration of C defects, as determined from IR measurements and the absorption at 400 nm (or 3.10 eV) after HPHT annealing of colourless type IaA diamonds. From the extrapolation of this data, one can determine concentrations of down to a few hundred ppb of C defects, provided no N3 defect absorption is present.

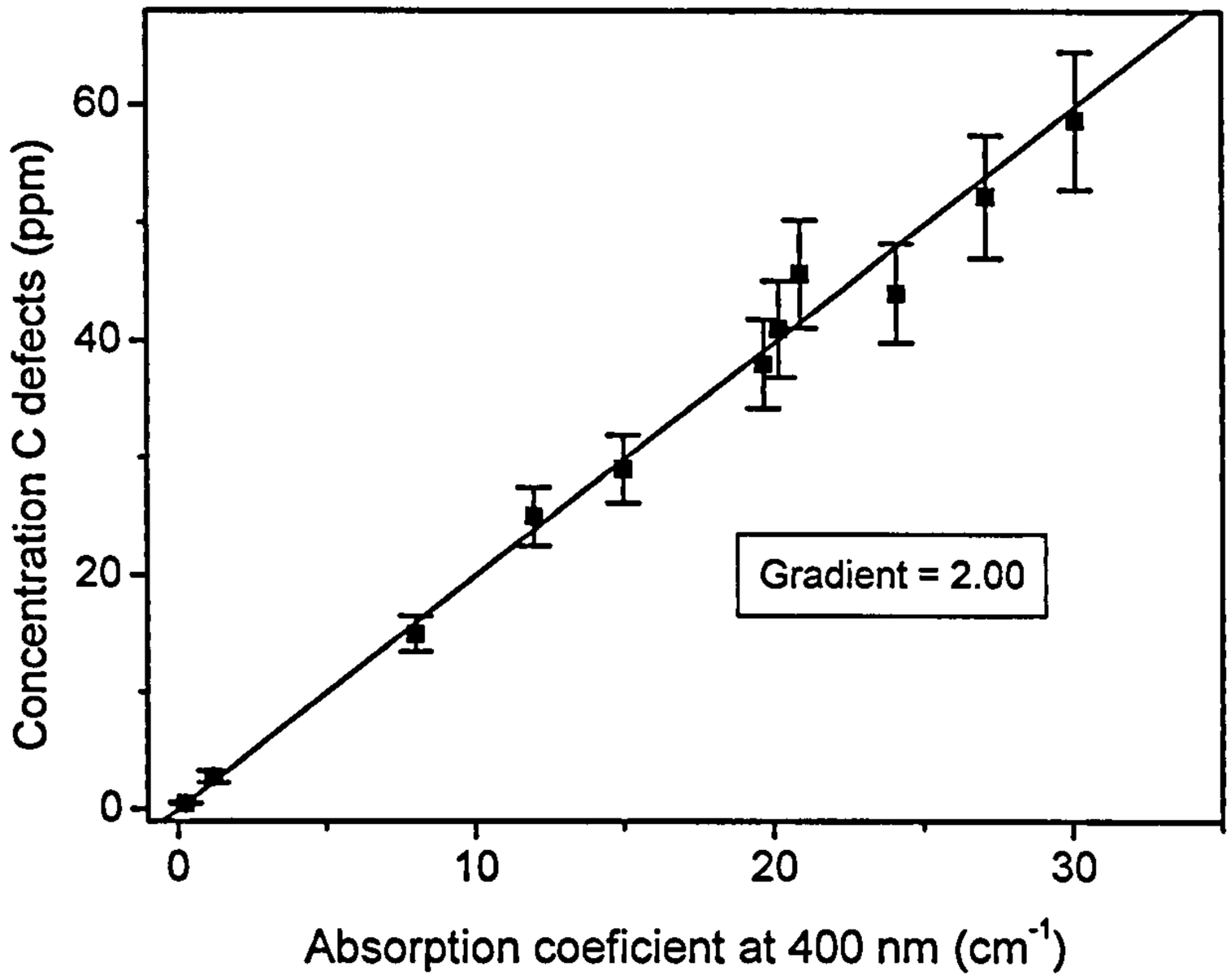

Figure 6.23. The absorption coefficient at 400 nm and the concentration of C defects in ppm as determined from the IR absorption spectrum. The two lowest C defect concentration datapoints are taken from Sumiya and Satoh (1996). The proportionality coefficient between the absorption at 400 nm and the concentration of C defects is 2.00 ± 0.04.

The eight type Ia diamonds HPHT annealed at 2300°C described in the previous section, a yellow synthetic sample and data of Sumiya and Satoh (1996) have been used to establish a correlation between the C defect concentration determined by IR and the absorption coefficient at 400 nm. Only absorption spectra of cubic growth sectors of synthetic diamonds were used, as the octahedral growth sectors are known to contain increased concentrations of nickel with additional broad absorption in the visible region (Furusawa and Ikeya 1990, Collins and Spear 1982).

For every measurement a metal mask was made to select an optical window on the appropriate part of the diamond and it was left in the mask for the IR and the UV-VIS absorption spectrum ensuring the measurement was made through exactly the same part of the sample. The results are given in figure 6.23.

This correlation enables us to estimate the concentration of C defects in samples annealed at low temperature (T = 1700°C, see section 6.4 of this chapter). We note that no N-V or H2 defects were detected in the UV-VIS absorption spectra of the

colourless natural type IaA HPHT annealed samples. N^+ is also absent because of the absence of electron trapping defects like vacancies, H2 and N-V defects.

The concentration of C defects in the samples annealed at 1700°C has also been determined by EPR measurements, following the procedure described in chapter 1, section 1.5.3.

6.4. Influence of pressure

As discussed in Chapter 1, section 1.3.2.3. Pressure has an influence on the observed activation energy for the dissociation of A defects and equation 6.3.7 changes into (see chapter 1, section 1.3.2.3.):

$$\frac{[A]}{[C]^2} = f.\exp\left\{\frac{\left[E_a + P(V_C - V_A)\right]}{k_B T}\right\} \qquad (6.4.1)$$

$[A]$ and $[C]$ are the A and C defect concentrations respectively, E_a is the binding energy of the A defect, P is the pressure in GPa and V_A and V_C are the total volume of the A and C defects respectively. The volume difference between the A and C defect is between 0.03 and 0.4 times the volume of a carbon atom in the diamond lattice (see chapter 1, section 1.3.2.3). The effect of pressure changes on the activation energy is small: it is of the order of 0.012 eV for 1 Giga Pascal change in pressure (for the numerical values see chapter 1, section 1.3.2.3). The Gibbs free energy changes (see chapter 1, section 1.3.2.3):

$$g = E_a + P(V_C - V_A) \qquad (6.4.2)$$

The equation 6.4.1 becomes:

$$\frac{[C]^2}{[A]} = f.e^{\left[-\frac{(7.3 + 0.012\ .\ P(in\ GPa)\ .\ (n\ [C]\ -\ m[A]))}{k_B T}\right]} \qquad (6.4.3)$$

The dilatation coefficient of the A defect, m is between 1.22 and 1.05 and the dilatation coefficient of the C defect is $n = 1.35 \pm 0.10$. The concentrations of C and A defects are the absolute numbers of defects in the diamond. The total effect is that the concentration of C defects should increase when annealing under pressure, however the effect should be too small to be observed experimentally (see chapter 1, section 1.3.2.3).

This is experimentally verified and to remove the influence of vacancies or other impurities as much as possible, colourless type IaA diamonds with negligible concentrations of B defects have been subjected to annealing at 1700°C at 7 GPa and 0 GPa.

In sample 4-3, annealed at 1700°C in vacuum for one hour, the total created C defect concentration is 0.5 ppm, while in sample 4-1, cut from the same rough diamond, the total concentration of C defects created during HPHT annealing at 1700°C for one hour is 2.5 ppm. The colour of this diamond changed to very light yellow.

Table 6.13 summarises the concentrations of C defects in the samples after 1 hour annealing at 1700°C at high temperature and zero pressure and at high temperature and high pressure.

From the limited dataset, it appears that annealing under high pressure of type IaA diamond results in a greater increase of the C defect concentration compared with the samples annealed under vacuum. However, the effect appears to be larger than indicated by equation 6.4.3. because the numerical values of the parameters are very small (see also chapter 1, section 1.3.2.3.). Further research should be carried to investigate if the increased concentration in the HPHT annealed samples is a consequence of the difference in dilatation of the A and C defect or if other parameters are important.

After HPHT annealing at 1700°C, 1 h			
Sample	[*C*] UVVIS (ppm)	[*C*] EPR (ppm)	[*A*] IR (ppm)
Sample 1-2	broken	-----	-----
Sample 4-1	2.504	2.930	993
Sample 5-2	N3*	0.075	232
Sample 7-1	0.952	0.640	839
Sample 7-2	1.476	0.794	793

*this sample had N3 in the UV-VIS absorption spectrum

After HT annealing at 1700°C, 1 h			
Sample	[*C*] UVVIS (ppm)	[*C*] EPR (ppm)	[*A*] IR (ppm)
Sample 1-1	0.640	0.495	751
Sample 4-3	0.481	0.384	721
Sample 6-2	broken	----	----
Sample 7-3	0.555	0.319	705

Table 6.13. The concentration of C defects of different samples after HPHT and HT annealing at 1700°C for 1 hour. Sample starting with numbers 1, 4 and 7 were cut from the same rough diamond. Sample 5-2 had too high concentration of N3 defects before annealing, making the determination of C defect concentration from the UV-VIS spectrum unreliable. The uncertainty in the concentration of the defects, determined by IR measurements is 10%. Uncertainty in the concentration of C defects determined by EPR and UV-VIS measurements is 25 % and 27 % respectively.

6.5. HT annealing of irradiated pre-annealed diamonds

6.5.1. Study of irradiated type I diamonds, annealed at high temperature (T ~ 1500°C) and low pressure (P << 1 GPa)

During HPHT annealing of brown type Ia diamond, various nitrogen-vacancy complexes (H3, H4, ...) formation and dissociation processes occur and are coupled as both processes will be activated at elevated temperatures. Also A defects will dissociate into C defects. The C defect acts as an electron donor and gives rise to

negatively charged defects, some of which are less mobile than their neutral counterparts (for example V^0 and V^- (Davies 1992)). To eliminate the interference between a large number of processes, a study of HT annealing of irradiated diamond is the most suitable. Here we study the results of irradiation and annealing up to 1600°C (Kiflawi *et al.* 1997, Collins 1980, Collins *et al.* 2005) for different types of diamond.

Vacancies introduced by irradiation will increase the aggregation rate of C defects into A defects, by successive trapping and releasing of vacancies (Collins 1980). Since the precise mechanism is not known, this vacancy-enhanced aggregation is modelled by taking only a fraction Δ of the N-V and C defects into account. The frequencies of the main phonons interacting with the N-V and H3 defects are taken as vibrational pre-factors in the rate constants involving dissociation of the N-V and H3 defect, respectively. The data of Kiflawi *et al.* (1997) and Collins (1980) can adequately be simulated by solving the differential equations:

$$\frac{d[V(t)]}{dt} = -k_{1,fast}[V(t)] + k_1[H3(t)] + k_2[(N\text{-}V)^-(t)] - k_{1,fast}\left(1-\left(\alpha[A(t)]+\gamma[C(t)]\right)\right)[V(t)] \quad (6.5.1)$$

$$\frac{d[(A\text{-}V)(t)]}{dt} = \alpha k_{1,fast}[A(t)][V(t)] - k_3[(A\text{-}V)(t)] - k_{1,fast}[(A\text{-}V)(t)] \quad (6.5.2)$$

$$\frac{d[H3(t)]}{dt} = k_3[(A\text{-}V)(t)] - k_4[H3(t)] \quad (6.5.3)$$

$$\frac{d[A(t)]}{dt} = -\alpha k_{1,fast}[A(t)].[V(t)] - k_{diss}[A(t)] + \tfrac{1}{2}k_{aggr}[C(t)]^2 + k_4[H3(t)] + k_5[C(t)][(N\text{-}V)^-(t)] \quad (6.5.4)$$

$$\frac{d[C(t)]}{dt} = -k_{aggr}[C(t)]^2 + 2k_{diss}[A(t)] - \gamma k_{1,fast}[C(t)][V(t)] - \Delta k_5[C(t)][(N\text{-}V)^-(t)] + k_2[(N\text{-}V)^-(t)] \quad (6.5.5)$$

$$\frac{d\left[(N\text{-}V)^{-}(t)\right]}{dt} = \gamma k_{1,fast}\left[C(t)\right].\left[V(t)\right] - k_2\left[(N\text{-}V)^{-}(t)\right] \qquad (6.5.6)$$

The r.h.s. of the first equation (6.5.1) describes the diffusion of vacancies created by the irradiation (first term), the vacancies originating from dissociated H3 defects (second term), the vacancies from dissociated N-V defects (third term), and the loss of vacancies to surface, cracks and other stable traps (fourth term). This last term can be neglected as it will be shown below that a negligible fraction of vacancies is lost during annealing at 1500°C.

The first term of the r.h.s. of equation 6.5.2 describes the trapping of vacancies close by the A defects and formation of the A-V structure, the second term describes the restructuring of the A-V combination into a H3 defect, the last term describes the vacancies diffusing back into the bulk of diamond, away from the A-V structure. Equation 6.5.3 describes the formation of H3 and dissociation of H3 defects. The right hand side of equation 6.5.4 describes the loss of A defects by A-V structure formation (first term), the dissociation of A defects (second term) the increase of A defects by re-aggregation (third term), the increase of A defects by the removal of the vacancy from the H3 defect (fourth term), and the vacancy enhanced re-aggregation, which is proportional to the C and N-V defect concentration (fifth term). The C defect concentration varies with time (equation 6.5.5) due to the formation of A defects (r.h.s. first term), dissociation of A defects (r.h.s. second term), N-V defect formation (r.h.s. third term), vacancy enhanced re-aggregation (r.h.s. fourth term), and dissociation of N-V defects (r.h.s. fifth term). The last equation (6.5.6) describes the formation of N-V defects and the dissociation of N-V defects.

k_{1fast}, k_{diss} and k_{aggr} have already been determined in chapter 5 and in section 6.3 of this chapter, and the activation energies for the other reaction rate constants are found by fitting the equations until the values for nitrogen aggregation in irradiated and unirradiated synthetic type Ib diamonds, and the reduction of N-V and H3 defects, are in agreement with the experimental data obtained by Collins (1980) and Kiflawi (1997) (figures 6.25 and 6.26).

Factors α and γ have been determined in chapter five and are inversely proportional with the concentration of A (C) defects and pre-factors a (g), i.e. $\alpha = (a[A])^{-1}$ (or $\gamma = (g[C])^{-1}$). The same factors will be encountered throughout this chapter, i.e. α for A defects, β for B defects and γ for C defects and are calculated as described in chapter five. The factor Δ is the fraction of N-V defects involved in the vacancy assisted aggregation and must be determined experimentally.

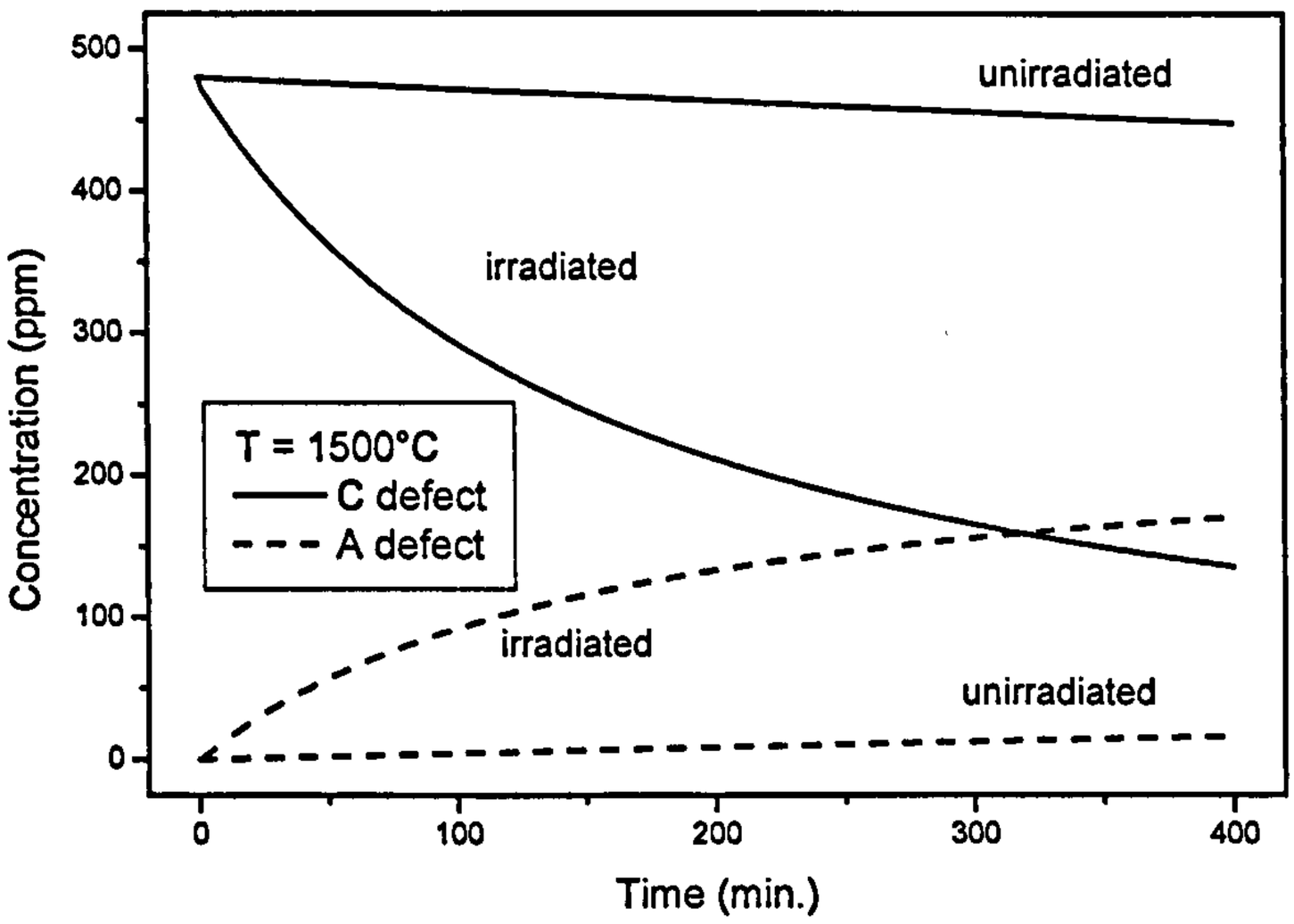

Figure 6.24. Simulation of the A and C defect concentrations of samples irradiated and annealed at 1500°C (Collins 1980) with equations 6.5.1 – 6.5.6.

Collins (1978, 1980) observed the creation of H3 defects in irradiated (1.0 10^{18} e^-/cm^2, 2 MeV, [V] ~ 7 ppm) and annealed type Ib synthetic diamonds. These diamonds were heated to 800°C for 2 hours after irradiation and then annealed at 1500°C for 4 hours. No H3 was detected before annealing at 1500°C, only $[(N\text{-}V)^-]$ (~ 6.5 ± 0.7 ppm) defects. This concentration of $(N\text{-}V)^-$ defects decreased by a factor or ~ 3 after annealing at 1500°C and a very weak H3 ZPL peak could be detected in the UV-VIS spectrum, corresponding to a defect concentration of ~ 1 ppm. The spectral range did not include the region with H2 absorption; however from the decomposition of the IR spectrum one can determine the concentration of H2 defects supposing that N-V defects and H2 defects are the major electron traps present in the sample. The concentration of H2 defects is then estimated by comparing the concentration of $[N^+]$ (~ 5 ppm) with $[(N\text{-}V)^-]$ ~ 2 ppm; there would then be ~ 3 ppm of H2 defects. The

total concentration of vacancies trapped at nitrogen (in $(N\text{-}V)^-$ defects) or nitrogen aggregates (H3 and H2 defects) is approximately 6 ppm, so the loss of vacancies is negligible.

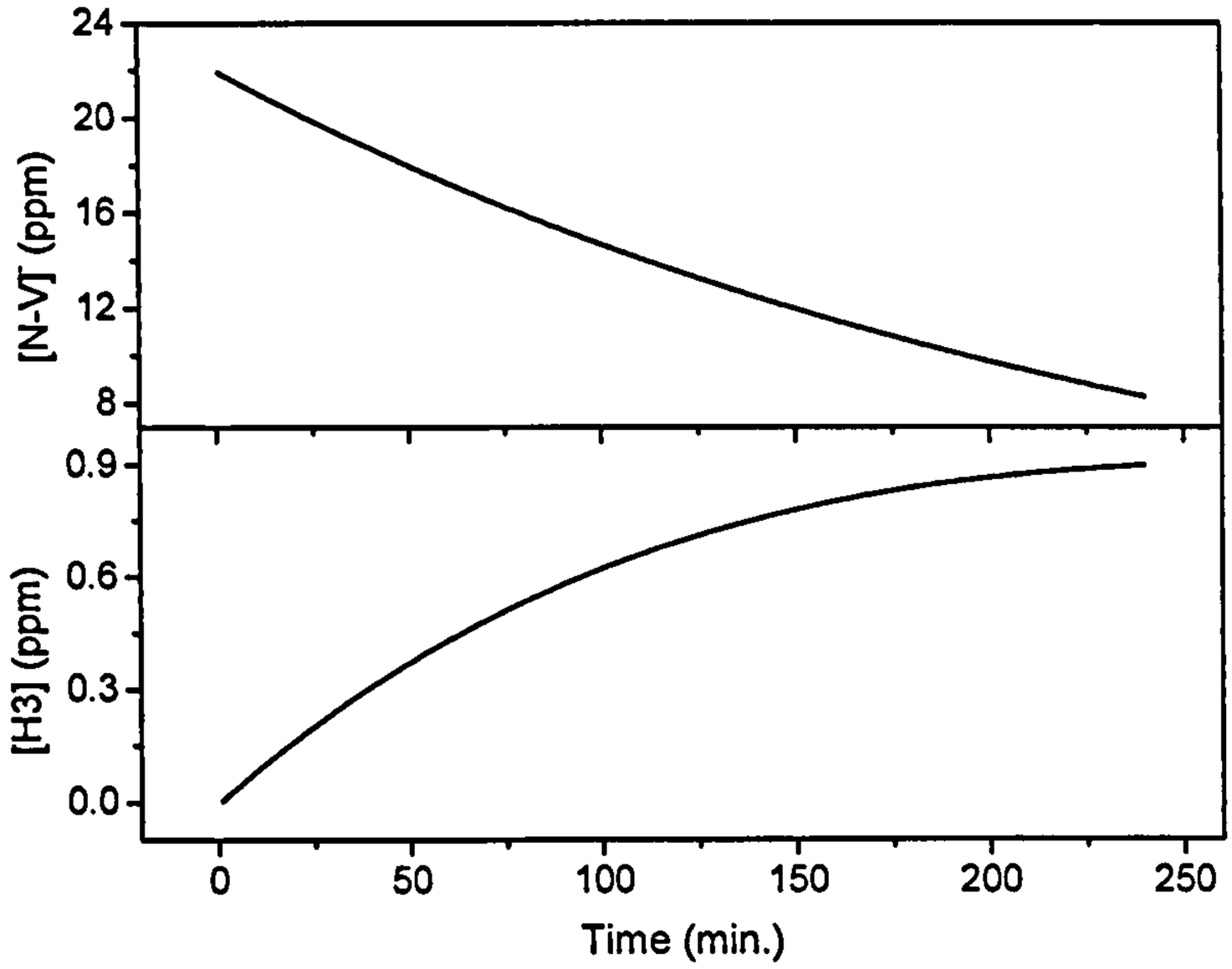

Figure 6.25. The data of Collins (1978) on N-V and H3 defect concentrations in irradiated and annealed type Ib diamond. The data of Collins (1980) of figure 6.24 is fitted with same parameters.

The activation energy used in the simulation with equations 6.5.1 – 6.5.6 for the vacancy assisted aggregation is 5.2 ± 0.2 eV and the $(N\text{-}V)^-$ dissociation energy is 5.2 eV ± 0.5 eV. With these values, one can simulate the behaviour of H3 and $(N\text{-}V)^-$ defects (figure 6.25).

Collins (1980) also reported a decrease of the H3 peak intensity by a factor ~ 3 in a type IaA diamond which was irradiated and heated with a similar procedure. From this data, the dissociation energy of the H3 defect can be estimated to be 5.1 ± 0.2 eV in good agreement with the value used here in the simulation of H3 dissociation in type Ia diamond. This value is also equal to the activation energy for the vacancy-assisted aggregation, which is very plausible. If vacancy assisted diffusion occurs, H3 will be created, and subsequently destroyed, leaving an A defect. If this last step is the rate-limiting step, then this step should have the highest activation energy, equal to the activation energy for vacancy-assisted aggregation.

One of the irradiated (10 ppm of vacancies) type Ib samples of K. Iakoubovskii, described in chapter 5 was annealed at 800°C and then at 1500°C for 1 hour and additionally for 3 hours at 1500°C. A simulation of the A and C concentrations after 1 hour and a total of 4 hours with parameters identical to those used in the previous simulations give a close fit to this experimental data (figure 6.26).

For reasons of clarity the concentrations of the A and C defects after 1 hour and 4 hour annealing at 1500°C are repeated here. The initial concentration of C defects was 160 ± 16 ppm. After 1 hour and 4 hours annealing, 15 ± 2 ppm and 48 ± 5 ppm of A defects were detected. The simulation indicates 14 ± 10 ppm and 37 ± 20 ppm of A defects after 1 hour and 4 hour annealing respectively.

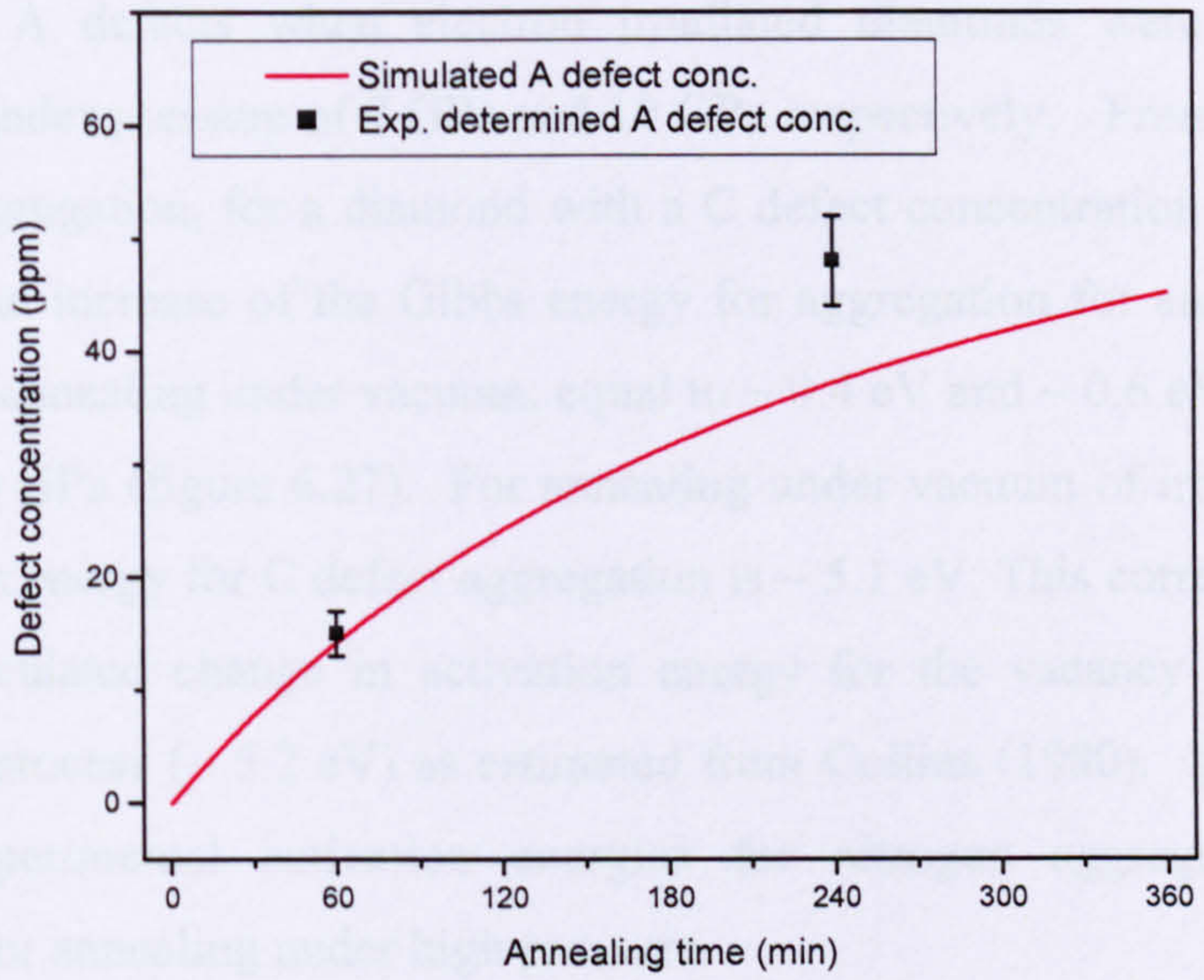

Figure 6.26. The simulated concentration of the A defect concentrations after 1 hour and 4 hours annealing at 1500°C of an irradiated type Ib diamond.

This discrepancy can be attributed to the presence of nickel in the diamonds, which can enhance the aggregation rate (Kiflawi *et al.* 1997 and 1998). A very weak 658 nm nickel related absorption line was detected in the samples. This second, nickel related, enhanced aggregation mechanism is not included in the simulations.

A remark should be made here: from the UV-VIS spectrum, a concentration of $(N\text{-}V)^-$ of 6.2 and 6.0 ppm could be detected after annealing at 800°C and after annealing at 1500°C for 1 hour respectively. No H3 was detected, but a very weak peak at 871 nm, the local mode of the H2 peak, can be detected. Again, this clearly indicates

almost all vacancies are retrapped by the C defect after being released from the H3 defect. This justifies, together with the data of Collins (1980), neglecting the vacancy loss term (fourth term in equation 6.5.1).

6.5.2. Study of irradiated and high temperature annealed (T ~ 1500°C) type I diamonds at various pressures (P up to 10 GPa)

Kiflawi *et al.* (1997) observed a decrease in the percentage of aggregated nitrogen when irradiated synthetic type Ib diamond samples ([*C*] ~ 280 ppm) were annealed at the same temperature (T= 1500°C) but with increasing pressure up to 10 GPa. In this study Kiflawi *et al.* observed after 4 hours ~ 60 %, ~ 30% and 4% aggregation of C defects into A defects when electron irradiated diamonds were annealed under vacuum, or under pressure of 7 GPa and 10 GPa respectively. From this variation of degree of aggregation, for a diamond with a C defect concentration of 280 ppm, one can deduce an increase of the Gibbs energy for aggregation for annealing at 7 GPa compared to annealing under vacuum, equal to ~ 0.4 eV and ~ 0.6 eV when annealing is done at 10 GPa (figure 6.27). For annealing under vacuum of irradiated diamond, the activation energy for C defect aggregation is ~ 5.1 eV. This corresponds very well with the calculated change in activation energy for the vacancy assisted nitrogen aggregation process (~ 5.2 eV) as estimated from Collins (1980). It should be noted that the experimental activation energies for nitrogen aggregation have been determined for annealing under high pressure.

When pressure is decreased, the A defect dissociation energy also changes, but lowering the dissociation energy by 0.6 eV, which is twice the calculated change of the aggregation activation energy, does not change the kinetics of A defect aggregation (figure 6.28).

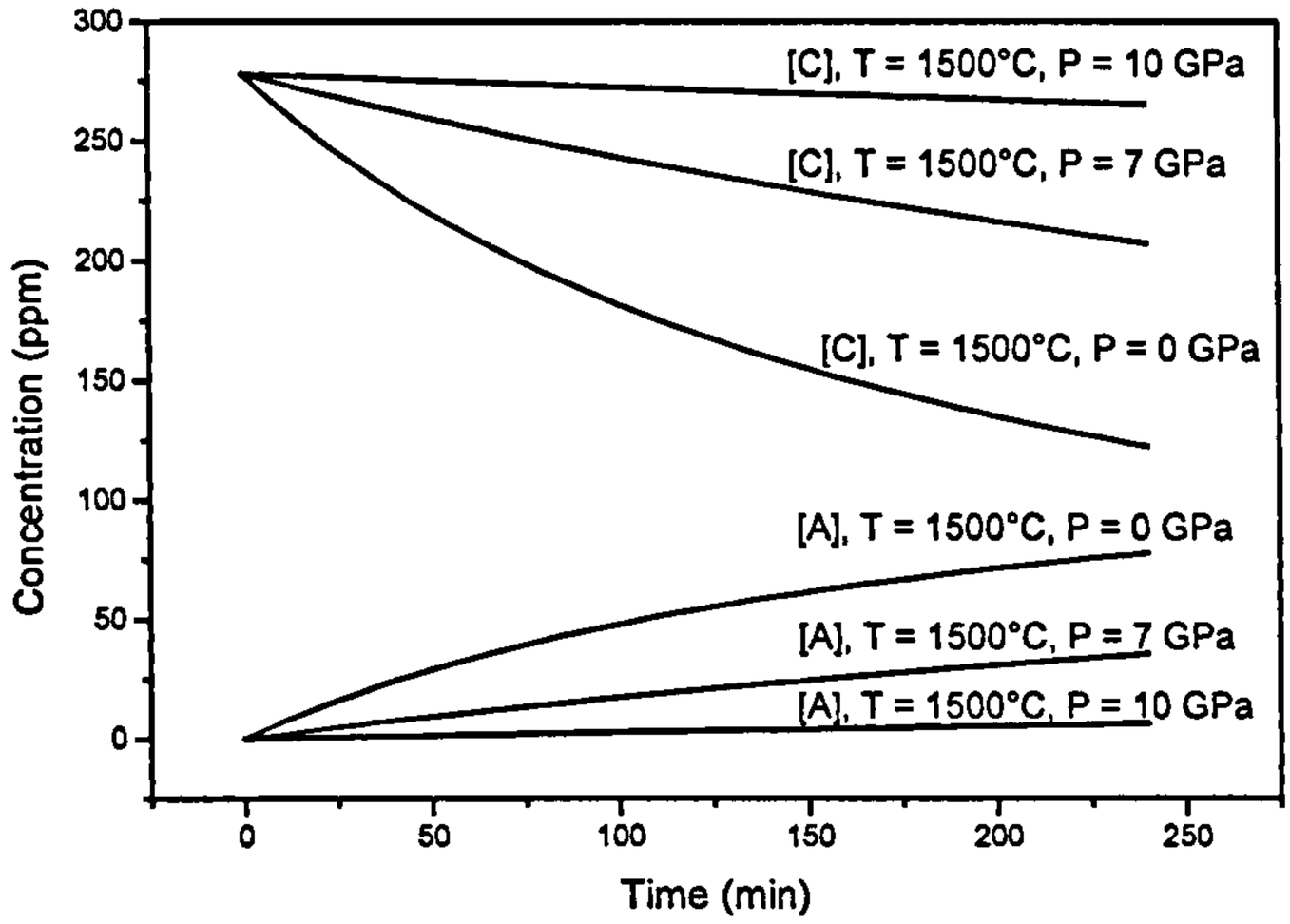

Figure 6.27. The concentrations of A and C defects in samples with 280 ppm of C defects and annealed under vacuum (0 GPa) or at 7 or 10 GPa and a temperature of 1500°C.

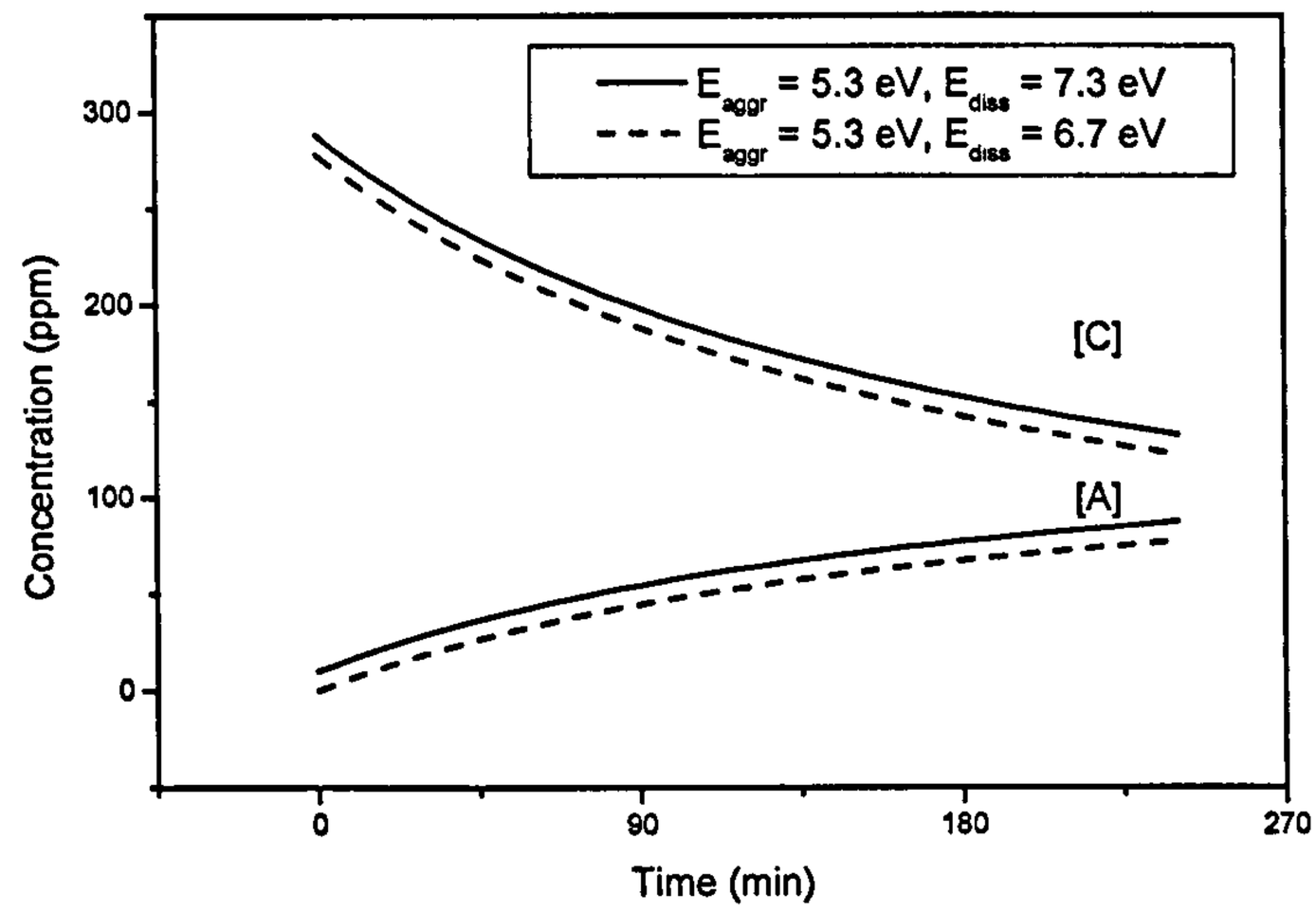

Figure 6.28. A change in the dissociation activation energy of the A defect does not change the kinetics of C defect aggregation at T = 1500°C. The curves have been displaced by 10 ppm for clarity.

Annealing at high pressure appears to suppress the vacancy enhanced diffusion effect significantly and this effect will be neglected in further simulations.

6.5.3. Summary

From these simulations, a summary can be made of the vibrational pre-factors and the activation energies involved in vacancy-enhanced nitrogen aggregation of irradiated

type Ib diamond under vacuum. The values of the vibration pre-factors and the activation energies are given in the table 6.14 below.

Rate constant	Process	Vibrational pre-factor (Hz)	Activation energy (eV)
$k_{1\,fast}$	vacancy diffusion	$7.1\ 10^{9}$	2.3 ± 0.2
k_1	H3 dissociation	$9.9\ 10^{12}$	5.1 ± 0.2
k_2	N-V defect diss.	$1.6\ 10^{13}$	5.2 ± 0.5
k_3	A-V struct. diss.	$7.1\ 10^{9}$	2.5 ± 0.2
k_4	Vacancy enh. aggr.	$7.1\ 10^{9}$	5.2 ± 0.2
k_{aggr}	A defect aggr. const.	$2.3\ 10^{11}$	5.2 ± 0.7
k_{diss}	A defect diss. const.	$5.0\ 10^{14}$	7.0 ± 0.6

Table 6.14. The activation energies and the vibrational pre-factors determined from the simulations of the annealing behaviour of the A, C, H3 and $(N\text{-}V)^-$ defects in irradiated and high temperature (T ~ 1500°C) annealed type Ib diamond.

Only the activation energy and vibrational pre-factors for nitrogen aggregation and dissociation will be used in section 6.7 on the HPHT annealing results of brown type Ia diamond. The values will be increased by 0.3 eV as the annealing is done under a stabilizing pressure of 7 GPa. The activation energy of the H3 dissociation will be determined in that section as the influence of pressure on the H3 defect is unknown.

6.6. Optical study of the annealing behaviour of the 3107 cm^{-1} defect in natural diamond

6.6.1. Experimental

The fourteen type Ia brown samples from the tlb and lb sample series were used in this study. Each diamond has different concentration of aggregated nitrogen in the A, B forms and D absorption strength. The samples were annealed at high pressure (P = 7 GPa) and high temperature (T > 2000°C) at Sundance Inc., using a prismatic press (De Weerdt *et al.* 2004).

The initial concentrations of the A and B defects at 1282 cm^{-1} and the integrated intensity of the platelet peak are summarised in table 6.7. The hydrogen-related absorption peak at 3107 cm^{-1} was fitted with a Lorentz function after subtraction of the diamond spectrum. The integrated intensities of this peak in the 14 specimens are listed in table 6.15. The 1405 cm^{-1} defect displays a similar behaviour to that of the 3107 cm^{-1} absorption line after successive HPHT annealings. This similarity could only be reliably verified for the samples tlb-3 and lb-5, the samples with the strongest 3107 cm^{-1} absorption (figure 6.29).

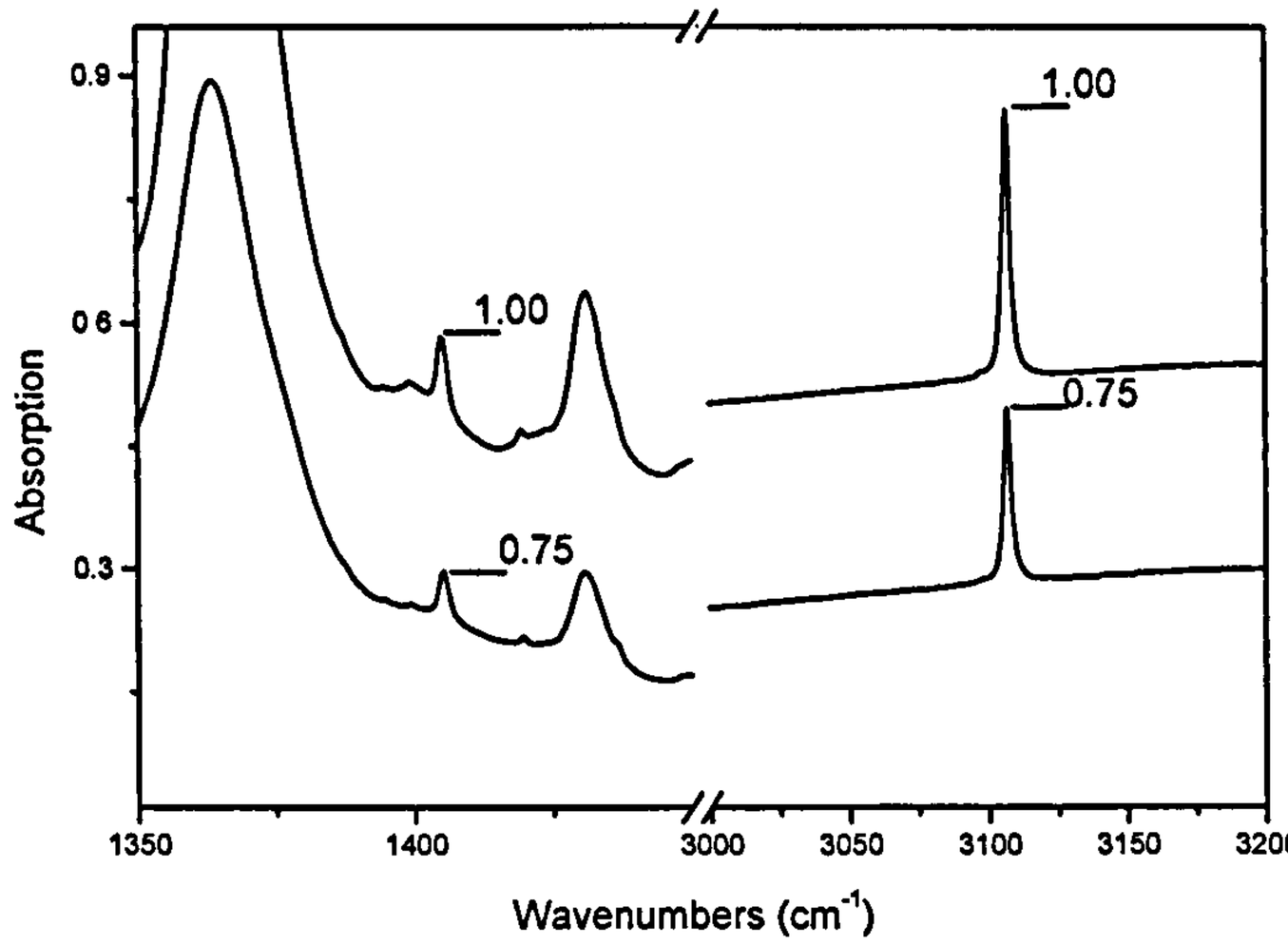

Figure 6.29. The hydrogen-related absorption lines at 1405 and 3107 cm^{-1} before (top) and after the final (bottom) HPHT annealing of sample tlb-3. The ratio of the intensities of these lines is similar after each annealing, and both have been reduced to approximately 75% of their initial intensities after the final annealing.

6.6.2. Results and discussion

All results and observations made here, and those reported in the literature, can be explained if there is an infrared-inactive hydrogen reservoir, from which hydrogen can be released, and subsequently trapped at a carbon atom, to form a 3107 cm^{-1} defect. However, the 3107 cm^{-1} defect itself is not stable at the high temperature used during the HPHT annealing; consequently there is a simultaneous dissociation of the defect.

As stated in the introduction of this chapter and chapter 1, section 1.3, there are different hydrogen-containing defects in diamond. Each of these will have a specific activation energy and dissociation rate constant for the release of the hydrogen atom because the binding force between the hydrogen atom and the remainder of the defect will differ. This is true, even for hydrogen dimers, because the binding energy of the hydrogen atoms in the bonding and anti-bonding sites will differ. As a consequence, in the aggregation-dissociation model of the 3107 cm^{-1} centre, below, we have assumed that the aggregation of hydrogen to form the 3107 cm^{-1} defect is a first order process with one rate constant. In a given diamond this will be a weighted average of different rate constants, because concentrations of the hydrogen sources are different for each sample. As a consequence, there is no physical significance in attempting to calculate the activation energy for the aggregation or dissociation process.

Time (min)	tlb-1	tlb-3	tlb-5	tlb-6	tlb-7	lb-1	lb-2	lb-3	lb-5	lb-6
0	5.24	11.02	8.35	5.08	6.87	5.35	6.35	6.82	11.21	8.43
3	3.18	8.59	2.54	3.07	6.90	3.06	3.48	4.15	7.17	4.61
6	3.17	8.76	2.54	3.41	5.76	3.31	3.16	4.83	6.66	3.85
9	3.03	8.27	2.76	2.80	6.22	2.89	2.94	4.87	6.60	3.47
12	2.78	7.90	2.47	3.01	4.98	2.41	2.90	4.92	6.09	2.99
15	2.59	7.89	2.54	br	3.65	2.57	2.51	4.91	br	3.06

Time (min)	tlb-4	lb-4	lb-7	lb-8
0	8.52	5.34	3.95	4.71
3	5.48	1.85	6.01	1.90
6	4.50	1.43	1.65	1.52
9	4.36	1.41	1.49	1.47
12	4.00	1.35	0.89	1.69

Table 6.15. The tables give the integrated intensity in cm^{-2} of the 3107 cm^{-1} line before (time t = 0) and after subsequent HPHT annealing (at times t = 3, 6, 9, 12 and 15 min) at 2100°C (top table) and at times t = 3, 6, 9 and 12 min at 2200°C (bottom table). The uncertainties are ± 5 %. The "br" means the sample broke during annealing.

In addition to this sample-dependence, deviations between the calculated values of the different dissociation and aggregation rate constants are partly due to the fact that temperature gradients in the HPHT cell will result in a slightly different annealing temperature for each sample.

For ease of analysis, all data are normalised with respect to the initial value of the integrated intensity of the 3107 cm^{-1} defect.

6.6.2.1. Aggregation-dissociation kinetics of the 3107 cm^{-1} defect

The model is based on the proposal that there is a hydrogen reservoir in the diamond, and that, during HPHT annealing, this reservoir will release hydrogen atoms, which will be trapped to form 3107 cm^{-1} defects until the reservoir is depleted. This situation is described by two coupled differential equations, similar to the radioactive decay of a parent element to a daughter element, which further decays to a granddaughter element. In our case, the 3107 cm^{-1} defect would be the "daughter element". We will refer to the model as the Two Stage Decay (TSD) model. The differential equations describing the kinetics are:

$$\frac{dH(t)}{dt} = -k_1 H(t) \qquad (6.6.1)$$

$$\frac{dE(t)}{dt} = k_1 \alpha H(t) - k_2 E(t) \qquad (6.6.2)$$

Here α is the fraction of hydrogen atoms released by the hydrogen source and converted into a 3107 cm^{-1} defect, $E(t)$ is the concentration of the 3107 cm^{-1} defect at time t, $H(t)$ is the concentration of the hydrogen in the source at time t, k_1 and k_2 are the aggregation and dissociation rate constants. $E(0)$ and $H(0)$ are the initial concentrations of the 3107 cm^{-1} defect and the hydrogen source respectively. The coupled differential equations for $E(t)$ can easily be solved by the use of Laplace transforms (Abramowitch and Stegun 1972). The Laplace transformation transforms a coupled differential equation into a set of algebraic equations, and the inverse transformation gives the solution of the differential equation.

Using the Laplace transform for a first order differential equation of a function N

$$\frac{d(N(t))}{dt} = -\lambda N(t) \qquad (6.6.3)$$

becomes, after Laplace transforming:

$$sN(s)-N(0)=-\lambda N(s) \tag{6.6.4}$$

The Laplace transformation of equations 6.6.1 and 6.6.2 gives two algebraic equations:

$$sH(s)-H(0)=-k_1 H(s) \tag{6.6.5}$$

$$sE(s)-E(0)=k_1\alpha H(s)-k_2 E(s) \tag{6.6.6}$$

Solving to function $E(s)$

$$\dot{E}(s)=\frac{k_1\alpha H(s)+E(0)}{(s+k_2)}$$

$$=\frac{E(0)}{(s+k_2)}+\frac{k_1\alpha H(s)}{(s+k_2)} \text{ with } H(s)=\frac{H(0)}{(s+k_1)} \tag{6.6.7}$$

$$=\frac{E(0)}{(s+k_2)}+\frac{k_1\alpha H(0)}{(s+k_2)(s+k_1)}$$

Using the inverse Laplace transformations on equations 6.6.5 and 6.6.7

$$\frac{1}{(s+\alpha)^n}=\frac{t^{n-1}}{(n-1)!}\exp(-\alpha t) \text{ and } \frac{1}{(s+\alpha)(s+\beta)}=\frac{\exp(-\alpha t)-\exp(-\beta t)}{(\beta-\alpha)}$$

gives

$$H(t)=H(0)e^{(-k_1 t)} \tag{6.6.8}$$

$$E(t)=E(0)e^{-k_2 t}+\alpha\frac{E(0)\,k_1}{k_2-k_1}\left[e^{-k_1 t}-e^{-k_2 t}\right] \tag{6.6.9}$$

Equation 6.6.8 describes the release of hydrogen from the hydrogen source. The first term on the right hand side of equation 6.6.9 describes the dissociation of the initial concentration of 3107 cm^{-1} defects. The second term describes the aggregation and simultaneous dissociation of the 3107 cm^{-1} defect, where the hydrogen originates from a finite hydrogen source which is undetectable using infrared absorption.

There are two cases of interest:

In the first case, the dissociation rate is the higher and $k_1 << k_2$. The concentration of the 3107 cm^{-1} defect has a strong initial decrease and a weaker decrease with longer annealing time (figure 6.30a). For most of the samples, the 3107 cm^{-1} defect displays this behaviour.

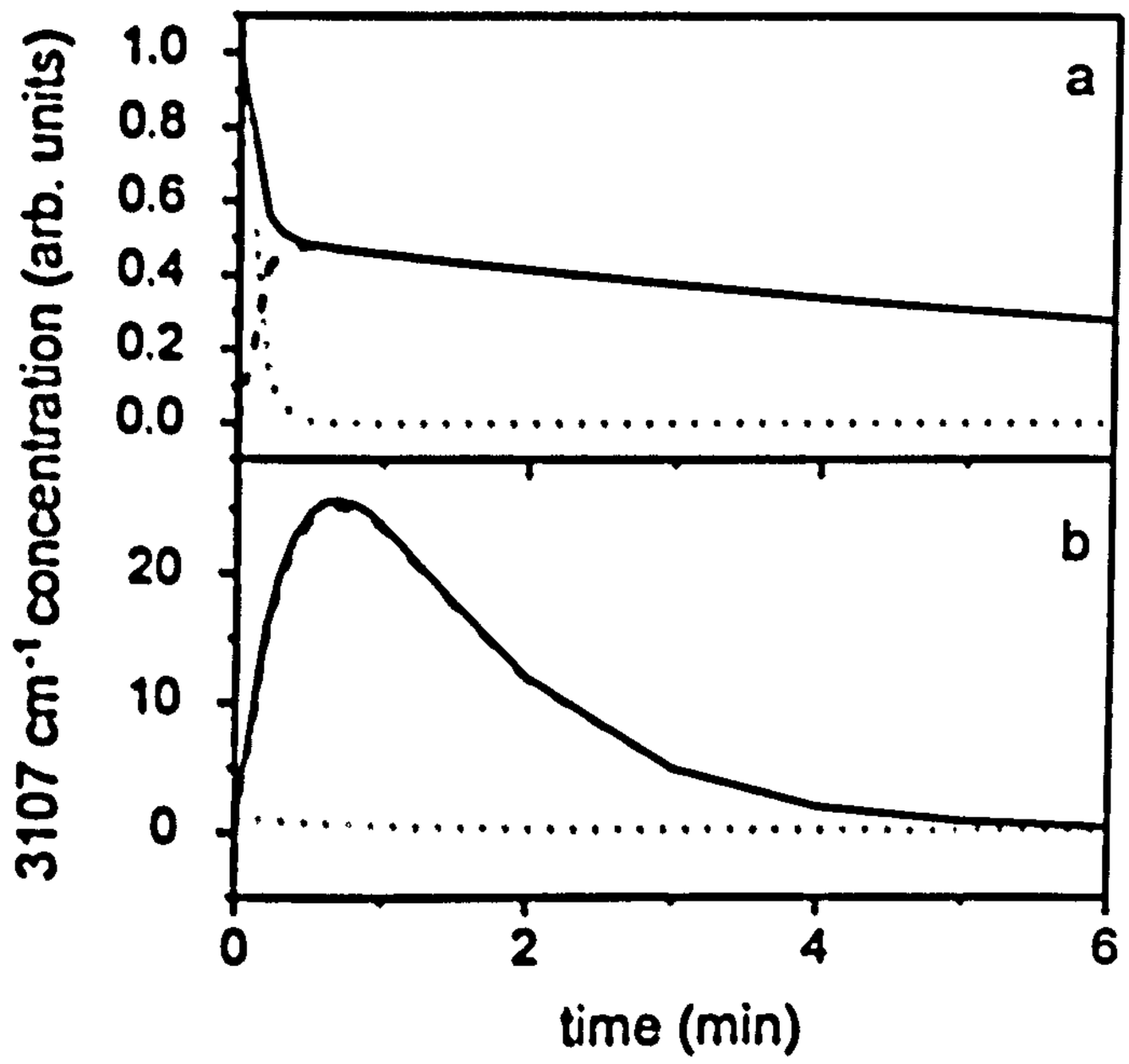

Figure 6.30. Two cases of interest: a) where dissociation dominates the kinetics, and b) where aggregation of the 3107 cm^{-1} defect is dominant. In each graph, the dotted curve represents the dissociation of the initial 3107 cm^{-1} concentration, the broken curve represents the aggregation and dissociation of the 3107 cm^{-1} defect and the full curve indicates the total concentration. It is assumed that the hydrogen originates from a source, which is undetectable using infrared absorption.

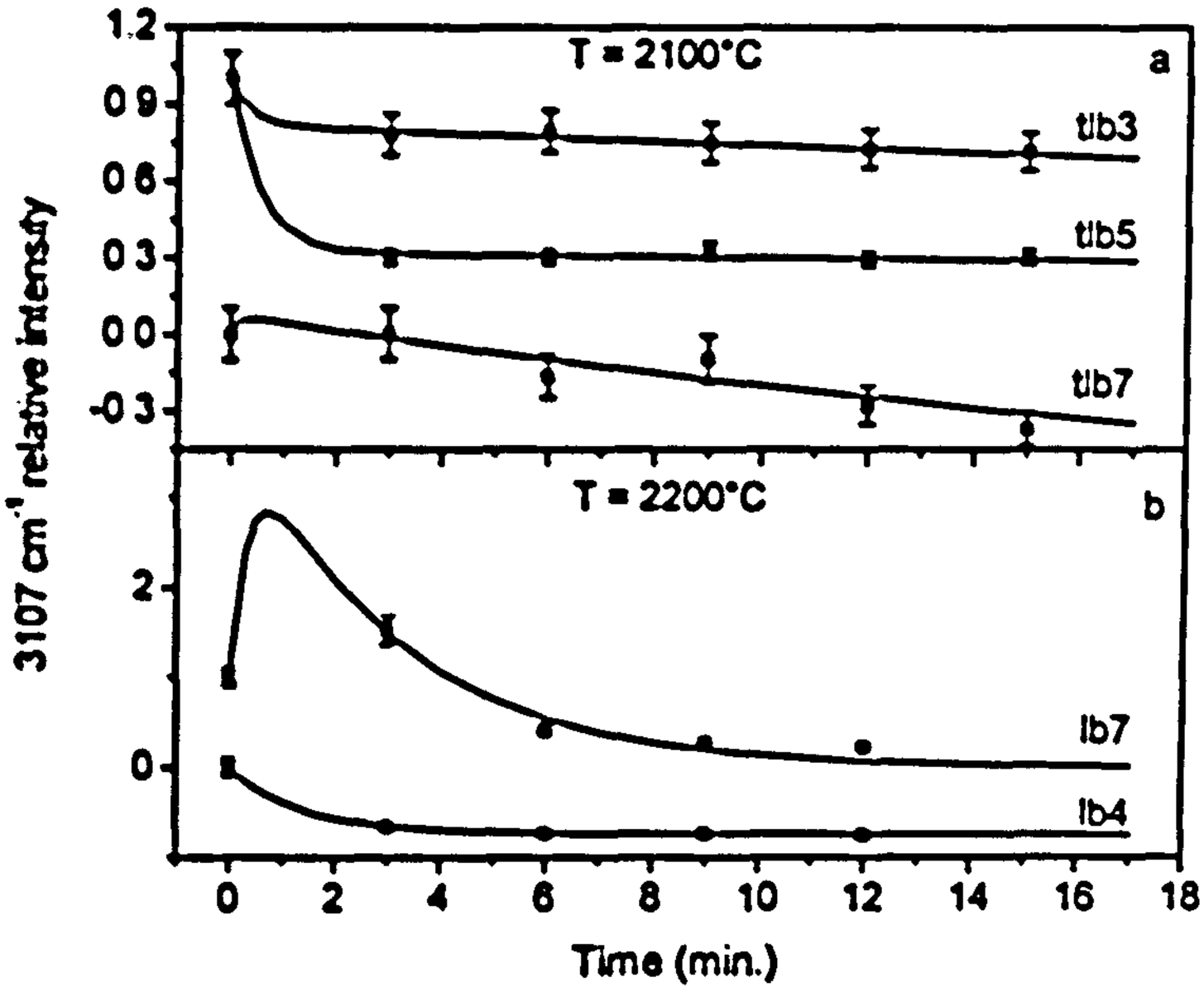

Figure 6.31. Three examples of datapoints from samples annealed at 2100°C (a), and two examples of data from samples annealed at 2200°C (b), fitted with equation 6.6.9. The lower curves in figure 6.31a and 6.31b have been shifted for clarity.

In the second case, the aggregation and dissociation rates are almost equal. There will be an initial increase, and then a decrease, in the concentration of the 3107 cm^{-1} defect (figure 6.30b). Only two samples (tlb-7 and lb-7) display this behaviour.

sample	tlb-1	tlb-3	tlb-5	tlb-6	tlb-7	lb-1	lb-2	lb-3	lb-5	lb-6
$\alpha I/I(0)$	250 ± 100	468 ± 150	200 ± 150	160 ± 90	170 ± 50	316 ± 20	399 ± 200	726 ± 150	175 ± 20	39 ± 20
k_1	0.008 ± 0.001	0.003 ± 0.001	0.006 ± 0.002	0.014 ± 0.004	0.020 ± 0.005	0.008 ± 0.003	0.004 ± 0.001	0.002 ± 0.001	0.014 ± 0.002	0.048 ± 0.002
k_2	3.18 ± 0.59	3.36 ± 0.12	3.40 ± 0.11	3.38 ± 0.16	3.28 ± 1.00	3.98 ± 0.80	3.24 ± 0.02	3.04 ± 0.70	3.76 ± 0.80	3.10 ± 0.14
χ^2	0.984	0.992	0.999	0.974	0.925	0.983	0.992	0.910	0.997	0.996

sample	tlb-4	lb-4	lb-7	lb-8
$\alpha I/I(0)$	131 ± 15	59 ± 25	113 ± 15	75 ± 13
k_1	0.052 ± 0.001	0.072 ± 0.001	0.432 ± 0.001	0.074 ± 0.001
k_2	9.36 ± 1.51	10.20 ± 2.10	9.22 ± 1.00	11.22 ± 1.10
χ^2	0.998	0.999	0.979	0.997

Table 6.16. The parameters used in equation 6.6.9 to fit the datapoints, normalized with respect to the initial integrated intensity of the 3107 cm^{-1} line. The Chi square value of is also given.

Equation 6.6.9 was added as a user defined equation in the fitting routine of Origin 7.0 software and was used to fit the datapoints (figure 6.31). The values of the parameters $\alpha H(0)$, k_1 and k_2 used in the fitting are summarised in table 6.16.

6.6.2.2. Hydrogen source - nitrogen correlation

From the limited dataset, it can be seen that the total hydrogen concentration in the hydrogen source, proportional to coefficient $\alpha H(0)$ is not correlated with the total nitrogen concentration of the samples (figure 6.32a). Also, figures 6.32b and 6.32c, indicate no correlation with [A] or [B], respectively.

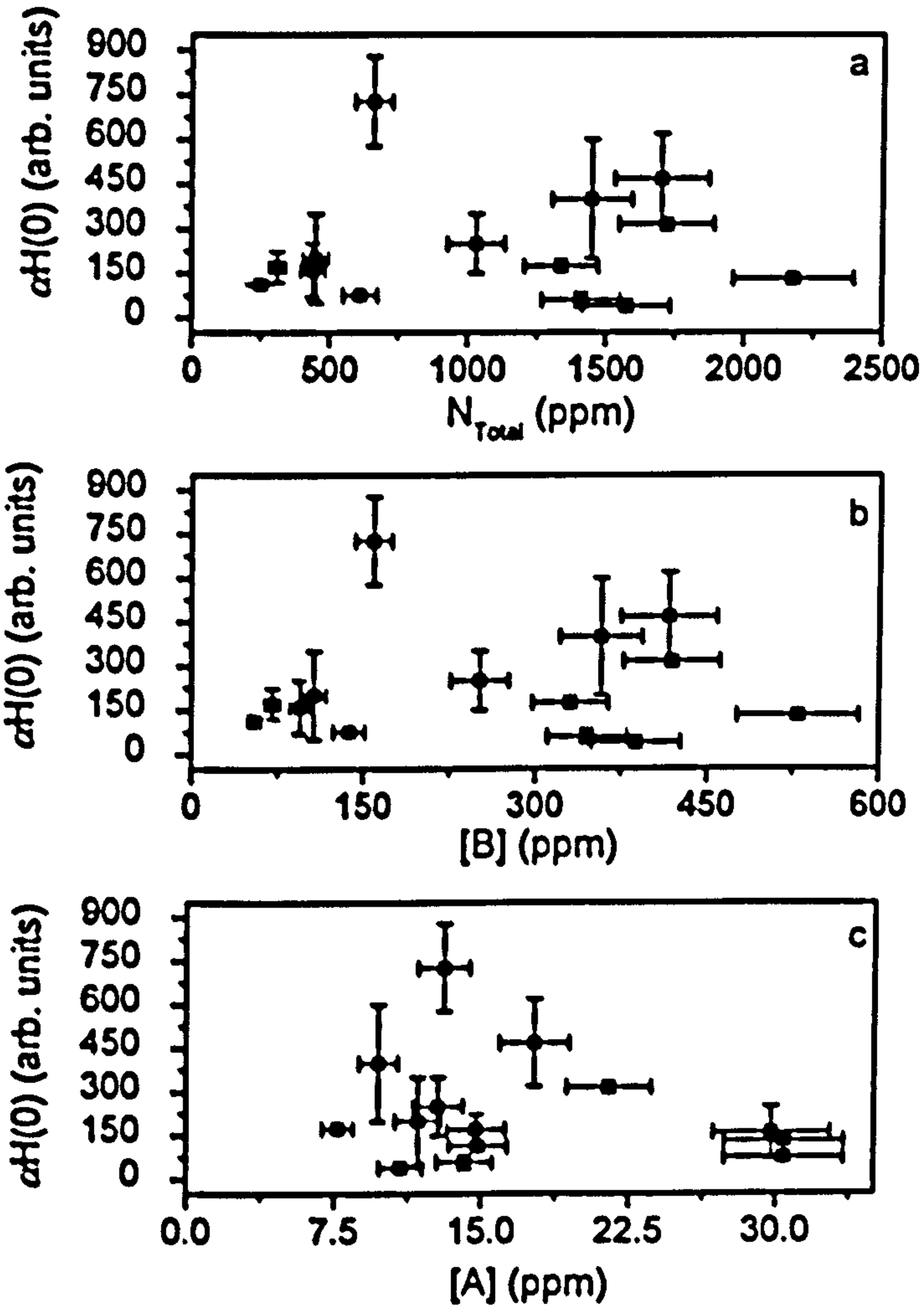

Figure 6.32. The factor proportional to the initial hydrogen concentration in the hydrogen source as function of the initial (a) total atomic nitrogen concentration, (b) B defect concentration and (c) A defect concentration.

6.7. Colour changes in HPHT annealed brown type Ia diamonds

6.7.1. Initial experiments

Before HPHT annealing, all UV-VIS spectra of the brown diamonds show a typical increasing absorption with shorter wavelength and a broad absorption band at 550 – 560 nm. This broadband absorption, centred at 550 – 560 nm, is typical for brown type Ia diamonds (figure 6.33).

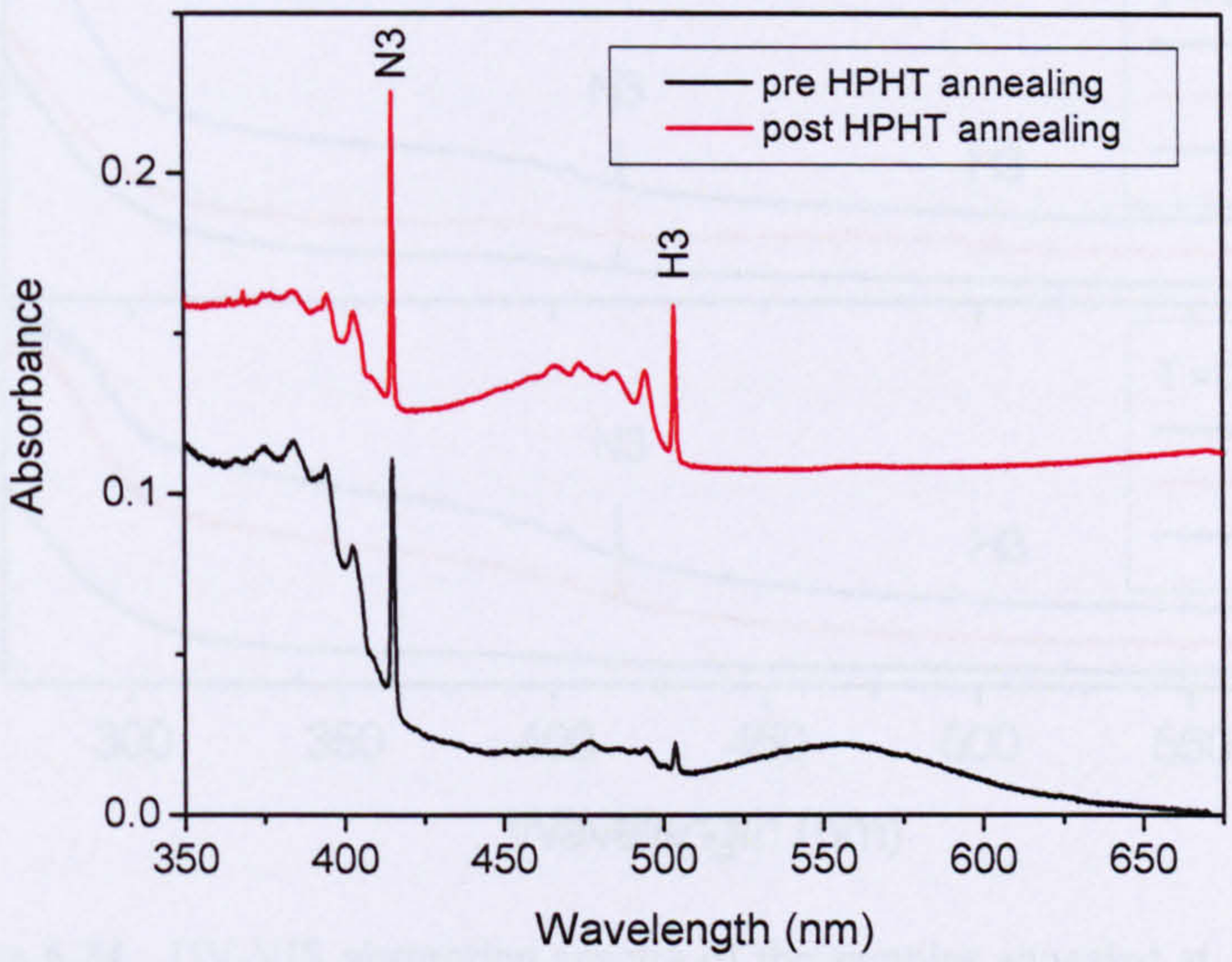

Figure 6.33. A typical absorption spectrum of a brown diamond before (bottom) and after (top) HPHT annealing. Both H3 (ZPL at 503.2 nm) and N3 (ZPL at 415 nm) defect concentrations increase after HPHT annealing. Spectra have been shifted for clarity.

The samples annealed at 1900°C temperature did not display a visible change in colour, and only a weak increase in the H3 absorption was detected. Samples annealed at 2100°C showed a strong increase of H3 absorption. The samples annealed at the highest temperature (2300°C) displayed a lower increase of H3 absorption compared to the samples annealed at 2100°C (figure 6.34) and a relatively high C centre absorption in the IR spectrum. A summary of the properties of the diamond samples is listed in table 6.2.

The second annealing of the diamonds was performed in order to check if the concentrations of the defects indeed reached their thermodynamic equilibrium. For

the samples annealed at 2300°C, only minor changes of H3 and C defect concentrations were observed after the second annealing.

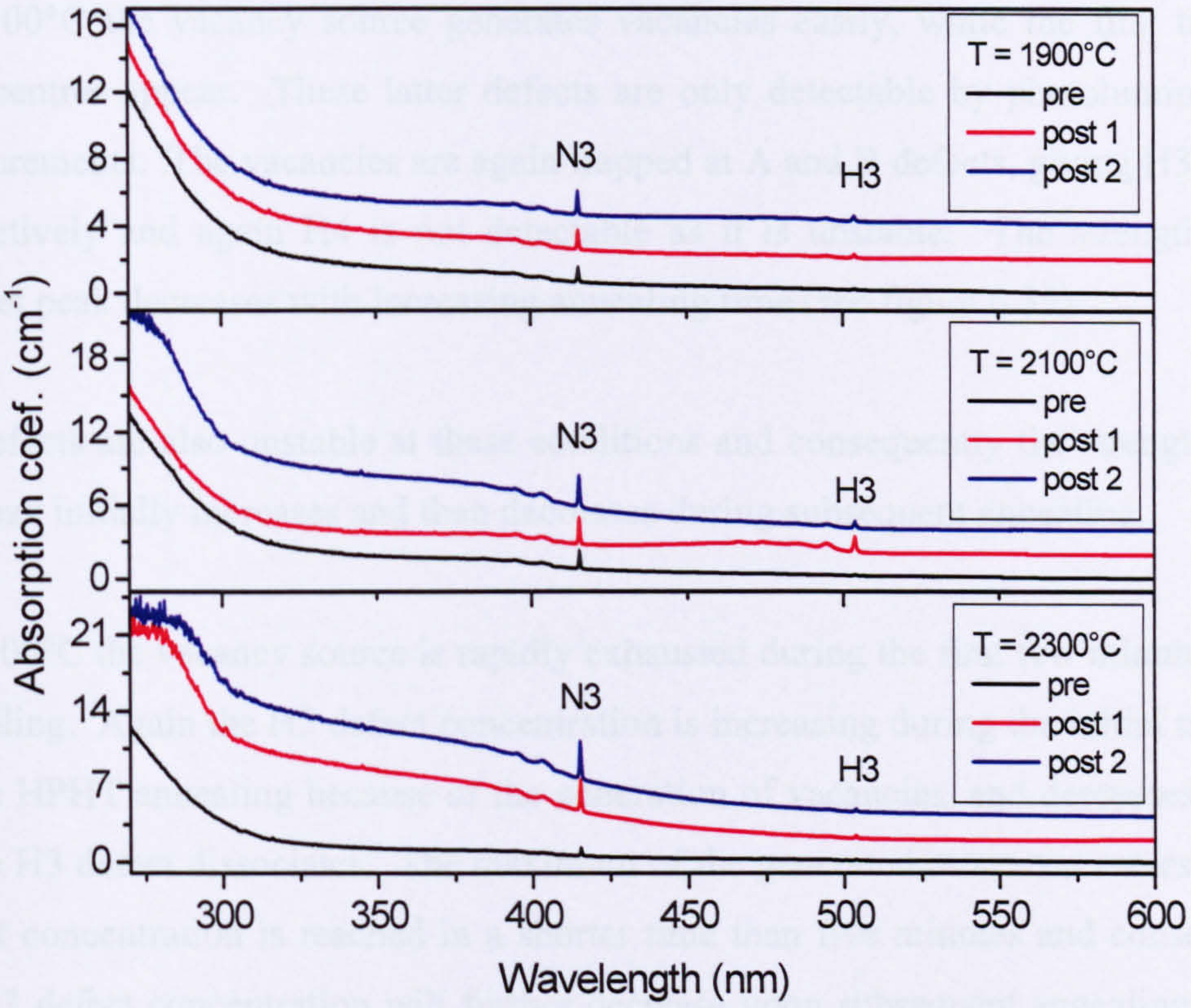

Figure 6.34. UV-VIS absorption spectra of the samples annealed at 1900°C (a), 2100°C (b) and 2300°C (c). Three spectra were recorded for every sample. In every set, the bottom, middle and top spectra are the pre HPHT annealing, after the first and second HPHT annealing, respectively. The spectra have been shifted for clarity. Note the change in the shape of the absorption spectra below 325 nm for the samples annealed at 2100°C and 2300°C, caused by the onset of the broad UV absorption band at 270 nm due to C defects. There is also a strong increase in the N3 absorption when the samples are annealed at 2300°C.

These experiments indicate the following: at 1900°C, a low concentration of vacancies is generated because of the low temperature. These vacancies are highly mobile at the high temperature, and are trapped by an A defect or a B defect, or various other traps (dislocations, surface, platelets, …). These vacancies, trapped at A defects, give rise to the observed weak increase in the concentration of the H3 defects. The strength of the H3 peak increases gradually with every annealing. H4 appears to be unstable at these conditions or higher temperatures as it is not detected and this is

consistent with Collins *et al.* (2005). A weak increase of N3 is detected after annealing at 1900°C.

At 2100°C the vacancy source generates vacancies easily, while the first traces of N-V centres appear. These latter defects are only detectable by photoluminescence measurements. The vacancies are again trapped at A and B defects, giving H3 and H4 respectively and again H4 is not detectable as it is unstable. The strength of the platelet peak decreases with increasing annealing time (see figure 6.35).

H3 defects are also unstable at these conditions and consequently the strength of the H3 peak initially increases and then decreases during subsequent annealing.

At 2300°C the vacancy source is rapidly exhausted during the first few minutes of the annealing. Again the H3 defect concentration is increasing during the initial moments of the HPHT annealing because of the generation of vacancies, and decreases rapidly as the H3 defect dissociates. The maximum of the generated mono-vacancies and H3 defect concentration is reached in a shorter time than five minutes and consequently the H3 defect concentration will further decrease upon subsequent annealing and the change is not as dramatic as with the samples annealed at 2100°C.

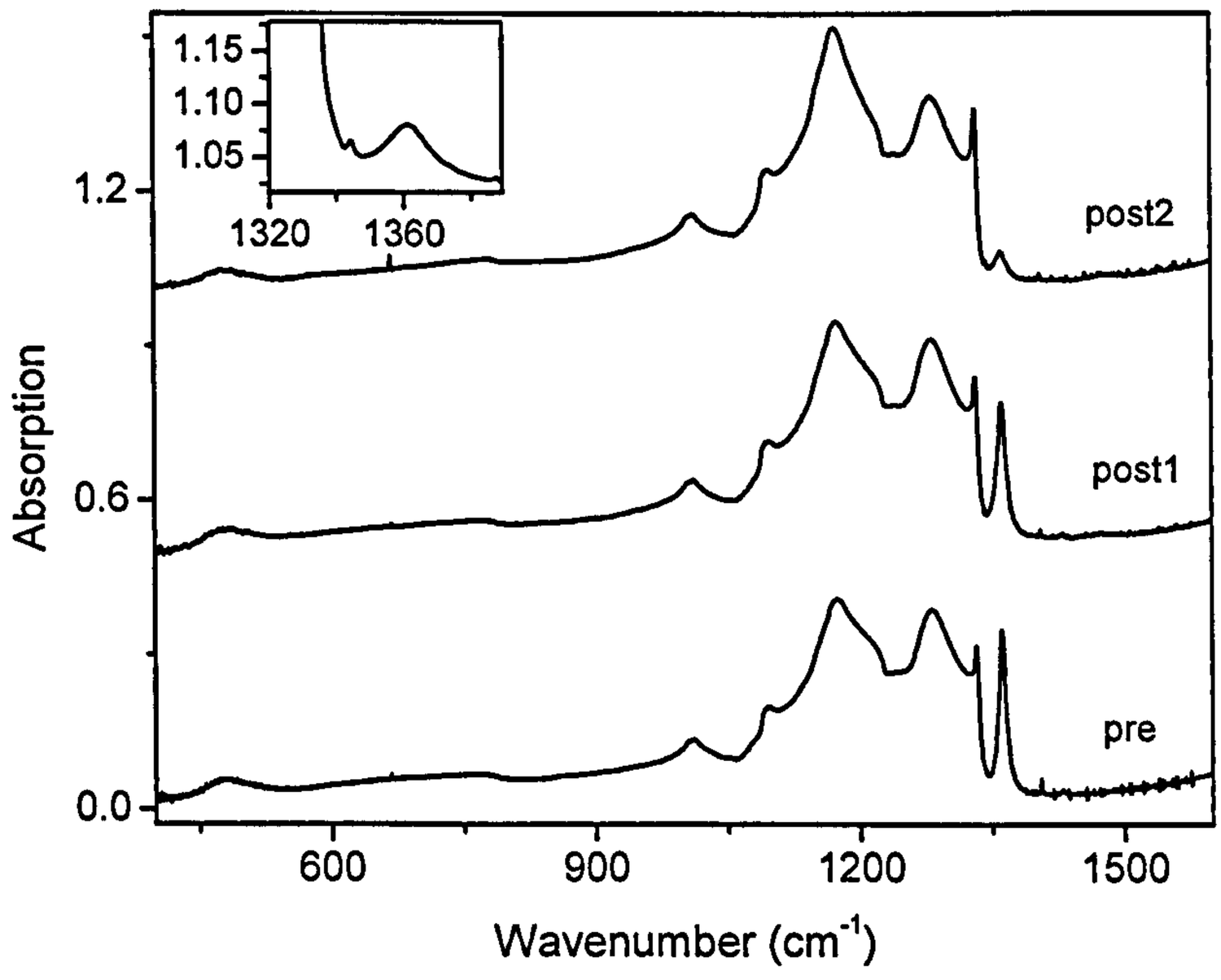

Figure 6.35. IR spectra of a sample prior to, after the first and second annealing at 2100°C. The platelet peak decreases in strength and a peak at 1344 cm^{-1} (see inset) appears after the second annealing.

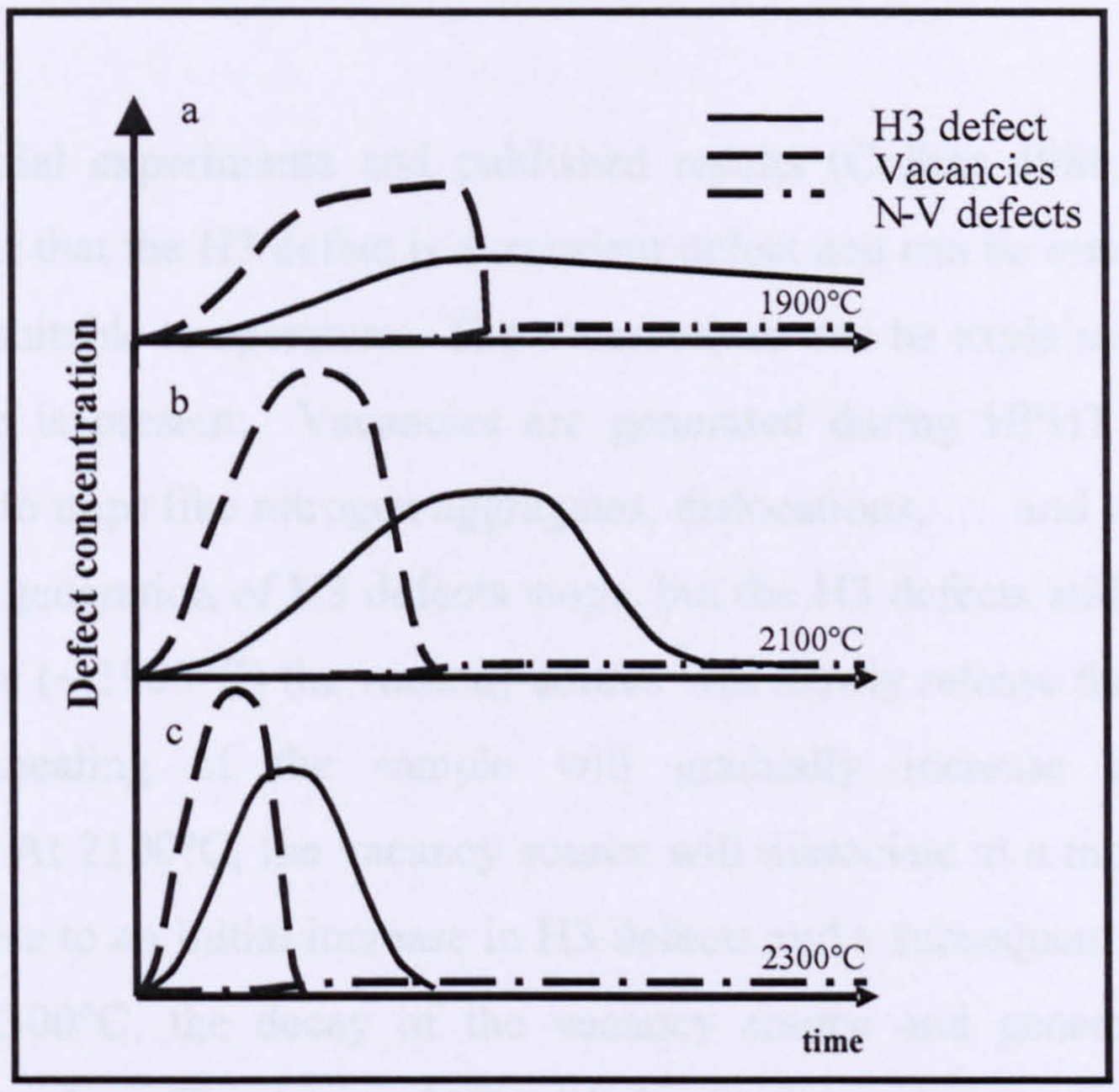

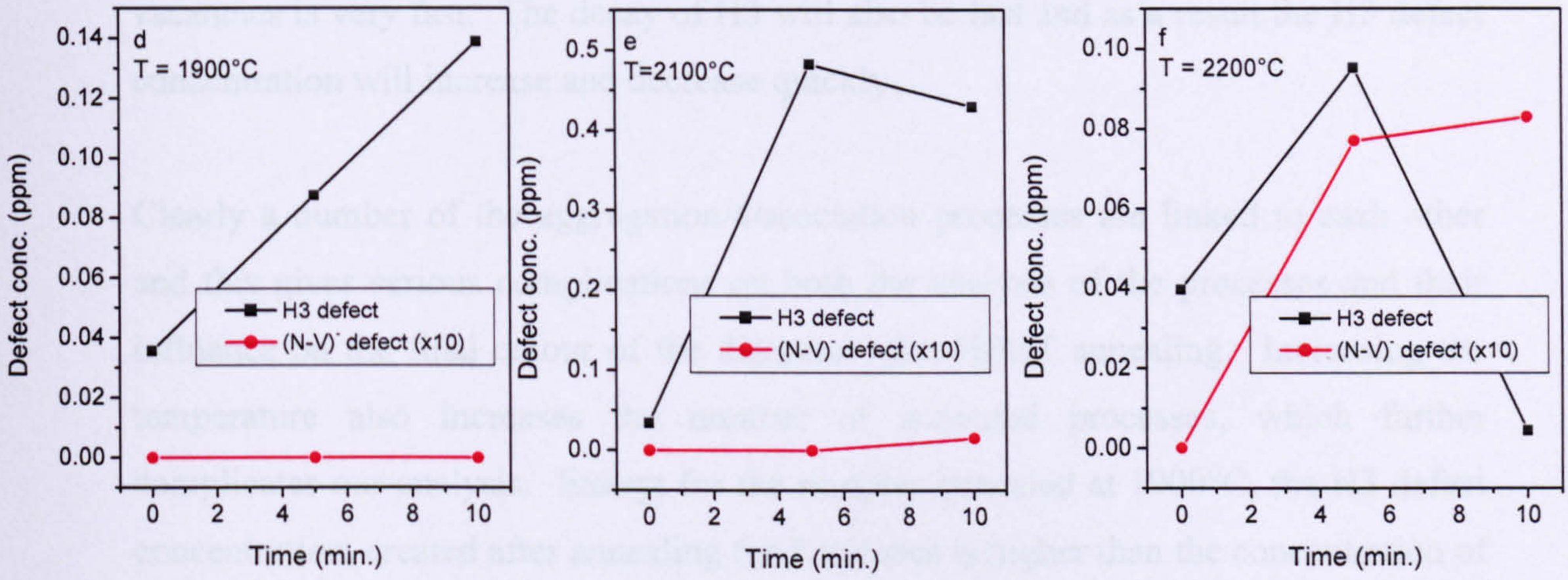

Figure 6.36. Schematic representation (not to scale) of the different processes during the HPHT annealing of type Ia brown diamond. Figure 6.36.a represents the processes, which occur when the diamond sample is annealed at relatively low temperature $T \leq 1900°C$. A low concentration of mono-vacancies is created due to dissociating of a vacancy source. At higher temperatures ($1900°C < T < 2200°C$), the same processes occur as at low temperatures, and a low concentration of NV defects is also created; this is due either to the dissociation of H3 defects into N + NV or the dissociation of A defects into N + N and subsequent trapping of a vacancy. Because the vacancy source is depleted after a certain time, no increase of H3 should be observed after some time during the annealing (Figure 6.36.b). At high temperatures ($T > 2300°C$) a high concentration of NV centres is created because a large concentration of C defects is created from dissociated A defects (6.36.c), which will trap the mono-vacancies. Figures d, e and f are the H3 and (N-V)- defect concentrations of samples 1H3, 1H6 and 1H8 respectively from which the schematic representation (6.37.a - c) is derived.

From these initial experiments and published results (Collins 1980, Collins *et al.* 2005), it is clear that the H3 defect is a transient defect and can be removed by HPHT annealing at a suitable temperature. The observations can be explained when a finite vacancy source is present. Vacancies are generated during HPHT annealing and diffuse rapidly to traps like nitrogen aggregates, dislocations, ... and when the source is depleted the generation of H3 defects stops, but the H3 defects still dissociate. At low temperature (~ 1900°C) the vacancy source will slowly release the vacancies and subsequent annealing of the sample will gradually increase the H3 defect concentration. At 2100°C, the vacancy source will dissociate at a moderate rate and this will give rise to an initial increase in H3 defects and a subsequent decrease of H3 defects. At 2300°C, the decay of the vacancy source and generation of mono-vacancies is very fast. The decay of H3 will also be fast and as a result the H3 defect concentration will increase and decrease quickly.

Clearly a number of the aggregation/dissociation processes are linked to each other and this gives serious complications on both the analysis of the processes and their influence on the final colour of the diamond after HPHT annealing. Increasing the temperature also increases the number of activated processes, which further complicates our analysis. Except for the samples annealed at 1900°C, the H3 defect concentration, created after annealing for 5 minutes is higher than the concentration of H3 defects after 10 minutes annealing. This indicates that the created H3 defect concentration might not be at its maximum after 5 minutes annealing: it is situated on the lowering flank in of the H3 concentration curves in figure 6.36b. The increase of H3 at 1900°C is slow and steady, indicating it is still on the increasing flank of the H3 defect concentration curve in figure 6.36a. Therefore other annealing experiments were carried out with the shortest experimental significant time interval, which is three minutes. The temperatures (2100 and 2200°C) are chosen so that results can be obtained after a reasonably short annealing time and the first datapoints should be located close to the maximum of the H3 concentration generated. By adopting this method we hope to resolve the maximum of the generated H3 defect concentration and the rising and decreasing flank of the H3 defect concentration curve as function of time.

To investigate the influence of different defects (A and B defects) on the H3 formation and dissociation in brown type Ia diamonds, the samples have been divided into four different groups, and have been HPHT annealed at 2100°C or 2200°C respectively:

- Group 1 consists of the tlb and lb samples, HPHT annealed at 2100°C with intervals of 3 minutes.
- Samples of group 2 are the tlb and lb samples, HPHT annealed at 2200°C with intervals of 3 minutes. Samples of groups 1 and 2 are the same samples as in section 6.5 of this chapter.
- Group 3 consists of the brown type IaA diamonds (1D1, 1B1 to 1B3), annealed at 2100°C for 3 minutes to study the generation and dissociation of H3 defects.
- Group 4 consists of 4 type IaB brown diamonds (B1a, B1b, Al84a, Al84b), sample pairs cut from 2 different diamonds. One half of each pair was annealed at 2100°C, the other half at 2200°C for 6 minutes. The purpose of this experiment was to generate H3 defects by dissociation of H4 defects.

One additional brown type IaA/B sample was cut into two plates, nearly parallel to (100) (samples 2a and 2b) and one of the samples (2a) was annealed at 1900°C for 20 h.

In the analysis of the data of the samples of group 1 and 2, we investigate the parameters influencing the H3 formation. We will start with the vacancy formation by release of vacancies from the vacancy source, and the effects of formation and dissociation of H3 defects by the capture of a vacancy by A defects, release of the vacancy and retrapping of vacancies by an A defect. Finally perturbations to the H3 defect formation and dissociation kinetics by the presence of H4 defects is investigated.

6.7.2. Correlation between the degree of the brown colour of a type Ia diamond and the created H3 concentration

Because the H3 defect ZPL and side band are superimposed on the side of the 550 nm centred absorption band, the integrated intensity of this band cannot be taken as a

measure of the concentration of the defect causing the absorption. Instead, the absorption coefficient at 550 nm is taken as a measure of the degree of brown colour of the diamond.

After the first HPHT annealing, a very strong increase in the H3 concentration is observed (figure 6.34) and the underlying broadband absorption, is removed. From the results of the samples of group 1, 2 and 3, an increasing trend between the increase of the concentration of H3 defects after the first annealing, and the intensity of the brown colour of the sample prior to HPHT annealing can be observed (figure 6.37). This indicates that the defect responsible for the brown colour of the diamond releases vacancies during HPHT annealing.

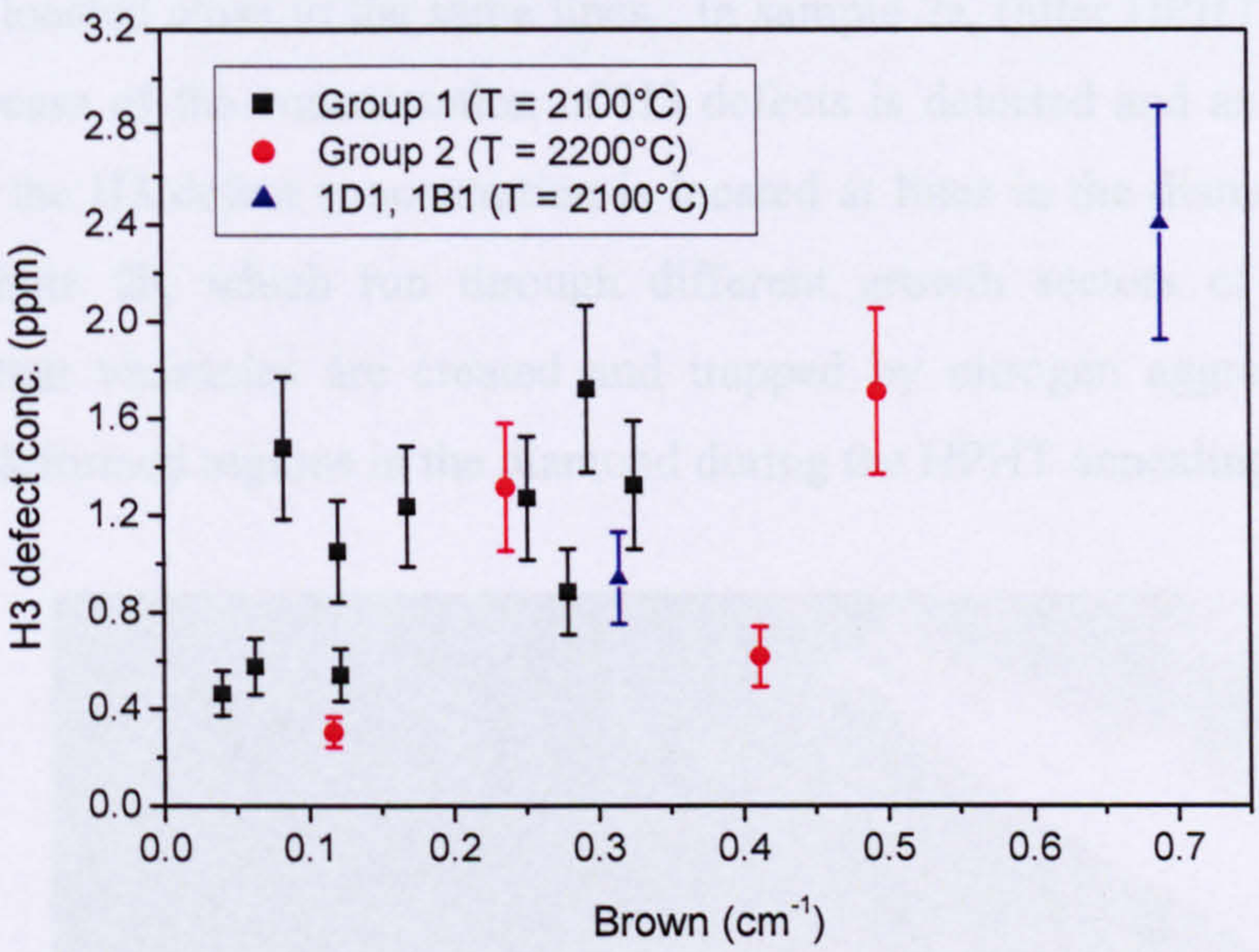

Figure 6.37. Analysis of the samples of the preliminary annealed samples and samples of groups 1, 2 and 3 show a correlation between the increase of H3 concentration and the saturation brown colour of the sample prior to HPHT annealing. The black squares are the datapoints of the samples annealed at 2100°C, red circles are of the samples annealed at 2200°C and the blue triangles are datapoints of brown type IaA samples annealed at 2100°C.

Stress and slip patterns in brown type Ia diamonds can be visualised by keeping the diamond between polarizing filters (Collins *et al.* 2000). In some commercially available HPHT annealed type Ia diamonds, green H3 luminescence can be observed. In some cases, these green luminescent lines appear to be correlated with the plastic deformation patterns. CL line scans on the surface of natural and HPHT annealed

brown diamonds should prove this correlation, thereby linking the plastic deformation to the generation of vacancies in brown type Ia diamond.

Regions for line scans on samples 2a and 2b were selected from CL images (figure 6.38 and 6.39). A spectral region between 365 and 630 nm was selected which allows clear identification of the presence of N3 defects with a zero phonon line at 415 nm and the H3 defect. The CL spectra of each line scan are shown in figure 6.41 (sample 2a, after annealing) and 6.40 (sample 2b, before annealing). In sample 2b, an additional defect related to the plastic deformation (Collins *et al.* 2000), with a ZPL at 490.7 nm can also be detected, with elevated concentrations pinned at lines through different growth regions of the diamond. Also, increased concentrations of H3 defects are located close to the same lines. In sample 2a, (after HPHT annealing) an overall increase of the concentration of H3 defects is detected and an even stronger increase of the H3 defect concentration is located at lines in the diamond, similar to that in sample 2b, which run through different growth sectors of the diamond, indicating that vacancies are created and trapped by nitrogen aggregates close to plastically deformed regions in the diamond during the HPHT annealing.

Figure 6.38. Cathodoluminescence image of the surface of sample 2b (before annealing) monochromatized at 530 nm. The white line indicates where the CL line scan has been done. The angle between the octahedral growth horizons with <110> direction on the nearly {100} surface and lines where the line scan is measured is ~ 23° so the lines are parallel with the <210> direction (see also figure 6.44).

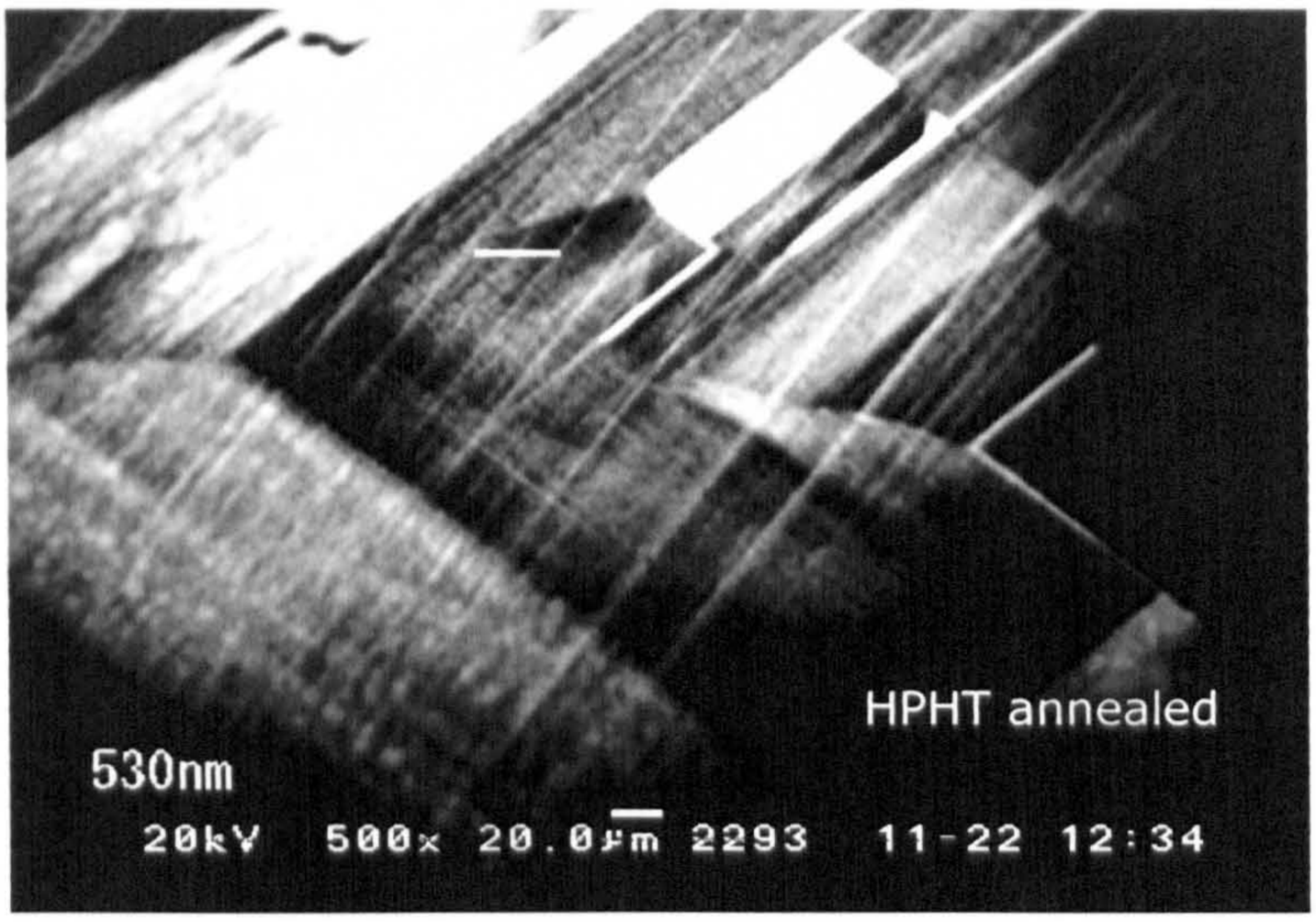

Figure 6.39. Cathodoluminescence image of the surface of sample 2a (after annealing) monochromatized at 530 nm. The white horizontal line indicates where the CL line scan has been done.

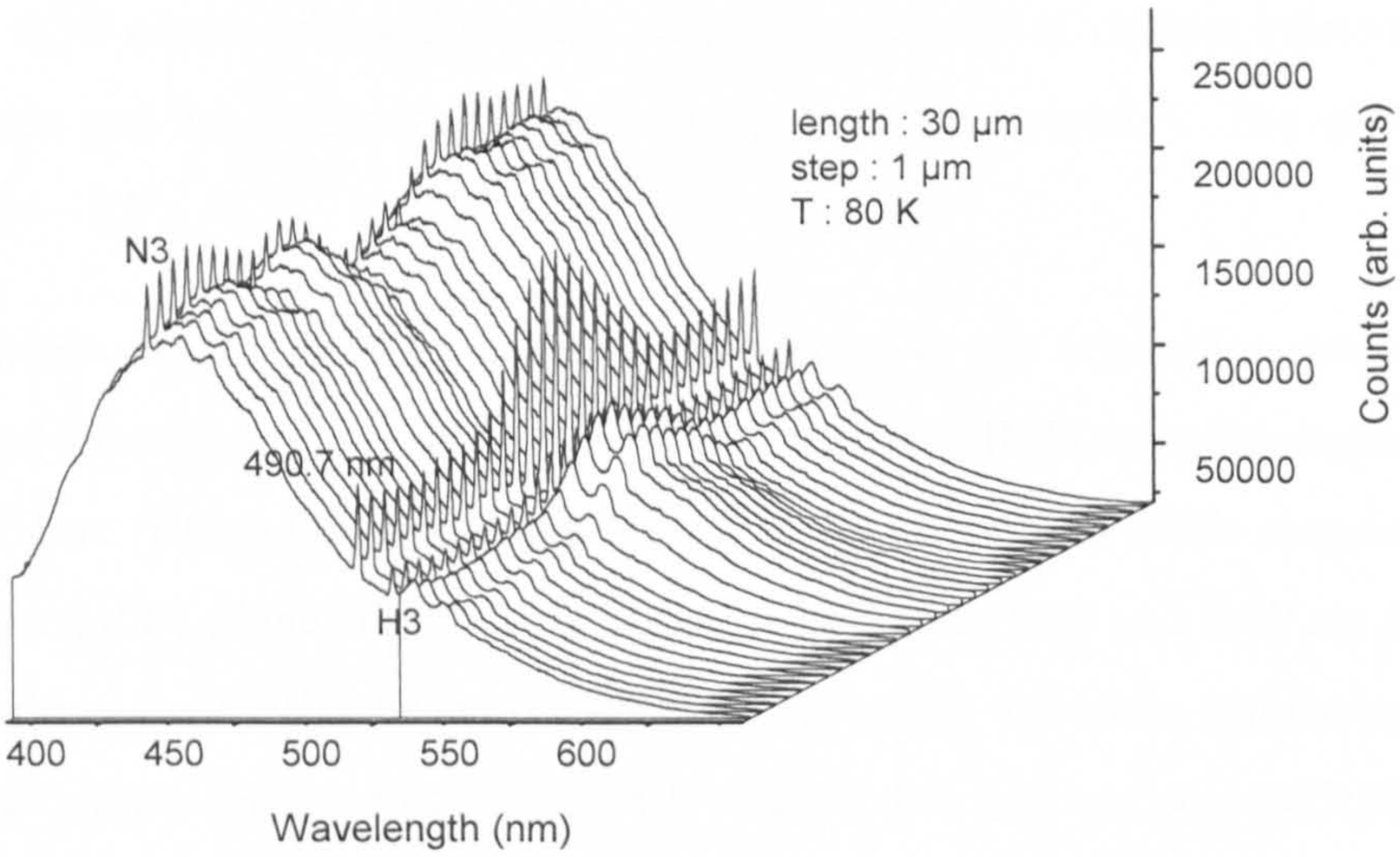

Figure 6.40. A CL line scan on the surface of the brown type Ia diamond (sample 2b) reveals that H3 and other defects are inhomogeneously dispersed in the diamond. Increased concentrations of H3 and 490.7 nm defects are located at lines in the diamond, which run through different growth sectors, indicating post growth formation. The step size along the line is 1 µm.

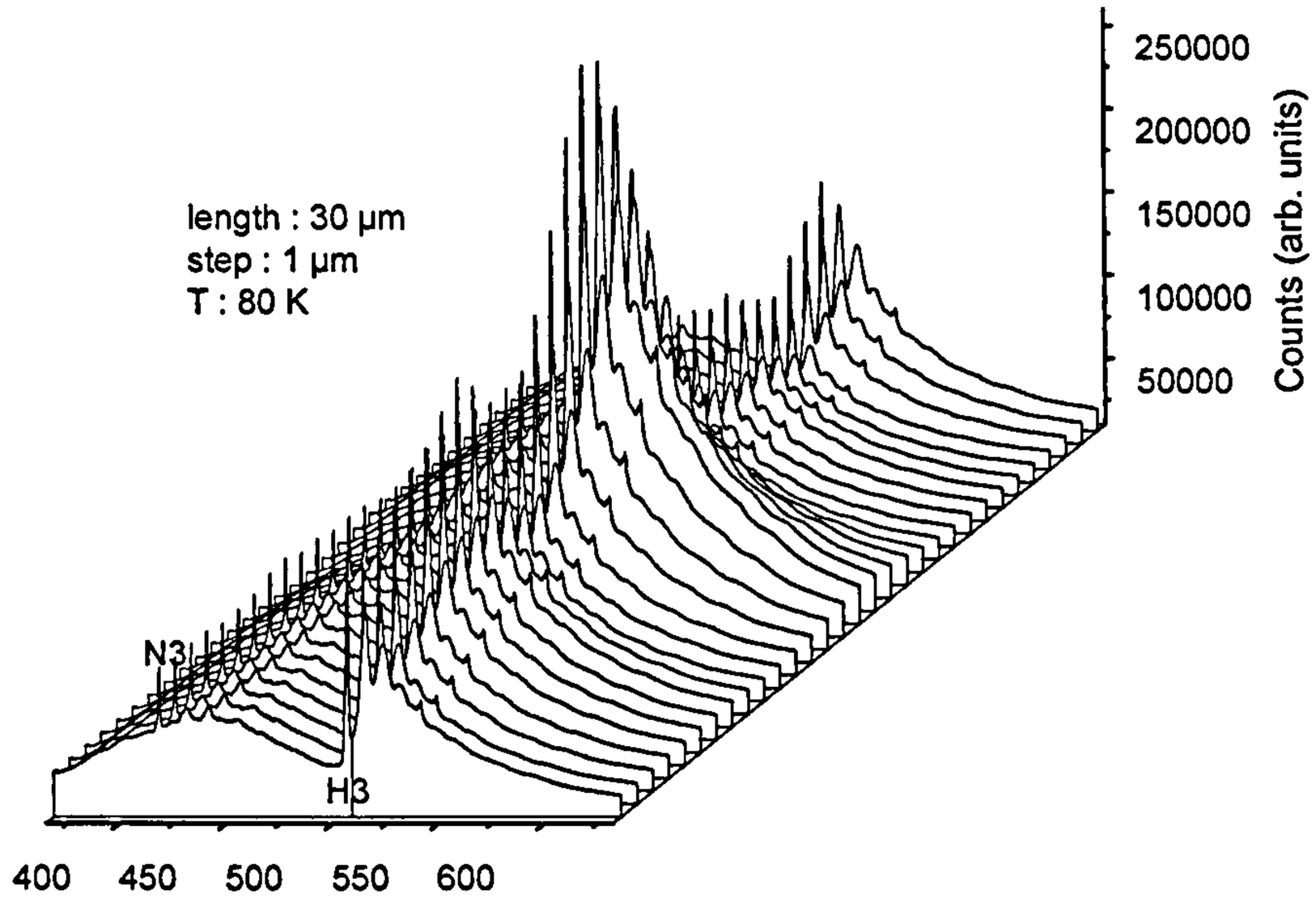

Figure 6.41. A CL line scan on the surface of the HPHT annealed brown type Ia diamond (sample 2a) reveals an overall increase of H3 defects especially around lines in the diamond. The step size along the line is 1 µm.

Shear of crystallographic planes because of plastic deformation should occur along the planes with closest stacking, i.e. parallel to the octahedral plane. However, figure 6.38 and 6.39 clearly show the plane with high density of defects related to plastic deformation and the octahedral growth sectors to be non-parallel. The angle between the lines is ~ 23°.

The orientation of the sample surface with respect to the crystalline orientation was determined from Electron BackScattered Diffraction (EBSD) measurements and from the pole figure (figure 6.42), and it is clear that the orientation of the sample surface is close to the {100} plane. The growth horizons in figures 6.39 and 6.40 are found to be oriented along the <110> or symmetrically equivalent direction, indicating these are octahedral planes intersecting the {100} surface, but are not perpendicular. This is because the polished surfaces are not perpendicular to the {100} plane (figure 6.42) so the intersection between {111}, $\{1\,\bar{1}\,1\}$ and {001} surfaces does not result in perpendicular <110> and $<1\,\bar{1}\,0>$ lines (figure 6.42).

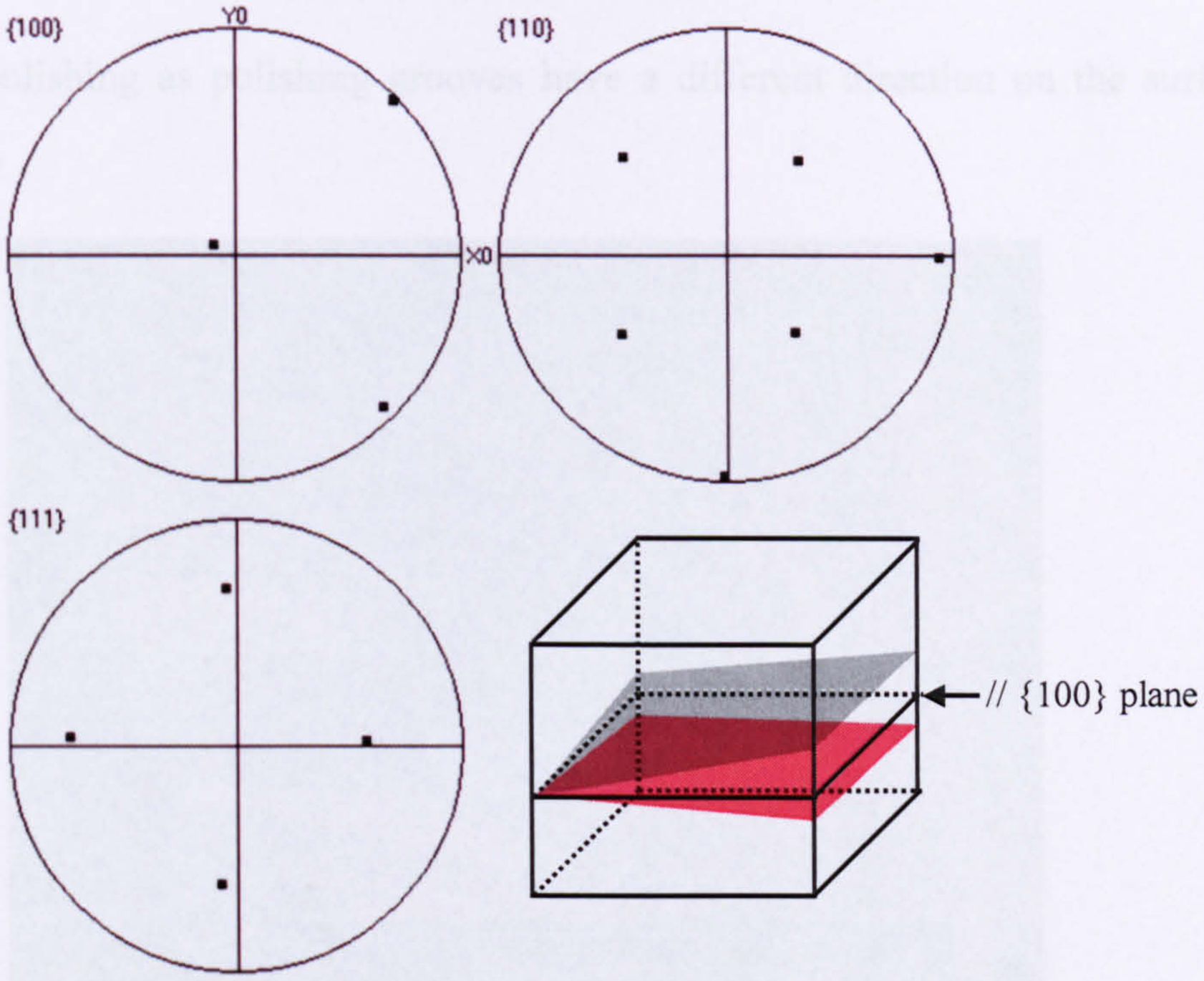

Figure 6.42. The pole figure of the diamond 2a. The surface of the sample is close to the {100} plane because sample was not exactly cut along a plane parallel to the {100} crystallographic plane: the orientation of the surface of samples 2a and 2b is more like the red and grey surfaces in the schematic drawing bottom right. As a consequence the angle between the equivalent octahedral planes intersecting the {100} plane in the CL images are not perpendicular.

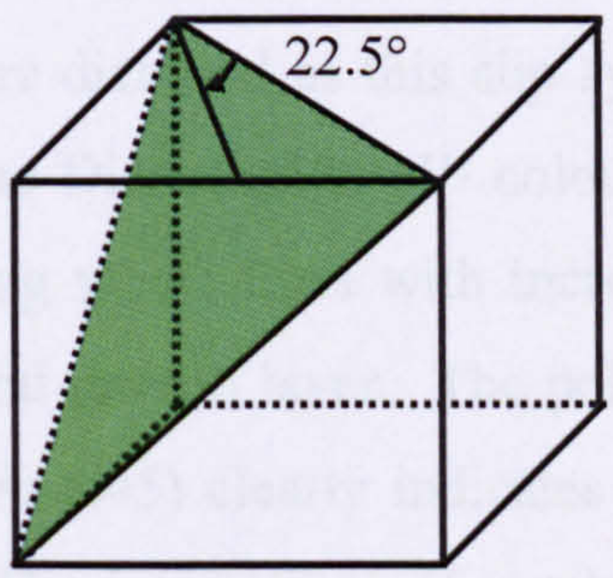

Figure 6.43. The intersection of a growth horizon of an octahedral plane with the {100} plane gives a line parallel to the <110> direction. The angle between the intersection of the octahedral plane and the {211} plane intersecting a cubic surface is 22.5°.

From CL images over a larger surface, we can clearly see that lines with increased H3 defects must be parallel to a <210> direction, which can form when a {211} intersects a {100} plane (figure 6.43). The lines with increased H3 concentration are certainly

not due to polishing as polishing grooves have a different direction on the surface (figure 6.44).

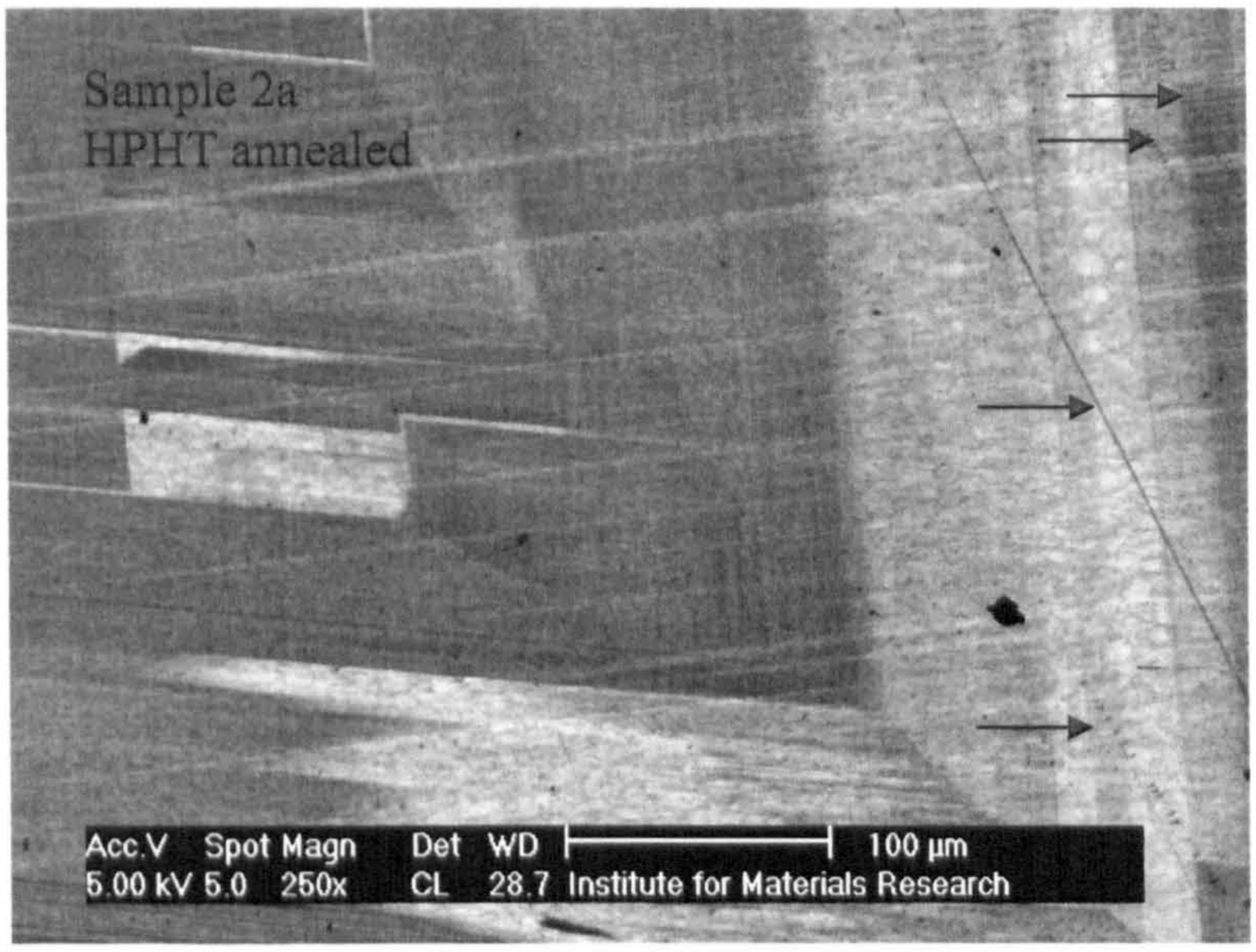

Figure 6.44. The CL image of the surface of sample 2a, recorded over a larger area than shown in figure 6.36. The sample image is recorded with the diamond rotated over 90 degree with respect to the image of the sample in figure 6.22. Arrows point to non-luminescent lines on the surface of the diamond, which are polishing grooves.

It is possible this is a very rare diamond as this slip system is usually not observed; however figure 6.45 shows the DiamondView™ colour image of a type brown IaA diamond after HPHT annealing where lines with increased H3 defect concentration are not parallel to an octahedral growth layer. The pole figure of two measurements on the diamond surface (figure 6.45) clearly indicates the polished surface is nearly parallel to the {111} plane. The intersection of octahedral planes on an octahedral surface is trigonal in shape and thus at 60° with respect to each other. The lines with clear increased concentrations of H3 defects intersecting the (octahedral) surface are at 45° angle with another octahedral plane (figure 6.45) and are thus not parallel to any other octahedral growth layer. The angle between the other octahedral growth layers is 60°.

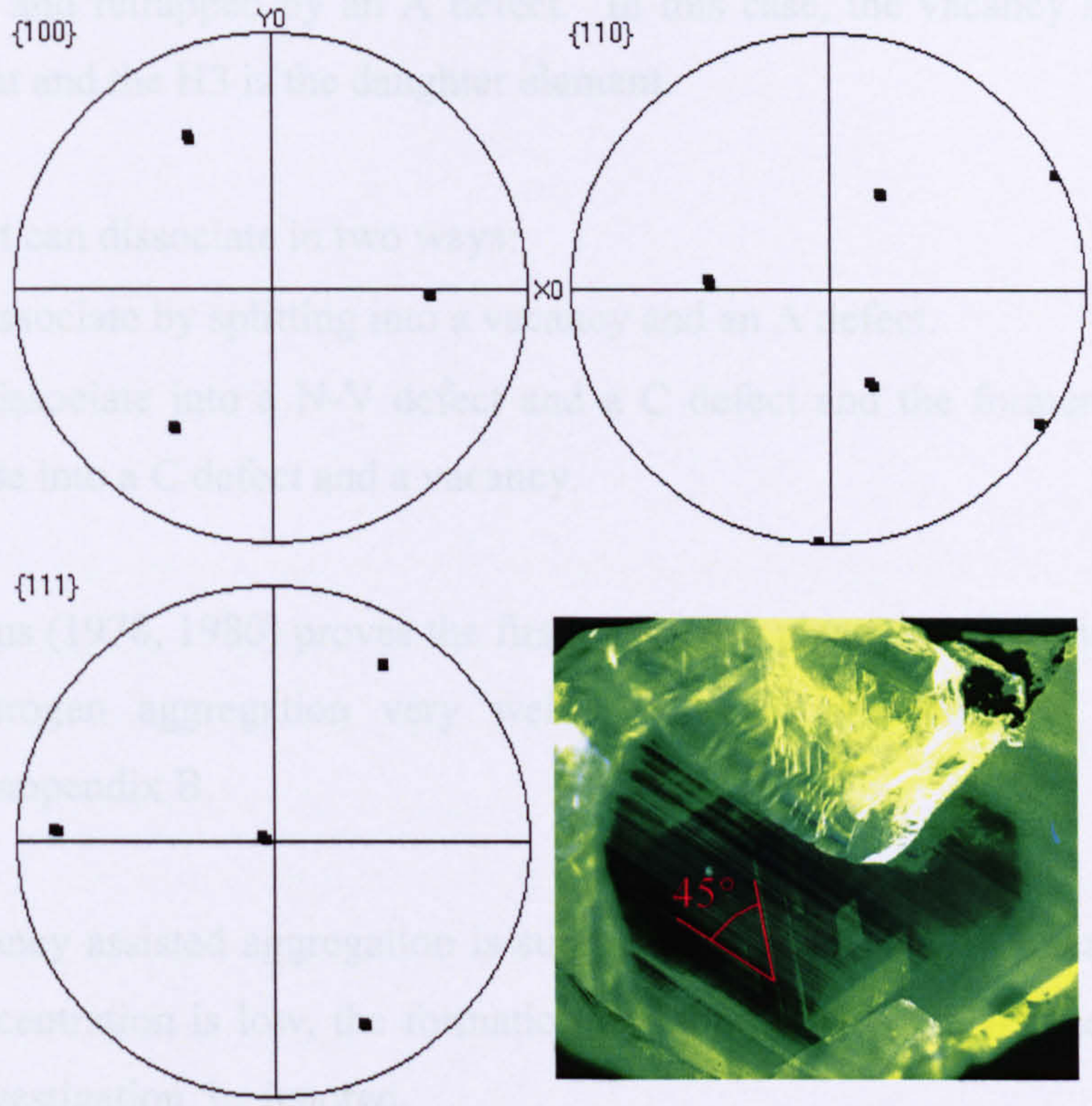

Figure 6.45. The DiamondView™ image and pole figure of one of the brown type IaA diamonds after HPHT annealing. Note the H3 defect rich lines are at 45° to one of the octahedral growth horizons intersecting the polished surface of the diamonds, so these lines cannot be parallel to an octahedral plane (the angle between octahedral planes intersecting another octahedral plane must be 60°).

Clearly other slip systems are activated at high temperature and pressure experienced by the diamond when it was plastically deformed in Nature. There are indications that different slip systems can indeed be activated at high temperature (Evans and Wild 1965, DeVries 1975, Sumiya 2006).

6.7.3. H3 defect formation and dissociation including vacancy release from H3 defects and retrapping by A defects and excluding B defects

The H3 defects created by the trapping of the vacancies from the vacancy source are not stable at the applied HPHT conditions and will also dissociate, which is experimentally observed in the samples of the two groups (figure 6.10 and 6.11). The reaction should proceed as a modified TSD model where vacancies can be released by

an H3 defect and retrapped by an A defect. In this case, the vacancy source is the parent element and the H3 is the daughter element.

The H3 defect can dissociate in two ways:

- H3 can dissociate by splitting into a vacancy and an A defect.
- H3 can dissociate into a N-V defect and a C defect and the former will further decompose into a C defect and a vacancy.

Data of Collins (1978, 1980) proves the first path takes place as this explains vacancy enhanced nitrogen aggregation very well. The second option is investigated separately in appendix B.

Because vacancy assisted aggregation is suppressed during HPHT annealing and the C defect concentration is low, the formation and dissociation of N-V defects will in this initial investigation, be ignored.

To include H3 defect formation and dissociation, vacancy retrapping by A defects, and the energy barrier which must be overcome to allow the A-V complex to restructure into H3, the reaction kinetics of the H3 defect can be described by five coupled differential equations:

$$\frac{d[V_{cl}(t)]}{dt} = -k_1[V_{cl}(t)] \tag{6.7.1}$$

$$\frac{d[V_{total}(t)]}{dt} = k_{1,fast}[V_{cl}(t)] + k_3[H3(t)] + k_{1,fast}[(A\text{-}V_{total})(t)] - k_{1,fast}(1-\alpha[A(t)])[V_{total}(t)] \tag{6.7.2}$$

$$\frac{d[(A\text{-}V_{total})(t)]}{dt} = \alpha k_{1,fast}[A(t)][V_{total}(t)] - k_2[(A\text{-}V_{total})(t)] - k_{1,fast}[(A\text{-}V_{total})(t)] \tag{6.7.3}$$

$$\frac{d[H3(t)]}{dt} = k_2\left[(A\text{-}V_{total})(t)\right] - k_3\left[H3(t)\right] \qquad (6.7.4)$$

$$\frac{d[A(t)]}{dt} = -\alpha k_{1,fast}\left[A(t)\right].\left[V_{total}(t)\right] + k_3\left[H3(t)\right] - k_{diss}\left[A(t)\right] + \tfrac{1}{2} k_{aggr}\left[C(t)\right]^2 \qquad (6.7.5)$$

Here $[V_{cl}(t)]$ is the mono-vacancy concentration released by the vacancy source at time t, α is the fraction of vacancies captured by the A defect. $[H3(t)]$ is the H3 defect concentration at time t, k_1 is the rate constant for the release of vacancies from the source and k_2 is the dissociation constant of the H3 defect itself. The constant $k_{1,fast}$ is the fast vacancy diffusion rate constant (see chapter 5). The last equation describes the loss of A defects by H3 defect formation and the generation of A defects by H3 dissociation into a vacancy and an A defect.

The vibrational pre-factor and the activation energy of the rate constants $k_{1,fast}$ and k_2 are tabulated in table 6.14. The other rate constants, k_1 and k_3, are determined from fitting of equations 6.7.1 – 6.7.5 to the experimental data by fitting the H3 defect concentration change described by the five coupled differential equations 6.7.1 – 6.7.5. The equations are solved numerically and parameters are varied until a close fit to the experimental data is reached. The uncertainty on the fitting procedure can be reduced by keeping in mind that the rate constants depend exponentially on the ratio of the temperature and activation energy for each i-th process:

$$k_i = A_i.\exp\left[{}^{-E_{a,i}}\!/_{k_B T}\right] \qquad (6.7.6)$$

with k_i the rate constant, A_i the exponential pre-factor, E_a the activation energy, k_B the Boltzmann constant, and T the temperature in Kelvin. These parameters should be the same for the two groups and upon substitution of the rate constants in equations 6.7.1 - 6.7.5 by equation (6.7.6), all datapoints acquired at T = 2100°C and 2200°C can be fitted in one least squares fitting procedure. However in practice, no increase and decrease of the H3 defect concentration at two different temperatures can be fitted

simultaneously in detail by this procedure: parameters which give a good fit of the data of group 1 gives a bad fit for the data of the samples of group 2 and vice versa. This indicates that this process is certainly not the only process describing the H3 formation. Also, the model should include vacancy diffusion and trapping of a vacancy by the A defect outlined in chapter five. A final note is that all fitted curves deviate substantially from the experimental data (figure 6.46) at long annealing time.

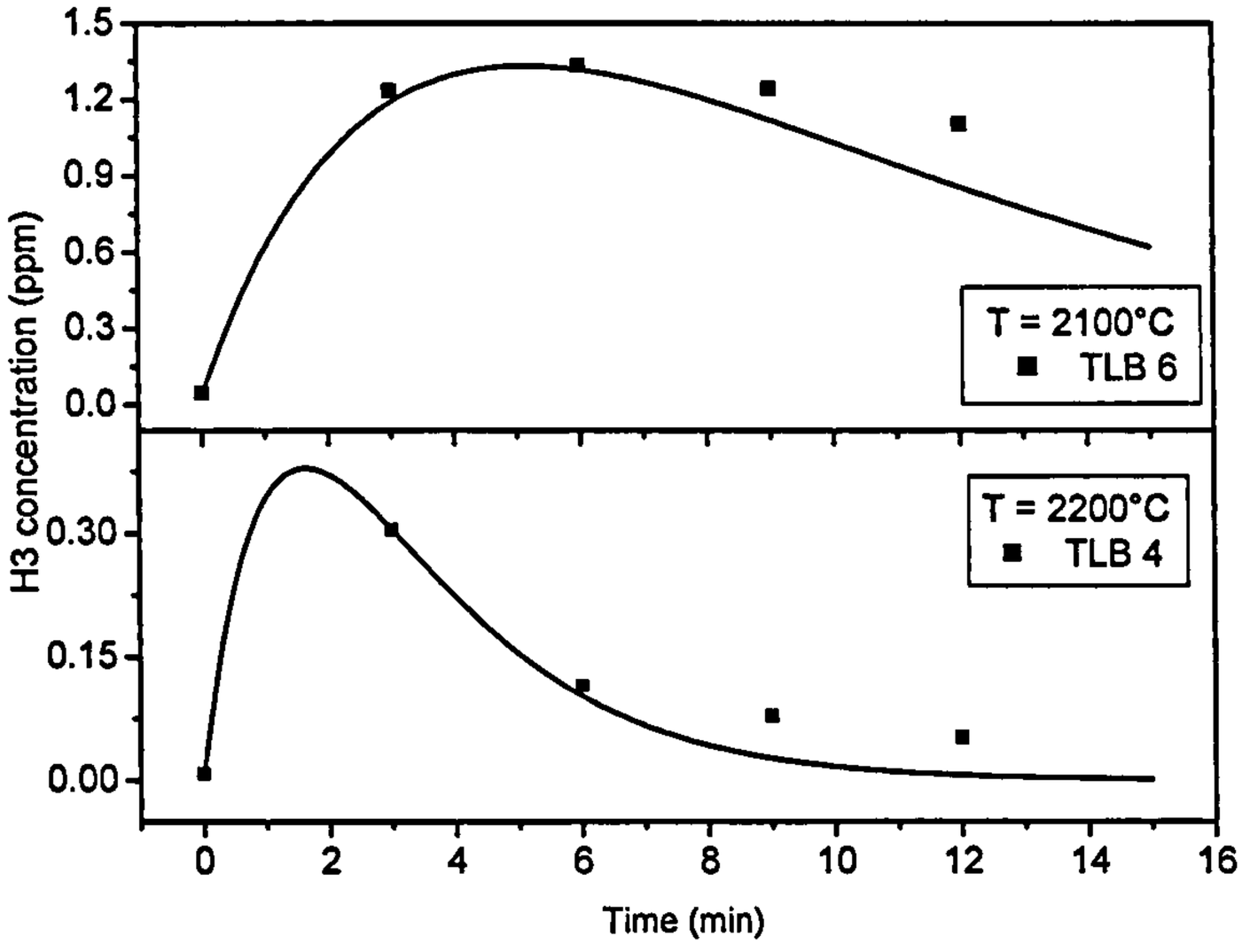

Figure 6.46. Examples of the change of H3 concentration with annealing time, fitted with equations 6.7.1-6.7.5 to the tlb and lb samples of group one and two annealed at two different temperatures (2100°C and 2200°C).

The activation energies of the processes used to calculate the curves in figure 6.46 are summarised in table 6.17.

Parameter	tlb-6	tlb-4
Monovac. in clusters (ppm)	30 ± 5	3 ± 1
Diss. energy vac. Clusters (eV)	6.5 ± 0.2	6.5 ± 0.2
Temperature (K)	2374 ± 50	2474 ± 50
[A] (ppm)	30 ± 3	14 ± 1
Diss. energy H3 defect (eV)	6.0 ± 0.2	5.7 ± 0.2

Table 6.17. The parameters used in the simulation of the change with annealing time of the H3 defect concentration.

From table 6.17 one can notice a deviation for the dissociation energy of H3 defects compared to the values used to simulate H3 defect concentration in irradiated high temperature annealed diamonds (5.2 eV). Also the values at two different temperatures are different: the activation energy used to simulate the H3 defect dissociation is systematically lower for the samples annealed at 2200°C. Replacing the low temperature value by the high temperature value and vice versa gives significant differences in the simulated H3 defect concentration behaviour, so the model presented above clearly cannot explain all observed phenomena.

6.7.4. Influence of the B/H4 defects on the H3 defect kinetics

H4 defects should be present in the samples of group 1 and 2 as all samples have high concentrations of B defects. However, no H4 is detected in the UV-VIS absorption spectra recorded with the sample at 80 K. Clearly the H4 defect dissociates during the HPHT annealing and these results are in agreement with previous data suggesting that H4 dissociates during annealing at temperatures below 2000°C (Collins 1979 and 1982, Collins *et al.* 2005). Two possible dissociation mechanisms for the H4 defect are proposed here:

$$H4 \rightarrow B + V \qquad (6.7.7)$$

or

$$H4 \rightarrow 2.H3 \qquad (6.7.8)$$

In the first option, the H4 dissociates into a B defect and a vacancy, where the vacancy can be retrapped by an B defect to give an H4 centre, or by an A defect to give an H3 defect, or diffuse to the surface or another trap and disappear. In that case, the presence of B defects should not have an influence on the created H3 concentration. This first model does not explain the experimental behaviour of the H3 defect concentration with time. In the second option, B defects trap a vacancy and split into two H3 defects, so B defects clearly have a strong influence on the time evolution of H3 defects. Also, there is evidence that the second option is the most plausible (Collins *et al.* 2005, Shirayev *et al.* 2001) so the second option is chosen to

simulate all further annealing data of the different defects which occur during HPHT annealing.

Including the reaction described by equation 6.7.8, the kinetics for H3, H4, N-V and C defect formation is described by a set of differential equations:

$$\frac{d\left[V_{cl}(\mathrm{t})\right]}{dt} = -\mathrm{k}_{\mathrm{cl}}\left[V_{cl}(\mathrm{t})\right] \tag{6.7.9}$$

$$\frac{d\left[V_{total}(\mathrm{t})\right]}{dt} = \mathrm{k}_{1,\mathrm{fast}}\left[V_{cl}(\mathrm{t})\right] + \mathrm{k}_4\left[H3(\mathrm{t})\right] + \mathrm{k}_7\left[(N\text{-}V)^{-}(\mathrm{t})\right] - \mathrm{k}_{1,\mathrm{fast}}\left(1-\left(\alpha\left[A(\mathrm{t})\right]+\beta\left[B(\mathrm{t})\right]+\gamma\left[C(\mathrm{t})\right]\right)\right)\left[V_{total}(\mathrm{t})\right] \tag{6.7.10}$$

$$\frac{d\left[(A\text{-}V)(\mathrm{t})\right]}{dt} = \mathrm{k}_{1,\mathrm{fast}}\alpha\left[A(\mathrm{t})\right]\left[V_{total}(\mathrm{t})\right] - \mathrm{k}_2\left[(A\text{-}V)(\mathrm{t})\right] - \mathrm{k}_{1,\mathrm{fast}}\left[(A\text{-}V)(\mathrm{t})\right] \tag{6.7.11}$$

$$\frac{d\left[H3(\mathrm{t})\right]}{dt} = \mathrm{k}_2\left[(A\text{-}V)(\mathrm{t})\right] + 2.\mathrm{k}_5\left[H4(\mathrm{t})\right] - \mathrm{k}_4\left[H3(\mathrm{t})\right] \tag{6.7.12}$$

$$\frac{d\left[(B\text{-}V)(\mathrm{t})\right]}{dt} = \beta\mathrm{k}_{1,\mathrm{fast}}\left[B(\mathrm{t})\right]\left[\mathrm{V}_{\mathrm{total}}(\mathrm{t})\right] - \mathrm{k}_3\left[(B\text{-}V)(\mathrm{t})\right] - \mathrm{k}_{1,\mathrm{fast}}\left[(B\text{-}V)(\mathrm{t})\right] \tag{6.7.13}$$

$$\frac{\mathrm{d}\left[H4(\mathrm{t})\right]}{\mathrm{dt}} = \mathrm{k}_3\left[(B\text{-}V)(\mathrm{t})\right] - \mathrm{k}_5\left[H4(\mathrm{t})\right] \tag{6.7.14}$$

$$\frac{d\left[A(\mathrm{t})\right]}{d\mathrm{t}} = -\alpha\mathrm{k}_{1,\mathrm{fast}}\left[A(\mathrm{t})\right].\left[V_{total}(\mathrm{t})\right] - \mathrm{k}_{\mathrm{diss}}[A(\mathrm{t})] + \tfrac{1}{2}\mathrm{k}_{\mathrm{aggr}}[C(\mathrm{t})]^2 + \mathrm{k}_4\left[H3(\mathrm{t})\right] \tag{6.7.15}$$

$$\frac{d[C(\mathrm{t})]}{d\mathrm{t}} = -\mathrm{k}_{\mathrm{aggr}}[C(\mathrm{t})]^2 + 2\mathrm{k}_{\mathrm{diss}}[A(\mathrm{t})] - \mathrm{k}_{1,\mathrm{fast}}\gamma\left[C(\mathrm{t})\right]\left[V_{total}(\mathrm{t})\right] + \mathrm{k}_6\left[(N\text{-}V)^{-}(\mathrm{t})\right] \tag{6.7.16}$$

$$\frac{d\left[B(\mathrm{t})\right]}{d\mathrm{t}} = -\beta \mathrm{k}_{1,fast}\left[B(\mathrm{t})\right].\left[V_{total}(\mathrm{t})\right] \qquad (6.7.17)$$

$$\frac{d\left[(N\text{-}V)^{-}(\mathrm{t})\right]}{d\mathrm{t}} = \gamma \mathrm{k}_{1,fast}\left[C(\mathrm{t})\right].\left[V_{total}(\mathrm{t})\right] - \mathrm{k}_{6}\left[(N\text{-}V)^{-}(\mathrm{t})\right] \qquad (6.7.18)$$

Again each rate constant depends on the pre-exponential factor and exponentially on the activation energy and the inverse of the temperature. The rate constants k_{aggr}, and k_{diss} are already determined and tabulated in table 6.14. The rate constants $k_{1,fast}$, k_2 and k_3 have been determined in chapter 5. The other rate constants k_4, k_5 and k_6 are determined from fitting of equations 6.7.9 – 6.7.18 to the experimental data.

The pre-exponential constant for k_4 and k_5 is set to the frequency of the main phonon interacting with the H3 and H4 defect (the phonon of 41 meV and 40 meV respectively).

The pre-exponential constant for k_6 is set equal to the main phonon interacting with the N-V defect (the phonon of 65 meV).

In all fittings, the boundary conditions are:

$[V_{cl}(0)]$ = total concentration of vacancies in the vacancy clusters (to be determined by fitting of the data).

$[V_{H3}(0)] = 0$ and $[V_{H4}(0)] = 0$, as there are no H3 (H4) defects which dissociate at room temperature.

$[H3(0)]$ = the initial concentration of H3 defects.

$[H4(0)] = 0$, as the initial H4 concentration is not detectable by UV-VIS absorption.

The initial A and B defect concentrations are the concentrations as determined from IR measurements.

In the next section the six unknown variables (the vacancy cluster concentration [$V_{cl}(0)$], the vacancy cluster dissociation energy $E_{diss.\ vac.\ cl}$ and the vibrational pre-factor $\nu_{diss.\ vac.\ cl}$, the H3 ($E_{H3\ diss}$) and H4 ($E_{H4\ diss}$) defect dissociation energy) will be determined and the influence of B defects on the time dependent behaviour of the H3 defect concentration will be emphasized.

6.7.5. Influence of different relative concentrations of A and B defects

A fitting of the data of the type IaA samples was carried out first as this eliminates the influence of B defects (figure 6.47). The activation energies for the dissociation of vacancy clusters and H3 defects are given in table 6.18. The maximum concentration of H3 defects is reached within 3 minutes (figure 6.48). The total mono-vacancy concentration in the vacancy clusters is 15.0 ± 1.0 ppm for sample 1B2 and 5.0 ± 0.5 for sample 1B1. The H3 defect data for samples 1B3 and 1D1 can be fitted with the same parameters and with 5.0 ± 0.5 and 40.0 ± 1 ppm of mono-vacancies.

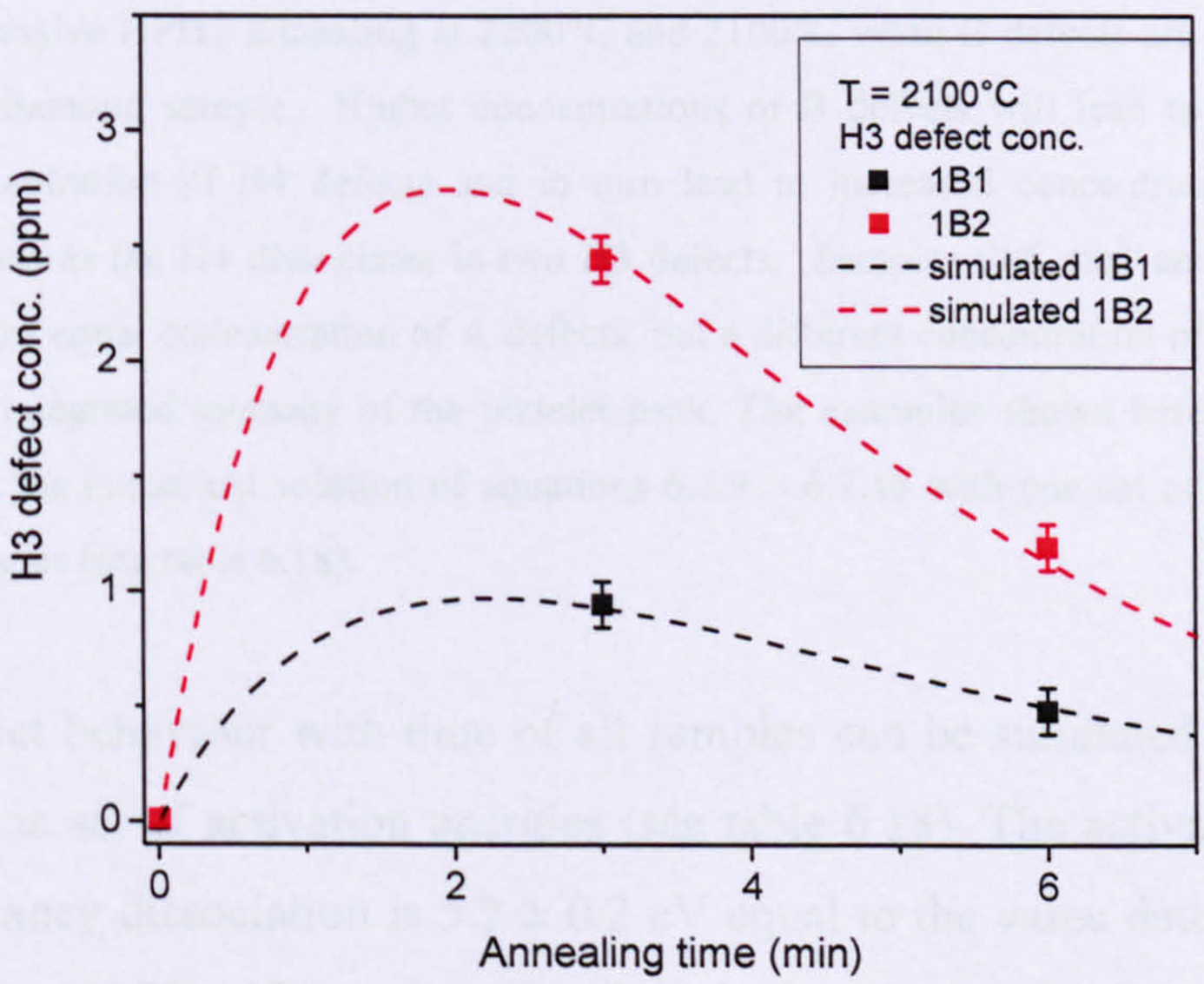

Figure 6.47. The H3 defect concentration after successive HPHT annealing and the fit of H3 defect concentration as calculated by equations (6.7.9) - (6.7.18) to the data. The activation energies of the processes are tabulated in table 6.18.

To simulate the behaviour of the H3 defect concentration in the HPHT annealed type IaA/B diamonds, all exponential pre-constants and activation energies are kept constant and equal to the constants used to simulate the H3 defect behaviour in the type IaA diamonds. The influence of an increasing concentration of B defect clearly manifests itself in an increase of the H3 defect concentration (figure 6.48).

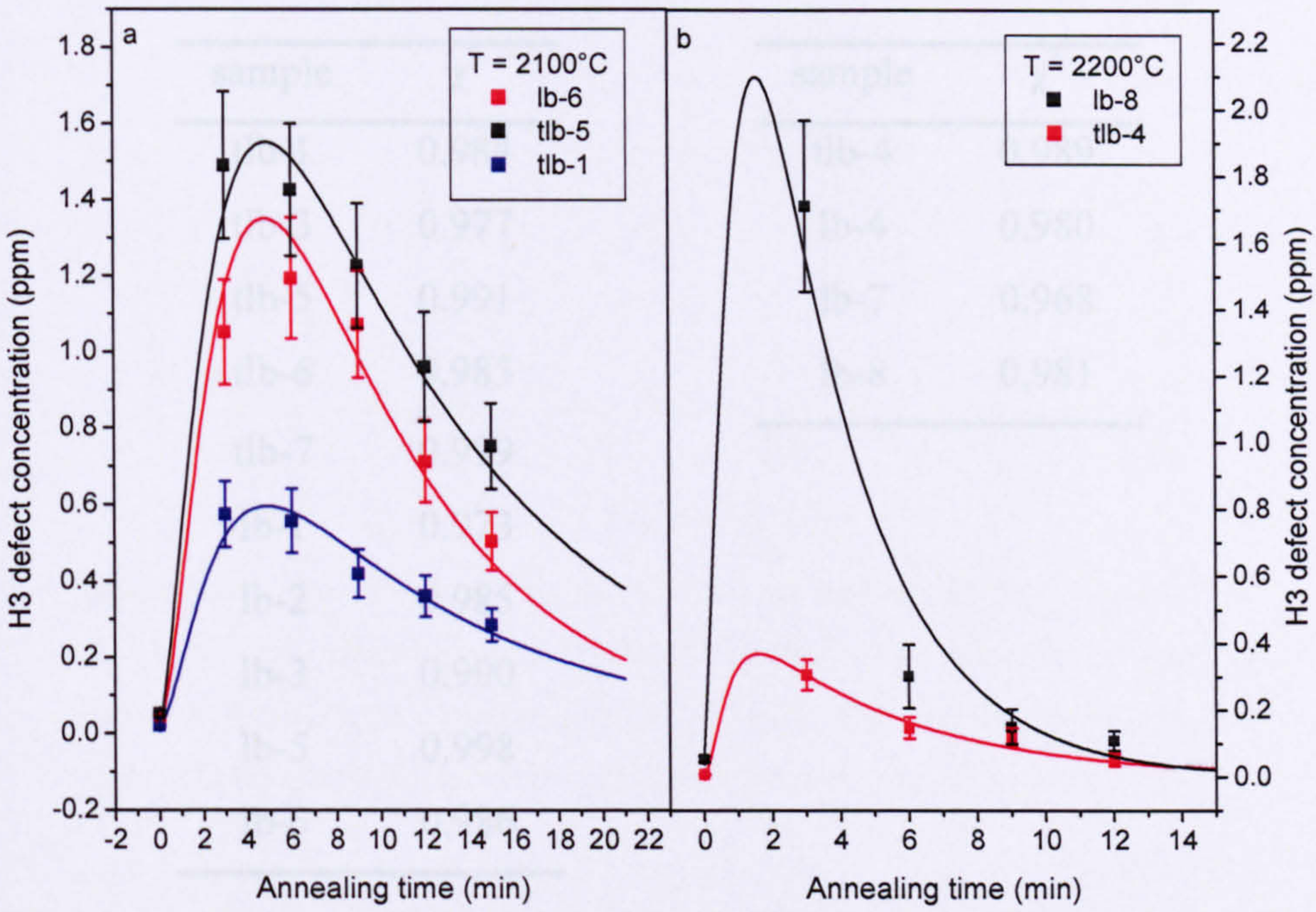

Figure 6.48. Two examples of the H3 defect concentration change upon successive HPHT annealing at 2200°C and 2100°C when B defects are present in the diamond sample. Higher concentrations of B defects will lead to increased concentration of H4 defects and in turn lead to increased concentration of H3 defects as the H4 dissociates in two H3 defects. Samples tlb5, tlb1 and lb6 have almost equal concentration of A defects, but a different concentration of B defects and integrated intensity of the platelet peak. The examples shown here are fitted with the numerical solution of equations 6.7.9 – 6.7.18 with one set of activation energies (see table 6.18).

The H3 defect behaviour with time of all samples can be simulated (figure 6.47 and 6.48) with one set of activation energies (see table 6.18). The activation energies for nitrogen-vacancy dissociation is 5.2 ± 0.2 eV equal to the value determined from the data of Collins (1978, 1980) and section 6.4 of this chapter. Only three samples could not be fitted with chi-square larger than 0.980 (see table 6.19).

$E_{diss.\ vac.\ cl}$	$E_{H3\ diss}$	$E_{H4\ diss}$
6.2 ± 0.2 eV	5.2 ± 0.2 eV	4.4 ± 0.2 eV

Table 6.18. The vacancy cluster, H3 and H4 defect dissociation energies, which fit the change of the H3 defect dissociation data with time in all samples.

sample	χ^2
tlb-1	0.984
tlb-3	0.977
tlb-5	0.991
tlb-6	0.985
tlb-7	0.999
lb-1	0.973
lb-2	0.985
lb-3	0.990
lb-5	0.998
lb-6	0.986

sample	χ^2
tlb-4	0.989
lb-4	0.980
lb-7	0.968
lb-8	0.981

Table 6.19. The χ^2 values calculated from the fit of equations 6.7.1 – 6.7.18 to the H3 defect data of samples of group 1 (left) and 2 (right).

If a certain degree of brown colour is caused by a certain concentration of vacancy clusters, then a darker brown type Ia diamond should release more vacancies than a lighter brown type Ia diamond with identical concentrations of A and B defects. During HPHT annealing, H3 defects are created by two different paths:

- Direct H3 defect formation when an A defect captures a vacancy
- Indirect H3 defect formation when a B defect captures a vacancy, converts into a H4 defect, which dissociates into two H3 defects.

Therefore, for a group of diamonds annealed under the same HPHT conditions, the concentration of H3 defects should increase when the brown colour intensity increases, on the condition that the A and B defect concentrations are equal within experimental uncertainty. This is indeed observed (figure 6.49).

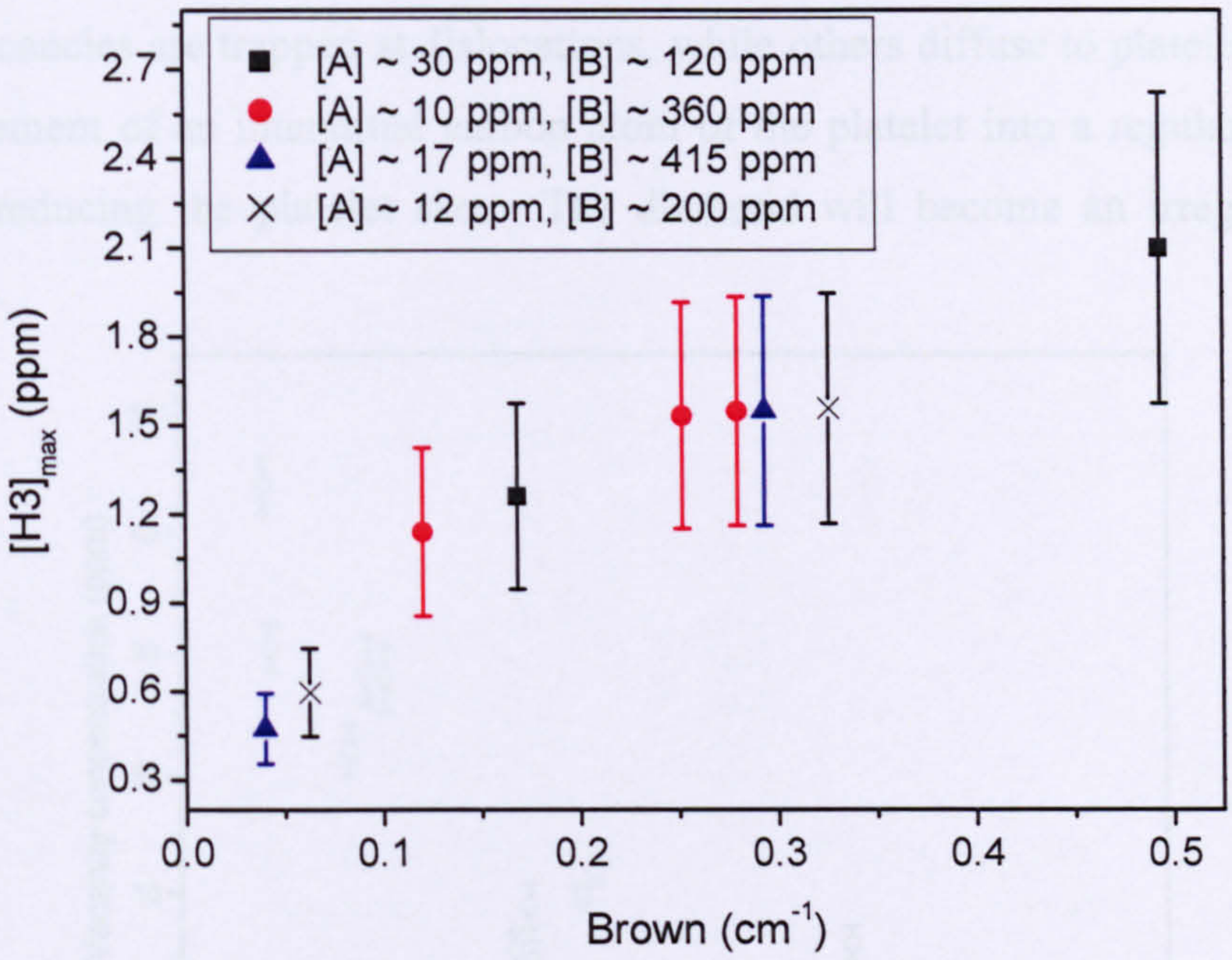

Figure 6.49. The calculated maximum of H3 as function of the intensity of the band at 550 nm, typical for brown type Ia diamond. The values are grouped for diamonds with similar concentrations of A and B defects. In general a higher degree of brown coloration results in a higher concentration of H3 defects.

In section 6.7.7, the accuracy of the activation energies for dissociation of H3 and H4 defects will be tested by simulating the results of irradiated and HPHT annealed and high temperature annealed (800°C < T < 1750°C) type Ia diamonds.

6.7.6. Released mono-vacancy concentration-platelet relation.

As can be deduced from figure 6.49, the total concentration of mono-vacancies ($[V_{cl}]$) released by the clusters varies strongly between 44 and 2 ppm with an apparent anti-correlation with the platelet integrated intensity (figure 6.50).

This anti-correlation can be explained in the following way: the diamond is grown in the Earth and the high temperature of the environment causes nitrogen aggregation into A and B defects, and platelet formation. Such a sample is a regular type Ia diamond. Then the sample is plastically deformed, and a very high concentration of vacancies is created rapidly during the deformation (Mott 1951, Leipner *et al.* 2000, Krause-Rehberg *et al.* 1993). This supersaturation of vacancies causes nucleation and

growth of vacancy clusters (Leipner *et al.* 2000, Krause-Rehberg *et al.* 1993). Some of the vacancies are trapped at dislocations, while others diffuse to platelets and cause the movement of an interstitial carbon atom of the platelet into a regular lattice site, thereby reducing the platelet size. The diamond will become an irregular type Ia diamond.

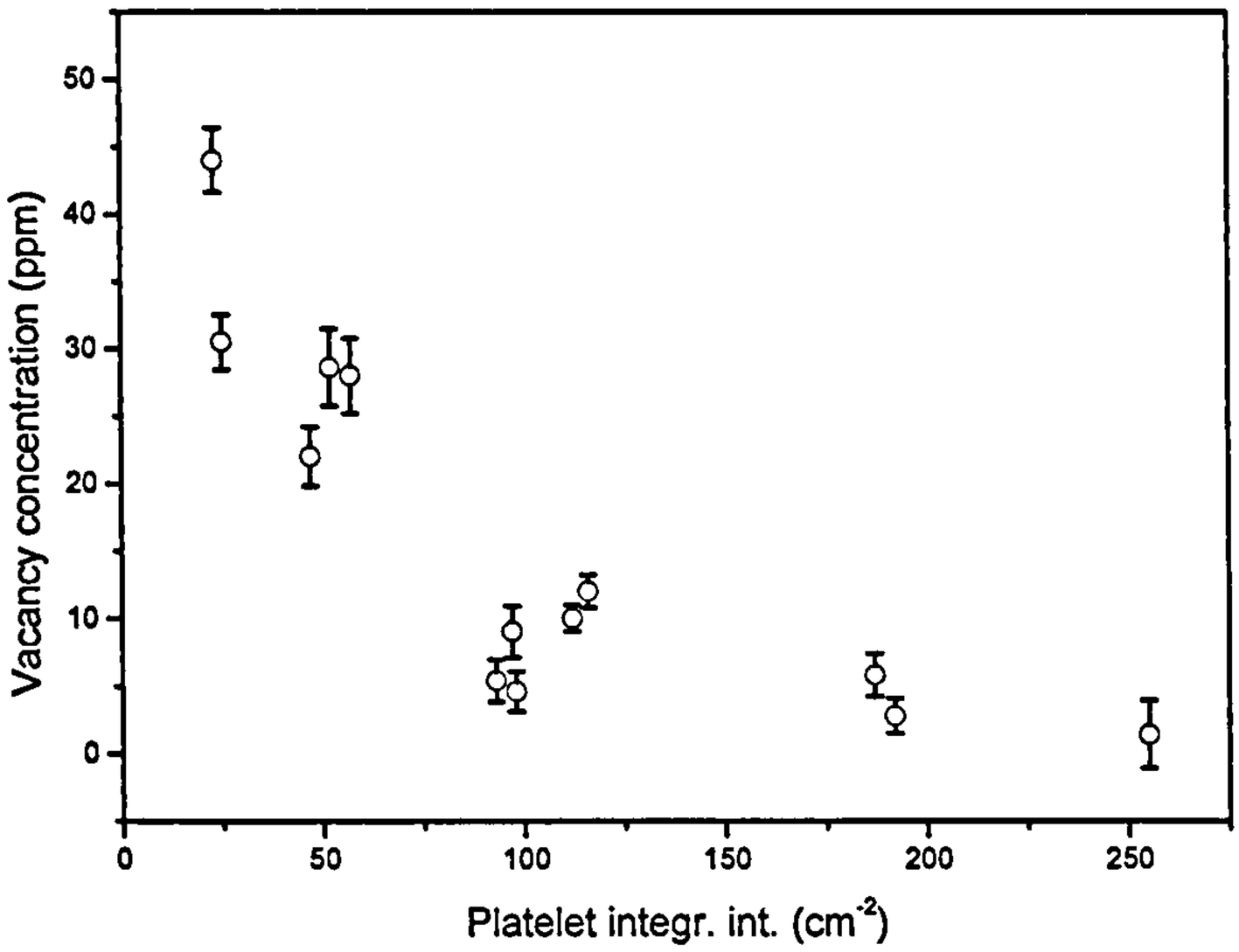

Figure 6.50. The released mono-vacancy concentration as function of the integrated intensity of the initial platelet peak in the IR spectrum. There is clearly an anti-correlation between the mono-vacancies available for trapping at nitrogen defects and the concentration of platelets.

The migration of vacancies to the platelets and the Ostwald ripening of the vacancy clusters will compete for the mobile mono-vacancies and both reduce the number of mono-vacancies and small vacancy clusters in the diamond. Depending on the total concentration of interstitials in the platelets, its presence can reduce the supersaturation of vacancies rapidly eliminating the population of small clusters.

The additional high temperature annealing in a laboratory HPHT press will cause further Ostwald ripening of vacancy clusters and platelets. Mono-vacancies released by the vacancy clusters may be trapped by nitrogen aggregates, platelets, ...

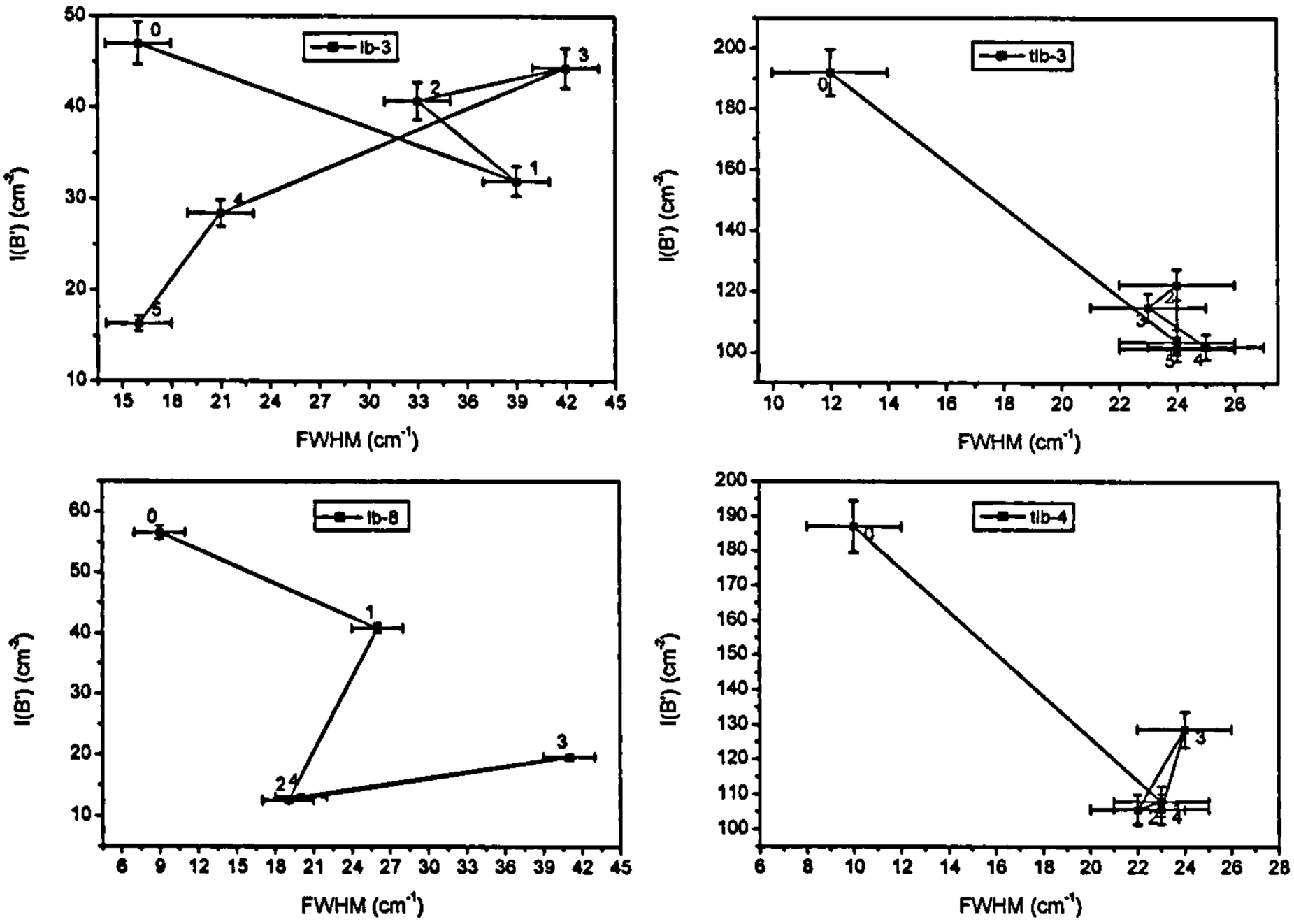

Figure 6.51. The integrated intensity of the platelet peaks as function of the FWHM of the platelet peak. Samples with high concentrations of released mono-vacancies have a very complicated behaviour.

The Ostwald ripening process continues until the vacancy clusters collapse into dislocation loops, or is exhausted as vacancies move to the surface or other sinks like cracks where they disappear or in climb movement of dislocations. H3 and H4 defects act as a second source of mono-vacancies after the source of mono-vacancies is depleted. The dissociation process continues until depletion of the latter two.

The destruction of platelets by trapping of vacancies released from the vacancy source and simultaneous growth of platelets will induce a very complicated behaviour of the platelet peak: growth of the platelets will increase the FWHM of the peak and shift the peak position to lower wavenumbers (Clackson, *et al.* 1990), while trapping of vacancies will reduce its size or destroy small platelets. This can initially broaden the platelet peak as vacancies are released at high rate from vacancy clusters. The large platelets have a larger capture cross-section for vacancies and as a result the distribution of platelet size alters rapidly. Because of platelet growth competes with platelet destruction by vacancies, prolonged HPHT annealing may increase or decrease the mean platelet size. As a result the mean size and size distribution of small platelets will tend to change faster and in a more unpredictable fashion. This is

indeed observed (figure 6.51 and 6.52): samples with low integrated intensity of the platelet peak release more mono-vacancies from the vacancy source and display large variations in FWHM and integrated intensity of the platelet peak, while samples with strong platelet absorption should display smaller variations in FWHM and integrated intensity of the platelet peak.

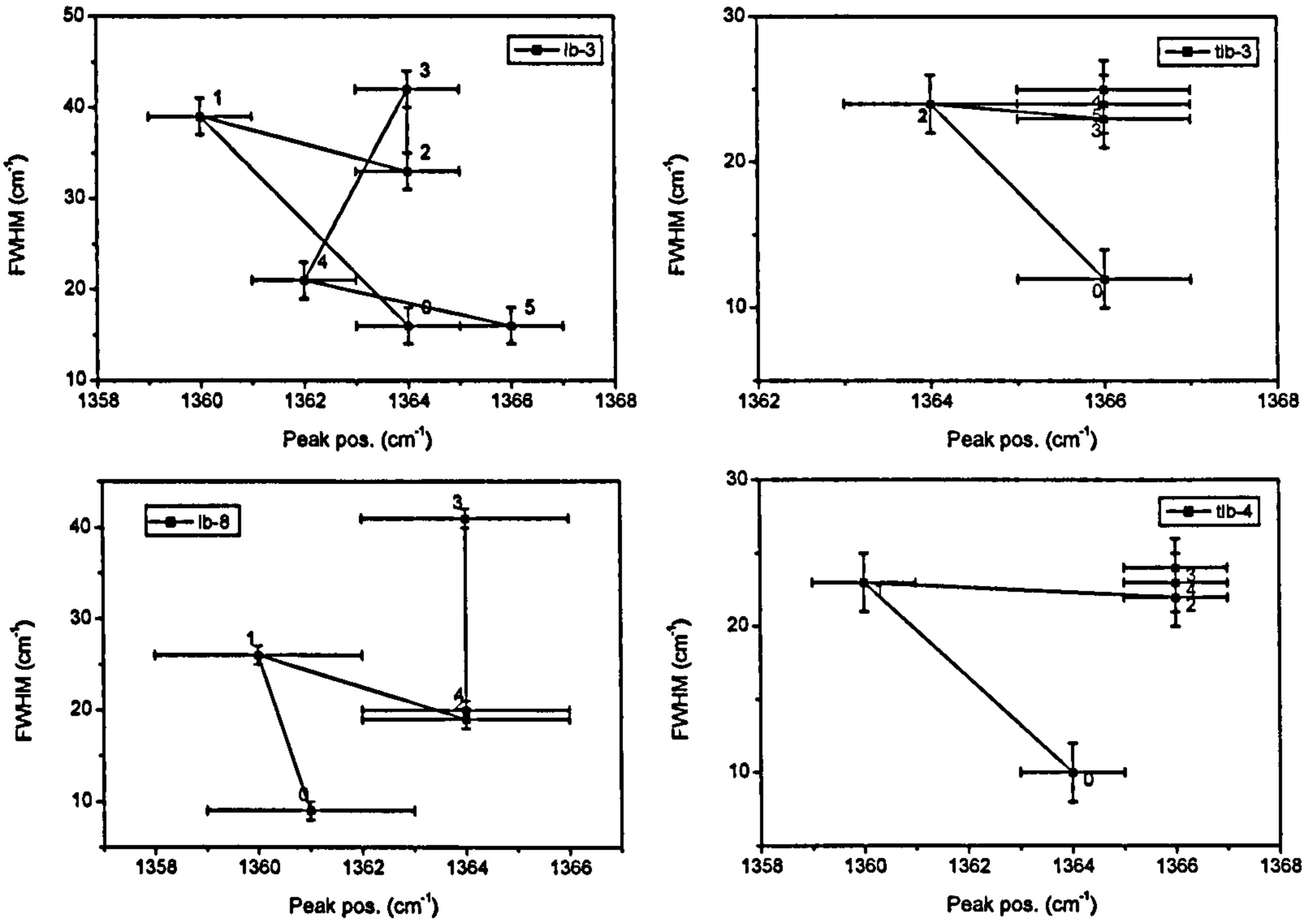

Figure 6.52. The FWHM of the platelet peak as a function of the position of the maximum absorption. In samples with low concentration of released mono-vacancies, the mean platelet size decreases weakly upon successive annealing. In samples with a high concentration of released mono-vacancies, the mean platelet size can grow and shrink upon successive HPHT annealing. The uncertainty for the FWHM and the peak position is 2 cm^{-1}.

Clearly more detailed knowledge on the growth and annealing behaviour of platelets in type I diamonds and their interaction with radiation damage products (interstitials and vacancies) is necessary.

6.7.7. HPHT annealing of irradiated and annealed type Ia samples.

Four irradiated samples were annealed at 2100°C (sample 14), 2200°C (sample 2) and 2300°C (samples 6-1 and 4-2) respectively. Only sample 14 showed a detectable H3 ZPL peak in the UV-VIS absorption spectrum (figure 6.53) corresponding to a

concentration of ~ 55 ppb. Table 6.20 shows the concentrations of C defects after annealing and the predicted concentrations of C defects when only direct A to C defect dissociation is taken into account.

To simulate the annealing of radiation induced vacancy concentration, the model must be modified as the vacancy concentration now decreases exponentially in time with an activation energy of 2.3 ± 0.2 eV (Davies *et al.* 1992). Equation 6.7.9 is eliminated from the equation set, and constant k_{cl} is set equal to $k_{1,fast}$. $[V_{cl}(0)]$ is set equal to the initial mono-vacancy concentration. All other parameters are kept constant. The model predicts ~ 40 ppb of H3 defects should be observed after annealing at 2100°C (figure 6.54).

The other samples did not show detectable H3 absorption peak; however in some cases weak H3 luminescence was detectable in the PL spectrum. Clearly the concentration of H3 defects was below the UV-VIS absorption detection limit (~ 10 ppb) as predicted by our model. None of the samples showed detectable 637 nm or a H2 absorption peak, but all showed a small emission peak at 637 nm in the PL spectrum. Other radiation damage related defects (GR1, TH5, 594 nm, H1b, H1c, ...) were not observed after HPHT annealing, which is expected as these are not stable above ~ 1500°C (Collins *et al.* 2005).

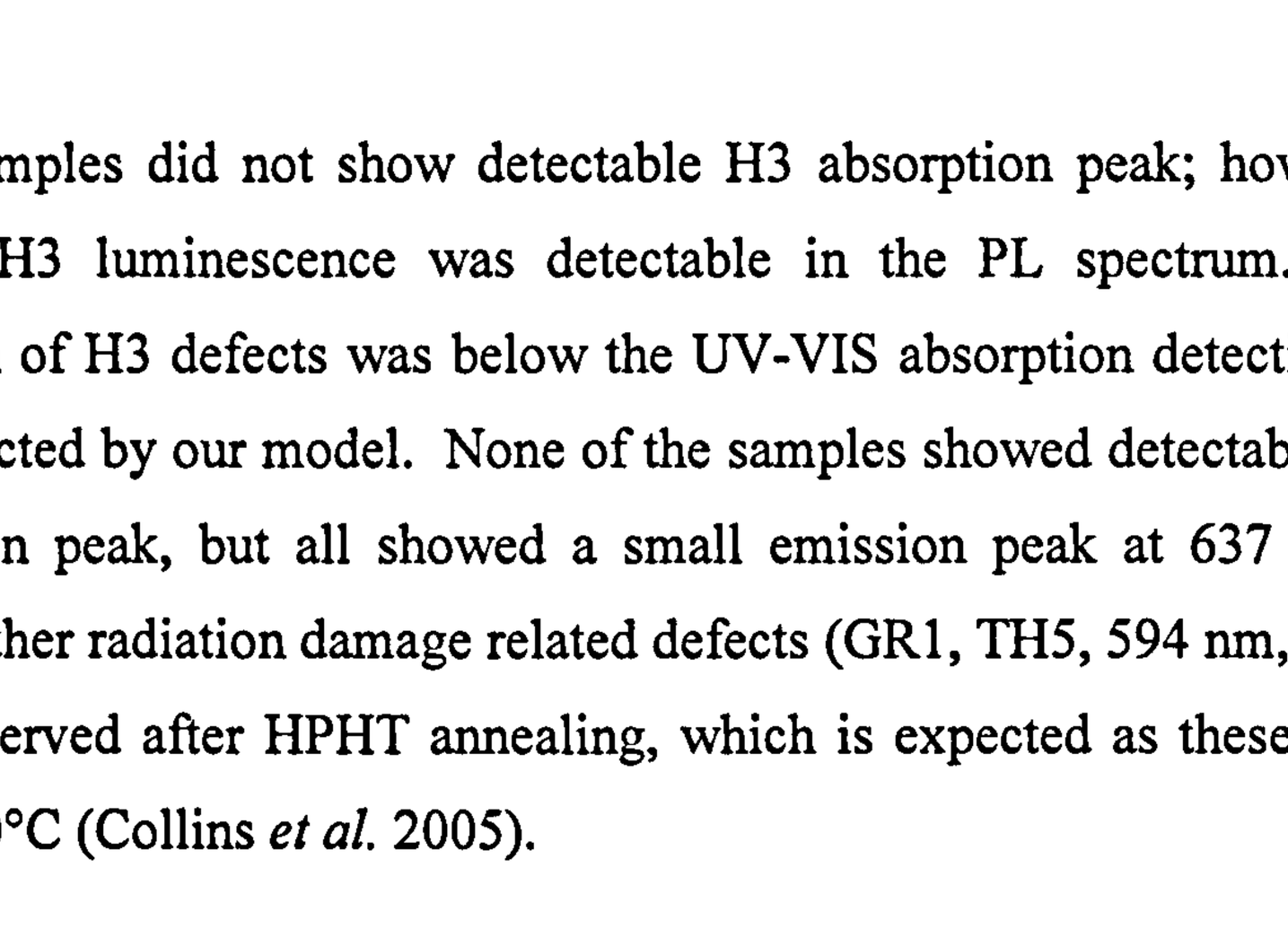

Figure 6.53. The UV-VIS absorption spectrum of an irradiated (6 MeV, 10^{17} e^- /cm^2) diamond after HPHT annealing at 2100°C for three minutes. The inset is a detail of the absorption spectrum, showing weak H3 absorption.

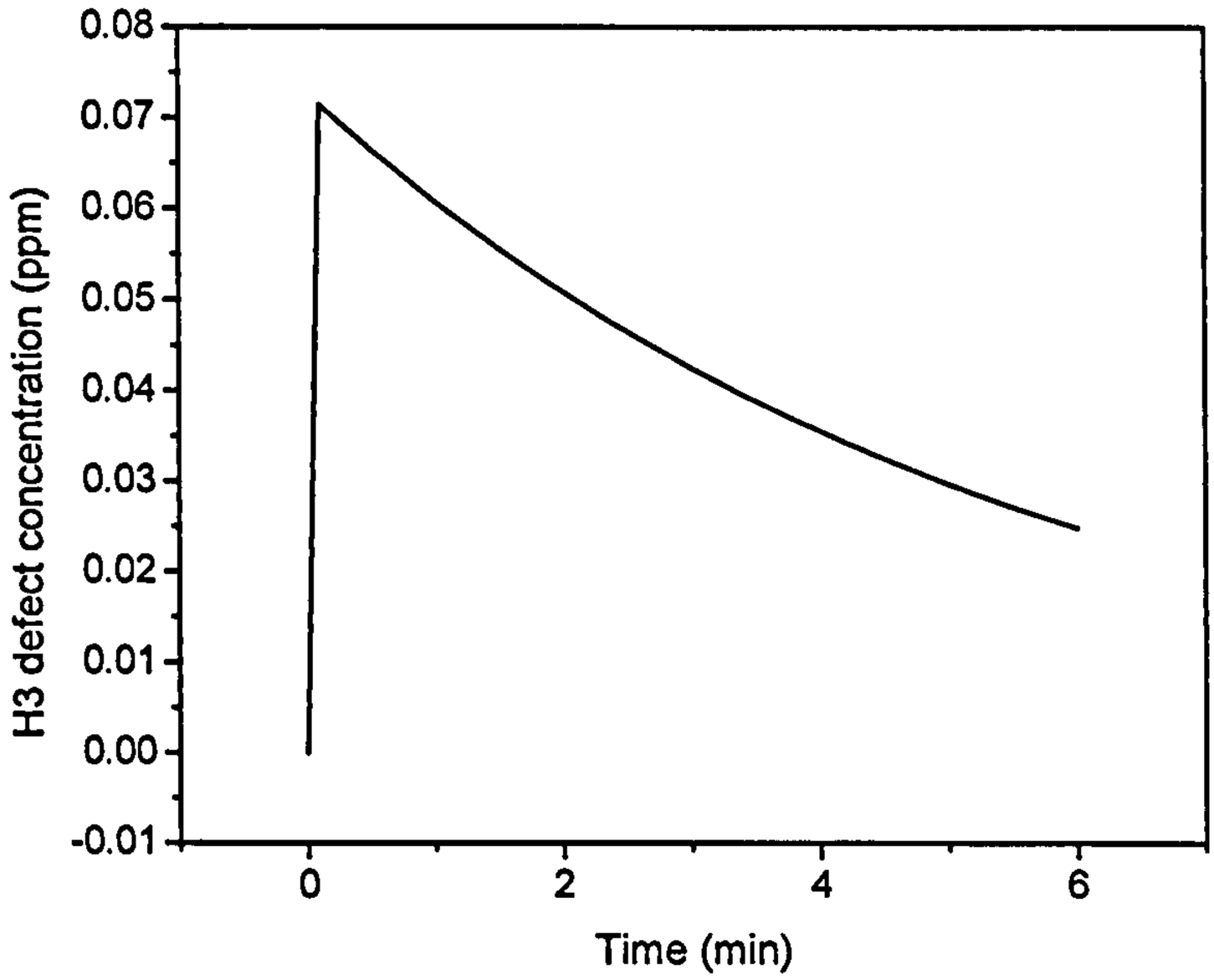

Figure 6.54. Simulation of H3 defect concentration in the irradiated HPHT annealed diamond, including H3 and H4 defect formation. The H4 defect concentration (not shown here) is below the detection limit by UV-VIS absorption. H4 defect is only weakly detectable by luminescence.

Sample	Annealing time (min)	Annealing temp. (°C)	[C] (ppm) UV-VIS	[C] (ppm) EPR	[C] (ppm) IR	[C] ppm predicted
Sample 2	3	2200	30	26	18	34
Sample 14	3	2100	3	-----	0	13
Sample 4-2	3	2300	54	60	52	47
Sample 6-1	3	2300	60	35	59	38

Table 6.20. The C defect concentrations in the irradiated and HPHT annealed type Ia diamonds. The concentrations of C defects were measured by IR, UV-VIS and EPR absorption spectroscopy. Uncertainty in the concentration of C defects determined by EPR, IR and UV-VIS measurements is 25%, 10% and 27% respectively.

The observed H4 defect dissociation and increase in the concentration of H3 defects, when samples are annealed between 900 and 1700°C (Collins *et al.* 2005), can now be explained by our model. Figure 6.55 is taken from the paper by Collins *et al.* (2005). The sample was a type IaB diamond and after irradiation and annealing at 900°C, no H3 was detected. The H4 ZPL intensity is approximately constant up to ~ 1300°C and then decreases in strength. At the same time, H3 defects are created. At higher

temperature (T > 1600°C) H3 defects start to dissociate and vacancies can, in principle, be retrapped by B defects. However, one has to keep in mind that one vacancy and a B defect form a H4 defect, which splits into two H3 defects. The H4 defect dissociates into two vacancies and two A defects, so there are now two vacancies which can be trapped by B defects. In the simulation of the H3 and H4 defect behaviour under isochronal (1 h) annealing at different temperatures, equation 6.7.16 and all other functions connected to A defect dissociation and C defect aggregation is eliminated. Again equation 6.7.9 is eliminated from the equation set and $[V_{cl}(t)]$ is set equal to the initial mono-vacancy concentration the boundary conditions are the following, at time t = 0:

- $[B] = 400$ ppm
- $[H4] = 5$ ppm
- $[H3] = [C] = [A] = [(N\text{-}V)^-] = 0$

After every simulated one hour annealing, the end values of the vacancy, H3 and H4 defect concentrations are taken as the initial values for the next simulation at 50°C higher temperature (figure 6.55), exactly like the experimental conditions used by Collins *et al.* (2005). The qualitative picture of the annealing behaviour correlates relatively well with the data of Collins *et al.* (2005) (figure 6.56).

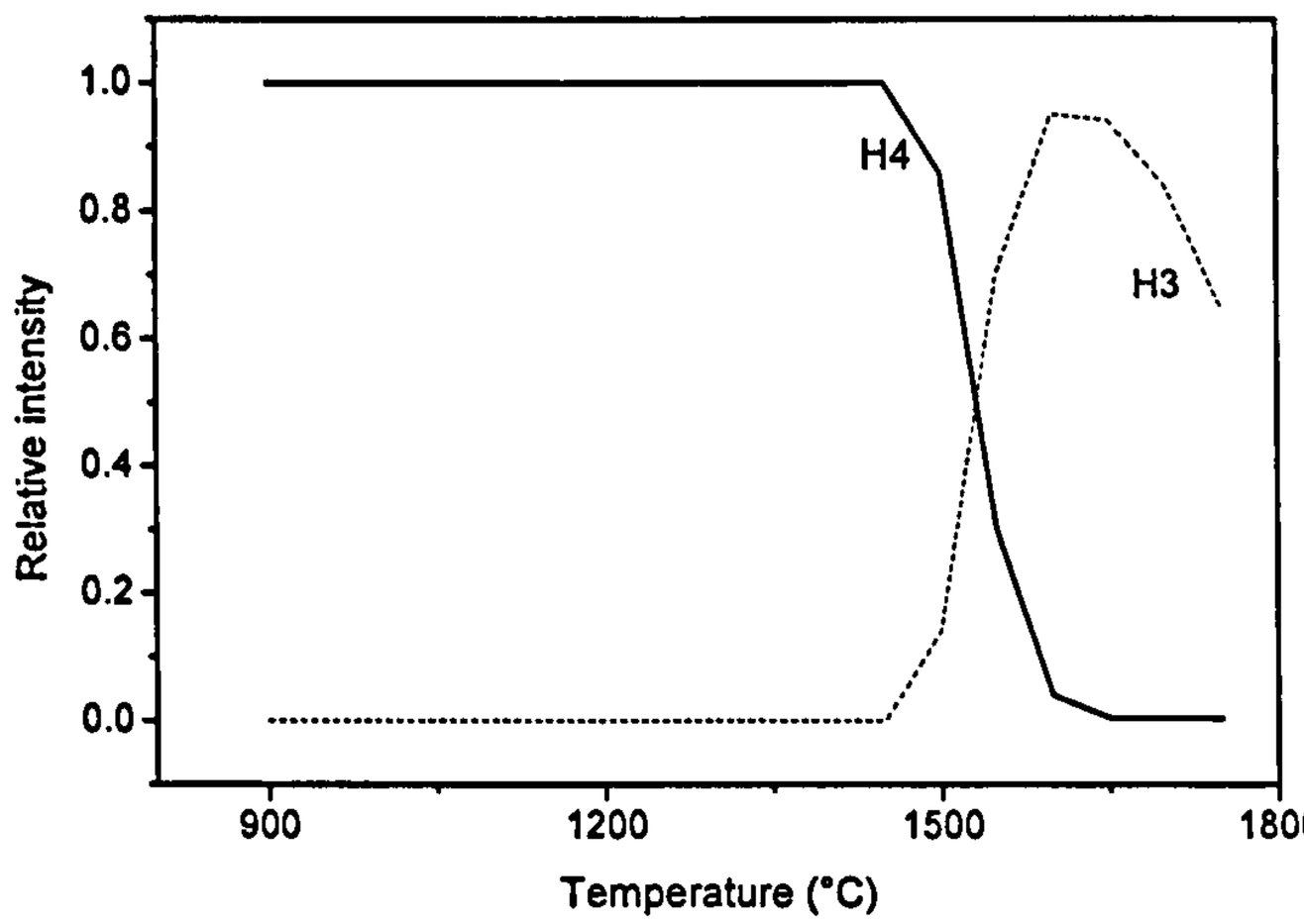

Figure 6.55. The relative absorption strength of H3 and H4 defects during isochronal annealing of irradiated type IaB diamond. The point where H4 defects begin to decay is ~ 50°C lower than observed experimentally, but the gradient of the H4 decay curve is the same. The curves are renormalized with respect to the maximum defect concentration.

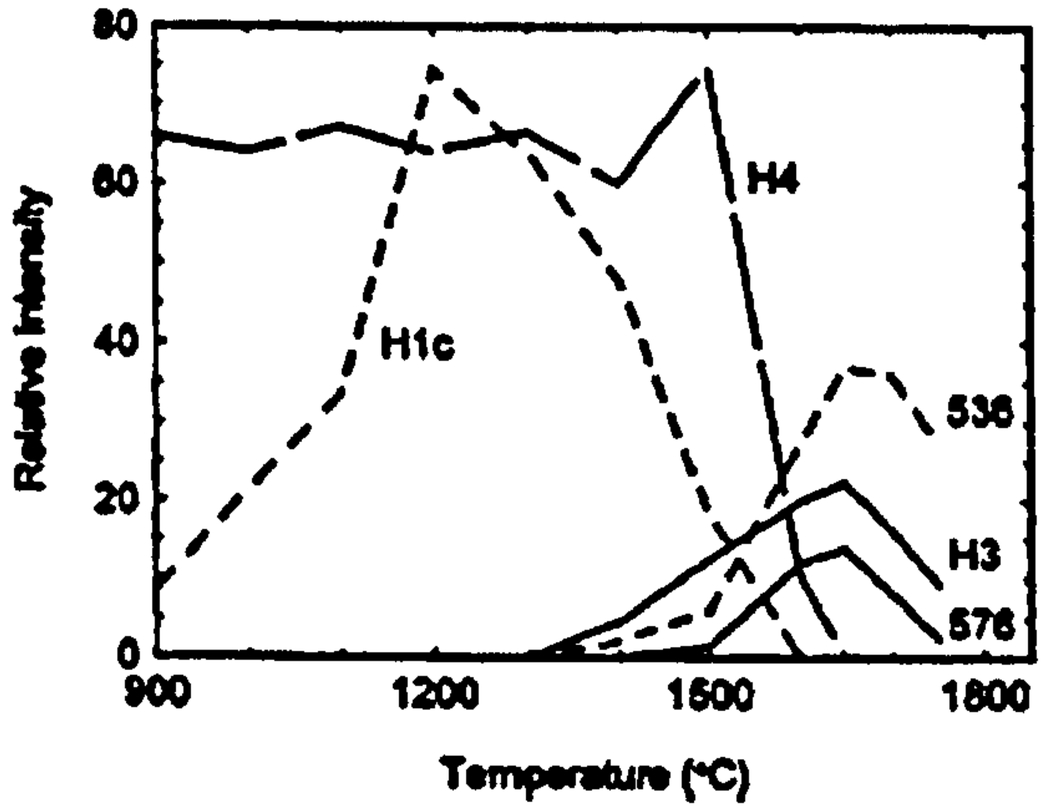

Figure 6.56. The relative absorption strength of a number of defects during isochronal annealing of irradiated type IaB diamond (figure 7 from Collins *et al.* (2005)).

The analysis provides additional evidence for the process $H3 \rightarrow A + V$, because N-V defects were not detected after annealing at 1700°C, where H3 defect concentration decreased in intensity.

6.7.8. Final remarks

As a first final remark, we wish to point to one other possible H4 defect dissociation mechanism: the H4 defect might dissociate by removal of a N-V defect, explaining an observed increase of N3 defect concentration (Collins *et al.* 2005). N3 defects have not been involved in the analysis presented. This dissociation path could have an influence on the created H3 defect concentration as this is a competitive H4 dissociation path. This is a point which clearly needs further investigation. Also in the analysis we did not include the formation and dissociation of H2 defects for three reasons:

- only semi-quantitative measurements could be carried out in the NIR region
- in the study here, the H2 peak is always lower in intensity than the H3 peak (figures 6-1 and 6.3) so the H2 concentration is very low compared to the H3 defect concentration.
- there is insufficient data on the dissociation of H2 defects. A study of the destruction of the H2 defect at lower temperatures (T ~ 1500°C) could clarify this point.

A second remark is the fact that vibrational frequencies and activation energies for formation and dissociation of H3, H4 and $(N\text{-}V)^-$ defects do not appear to be affected by a difference in pressure.

In chapter two, it is remarked that broad band luminescence can be observed in brown type Ia, and disappears upon HPHT annealing. The one-phonon spectrum of this broad band has two maxima at 17 and 44 meV. The 17 meV is a very low vibrational frequency for diamond. This low frequency vibration could be because of the combination of vacancy disks and the nitrogen B aggregate. Low frequency vibrations are not uncommon for extended defects: platelets are known to have an absorption peak in the IR spectrum at 328 cm^{-1} (Woods 1989).

6.8. Conclusion

6.8.1. Dissociation of A defects in diamond

The activation energy for the dissociation of A centres into C centres has been calculated in two different ways, and values of 5.6 ± 1.4 and 7.66 ± 0.6 eV have been found. The weighted average of 7.3 ± 0.6 eV is in agreement with theoretically calculated values of Mainwood (1994).

The dissociation of A defects is responsible for the colourless to yellow colour change of type Ia diamonds.

6.8.2. Influence of pressure on the dissociation of A defects

The dissociation of A centres into C centres is dependent not only on the temperature but also on the pressure during the HPHT annealing. The enhancement is approximately a factor of 10 when a pressure of 5 - 6 GPa is used instead of 8.5 GPa at 2300°C. Further experiments are being carried out to allow a more detailed analysis of the influence of pressure on the dissociation of nitrogen aggregates during HPHT annealing.

The activation energy of the nitrogen aggregation and dissociation process changes with pressure because there is a volume difference between two C defects and an A defect. As a consequence of the dilatation difference between nitrogen atoms in the A and C defect, a higher concentration of C defects is created during HPHT annealing of type Ia diamond when pressure increases.

The change in dilatation because of the aggregation of C defects into A defects is too small to induce a sufficient change in activation energy to explain the experimental results and further investigation into the dilatation and A defect dissociation at low pressure is needed.

6.8.3. High temperature annealing of irradiated type Ib diamond under varying pressure

This study indicates vacancy assisted aggregation follows the following path, as originally proposed by Collins (1980):

$$N + V \rightarrow N\text{-}V$$

$$N\text{-}V + C \rightarrow H3$$

$$H3 \rightarrow A + V$$

The vacancy which is removed from the H3 defect can efficiently be recycled by the C defect because of the large capture cross-section for vacancies. The whole process can then start over again, and this explains why a relatively low concentration of vacancies is lost to the surface or other traps.

Annealing under pressure appears to suppress the vacancy assisted aggregation, a fact also observed by Allen and Evans (1981).

6.8.4. Optical study of the annealing behaviour of the 3107 cm^{-1} defect in natural diamond

Hydrogen diffusion in diamond is important as hydrogen is present in all diamonds and can alter its properties. In this thesis the annealing behaviour of the 3107 cm-1 defect is studied.

The annealing behaviour of the 3107 cm^{-1} hydrogen defect is very complicated, indicating that it can be formed by capturing hydrogen atoms, released from other defects, but the 3107 cm^{-1} defect itself can also be destroyed.

The absence of correlation between the absorption strength of the 3107 cm-1 peak and the A, B or C defect concentration confirms the idea that nitrogen is not directly involved in the defect.

6.8.5. Dynamics of defects in brown type Ia diamond

The main goal of the thesis is to understand the colour changes induced by HPHT annealing of brown type Ia diamond. Brown diamonds can become yellow-green or yellow, depending on the annealing conditions and annealing time. Up to now, the reasons why diamonds become yellow-green or yellow after HPHT annealing are unclear and this study aims to understand the processes between defects responsible for the colouration.

There is a correlation between the degree of colour saturation of brown diamonds and the concentration of H3 defects, created after HPHT annealing; CL indicates that vacancies are released from defects pinned at or close to plastically deformed regions in the brown colour in diamond.

The measurements and analysis, presented here support the view that the brown colour in type Ia diamonds is probably caused by multi-vacancy clusters and that, during HPHT annealing, vacancies are evaporated from these clusters to form nitrogen-vacancy complexes.

The activation energy for release of the vacancy from the vacancy source is 6.2 ± 0.2 eV. The H3 defect dissociates with an activation energy of 5.2 ± 0.2 eV. During the HPHT annealing, the H4 defect converts into two H3 defects with an activation energy of 4.4 ± 0.2 eV.

The dissociation of the H4 defect explains the absence of detectable H4 defect concentrations in the UV-VIS absorption spectrum after HPHT annealing. This view is supported by the high temperature annealing data of irradiated type IaB diamonds of Collins *et al.* (2005) where there is a correlation between the destruction of H4 defects and the growth of H3 defects.

The fact that an H4 defect dissociates into two H3 defects has significant consequences and partly explains the observed differences between the diamonds with similar concentrations of A defects and similar initial colour, but with different concentrations of B defects.

The presence of platelets clearly has an indirect influence on the colour change of an HPHT annealed diamond: higher platelet concentrations decrease the available mono-vacancy concentration and thus reduce the created concentration of H3 defects in HPHT annealed brown type Ia diamond. As platelets have a large size, they should be efficient vacancy sinks. Further research should be carried out by irradiating and annealing type Ia diamonds with different concentrations of platelets. Also a systematic study of the annealing and formation behaviour of platelets in type Ia diamond should be carried out as platelet formation and destruction is not understood properly.

The H3 defect formation and dissociation model, including the H4 defect formation and dissociation, proposed here is tested against data of Collins *et al.* (2005) on irradiated and isochronally annealed diamonds to temperatures up to ~ 1700°C, and on data of irradiated and HPHT annealed diamonds. The isothermal annealing curves of the H3 and H4 defect concentrations can be understood by application of this proposed model, but the exact annealing behaviour might depend on other factors like different charged states of defects. It is possible that a charged defect needs to be ionised before it can dissociate, and this is not included in the model proposed here.

Further work should include detailed data on the platelet growth and destruction by HPHT annealing, and the interaction of platelets with radiation damage products like vacancies and interstitials. A model should then be constructed describing the platelet growth as function of platelet size. A similar model should be developed for vacancy cluster growth and destruction. This has not been attempted here.

An attempt should be made to look at the annealing behaviour of H2 when a diamond is irradiated and annealed or HPHT annealed. To do this, additional equations should be introduced to describe the charge transfer between C defects and H2 and N-V defects and vacancies. This perturbation on the model proposed here is ignored as these parameters are not known, and the concentrations of H2, $(N\text{-}V)^-$ (~ ppb) defects are much smaller than the H3 and N3 concentrations (~ ppm). Negatively charged mono vacancies are even not detected after HPHT annealing.

Chapter Seven

Summary, conclusions and further work

7.1. Summary and Conclusions

This thesis has been concerned with colour in diamond and the defects causing it, which is of importance for gem-testing laboratories. An attempt has been made to understand the physical mechanisms giving rise to colour of a diamond and the defect dynamics during annealing, which cause colour changes. When trying to judge the possible future types and economic feasibility of treatments, this knowledge is paramount.

The study has employed various spectroscopic techniques and models have been made to understand the colour changes of diamond. Three major topics are investigated in this thesis:

1. Linear electron-phonon coupling in diamond.
2. HPHT annealing of brown type Ia diamond.
3. Hydrogen in diamond.

The reason why electron-phonon coupling is important is because the side band of a sharp zero phonon line causes the colour in diamond, and the various consequences of linear electron-phonon coupling theory are demonstrated. The theory allows calculation of the shape of the spectrum caused by a defect, and gives a possible explanation of sub-threshold excitation of defects.

Colour changes as induced by HPHT annealing are not well understood and this study aims to elucidate some of the defect chemistry occurring during HPHT annealing. In addition, the 3107 cm^{-1} hydrogen-related absorption in the IR spectrum of type Ia diamond has been studied.

7.1.1. Linear electron-phonon coupling

Using linear electron-phonon coupling, we calculated the side bands of two common defects in brown type Ia diamond, the 490.7 nm defect and the broad band centred at ~ 710 nm. The validity is tested by various methods: by predicting the experimental results of the behaviour of the zero phonon line at different temperatures and by decomposing spectra of different samples in calculated curves. In due course, it was discovered that other processes might play a crucial role in the relaxation of the electron from the excited state to the ground state of the defect, causing the anomalous temperature behaviour of the 490.7 nm and 3H defects. This might be because of defect-defect interactions or stress in the diamond. Defect-defect interactions may thus play a crucial role in the detectability of a defect by photoluminescence, and therefore further investigation is important from the technological and fundamental points of view.

Sub-threshold excitation of a defect in diamond is the excitation of an electron, from a vibronic level with non-zero quantum number in the electronic ground state, to a vibronic level of the excited state. The energy of the photon used to excite the centre in this way is then less than the energy of the zero-phonon line. Hence the name "sub-threshold" is given to the process. Luminescent de-excitation of the electron gives rise to the observed sub-threshold luminescence spectrum of the defect. Sub-threshold excitation is not limited to diamond: it should be observed in all materials, but especially in materials with sharp zero-phonon lines.

When analysing the sub-threshold excitation data it was found that the deviations of Arrhenius behaviour of the integrated intensity of the ZPL of a defect can be explained when corrections are allowed for the change in transition probability with temperature. When more than one defect is simultaneously excited by the sub-threshold mechanism, strong deviations of the Arrhenius behaviour are observed in some cases. In particular, the data suggests a thermally activated energy transfer mechanism between the H3 and H4 defects.

7.1.2. Annealing of brown type Ia diamond

The study of the kinetics of colour changes of the diamond and thus the defect formation and dissociation is divided into a number of sub-problems:

- Study of the capture of vacancies by nitrogen aggregates.
- Study of the dissociation of nitrogen-vacancy complexes.
- Study of the dissociation of nitrogen aggregates.
- Determination of prefactors of the rate constants involved in all processes.

The effect of combining all the processes above leads to an understanding of the colour change of brown diamonds during HPHT annealing and the differences that arise when annealing is done at low temperature (~ 1900°C to 2000°C) or high temperature (2300°C or higher) and a short vs. a long annealing time.

7.1.2.1. Study of the capture of vacancies by nitrogen aggregates

The study of the capture of vacancies by irradiation and annealing of type Ia diamonds has been carried out by analysis of results from the literature and from our own experiments. A main conclusion drawn from this study is the suppression of di-vacancy formation when type Ia diamond is annealed. Also an activation energy barrier for vacancy diffusion around the A and B defects would explain phenomena like the presence of a fast and slow diffusion process and the disappearance of the slow diffusion process at higher annealing temperature (Davies *et al.* 1992).

7.1.2.2. Study of the dissociation of nitrogen-vacancy complexes

H4 defects dissociate into two H3 defects with an activation energy of 4.4 ± 0.2 eV, while the H3 defect itself dissociates into an A defect and a vacancy, with an activation energy of 5.2 ± 0.2 eV.

The H4 defect dissociation into two H3 defects, and with a lower activation energy than that of the H3 defect, explains the isothermal annealing curves of the concentrations of H3 and H4 defects (Collins *et al.* 2005).

7.1.2.3. Study of the dissociation of nitrogen aggregates

The dissociation process is of importance, as C defects can be created by HPHT annealing and can have an influence on the kinetics of other defects (for example vacancies (Davies *et al.* 1992)). Dissociation of A defects and aggregation of C defects occur simultaneously and a model should include both processes.

The dissociation of nitrogen A aggregates has been studied by HPHT annealing of colourless type IaA diamonds. This allows the study of the dissociation process without the influence of vacancies. The influence of vacancies can be significant: when type Ib diamond is irradiated prior to annealing under vacuum the aggregation rate is significantly enhanced (Collins 1978b, 1980). This enhancement is in turn suppressed when irradiated diamond is annealed under pressure at the same temperature, even when multiple irradiation and annealing steps are carried out (Allen and Evans 1981, Kiflawi *et al.* 1996).

During HPHT annealing of type IaA diamond, the relative concentrations of A and C defects will change to an equilibrium level. This equilibrium level is determined by the relative rates of aggregation and dissociation and is proportional to the activation energy for the A defect dissociation (7.3 ± 0.6 eV).

7.1.2.4. Prefactors of the rate constants involved in all processes

When a defect diffuses or dissociates, it needs to overcome an energy barrier. The rate at which the defect crosses the energy barrier is proportional to the attempt frequency and the exponential of the ratio of the activation energy and the thermal energy. The attempt frequency to cross the activation energy barrier should be proportional to the vibrational properties of the defect itself (the so-called exponential prefactor).

An attempt has been made to determine which vibrations are stretch vibrations by isotopic substitution of ^{12}C by ^{13}C, and thus to determine the prefactor in nitrogen aggregation and dissociation processes. A shift of the absorption peaks of the A defect at 1282, 1212, 1064 and 480 cm^{-1} is observed in the IR spectrum of diamond

isotopically enriched with ^{13}C. The different magnitudes of the shifts suggests the 1282 cm^{-1} peak involves the vibration of both nitrogen and carbon atoms, while the 1212 and 1064 cm^{-1} peaks involve only carbon atoms. The 480 cm^{-1} peak is due to nitrogen only. However, as observed in later chapters, the prefactors are rarely equal to vibrational frequencies.

7.1.2.5. Colour changes of brown diamond by variation of the HPHT annealing parameters.

Nitrogen aggregate – vacancy complexes are created during HPHT annealing of brown type Ia diamond. The source of the vacancies is not identified, but positron annihilation studies (Mäki *et al.* 2005, T. Anthony: pers. comm.) have indicated that vacancy clusters or disks are present in brown diamond. Theoretical studies have indicated that these clusters may be the cause of the brown colour of plastically deformed brown diamonds (Hounsome *et al.* 2005a, b). These vacancy clusters or disks can form when large concentrations of vacancies are created during plastic deformation (Leipner *et al.* 2000). They can grow by the Ostwald ripening process.

During the HPHT annealing process, mono-vacancies are generated and in type Ia diamond some of these are trapped at nitrogen aggregates, leading to the formation of H3, H4 and N-V defects. The simultaneous destruction of these nitrogen-vacancy type defects leads to a decrease of their concentration. The behaviour of the different defects has been modelled and fitting of data indicates the activation energy for the release of a vacancy from the vacancy cluster or disk is 6.2 ± 0.2 eV.

Furthermore, the model is able to simulate the high temperature ($T > 1400°C$) annealing data of irradiated and pre-annealed ($T \sim 800°C$) diamonds, employing the same parameters as those used to simulate the H3, H4 and N-V defect behaviour in HPHT annealed diamond. The only change that needs to be made is the substitution of the rate constant for the generation of mono-vacancies from vacancy clusters by the rate constant for mono-vacancy diffusion.

The apparent anti-correlation between the concentration of mono-vacancies available for trapping at nitrogen aggregates and the integrated intensity of the platelets

explains why some brown diamonds from the Argyle mine are irregular type diamonds. Harris and Collins (1985) commented that, using the activation energy of 7 eV deduced from the work of Evans and Qi (1982) for conversion of A defects into B defects, the calculated age of these diamonds would be higher than the age of the Earth. Furthermore, when a regular type IaA/B Cape Yellow diamond is converted into a irregular type IaA/B diamond, more extreme conditions (T > 2500°C) are required (Kiflawi and Bruley 2000), indicating this process has an even higher activation energy. This means that the irregular type IaB diamond would be even older than a regular type IaB. However, these methods do not take vacancy-enhanced destruction of platelets or other processes into account.

7.1.3. Hydrogen in diamond

The nature of the 3107 cm^{-1} defect has also been investigated by isotopic substitution of ^{12}C by ^{13}C and it is confirmed that the hydrogen is bonded to a single carbon atom, as suggested by Collins and Woods (1983).

There is no correlation between the concentration of the 3107 cm^{-1} defect and the nitrogen concentration in either the A or B defects, or the total nitrogen concentration in diamond.

7.2. Further work

7.2.1. Linear electron-phonon coupling

Linear electron-phonon coupling has been studied and it is illustrated that the theory can predict the behaviour of the ZPL at different temperatures for many defects. However, there are clearly a number of defects with deviations from this behaviour: the 490.7 nm defect in brown type Ia diamonds is such an example. The reason for this behaviour can only be understood when more information about this defect is known: there can be nearly degenerate states, interactions with other defects, ...

Sub-threshold excitation can be accounted for when one type of defect is present in the diamond. However, in some cases when more than one defect is detected in sub-threshold excitation, the temperature behaviour is not fully understood. This has been

attributed to defect-defect interaction, but detailed investigation of samples with different H3 and H4 concentrations, spanning a wide range, is necessary to confirm this proposal.

7.2.2. Photochromic effects

Photo-induced changes of defects when illuminated with light have been observed for several irradiated and annealed samples, and comparing data of different samples with data of other research groups clearly points to a sample-dependent behaviour of the photo-induced changes. This can have a significant influence on the detection limit of these defects. A great deal of additional experimental work is required to understand these phenomena properly. It is very important to have accurate data on the ratio of the change of the GR1/ND1 absorption strength as this forms the basis for the determination of the oscillator strength of the GR1 and ND1 defects. This is important as the oscillator strength of H3, H4 and $(N\text{-}V)^-$ is determined from the oscillator strength of the GR1 and ND1. More experiments should be carried out to determine the GR1/ND1 absorption change upon illumination.

7.2.3. Vacancy capture by nitrogen aggregates in diamond

Davies *et al.* (1992) observed 40% of the vacancies in electron-irradiated diamond are more strained, diffuse faster than in bulk and are presumed to be created close to A defects; furthermore they showed that more vacancies are created in type Ia diamonds ($[V]_{\text{type Ia}} = 1.6\ [V]_{\text{type IIa}}$). The increased concentration of vacancies created by electron irradiation is also observed when C defects are present in the diamond. The physical mechanism for this enhancement is not clear. Reduction of recombination-enhanced interstitial diffusion because of the presence of defects could be one of the reasons for the increased vacancy concentration in type IIa diamond. The study of vacancy and interstitial creation in type Ia diamond by electron irradiation at different temperatures should also contribute to the understanding of the recombination-enhanced diffusion of the interstitial in the presence of nitrogen aggregates. Also, a simulation of the diffusion properties of a vacancy close to an A or B nitrogen aggregate should be investigated in more detail.

The C defect in diamond is a very efficient vacancy trap for vacancies compared to A and B defects. Mainwood (1994) pointed out that the activation energy for vacancy diffusion is lowered close to the C defect, which might be the cause of the increased trapping of vacancies by C defects. This point needs further investigation, as it is not clear why the C defect is a more efficient vacancy trap.

7.2.4. Brown colour in diamond and vacancy clusters

Large concentrations of vacancies are created during plastic deformation, leading to supersaturation of the diamond with vacancies. The vacancies precipitate and grow, probably in an Ostwald type ripening process.

There is still considerable work that needs to be done on vacancy disks or clusters in brown type Ia diamond, and a detailed study of positron annihilation experiments as a function of annealing temperature and time is highly desirable. However, this technique cannot be applied to large vacancy clusters or disks which may exist, so a second approach like small angle X-ray scattering, or laser scattering tomography, should be used to investigate the possibility of even larger aggregates in brown diamonds.

7.2.5. Crystallographic directions of plastically deformed regions in diamond

In a large number of samples, it is seen that lines with increased concentrations of H3 defects, associated with H3 defects created close to slip planes, are not parallel with low index crystallographic (octahedral and cubic) directions in diamond, but are tilted at an angle with respect to the planes (see chapter 6, section 6.7.2). This might be because these non-principal slip directions are activated when the diamond is deformed at high temperature, but this point clearly needs further research.

7.2.6. Platelet formation and destruction

The influence of platelets on the annealing of vacancies is not understood, but the HPHT annealing data points to the importance of a proper understanding of the platelet-vacancy interaction. Platelets are clearly influenced during irradiation but not by the subsequent annealing.

Formation and aggregation of platelets is not very well understood and may be a process similar to Ostwald ripening. It is suggested the B defects could act as a nucleation site for platelets, so one should be able to create platelets, or increase the absorption strength due to platelets, in heavily irradiated, annealed type IaB diamonds. This has partly been investigated by Allen and Evans (1981) but there is insufficient data to study the platelet creation/destruction in detail so more data is required.

The behaviour of platelets as function of annealing temperature and time in regular diamonds has not been investigated in this thesis and only scattered data is found in literature. From the work of Evans and Woods (1983), we know platelets are formed in type I diamond after substantial nitrogen aggregation. Subsequent annealing distorts the platelet peak shape and in regular type Ia diamonds the width decreases and the position of the peak shifts to lower wavenumbers when the nitrogen in the diamond has aggregated more into B defects, indicating the platelets grow in size and the size distribution narrows. The brown type Ia samples under study in this thesis do not display this behaviour, which is attributed here to the release of high concentrations of mono-vacancies from the vacancy sources in the diamond interfering with the normal ripening process of platelets. A more in-depth study of the platelet properties appears to be urgently necessary to support the conclusions of chapter six on the platelet peak behaviour with time when the diamond is subjected to HPHT annealing.

7.2.7. Defect kinetics

We remark here that the changes of the N3 defect concentration have not been taken into account in any analysis. An alternative H4 dissociation path could be the following: H4 → N-V + N3. This could account for the observed deviation from the expected behaviour of N-V defect concentrations. Resolving this anomalous annealing behaviour of N-V defects clearly needs further investigation.

Appendix A

Colour and colour coordinate calculation

1. Introduction

This appendix will give a concise introduction to the colour and colour coordinate calculation. For a detailed treatment of colour and vision, the interested reader is referred to Wyszecki and Stiles (2000).

The coordinates in colour space are calculated and displayed on the CIE (Comission International d'Eclarage) diagram. There are different CIE models to calculate the colour coordinate, and the method adopted here is the 1931, 2 degree observer.

The colour coordinate of a spectrum is calculated by convolution of the transmission spectrum of the sample with the spectrum of standardized lamp (D65 lamp; northern daylight equivalent or black body emission of a subject of 6500 K) and the response curve of the human eye.

For ease of interpretation, the colour coordinate is displayed on the chromaticity diagram. On this diagram the edge is 100% colour saturation and the dominant wavelength of the light is indicated. The dominant wavelength represents the colour observed by a human colour grader. This wavelength is determined by drawing a line from the white point (colour coordinate of the D65 lamp) through the colour coordinate to the edge on the diagram. The distance between the white point and the colour coordinate along this line determines the excitation purity.

2. Colour coordinate calculation

The colour coordinate is calculated from a spectrum by the following way:

First the tristimulus values X,Y and Z are calculated by integrating the transmission spectrum of the sample with the colour matching function and the spectrum of the D65 lamp.

$$X = \int_{360}^{830} I(\lambda)\bar{x}(\lambda)D65(\lambda)d\lambda$$

$$Y = \int_{360}^{830} I(\lambda)\bar{y}(\lambda)D65(\lambda)d\lambda$$

$$Z = \int_{360}^{830} I(\lambda)\bar{z}(\lambda)D65(\lambda)d\lambda$$

Here $I(\lambda)$ is the spectrum as function of the wavelength of the light. $D65(\lambda)$ is the spectrum of a D65 illumination (northern daylight or blackbody radiation of 6500K).

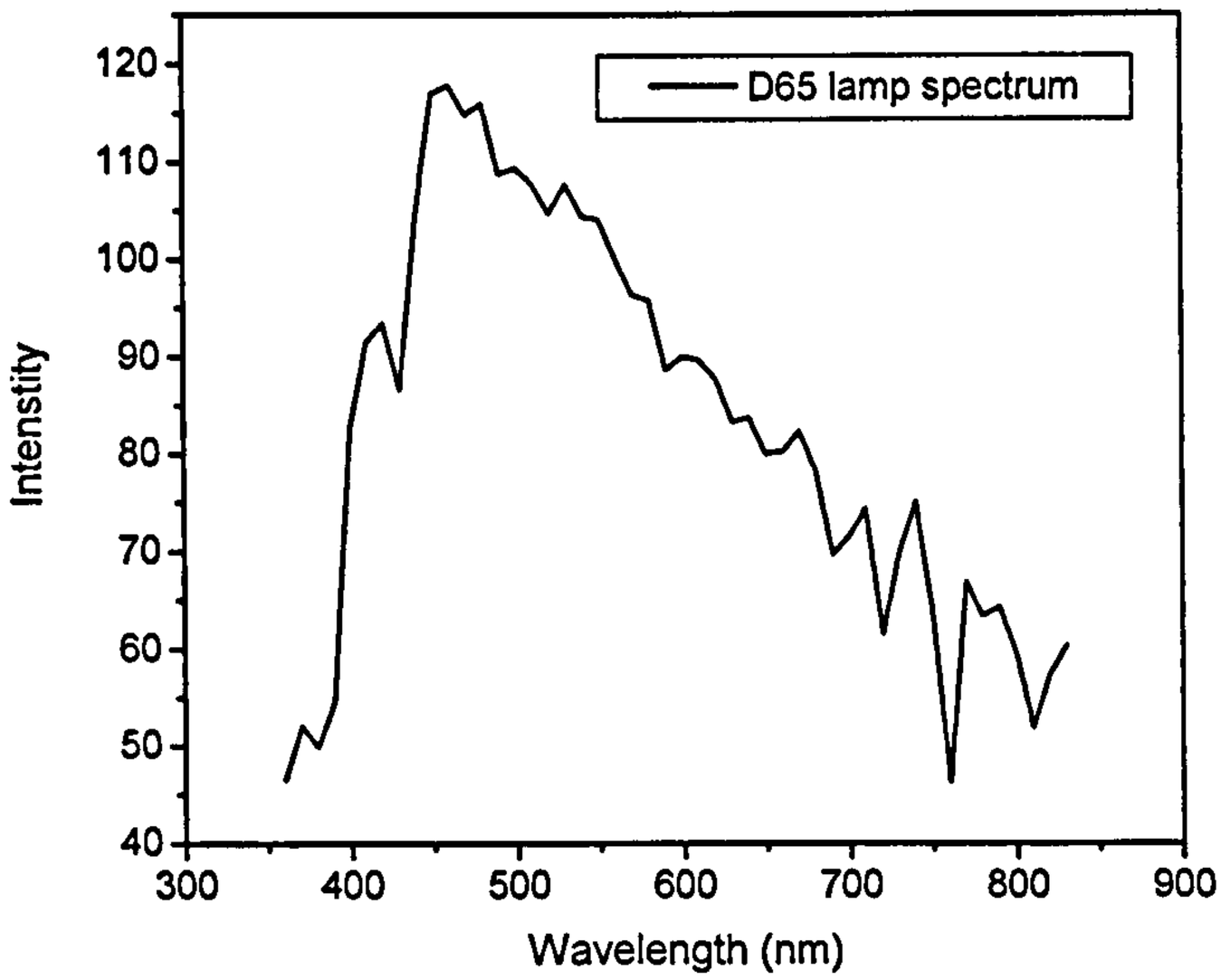

Figure A.1. The D65 spectrum, imitating northern daylight.

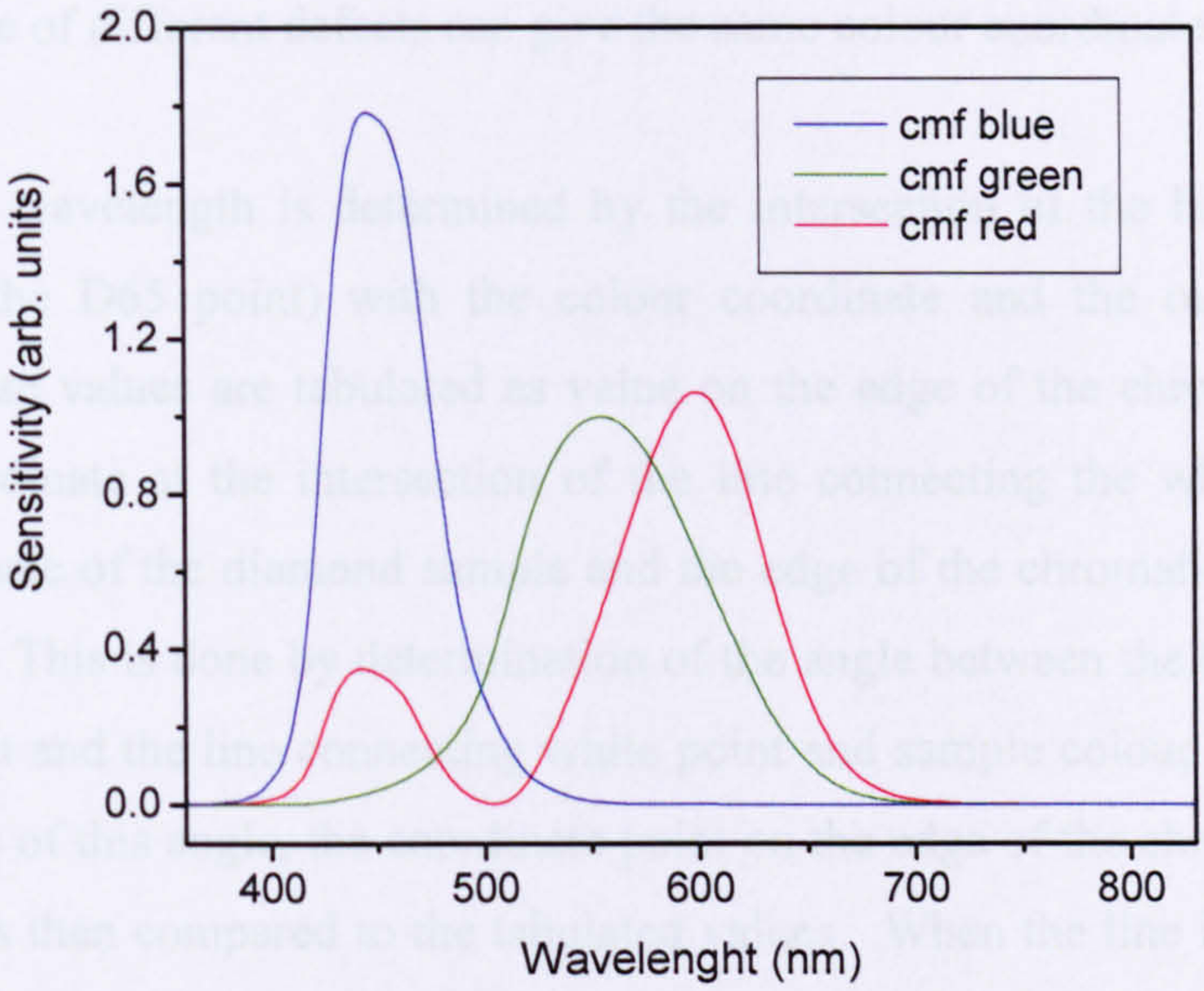

Figure A.2. The colour matching functions of the eye. These reflect the response function of the eye as function of the wavelength of the light.

$\bar{x}(\lambda)$, $\bar{y}(\lambda)$ and $\bar{z}(\lambda)$ are the "colour matching functions", which are the response function of the eye for red, green and blue respectively. The colour coordinate on the CIE diagram is determined by the following functions:

$$x = \frac{X}{X+Y+Z}$$

$$y = \frac{Y}{X+Y+Z}$$

$$z = \frac{Z}{X+Y+Z}$$

x and y determine the colour coordinate on the CIE 1931 chromaticity diagram.

Because the primaries are integrals over the entire visible spectrum, different spectra could give similar results. The convolution functions A.1 – A.3 will reduce a spectrum

into three numbers, thereby losing additional information in the spectrum. Similar spectra because of different defects can give the same colour coordinate.

The dominant wavelength is determined by the intersection of the line connecting the white point (the D65 point) with the colour coordinate and the outside of the CIE diagram. These values are tabulated as value on the edge of the chromaticity diagram. Thus the coordinate at the intersection of the line connecting the white point and the colour coordinate of the diamond sample and the edge of the chromaticity diagram must be calculated. This is done by determination of the angle between the horizontal through the white point and the line connecting white point and sample colour coordinate. From the knowledge of this angle, the coordinate point on the edge of the chromaticity diagram is found and is then compared to the tabulated values. When the line intersects the edge of the chromaticity diagram between two values in the tables, a linear interpolation is done between the two tabulated values.

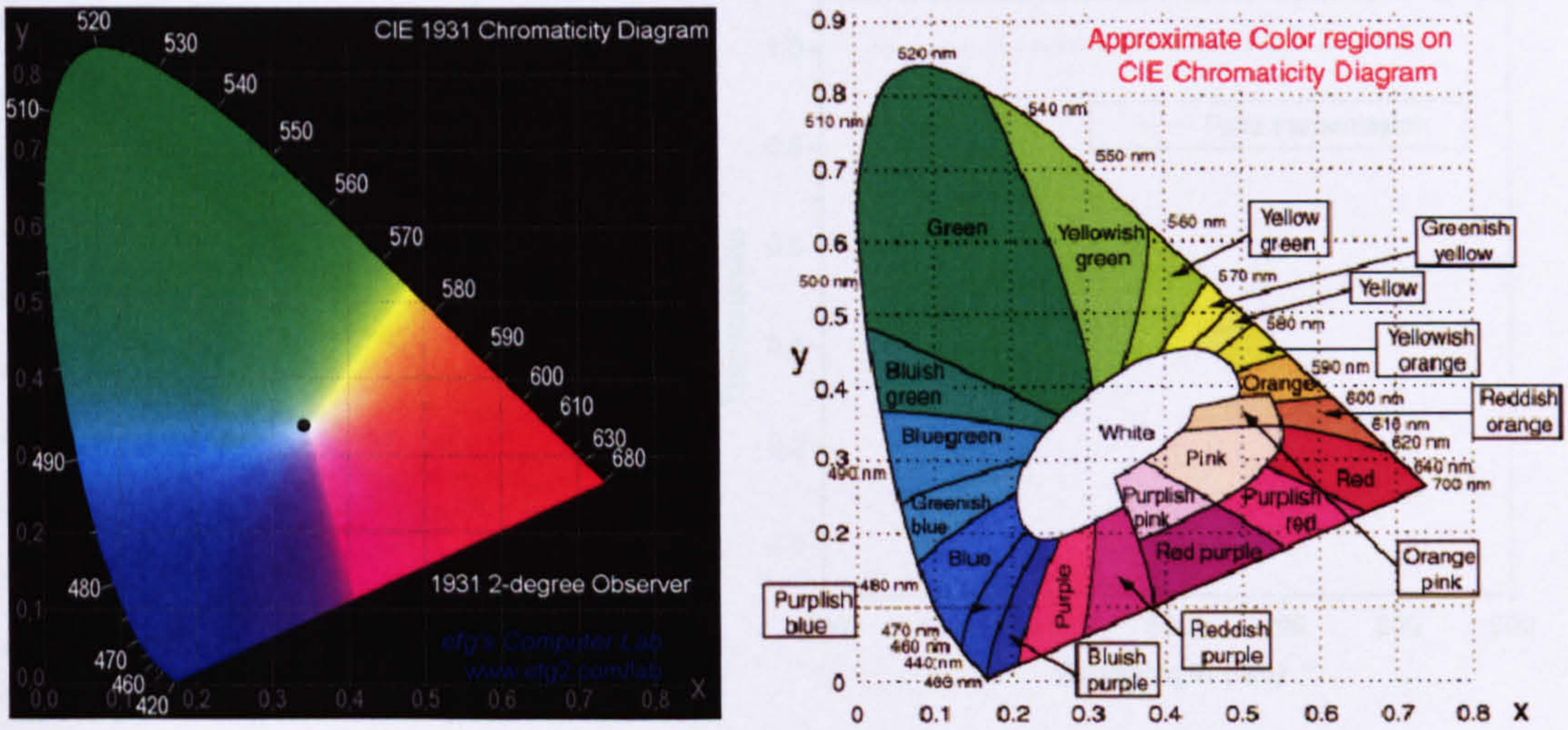

Figure A.3. The CIE 1931 chromaticity diagrams with the approximate colour name regions (right) and the real CIE colour space (left). The black dot is the D65 reference point

3. Examples

To get some feeling on how the colour coordinate calculation works, a number of artificially generated spectra will be shown and the calculated colour coordinate and dominant wavelength will be given. The coordinate of the D65 illuminant white point is x = 0.3127 and y = 0.3290.

Total transmission

In this case, the calculated colour coordinate should coincide with the white point of the D65 reference lamp, as the primaries are the integrals over the D65 lamp and CMF only.

This is indeed the case (figure A.4.). The calculated coordinate is at x = 0.3127 and y = 0.3290.

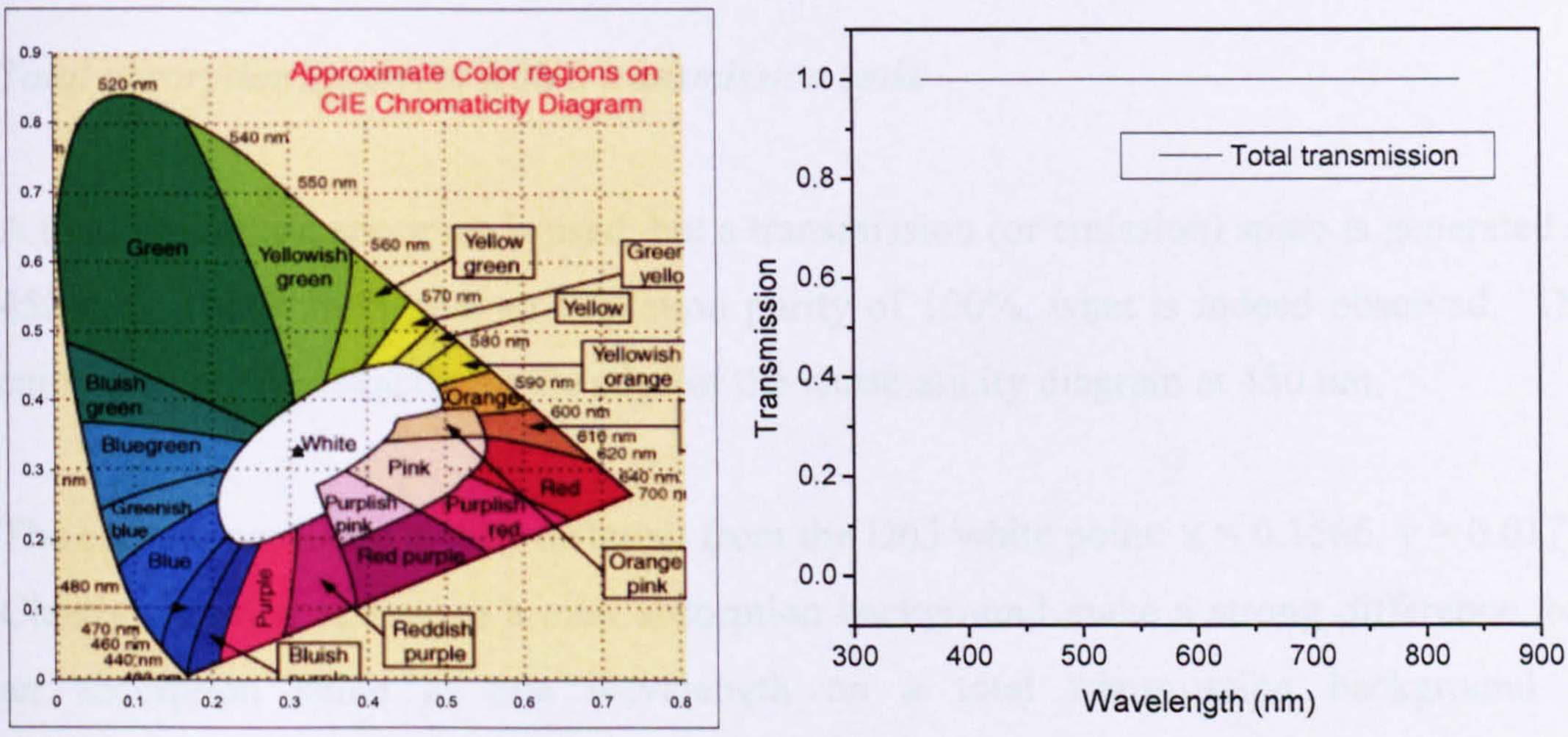

Figure A.4. The colour coordinate of a total transmission spectrum.

Total transmission except at one particular wavelength

The same spectrum as in the previous paragraph is used, but with a single absorption spike at 450 nm. Almost no change compared with the total transmission spectrum is detected. The calculated colour coordinate is x = 0.3139 and y = 0.3315

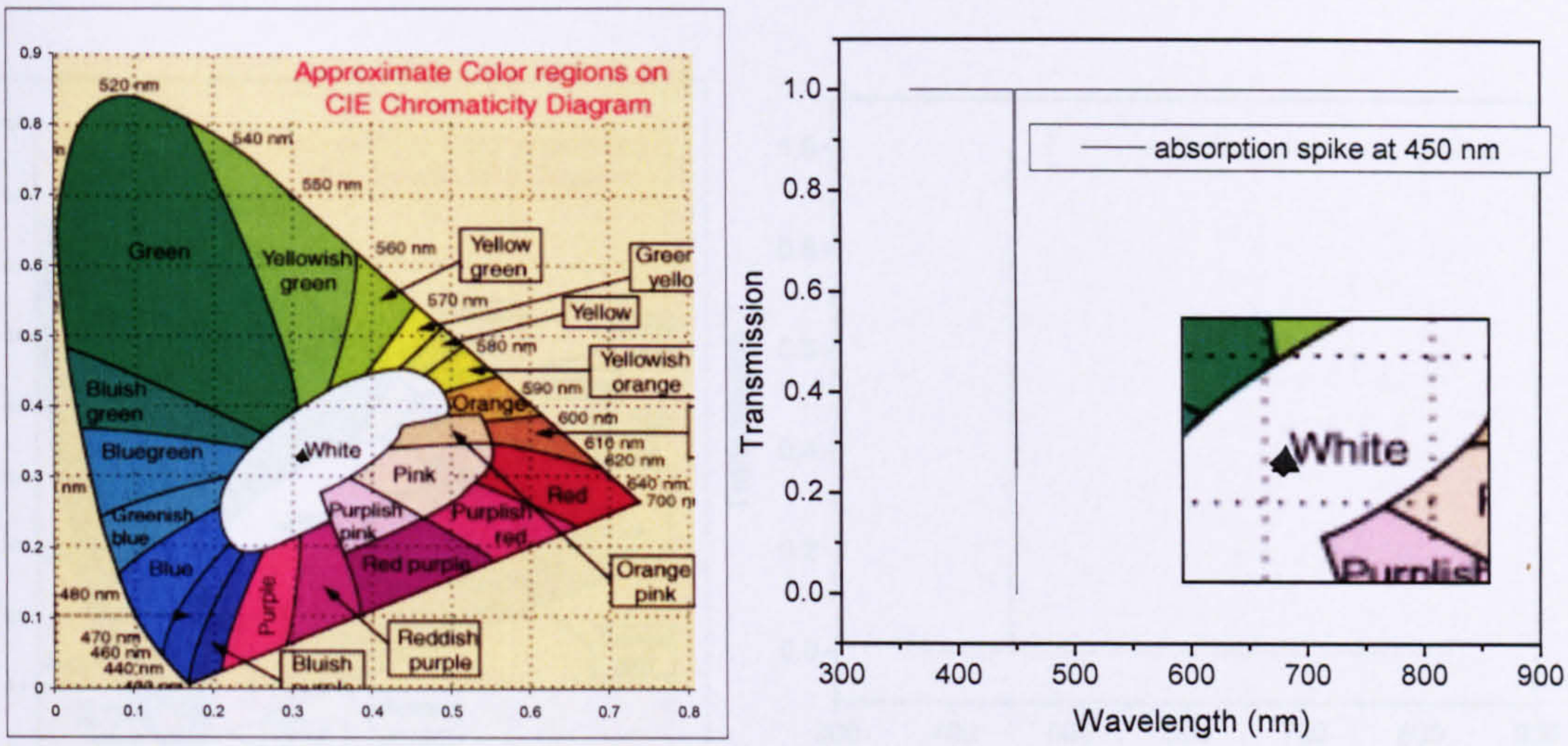

Figure A.5. The colour coordinate calculation result of a total transmission spectrum with an absorption spike at 450 nm. The inset in the spectrum shows the coordinate of spectrum in the chromaticity diagram together with the D65 white point. There is almost no difference.

Total absorption spectrum with a transmission spike

A total absorption spectrum is used, but a transmission (or emission) spike is generated at 450 nm. This should give an excitation purity of 100%, what is indeed observed. The calculated point is exactly on the edge of the chromaticity diagram at 450 nm.

The colour coordinate is very different from the D65 white point: $x = 0.1566$, $y = 0.0177$. Clearly emission spikes on a total absorption background make a strong difference, but an absorption spike at one wavelength on a total transmission background is undetectable.

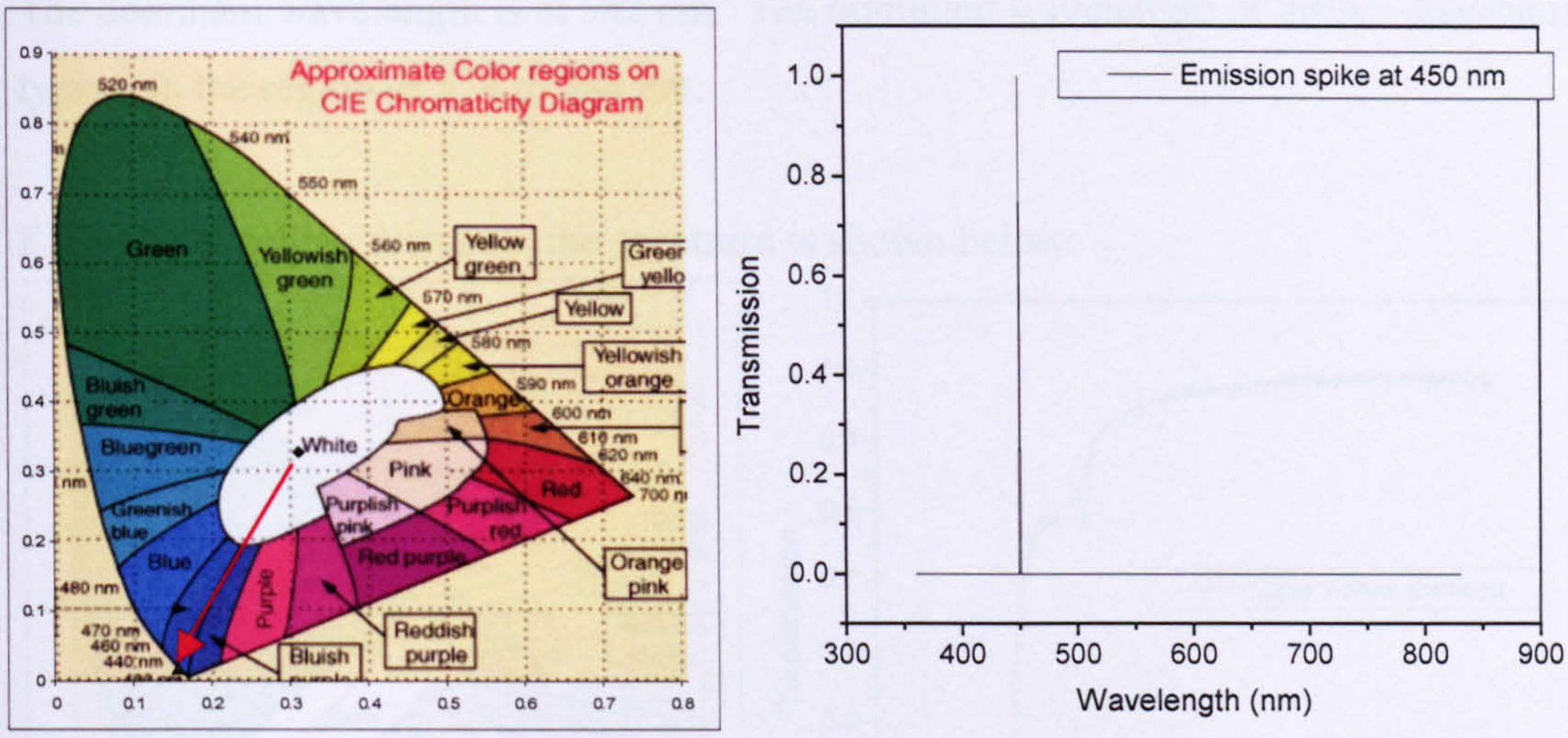

Figure A.6. The colour coordinate calculation result of a total absorption spectrum with an emission spike at 450 nm. The red arrow indicates the dominant wavelength with respect to the D65 illuminant.

Examples of real spectra of coloured diamonds

The spectrum of a brown type IaA diamond is as in the figure below

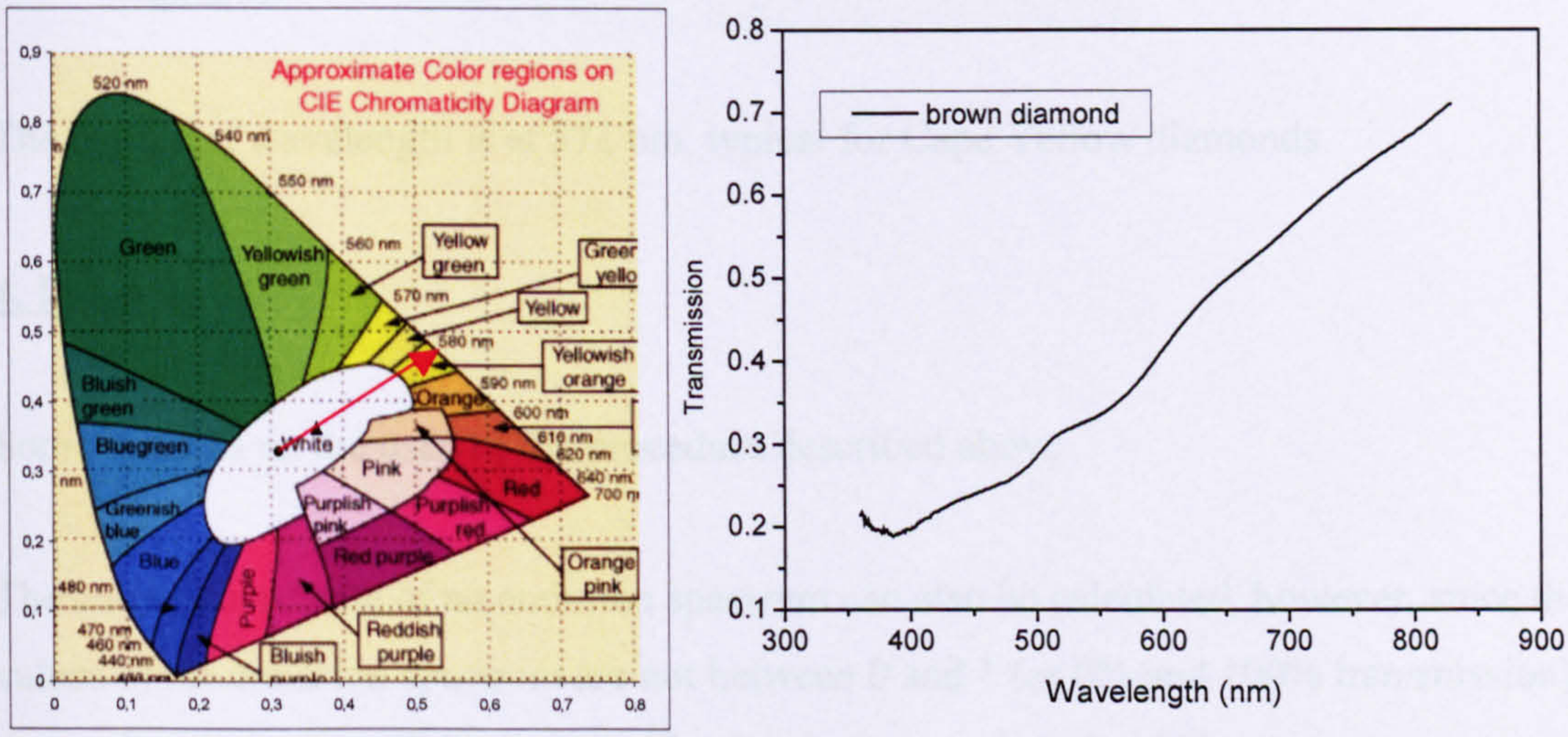

Figure A.7. The colour coordinate calculation result of a brown type IaA diamond. The red arrow indicates the dominant wavelength with respect to the D65 illuminant. The black triangle indicates the calculated colour coordinate of the spectrum.

The dominant wavelength is at 582 nm. The dominant wavelength of brown diamonds is typical in the region of 579 to 584 nm.

For a Cape Yellow diamond, the spectrum is shown below:

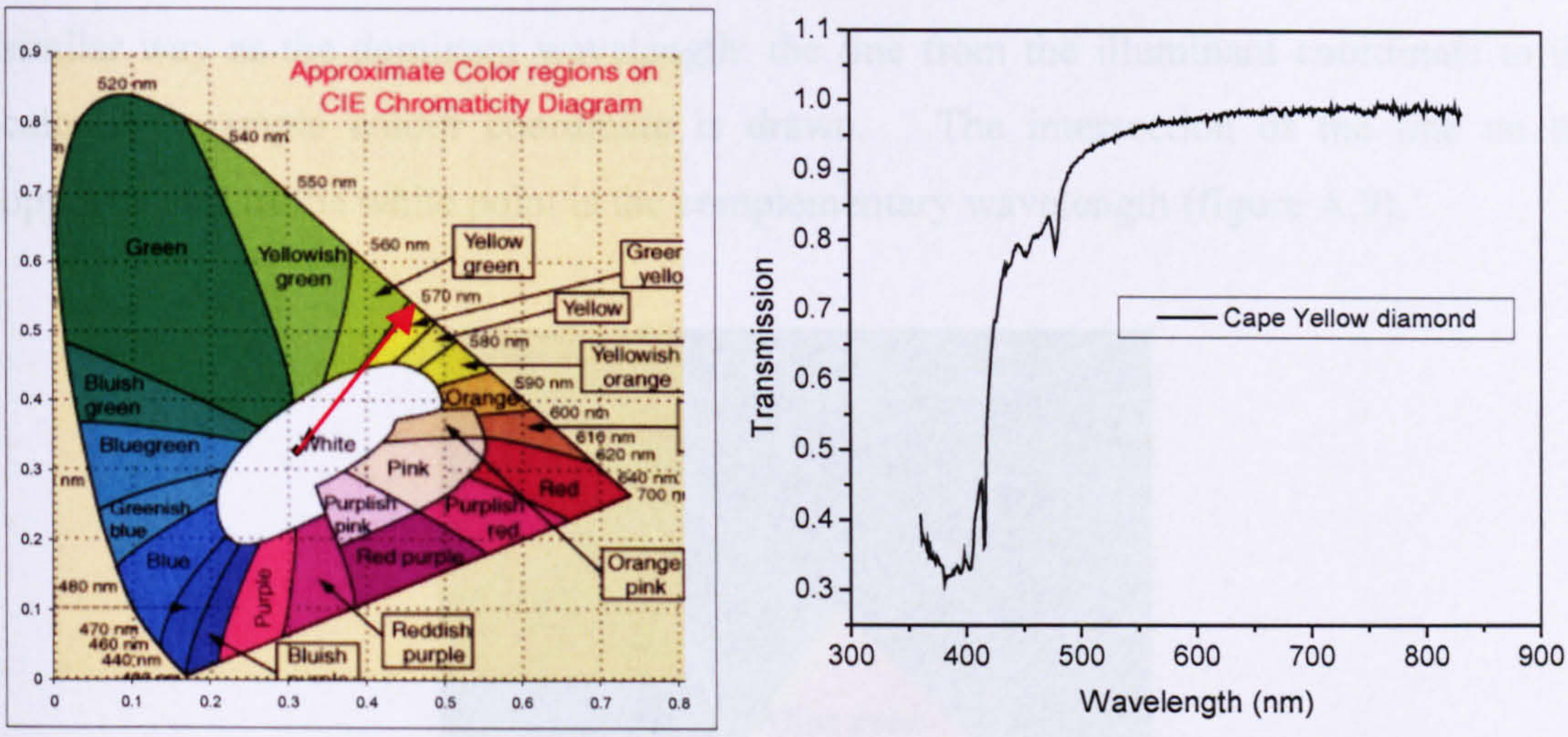

Figure A.8. The colour coordinate calculation result of a Cape Yellow diamond. The red arrow indicates the dominant wavelength with respect to the D65 illuminant. The black triangle indicates the calculated colour coordinate of the spectrum.

The dominant wavelength is at 571 nm, typical for Cape Yellow diamonds.

4. Remarks

Some remarks on the used of the procedure described above.

The colour coordinate of an emission spectrum can also be calculated, however, since the values of the emission spectrum are not between 0 and 1 (or 0% and 100% transmission), the excitation purity will be wrong. The dominant wavelength will be correct.

Black, white and various degrees of grey have the same colour coordinate. This is caused by the fact that various degrees of grey are projected perpendicular to the chromaticity diagram by the transformation of XYZ primaries space into xyY space.

Purple colours are on the so-called purple line and have no dominant wavelength because these cannot be represented by a single dominant wavelength. These colours are characterised by the complementary wavelength. This wavelength is determined in a similar way as the dominant wavelength: the line from the illuminant coordinate to the calculated sample colour coordinate is drawn. The intersection of the line on the opposite side of the white point is the complementary wavelength (figure A.9).

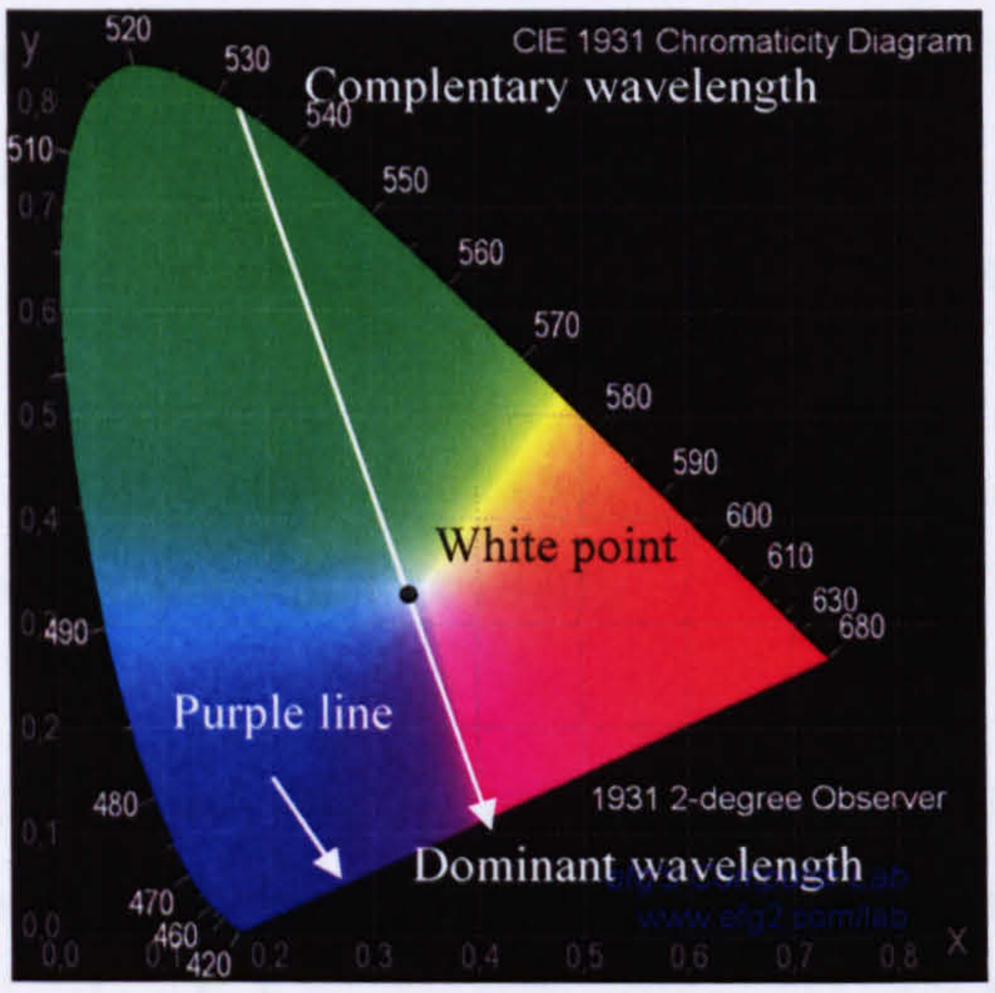

Figure A.9. The complementary and dominant wavelength in the 1931 CIE chromaticity diagram.

Appendix B

Alternative dissociation path of H3 defects: H3 → N + N-V

As mentioned in the chapter 6, paragraph 7.3, the H3 defect can dissociate by:

- removal of the vacancy or
- by dissociating into a nitrogen-vacancy pair plus a single substitutional nitrogen defect.

Earlier and more recent experimental results suggest that the vacancy is removed from the H3 defects (Collins *et al.* 2005, Collins 1980).

To investigate this properly, we need to include the formation of C defects and the vacancy enhanced aggregation during the HPHT annealing by formation and dissociation of N-V defects. This has already been investigated in chapter 6, paragraph 7.3, and can easily be added to equations 6.31-6.25:

$$\frac{d[V_{cl}(t)]}{dt} = -k_1[V_{cl}(t)] \tag{B.1}$$

$$\frac{d[V_{tot}(t)]}{dt} = k_1[V_{cl}(t)] - k_{1,fast}\left(1-\left(\alpha[A(t)]+\gamma[C(t)]\right)\right)[V_{tot}(t)] + k_6[(N\text{-}V)(t)] + k_{1,fast}[(A\text{-}V)(t)] \tag{B.2}$$

$$\frac{d[(A\text{-}V)(t)]}{dt} = \alpha k_{1,fast}[A(t)][V_{total}(t)] - k_2[(A\text{-}V)(t)] - k_{1,fast}[(A\text{-}V)(t)] \tag{B.3}$$

$$\frac{d[H3(t)]}{dt} = k_2[(A\text{-}V)(t)] - k_3[H3(t)] \quad \text{(B.4)}$$

$$\frac{d[A(t)]}{dt} = -\alpha k_{1,fast}[A(t)].[V_{total}(t)] - 2k_{diss}[A(t)] + k_{aggr}[C(t)]^2 \quad \text{(B.5)}$$

$$\frac{d[C(t)]}{dt} = -k_{aggr}[C(t)]^2 + 2k_{diss}[A(t)] - \gamma k_{1,fast}[C(t)][V_{total}(t)] + k_4[H3(t)] + k_6[(N\text{-}V)(t)] \quad \text{(B.6)}$$

$$\frac{d[(N\text{-}V)(t)]}{dt} = \gamma k_{1,fast}[C(t)].[V_{total}(t)] - k_6[N\text{-}V(t)] + k_4[H3(t)] \quad \text{(B.7)}$$

α and γ are the fraction of A and C defects respectively which capture a vacancy and these have been determined in chapter five. Equation B.1 describes the release of mono-vacancies from the vacancy source, the first term of the r.h.s. of equation B.2 describes the migration of the mono-vacancies from the vacancy source, the second term describes the loss of vacancies to dislocations, the surface or other vacancy traps, the last term describes the generation of vacancies from the nitrogen-vacancy complexes. The r.h.s. of equation B.3 describes the trapping and release of vacancies by the A defect and the formation of H3 defects. Equation B.4 describes the formation and dissociation of the H3 defects. The r.h.s. of equation B.5 describes the increase in A defect concentration by re-aggregation, the loss of A defects by dissociation of A defects and vacancy trapping. The r.h.s. of the C defect formation equation (equation B.6) includes the re-aggregation of C defects, the increase in C defects due to dissociation of A defects, loss of C defects by the formation of N-V defects, the increase in C defects by H3 dissociation and N-V dissociation in a nitrogen atom and a vacancy. Equation B.7 describes the N-V defect formation and dissociation. The right hand side of the equation describes the formation of N-V defects, the dissociation of N-V defects and the formation of N-V defects by removing a single nitrogen atom from the H3 defect.

The rate constants $k_{1,fast}$, k_{diss}, k_{aggr}, are tabulated in table 6.14 of chapter 6 and k_1, k_2, k_3 need to be determined experimentally by numerically solving equations B.1 to B.7 and varying the respective pre-exponential factor and activation energy to the experimental data.

The dissociation of H3 defects into a C and an N-V defect leads to a supersaturation of C defects during the initial stages of the annealing (see figure B.1) and this supersaturation decreases quickly to the thermodynamically stable level. Lowering the temperature will slow down the processes at a different rate, because every process has a different activation energy. However, the difference in C defect concentration at lower temperature (T = 2100°C) will not be sufficient to distinguish between the two H3 defect decay modes (figure B.1).

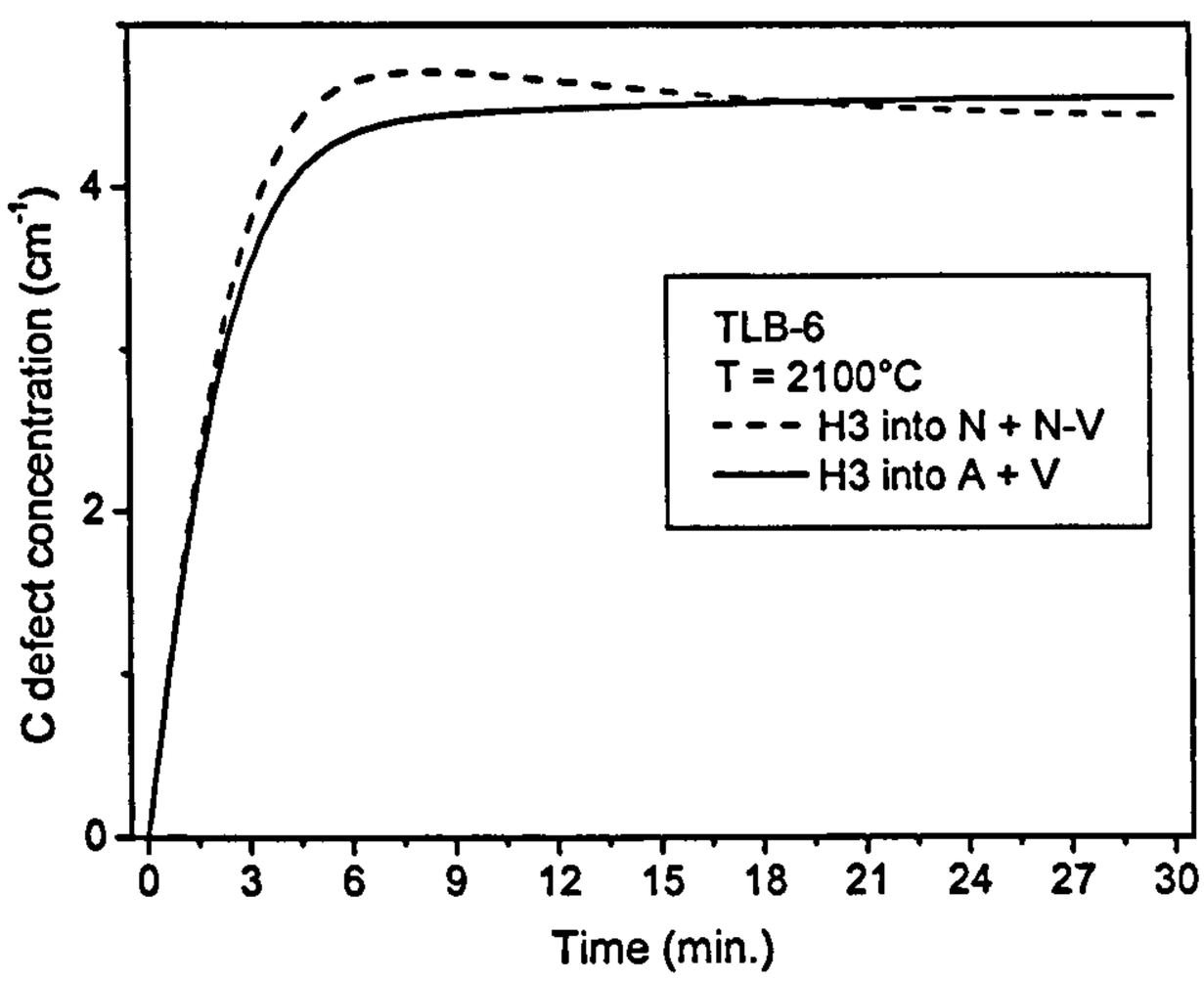

Figure B.1. The concentration of C defects after HPHT annealing when H3 dissociates in A + V or N + N-V.

Since this initial supersaturation of C defects is too small to be resolved experimentally, it is possible that the different concentration of N-V defects created by the two different H3 decay modes, might give a hint on the dissociation process for H3 defects.

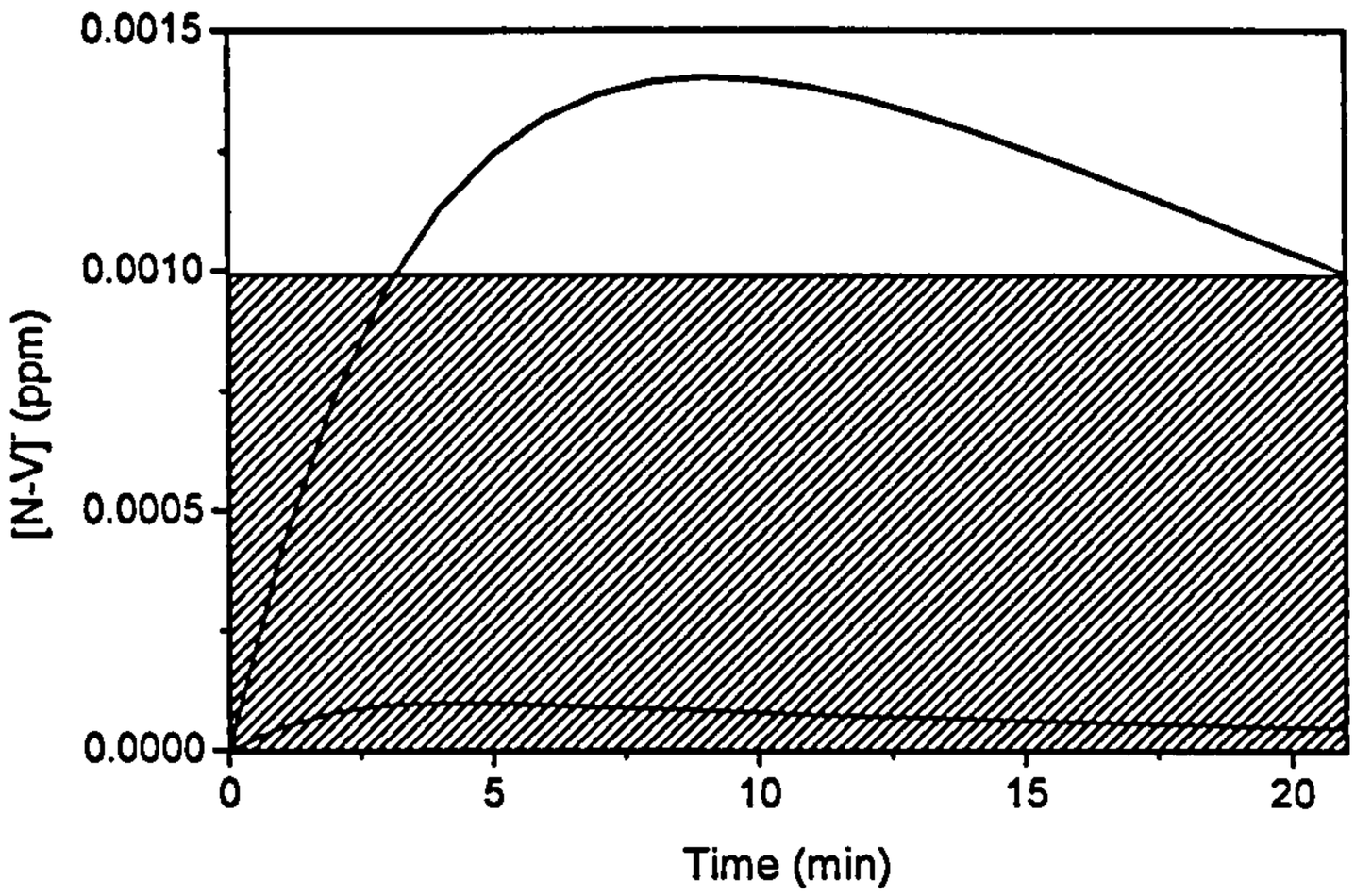

Figure B.2. The simulation of the concentration of N-V defects, generated during HPHT annealing of brown type Ia diamond with [A] = 20 ppm and [B] = 300 ppm. The hatched region is where the N-V concentration is below the UV-VIS absorption detection limit. The top curve is the concentration of N-V defects when H3 dissociates into single nitrogen and N-V defect combination, the lower curve is when H3 splits into and A defect and a vacancy. The maximum concentration of N-V defects should be detected after ~ 9 minutes.

The time-evolution of N-V defects suggests the split up of H3 defects into a nitrogen plus an N-V defect combination. Annealing at higher temperatures results in a similar picture like figure B.2, but the maximum of N-V concentration occurs after 2 minutes in the H3 $\rightarrow$ A + V reaction and after 4 minutes for the H3 $\rightarrow$ N + N-V reaction (figure B.2). Again, the concentration of N-V defects is below absorption detection limit when the H3 $\rightarrow$ A + V reaction occurs. Note that both models of H3 defect destruction results in a very small and experimentally not resolvable difference in H3 defect concentrations.

A simulation of the HT annealing data of Collins (1978, 1980) and with equations B.1 – B.7 to model the H3 $\rightarrow$ N + N-V reaction instead of the H3 $\rightarrow$ A + V reaction results in very small nitrogen aggregation in contradiction to the results of Collins (1980) and clearly proves the H3 defect dissociates by removal of the vacancy: H3 $\rightarrow$ A + V. Therefore in all simulations we use the model where H3 defects dissociate in an A defect and a vacancy.

Appendix C

Examples of colour changes by treatments

C.1. Introduction

In this appendix, a number of photos of typical colours of diamonds after various colour treatments (irradiation, annealing, HPHT annealing, or combinations thereof). The examples shown here are:

- The colour of diamond after irradiation with electrons.
- The change of the colour of a diamond after irradiation with electrons and subsequent annealing at 800°C.
- The colour change after HPHT annealing of brown type IaA/B diamond, and the colour change if this is followed by irradiation and annealing at 800°C.

Each of the colour treatments will induce a different colour in the diamond and as will be shown below, a combination of treatments will also give the diamond a different colour.

C.2. Irradiation

After irradiation of a colourless diamond, the diamond has a blue-green to green colour, depending on the irradiation dose and energy (figures C.1. and C.2.).

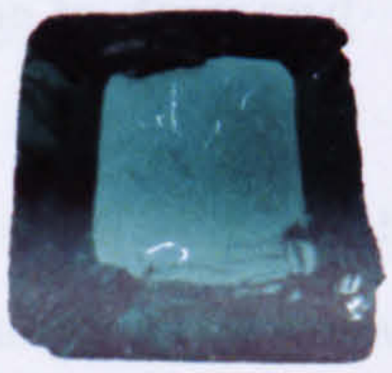

Figure C.1. A green diamond sample after irradiation with electrons (dose: $8\ 10^{18}$ e^-/cm^2, energy: 8 MeV).

Figure C.2. The various colours of diamonds after irradiation (irradiation conditions unknown). From left to right: depending on the irradiation dose and energy, the diamond can be black, green or blue.

C.3. Irradiation and annealing (T = 800°C, 1h)

By annealing of irradiated type Ia diamond, H3 and H4 defects are created. The absorption because of 594 nm defects is also increased in strength, and the net result is a golden yellow colour of the diamond (figure C.3).

Figure C.3. A diamond after irradiation and annealing at 800°C. The colour of the diamond changed from green to golden yellow.

C.4. HPHT annealing of brown type Ia diamond

Depending on the length of the annealing time and the annealing temperature, the colour of a brown type Ia diamond can change from brown to yellow-green or yellow. After irradiation and annealing, N-V defects can be created, leading to a purple-red colour (figure C .4.).

Figure C.4. The different colours of a brown type Ia diamond after HPHT annealing, and irradiation and heat treatment. After HPHT annealing the colour of the brown diamond changed into a yellow-green colour. After irradiation and annealing the colour of the diamond changes into purple-red.

Figure C.5. Brilliant polished diamonds after HPHT annealing. Annealing for a shorter time or at lower temperature will give the diamond a yellow-green colour (diamonds on left and right side). Prolonged annealing or annealing at higher temperature will give the diamond a yellow to orange colour (diamond in the centre).

Shorter annealing at relatively lower temperature of brown type IaA/B diamond results in a yellow-green colour change (the diamonds on left and right side of figure C.5.). This is caused by the creation of large concentrations of H3 defects in the diamonds, responsible for the increase in yellow colour. The fluorescence because of the H3 defect gives the diamond a green colour.

Longer annealing or annealing at very high temperature will result in a type Ib like colour because of the formation of relatively large concentrations of C defects. Depending on the concentration of C defects, the colour can be light yellow (low colour saturation) to orange (high colour saturation) (figure C.4., the diamond in the middle).

References

M. Abramowitz and I. Stegun, 1972, *Handbook of mathematical functions, Graphs and Mathematical tables*, Dover Publications, ISBN 486-61272-4

F. Agullo-Lopez, C.R.A. Catlow, P.D. Townsend, *Point defects in materials*, Academic press, 1988, ISBN 0-12-044510-7

B.P. Allen, T. Evans, 1981, Proc. R. Soc. A, **375**, p. 93

L. Allers, A.T. Collins, J. Hiscock, Diam. Relat. Mater, **7**, p. 228

C.A.J. Ammerlaan, E.A. Burgemeister, 1981, Phys. Rev. Lett., **47**, p. 954

J.A. Angress, S.A. Hall, 1979, J. Phys. C: Solid State Phys., **12**, p. 4623

V. Avalos, S. Dannefaer, 2003, Physica B, **340**, p. 76

J.C. Barry, L.A. Bursill, J.L. Hutchison, A.R. Lang, G.M. Rackham, N. Sumida, 1987, Proc. R. Soc. Lond. A, **321**, p. 361

G. Beaucarne, M.A. Green, 2003, Solid State Electr., **47**, p. 685

F. Béjina, O. Jaoul, R.C. Liebermann, 2003, Phys. Earth Planet. Inter., **139**, p. 3

H. Bilz, 1966, *Phonons in perfect lattices and in lattices with point imperfections*, edited by R.W.H. Stevenson, Oliver & Boyd, Edinburgh

H. Bilz and Kress, 1979, *Phonon dispersion relations in insulators*, Solid State Sciences 10, Springer-Verlag, p. 92.

S.R. Boyd, I. Kiflawi, G.S Woods, 1994, Phil. Mag. B, **69**, p. 1149

S.R. Boyd, I. Kiflawi, G.S Woods, 1995, Phil. Mag. B, **72**, p. 351

Yu. Borzdov, Yu. Pal'yanov, I. Kupriyanov, V. Gusev, A. Khokhryakov, A. Sokol, A. Efremov, 2002, Diam. Relat. Mater., **11, p.** 1863

P.R. Briddon, R. Jones, 1993, Physics B, **185**, p. 179

E.J. Brookes, A.T. Collins, G.S. Woods, 1993, J. Hard Mater. **4**, p. 97

E.J. Brookes, P. Greenwood, G. Xing, 1999, Diam. Relat. Mater., **8**, p 1536

E.J. Brookes, J.D. Comins, R.D. Daniel, R.M. Erasmus, 2000, Diam. Rel. Mater., **9**, p. 1115

M.R. Brozel, T. Evans, R.F. Stephenson, 1978, Proc. R. Soc. Lond. A, **361**, p. 109

H. Buijs, 1996, *Atomic, Molecular & optical physics handbook*, ed. G.F. Drake, (New York: AIP press), ISBN 1-56396-242-X

F.P. Bundy, H.T. Hall, H.M. Strong, H.M. Strong, R.H. Wentorf Jr., 1955, Nature, **176**, p. 51

F.P. Bundy, 1961, J. Appl. Phys., **32**, p. 483

W.E. Burcham, M. Jobes, 1995, *Nuclear and Particle Physics*, (Longman Scientific & Technical, Essex), ISBN 0-582-45088-8

R.C. Burns, G.J. Davies, 1992, *Properties of natural and synthetic diamond*, ed. J.E. Field, Academic Press, ISBN: 0-12-255352-7

S.J. Bruer, P.R. Briddon, (1996) Phys. Rev. B, **53**, p. 7819

B. Campbell, A. Mainwood, 2000, Phys. Stat Sol. a, **181**, p. 99

B. Campbell, W. Choudhury, A. Mainwood, M. Newton, G. Davies, 2002, Nucl. Instr. and Meth. A, **476**, p. 680

G.R. Carlow, S.Yu. Krylov, M. Zinke-Allmang, 1998, Physica A, **261**, p. 115

K.J. Chang, D.J. Chadi, 1989, Phys. Rev. B, **40**, p. 11644

S.P. Chauhan, J.C. Angus, N.C. Gardner, 1974, J. Vac. Sci. Technol., **11**, p. 423

S.P. Chauhan, J.C. Angus, N.C. Gardner, 1976, J. Appl. Phys., **47**, p. 4746

J.J. Charette, 1961, Physica, **27**, p. 1061

S.J. Charles, J.E. Butler, B.N. Feygelson, M.E. Newton, D.L. Carroll, J.W. Steeds, H. Darwish, C.S. Yan, H.K. Mao, R.J. Hemley, 2004, Phys. Stat. Sol. a, vol. **201**, p. 2473

J. Chevallier, B. Theys, A. Lusson, C. Grattepain, A. Deneuville, E. Gheeraert, 1998 Phys. Rev. B, **58**, 7966

J. Chevallier, F. Jomard, Z. Teukam, S. Koizumi, H. Kanda, Y. Sato, A. Deneuville, M. Bernard, 2002, Diam. Relat. Mater., **11**, p. 1566

R.M. Chrenko, H.M. Strong, R.E. Tuft, 1971, Phil. Mag., **23**, p. 313

R.M. Chrenko, R.E. Strong, H.M. Tuft, 1977, Nature, **270**, p.141

S.G. Clackson, M. Moore, J.C. Wamsley, G.S. Woods, 1990, Phil. Mag. B, **62**, p. 115

C.D. Clark, R.W. Ditchburn, H.B. Dyer, 1956a, Proc. R. Soc. London A, **234**, p. 363

C.D. Clark, R.W. Ditchburn, H.B. Dyer, 1956b, Proc. R. Soc. London A, **237**, p. 75

C.D. Clark, P.J. Dean, P.V. Harris, 1964, Proc. Phys. Soc. Lond. A, **277**, p. 312

C.D Clark, C.A. Norris, 1971, J. Phys. C: Solid State Phys., **4**, p. 2223

C.D Clark , S.T. Davey, 1984, J. Phys. C: Solid State Phys., **17**, p. L399

A.T. Collins, 1978a, J. Phys. C: Solid State Phys., **11**, p. 1957

A.T. Collins, 1978b, J. Phys. C: Solid State Phys., **11**, p. L417

A.T. Collins, 1979, Inst. Phys. Conf. Series, **46**, p. 327

A.T. Collins, S. Rafique, 1979, Proc. R. Soc. Lond A, **367**, p. 81

A.T. Collins, 1980, J. Phys. C: Solid State Phys., **13**, p. 2641

A.T. Collins, 1982, J. Phys. D: Appl. Phys., **15**, p. 1431

A.T. Collins, K. Mohammed, 1982, J. Phys. C: Solid State Phys., **15**, p. 147

A.T. Collins, P.M. Spear, 1982, J. Phys. D: Appl. Phys., **15**, p. L183

A.T. Collins, G.S. Woods, 1982, Phil. Mag. B, **45**, p. 385

A.T. Collins, 1983, J. Phys. C: Solid State Phys., **16**, p. 6691

A.T. Collins, G. Davies, G.S. Woods, 1986, J. Phys. C: Solid State Phys., **19**, p. 3933

A.T. Collins, M. Stanley, G.S. Woods, 1987, J. Phys. D: Appl. Phys., p. 969

A.T. Collins, G. Davies, H. Kanda, G.S. Woods, 1988, J. Phys. C: Solid State Phys., **21**, p. 1363

A.T. Collins, 1998, Diam. Rel. Mater., **7**, p. 1257

A.T. Collins, P.J. Woad, G.S. Woods, H. Kanda, 1993, Diam. Relat. Mater., **2**, p. 136

A.T. Collins, 1999, Diam. Rel. Mater., **8**, p. 1455

A.T. Collins, H. Kanda, H. Kitawaki, 2000, Diam. Rel. Mater, **9**, p. 113

A. T. Collins, 2001. *Proceedings of the Sixth Applied Diamond Conference / Second Frontier Carbon Technology Joint Conference (ADC/FCT 2001)*, eds. Y. Tzeng, K. Miyoshi, M. Yoshikawa, M. Murakawa, Y. Koga, K. Kobashi and G.A.J. Amaratunga, National Aeronautics and Space Administration.

A.T. Collins, A. Dahwich, 2003, J. Phys.: Condens. Matter, p. L591

A.T. Collins, A. Connor, C.-H. Ly, A. Shareef, P.M. Spear, 2005, J. Appl. Phys., **97**, p. 083517

B. Colombeau, N.E.B. Cowern, F. Cristiano, P. Calvo, N. Cherkashin, Y. Lamrani, A. Claverie, Appl. Phys. Lett., 2003, **83**, p. 1953

N.E.B. Cowern, G. Mannino,P.A. Stolk,F. Roozeboom,H.G.A. Huizing,J.G.M. van Berkum, F. Cristiano, A. Claverie, M. Jaraiz, 1999, Phys. Rev. Lett., **82**, p. 4460

A. Cox, M.E. Newton, J.M. Baker, 1992, J. Phys.: Condens. Matter, **3**, p. 8119

M.D. Crossfield, G. Davies, A.T. Collins, E.C. Lightowlers, 1974, J. Phys. C: Solid State Phys., **7**, p. 1909

G. Davies, 1970, J. Phys. C: Solid State Phys., **3**, p. 2474

G. Davies, 1972, J. Phys. C: Solid State Phys., **5**, p. 2534

G. Davies, M. Crossfield, 1973, J. Phys. C: Solid State Phys., **6**, p. L104

G. Davies, 1974a, J. Phys. C: Solid State Phys., **7**, p. 3797

G. Davies, 1974b, Proc. R. Soc. Lond. A, **336**, p. 507

G. Davies, 1976, J. Phys. C: Solid State Phys., **9** p. L537

G. Davies, M.H. Nazaré, M.F. Hamer, 1976, Proc. R. Soc. Lond. A, **351**, p. 241

G. Davies, M.F. Hamer, 1976, Proc. R. Soc. Lond. A, **348**, p. 285

G. Davies, 1977, Nature, **269**, p. 498

G. Davies, M.H. Nazaré, 1979, Proc. R. Soc. Lond. A, **365**, p. 75

G. Davies, C. Foy, 1980, J. Phys. C: Solid State Phys., **13**, p. 2203

G. Davies, 1981a, Rep. Prog. Phys., **44**, p. 787

G. Davies, 1981b, J. Phys. C: Solid State Phys., **14**, p. L391

G. Davies, A.T. Collins, P.M. Spear, 1984, Solid State Commun., **49**, p. 433

G. Davies, S.C. Lawson, A.T. Collins, A. Mainwood, S.J. Sharp, 1992, Phys. Rev. B, **46**, p. 13157

G. Davies, I. Kiflawi, G. Sittas, H. Kanda, 1997, J. Phys.: Condens. Matter, **9**, p. 3871

G. Davies, 1999, Physica B, **273-274**, p. 15

G. Davies, H.E. Smith, H. Kanda, 2000, Phys. Rev. B, **62**, p. 1528

G. Davies, B. Campbell, A. Mainwood, M.E. Newton, M. Watkins, H. Kanda, T.R. Anthony, 2001, Phys. Stat. Sol. a, **186**, p. 187

P.G. Dawber, R.J. Elliot, 1963, Proc. R. Soc. A, **273**, p. 222

D. L. Decker, W. A. Bassett, L. Merrill, H. T. Hall, J. D. Barnett, 1972, J. Phys. Chem. Ref. Data, **1**, p 1

P. Denham, E.C. Lightowlers, P.J. Dean, 1967, Phys. Rev., **161**, p. 762

C.S. Deo, D.J. Srolovitz, W. Cai, V.V. Bulatov, 2005, Phys. Rev. B, **71**, art. nr. 014106

F. De Weerdt, J. Van Royen, 2000, J.Gemm., **27**, p. 201

F. De Weerdt, 2001. *Proceedings of the Sixth Applied Diamond Conference / Second Frontier Carbon Technology Joint Conference (ADC/FCT 2001)*, eds. Y. Tzeng, K. Miyoshi, M. Yoshikawa, M. Murakawa, Y. Koga, K. Kobashi and G. A. J. Amaratunga, National Aeronautics and Space Administration.

F. De Weerdt, J. Van Royen, 2001, Diam. Rel. Mater, **10**, p. 474

F. De Weerdt, I. Kupriyanov, 2002, Diam. Rel. Mat., **11**, 714

F. De Weerdt, A.T. Collins, 2003, Diam. Rel. Mater, **12**, p. 507

F. De Weerdt, A. Anthonis, 2004, Diamond Conf. (unpublished abstracts)

F. De Weerdt, R. Galloway, A. Anthonis, 2004, Defect and Diffusion Forum (Annual Retrospective - Ceramics VI), **226-228**, p. 49

F. De Weerdt, A. T. Collins, M. Zugik, A. Conner, 2005, J. Phys.: Condens. Matter, **17**, p. 8005

T.E. Derry, R.W. Fearick, J.P.F Sellschop, 1982, Phys. Rev. B, **26**, p. 17

H.B. Dyer, F.A. Raal, L. du Preez, J.H.N. Loubser, 1965a, Phil. Mag., **11**, p. 763

H.B. Dyer, L. du Preez, 1965b, J. Chem. Phys., **42**, p. 1898

H.B. Dyer, P. Ferdinando, 1966, Brit. J. Appl. Phys., **17**, p. 419

E. Elliot, 1966, *Phonons in perfect lattices and in lattices with point imperfections*, edited by R.W.H. Stevenson, Oliver & Boyd, Edinburgh

T. Evans, C. Phaal, 1962, Proc. R. Soc. Lond., **270**, p. 538

T. Evans, P. Rainey, 1975, Proc. R. Soc. Lond. A, **344**, p. 111

T. Evans, Z. Qi, 1982, Proc. R. Soc. Lond. A, **381**, p. 159

T. Evans, I. Kiflawi, W. Luyten, G. Van Tendeloo, G.S. Woods, 1995, Proc. R. Soc. London A, **449**, p. 295

R.G. Farrer, L.A. Vermeulen, 1972, J. Phys. C: Solid State Phys., **5**, p. 2762

J. Field, 1992, *Properties of natural and synthetic diamond*, ed. J.E. Field, Academic Press, ISBN: 0-12-255352-7

B. Fortner, (1996), SciTech Journal, **6**, p32

E. Fritsch, K. Scarratt, A.T. Collins, 1991, *New Diamond Science and Technology - Proc. Second Int. Conf. on the New Diamond Sci. and Tech.*, eds. R. Messier, J.T. Glass, J.E. Butler and Rustum Roy, 1991, Materials Research Society, Pittsburgh, PA, pp. 671

M. Furusawa, M. Ikeya, 1990, J. Phys. Soc. Japan, **59**, p. 2340

E. Gaillou, E. Fritsch, F. Notari, 2005, Diamond 2005 conf., Diam. Rel. Mater, to be published.

S. Gierlotka, B. Palosz, A. Grzegorczyk, P. Biczyk, R. Pielaszek, E. Grzanka, Hasylab Annual Report 1999

W. Greiner, L. Neise, H. Stöcker, *Thermodynamics and statistical mechanics*, 1995, Springer-Verlag, New York, ISBN 3-540-94299-8

C. Glover, M. Newton, P. Martineau, D. Twitchen, J. Baker, 2003, Phys. Rev. Lett., **90**, p. 185507

J.P. Goss, B.J. Coomer, R. Jones, C.J. Fall, P.R. Briddon, S. Öberg, 2003, Phys. Rev. B, **67**, p. 165208

J.P. Goss, 2003, J. Phys.: Cond. Matter, **15**, p. R551

J.P. Goss, P.R. Briddon, R. Jones, S. Sque, 2003, J. Phys.: Cond. Matter, **15**, P. S2903

J.P. Goss, M.J. Rayson, P.R. Briddon, J.M. Baker, SBDD XI conference, personal communication.

A.M. Gusak, G.V. Lutsenko, K.N. Tu, 2006, Acta Mater. **54**, p. 785

R.N. Hall, 1952, Phys. Rev., **87**, p. 387

F.S. Ham, 1965, Phys. Rev., **138**, p. 1727

P.L. Hanley, I. Kiflawi, A.R. Lang, 1977, Phil. Trans. R. Soc. A, **284**, p. 329

K.C. Hass, M.A. Tamor, T.R. Anthony, W.F. Banholzer, 1992, Phys. Rev. B, **45**, p. 7171

M.I. Heggie, S. Jenkins, C.P. Ewels, P. Jemmer, R. Jones, P.R. Briddon, 2000, J. Phys.: Condens. Matter, **12**, p. 10263

M.I. Heggie, C.P. Ewels, N. Martsinovich, S. Scarle ,R. Jones, J.P. Goss, B. Hourahine, P.R. Briddon, 2002, J. Phys.: Cond. Matter, **14**, p. 12689

J.P. Hirth, J. Lothe, 1982, *Theory of dislocations*, (New York: Wiley), p. 531

P.B. Hirsch, P. Pirouz, J.C. Barry, 1986, Proc. R. Soc. Lond. A, **407**, p. 239

L.S. Hounsome, R. Jones, P.M. Martineau, M.J. Shaw, P.R. Briddon, S. Öberg, A.T. Blumenau, N. Fujita, 2005a, Phys. Stat. Sol. a, **202**, p. 2182

L.S. Hounsome, R. Jones, P.M. Martineau, D. Fisher, M.J. Shaw, P.R. Briddon, S. Öberg, 2005b, Diamond conference, Unpublished abstracts

P.R.W. Hudson, I.S.T. Tsong, 1977, J. Mat. Science, **12**, p. 2389

F.J. Humphreys, M. Hatherly, 1996, *Recrystallization and related annealing phenomena*, Pergamon Press, ISBN 0080418848

K. Iakoubovskii, G.J. Adriaenssens, M. Nesladek, 2000, J. Phys.: Condens. Matter, **12**, p. 189

K. Iakoubovskii, G. J. Adriaenssens, N. N. Dogadkin, A. A. Shiryaev, 2001, Diam. Rel. Mater., **10**, p. 18.

K. Iakoubovskii, I. Kiflawi, K. Johnston, A.T. Collins, G. Davies, A. Stesmans, 2003, Physica B, **340-342**, p 67

K. Iakoubovskii, S. Dannefaer, A. Stesmans, 2005, Phys. Rev. B, **71**, 233201

J. Isoya, H. Kanda, J.R. Norris, J. Tang, M.K. Bowman, 1990, Phys. Rev. B, **42**, p. 9843.

H.A. Jahn, E. Teller, 1934, Proc. R. Soc. Lond. A, **161**, p. 220

R.N. Jeffery, J.D. Barnett, H.B. Vanfleet, H.T. Hall, 1966, J. Appl. Phys., **37**, p. 3172

R. Jones, P.R. Briddon, S. Öberg, 1992, Phil. Mag. Letters, **66**, p. 67

R. Jones, V.J.B. Torres, P.R. Briddon, S. Öberg, 1994, Mater. Scie. Forum, **143-147**, p. 45

R. Jones, 1995, Phil. Trans. R. Soc. Lond. A, **350**, p. 189

H. Kanda, 1994, ICNDST-4 proceedings, p. 507

H. Kanda, A. Ahmadjan, H. Kitawaki, 2005, Diam. Rel. Mater., **14**, p. 1928

H. Kanda, K. Watanabe, 2004, Diam. Rel. Mater., **13**, p. 904

K. Kaneko, A.R. Lang, 1993, Ind. Diam. Rev., **6**, p. 334

M. Kasha, 1950, Discuss. Faraday Soc., **9**, p. 14

W. Kaiser, W.L. Bond, 1959, Phys. Rev., **115**, p. 857

J. Kulda, B. Darner, B. Roessli, H. Sterner, R. Bauer, Th. May, K. Karch, P. Pavone, D. Strauch, 1996, Solid State Comm., **99**, p. 799

J. Kulda, H. Kainzmaier, D. Strauch, B. Dorner, M. Lorenzen, M. Krisch, 2002, Phys. Rev. B, **66**, art. nr. 241202

I. Kiflawi, A.R. Lang, 1976, Phil. Mag., **33**, p. 679

I. Kiflawi, A.E. Mayer, P.M. Spear, J.A. van Wyk, G.S. Woods, 1994, Phil. Mag. B, **69**, p. 1141

I. Kiflawi, G. Sittas, D. Fisher, H. Kanda, 1996, Diam. Rel. Mater., **5**, p. 1516

I. Kiflawi, H. Kanda, D. Fisher, S.C. Lawson, 1997, Diam. Rel. Mater., **6**, p. 1643

I. Kiflawi, H. Kanda, A. Mainwood, 1998, Diam. Rel. Mater., **7**, p. 327

I. Kiflawi, G. Davies, D. Fisher, H. Kanda, 1999, Diam. Rel. Mater, **8**, p. 1576

I. Kiflawi, J. Bruley, 2000, Diam. Rel. Mater., **9**, p. 87

I. Kiflawi, 2001, *Properties, growth and applications of diamond*, ed. M.H. Nazaré, A.J. Neves, INSPEC London, ISBN 0-85296-785-3

I. Kiflawi, A.T. Collins, G. Davies, D. Fisher, K. Iakoubovskii, 2005, Diamond Conf., (unpublished abstracts)

J.K. Kiriu, J.A. Van Wyk, M.J.R. Hoch, 1999, Diam. Rel. Mater., **8**, p. 1569

M. Kizilyalli, J. Corish, R.Metselaar, 1999, Pure Appl. Chem., **71**, p. 1307

R. Krause-Rehberg, M. Brohl, H. S. Leipner, Th. Drost, A. Polity, and U. Beyer, H. Alexander, (1993), Phys. Rev. B, **47**, p. 13266

I.N. Kupriyanov, V.A. Gusev, Yu. N. Pal'yanov, Yu. M. Borzdov, 2000, J. Phys.: Condens. Matter, **12**, p. 7843

H. Kuzmany, 1998, *Solid State Spectroscopy, An Introduction*, (Berlin: Springer-Verlag), ISBN 540-63913-6

A.R. Lang, 1967, Nature, **213**, p. 248

A.R. Lang, M. Moore, A.P.W. Makepeace, W. Wierzchowski, C.M. Welbourn, 1991, Phil. Trans.: Phys. Scien. Eng., **337**, p. 497

A.R. Lang, G. Pang, 1998, Phil. Trans.: Phys. Scien. Eng., **356**, p. 1397

A.R. Lang, A.P. Yelisseyev, N.P. Pokhilenko, J.W. Steeds, A. Wotherspoon, 2004, J. Cryst. Growth, **263**, p. 575

D.V. Lang, 1982, Ann. Rev. Mater. Sci., **12**, p. 377

M. Lannoo, J. Bourgoin 1983 *Point defects in Semiconductors II: Experimental Aspects*, (NY: Springer-Verlag), ISBN 0387115153

S.C. Lawson, G. Davies, A.T. Collins, A. Mainwood, 1992a, J. Phys.: Condens. Matter, **4**, p. 3439

S.C. Lawson, G. Davies, A.T. Collins, A. Mainwood, 1992b, J. Phys.: Cond. Matter, **4**, p. L125

S.C. Lawson, D. Fisher, D.C. Hunt, M.E. Newton, 1998, J. Phys.: Cond. Matter, **10**, p. 6171

M. Lax, E. Burstein, 1955, Phys. Rev., **97**, p. 39

H.S. Leipner, C.G. Hübner, T.E.M. Staab, M. Haugk, A Sieck, R. Krause-Rehberg, T. Frauenheim, 2000, J. Phys.: Condens. Matter, **12**, p.10071

I.M. Lifshitz, V.V. Slyozov, 1961, J. Phys. Chem. Solids, **19**, p. 35

E.C. Lightowlers, A.T. Collins, 1976, J. Phys. D: Appl. Phys., **9**, p. 951

H. Liander, 1953, ASEA Journal, **28**, p. 97

C. A. Londos, M. S. Potsidi, J. Bak-Misiuk, A. Misiuk, V. V. Emtsev, 2003, Cryst. Res. Technol., **38**, p. 1058

H.C. Longuet-Higgens, U. Opik, M.H.L. Pryce, R.A. Sack, 1958, Proc. R. Soc. London A, **244**, p. 1

J.H.N. Loubser, W.P. van Ryneveld, 1967, Brit. J. Appl. Phys., **18**, p 1029

J.H.N. Loubser, J.A. van Wyk, 1978, Rep. Prog. Phys., **41**, p. 1201

R. Loudon, 1964, Proc. Phys., **84**, p. 379

J.E. Lowther, 1978, J. Phys. C: Solid State Phys., **11**, p. 373

R. Luchsinger, P.F. Meier, N. Paschedag, H.U. Suter, Yu. Zhou, 1995, Phil. Trans. R. Soc. Lond. A, **350**, p. 203

W. Luyten, 1994, PhD thesis, University of Antwerp

G. Madras, B.J. McCoy, 2003, Chem. Eng. Science, **58**, p. 2903

G. Madras, B.J. McCoy, 2004, Chem. Eng. Science, **59**, p. 2753

H.K. Mao, P.M. Bell, 1978, Science, **200**, p. 1145

A. Mainwood, 1994, Phys. Rev. B, **49**, p. 7934

J.-M. Mäki, V. Ranki, K. Saarinen, P. Martineau, D. Fisher, 2005, Diamond conf., (unpublished abstracts)

S.P. Marsh, M.E. Glicksman, 1997, Mat. Scie. Eng., **A238**, p. 140

N. Martsinovich, M.I. Heggie, C.P. Ewels, 2003, J. Phys.: Cond. Matter, **15**, p. S2815

W.A. McKinley, H. Feshbach, 1948, Phys. Rev., **74**, p. 1759

M.J. Mendelssohn, H.J. Milledge, P.A. Woods, M. Seal, S.R. Boyd, D.P. Mattey, C.T. Pillinger, 1986, *Diamond Conference*, Royal Holloway and Bedford New College (unpublished abstracts).

Y. Mita, Y. Nisida, K. Suito, A. Onodera, S. Yazu, 1990, Phys.: Condens. Matter, **2**, p. 8567

Y. Mita, 1993, Phys. Rev. B, **53**, p. 11360

N.F. Mott, 1929, Proc. R. Soc. Lond. A, **124**, p. 426

N.F. Mott, 1932, Proc. R. Soc. Lond. A, **135**, p. 429

N.F. Mott, 1951, Proc. Phys. Soc., **64**, p. 729

V.A. Nadolinny, A.P. Yelisseyev, J.M. Baker, M.E. Newton, D.J. Twitchen, S.C. Lawson, O.P. Yuryeva, B.N. Feigelson, 1999, J. Phys. Cond. Matter, **11**, p. 7357

Y. Nagai, K. Inoue, Z. Tang, I. Yonenaga, T. Chiba, M. Saito, M. Hasegawa, 2003, Physica B, **340-342**, p. 518

M.H. Nazaré, M.I.B. Jorge, M.F. Thomaz, 1985a, J. Phys. C: Solid State Phys., 18, p. 2371

M.H. Nazaré, M.I.B. Jorge, M.F. Thomaz, 1985b, Solid State Comm., 55, p. 577

E. Nes, 1995, Acta metall. mater., **43**, p. 2189

R.C. Newman, 1995, Phil. Trans. R. Soc. Lond. A, **350**, p. 215

M.E. Newton, J.M. Baker, 1992a, J. Phys.: Condens. Matter, **9**, p. 3591

M.E. Newton, J.M. Baker, 1992b, J. Phys.: Condens. Matter **9**, p. 3605

M.E. Newton, 1994, *Properties and growth of diamond*, (London: INSPEC), ed. G. Davies, ISBN: 0-85296-875-2

M.E. Newton, B.A. Campbell, D.J. Twitchen, J.M. Baker, T.R. Anthony, 2002, Diam. Rel. Mater, **11**, p. 618

M.E. Newton, 2005b, Diamond Conference (Unpublished abstracts)

M. Newton, ADC 2005 conference proceedings, Argonne Nat. Lab., to be published

M. Newton, 2006, personal communication.

C.J. Noble, Th. Pawlik, J.-M. Spaeth, 1998, J. Phys.: Condens. Matter, **10**, p.11781.

U. Opik, M.H.L. Pryce, 1957, Proc. R. Soc. London A, **238**, p. 425

S. Olive, U. Grafe, I. Steinbach, 1996, Comp. Mat. Science, **7**, p. 94

Yu. N. Pal'yanov, A.F. Khokhryakov, Yu. M. Borzdov, A.G. Sokol, V.A. Gusev, G.M. Rydov, N.V. Sobolev, 1997, Geol. Geofiz. **38**, p. 882

P. Pavone, K. Karch, O. Schütt, W. Windl, D. Strauch, P. Giannozzi, S. Baroni, 1993, Phys. Rev. B, **48**, p. 3156

W. Paszkowicz, W. Szuszkiewicz, E. Dynowska, J.Z. Domagala, C. Lathe, Hasylab Annual Report 2000

E. Pereira, M.I.B. Jorge, 1987, Solid State Comm., 61, p. 75

V.I. Petrov, 1996, Physics – Uspekhi, **39**, p. 807

A. Porter, K.E. Easterling, 1992, *Phase transformations in Metals and Alloys* , CRC press, ISBN 0-7487-5741-4

J.F. Prins, 2001, Diam. Rel. Mater., **10**, p. 87

A. Pu, V. Avalos, S. Dannefaer, 2001, Diam. Rel. Mater, **10**, p. 585

Rapaport, 1999, News Flash, 19 March 1999, p. 6

J. Robertson, J.J. Fox, A.E. Martin, 1934, Phil. Trans. R. Soc., A, **232**, p. 463

P. Rudolph, 2005, Cryst. Res. Technol., **40**, p. 7

T. Ruf, M. Cardona, H. Sternshulte, S. Wahl, K. Thonke, R. Sauer, P. Pavone, T.R. Anthony, 1998, Solid State Commun., **105**, p. 311

W.A. Runciman, T. Carter, 1971, Solid State Commun., **9**, p. 315

P. Saarinen, J. Kauppinnen, 1992, Appl. Optics, **31**, p. 2353

A. Shareef, A.T. Collins, 2003, Diamond conf., (unpublished abstracts)

A.A. Shirayev, M.T. Hutchison, K.A. Dembo, A.T. Dembo, K. Iakoubovskii, Yu.A. Klyuev, A.M. Naletov, (2001), Physica B, p. 598

W. Shockely, W.T. Read, (1952), Phys. Rev., **87**, p. 835

J.P.F. Sellschop, 1992, *The properties of natural and synthetic diamond*, edited by J.E. Field, Academic Press, New York, p. 81

P.K. Sitch, R. Jones, S. Öberg, M.I. Heggie, 1997, J. Physique III, **7**, p. 1381

H.E. Smith, G. Davies, M.E. Newton, H. Kanda, (2004), Phys. Rev. B, **69**, p. 045203

W.V. Smith, P.P. Sorokin, I.L. Gelles, G.J. Lasher, 1959, Phys. Rev., **115**, p. 1546

C.P. Smith, G. Bosshart, J. Ponahlo, V.M.F. Hammer, H. Klapper, K. Schmetzer, 2000, Gems & Gemol., **36**, p. 192

J.-M. Spaeth, J.R. Niklas, R.H. Bartram, 1992, *Structural analysis of point defects in solids, An Introduction to Multiple Magnetic Resonance Spectroscopy*, Springer-Verlag: Berlin, ISBN 3-540-53615-9

J.W. Steeds, T.J. Davis, S.J. Charles, J.M. Hayes, J.E. Butler, 1999, Diam. Rel. Mater., **8**, p. 1847

H. Sumiya, S. Satoh, 1996, Diam. Rel. Mater, **5**, p. 1359

H. Sumiya, N. Toda, S. Satoh, 2005, SEI tech. review, **60**, p. 1

H. Sumiya, Diam. Relat. Mater., to be published.

R.J. Sweeney, V.M. Prozesky, K.S. Viljoen, S. Conell, 1999, NIMB, **158**, p. 587

T. Templeman, 2000, Rapaport diamond report, **23**, p. 29

M.F. Thomaz, G. Davies, 1978, Proc. R. Soc. London A, **362**, p. 405

D.J. Twitchen, M.E. Newton, J.M. Baker, T.R. Anthony, W.F. Banholzer, 2001, J. Phys.: Condens. Matter, **13**, p. 2045

C. Uzan-Saguy, A. Reznik, C. Cytermann, R. Brener, R. Kalish, E. Bustarret, M. Bernard, A. Deneuville, E. Gheeraert, J. Chevallier, 2001, Diam. Relat. Mater., **10**, p. 453

R.C. Weast, 1989, *CRC Handbook of Chemistry and Physics, 69th ed.*, CRC Press Inc., ISBN 0-8493-0469-5

J.A. van Wyk, E.C. Reynhardt, G.L. High, I. Kiflawi, 1997, J. Phys. D: Appl. Phys., **30**, p. 1790

J.A. van Wyk, 1982, J. Phys. C: Solid State Phys., **15**, p. L981

J.A. van Wyk, J.H.N. Loubser, 1993, J. Phys. C: Solid State Phys., **5**, p. 3019

J.A. van Wyk, E.C. Reynhardt, G.L. High, I. Kiflawi, 1997, J. Phys. D: Appl. Phys., **30**, p.1790

I.I. Vlasov, V.G. Ralchenko, V.I. Konov, 2001, Phys. Stat. Sol. a, **186**, p. 221

I.I. Vlasov, V.G. Ralchenko, E. Goovaerts, 2002, Phys. Stat. Sol. a, **193**, p. 489

R. Vogelgesang, A.K. Ramdas, S. Rodriguez, M. Grimsditch, T.R. Anthony, 1996 Phys. Rev. B, **54** p. 3989

W. Wang, M. Hall, T. Moses, J. Shigley, 2006, Diamond Conf. (unpublished abstracts)

C. Wagner, 1961, Z. Elektrochem., **65**, p. 581

J. Walker, 1979, Rep. Prog. Phys., **42**, p. 1607

D.J. Weidner, Y. Wang, M.T. Vaughan, 1994, Science, **266**, p. 419

C.M. Welbourn, 1978, Solid State Comm., **26**, p. 255.

B. Willems, R. Barnes, U. Bangert, J. Van Royen, G. Bertoni, J. Verbeeck, P.M. Martineau, D. Fisher, G. Van Tendeloo, 2006, SBDD-XI presentation.

W. Windl, P. Pavone, K. Karch, O. Schütt, D. Strauch, 1993, Phys. Rev. B, **48**, p.3164

G.S. Woods, A.T. Collins, 1983, J. Phys. Chem. Solids, **44**, p. 471

G.S. Woods, 1986, Proc. R. Soc. London A, **407**, p.219

G.S. Woods, 1989, Phil. Mag. A, **59**, p. 339

G.S. Woods, J.A. van Wyk, A.T. Collins, 1990, Phil. Mag. B, **62**, p. 589

G.S. Woods, G.C. Purser, A.S.S. Mtikulu, A.T. Collins, 1990, J. Phys. Chem. Solids, **51**, p. 1191

Y. Yamashita, F. Jyobe, Y. Kamiura, K. Maede, 1999, Phys. Stat. Sol. a, **171**, p. 27

P.Y. Yu, M. Cardona, 2003, *Fundamentals of semi-conductors, Physics and Materials properties*, Springer-Verlag, Berlin, ISBN 3-540-41323-5, p. 183

R. Zeisel, C.E. Nebel, M. Stutzmann, 1999, Appl. Phys. Lett., **74**, p. 1875

A. M. Zaitsev 2001, *Optical properties of diamond*, ISBN : 3-540-66582-x

S. Zhang, S.C.Ke, M.E. Zvanut, H.T. Tohver, Y.K. Vohra, 1994, Phys. Rev. B, **49**, p. 15493

X. Zhou, G. Watkins, K.M. McNamara-Rutledge, R.P. Messmer, S. Chawla, 1996, Phys. Rev. B, **54**, p. 7881